

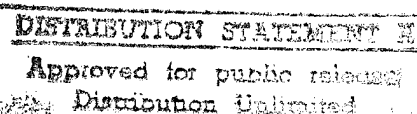
MASSACHUSETTS INSTITUTE OF TECHNOLOGY

The RESEARCH LABORATORY *of* ELECTRONICS

PROGRESS REPORT

NO. 137

JANUARY 1-DECEMBER 31, 1994



19950703 240

REPORT DOCUMENTATION PAGE

Form Approved
OMB No. 0704-0188

Public reporting burden for this collection of information is estimated to average 1 hour per response, including the time for reviewing instructions, searching existing data sources, gathering and maintaining the data needed, and completing and reviewing the collection of information. Send comments regarding this burden estimate or any other aspect of this collection of information, including suggestions for reducing this burden, to Washington Headquarters Services, Directorate for Information Operations and Reports, 1215 Jefferson Davis Highway, Suite 1204, Arlington, VA 22202-4302, and to the Office of Management and Budget, Paperwork Reduction Project (0704-0188), Washington, DC 20503.

1. AGENCY USE ONLY (Leave blank)	2. REPORT DATE	3. REPORT TYPE AND DATES COVERED	
	June 95	Technical Report 1 Jan-Dec 31, 94	
4. TITLE AND SUBTITLE		5. FUNDING NUMBERS	
The Research Laboratory of Electronics Progress Report No. 137		DAAL03-92-C-0001	
6. AUTHOR(S)			
Jonathan Allen Daniel Kleppner			
7. PERFORMING ORGANIZATION NAME(S) AND ADDRESS(ES)		8. PERFORMING ORGANIZATION REPORT NUMBER	
Massachusetts Institute of Technology Cambridge, MA 02139-4307			
9. SPONSORING/MONITORING AGENCY NAME(S) AND ADDRESS(ES)		10. SPONSORING/MONITORING AGENCY REPORT NUMBER	
U.S. Army Research Office P.O. Box 12211 Research Triangle Park, NC 27709-2211		ARO 28925.180-EL-JSEP	
11. SUPPLEMENTARY NOTES The views, opinions and/or findings contained in this report are those of the author(s) and should not be construed as an official Department of the Army position, policy, or decision, unless so designated by other documentation.			
12a. DISTRIBUTION/AVAILABILITY STATEMENT		12b. DISTRIBUTION CODE	
Approved for public release; distribution unlimited.			
13. ABSTRACT RLE Progress Report Number 137 describes research programs at RLE for the period January 1 through December 31, 1994. Each chapter of the Progress Report includes a summary of research efforts for research projects listed. Faculty, research staff, students and others who participated in these projects are identified at the beginning of each project, along with sources of funding. There are four appendices at the end of the report: Appendix A is a bibliography of RLE publications and papers presented by RLE staff during 1994; Appendix B is a roster of current RLE staff; Appendix C is a list of RLE faculty and staff milestones and honors received during 1994; and Appendix D is an index of RLE sponsors. The Project Staff and Subject Index provides additional access to the information in this report.			
14. SUBJECT TERMS		15. NUMBER OF PAGES	
		16. PRICE CODE	
17. SECURITY CLASSIFICATION OF REPORT UNCLASSIFIED		18. SECURITY CLASSIFICATION OF THIS PAGE UNCLASSIFIED	
19. SECURITY CLASSIFICATION OF ABSTRACT UNCLASSIFIED		20. LIMITATION OF ABSTRACT UL	

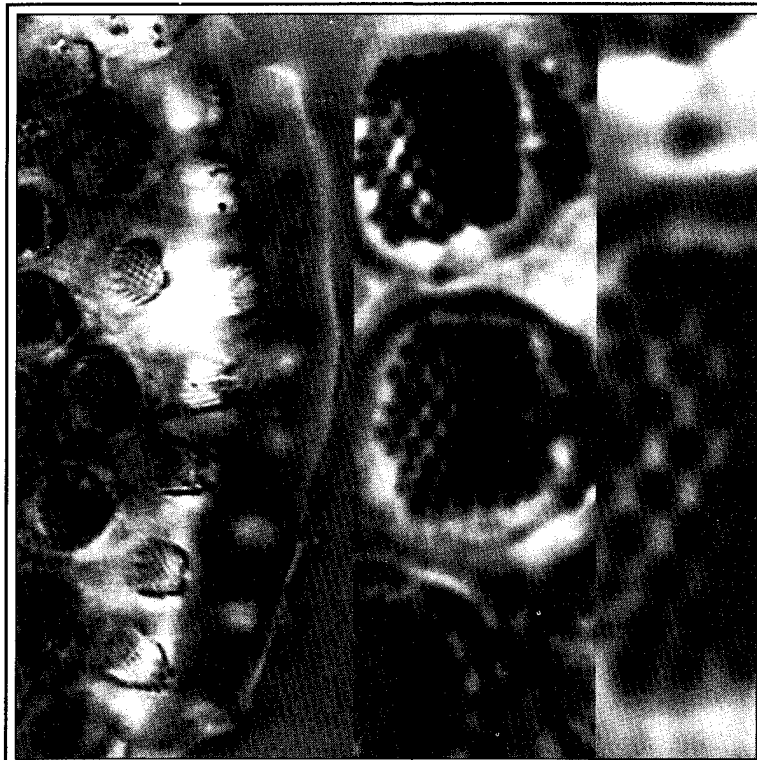
RLE Progress Report

No. 137

January 1 - December 31, 1994

Submitted by

Professor Jonathan Allen
Professor Daniel Kleppner



Accesion For	
NTIS	CRA&I
DTIC	TAB
Unannounced	
Justification _____	
By _____	
Distribution / _____	
Availability Codes	
Dist	Avail and / or Special
A-1	

The RESEARCH LABORATORY of ELECTRONICS

MASSACHUSETTS INSTITUTE of TECHNOLOGY

CAMBRIDGE, MASSACHUSETTS 02139-4307

RLE Progress Report Number 137

Cover and title page: Zooming in on Hearing

Microscopic mechanics of single sensory receptor cells play an important signal processing role in the inner ear. However, there are few direct measurements—in large part because the measurements are technically challenging. The important structures are small (micrometer scale) and the motions are even smaller as well as fast (20 Hz to 20 kHz).

Recently, members of RLE's Auditory Physiology Group have developed a video microscopic system in which stroboscopic illumination is used to take stop-action images of sound-induced motions of inner ear structures. Motions as small as 14 nm are determined directly from video images using a new algorithm based on optical flow techniques that are commonly used in machine vision.

The system has been applied to characterize inner ear motions at three levels of organization, illustrated on the cover. The left panel shows a cluster of approximately 25 sensory cells and associated structures. The center panel shows a magnified view of three of the cells. Each cell (8 micrometer diameter) contains a bundle of approximately 50 sensory hairs (0.7 micrometer diameter). The right panel shows a magnified view of the sensory hairs of a single cell. Analysis of images at these three different levels provides information about the coding of sounds at a systems level, at a cellular level, and at a level that provides insight into the molecular mechanisms of transduction.

These photomicrographs were taken by C. Quentin Davis, a graduate student in the Department of Electrical Engineering and Computer Science and in the Medical Engineering/Medical Physics (MEMP) program in Health Sciences Technology, and by Dr. Dennis M. Freeman, research scientist in RLE. More information and slow-motion video sequences of these structures are available through the Cochlear Physiology home page on the World Wide Web (<http://behn.mit.edu>). For background information on the work of the Auditory Physiology Group, write the RLE Communications Group for a copy of *RLE currents* (volume 3, number 1, Fall 1989).

Our special thanks to the following staff members of the RLE Communications Group: Mary J. Ziegler for her exceptional organizational skills, editing, and graphics scanning and processing; Michelle M. Scheer for her excellent formatting and technical typing; Rita C. McKinnon for proofreading, and Andrew Beharrie for formatting. We also want to thank David W. Foss, Manager of the RLE Computer Facility, for his time and invaluable technical assistance, and Mary S. Greene for inputting information for the publications chapter.

We thank the faculty, staff, and students of RLE for their generous cooperation.

Editor:	Barbara Passero
Associate Editor:	Mary J. Ziegler
Design and photography:	John F. Cook
Printer:	ZBR Publications, Wilmington, Massachusetts
Typesetting:	This report was produced with IBM's BookMaster Software.

Table of Contents

The Research Laboratory of Electronics	1
PART I Solid State Physics, Electronics and Optics	
Section 1 Materials and Fabrication	
Chapter 1 Heterostructures for High-Performance Devices	7
<i>Professor Clifton J. Fonstad, Jr.</i>	
• 1.1 Introduction	7
• 1.2 High-Temperature Stability of GaAs Integrated Circuits	7
• 1.3 High Peak-to-Valley Current Ratio Resonant-Tunneling Diodes on GaAs Substrates	8
• 1.4 Monolithic Integration of Resonant-Tunneling Diodes on GaAs Integrated Circuits	9
1.5 Phosphide-Based Optical Emitters for Monolithic Integration with GaAs MESFETs	10
1.6 Monolithic Integration of LEDs and VLSI GaAs MESFET Circuits	12
1.7 Development of an Epi-on-Electronics OEIC Technology	13
1.8 Integrated Optics Circuits Based on Commercial GaAs Integrated Circuits	15
1.9 Growth of Distributed Bragg Reflector and Multiple Quantum Well Heterostructures at Reduced Temperature	17
1.10 Reactive Ion Etching of InGaAlAs and InGaAsP Heterostructures	18
1.11 Tunable Semiconductor Lasers	19
1.12 Application of the Spectral Index Method to Laser Diode Design	21
1.13 Normal Incidence Quantum Well Infrared Photodetector	22
1.14 Fourteen-Band $k \cdot p$ Analysis of Intersubband Transitions in Conduction Band Quantum Wells	24
1.15 Study of Intersubband Transitions in Ultra-Narrow Quantum Wells	25
1.16 In-plane and Tilted Field Magneto-Tunneling Spectroscopy in Double InGaAs/InAlAs Quantum Well Structures on [001] and [111]B InP Substrates	25
1.17 High-Frequency/High-Speed Characterization of Optoelectronic Devices and Integrated Circuits	26
1.18 In-Situ Supersonic Beam Etching of III-V Heterostructures	27
1.19 Publications	27
Chapter 2 Physics of InAlAs/InGaAs Heterostructure Field-Effect Transistors	29
<i>Professor Jesús A. del Alamo</i>	
• 2.1 Introduction	29
• 2.2 An Integratable S-passivation Process for the InAlAs/InGaAs System	30
• 2.3 S-passivated InAlAs/InGaAs MODFETs	30
• 2.4 Publications	33
Chapter 3 Gas Source Molecular Beam Epitaxy of Compound Semiconductors	35
<i>Professor Leslie A. Kolodziejski</i>	
• 3.1 Introduction	35
• 3.2 Gas Source Molecular Beam Epitaxy of ZnSe, ZnSe:Cl and ZnSe:N	36
3.3 Novel Epitaxial III-V Buffer Layers for Wide Bandgap II-VI Visible Sources	40
• 3.4 Heterovalent Interfaces Composed of II-VI/III-V Semiconductors	42

Table of Contents

3.5	(In,Ga)(As,P)/InP Semiconductor Waveguide Design for Synchronously Side-Coupled Bragg Resonators	43
3.6	Phosphide-Based Optical Emitters for Monolithic Integration with GaAs MESFETs	46
3.7	Photonic Bandgap Structures	47
• 3.8	Heteroepitaxy of GaAs onto Corrugated Surfaces of Si	49
Section 2 Quantum-Effect Devices		
Chapter 1	Statistical Mechanics of Quantum Dots	53
<i>Professor Boris L. Altshuler</i>		
• 1.1	Project Description	53
• 1.2	Publications	54
Chapter 2	Artificial Atoms	55
<i>Professor Marc A. Kastner</i>		
• 2.1	Goals and Objectives	55
• 2.2	Quantization of Energy and Charge	56
• 2.3	Spectroscopy of Artificial Atoms: the Three Energy Scales	57
• 2.4	Criterion for Single-Electron Effects	59
• 2.5	Crossover from Single to Multilevel Transport	61
• 2.6	Ground State of the Artificial Atom in Strong Magnetic Fields	62
• 2.7	Development of Process for Si Single Electron Transistors	65
• 2.8	Publications	66
Chapter 3	Coulomb Blockade in a Quantum Dot	67
<i>Professor Patrick A. Lee</i>		
• 3.1	Project Description	67
• 3.2	Publications	68
Chapter 4	Superconducting and Quantum-Effect Devices	69
<i>Professor Terry P. Orlando</i>		
4.1	Simulations of Vortices in Arrays of Josephson Junctions	69
4.2	Superconducting Transmission Lines	70
4.3	Discrete Superconducting Vortex Flow Transistors	70
4.4	Fiske Modes in One-Dimensional Parallel Josephson-junction Arrays	71
4.5	Novel Mesoscopic Superconducting Devices	71
4.6	Single Charging Effects and Tunneling in Quantum Dot Nanostructures	72
4.7	One-dimensional Parallel Josephson-junction Arrays as a Tool for Diagnostics	72
4.8	Nonlinear Dynamics of Discrete Josephson Rings	72
4.9	Discrete Underdamped Vortex Flow Devices	73
4.10	Publications	73
Chapter 5	Nanostructures Technology, Research, and Applications	75
<i>Professor Henry I. Smith</i>		
• 5.1	NanoStructures Laboratory	75
• 5.2	Scanning Electron Beam Lithography	75
• 5.3	Spatial-Phase-Locked Electron-Beam Lithography	76
• 5.4	X-Ray Nanolithography	77
• 5.5	Improved Mask Technology for X-Ray Lithography	78
• 5.6	A High-Precision Mask Alignment System	81

• 5.7	Interferometric Lithography	83
• 5.8	Ion-Beam Lithography	85
• 5.9	High-Performance Self-aligned Sub-100 nm MOSFETs Using X-ray Lithography	85
5.10	Fabrication of T-gate Devices using X-ray Lithography	89
• 5.11	Studies of Coulomb Charging Effects and Tunneling in Semiconductor Nanostructures	90
• 5.12	Superconductor/Semiconductor Interface of V ₃ Si and Si	92
• 5.13	Laterally-Coupled Distributed-Feedback Lasers Fabricated by X-Ray Lithography	93
• 5.14	Combined Spatial-Phase-Locked Electron-Beam, X-ray, and Optical Lithography for Channel-Dropping Filters	95
5.15	High-Dispersion, High-Efficiency Transmission Gratings for Astrophysical X-ray Spectroscopy	99
• 5.16	Submicrometer-Period Transmission Gratings for X-ray and Atom-Beam Spectroscopy and Interferometry	100
• 5.17	GaAs Epitaxy on Sawtooth-Patterned Silicon	100
• 5.18	Publications	101

Chapter 6 Single-Electron Spectroscopy 103

Professor Raymond Ashoori

• 6.1	Goals and Objectives	103
• 6.2	Traps Created by Disorder and Impurities in Semiconductor Structures	104
• 6.3	Artificial Atoms	104
• 6.4	Spatially Resolved Charge Sensing	105
• 6.5	Single-Electron Transistors for Spectroscopy	105
• 6.6	Publications	105

Section 3 Optics and Devices

Chapter 1 Optics and Quantum Electronics 109

Professor Hermann A. Haus, Professor Erich P. Ippen, Professor James G. Fujimoto, Professor Peter L. Hagelstein, Dr. Brett E. Bouma, Dr. Joseph A. Izatt

• 1.1	Fiber Ring Lasers	109
1.2	Fiber Storage Ring	111
1.3	Long-Distance Fiber Communications	111
1.4	Squeezing	112
1.5	Optical Channel Dropping Filters	113
• 1.6	Overdriven Additive Pulse Modelocking	114
• 1.7	A Broadband-Tunable Femtosecond Source for 1.55 μm Diagnostics	115
• 1.8	Ultrafast Nonlinearities in Active Semiconductors	116
• 1.9	Nonlinear Interactions of Continuous and Pulsed Light in Optical Fibers	117
• 1.10	Intensity Autocorrelation of Light Sources for Fiber Optical Gyroscopes	119
• 1.11	Wavelength Shifting by Four-Wave Mixing in Passive Semiconductor Waveguides	119
• 1.12	Ultrashort Pulse Generation in Solid State Lasers	120
• 1.13	Ultrafast Phenomena in Materials and Devices	122
1.14	Laser Medicine	125
1.15	Optical Coherence Tomography Technology	125
1.16	EUV Laser Studies	130
1.17	Collisional and Recombination Schemes at Longer Wavelength	134
1.18	Toward a Novel End-Pumped EUV Laser	136
1.19	Photon Operators and Photon Configuration-Space Equations	137

Table of Contents

1.20	Neutron Hopping	139
1.21	Possible Phonon Laser Driven by Exothermic Desorption	140
Chapter 2	Optical Propagation and Communication	143
	<i>Professor Jeffrey H. Shapiro, Dr. Robert H. Rediker, Dr. Ngai C. Wong</i>	
2.1	Introduction	143
2.2	Nonlinear and Quantum Optics	143
2.3	Multiresolution Laser Radar Range Profiling	145
2.4	Optical Frequency Division and Synthesis	146
Chapter 3	High-Frequency (>100 GHz) and High-Speed (<1 ps) Electronic Devices	149
	<i>Professor Qing Hu</i>	
3.1	Introduction	149
3.2	Micromachined Millimeter-wave Devices	150
3.3	Far-infrared and Picosecond Time-resolved Transport Studies of Quantum-effect Devices	152
3.4	Intersubband Transitions in Coupled Double Quantum-well (DQW) Structures	158
3.5	Publications	163
Section 4	Surfaces and Interfaces	
Chapter 1	Synchrotron X-Ray Studies of Surface Disorder	167
	<i>Professor Robert J. Birgeneau</i>	
• 1.1	Introduction	167
• 1.2	Stability of Vicinal Si(111) Surfaces Under Metal Surface Studies	167
• 1.3	Publications	169
Chapter 2	Semiconductor Surface Studies	171
	<i>Professor John D. Joannopoulos</i>	
• 2.1	Introduction	171
• 2.2	Chemisorption	171
• 2.3	Cross-sectional Scanning Tunneling Microscopy	174
• 2.4	Publications	176
Chapter 3	Step Structures and Epitaxy on Semiconductor Surfaces	177
	<i>Professor Simon G.J. Mochrie</i>	
• 3.1	Introduction	177
• 3.2	Phase Behavior of Stepped Si(113) Surfaces	178
• 3.3	Faceting Kinetics of Stepped Si(113) Surfaces: Self-Assembled Nano-Scale Gratings	180
• 3.4	Publications	181
PART II	Applied Physics	
Section 1	Atomic, Molecular and Optical Physics	
Chapter 1	Quantum Optics and Photonics	187
	<i>Professor Shaoul Ezekiel</i>	

Table of Contents

1.1	Distributed Fiberoptic Sensor for Quench Detection in Superconducting Tokamak Magnets	187
1.2	Measurement of Liquid Helium Flow in Superconducting Tokamak Magnets	188
1.3	Efficient, Low-Intensity Optical Phase Conjugation using Coherent Population Trapping in Sodium	190
1.4	Highly Selective Nonspatial-Filters Using Porous Matrix Based Thick Holograms	192
1.5	Cache Memory using Optically Induced Spin Echo	194
1.6	Doppler Cooling in Traveling Wave Velocity Selective Coherent Population Trapping	196
1.7	Near-perfect Squeezing in a Folded Three-Level System	198
Chapter 2	Basic Atomic Physics	201
<i>Professor Daniel Kleppner, Professor David E. Pritchard</i>		
• 2.1	Studies in Quantum Chaos: High Resolution Periodic Orbit Spectroscopy	201
• 2.2	Determination of the Rydberg Frequency	205
• 2.3	Precision Mass Spectrometry of Ions	208
• 2.4	Atom Interferometry	211
• 2.5	Cooling and Trapping Neutral Atoms	215
Section 2	Plasma Physics	
Chapter 1	Plasma Dynamics	223
<i>Professor George Bekefi, Professor Abraham Bers, Professor Bruno Coppi, Professor Jonathan S. Wurtele, Dr. Stefano Migliuolo, Dr. Abhay K. Ram, Dr. Linda E. Sugiyama</i>		
1.1	Relativistic Electron Beams	223
1.2	Plasma Wave Interactions - RF Heating and Current Generation	229
1.3	Physics of Thermonuclear Plasmas	237
Section 3	Electromagnetics	
Chapter 1	Electromagnetic Wave Theory and Applications	245
<i>Professor Jin Au Kong, Dr. Kung Hao Ding, Dr. Robert T. Shin, Dr. Y. Eric Yang</i>		
1.1	Remote Sensing of Earth Terrain	245
• 1.2	Electromagnetic Waves in Multilayer Media	246
1.3	Simulation of Electromagnetic Wave Scattering	247
1.4	Publications	247
Section 4	Radio Astronomy	
Chapter 1	Radio Astronomy	251
<i>Professor Bernard F. Burke, Professor David H. Staelin, Professor Jacqueline N. Hewitt, Dr. Philip W. Rosenkranz</i>		
1.1	Extragalactic Radio Source Studies	251
1.2	Studies of Gravitational Lenses	252
1.3	The Detection of Astronomical Radio Transients	254
1.4	Algorithms for Advanced Microwave Sounding Unit Operational Use	255
1.5	Earth Observing System: Advanced Microwave Sounding Unit	255
1.6	High-Resolution Passive Microwave Imaging of Atmospheric Structure	256
1.7	Reduction of Variation	256

PART III Systems and Signals

Section 1 Computer-Aided Design

Chapter 1 Custom Integrated Circuits	263
<i>Professor Jonathan Allen, Professor John L. Wyatt, Jr., Professor Jacob White, Professor Srinivas Devadas</i>	
1.1 Custom Integrated Circuits	263
1.2 Analog VLSI Systems for Integrated Image Acquisition and Early Vision Processing .	266
1.3 Parallel Algorithms for Device Simulation	273
1.4 Numerical Simulation of Short Channel MOS Devices	274
1.5 Coupled Simulation Algorithms for Microelectromechanical CAD (MEMCAD) . .	274
1.6 Numerical Techniques for Simulating Josephson Junction Arrays	275
1.7 Efficient 3-D Interconnect Analysis	276
1.8 Adaptive Gridding Techniques for Multipole-Accelerated Solution of Integral Equations	278
1.9 Circuit Simulation Algorithms	278
1.10 Techniques for High-Performance Low-Power Embedded System Design . .	280
Chapter 2 Computer-Integrated Fabrication System Structure	285
<i>Professor Donald E. Troxel</i>	
2.1 Introduction	285
2.2 CAFE Applications	285
2.3 Organization of Data and Algorithms for Factory Design and Control	286
2.4 Statistical Process Control Charts for the Computer-Aided Fabrication Environment .	286
2.5 Run-by-Run Control: Interfaces, Implementations, and Integration	286
2.6 Hardware Setup for a Remote Microscope	288
2.7 First-Order Model for Remote Fabrication	288
2.8 Estimating the Lead Time Distribution of Priority Lots in a Semiconductor Factory .	289
2.9 Factory Display Software	289
2.10 Message Passing Tools for Software Integration	289
2.11 CAFE at MIT Lincoln Laboratory	290
2.12 Error Handling Within CAFE	291
2.13 Semiconductor Manufacturing Process Flow Representation	291
2.14 Computer-Aided Technology Design	293
2.15 Publications	295
Section 2 Digital Signal Processing	
Chapter 1 Digital Signal Processing Research Program	299
<i>Professor Alan V. Oppenheim, Professor Arthur B. Baggeroer, Professor Gregory W. Wornell</i>	
1.1 Introduction	299
1.2 Single Mode Excitation in the Shallow Water Acoustic Channel	300
1.3 Self-Synchronization of Chaotic Systems: Analysis, Synthesis, and Applications .	300
1.4 Algebraic and Probabilistic Structure in Fault-Tolerant Computation	301
1.5 Signal Processing Applications of Chaotic Dynamical Systems	301
1.6 Wavelet-Based Representation and Algorithms for Generalized Fractal Signals .	302
1.7 Approximate Signal Processing	302
1.8 CDMA for Digital Storage	303
1.9 Estimation and Detection of a Class of Chaotic Signals	303
1.10 Real Time Active Noise Cancellation	303
1.11 State and Parameter Estimation with Chaotic Systems	304
1.12 Model Based Analysis of Music	305
1.13 Nonlinear Models for Signal Processing	305
1.14 Environmental Robustness in Automatic Speech Recognition	305

Table of Contents

1.15	Active Noise Cancellation	306
1.16	Oceanographic Signal Processing	306
Chapter 2	Advanced Telecommunications and Signal Processing Program	309
	<i>Professor Jae S. Lim</i>	
2.1	Introduction	309
2.2	ATRP Facilities	309
2.3	Signal Representations for Very-low-bit-rate Video Compression	310
2.4	Constant Quality Video Coding	310
2.5	Signal Representations in Audio Compression	311
2.6	Pre-Echo detection and Reduction	312
2.7	Video Source Coding for High-Definition Television	312
2.8	Transmission of HDTV Signals in a Terrestrial Broadcast Environment	313
2.9	Position-Dependent Encoding	313
2.10	MPEG Compression	313
2.11	HDTV Transmission Format Conversion and the HDTV Migration Path	314
2.12	Removing Degradations in Image Sequences	314
2.13	Speech Enhancement	314
Chapter 3	Combined Source and Channel Coding for High-Definition Television	317
	<i>Professor William F. Schreiber</i>	
3.1	Project Description	317
3.2	Technology	318
3.3	Current Status	318
3.4	Future Plans	318
3.5	Publications	319
PART IV	Bioelectronics	
Section 1	Genetic Analysis	
Chapter 1	Genosensor Technology Development	325
	<i>Dr. Mark Hollis, Dr. Daniel J. Ehrlich, Dr. Dennis D. Rathman</i>	
1.1	Introduction	325
1.2	Development of Genosensor Arrays for DNA Decoding	325
1.3	Microdetection Technology for Automated DNA Sequencing	328
PART V	Language, Speech and Hearing	
Section 1	Speech Communication	
Chapter 1	Speech Communication	333
	<i>Professor Kenneth N. Stevens, Dr. Joseph S. Perkell, Dr. Stefanie Shattuck-Hufnagel</i>	
1.1	Studies of Normal Speech Production	334
1.2	Speech Research Relating to Special Populations	336
1.3	Speech Production Planning and Prosody	340
1.4	Studies of the Acoustics, Perception, and Modeling of Speech Sounds	342
1.5	Models for Lexical Representation and Lexical Access	344
1.6	Development of Computer and Data Processing Facilities	344
1.7	Publications	345
Section 2	Sensory Communication	
Chapter 1	Sensory Communication	349

Table of Contents

*Professor Louis D. Braida, Nathaniel I. Durlach, Dr. William M. Rabinowitz,
Dr. Charlotte M. Reed, Dr. Mandayam A. Srinivasan, Dr. Thomas E.v. Wiegand,
Dr. David Zeltzer, Dr. Patrick M. Zurek*

1.1	Research on Hearing, Hearing Aids, and Tactile Communication of Speech	349
1.2	Haptics Research	360
1.3	Virtual Environment Technology for Training	372
1.4	Research on Improved Sonar Displays: A Human/Machine Processing System	376
1.5	Development of Inertial Head-Tracking Technology	378

Section 3 Auditory Physiology

Chapter 1 Signal Transmission in the Auditory System 383

Professor Lawrence S. Frishkopf, Professor Nelson Y.S. Kiang, Professor William T. Peake, Professor William M. Siebert, Professor Thomas F. Weiss, Dr. Bertrand Delgutte, Dr. Donald K. Eddington, Dr. Dennis M. Freeman, Dr. John J. Guinan, Jr., Dr. John J. Rosowski

1.1	Introduction	383
1.2	Signal Transmission through the External and Middle Ear	383
1.3	Cochlear Mechanisms	385
1.4	Stimulus Coding in the Auditory Nerve and Cochlear Nucleus	387
1.5	Interactions of Middle-Ear Muscles and Olivocochlear Efferents	390
1.6	Cochlear Efferent System	390
1.7	Cochlear Implants	392

Section 4 Linguistics

Chapter 1 Linguistics 397

Professor Noam Chomsky, Professor Morris Halle

1.1	Introduction	397
1.2	Abstracts of Doctoral Dissertations	397

APPENDICES

Appendix A RLE Publications and Papers Presented 401

A.1	Meeting Papers	401
A.2	Journal Articles	412
A.3	Books/Chapters in Books	421
A.4	RLE Publications	422
A.5	RLE Theses	423

Appendix B Current RLE Personnel 427

Appendix C Milestones 433

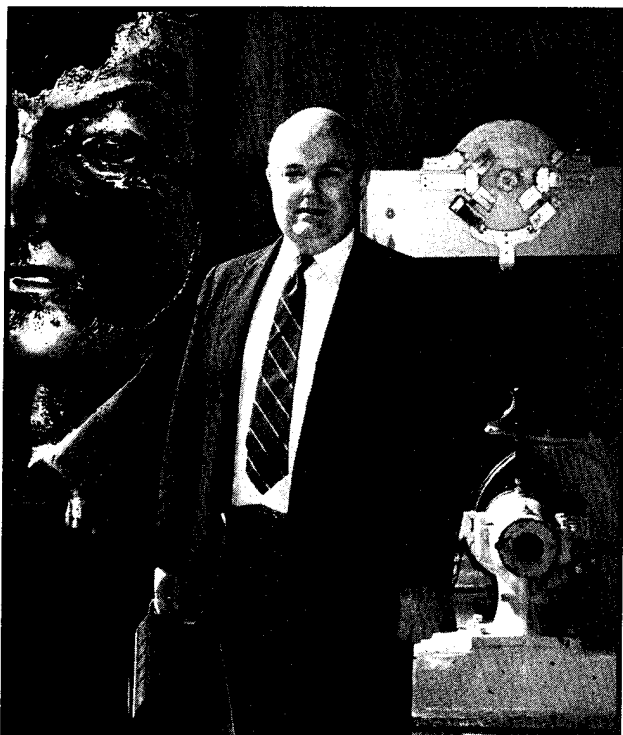
C.1	New Faculty and Staff	433
C.2	Promotions	433
C.3	Appointments	433
C.4	Awards and Honors	433

Appendix D RLE Research Support Index 435

Project Staff and Subject Index 439

The Research Laboratory of Electronics

The Research Laboratory of Electronics (RLE) was established in 1946 as the Institute's first interdepartmental laboratory. Originally organized under the joint sponsorship of the Departments of Physics and Electrical Engineering, RLE has broadened its interests to cover a wide range of research.



Professor Jonathan Allen, Director, Research Laboratory of Electronics (Photo by John F. Cook)

The RLE environment provides both the freedom of action essential in an academic institution and the availability of large-scale laboratory facilities and services required by researchers. RLE's interdisciplinary setting offers many opportunities for creative and collaborative research. By fostering this powerful combination of research and education, RLE effectively penetrates beyond the horizon of new ideas and information.

RLE Progress Report

RLE Progress Report Number 137 describes research programs at RLE for the period January 1 through December 31, 1994. Each chapter of the *Progress Report* includes a summary of research efforts for research projects listed. Faculty, research staff, students and others who participated in these projects are identified at the beginning of each project, along with sources of funding.

There are four appendices at the end of the report: Appendix A is a bibliography of RLE publications and papers presented by RLE staff during 1994; Appendix B is a roster of current RLE staff; Appendix C is a list of RLE faculty and staff milestones and honors received during 1994; and Appendix D is an index of RLE sponsors. The Project Staff and Subject Index provides additional access to the information in this report.

RLE Publications

RLE also publishes *RLE currents*, a biannual newsletter which focuses on RLE research interests; a technical report series; *Speech Group Working Papers*; and other information related to the Laboratory. The *RLE Brochure*, published in 1991 for RLE's 45th anniversary, is also available at no charge.

RLE has a presence on the World Wide Web (<http://rleweb.mit.edu>). RLE web pages include an introduction to RLE research and services; information about RLE's history, research groups, staff, and publications along with news of RLE events, and a history of the Radiation Laboratory (1940-1945).

Massachusetts Institute of Technology
Research Laboratory of Electronics
Communications Office
Room 36-412
Cambridge, Massachusetts 02139-4307
Tel. (617) 253-2566
Fax (617) 258-7864

Part I Solid State Physics, Electronics and Optics

Section 1 Materials and Fabrication

Section 2 Quantum-Effect Devices

Section 3 Optics and Devices

Section 4 Surfaces and Interfaces

Section 1 Materials and Fabrication

Chapter 1 Heterostructures for High-Performance Devices

Chapter 2 Physics of InAlAs/InGaAs Heterostructure
Field-Effect Transistors

Chapter 3 Gas Source Molecular Beam Epitaxy of
Compound Semiconductors

Chapter 1. Heterostructures for High-Performance Devices

Academic and Research Staff

Professor Clifton G. Fonstad, Jr.

Visiting Scientists and Research Affiliates

Paul Gavrilovich,¹ Norio Iisuka,² Kathy Meehan,¹ Dr. Sheila Prasad³

Graduate Students

Rajni J. Aggarwal, Joseph F. Ahadian, Eric K. Braun, Woo-Young Choi, Isako Hoshino, Paul S. Martin, Janet L. Pan, Lung-Han Peng, Yakov Royter, Krishna V. Shenoy, Jurgen H. Smet, Hao Wang

Undergraduate Students

Cade Murray, Michael Rosenthal

Technical and Support Staff

Charmaine A. Cudjoe-Flanders, Angela R. Odoardi

1.1 Introduction

The broad focus of our research program is on the development of III-V quantum heterostructures for high performance electronic, optoelectronic, and photonic devices, and on the integration of such devices with high density GaAs MESFET electronics for applications in high speed signal processing, computation, and communication. A major portion of our current effort is directed at a novel epitaxy-on-electronics integration process we have invented which allows us to monolithically integrate complex heterostructure optoelectronic and quantum effect devices with commercially processed, fully metalized gallium arsenide VLSI circuits. In this manner we can achieve levels of integration and functionality impossible by any other technique.

Our group works closely with Professors Hermann A. Haus, Erich P. Ippen, Leslie A. Kolodziejski, Henry I. Smith, and Cardinal Warde at MIT, and on ongoing collaborations with other universities and within industry. These include joint work within the National Center for Integrated Photonics Tech-

nology with Professors Wen Wang and Richard Osgood at Columbia University, and Professors Elsa Garmire, Sandy Sawchuck, and Dan Dapkus at the University of Southern California. Other collaborations involve Professor William Goodhue of the University of Massachusetts at Lowell, Professor Demetri Psaltis of California Institute of Technology, and Professor Sheila Prasad of Northeastern University. In early 1995, we will be initiating a new effort, the OPTOCHIP Project, to make our epi-on-electronics optoelectronic integration technology available to an even broader community of users.

1.2 High-Temperature Stability of GaAs Integrated Circuits

Sponsors

Advanced Research Projects Agency/National
Center for Integrated Photonics Technology
Fannie and John Hertz Foundation
Graduate Fellowship

¹ Polaroid Corporation, Cambridge, Massachusetts.

² Toshiba Corporation Ltd., Kawasaki, Japan.

³ Northeastern University, Boston, Massachusetts.

Joint Services Electronics Program
 Contract DAAL03-92-C-0001
 Grant DAAH04-95-1-0038
 National Science Foundation
 Graduate Fellowship

Project Staff

Eric K. Braun,⁴ Krishna V. Shenoy, Professor Clifton G. Fonstad, Jr., J.M. Mikkelsen⁵

The optical device quality in optoelectronic integrated circuits formed by selective-area growth (see epi-on-electronics section) depends strongly on the epitaxial growth temperature. The upper temperature bound is set by the thermal stability of the underlying electronics. In our studies of the stability of GaAs electronics, we have investigated the HGaAs₂⁶ and HGaAs₃⁷ process of Vitesse Semiconductor Corporation and the CS-1 process of Motorola. Both lines produce VLSI density GaAs enhancement-mode and depletion-mode MESFETs with refractory metal gates (tungsten-nitride based) and ohmic contacts (nickel based); the upper level interconnect lines are aluminum-copper (standard in silicon CMOS) bounded by tungsten nitride. Such refractory metal circuits have demonstrated excellent high operating-temperature performance as well as tolerance to elevated-temperature thermal cycles.

We have shown that the thermally-weak link in the structures is the multilayer metal film used in the upper level interconnect lines, which typically limits us to epitaxy temperatures below 500°C, preferably under 475°C. The ohmic contacts are stable to somewhat higher temperatures and the GaAs intrinsic transistor structures are stable to much higher temperatures. We have suggested changes in the HGaAs₃ interconnect metal compositions to Vitesse and have demonstrated increased stability at high temperatures in test samples prepared by Vitesse. We have also incorporated measured changes in device parameters after elevated temperature thermal cycles into circuit models and have successfully used them to predict circuit failures seen experimentally after extended periods at very high temperatures. These thermal stability studies have permitted the first successful inte-

gration of optical devices with commercial VLSI GaAs electronics.

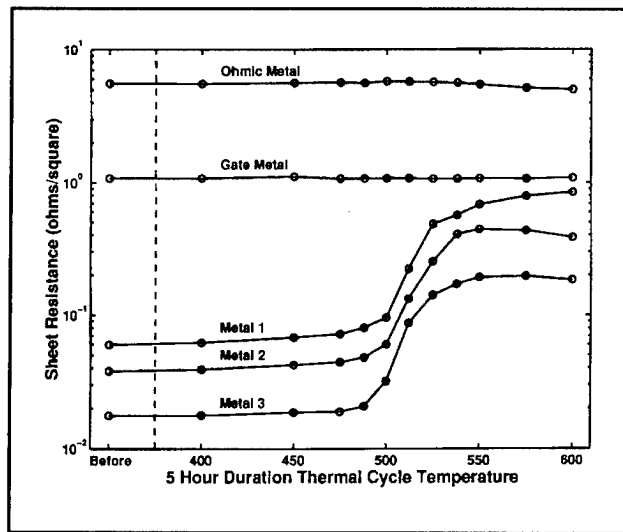


Figure 1. Metal layer sheet resistance after five-hour thermal cycles. At elevated temperatures a metallurgical reaction, $\text{AlCu}_x + \text{WN}_x \rightarrow \text{Al}-\text{Cu}-\text{W}-\text{N}$, occurs within the interconnect metal layers which increases their sheet resistance.

1.3 High Peak-to-Valley Current Ratio Resonant-Tunneling Diodes on GaAs Substrates

Sponsor

Joint Services Electronics Program
 Contract DAAL03-92-C-0001
 Grant DAAH04-95-1-0038

Project Staff

Rajni J. Aggarwal, Professor Clifton G. Fonstad, Jr.

The peak-to-valley current ratio (PVCR) of GaAs/Al_xGa_{1-x}As resonant-tunneling diodes (RTDs) grown on GaAs can be improved upon by replacing GaAs with In_xGa_{1-x}As. Because In_xGa_{1-x}As is not lattice matched to GaAs, strained layer thickness limits restrict the indium content of the In_xGa_{1-x}As

⁴ Maxim Corporation, Sunnyvale, California.

⁵ Vitesse Semiconductor Corporation, Camarillo, California.

⁶ K.V. Shenoy, C.G. Fonstad, Jr., and J.M. Mikkelsen, "High Temperature Stability of Refractory-Metal VLSI GaAs MESFETs," *IEEE Electron Dev. Lett.* 15: 106-108 (1994).

⁷ E.K. Braun, K.V. Shenoy, C.G. Fonstad, Jr., and J.M. Mikkelsen, "Elevated Temperature Stability of GaAs Digital Integrated Circuits," submitted to *IEEE Electron Dev. Lett.*

layers, and therefore limit the utility of this approach. By using a strain relieved buffer, the substrate lattice constant can be changed to match that of higher indium-fraction $\text{In}_x\text{Ga}_{1-x}\text{As}$ layers. We are using this approach to design high PVCR RTDs suitable for circuit applications.

We have demonstrated the highest PVCR reported for $\text{In}_x\text{Ga}_{1-x}\text{As}$ based RTDs on GaAs.⁸ Figure 2 shows the electrical characteristics of an $\text{In}_{0.22}\text{Ga}_{0.78}\text{As}/\text{AlAs}$ RTD grown on a two-step relaxed buffer structure. Photoluminescence and x-ray diffraction were used to confirm the relaxed nature of the buffer. Dislocations are visible to the naked eye, however, the electrical performance suggests that the RTD structures are robust and can withstand the presence of some dislocations in the active layers.

Early relaxed-buffer RTDs had resonance voltages beyond those suitable for circuit applications. Two series of relaxed buffer diodes were grown to determine the contribution of the relaxed buffer to the resonance voltage of the devices. In each series, the heavily doped relaxed buffer and the RTD structure were held constant and the contact doping was varied. As expected, diodes with lower contact doping had higher resonance voltages. Both series indicate that only tens of millivolts are being dropped across the heavily doped relaxed buffer. RTDs using heavily doped relaxed buffers in combination with highly doped contacts will be suitable for circuit applications.

We have developed a repeatable technique for growing high performance $\text{In}_x\text{Ga}_{1-x}\text{As}/\text{AlAs}$ RTDs on GaAs substrates. Future work will focus on increasing the indium content of the diodes as well as investigating $\text{In}_x\text{Ga}_{1-x}\text{As}/\text{AlAs}/\text{In}_y\text{Ga}_{1-y}\text{As}$ diodes.

1.4 Monolithic Integration of Resonant-Tunneling Diodes on GaAs Integrated Circuits

Sponsors

Advanced Research Projects Agency/National Center for Integrated Photonics Technology
Fannie and John Hertz Foundation

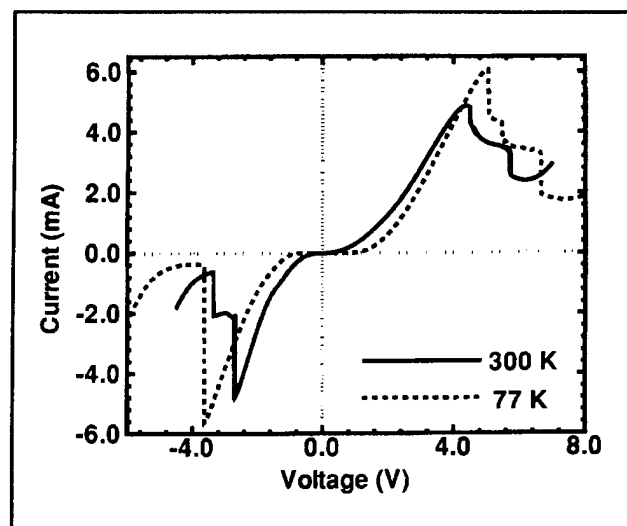


Figure 2. The current-voltage characteristic of a typical $25 \mu\text{m}^2$ relaxed buffer RTD at 77 K (broken line) and 300 K (solid line).

Graduate Fellowship
Joint Services Electronics Program
Contract DAAL03-92-C-0001
Grant DAAH04-95-1-0038
National Science Foundation
Graduate Fellowship

Project Staff

Rajni J. Aggarwal, Professor Clifton G. Fonstad, Jr.

GaAs integrated circuits have reached VLSI densities, but there remains a need for a compact GaAs random access memory cell. Fujitsu initially proposed a monolithic resonant-tunneling diode (RTD) based static random access memory (SRAM) using a single-transistor, two-diode architecture.⁹ However, the HEMT was not the appropriate device to build the necessary memory array addressing circuitry and therefore this approach was abandoned. We utilize MBE growth on commercial circuits to combine a proven GaAs FET technology with RTDs. We use the Vitesse HGaAs₃ process to fabricate high-performance GaAs DCFL circuits on which we epitaxially grow RTDs. In this fashion, we free ourselves from development of the transistor technology, and yet maintain a monolithic SRAM. We have chosen a two EFET, two RTD architecture similar to that used by Fujitsu.

⁸ R.J. Aggarwal and C.G. Fonstad, Jr., "High Peak-to-valley Current Ratio $\text{In}_{0.22}\text{Ga}_{0.78}\text{As}/\text{AlAs}$ RTDs on GaAs Using Relaxed $\text{In}_x\text{Ga}_{1-x}\text{As}$ Buffers," *Electron. Lett.* 31(1): 75-77 (1995).

⁹ Y. Watanabe, et al., "Monolithic Integration of InGaAs/InAlAs Resonant Tunneling Diode and HEMT for Single-transistor SRAM Application," *Proceedings of the 1992 International Electron Devices Meeting*, San Francisco, California, December 13-16, 1992.

We are developing analytic expressions for the operation of the memory cell. Initially, these were derived using linearized models of the EFET and the RTD. Improved models which more accurately describe the electrical characteristics will be used in subsequent analyses. These new expressions will be used to theoretically estimate the speed limits of the cell.

Initial studies on RTD structures yielded large-signal design parameter information. This information was used to design three basic circuits to study the feasibility of integrating RTDs with GaAs ICs: a diode

array, a single-bit memory cell, and a 4-bit memory array. The diode array will be used to study the quality of the RTD material grown on the GaAs ICs. The single-bit memory cells will be used to characterize the basic operation of the memory cell. Figure 3 shows the simulated operation of a single cell. The 4-bit memory array will be used to address density issues such as the effect of RTD variation on the performance of the memory. The performance of the individual memory cells and the memory array will be evaluated at a variety of frequencies. Based on our results, we will assess the commercial potential of this technology.

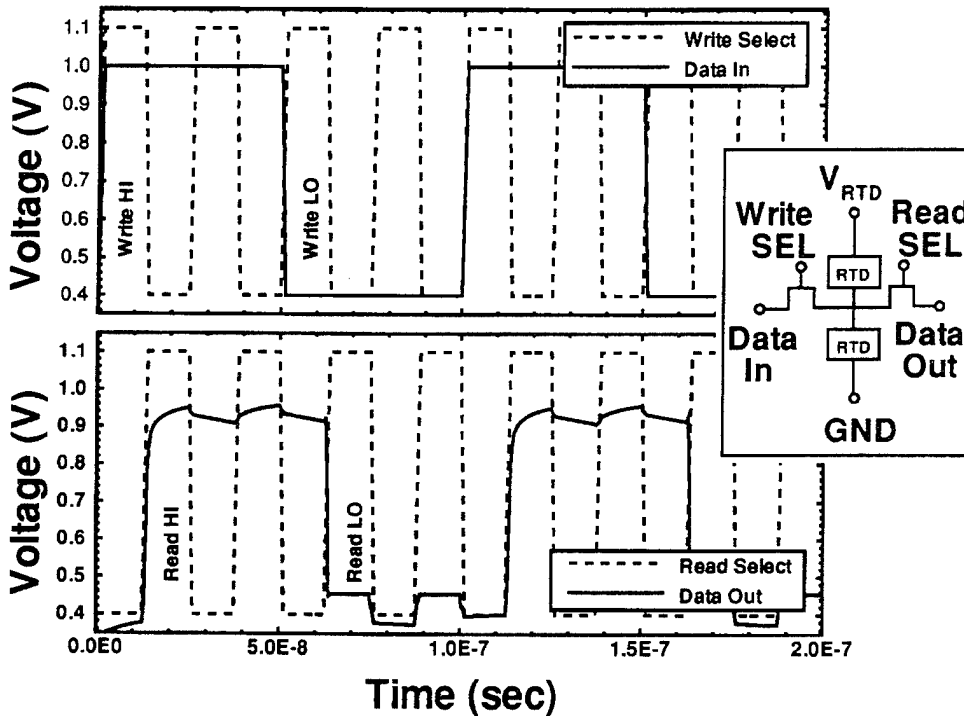


Figure 3. Simulated operation of a 1-bit memory cell using $240 \mu\text{m} \times 1.2 \mu\text{m}$ FETs and $1.2 \mu\text{m} \times 10 \mu\text{m}$ RTDs. The upper panel shows the activity on the input lines of the cell. The lower panel shows the simultaneous activity on the output lines of the cell. The inset shows the schematic of the cell.

1.5 Phosphide-Based Optical Emitters for Monolithic Integration with GaAs MESFETS

Sponsors

Advanced Research Projects Agency/National Center for Integrated Photonics Technology
National Security Agency¹⁰

Project Staff

Joseph F. Ahadian, Krishna V. Shenoy, Dr. Gale S. Petrich, Professor Leslie A. Kolodziejski, Professor Clifton G. Fonstad, Jr.

A technology thrust aimed at developing a VLSI OEIC platform has, under the direction of Professor Clifton G. Fonstad, produced an "Epi-on-

¹⁰ Ft. Meade with MIT Lincoln Laboratory.

Electronics" (E-o-E) monolithic integration method in which optical devices are grown in foundry opened "epitaxy windows" on fully-processed refractory metal GaAs VLSI MESFET circuits. These VLSI chips, commercially manufactured by Vitesse Semiconductor Corporation and available through MOSIS, have been found to withstand extended temperature cycles of up to approximately 500°C without significant degradation of the electronic performance, suggesting the possibility of subsequent growth by molecular beam epitaxy (MBE). However, a substrate temperature of less than 500°C is not optimal for the conventional growth of AlGaAs-containing LEDs and lasers; these devices exhibit compromised performance. High-performance lasers utilizing InGaP ($\text{In}_{0.49}\text{Ga}_{0.51}\text{P}$ is lattice matched to GaAs) as the wide bandgap material have been realized by a number of groups.¹¹ Since phosphorus-containing alloys are nominally grown by gas source MBE below 500°C, the integration of high quality LEDs and lasers based on this material system is the objective of the current project.

InGaAs/GaAs/InGaP quantum well separate confinement heterostructure lasers having threshold current densities of 220 A/cm² (for pulsed room temperature broad-area devices) have been fabricated. Electroluminescence measurements on GaAs/InGaP double heterostructures have shown the efficacy of LEDs based on this structure. The aforementioned structures were grown by gas-source molecular beam epitaxy at a constant substrate temperature of 470°C on bulk GaAs. Two remaining challenges to the integration process are being addressed. First, the normal MBE practice of briefly elevating the substrate temperature (to around 600°C) to desorb the native GaAs oxide prior to epitaxy must be eliminated since it results in damage to upper-level metal interconnects. A technique under investigation uses a hydrogen plasma to remove the oxide at a substrate temperature of 300°C. The second challenge is to develop a more robust procedure for preparing the epitaxy windows for growth, ensuring more reliable epitaxy results. These innovations will allow the integration of state-of-the-art emitters onto a VLSI OEIC.

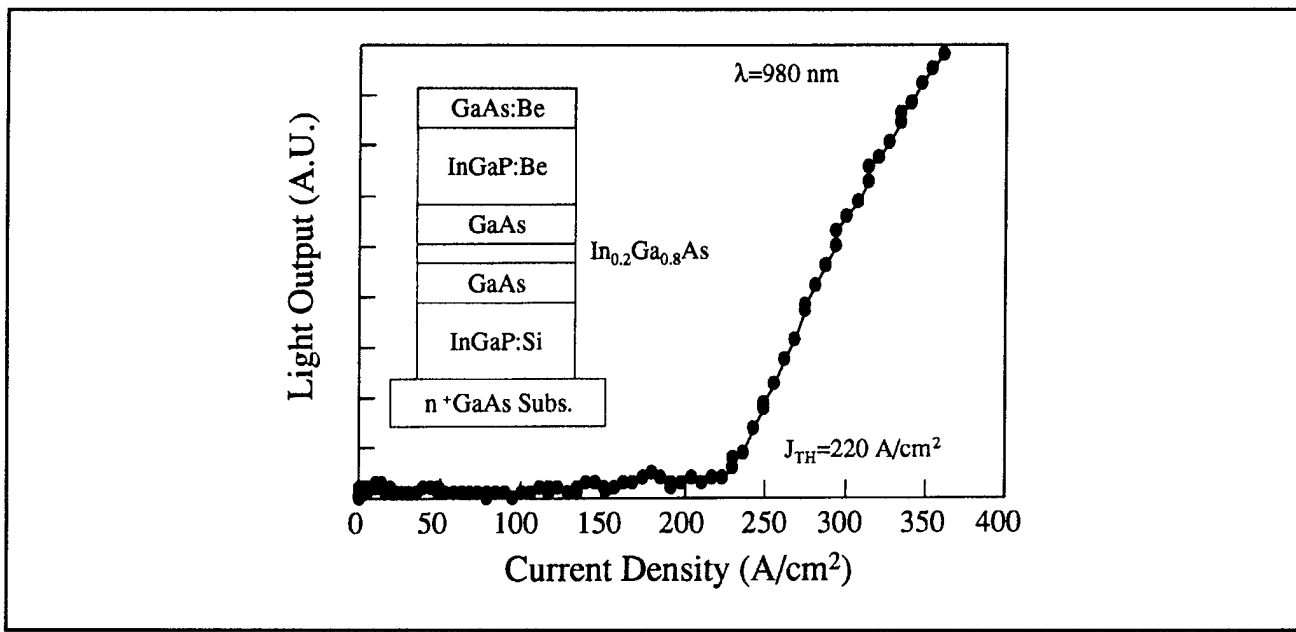


Figure 4. Light output versus current density for a room temperature pulsed broad-area InGaAs/GaAs/InGaP quantum-well separate confinement heterostructure laser. The low threshold current density verifies that high quality optical emitters based on this material system which was grown at 470°C are possible.

¹¹ T. Ijichi, M. Ohkubo, N. Matsumoto, and H. Okamoto, *Proceedings of the 12th IEEE International Semiconductor Laser Conference*, Davos, Switzerland, September 9-14, 1990; J.M. Kou, Y.K. Chen, M.C. Wu, and M.A. Chin, "InGaAs/GaAs/InGaP Multiple-Quantum-Well Lasers Prepared by Gas-Source Molecular Beam Epitaxy," *Appl. Phys. Lett.* 59(22): 2781-2783 (1991); G. Zhang, J. Nappi, K. Vanttinen, H. Asonen, and M. Pessa, "Low Threshold Current Strained-Layer InGaAs/GaAs/InGaP Lasers Grown By Gas-Source Molecular Beam Epitaxy," *Appl. Phys. Lett.* 61(1): 96-98 (1992).

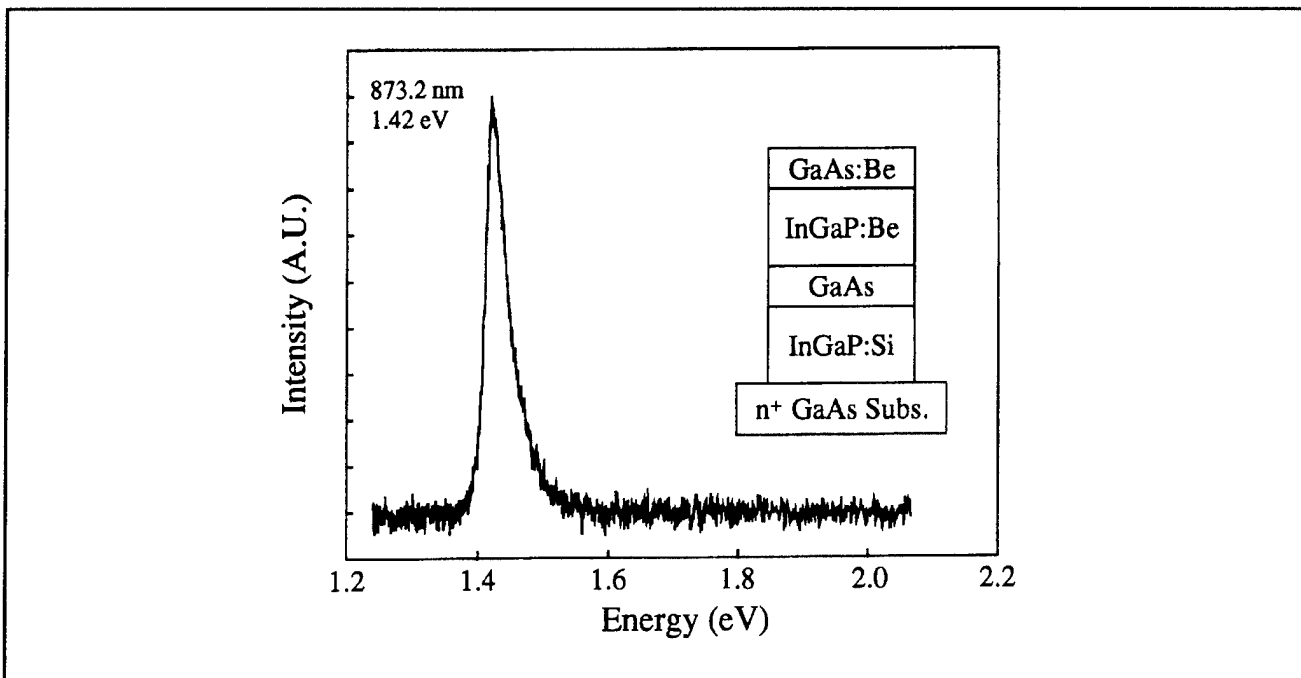


Figure 5. Electroluminescence from a GaAs/InGaP double heterostructure grown at 470°C. LEDs compatible with GaAs m-s-m photodetectors will be fabricated using this epitaxial structure.

1.6 Monolithic Integration of LEDs and VLSI GaAs MESFET Circuits

Sponsors

Advanced Research Projects Agency/National Center for Integrated Photonics Technology
 Fannie and John Hertz Foundation
 Graduate Fellowship
 Motorola Corporation
 National Science Foundation
 Graduate Fellowship

Project Staff

Krishna V. Shenoy, Professor Clifton G. Fonstad, Jr. in collaboration with A.C. Grot,¹² Dr. Demetri Psaltis¹³

Recently, we have reported that fully processed, commercially available (Vitesse Semiconductor Corporation through MOSIS) VLSI GaAs MESFET inte-

grated circuits are electrically stable after thermal cycles such as those encountered in reduced-temperature molecular beam epitaxy. A novel optoelectronic integration technique was proposed based on this circuit stability. Consequently the monolithic integration of LEDs and GaAs circuits by molecular beam epitaxial (MBE) growth (to form an optoelectronic thresholding circuit) was demonstrated.¹⁴ In the initial work the circuits and LEDs occupied distinct halves of the chip, one large dielectric growth window was wet etched after circuit fabrication, and the LEDs required both n and p ohmic contacts to be formed after growth. Advances in these areas are required to achieve higher levels of integration and thus to take full advantage of the highly uniform VLSI circuitry inherent to this optoelectronic integration technique.

With these challenges in mind, we have successfully demonstrated the use of standard foundry process etches to open dielectric growth windows intermixed with circuitry and the growth of n-side down LEDs on a source/drain ion-implanted n⁺

¹² Hewlett-Packard, Palo Alto, California.

¹³ California Institute of Technology, Pasadena, California.

¹⁴ A.C. Grot, D. Psaltis, K.V. Shenoy, and C.G. Fonstad, Jr., "Integration of LEDs and GaAs Circuits by MBE Regrowth," *IEEE Photon. Tech. Lett.* 6(7): 819-821 (1994).

region serving as the n ohmic contact.¹⁵ We designed and fabricated a three-unit winner-take-all (WTA) neural circuit which consists of three LEDs grown in $50 \mu\text{m} \times 50 \mu\text{m}$ dielectric growth windows with source/drain implant contacts, associated optical-FET detectors, and four FETs per unit. These advances are important steps toward realizing higher levels of circuit integration.¹⁶ A 100-unit WTA circuit array and various schemes to suppress

both optical and electrical cross-talk in high-density optoelectronic circuits are currently in progress.

By epitaxially growing LEDs on custom designed commercial VLSI GaAs MESFET integrated circuits with S/D n⁺ regions beneath foundry etched dielectric growth windows, large-scale high-density optoelectronic circuits and systems fabrication should now be possible.

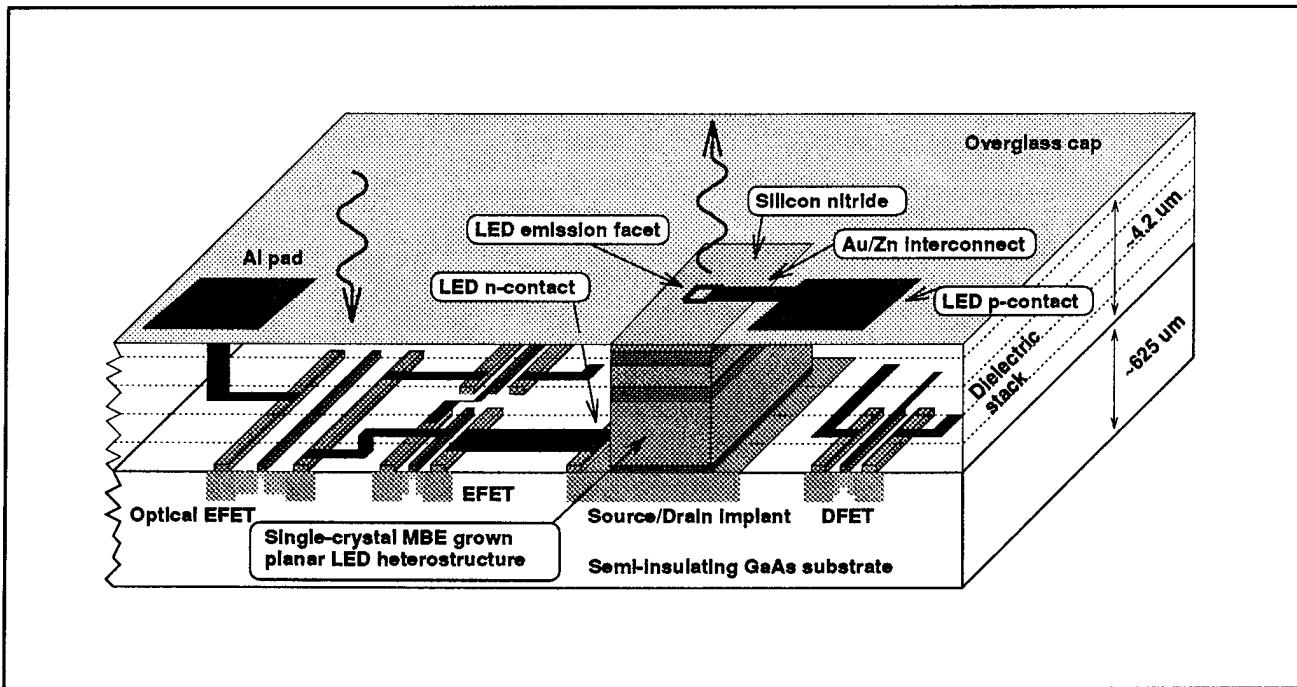


Figure 6. Artist's perspective of the third of three stages of optoelectronic circuit fabrication: (a) custom designed chip with dielectric growth window as received from the foundry; (b) single-crystal material grows in the dielectric growth window and polycrystalline material deposits on the top overglass and bond pads; and (c) as pictured, planarizing polycrystalline etch, current-confining mesa etch, Si₃N₄ chemical vapor deposition, and AuZn/Au p ohmic contact evaporation completes the fabrication sequence.

1.7 Development of an Epi-on-Electronics OEIC Technology

Sponsors

Advanced Research Projects Agency/National Center for Integrated Photonics Technology
Fannie and John Hertz Foundation Graduate Fellowship
Motorola Corporation
National Science Foundation Graduate Fellowship

Project Staff

Krishna V. Shenoy, Professor Clifton G. Fonstad, Jr.

At MIT, we are coordinating and leading a Directed Technology Project within the National Center for Integrated Photonics Technology (NCIPT) focused on developing a technology to produce high-density monolithic optoelectronic circuits for optical interconnect and smart pixel applications. While several

¹⁵ K.V. Shenoy, C.G. Fonstad, Jr., A.C. Grot, and D. Psaltis, "Monolithic Optoelectronic Circuit Design and Fabrication by Epitaxial Growth on Commercial VLSI GaAs MESFETs," *IEEE Photon. Tech. Lett.*, forthcoming.

¹⁶ A.C. Grot, D. Psaltis, K.V. Shenoy, and C.G. Fonstad, Jr., "GaAs Optoelectronic Winner-Take-All Circuit," OSA/IEEE/CLEO Annual Meeting Digest (paper CThP5), Anaheim, California, May 8-13, 1994.

approaches such as epitaxial lift-off and flip-chip bonding are currently being investigated at other sites, none offer the potential of true VLSI densities of electrical and optical devices. Our starting point is commercial VLSI gallium-arsenide (GaAs) metal-semiconductor field-effect transistor (MESFET) circuitry available at foundries such as Vitesse Semiconductor Corporation through the MOSIS service. We have demonstrated that these refractory-metal based circuits can withstand thermal cycles of up to five hours at close to 500°C, which is within the range of certain molecular beam epitaxy (MBE) techniques capable of growing sophisticated optical devices. By overlaying existing standard foundry process etches, it is possible to specify dielectric growth windows (DGWs) during circuit layout. The second fabrication step is to epitaxially grow optical heterostructures on the fully processed commercial electronics-only GaAs wafer or chip. Single-crystal, device-quality material grows from the GaAs wafer to the top of the interlevel-metal dielectric stack (DWG sidewalls) in the DWGs while polycrystalline material deposits in the inter-DWG areas. The optical devices are then fabricated by removing the polycrystalline deposits and defining the optical devices with standard photolithography, wet/dry etches and metallization

processes. The fourth and final optoelectronic fabrication step is to monolithically interconnect the optical and electrical devices which can often be combined with the device metallization.

We have successfully demonstrated the integration of LEDs with several circuits¹⁷ and are currently working on large-scale arrays¹⁸ and expanding the library of optical devices for integration. A multi-project OEIC chip (MIT-OEIC-3/NCIPT-OEVLSI-1 submitted to MOSIS in November 1994) is our initial attempt at involving many groups (five) from around the country in an epi-on-electronics OEIC chip.¹⁹ It involves cell designs for both smart pixel (i.e., surface-normal configuration) OEICs and integrated optics (i.e., in-plane, fiber-coupled configuration) OEICs. Cells are included for LED drives and arrays, edge- and surface-emitting laser diodes with and without drivers, SEEDs and window modulators with high-voltage drive circuits, MSM detectors and transimpedance amplifiers, fiber-coupled detectors, and guided-wave-optics modulators. Additional test and process monitor structures are also included. We have also initiated a project, OPTOCHIP, to provide eight groups from around the world with optoelectronic ASICs with LEDs, optical-FETs, MSM detectors with transimpedance amplifiers and VLSI density GaAs analog and digital circuitry.

¹⁷ K.V. Shenoy, C.G. Fonstad, Jr., A.C. Grot, and D. Psaltis, "Monolithic Optoelectronic Circuit Design and Fabrication by Epitaxial Growth on Commercial VLSI GaAs MESFETs," *IEEE Photon. Tech. Lett.*, forthcoming; A.C. Grot, D. Psaltis, K.V. Shenoy, and C.G. Fonstad, Jr., "Integration of LEDs and GaAs Circuits by MBE Regrowth," *IEEE Photon. Tech. Lett.* 6(7): 819-821 (1994).

¹⁸ A.C. Grot, D. Psaltis, K.V. Shenoy, and C.G. Fonstad, Jr., "Large Scale Integration of LEDs and GaAs Circuits Fabricated through MOSIS," ICO/OSA/SPIE/LEOS 1994 International Conference on Optical Computing Digest (Invited plenary paper), Scotland, United Kingdom, August 22-25, 1994.

¹⁹ C.G. Fonstad and K.V. Shenoy, "Application Specific OEICs Fabricated using GaAs IC Foundry Services," IEEE/LEOS 1994 Summer Topical Meeting on Integrated Optoelectronics Digest (Invited paper W3.4), Lake Tahoe, Nevada, July 6, 1994.

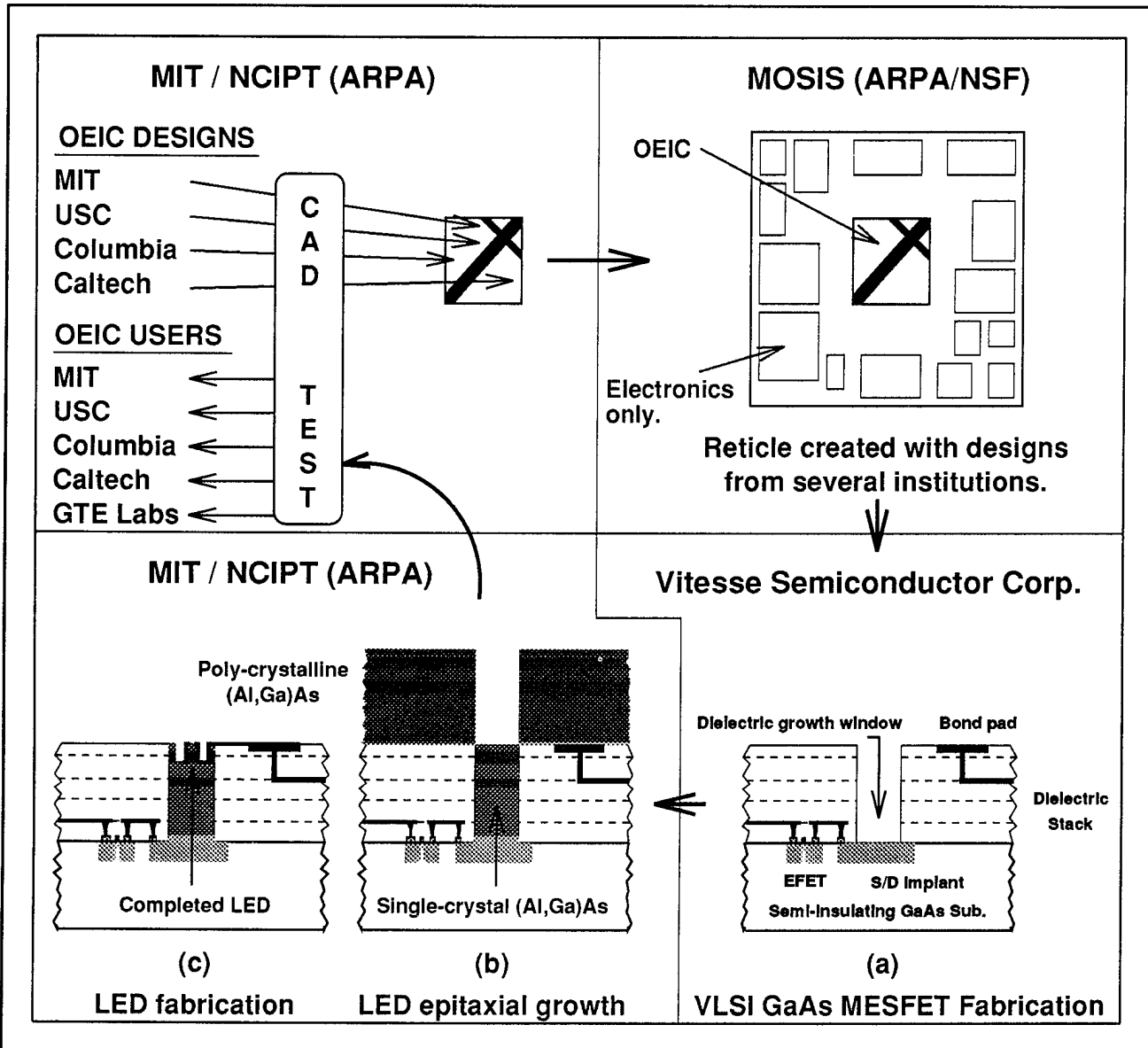


Figure 7. Schematic illustration of the Epi-on-Electronics fabrication flow (read clockwise starting from upper-left). OEIC designs are combined at MIT and the VLSI GaAs circuits are fabricated at Vitesse Semiconductor Corporation via the MOSIS foundry service. Heterostructures (LEDs) are then grown in dielectric openings, which expose the underlying GaAs substrate, and the resulting epi-islands are processed into functional devices. Finally, the optical and electrical devices are monolithically interconnected and the chips are disseminated.

1.8 Integrated Optics Circuits Based on Commercial GaAs Integrated Circuits

Sponsors

Advanced Research Projects Agency/National Center for Integrated Photonics Technology
Motorola Corporation

Project Staff

Yakov Royter, Professor Clifton G. Fonstad, Jr.

Recently, due to the fiber optic telecommunications boom, much work has been done in the area of integration of semiconductor optical devices, such as modulators, detectors, and lasers, with driving electronics made up of MESFETs, MODFETs, and HBTs. However, the necessity to optimize both the optical and electronic devices simultaneously make this approach slow. Our project is to integrate mature GaAs electronic ICs with optical components, by selectively growing using MBE our optical devices on open areas of commercial quality IC chips. This has already been successfully achieved

for integrating light emitting diode array with such electronics.²⁰ Our goal is to demonstrate a working integrated optics switching circuit fabricated on and integrated with a GaAs IC chip. The basic optical components of this system are passive waveguides, waveguide couplers and Y-junctions, phase modulators, and detectors. The electronics will consist of driving and amplifying circuits for the modulators, and detectors, as well as signal detection and routing decision digital circuits.

The first version of the circuit will consist of conventional double heterostructure waveguides and electro-optic modulators, with total internal reflection mirror coupled MSM detectors.²¹ A schematic of a waveguide integrated with a modulator, a detector, and the electronics is shown in figure 8. A quantum well heterostructure version of the system will also be attempted to take advantage of the strong electro-optic effect in QW structures. The

AlGaAs growth will have to be done below 500°C to not cause drastic deterioration of the IC performance.²² Therefore, a study of lower temperature grown AlGaAs is being performed. Finally, a structure with an InGaAs detector layer will be attempted, which will enable the system to operate at the industry standard wavelength of 1.3 μm .

In addition to optical device design, circuit design is also being carried out. The modulator driver circuitry has been designed, laid out, and sent to the Vitesse MOSIS foundry. These circuits are expected to be able to drive the modulators from 0-9V with DCFL inputs of 0-0.6V, with speeds of up to 200 MHz, providing up to 1 mA of leakage current, and without gate breakdown. (The simulations were done using Vitesse HSPICE device parameters.) To control the backgating effect, a guard-ring layout technique was employed.

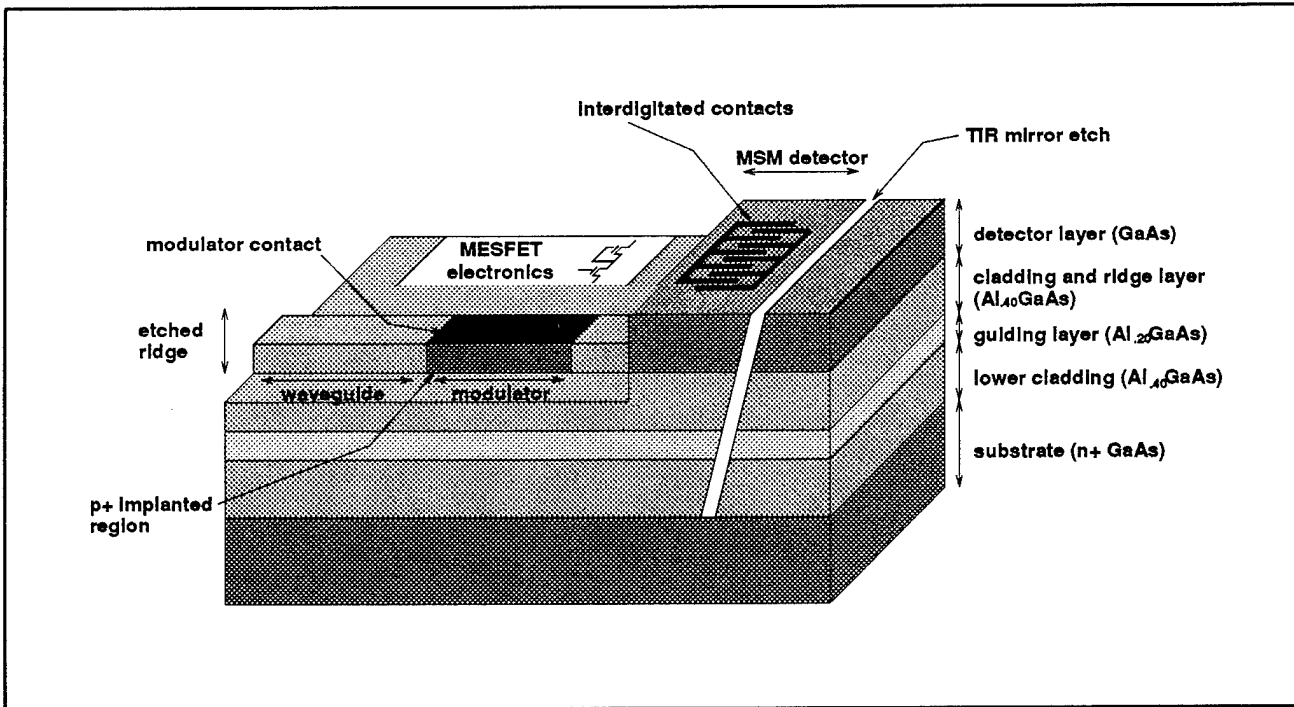


Figure 8. A waveguide/modulator/detector/electronics integration scheme.

²⁰ K.V. Shenoy, P.R. Nuykens, C.G. Fonstad, G.D. Johnson, W.D Goodhue, and J. P. Donnelly, *Proceedings of the IEEE/LEOS Annual Meeting*, San Jose, California, November 15-18, 1993.

²¹ D.E. Bossi, R.W. Ade, R.P. Basilica, and J.M. Berak, *IEEE Photon. Tech. Lett.* 5(2): 166-169 (1991).

²² E. Braun, *Elevated Temperature Stability of Gallium Arsenide Integrated Circuits*, S.M. thesis, Dept. of Electr. Eng. and Comput. Sci., MIT, 1995.

1.9 Growth of Distributed Bragg Reflector and Multiple Quantum Well Heterostructures at Reduced Temperature

Sponsors

Advanced Research Projects Agency/National Center for Integrated Photonics Technology
 Fannie and John Hertz Foundation Graduate Fellowship
 National Science Foundation Graduate Fellowship

Project Staff

Hao Wang, Paul S. Martin, Krishna V. Shenoy, Professor Clifton G. Fonstad, Jr.

Growth of optical devices on commercially available VLSI GaAs electronic circuits via the epi-on-electronics (E-o-E) integration technique employing molecular beam epitaxy (MBE) requires growth temperatures below 500°C to avoid deterioration of the underlying circuitry.²³ Furthermore, a temperature even lower than 500°C is required to grow thick, and therefore lengthy, growth sequences of optical devices such as vertical cavity surface emitting lasers (VCSELs) and self electro-optic effect device (SEED) modulators.

An important issue to be addressed is whether the reduced temperature MBE growth can produce high

quality optical devices and how the optical quality at low growth temperatures can be optimized. We are currently investigating lowered-temperature growth of distributed Bragg reflectors (DBRs) and multiple quantum wells (MQWs), which are constituent elements of VCSELs and SEEDs; we are also growing complete VCSELs and SEEDs. While the growth temperature constraint does not allow fully optimized quantum well formation and ideal interfacial quality in superlattices during conventional MBE, we are exploiting alternative methods of low-temperature epitaxy, such as atomic layer epitaxy (ALE) via MBE, pulsed arsenic MBE and stoichiometric (unity group III to group V flux ratio) MBE. By reducing the arsenic overpressure, while still staying above unity group III-V flux ratio, we have demonstrated growth-temperature independent AlGaAs DBRs reflectivity down to growth temperature as low as 400°C.

In addition to high optical quality mirrors, low modulation-voltage MQWs are also essential for integration with low-voltage digital circuits which typically have 0 V and -2.0 V rails. SEED devices grown at 500°C have been fabricated and function well with an 8 V voltage swing. Asymmetric triangular quantum wells promise reduced drive voltages. SEEDs will soon be integrated with enhancement- and depletion-mode MESFET VLSI circuits, which were designed as a part of the E-o-E development chip, to produce dual-rail digital optical logic circuits which will effectively compete with ATC depletion-mode only MESFET-SEED technology.

²³ K.V. Shenoy, C.G. Fonstad, Jr., and J.M. Mikkelsen, "High Temperature Stability of Refractory-Metal VLSI GaAs MESFETs," *IEEE Electron Dev. Lett.* 15: 106-108 (1994); E.K. Braun, K.V. Shenoy, C.G. Fonstad, Jr., and J.M. Mikkelsen, "Elevated Temperature Stability of GaAs Digital Integrated Circuits," submitted to *IEEE Electron Dev. Lett.*

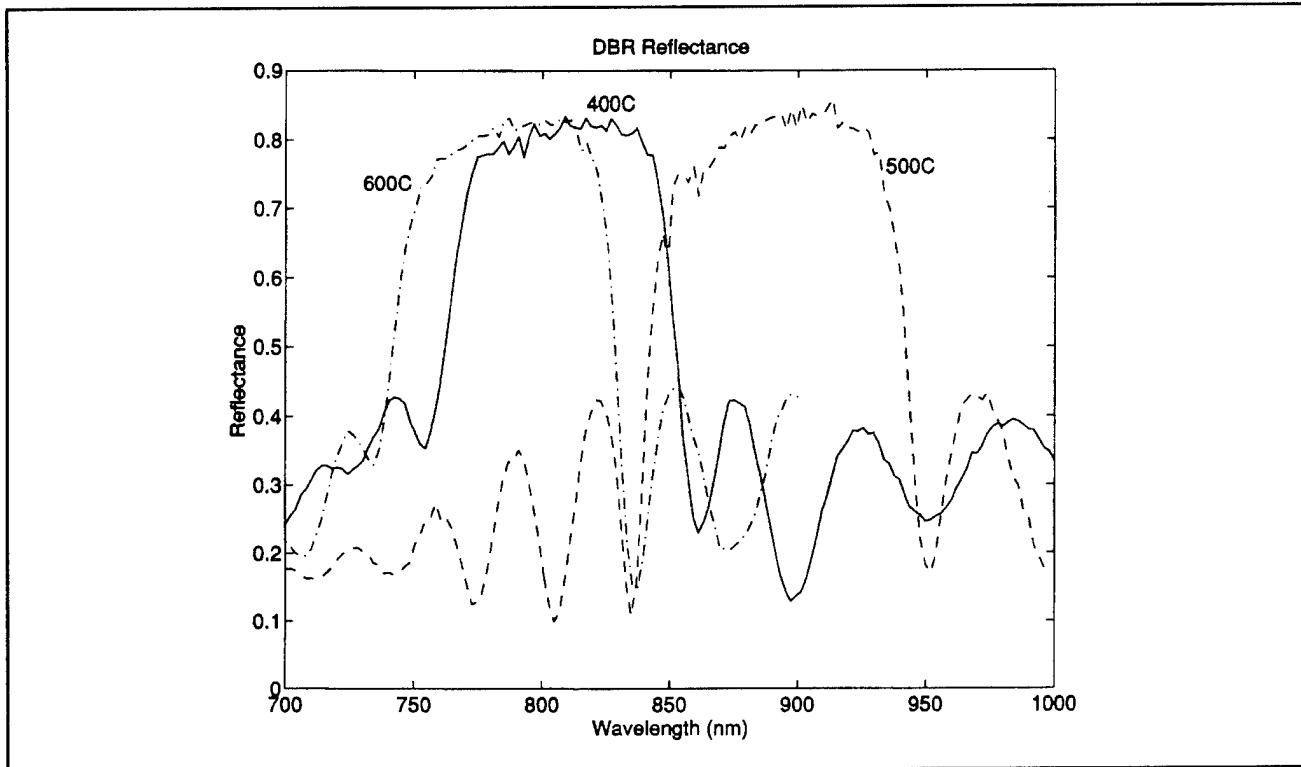


Figure 9. Reflectivities of 16 periods $\text{AlAs}/\text{Al}_{0.11}\text{Ga}_{0.89}\text{As}$ DBRs grown at temperatures ranging from 600°C down to 400°C .

1.10 Reactive Ion Etching of InGaAlAs and InGaAsP Heterostructures

Sponsor

Advanced Research Projects Agency/National Center for Integrated Photonics Technology

Project Staff

Paul S. Martin, Professor Clifton G. Fonstad, Jr.

Reactive ion etching (RIE) is an important technology for integrating optical devices on existing GaAs VLSI circuits because RIE can be done without exposing the chip to chemical etchants that damage the VLSI circuits. Also, RIE is ideal for etching vertical structures in III-V heterostructures that can be used as mirrors, distributed feedback (DFB) gratings and device isolation. Figure 10 shows a GaAs VLSI chip that has been etched in $\text{CF}_4:\text{O}_2$ and is now ready to be introduced into the molecular beam epitaxy (MBE) chamber. The growth wells are the dark colored rectangles near the top of the photo and the GaAs VLSI electronics are shown at the bottom. Figure 11 shows the face of a GaAlAs optical waveguide etched using

$\text{BCl}_3:\text{SiCl}_4$ for the RIE gases. The wall is nearly vertical and smooth enough to have minimal effect on the optical loss in the waveguide. Residual granularity in the PECVD deposited SiO_2 mask and not the RIE process are responsible for remaining roughness. Processes for etching InGaAsP based on $\text{CH}_4:\text{H}_2:\text{Ar}$ have also been implemented and are being used to etch DFB gratings for laser devices.

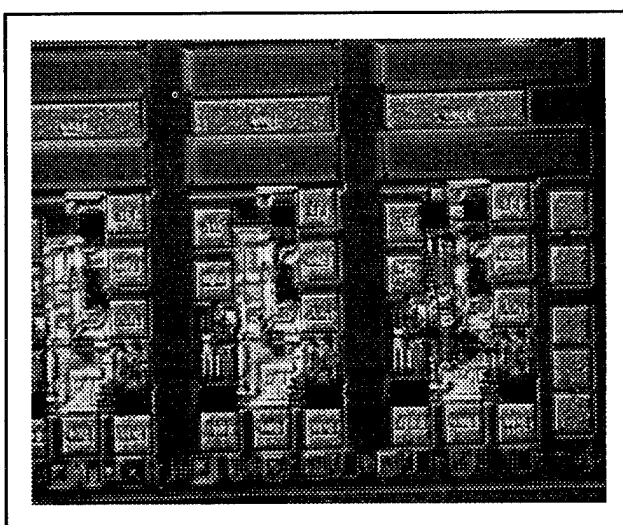


Figure 10. VLSI chip ready for epitaxy.

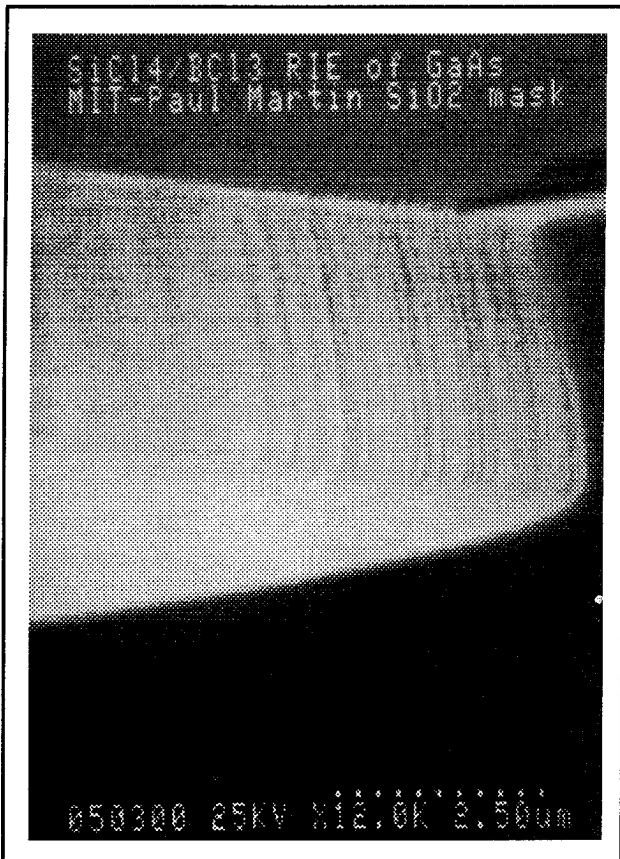


Figure 11. Edge of GaAs waveguide etched using BCl_3 and SiCl_4 .

1.11 Tunable Semiconductor Lasers

Sponsor

Advanced Research Projects Agency/National Center for Integrated Photonics Technology

Project Staff

Paul S. Martin, Professor Clifton G. Fonstad, Jr., Professor Hermann A. Haus

Wavelength division multiplexing (WDM) applications such as the channel dropping filter proposed by H.A. Haus and Y. Lai²⁴ require tunable lasers and/or optical amplifiers. We have proposed a new three-terminal independently addressable asymmetric double quantum well (IAADQW) structure (shown in figure 12), in which current injection into two quantum wells located within a single mode rib waveguide can be independently controlled. Simulations for both optical modes using the spectral index method²⁵ and tuning characteristics show a continuous tuning range of more than 20 nm about a center wavelength of $1.5 \mu\text{m}$ for the structure shown below with one 95 \AA well and one 100 \AA well as shown in figure 13. This is significantly larger than the continuous tuning range of both three-section distributed Bragg reflector (DBR) and tunable twin-guide (TTG) lasers that are competing for use in WDM systems. Furthermore, because the IAADQW laser is a three terminal device, light output power can be held constant over the entire tuning range making the IAADQW an important candidate for WDM applications. Fabrication of the IAADQW devices has begun using a self-aligned technique we developed. In this technique, a single photolithography step defines a photoresist/silicon diode layer used as: (1) an etch mask for the definition of an optical waveguide using reactive ion etching (RIE); (2) an ion implant mask that we use to confine the current injection in the lower quantum well; and (3) a lift-off stencil for defining the N-type contact to the center well region. Using this technique eliminates critical lithographic alignments that can make the fabrication of three-terminal devices prohibitively complex.

²⁴ H.A. Haus and Y. Lai, "Narrow-band Optical Channel Dropping Filter," *IEEE J. Lightwave Tech.* 10: 57-62 (1992).

²⁵ P. Martin, J. Chen, C.G. Fonstad, and H.A. Haus, "Application of the Spectral Index Method to Laser Diode Design," *IEEE J. Lightwave Tech.*, forthcoming.

IAADQW Process Summary

- 1) SiO₂ Deposition
- 2) Photolithographic Definition of Ridge Waveguide
- 3) RIE of SiO₂ and P AlGaAs Clad
- 4) Ion Implantation of Hydrogen Current Confinement Layer
- 5) AuGe Evaporation and SiO₂ Assisted Liftoff
- 6) SiO₂ RIE Planarization
- 7) AuZn P Contact Evaporation

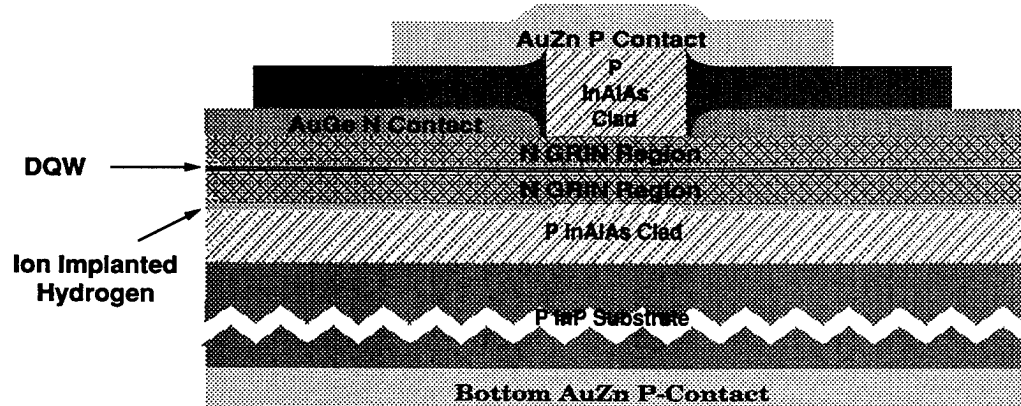


Figure 12. IAADQW Process Description.

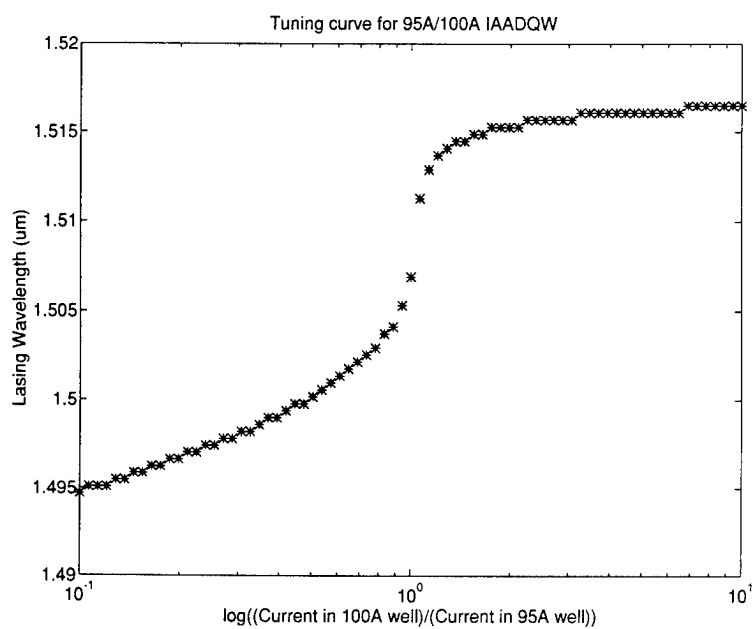


Figure 13. IAADQW Simulated Tuning Range.

1.12 Application of the Spectral Index Method to Laser Diode Design

Sponsor

Advanced Research Projects Agency/National Center for Integrated Photonics Technology

Project Staff

Jerry C. Chen, Paul S. Martin, Professor Clifton G. Fonstad, Jr., Professor Hermann A. Haus

The spectral index method (SIM) has been compared to the effective index method (EIM) and the beam propagation method (BPM) for the calculation of the optical mode index and mode profile in a

prototypical distributed feedback (DFB) rib waveguide laser diode. The performance metric normally used to evaluate such methods, modal index, was shown to be insufficient as a metric of comparison when one is interested in designing a DFB laser diode cavity. Therefore, in addition to n_{mode} , the quantum well filling factor, Γ , and grating coupling coefficient, κ , are included in the metric for comparison. Table 1 shows the results of the analysis for the DFB laser diode shown in figure 14. Although n_{mode} and b are similar for the three methods, the important device parameters, Γ and κ , are significantly different illustrating the importance of using the proper metric. Using this analysis, SIM is found to yield superior results to EIM and to give results comparable to BPM as shown by the mode profile in figure 15, almost two orders of magnitude faster.²⁶

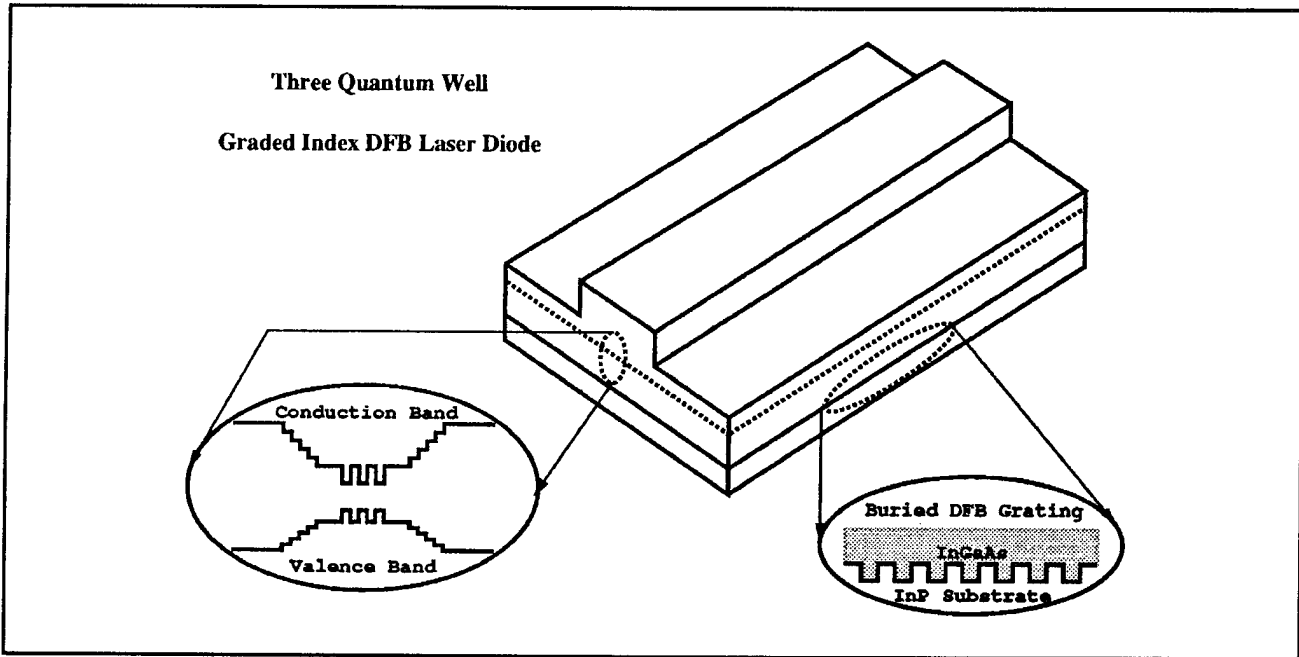


Figure 14. DFB Laser Diode Schematic.

²⁶ P. Martin, J. Chen, C.G. Fonstad, and H.A. Haus, "Application of the Spectral Index Method to Laser Diode Design," *IEEE J. Lightwave Tech.*, forthcoming.

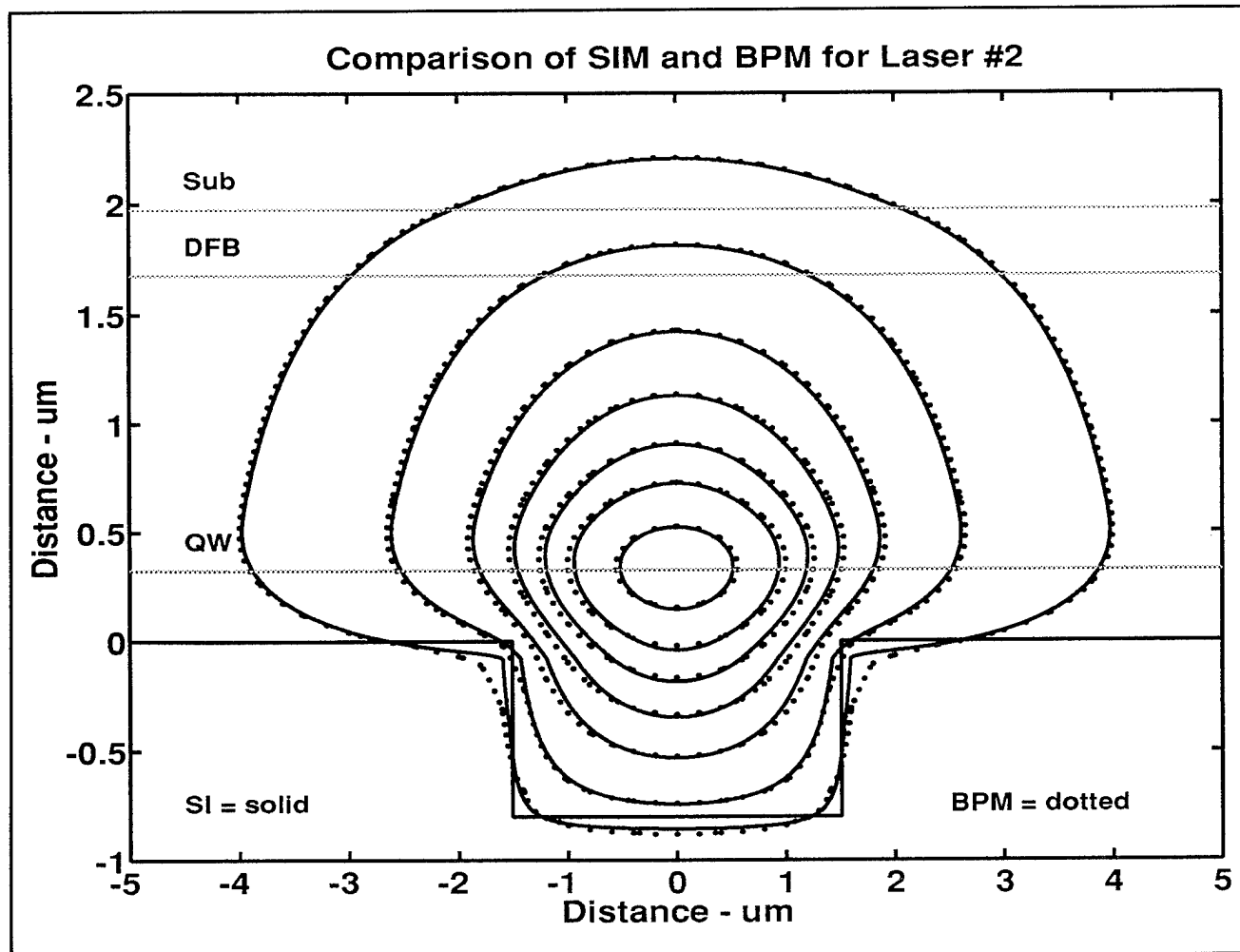


Figure 15. Mode Profile Comparison of SIM and BPM.

1.13 Normal Incidence Quantum Well Infrared Photodetector

Sponsors

National Science Foundation
U.S. Navy - Office of Naval Research²⁷

Project Staff

Hao Wang, Paul S. Martin, Janet L. Pan, Professor
Clifton G. Fonstad, Jr.

Recent work by Peng et al. at MIT²⁸ has shown that TE intersubband absorption in strained narrow quantum wells can have an absorption strength as large as the well known TM intersubband absorption on which current QWIP devices are based. This important finding has led us to begin the development of normal incidence QWIP devices that take advantage of TE intersubband absorption. Because these devices are normal incidence, no surface lenses or beveled surfaces are needed to direct the light into the quantum well active region, thus making the devices ideal for integration with existing GaAs electronic circuits both as individual devices and as large area arrays. Figure 16a shows the TE absorption from a single strained

²⁷ STTR contract with Advanced Device Technology, Nashua, New Hampshire.

²⁸ L.-H. Peng, J.H. Smet, T.P.E. Broekaert, and C.G. Fonstad, "Transverse Electric and Transverse Magnetic Polarization Active Intersubband Transitions in Narrow InGaAs Quantum Wells," *Appl. Phys. Lett.* 61(17): 2078-2080 (1992); L.-H. Peng and C.G. Fonstad, "Normal Incidence Intersubband Transitions in Si-doped InGaAs Multiple Quantum Wells," *Appl. Phys. Lett.* 62(19): 2413-2415 (1993).

quantum well on InP as measured at MIT. Figure 16b shows the schematic of our current normal incidence QWIPs.

An important aspect of our effort involves the combination of our work on normal incidence QWIPs with the epitaxy-on-electronics monolithic integration

process. Working with Advanced Device Technologies, Inc., Nashua, New Hampshire, we are investigating integration of normal incident QWIPs with gallium arsenide, addressing electronics and transimpedance amplifiers to produce monolithic infrared focal plane arrays.

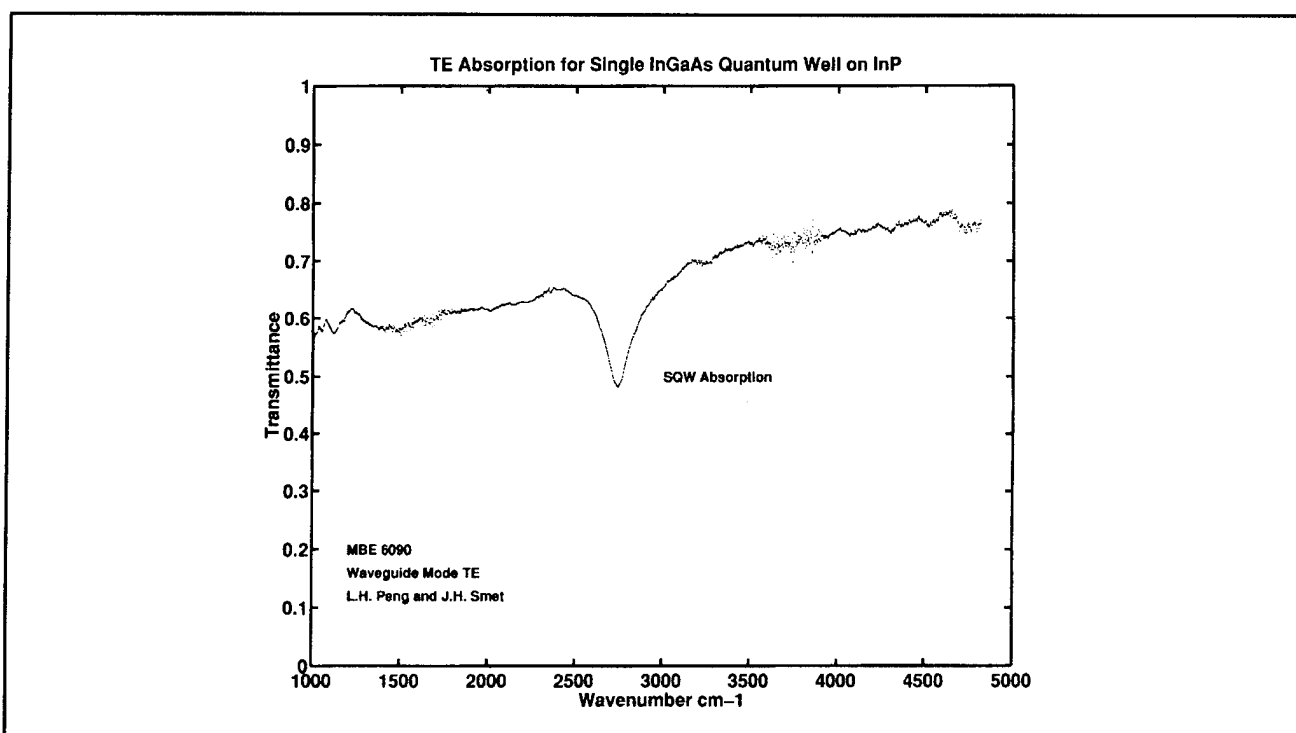


Figure 16(a). TE absorption from single InGaAs quantum well.

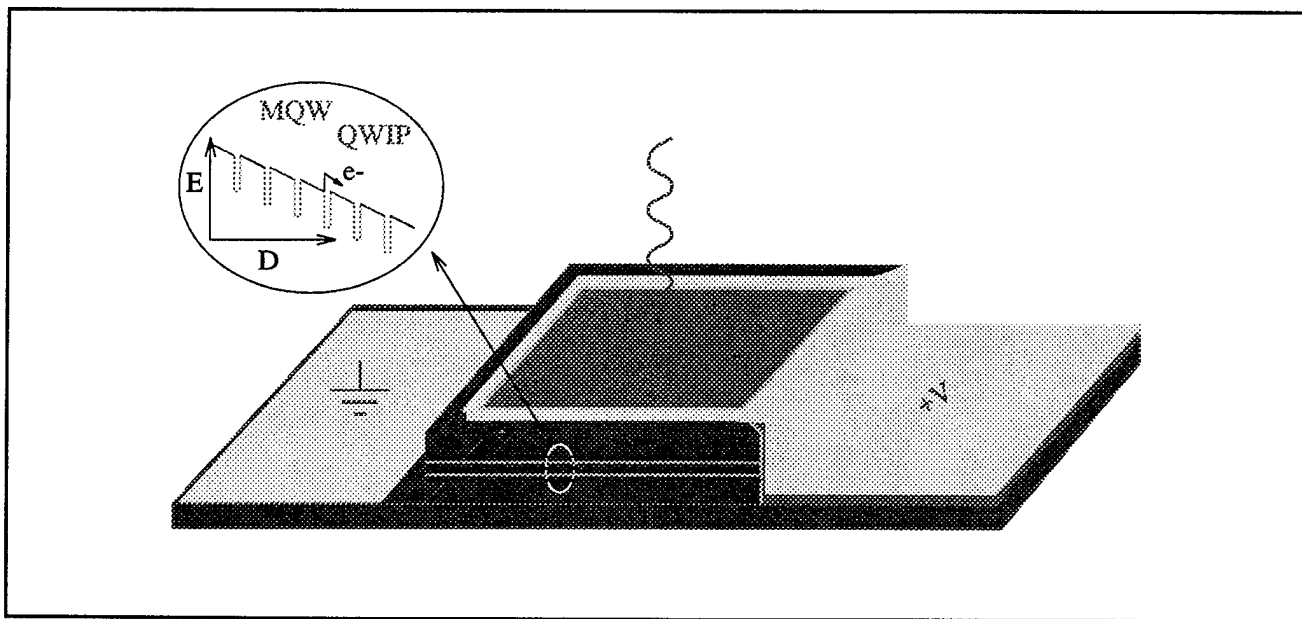


Figure 16(b) QWIP device schematic.

1.14 Fourteen-Band $k \cdot p$ Analysis of Intersubband Transitions in Conduction Band Quantum Wells

Sponsor

National Science Foundation

Project Staff

Lung-Han Peng, Professor Clifton G. Fonstad, Jr.

Quantum wells (QWs) are layered semiconductor structures engineered so that electrons are confined to move within a thin planar layer. Intersubband transitions are observed between the quantized QW conduction subbands. Two types of QW intersubband single particle excitation (SPE) activity are depicted in figure 17a. The first one is a direct infrared (IR) absorption process that involves two conduction subbands. The second one is an indirect Raman scattering process that invokes an additional intermediate state, e.g., heavy hole in figure 17b. The energies involved in QW intersubband transitions are typically in the IR spectral range from 0.1 to 0.8 eV²⁹ depending on the structure design. The main driving force for pursuing III-V QW IR intersubband devices (detectors, modulations, and lasers) is to take advantage of the reliable III-V materials growth and device process techniques. In addition, intersubband transitions are expected to have stronger oscillator strengths and fast relaxation times that make them attractive for studying linear and nonlinear optical effects.

We discuss multiband coupling effects on electronic intersubband single particle excitations (SPE) of infrared (IR) and Raman processes in type I quantum wells (QWs). Interband couplings between $\Gamma_7^c - \Gamma_5^c$, $\Gamma_7^c - \Gamma_5^s$, and $\Gamma_5^s - \Gamma_5^c$ bulk band edges are treated within 14-band $k \cdot p$ first-order perturbation theory. Enhanced band-mixing effects are observed at Brillouin zone center ($k_{\parallel} = 0$) because of quantization effects ($k_2 \neq 0$). For zinc-blende-type QWs, $\Gamma_5^s - \Gamma_5^c$ band-mixing effects at high-lying Γ_7^c conduction subbands contribute (x,y)-

polarized IR and $z(x,x)\bar{z}$ - and $z(x,y)\bar{z}$ -polarized Raman intersubband SPE. Intersubband polarization splittings occur when the QWs are under biaxial strains.

In particular, we found that the ratio of the TM to TE IR intersubband metrix element is

$$(TM)_{\text{inter}}:(TE)_{\text{inter}}$$

$$= p_{T,m=2} \left(\frac{mP_0^2}{E_0 + E_{m=2}} - \frac{mP_1^2}{E_1 - E_{m=2}} \right)$$

$$: p_{T,m=2} \left(\frac{mP_0^2}{E_0 + E_{m=2}} \frac{Q}{P_0} + \frac{mP_1^2}{E_1 - E_{m=2}} \frac{Q}{P_1} \right)$$

Using very conservative numbers for a GaAs/AlAs QW structure with a QW width of ~ 4.0 - 5.0 nm, we find the TM/TE ratio in the above equation to be approximately 1. This result is supported by recent measurements on GaAs/AlAs QWs and has important implications for the development of normal incidence QW devices.

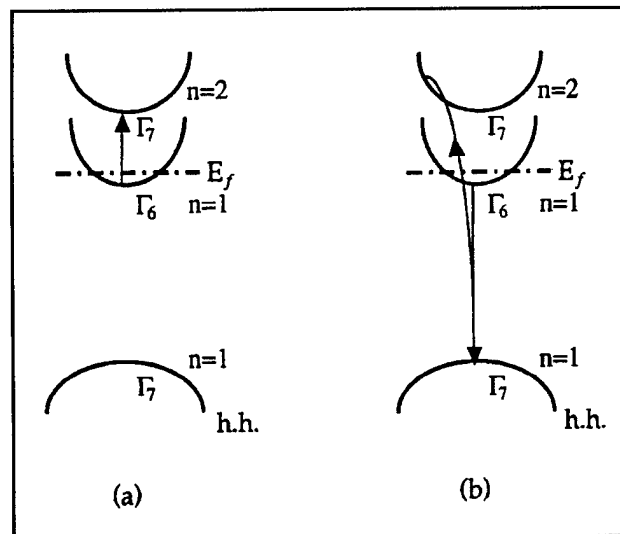


Figure 17. (a) Infrared absorption; (b) Raman scattering.

²⁹ L.C. West and S.J. Egash, "First Observation of an Extremely Large-dipole Infrared Transition within the Conduction Band of a GaAs Quantum Well," *Appl. Phys. Lett.* 46(12): 1156-1158 (1985); J.H. Smet, L.H. Peng, Y. Hirayama, and C.G. Fonstad, "Electron Intersubband Transitions to 0.8 eV (1.55 μm) in InGaAs/AlAs Single Quantum Well," *Appl. Phys. Lett.* 64(8): 986-987 (1994).

1.15 Study of Intersubband Transitions in Ultra-Narrow Quantum Wells

Sponsors

National Science Foundation
Toshiba Corporation

Project Staff

Janet L. Pan, Norio Iisuka, Lung-Han Peng, Professor Clifton G. Fonstad, Jr.

We are studying intersubband transitions in very narrow quantum wells for the purpose of making high speed, high responsivity detectors compatible with optical fibers. In future work, we envision arrays of such devices to be monolithically integrated in optical circuits.

Previous work³⁰ has already demonstrated the observation of intersubband transitions at 1.5 microns in highly strained InGaAs quantum wells grown between InAlAs/AlAs layers on InP substrates. Present efforts use InGaAs/AlAs quantum well structures on both InP and GaAs substrates and are focused on demonstrating intersubband transitions at shorter wavelengths. We are also developing similar structures using the InGaAlP quaternary system on GaAs substrates. As intersubband transition energy increases, mass nonparabolicity has a larger effect on the position of the upper quantum well state. We are investigating the effects of mass nonparabolicity for more accurate modeling of the intersubband transition energy.

We are growing narrow GaAs quantum wells between AlAs layers on a GaAs substrate. We have chosen to study these AlAs/GaAs quantum wells because the large conduction band discontinuity between GaAs and AlAs allows for large intersubband transition energies. Further, such quantum wells are easier to grow because they are not strained. The use of GaAs substrates allows the growth of detectors compatible with present commercial GaAs VLSI.

We are looking for absorption resulting from intersubband transitions by studying the transmission characteristics of these quantum wells in modulation spectroscopy. For GaAs/AlAs multiple quantum wells, intersubband transition energies less than 650 meV ($1.9\mu\text{m}$) are predicted. To obtain higher energy intersubband transitions, thin

pseudomorphic InGaAs layers will be grown into the GaAs/AlAs multiple quantum wells.

Fast (picosecond) relaxation times are expected for intersubband transitions. Intersubband transitions at 1.5 microns are compatible with existing short pulse, high speed laser systems. Eventually, we hope to characterize the speed of devices based on intersubband transitions.

1.16 In-plane and Tilted Field Magneto-Tunneling Spectroscopy in Double InGaAs/InAlAs Quantum Well Structures on [001] and [111]B InP Substrates

Sponsor

U.S. Army Research Office

Project Staff

Jurgen H. Smet, Professor Clifton G. Fonstad, Jr., Professor Qing Hu

Of the available techniques used to analyze the energy spectra of multiple quantum well structures, one has proven to be the most powerful: magneto-quantum oscillations observed in the tunnel current as a function of applied bias when sweeping the magnetic field $B \parallel J$. Although this magnetic field configuration is a wonderful diagnostic tool to probe the subband spacings in adjacent wells as a function of applied bias, signal levels corresponding to inter-Landau level transitions are typically small. This is because higher order elastic or inelastic scattering mechanisms have to account for a change in the orbital momentum. In addition, the technique can not be used in negative differential resistance regions where the measurement circuit may be unstable. Also, at high bias voltages the magneto-oscillations due to charge storage in the first quantum well appear to dominate and inter-Landau level transition signals can not be resolved.

Tilted magnetic fields provide an alternative to alleviate many of these encountered difficulties and extend the magneto-tunneling spectroscopy capabilities. The negative differential conductance is considerably reduced in tilted magnetic fields and the main resonant peaks are broadened. As a result the analysis can be extended up to higher applied

³⁰ J.H. Smet, L.-H. Peng, Y. Hirayama, and C.G. Fonstad, "Electron Intersubband Transitions to 0.8eV (1.55 μm) in InGaAs/AlAs Single Quantum Wells," *Appl. Phys. Lett.* 64(8): 986-987 (1994).

voltages and unstable regions are no longer present. However the true benefit from the in-the-plane field component B_{\perp} stems from strongly enhanced inter-Landau transition signals. The Lorentz force associated with crossed electric and magnetic fields induces an in-the-plane direction during barrier traversal for inter-Landau level transitions to occur. Higher order scattering no longer needs to be invoked.

An interesting byproduct of these in-plane B_{\perp} measurements is the electronic dispersion of the collector well subbands. The field is related to the in-plane wavevector $\Delta k_y^{ew} - cw$ at which the dispersion curve is probed through $eB_{\perp}(\langle Z \rangle_{cw} - \langle Z \rangle_{ew})/\hbar$, where $\Delta k_y^{ew} - cw$ is acquired in-plane momentum under the action of the Lorentz force over an average distance $(\langle Z \rangle_{cw} - \langle Z \rangle_{ew})$. The averaged values are obtained using the unperturbed subband

wavefunctions. Figure 18 presents the simulated and experimental dispersion curves of the lowest valence band subbands for an $In_{0.53}Ga_{0.47}As$ quantum well on a [111] B-growth-axis InP substrate. To ensure a sufficient number of quasi-bound states, a well width of 100 Å was chosen. The current density was kept low by choosing a thick injector barrier of 90 Å to avoid significant resistive voltage drops, thereby improving the accuracy in the voltage to energy conversion. The small quantization energy of the heavy-hole subbands calls for an injector well of, in this case, 120 Å and guarantees injection from a clean two-dimensional reservoir even at low bias voltages. The experiment reproduces at least qualitatively the simulated dispersion curves. The extracted Luttinger parameters from the experiment are 10.3, 3.94, 4.42 for γ_1 , γ_2 , and γ_3 , respectively.

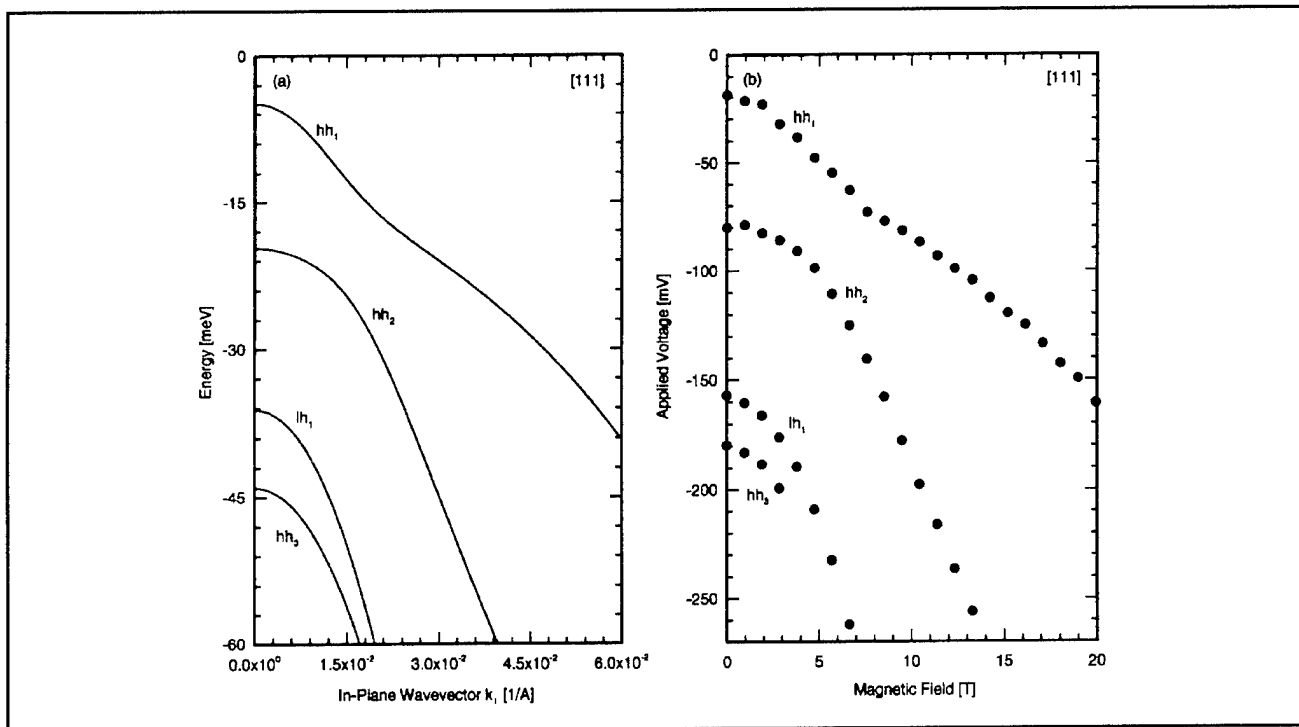


Figure 18. Simulated dispersions (a) of the lowest valence subbands for a 100 Å $In_{0.53}Ga_{0.47}As$ quantum well on [111]-growth-axis InP. Also shown in (b) are the experimental results obtained from magneto-tunneling. The peak-voltages in the I-V characteristic are plotted as a function of the in-plane magnetic field.

1.17 High-Frequency/High-Speed Characterization of Optoelectronic Devices and Integrated Circuits

Sponsor

National Science Foundation

Project Staff

Dr. Sheila Prasad, Professor Clifton G. Fonstad, Jr.

The investigation of the high-frequency and high-speed performance of optoelectronic devices and integrated circuits has been initiated. The optical and electrical components of the optoelectronic integrated circuits are to be characterized separately following which the entire OEIC is to be characterized. There are certain significant issues

arising in optoelectronic integration that directly affect the high frequency/high speed performance of the OEICs. It is proposed to explore these issues in the course of the investigation. A Hewlett-Packard 8510B automatic network analyzer and Cascade Microtech on-wafer probe station are to be used to make on-wafer scattering parameter measurements from 45 MHz to 40 GHz. Thus, microwave methods of measurement are to be used with a photodetector and auxiliary optical equipment. It has been determined that a broadband photodetector (400-1650 nm) operating from DC to 25 GHz, 17 ps rise time and 5 V/W would be the most suitable for initiating the experiments. The responsivity of this photodetector is approximately 0.2 A/W over the entire wavelength. This performance is adequate for the optical devices that are to be fabricated in the laboratory. The auxiliary optical equipment such as optical mounts, GRIN rods and fibers are being assembled.

The design of the experiment to characterize both edge emitting and surface emitting lasers is continuing. The modification of the probe station to accommodate the optical measurement system is being investigated. The method of performing measurements with ECL inputs and outputs for high speed characterization is also being investigated.

When the experimental set-up is completed, it is anticipated that measurements can be performed on optoelectronic transceivers with LED sources and lasers, M-S-M detectors and GaAs MESFET VLSI electronics. The measurement and characterization methods developed will be sufficiently general so that they are applicable to other optoelectronic circuits and systems.

1.18 In-Situ Supersonic Beam Etching of III-V Heterostructures

Sponsor

Advanced Research Projects Agency/National Center for Integrated Photonics Technology
AT&T Foundation Graduate Fellowship
National Science Foundation

Project Staff

Isako Hoshino, Professor Clifton G. Fonstad, Jr.

The development of damage-free, ultra high-vacuum (UHV) etching, cleaning, and regrowth techniques compatible with molecular beam epitaxy (MBE) and ex-situ processing of III-V heterostructures is a major challenge for device researchers. The ability to selectively pattern, etch, and overgrow

quantum heterostructures is crucial to the effective realization of integrated optical circuitry and quantum effect electronic structures. Present techniques to do this involve relatively high energy ions or plasma sources which cause substantial subsurface or structural damage, much of which is impossible to remove or repair, especially on compound semiconductors which are more susceptible to such damage than silicon.

As a solution to the problem of process-induced damages, we have begun investigating use of molecular beam (hot neutral beam, or also known as kinetic beam) techniques to etch and clean III-V substrates and heterostructures with a minimum of surface damage and allowing maximum flexibility in attaining various etch profiles. Depending on the etchant gas, it is anticipated that low energy (0.5 to 30 eV) kinetic beams can be used to (1) both directionally and isotropically etch-pattern III-V heterostructure wafers with no damage; (2) clean surfaces allowing epitaxial growth on wafers that have been removed from the UHV environment for external processing; and (3) selectively remove masking materials and clean surfaces suitable for subsequent overgrowth.

Currently, the construction of the differentially pumped UHV kinetic beam etch (KBE) system designed to use a methane-hydrogen gas mixture using a supersonic beam source is near completion. The system is designed such that it can be connected to the existing Riber 2300 solid source MBE system in the future through a transfer mechanism of special design. The initial function tests of the KBE system are scheduled to be performed in the near future. Subsequently, a full-scale characterization of the ability of the KBE system will be performed, mainly concentrating on etch rate, etch profile, and surface damage assessment. Any surface damage will be determined through photoluminescence and carrier mobility measurements using various III-V heterostructures grown by MBE.

1.19 Publications

Aggarwal R. J., and C. G. Fonstad, "High Peak-to-valley Current Ratio InGaAs/AlAs RTSs on GaAs using Relaxed InGaAs Buffers," *Electronics Letters*. Forthcoming.

Braun, E.K., K.V. Shenoy, and C.G. Fonstad. "Elevated Temperature Stability of GaAs Digital Integrated Circuits." *IEEE Electron Device Lett.* Forthcoming.

Fonstad, C.G., and K.V. Shenoy. "Application Specific OEICs Fabricated usimm GaAs IC Foundry

- Services." LEOS 1994 Summer Topical Meeting on Integrated Optoelectronics Digest, WHERE?, July 6, 1994.
- Grot, A.C., D. Psaltis, K.V. Shenoy, and C.G. Fonstad. "Integration of LED's and GaAs Circuits by MBE Regrowth," *IEEE Photon. Tech. Lett.* 6: 819-821 (1994).
- Martin, P. S., J. C. Chen, C. G. Fonstad, and H. A. Haus. "Application of the Spectral Index Method to Laser Diode Design." *IEEE Photonics Technology Lett.* Forthcoming.
- Peng, L.-H., and C.G. Fonstad. "Multiband Coupling Effects on Electron Quantum Well Intersubband Transitions." *J. Appl. Phys.* 77: 747-754 (1995).
- Peng, L.-H., and C.G. Fonstad. "Spatial Confinement Effects on Type II Quantum Well Intersubband Transitions." *Appl. Phys. Lett.* Forthcoming.
- Shenoy, K.V., C.G. Fonstad, and J.M. Mikkelsen. "High-Temperature Stability of Refractory-Metal VLSI GaAs MESFETs." *IEEE Electron Device Lett.* 15:106-108 (1994).
- Shenoy, K.V., C.G. Fonstad, A.C. Grot, and D. Psaltis. "Monolithic Optoelectronic Circuit Design and Fabrication by Epitaxial Growth on Commercial VLSI GaAs MESFETs," *IEEE Photon. Tech. Lett.* Forthcoming
- Smet, J.H., L.H. Peng, Y. Hirayama, and C.G. Fonstad. "Electron Intersubband Transitions to 0.8 eV (1.55 μ m) in InGaAs/AlAs Single Quantum Wells." *Appl. Phys. Lett.* 64: 986-988 (1994).

Theses

- Braun, E. *Elevated Temperature Stability of Gallium Arsenide Integrated Circuits*. S.M. thesis. Dept. of Electr. Eng. and Comput. Sci., MIT, 1995.
- Peng, L.-H. *Electron Intersubband Transitions in n+ InGaAs Quantum Wells: Optical Selection Rules and Strain Effects*. Ph.D. diss. Dept. of Applied Physics, Harvard University, 1994.
- Smet, J.H. *Intrawell and Interwell Intersubband Transitions in Single and Multiple Quantum Well Heterostructures*. Ph.D. diss. Dept. of Electr. Eng. and Comput. Sci., MIT, 1994.

Chapter 2. Physics of InAlAs/InGaAs Heterostructure Field-Effect Transistors

Academic and Research Staff

Professor Jesús A. del Alamo

Graduate Students

Mark H. Somerville

Undergraduate Students

Tracy E. Adams, James W. Reiner

Technical and Support Staff

Michael J. Weinberg

2.1 Introduction

Sponsors

Joint Services Electronics Program
 Contract DAAL03-92-C-0001
 Grant DAAH04-95-1-0038

Raytheon Corporation
 Contract 90-58203

Texas Instruments
 Agreement dated 08/14/91

The goal of this project is to develop InAlAs/InGaAs heterostructure field-effect transistors suitable for millimeter-wave high-power applications. The suitability of this material system for low-noise amplification is now unquestionable. Obtaining a high breakdown voltage is, however, still rather difficult, and it usually comes with severe trade offs. This fact seriously limits the suitability of this material system for high-power millimeter-wave applications.

Over the last few years, we have been engaged in research on how to improve the breakdown voltage of InAlAs/InGaAs HFETs, that is, the maximum voltage that the device can handle. Our work has provided technological design criteria that are now

widely used in industry, such as employing AlAs-rich InAlAs pseudoinsulators¹ and carrying out selective recessed-mesa sidewall isolation.² We also recently identified the detailed physical mechanisms responsible for breakdown in InAlAs/n⁻-InGaAs HFETs fabricated at MIT.³ We found that the breakdown path involves two different processes in series. First, electron thermionic field emission takes place from the gate over the InAlAs barrier into the InGaAs channel. This is followed by hot electron relaxation in the channel with impact ionization of electron-hole pairs. More recently, in collaboration with Daimler-Benz in Ulm, Germany, we identified the same mechanisms in action in state-of-the-art InAlAs/InGaAs Modulation-Doped Field-Effect Transistors (MODFETs).⁴ Finally, last year we identified the existence of substantial impact ionization in the channel of our own InAlAs/InGaAs HFETs under regular operating conditions. This is important for understanding noise in these devices.

In the last period of performance, we have developed S-passivation technology for InAlAs/InGaAs MODFETs, and we have integrated it into a complete 0.8 μm gate length device process. S passivation is claimed to reduce Fermi level pinning

¹ S.R. Bahl, W.J. Azzam, and J.A. del Alamo, "Strained-Insulator In_xAl_{1-x}As/n⁻-In_{0.53}Ga_{0.47}As Heterostructure Field-Effect Transistors," *IEEE Trans. Electron Dev.* 38(9): 1986-1992 (1991).

² S.R. Bahl and J.A. del Alamo, "Elimination of Mesa-Sidewall Gate-Leakage in InAlAs/InGaAs Heterostructures by Selective Sidewall Recessing," *IEEE Electron Dev. Lett.* 13(4): 195-197 (1992).

³ S.R. Bahl and J.A. del Alamo, "Physics of Breakdown in InAlAs/n⁻-InGaAs Heterostructure Field-Effect Transistors," *IEEE Trans. Electron Dev.* 41(12): 2268-2275 (1994).

⁴ S.R. Bahl, J.A. del Alamo, J. Dickmann, and S. Schildberg, "Off-State Breakdown in InAlAs/InGaAs MODFETs," *IEEE Trans. Electron Dev.* 42(1): 15-22 (1995).

at the surface of III-V compound semiconductors. There are two ways in which this could be exploited to improve the power handling capability of InAlAs/InGaAs MODFETs. First, if the Fermi level can be unpinned, S passivation at the exposed gap between the gate and the drain should smooth the electric field at the drain end of the channel. This ought to result in an improvement of the breakdown voltage. Furthermore, if S passivation is applied to the interface between an appropriate gate metal and the semiconductor, the Schottky barrier height of the gate could be improved. This should result in a reduction of gate leakage and an improvement of the breakdown voltage. Our first experimental results indicate modest improvements in the expected direction but it is yet unclear the physics that are at play. The following sections describe in more detail our technical findings and our key conclusions.

2.2 An Integratable S-passivation Process for the InAlAs/InGaAs System

For several years, the use of sulfur-containing compounds for the passivation of the surfaces of both GaAs and InP has received considerable attention. It has been demonstrated that treatment with sulfur-containing compounds prior to evaporation can yield substantial shifts in Schottky barrier height towards the ideal value dictated by the metal work function.⁵ Recently, similar results were reported for Au Schottky barriers on InAlAs.⁶ While these results offer great promise, it is unclear whether the improvement in Schottky barrier height on InAlAs is due to reduction in pinning, or to a shift in the position of the pinned Fermi level. Furthermore, the work reported previously has utilized aggressive surface cleans prior to sulfur treatment. An effective S passivation process that is suitable to integration with a complete HFET fabrication process has yet to be developed.

Based on a literature search, we selected $(\text{NH}_4)_2\text{S}_x$ as the most likely candidate for an integratable S treatment of the InAlAs surface. We first carried out two process compatibility tests that any integratable process had to meet:

- We measured the etch rate of $(\text{NH}_4)_2\text{S}_x$ on InAlAs, InGaAs and GaAs. InGaAs and GaAs

exhibited minimal etch rates (less than 10 Å/hr). InAlAs was etched at a rate of about 100 Å/hr. These results are adequate for process integration.

- We established that the S treatment is compatible with conventional photolithography. No pattern degradation or adhesion difficulties were observed after $(\text{NH}_4)_2\text{S}_x$ treatment of a photoresist patterned wafer.

Following these process compatibility tests, we carried out an additional test to select the proper chemical treatment prior to $(\text{NH}_4)_2\text{S}_x$ application. We fabricated Van der Pauw structures in typical InAlAs/InGaAs MODFET heterostructures. These structures were subject to several pretreatments as summarized in table 1. In all cases, a selective succinic-acid based gate recess was performed just prior to S treatment as this is a key constrain in the process. In addition to a reference sample without S treatment, four different pretreatment processes were examined, as listed in table 1. The sheet carrier concentration before and after S passivation was measured for all samples.

The results summarized in table 1 indicate that the omission of a pretreatment before $(\text{NH}_4)_2\text{S}_x$ application resulted in the maximum change in the sheet carrier concentration (with respect to the reference sample) as a result of S passivation. The other approaches were much less effective. From a process integration point of view, this is also a favorable alternative because of its simplicity. In consequence we decided not to perform any pre-treatment between succinic acid selective etching and $(\text{NH}_4)_2\text{S}_x$ application.

2.3 S-passivated InAlAs/InGaAs MODFETs

Having selected the process parameters of the S treatment, we proceeded to carry out a complete fabrication run of InAlAs/InGaAs MODFETs. The starting heterostructure is shown in figure 1. This heterostructure was designed in collaboration with Raytheon Research Division, and it was MBE-grown at Raytheon by Bill Hoke. This design incorporates a number of features that are targeted for power applications. First, it is a double-

⁵ M.S. Carpenter, M.R. Melloch, and T.E. Dungan, "Schottky Barrier Formation on NH_4S -treated N- and P-type (100) GaAs," *App. Phys. Lett.* 53(1): 66-68 (1988); J. Fan, H. Oigawa, and Y. Nannichi, "Metal-dependent S-barrier Height with the $(\text{NH}_4)_2\text{S}_x$ -treated GaAs," *Jap. J. App. Phys.* 27(11): L2125-2127 (1988).

⁶ N. Yoshida, M. Totsuka, J. Ino, and S. Matsumoto, "Surface Passivation of InAlAs using $(\text{NH}_4)_2\text{S}_x$ and $\text{P}_2\text{S}_5/\text{NH}_4\text{S}$," *Jap. J. App. Phys.* 33(3A) part 1: 1248 (1994).

Sample ID	E	F	G	H	I
Gate Recess	Succinic	Succinic	Succinic	Succinic	Succinic
Pre-Treatment	-	-	Semico Clean	5% NH ₄ OH	Dilute H ₂ SO ₄ :H ₂ O ₂
(NH ₄) ₂ S _x Treatment	-	10 min.	10 min.	10 min.	10 min.
Relative change in sheet concentration ($\Delta n_s/n_s$)	- 2%	- 16%	- 6%	- 5%	- 3%

Table 1. Summary of process and sheet charge concentration results in five samples as a function of the chemical treatment applied prior to S passivation.

heterostructure with doping above and below the channel. Second, we used delta-doping on both layers. Third, we incorporated a thin undoped cap that is to be selectively etched. Our insulator is thicker than usual, 300 Å, in order to obtain a high breakdown voltage. The channel is thick so as to get high transconductance and low output conductance and therefore high gain.

Our process is standard. We use SiN_x-assisted liftoff for all our metal layers with the exception of the pads which are performed using chlorobenzene. The ohmic contacts are made by rapid-thermally annealing a AuGe bilayer. Before S treatment and gate evaporation, we perform selective mesa sidewall recessing to eliminate a very deleterious

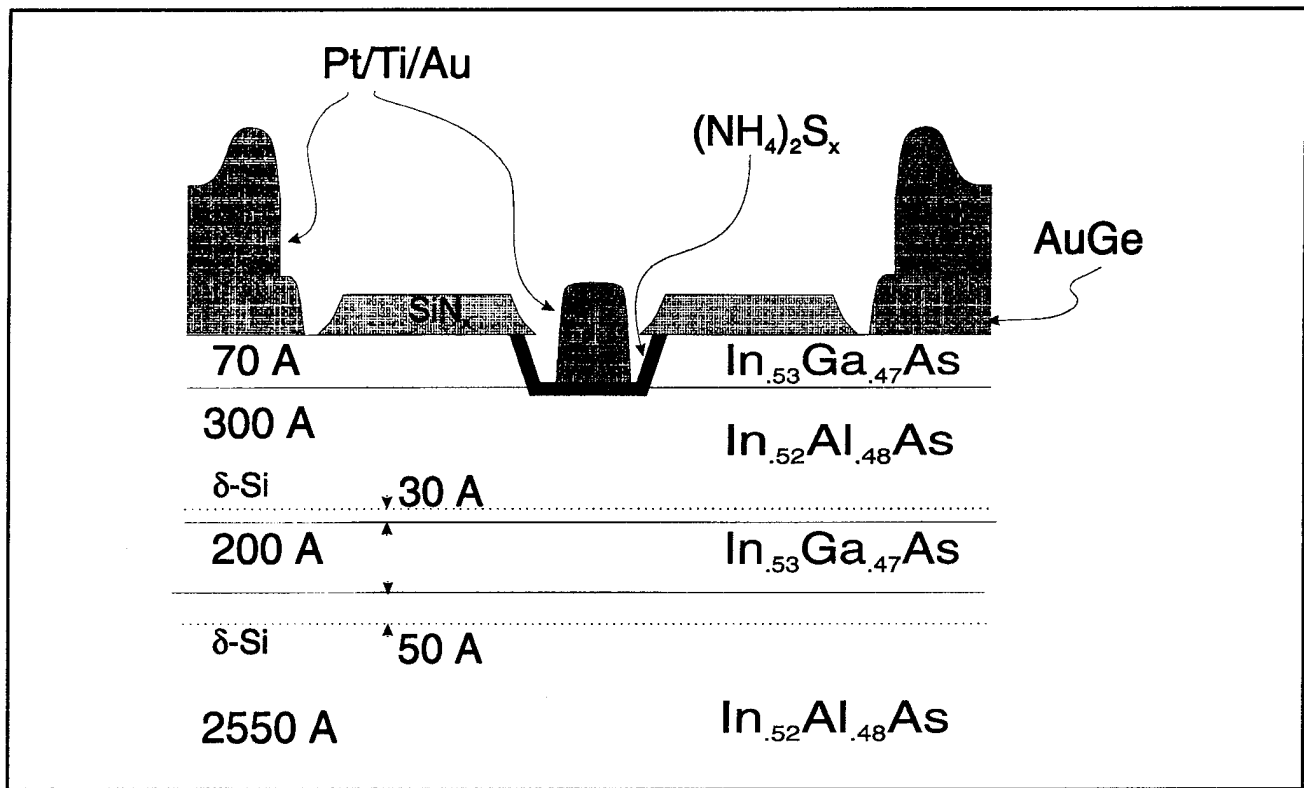


Figure 1. Schematic cross-section of fabricated modulation-doped field-effect transistor. The heterostructure was grown at Raytheon Research Division by Bill Hoke.

leakage path between the gate and the channel.⁷ For this we use a succinic acid solution. This simultaneously etches in a selective way the InGaAs cap in the intrinsic portion of the device exposing the InAlAs insulator. The sample was cleaved at this point into two pieces. One half underwent the S treatment presented in the previous section. The second half was a reference sample that followed a conventional 5 percent NH₄OH pre-gate treatment. Both halves were joined again for gate evaporation. This consisted of a Pt/Ti/Au stack. The process finished with the evaporation and lift-off of Ti/Au pads.

Devices with gate lengths 0.8 μm long and 50 μm wide have been tested. Typical output characteristics of a S-treated device are shown in figure 2. Qualitatively, they do not differ much from the untreated devices. A summary of average values of important figures of merit for both technologies is listed in table 2. Mean values for the maximum current that these devices can handle are 450 and 475 mA/mm, for the S-treated and untreated devices respectively. A plot of transconductance and drain current versus V_{GS} is shown in figure 3 for different values of V_{DS} . The average peak transconductance of the S-treated devices is 440 mS/mm. This contrasts with an average value of 380 mS/mm for the reference devices. This significant improvement in g_m could be explained by a slight etching of the InAlAs insulator or by the elimination of a surface oxide that is unavoidably present between the gate and the InAlAs insulator in conventional processing. In fact, the threshold voltage has shifted slightly from -0.7 V to -0.55 V as a result of the treatment.

Sample ID	No Sulfur	Sulfur
$\langle V_T \rangle$	-0.7 V	-0.55 V
$\langle g_m \text{-peak} \rangle$	380 mS/mm	440 mS/mm
$\langle I_{DSS} \rangle$	475 mA/mm	450 mA/mm
$\langle BV_{DS} \rangle$	7.5 V	8.3 V

Table 2. Summary of MODFET results for S-treated and reference devices with $L_g = 0.8 \mu\text{m}$ and $W_g = 50 \mu\text{m}$.

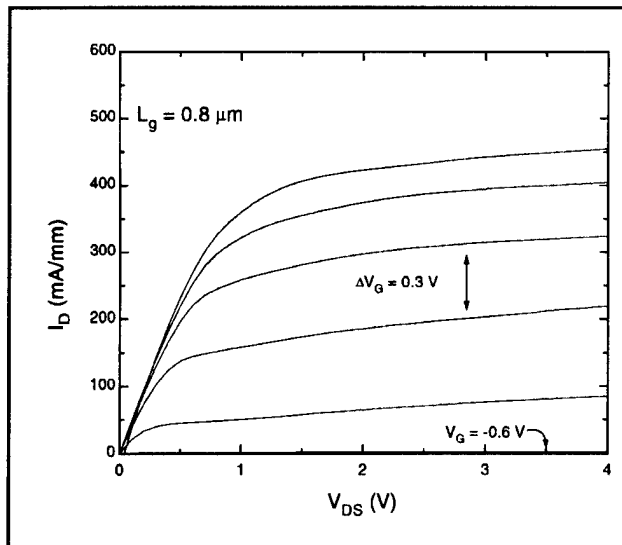


Figure 2. Output characteristics of a S-treated $L_g = 0.8 \mu\text{m}$, $W_g = 50 \mu\text{m}$ MODFET.

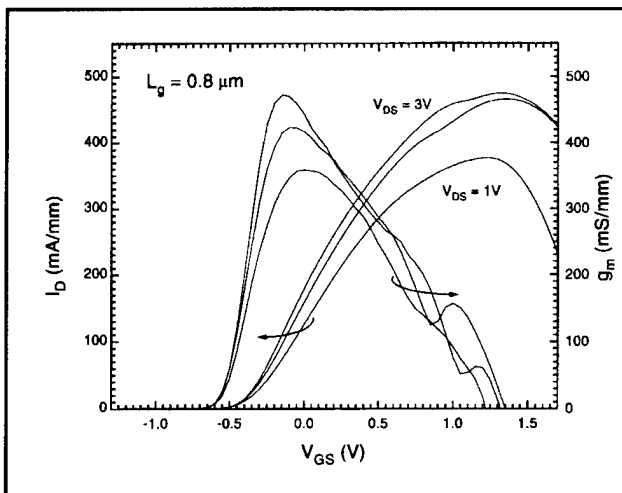


Figure 3. Plot of transconductance and drain current vs. V_{GS} for a S-treated $L_g = 0.8 \mu\text{m}$, $W_g = 50 \mu\text{m}$ MODFET for three values of V_{DS} .

In spite of this, the breakdown voltage of these devices is excellent. We have measured an average off-state three-terminal breakdown voltage of 7.5 V in the conventional device (defined at a current of 1 mA/mm). For the S-treated device, this value improved to 8.3 V. Figure 4 shows a plot of the drain-current injection technique⁸ applied to a S-treated device. A three-terminal breakdown voltage in excess of 8 V is obtained.

⁷ S.R. Bahl and J.A. del Alamo, "Elimination of Mesa-Sidewall Gate-Leakage in InAlAs/InGaAs Heterostructures by Selective Sidewall Recessing," *IEEE Electron Dev. Lett.* 13(4): 195-197 (1992).

⁸ S.R. Bahl and J.A. del Alamo, "A New Drain-Current Injection Technique for the Measurement of Breakdown Voltage in FETs," *IEEE Trans. Electron Dev.* 40(8): 1558-1560 (1993).

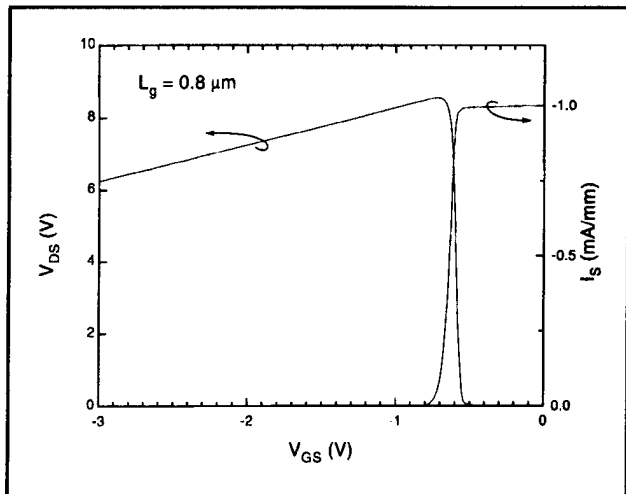


Figure 4. Plot of V_{DS} and I_S versus V_{GS} for $I_D = 1$ mA/mm for a S-treated $L_g = 0.8 \mu\text{m}$, $W_g = 50 \mu\text{m}$ MODFET showing a three-terminal breakdown voltage in excess of 8 V.

A detailed analysis of the impact of S passivation is currently under way. Our preliminary results indicate that S passivation improves the transconductance and the breakdown voltage of the device while it slightly degrades the maximum current drivability. In the near future, we will carry out detailed C-V characteristics of gate diodes so as to understand the charge control in the intrinsic portion of the device. We will also measure high-frequency S-parameters.

2.4 Publications and Conference Papers

Bahl, S.R., and J.A. del Alamo. "Physics of Breakdown in InAlAs/n⁺-InGaAs Heterostructure Field-Effect Transistors." *IEEE Trans. Electron Dev.* 41(12): 2268-2275 (1994).

Berthold, G., M. Mastrapasqua, C. Canali, M. Manfredi, E. Zanoni, S.R. Bahl, and J.A. del Alamo. "Electron and Hole Real Space Transfer in InAlAs/InGaAs Heterostructure Device." *Proceedings of the 24th European Solid State Device Research Conference*. Eds. C. Hill and P. Ashburn. Editions Frontieres. Edinburgh, United Kingdom, September 11-15, 1994. pp. 631-634.

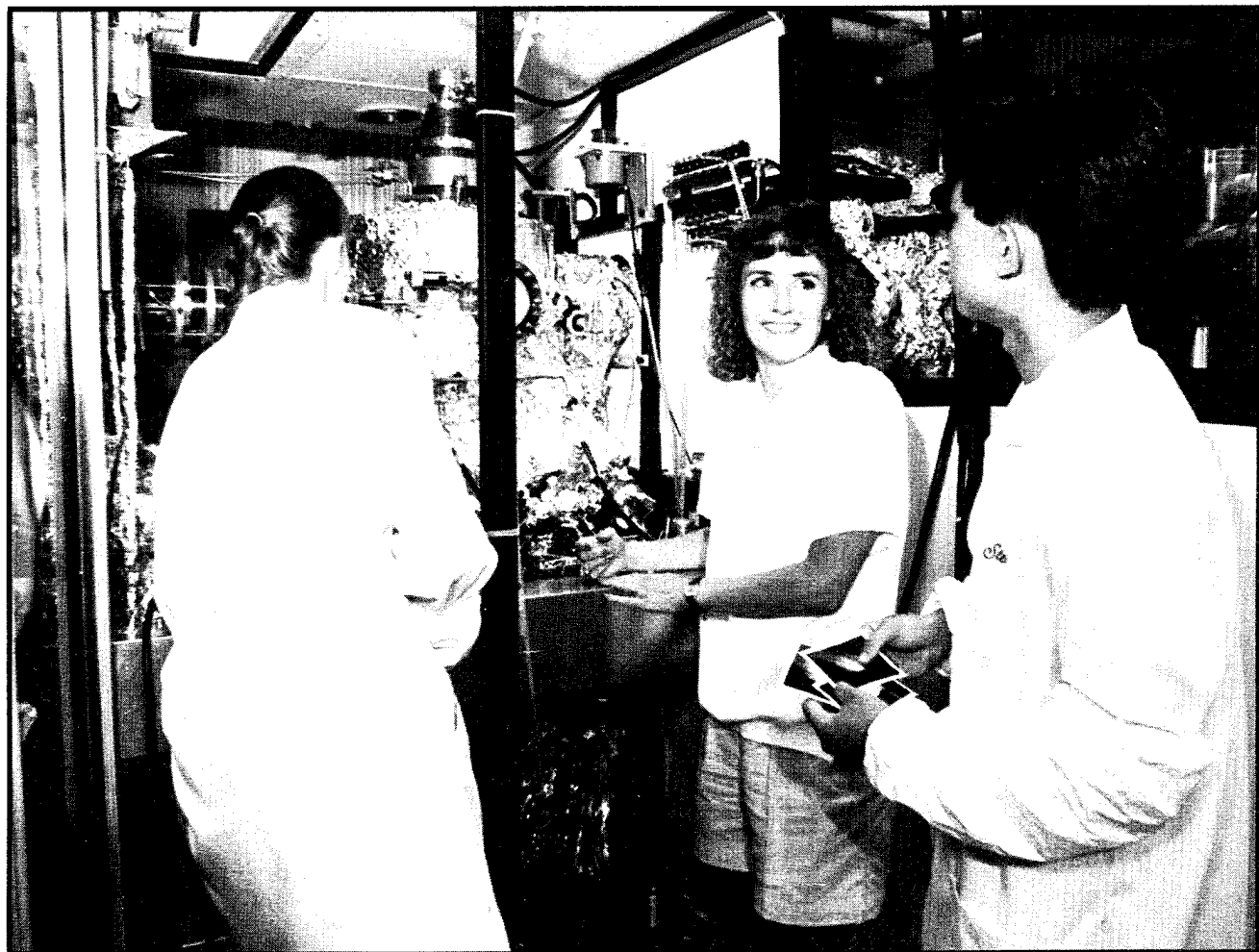
Berthold, G., E. Zanoni, M. Manfredi, M. Pavesi, C. Canali, J.A. del Alamo, and S.R. Bahl. "Electroluminescence and Gate Current Components of InAlAs/InGaAs HFETs." 52nd Annual Device Research Conference, Boulder, Colorado, June 20-22, 1994.

Moolji, A.A., S.R. Bahl, and J.A. del Alamo. "Impact Ionization in InAlAs/InGaAs HFETs." *IEEE Electron Dev. Lett.* 15(8): 313-315 (1994).

Theses

Adams, T. *Gate Delay in InP Heterostructure Field-Effect Transistors*. B.S. thesis. Dept. of Electr. Eng. and Comput. Sci., MIT, 1994.

Reiner, J.W. *A Small-Signal Model for Surface Effects in InAlAs/InGaAs HFETs*. B.S. thesis. Dept. of Electr. Eng. and Comput. Sci., MIT, 1994.



From left: graduate student Jody L. House, Professor Leslie A. Kolodziejki, and graduate student Kuo-Yi Lim (Photo by John F. Cook)

Chapter 3. Gas Source Molecular Beam Epitaxy of Compound Semiconductors

Academic and Research Staff

Professor Leslie A. Kolodziejski, Dr. Gale S. Petrich

Visiting Scientists and Research Affiliates

Dr. Hisashi Kanie¹

Graduate Students

Joseph F. Ahadian, Jay N. Damask, Sean M. Donovan, Philip A. Fisher, Easen Ho, Jody L. House, Kuo-Yi Lim, Elisabeth A. Marley, Kan Lu, Xiaofeng Tang

Undergraduate Students

James R. Geraci

Technical and Support Staff

Charmaine A. Cudjoe-Flanders, Angela R. Odoardi

3.1 Introduction

This research program utilizes the chemical beam epitaxy laboratory and emphasizes the epitaxial growth of a wide variety of compound semiconductors (both II-VI and III-V), as well as multilayered structures composed of II-VI/II-VI, II-VI/III-V and III-V/III-V heterostructures. The chemical beam epitaxy laboratory consists of two gaseous source epitaxy reactors (II-VI dedicated and III-V dedicated) interconnected to several smaller chambers which are used for sample introduction and *in-situ* surface analysis and metalization. Such a multi-chamber epitaxy system allows the fabrication of the aforementioned heterostructures within a continuous ultrahigh vacuum environment. The interconnected reactors enable an additional degree of freedom in device design by providing the ability to integrate the II-VI and III-V material families into a single device. For example, a variety of structures are grown (1) in a single reactor for binary or alloy II-VI or III-V epilayers, (2) with both reactors as in the case of II-VI/III-V heterostructures and quantum wells, and (3) in a single reactor as in the case of superlattice structures.

The III-V gas source molecular beam epitaxy (GSMBE) reactor uses solid elemental sources of Ga, In, Al, Si and Be and gaseous hydride sources of arsenic and phosphorus. The II-VI reactor cur-

rently uses solid elemental sources of Zn and Se and gaseous hydrogen selenide, in addition to a nitrogen plasma source and a solid ZnCl₂ source, to achieve p- and n-type doping, respectively. The plasma source is also used with a high purity hydrogen/argon mixture for hydrogen plasma cleaning of GaAs and ZnSe substrates. The highlighted region in figure 1 illustrates the wide range of lattice parameters and energy bandgaps which are accessible using the modular interconnected epitaxy system for the growth of II-VI and III-V compound semiconductors.

In the next section, we will describe our progress in the growth and doping of ZnSe using gas source molecular beam epitaxy; the II-VI effort is complemented by an investigation of the growth of ZnSe on alternative epitaxial III-V buffer layers. An additional II-VI/III-V effort involves the fabrication of ZnSe/GaAs quantum well structures, focusing on the formation of and resultant properties of the ZnSe/III-V heterovalent interface. The III-V GSMBE system is also utilized for the fabrication of (In,Ga)(As,P) waveguide devices that operate as filters at 1.55 μm , which is the wavelength used for optical fiber communication. Additional III-V-based projects include the fabrication of optoelectronic devices on premetallized GaAs MESFET integrated circuits for optoelectronic integrated circuits, an investigation into the growth of GaAs on patterned

¹ Professor, Science University of Tokyo, Japan.

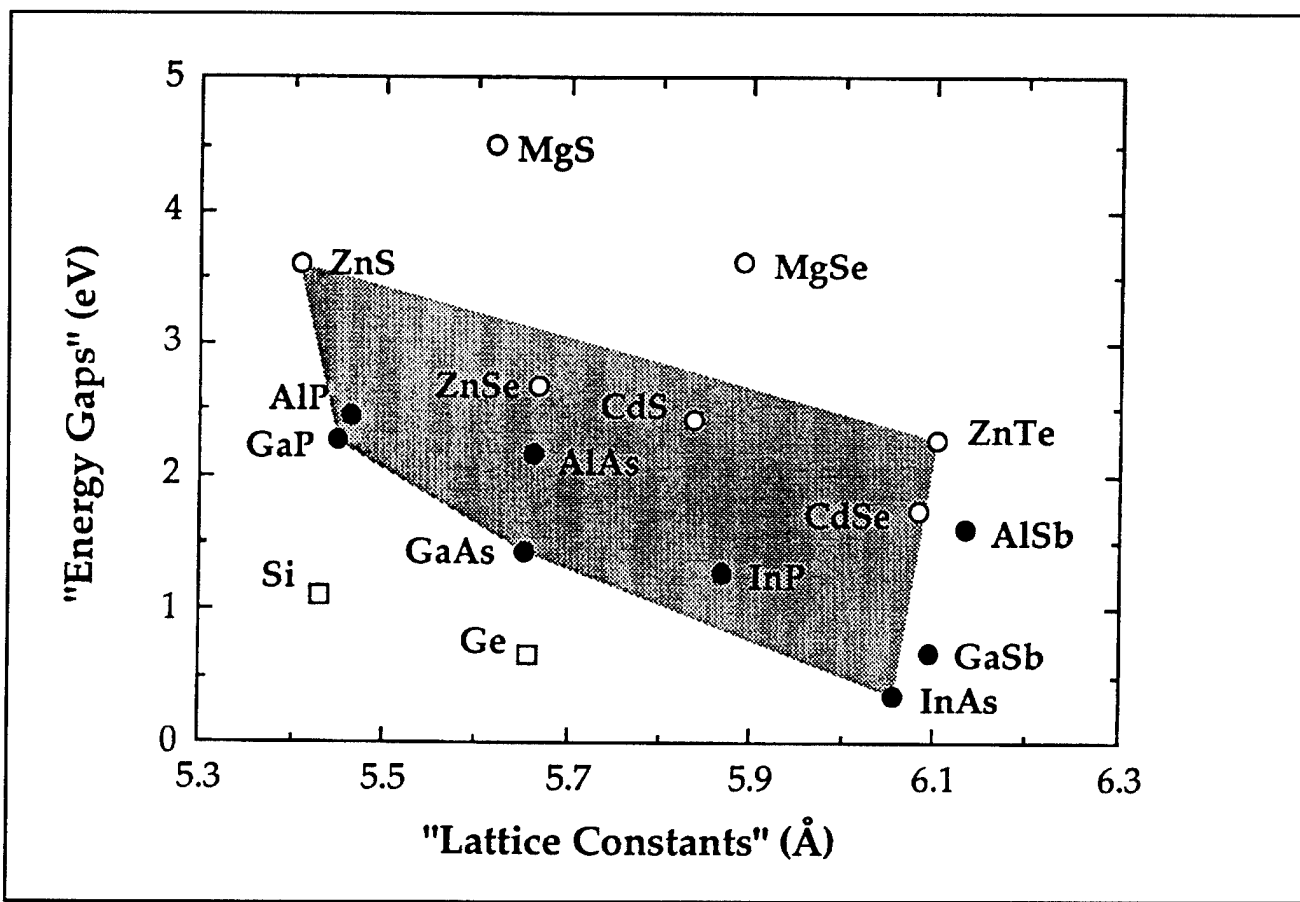


Figure 1. Energy bandgap as a function of lattice parameter for a wide variety of technologically important II-VI and III-V compound semiconductors. The highlighted region indicates the materials, heterostructure combinations, and quantum well structures which are accessible for study utilizing the modular interconnected epitaxy system.

Si substrates, and the fabrication of air bridge microcavities using the concepts of photonic bandgap crystals.

Project Staff

Professor Leslie A. Kolodziejski, Dr. Gale S. Petrich, Philip A. Fisher, Easen Ho, Jody L. House, James R. Geraci

3.2 Gas Source Molecular Beam Epitaxy of ZnSe, ZnSe:Cl and ZnSe:N

Sponsors

Advanced Research Projects Agency
Subcontract 284-25041
Joint Services Electronics Program
Contract DAAL03-92-C-0001
Grant DAAH-04-95-1-0038
National Center for Integrated Photonic Technology
Contract 542-381
Grant subcontract 652-693
U.S. Army Research Office/ AASERT
Contract DAAH04-93-G-0175

Under the university research initiative (URI) program sponsored by the Advanced Research Projects Agency through the Office of Naval Research, Professor Kolodziejski is a co-principal investigator along with Professor R.L. Gunshor, Purdue University, and Professor A.V. Nurmikko, Brown University. The focus of the URI is aimed towards achieving continuously operating, room temperature, short wavelength, visible light emitters operating in the blue and blue/green spectral ranges based on wide bandgap II-VI semiconductors. As the research effort continues toward eliminating the various technological barriers prohibiting the achievement of viable, commercial "blue" laser diodes, the heterostructures are becoming increasingly complex, requiring the use of advanced epitaxial growth techniques. Gas source molecular beam epitaxy (GSMBE) and/or chemical beam epitaxy (CBE) are anticipated to offer key advan-

tages for growing sophisticated heterostructures containing alloys composed of high vapor pressure species such as S and Se. The use of precision mass flow controllers, which provide a constant, uniform flux of gaseous species, eliminates the need for thermal effusion ovens operating at very low temperatures. The GSMBE technique will be particularly useful for the growth of both ternary and quaternary layers where two high vapor pressure group VI species are required, such as for Zn(Se,Te) or (Zn,Mg)(Se,S). In this project, the growth of ZnSe by GSMBE is being explored with particular emphasis on the controlled incorporation of donor and acceptor species for eventual fabrication of optical devices.

Using sources of elemental Zn and gaseous H₂Se, that was typically thermally decomposed at 1000°C, the ZnSe epilayers were doped p-type with atomic nitrogen derived from a radio frequency plasma source and n-type with chlorine from a ZnCl₂ effusion cell to film thicknesses of 1.5 to 4 μm. The substrate temperature was monitored using an optical pyrometer that was calibrated to the eutectic phase transition of 500 Å of Au on Ge. For the n-type layers, the substrate temperature during growth was 290°C; while for the p-type layers, the substrate temperature ranged from 250°C to 370°C. The Zn deposition rate was measured by depositing Zn onto a water-cooled crystal oscillator located at the substrate position. The H₂Se gas flow was adjusted to maintain a Zn-to-Se surface stoichiometry near unity. The surface stoichiometry was monitored by observing the reflection high energy electron diffraction surface reconstruction. For the p-type films, the nitrogen flow was regulated by a leak valve resulting in chamber pressures that ranged from 5.8×10^{-7} to 2.1×10^{-5} Torr. For the n-type films, the amount of chlorine incident onto the surface was controlled by the ZnCl₂ effusion cell temperature.

The optical properties of the epitaxial ZnSe layers were measured using low temperature photoluminescence (PL). The PL spectra were measured by optically exciting the samples with the 3250 Å line of a focused He-Cd laser, providing a power density of approximately 300 mW/cm². The luminescence was analyzed with a 0.5 m spectrometer and a photomultiplier. The PL spectra from the undoped ZnSe layers were dominated by the donor-bound exciton (I_d) and free exciton (E_x) transitions. The Y₀ and I_v transitions which have been reported to be observed in undoped ZnSe films were also

detected. Shahzad et. al.² have reported ZnSe films with carrier concentrations of $\sim 10^{15}$ cm⁻³ grown on GaAs substrates exhibiting similar PL features. Hall effect measurements of the undoped GSMBE-grown layers showed n-type conductivity with carrier concentrations ranging from high 10^{15} cm⁻³ to low 10^{17} cm⁻³.

Chlorine-doped ZnSe samples were analyzed using secondary ion mass spectroscopy (SIMS), photoluminescence, capacitance-voltage (C-V) measurements, and Hall effect measurements. The chlorine concentration, which varied from 9×10^{15} cm⁻³ to 8×10^{19} cm⁻³, was primarily measured with SIMS. For doping concentrations greater than 10^{20} cm⁻³, the growth rate decreased to below 1000 Å/hr, even though the undoped ZnSe growth rate was ~7000 Å/hr for identical growth conditions. The decrease in the growth rate is speculated to be due to a surface chemical reaction involving the Cl and the H present at the growth front in the GSMBE environment. The PL spectra of the ZnSe:Cl films with Cl concentrations up to 4×10^{18} cm⁻³ were dominated by a donor-bound excitonic transition at 2.795 eV with negligible defect-related deep level emission. At a Cl concentration of 8×10^{19} cm⁻³, the PL spectrum was dominated by a broad band of deep level emission centered at 2.2 eV.

Since thermally decomposed H₂Se is used as a source gas, the presence of hydrogen within the ZnSe lattice was investigated. SIMS was used to measure the amount of hydrogen that was incorporated during the chlorine doping of ZnSe epilayers. As seen in figure 2, the hydrogen concentration remains at or near the background level even though the Cl concentration was varied from $< 10^{17}$ cm⁻³ to 3×10^{18} cm⁻³, suggesting that Cl and H do not form a H-Cl complex. Electrical measurements of the epilayers indicated that the free electron concentration was comparable to the amount of Cl incorporated and that the electrical activation of the Cl donors was negligibly affected by the presence of hydrogen.

Nitrogen-doped ZnSe epilayers were primarily characterized by photoluminescence, secondary ion mass spectroscopy, and capacitance-voltage measurements. Low temperature photoluminescence showed that as the nitrogen concentration increased, the spectra evolved from one exhibiting a neutral N acceptor peak at 2.793 eV to spectra exhibiting a dominant donor-to-acceptor pair (DAP) transition with easily resolved longitudinal optical

² K. Shahzad, J. Petruzzello, D.J. Olego, D.A. Cammack, and J.M. Gaines, "Correlation Between Radiative Transitions and Structural Defects in Zinc Selenide Epitaxial Layers," *Appl. Phys. Lett.* 57: 2452-2455 (1990).

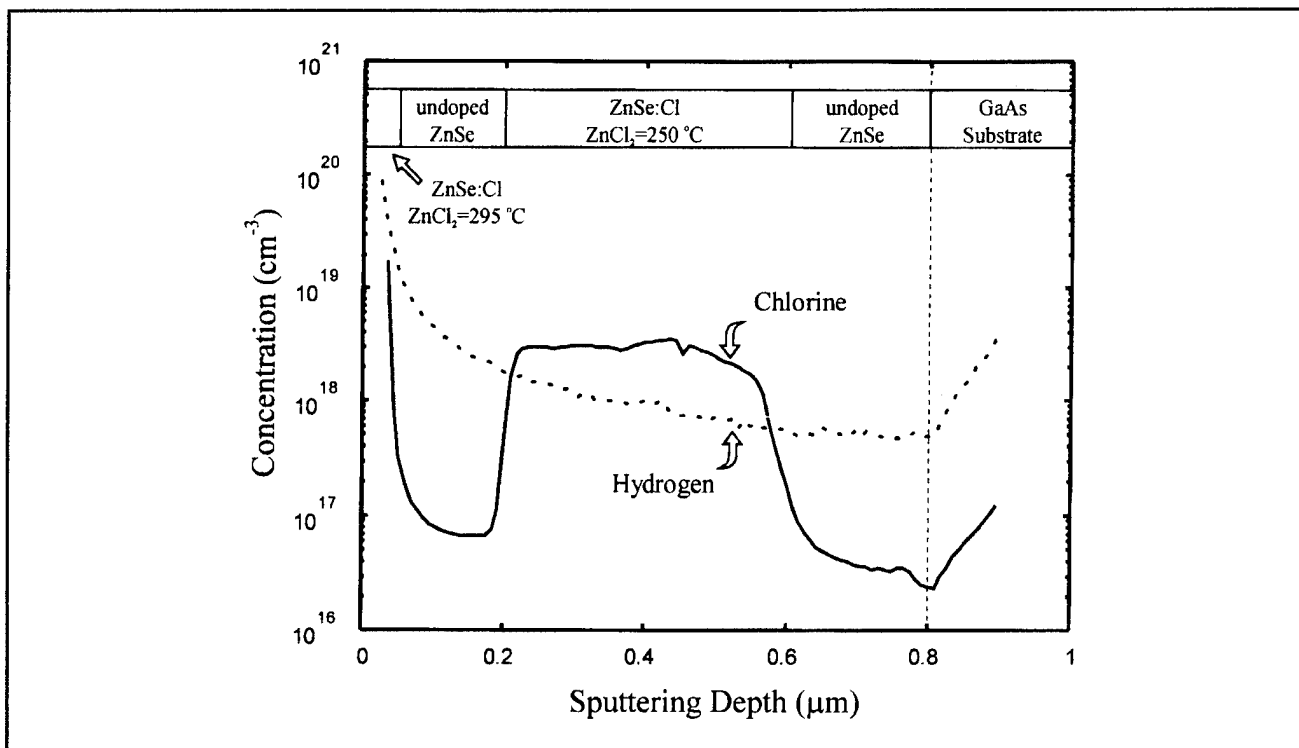


Figure 2. SIMS profile of a ZnSe:Cl structure grown by GSMBE with various ZnCl_2 effusion cell temperatures, as indicated schematically at the top of the figure. The high level of [H] near the surface is an artifact due to surface contamination.

phonon replicas, and finally to spectra exhibiting a single broad DAP feature. Using SIMS, the ZnSe:N epilayers that were grown with a Zn-rich surface stoichiometry, were found to exhibit measurable quantities of nitrogen atoms, while ZnSe:N epilayers that were grown with a Se-rich surface stoichiometry, were found to have N concentrations at or below the SIMS detection level (approximately 10^{17} cm^{-3}). The highest N concentration obtain thus far using GSMBE was $6 \times 10^{18} \text{ cm}^{-3}$. However, C-V measurements indicated that the ZnSe:N films were insulating instead of conductive.

The inability to achieve p-type conductivity suggested that the presence of hydrogen and its electrical passivation of the acceptors may be playing a role. Therefore, to examine the hydrogenation behavior of ZnSe:N films grown by GSMBE and MBE, an in-depth investigation using SIMS was initiated. In the case of GSMBE, the hydrogen was supplied by the thermal decomposition of H_2Se . Figure 3 shows a SIMS profile of a ZnSe:N layer that was grown by GSMBE on a p-type GaAs

substrate. An initial undoped layer of ZnSe was grown to provide a reference for the detection limits of the nitrogen and hydrogen concentrations ([N] and [H] respectively). Two other thin undoped layers were also grown in an otherwise uniformly doped ZnSe:N layer. As the figure shows, the [H] tracks the variation in the [N] throughout the film, decreasing to their respective background levels in the undoped layers. A similar hydrogenation behavior has been observed in other films that were grown under various Zn-to-Se ratios and doping conditions in which the [N] ranged from $\sim 10^{17} \text{ cm}^{-3}$ to $\sim 10^{19} \text{ cm}^{-3}$. The [H] relative to the [N] and their synergistic behavior suggest that N-H bonds may be formed within the lattice, leading to the observed electrical passivation. This is in agreement with the reported presence of N-H bonds in metalorganic vapor phase epitaxy-grown ZnSe films.³ By intentionally injecting H_2 into the chamber during growth, the incorporation of H in MBE-grown ZnSe:N epilayers was also investigated. (In MBE growth, elemental Zn and Se are the constituent species.) Figure 4 shows the SIMS profile of a MBE-grown

³ J.A. Wolk, J.W. Ager, K.J. Duxstand, E.E. Haller, M.R. Taskar, D.R. Dorman, and D.J. Olego, "Local Vibrational Mode Spectroscopy of Nitrogen-Hydrogen Complex in ZnSe," *Appl. Phys. Lett.* 63: 2756-2758 (1993); A. Kamata, H. Mitsuhashi, and H. Fujita, "Origin of the Low Doping Efficiency of Nitrogen Acceptors in ZnSe Grown by Metalorganic Chemical Vapor Deposition," *Appl. Phys. Lett.* 63: 3353-3354 (1993).

ZnSe:N structure incorporating an intentionally hydrogenated layer. The hydrogenated ZnSe:N layer (obtained by the injection of 3 sccm of H₂ through the H₂Se cracker) showed that the [H] was at an elevated concentration although slightly below the [N] level. The unhydrogenated MBE layer, that was grown under identical nitrogen doping conditions, showed that the [N] was at the same concentration but that the [H] was near the background level. The undoped ZnSe layer provided a reference for the background concentration of both nitrogen and hydrogen. Therefore, the presence of H₂ in the growth environment, either intentionally injected or derived from the thermal decomposition of H₂Se, results in an unambiguous dopant enhanced hydrogenation when nitrogen is used as a dopant. In addition, the diffusion of hydrogen in ZnSe:N is small as indicated by the relatively sharp transition in the [H] from the hydrogenated layer to the unhydrogenated layer in the conventionally-grown MBE layer. Based on the observation that the injection of H₂ during MBE, at flows in excess of those typically observed during GSMBE, resulted only in partial hydrogenation, sub-hydride species of

H₂Se that are present due to the incomplete cracking of H₂Se, play a major role in the observed passivation of the nitrogen acceptors. *Ex-situ* post-growth methods of removing the hydrogen, such as rapid thermal anneals at 500°C and long term anneals at 600°C for one hour, have been unsuccessful in creating conductive p-type ZnSe films that were grown by GSMBE.

In summary, significant hydrogenation in ZnSe:N grown by GSMBE has been observed. Unlike ZnSe:Cl layers grown by GSMBE, where hydrogen was found to be near the background level and was independent of the [Cl], the [H] was found to follow closely the profile of the [N] in ZnSe:N samples. When H₂ was intentionally introduced during the conventional MBE growth of ZnSe:N, enhanced hydrogen incorporation was observed. These results suggest that a significant source of the incorporated hydrogen in these ZnSe:N films may be the presence of a large amount of ambient H₂ in the growth environment, whether it is intentionally injected or present as a by-product of the H₂Se decomposition reaction.

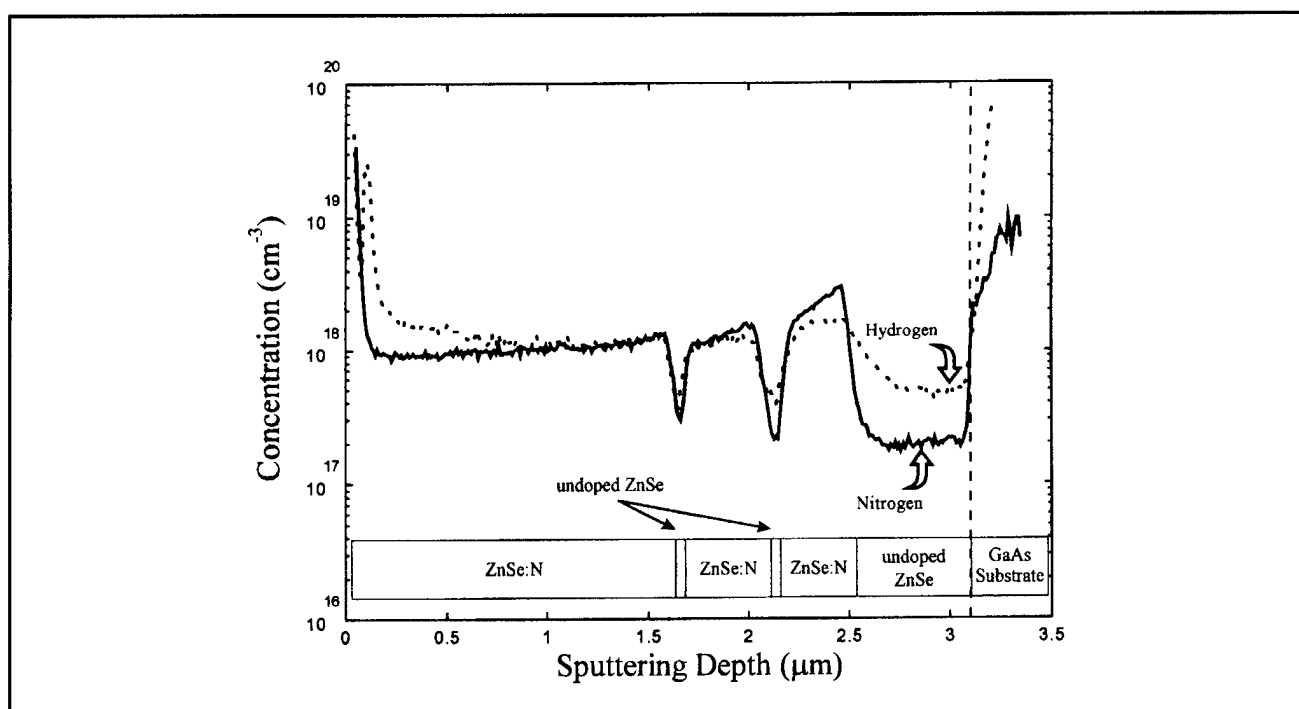


Figure 3. SIMS profile of a ZnSe:N structure grown by GSMBE having an initial undoped layer near the ZnSe/GaAs interface, followed by two thin undoped regions in an otherwise uniformly nitrogen-doped film as schematically indicated in the figure. The sudden rise in the [H] and [N] at the ZnSe/GaAs interface are artifacts of the data normalization process.

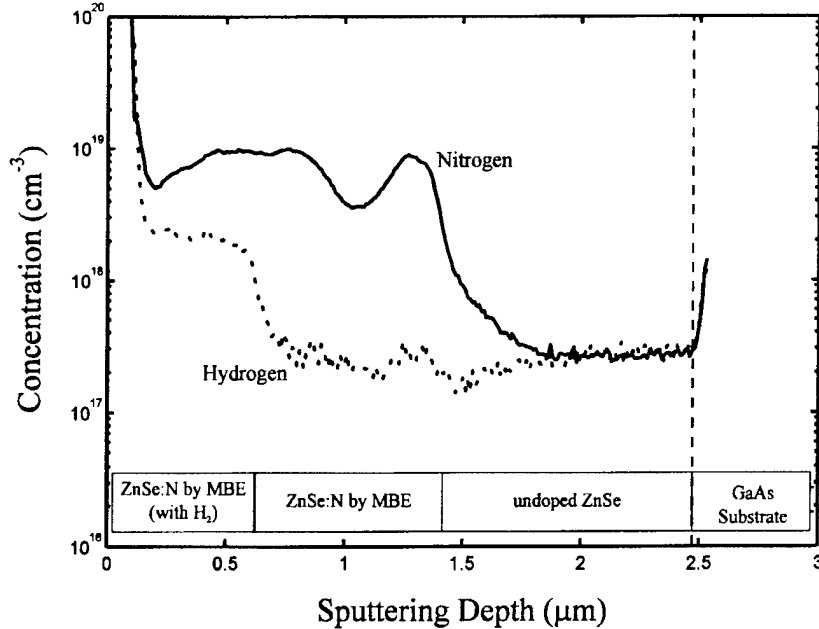


Figure 4. SIMS profile of a ZnSe:N structure (as indicated schematically in the figure) grown by MBE both with and without intentional injection of hydrogen through the H₂Se cracker held at 300°C. The sudden rise in the [H] and [N] at the ZnSe/GaAs interface are artifacts of the data normalization process.

3.2.1 Publications

Coronado, C.A., E. Ho, P.A. Fisher, J.L. House, K. Lu, G.S. Petrich, and L.A. Kolodziejski. "Gas Source Molecular Beam Epitaxy of ZnSe and ZnSe:N." *J. Electron. Mater.* 23: 269-273 (1994).

Fisher, P.A., E. Ho, J.L. House, G.S. Petrich, L.A. Kolodziejski, M.S. Brandt, and N.M. Johnson. "N- and P- Type doping of ZnSe using Gas Source Molecular Beam Epitaxy." *Mat. Res. Soc. Symp. Proc.* 340: 451-456 (1994).

Fisher, P.A., E. Ho, J.L. House, G.S. Petrich, L.A. Kolodziejski, J. Walker, and N.M. Johnson. "P- and N-type Doping of ZnSe: Effects of Hydrogen Incorporation." 8th International Conference on Molecular Beam Epitaxy, Osaka, Japan, August 29-September 2, 1994. *J. Cryst. Growth.* Forthcoming.

Ho, E., P.A. Fisher, J.L. House, G.S. Petrich, L.A. Kolodziejski, J. Walker, and N.M. Johnson. "Hydrogen Passivation in Nitrogen- and Chlorine-Doped ZnSe Films Grown by Gas Source Molecular Beam Epitaxy." *Appl. Phys. Lett.* Forthcoming.

3.3 Novel Epitaxial III-V Buffer Layers for Wide Bandgap II-VI Visible Sources

Sponsors

Advanced Research Projects Agency
Subcontract 284-25041

National Center for Integrated Photonic Technology
Contract 542-381
Grant subcontract 652-693
National Science Foundation
Grant DMR 92-02957

Project Staff

Professor Leslie A. Kolodziejski, Dr. Gale S. Petrich, Philip A. Fisher, Easen Ho, Jody L. House, Kan Lu

A number of important advantages are offered by the use of novel (In,Ga,Al)P epitaxial buffer layers for the subsequent growth of ZnSe-based optical devices. The optimum substrate is bulk ZnSe material; however, ZnSe bulk substrates are very expensive, have a small useable area, and the surface preparation techniques necessary for epitaxy are not well understood. In the past, therefore, the primary substrate employed for ZnSe-based optical devices was GaAs, possessing a small 0.27 percent lattice constant mismatch. As seen in figure 1, the use of the (In,Ga,Al)P quaternary alloy, as an epitaxial buffer layer for

ZnSe growth, provides the opportunity to vary the in-plane surface lattice constant (to match that of ZnSe) and also enables the variation of the energy bandgap of the III-V alloy buffer layer to facilitate the transport of carriers from the substrate into the active region of the II-VI overlayer. The valence-band offset between p-type GaAs and p-type ZnSe is approximately 1 eV. By the insertion of an (In,Al)P buffer layer between the GaAs and the ZnSe, the valence-band discontinuity is expected to be reduced to 0.34 eV, as opposed to 0.67 eV for (In,Ga)P. Appropriate doping and formation of the II-VI/III-V heterovalent interface may further reduce the barrier for hole injection. In addition to the aforementioned advantages, an important current research topic⁴ addresses the formation and propagation of extended defects in ZnSe-based optical emitters which eventually limit device lifetime. The ZnSe/GaAs heterointerface is believed to be the site for the nucleation of stacking faults, which then provide sources of dark line defects.⁵ The use of novel (In,Ga,Al)P buffer layers will offer an alternative interface surface chemistry for exploration, and thus may shed more insight into the problems involving the II-VI/III-V heterovalent interface.

The investigation into the growth of ZnSe on epitaxial (In,Al,Ga)P buffer layers represents an unique contribution to the area of II-VI-based semiconductors by our group at MIT. Our interconnected II-VI and III-V gas source molecular beam epitaxy reactors enable the investigation of the nucleation of ZnSe on epitaxial layers consisting of a multitude of III-V alloys. In the III-V reactor, the various (In,Al,Ga)P buffer layers are grown at 470°C (typically on an epitaxial 0.5 μm thick GaAs buffer layer) where the substrate temperature is calibrated using the melting point of InSb (525°C). Elemental In, Ga, Al and cracked phosphine (thermally decomposed at 900°C) are used as the constituent species. During growth, the (In,Ga,Al)P exhibits a (2x1) surface reconstruction as observed by reflection high energy electron diffraction. The (In,Ga,Al)P film thicknesses range from 0.5-4 μm, and the precise alloy composition and the amount of lattice relaxation are determined from (400) and (511) x-ray diffraction rocking curves. Following growth, the (In,Ga,Al)P films are *in situ* transferred

to the II-VI reactor and the ZnSe growth proceeds in the manner described in the previous section. A variety of characterization techniques are used to analyze the II-VI/III-V heterostructures, and include high resolution double crystal x-ray diffraction, low temperature photoluminescence, optical Nomarski microscopy, and transmission electron microscopy (TEM).

Two parallel paths of investigation have been pursued to address (1) the use of (In,Ga)P buffer layers designed to lattice-match to ZnSe, and (2) the use of (In,Ga,Al)P layers to facilitate transport of carriers from the p-type GaAs into p-type ZnSe. By varying the In mole fraction of (In,Ga)P from 50 percent to 56 percent and by increasing the buffer layer thickness from one to four microns, the (In,Ga)P is found to possess an in-plane surface lattice constant near to that of ZnSe. To release the build-up of strain energy due to the lattice constant mismatch with GaAs, edge-type misfit dislocations are found located at the (In,Ga)P/GaAs interface as evidenced by cross-sectional TEM. These dislocations propagate parallel to the interface and do not appear to propagate into the over-layer of ZnSe. However, the III-V buffer layer is not fully relaxed, and a small degree of lattice-mismatch still resides at the ZnSe/(In,Ga)P interface as evidenced by x-ray diffraction and photoluminescence measurements of the ZnSe.

The study of hole injection from the III-V quaternary buffer layer into the p-type ZnSe layer has thus far consisted primarily of an investigation into the heteroepitaxy of ZnSe on various III-V alloys. A variety of III-V surfaces have been grown consisting of (In,Ga)P, (In,Ga,Al)P, and (In,Al)P which are all pseudomorphic to the GaAs (and hence lattice-mismatched to the ZnSe). The nucleation of ZnSe on each epitaxial surface is observed to proceed in a layer-by-layer fashion due to the observation of reflection high energy electron diffraction intensity oscillations. Photoluminescence measurements of the 1200 Å pseudomorphic ZnSe layers on the various III-V surfaces show spectra exhibiting dominant free exciton transitions and the absence of deep level defect-related luminescence. In addition, all of the ZnSe films with (In,Ga,Al)P or GaAs

⁴ M.A. Haase, P.F. Boude, M.S. Hagedorn, J. Qiu, J.M. DePuydt, H. Cheng, S. Guha, G.E. Hofler, and B.J. Wu, "Low Threshold Buried Ridge II-VI Laser Diodes," *Appl. Phys. Lett.* 63: 2315-2317 (1993); S. Guha, J.M. DePuydt, J. Qiu, G.E. Hofler, M.A. Haase, B.J. Wu, and H. Cheng, "Role of Stacking Faults as Misfit Dislocation Sources and Nonradiative Recombination Centers in II-VI Heterostructures and Devices," *Appl. Phys. Lett.* 63: 3023-3025 (1993); S. Guha, J.M. DePuydt, M.A. Haase, J. Qiu, and H. Cheng, "Degradation of II-VI Based Blue-green Light Emitters," *Appl. Phys. Lett.* 63: 3107-3109 (1993).

⁵ D.C. Grillo, Y. Fan, M.D. Ringle, L. He, J. Han, R.L. Gunshor, A. Salokatve, H. Jeon, M. Hovinen, and A.V. Nurmikko, "MBE Growth and Characterization of II-VI Blue/Green Laser Diodes Having CW Operation at Room Temperature," *Mat. Res. Soc. Symp. Proc.* 340: 431-436 (1994).

buffer layers were featureless as observed by optical Nomarski microscopy.

3.3.1 Publications

Lu, K., P.A. Fisher, E. Ho, J.L. House, G.S. Petrich, L.A. Kolodziejski, G.C. Hua, and N. Otsuka. "Gas Source Molecular Beam Epitaxy Growth of ZnSe on (In,Ga)P." *Mat. Res. Soc. Symp. Proc.* 340: 497-502 (1994).

Lu, K., P.A. Fisher, J.L. House, E. Ho, C.A. Coronado, G.S. Petrich, and L.A. Kolodziejski. "Gas Source Molecular Beam Epitaxy Growth of ZnSe on Novel Buffer Layers." *J. Vac. Sci. Technol. B* 12(2): 1153-1155 (1994).

Lu, K., J.L. House, P.A. Fisher, C.A. Coronado, E. Ho, G.S. Petrich, and L.A. Kolodziejski. "(In,Ga)P Buffer Layers for ZnSe-Based Visible Emitters." *J. Cryst. Growth* 138: 1-7 (1994).

3.4 Heterovalent Interfaces Composed of II-VI/III-V Semiconductors

Sponsors

Joint Services Electronics Program
Contract DAAL03-92-C-0001
Grant DAAH04-95-1-0038

National Science Foundation
Grant DMR 92-02957
Grant DMR 90-22933

Project Staff

Professor Leslie A. Kolodziejski, Dr. Gale S. Petrich, Jody L. House

Traditionally, II-VI and III-V compound semiconductors have been treated as separate material systems, each having its own special applications. For example, GaAs has been extensively used in electronic and optical devices that exploit its high room temperature mobility and direct infrared bandgap. In contrast, ZnSe is currently the research focus for blue/blue-green light emitters that are made possible by its large room temperature bandgap of 2.7 eV. However, by jointly employing the properties of these two material families, it should be possible to create a new class of II-VI/III-V heterojunction devices that have unusual

optical and electronic properties due to differences in the energy bandgap, dielectric constants, refractive indices, etc. The energy bandgaps of the II-VI semiconductor cover the visible spectrum and are significantly wider than those of typical III-V compounds (see figure 1). It is also important to note that for every technologically important III-V semiconductor, such as GaAs or InP, there exists a perfectly lattice-matched II-VI ternary counterpart that, when layered together, can provide "defect-free" coherent II-VI/III-V heterointerfaces. (In addition, the thermal expansion coefficients of the II-VI and III-V compounds are, in many cases, quite similar.) In contrast to the similarities of the II-VI and III-V materials, there are large differences in their optical constants. The II-VI compounds typically have a smaller dielectric constant and a lower refractive index than its lattice-matched III-V counterpart. Combining the material properties of the II-VI and III-V compound semiconductors offers the device designer greater flexibility in specifying barrier layers, insulating layers, and waveguiding or optical confinement layers, while maintaining structural compatibility.

In collaboration with Professor E.P. Ippen, the nonlinear optical properties of II-VI/III-V quantum well structures, composed initially of ZnSe/GaAs multilayers, are under investigation. Due to the large differences in the dielectric constants (ZnSe: 8.1, GaAs: 12.0), the layered structures are referred to as dielectric quantum wells. Kumagai and Takagahara⁶ have theorized that for these dielectric quantum well structures an increase in the exciton reduced mass and thus, an enhanced excitonic binding energy, an enhanced oscillator strength, and an enhanced nonlinear optical response is anticipated. Not only can the optical properties of the dielectric quantum well be enhanced, but other material properties will be affected, such as the mobility of the carriers, the RC time constant, and the Frohlich interaction.

The initial structure under investigation is a ZnSe/GaAs/ZnSe single quantum well. The substrates which have been employed include GaAs and ZnSe bulk material, and (In,Ga)P epilayers on GaAs to facilitate appropriate confinement of carriers and to affect the lattice constant mismatch. Again, the interconnected II-VI and III-V GSMBE reactors are crucial for the fabrication of these sophisticated II-VI/III-V heterostructures. The growth of ZnSe on GaAs is well understood; however, the formation of the inverted interface,

⁶ M. Kumagai and T. Takagahara, "Excitonic and Nonlinear-Optical Properties of Dielectric Quantum-Well Structures," *Phys. Rev. B* 40: 12359-12381 (1989).

i.e., GaAs onto ZnSe, has not been previously investigated. Therefore, the initial investigative path consists of the growth of a III-V epilayer of GaAs onto a II-VI epitaxial ZnSe surface. In this case, the II-VI surface has been fabricated in the II-VI reactor and transferred via the transfer chamber into the III-V reactor. In order to avoid interdiffusion of the Zn and Se into the GaAs quantum well, the GaAs is grown at a substrate temperature of 350°C. The growth parameters of the III-V/II-VI heterostructures have been optimized to form abrupt heterointerfaces and to result in the two-dimensional growth of GaAs. The two-dimensional growth of GaAs on ZnSe was successfully achieved by carefully engineering the initial stages of nucleation. Monolayer-controlled GSMBE was employed to reduce the islanding of highly mobile Ga atoms on the ZnSe surface and was only performed during the formation of the interface to enable the careful engineering of the stoichiometry. The Group V-to-Group III flux ratio is carefully maintained at 12-to-1 during the initial nucleation. Following the growth of six monolayers, reflection high energy electron diffraction patterns suggest a smooth GaAs surface and a c(4x4) reconstructed surface.

The growth conditions of the optimized III-V/II-VI heterostructure have been used as the foundation for the growth of ZnSe/GaAs/ZnSe single quantum well (SQW) structures. As previously mentioned, the SQW structure has been grown on both GaAs and ZnSe substrates. (400) x-ray diffraction rocking curves have been used to examine the amount of strain in the quantum well. Figure 5 shows a (400) rocking curve of a 8 nm GaAs quantum well with 50 nm ZnSe barriers. When using either aforementioned substrate, the heterointerfaces are nucleated using the growth conditions which minimize the formation of Ga-Se bonds and thus leads to the most abrupt heterointerface.

The optical properties of the ZnSe/GaAs/ZnSe quantum well will be affected by the presence of the II-VI/III-V heterovalent interface, but is also affected by the growth of the GaAs quantum well at the unusually low temperature of 350°C (the usual growth temperature is 580°C). To enable separate assessment of the effect of the heterovalent interfaces from the effect of the low temperature growth of GaAs, a series of GaAs quantum wells have been fabricated with (In,Ga)P barrier layers. By varying the As-to-Ga flux ratio for growth of GaAs at 350°C, and by varying the quantum well width and growth temperature simultaneously, we have measured photoluminescence originating from a 15 Å GaAs single quantum well grown at 350°C (with (In,Ga)P barrier layers). By inserting this GaAs material between barrier layers of ZnSe and by

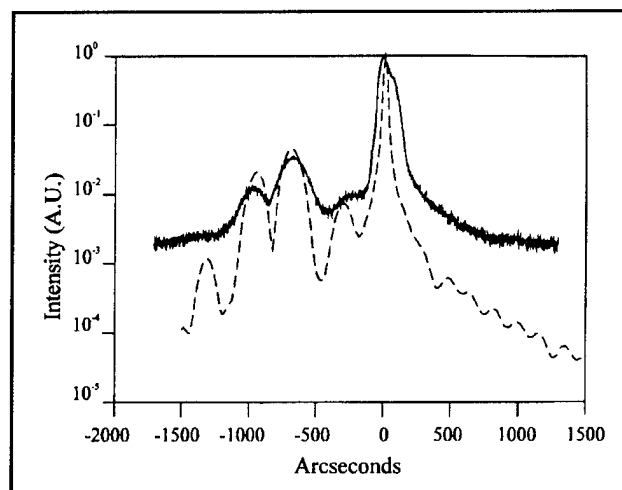


Figure 5. High resolution double crystal x-ray diffraction (400) rocking curve of a 8 nm single GaAs quantum well with ZnSe barriers. The dotted line corresponds to simulation results and the solid line corresponds to the experimental results.

varying the quantum well dimension, the affect of the heterovalent interface is isolated and assessed. Finally, upon the successful fabrication of single quantum well structures consisting of ZnSe/GaAs/ZnSe, the fabrication of superlattice structures will be attempted in a single reactor with gaseous sources for all of the constituent species. The II-VI reactor has been specially equipped to consider the growth of these II-VI/III-V quantum wells.

3.5 (In,Ga)(As,P)/InP Semiconductor Waveguide Design for Synchronously Side-Coupled Bragg Resonators

Sponsors

MIT Lincoln Laboratory
Contract BX-5411

National Center for Integrated Photonic Technology
Contract 542-383
Grant subcontract 652-693

Project Staff

Professor Hermann A. Haus, Professor Leslie A. Kolodziejski, Professor Henry I. Smith, Dr. Gale S. Petrich, Jay N. Damask, Elisabeth A. Marley

In collaboration with Professors Hermann A. Haus and Henry I. Smith, this project involves the fabrication of a channel dropping filter based on the (In,Ga)(As,P) materials system and designed to operate at the optimum wavelength of 1.55 μm for optical communication applications. The theory and

design component of the project resides with Professor Haus, while the fabrication of the layered structure and the formation of the appropriate gratings is performed in the groups of Professors Kolodziejki and Smith, respectively. The channel dropping filter represents a key optical component for wavelength division de-multiplexing applications. The unique attribute of the channel dropping filter is the ability to selectively "drop" a desired channel, or frequency, from the main waveguide or bus, while sending the other channels undistorted to their final destination. A significant effort is underway to simulate an InP-based channel dropping filter to provide device design constraints on the final fabricated structure.

The channel-dropping filter (figure 6) is constructed by weakly side-coupling two high-Q quarter-wave shifted distributed-Bragg-reflector (QWS-DBR) resonators to a rib waveguide. The resonators are created by etching gratings, each with an appropriately placed quarter-wave shift, on top of the two outer rib waveguides. The period of the grating, ~ 240 nm for the InP material system, is chosen to be the Bragg period of the filter center wavelength. The length of the gratings (e.g., 250-500 μm) are dictated by the required Q of each resonator and the depth of the grating corrugations. The spectral responses at the signal port (top left waveguide) and transmission port (top right waveguide) are shown in figure 6 for a filter designed to maximally

select the on-resonance signal from the center waveguide.

The spectral responses shown in figure 6 were calculated assuming that the phase velocities along the grating and blank waveguides are identical. However, this is generally not the case. The patterning of a grating corrugation on top of the grating waveguide necessarily reduces the effective index of the mode. When a grating waveguide is coupled to a guide with identical dimensions but with no grating, the phase velocities between the two guides are different. The fundamental unit of phase mismatch, ϕ_s , is the phase difference that is accrued over one decay length of the optical mode along the grating length. Figure 7 shows two plots of the same receiver spectrum as in figure 6 but where the phase velocities are mismatched. The spectra is clearly distorted.

Optimal design rules have been determined in order to derive the vertical and lateral dimensions of a coupled waveguide pair such that after the grating is etched, the two guides are synchronous. Figure 8 shows the mode profiles of a blank (rib) and resonator (grating) waveguide where the waveguide widths are 1.0 μm and 2.0 μm , respectively. The differences in effective indices, Δn_{eff} , for these two guides is $\Delta n_{\text{eff}} \approx 0.2 \times 10^{-3}$ or $\phi_s \approx \pi/100$. Such close phase matching would result in acceptable filter performance.

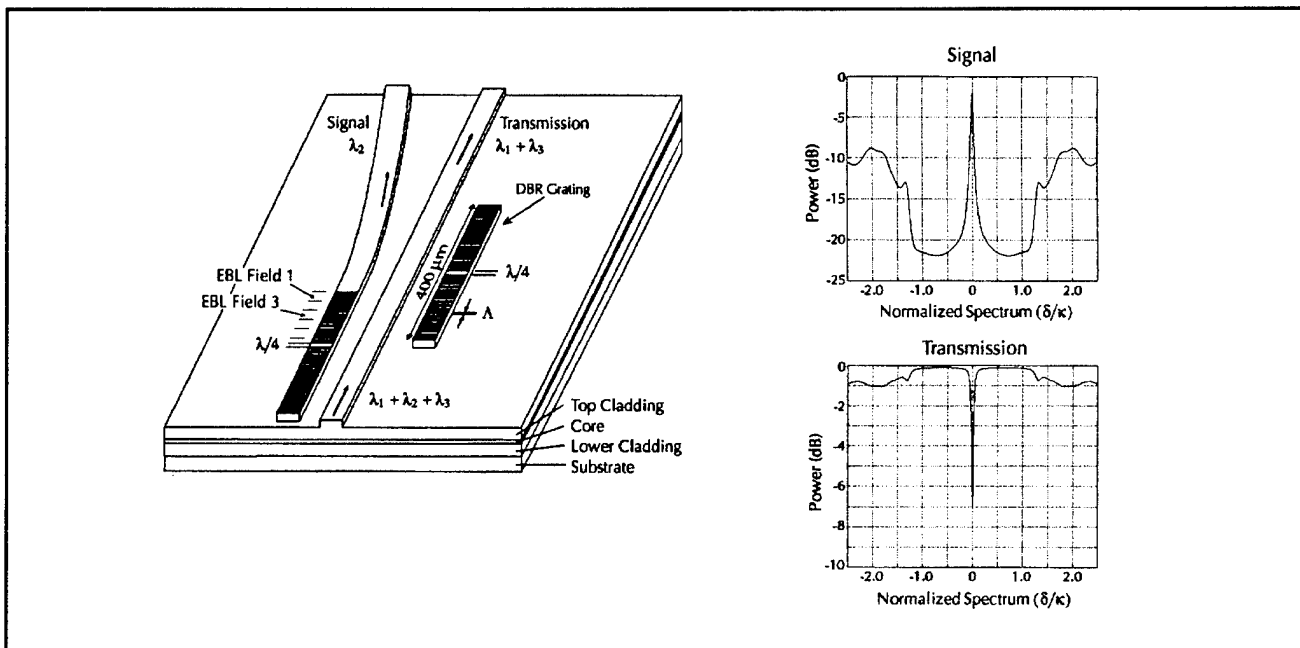


Figure 6. An illustration of the integrated-resonant channel-dropping filter. Two Bragg-grating resonators are weakly side-coupled to the center optical bus in order to remove only the on-resonant signal from the bus. The calculated receiver (signal) and transmission impulse responses show the channel selectivity.

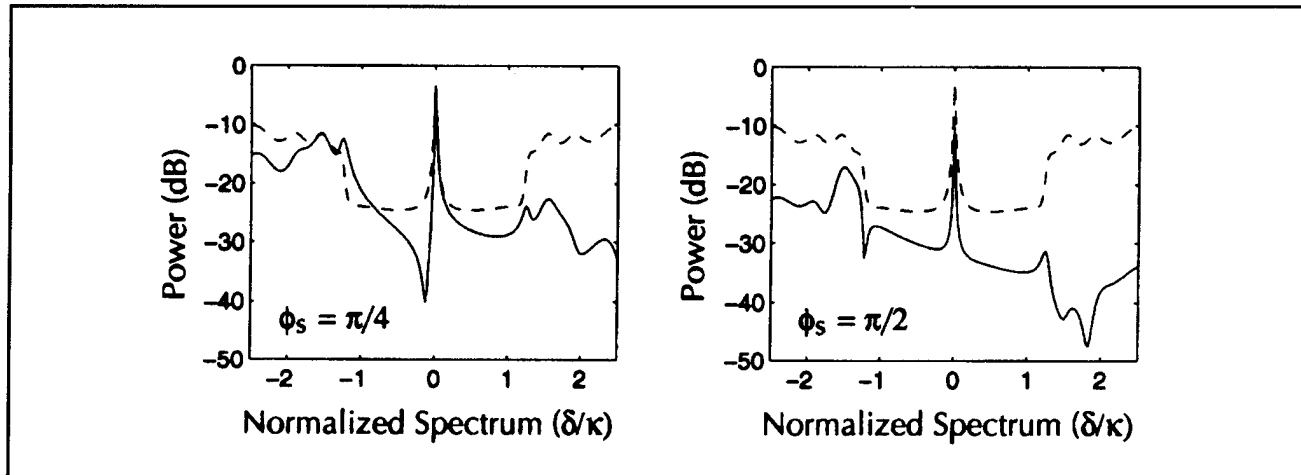


Figure 7. The phase mismatch between two asynchronous waveguides results in the distortion of the optical response of the channel-dropping filter. The phase slip is defined as $\phi_s = 2\pi \Delta n_{\text{eff}}/\kappa \lambda_0$ where κ is the grating strength.

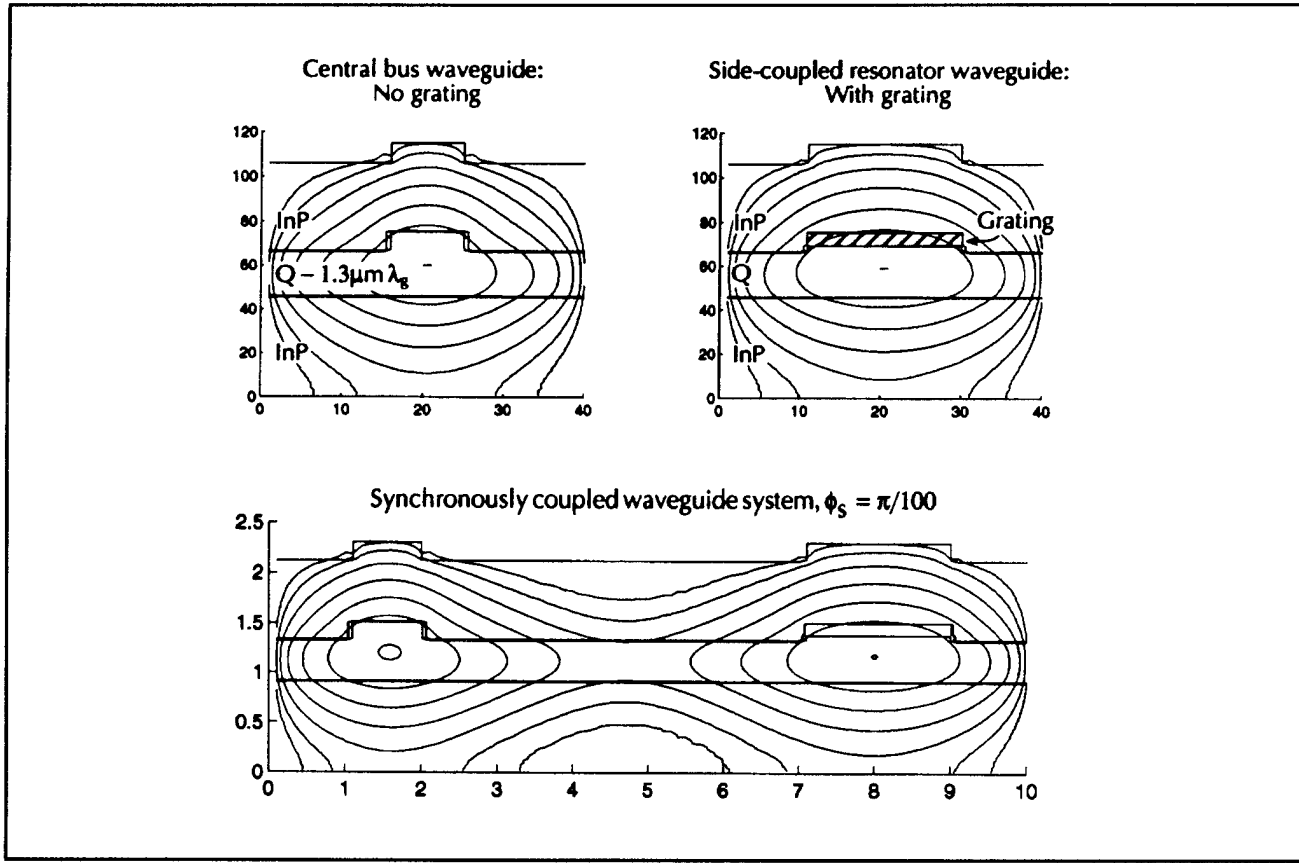


Figure 8. The top two figures show the calculated field profiles of the bus (rib) and resonator (grating) waveguides for an optimally-designed synchronous pair of waveguides. The mode overlap is as low as 99 percent while the effective index difference is only $\Delta n_{\text{eff}} \approx 0.2 \times 10^{-3}$. The grating strength is estimated to be $\sim 260 \text{ cm}^{-1}$, which would result in a $\sim 6 \text{ nm}$ stop band. The bottom shows the calculated field profiles of the coupled system. The inter-most circular field contours under the two waveguides show the difference in optical confinement that was built into the system. In the figure, Q refers to an (In,Ga)(As,P) quaternary alloy.

To fabricate the above design, the core (In,Ga)(As,P) material must be segmented into three layers with InP etch stops positioned at the

correct layer dimension. Tolerance calculations show that the core refractive index, which is related to the (In,Ga)(As,P) composition, must be controlled

to better than ± 0.6 percent to maintain an effective-index mismatch to within $|\Delta n_{\text{eff}}| \leq 0.001$. Furthermore, when the three-level segmented core is grown, the core thicknesses will only be estimated from a time/growth-rate product. If the actual growth rate changes from wafer to wafer, but the target times are held fixed, then the three thicknesses of the segmented core will scale. The tolerance on run-to-run growth-rate variation, as long as the growth rate remains constant during growth, is as large as ± 20 percent while Δn_{eff} remains within $|\Delta n_{\text{eff}}| \leq 0.001$.

Using the III-V-dedicated GSMBE reactor, the growth of a variety of $(\text{In},\text{Ga})(\text{As},\text{P})$ quaternary layers have been fabricated to understand the affect of the Group V overpressure on the quaternary composition. The Group III flux ratio is more easily maintained by establishing the proper effusion cell temperatures. Appropriate composition is necessary to establish the energy bandgap (and hence refractive index), but also to ensure that the layer remains lattice-matched to the InP substrate.

3.5.1 Publications

Damask, J.N., J. Ferrera, V.V. Wong, H.I. Smith, and H.A. Haus. "Limitations and Solutions for the Use of Integrated QWS-DBR Resonators in WDM Applications." *Proceedings of the SPIE International Symposium on Integrated Optical Conference on Nanofabrication Technologies and Device Integration*, Lindau, Germany, April 1994. 137: 2213, (1994).

Wong, V.V., J. Ferrera, J.N. Damask, J. Carter, E.E. Moon, H.A. Haus, H.I. Smith, and S. Rishton. "Spatial-Phase Locked E-beam Lithography and X-ray Lithography for the Fabrication of First-Order Gratings on Rib Waveguides." *J. Vac. Sci. Technol. B* 12(6): 3741-3745 (1994).

3.6 Phosphide-Based Optical Emitters for Monolithic Integration with GaAs MESFETs

Sponsor

National Center for Integrated Photonic Technology
Contract 542-381
Grant subcontract 652-693

Project Staff

Professor Clifton G. Fonstad, Jr., Professor Leslie A. Kolodziejski, Dr. Gale S. Petrich, Joseph F. Ahadian, Krishna V. Shenoy

A technology thrust aimed at developing a VLSI optoelectronic integrated circuit (OEIC) platform has, under the direction of Professor Fonstad, produced an "Epi-on-Electronics" (E-o-E) monolithic integration method in which optical devices are grown in foundry opened "epitaxy windows" on completed, fully-processed refractory metal GaAs VLSI MESFET circuits.⁷ These VLSI chips, commercially manufactured by Vitesse Semiconductor Co. and available through MOSIS, have been found to withstand extended temperature cycles of up to approximately 500°C without significant degradation of the electronic devices, and thus suggest the possibility of subsequent growth of optical devices using molecular beam epitaxy (MBE). A difficulty, however, is that substrate temperatures less than 500°C are not optimal for the conventional MBE-growth of AlGaAs-containing LEDs and lasers; these devices exhibit compromised performance. High performance lasers, utilizing InGaP ($\text{In}_{0.49}\text{Ga}_{0.51}\text{P}$ is lattice matched to GaAs) as the wide bandgap material, have been realized by a number of groups.⁸ Since phosphorus-containing alloys are nominally grown by gas source MBE below 500°C, the integration of high quality LEDs and lasers based on this material system is the objective of the current project utilizing our III-V-dedicated GSMBE reactor.

Our current emphasis involves $(\text{In},\text{Ga})\text{As}$ quantum wells inserted between cladding layers of GaAs, as well as $(\text{In},\text{Ga})\text{P}$. Although GaAs is typically grown at 580°C, for our study the thin layers of GaAs (and InGaAs) are grown at 470°C, which is the desired

⁷ A.C. Grot, D. Psaltis, K.V. Shenoy, and C.G. Fonstad Jr., "Integration of LED's and GaAs Circuits by MBE Regrowth," *IEEE Photon. Tech. Lett.* 6: 891-821 (1994); K. Shenoy, C.G. Fonstad Jr., and J.M. Mikkelsen, "High-Temperature Stability of Refractory-Metal VLSI GaAs MESFETs," *IEEE Electron. Dev. Lett.* 15: 106-108 (1994).

⁸ J.M. Kou, Y.K. Chen, M.C. Wu, and M.A. Chin, "InGaAs/GaAs/InGaP Multiple-Quantum-Well Lasers Prepared by Gas-Source Molecular Beam Epitaxy," *Appl. Phys. Lett.* 59: 2781-2783 (1991); G. Zhang, J. Nappi, K. Vanttilen, H. Asonen, and M. Pessa, "Low Threshold Current Strained-Layer InGaAs/GaAs/InGaP Lasers Grown By Gas-Source Molecular Beam Epitaxy," *Appl. Phys. Lett.* 61: 96-98 (1992).

temperature for growth of the (In,Ga)P and (In,Ga)As layers. InGaP/GaAs/InGaAs quantum well separate confinement heterostructure lasers having threshold current densities of 220 A/cm^2 (for pulsed room temperature broad-area devices) have been fabricated (figure 9). Electroluminescence measurements on InGaP/GaAs double heterostructures have shown the efficacy of LEDs based on this structure (figure 10). However, the aforementioned structures have, thus far, been grown on bulk GaAs. Simultaneous growth within the "epitaxy windows" on the VLSI chips resulted in a very rough, highly defective surface morphology, which contrasts to the occurrence of a smooth, nearly featureless morphology on the bulk substrate. It immediately became apparent that the surface of the "epitaxy windows" was not properly prepared for epitaxy. Therefore, two remaining challenges to the integration process are now being addressed. First, the normal MBE practice of briefly elevating the substrate temperature (to around 600°C) to desorb the native GaAs oxide prior to epitaxy must be eliminated since it damages the upper-level metal interconnects. The technique under investigation uses a hydrogen plasma in the II-VI reactor to remove the oxide at a substrate temperature of $\sim 300^\circ\text{C}$. The second challenge is to develop a more robust procedure for preparing the "epitaxy windows" for growth, ensuring more reliable epitaxy results. These innovations will allow the integration of state-of-the-art emitters onto a VLSI optoelectronic integrated circuit.

3.7 Photonic Bandgap Structures

Sponsor

National Science Foundation
DMR 94-00334

Project Staff

Professor John D. Joannopoulos, Professor Leslie A. Kolodziejski, Professor L. Rafael Reif, Dr. Gale S. Petrich, Kuo-Yi Lim, Xiaofeng Tang

A photonic bandgap crystal is a periodic arrangement of dielectric scattering centers within a host dielectric matrix. The effect of the photonic bandgap crystal on the properties of photons is much like the affect of a periodic arrangement of atoms on the behavior of charge carriers. In many ways, the creation of an energy bandgap for carriers in a semiconductor is directly analogous to the creation of a photonic bandgap for photons in a photonic bandgap crystal. The periodic arrangement of the dielectric scattering centers, the discontinuity in dielectric constant between the scatterer and the host matrix, and the length scale associated with the scatterers contribute to determining the size of the photonic bandgap, as well as the frequency or wavelength of the photons affected by the photonic bandgap crystal. In this research project, both one-dimensional and three-dimensional photonic bandgap crystals are under

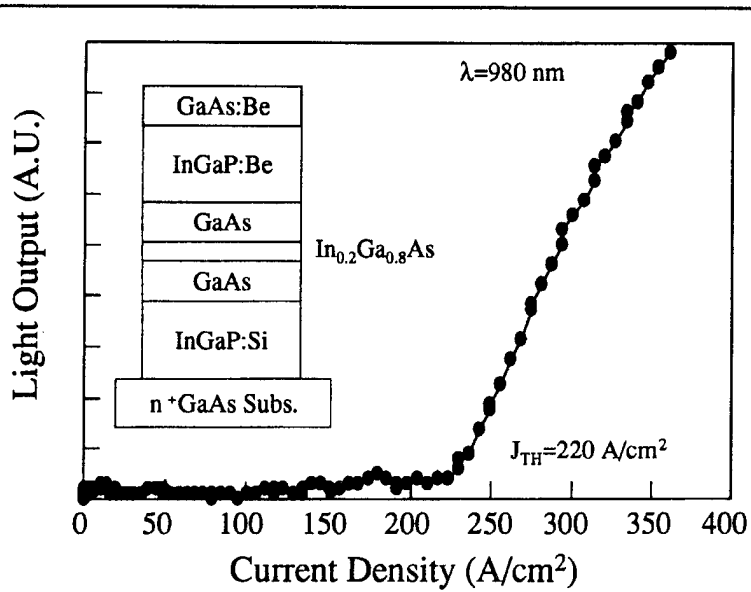


Figure 9. Light output versus current density for a room temperature pulsed broad-area InGaP/GaAs/InGaAs quantum-well separate confinement heterostructure laser. The measured low threshold current density verifies that high quality optical emitters based on this material system, and grown at 470°C , are possible. The inset shows a schematic of the laser structure.

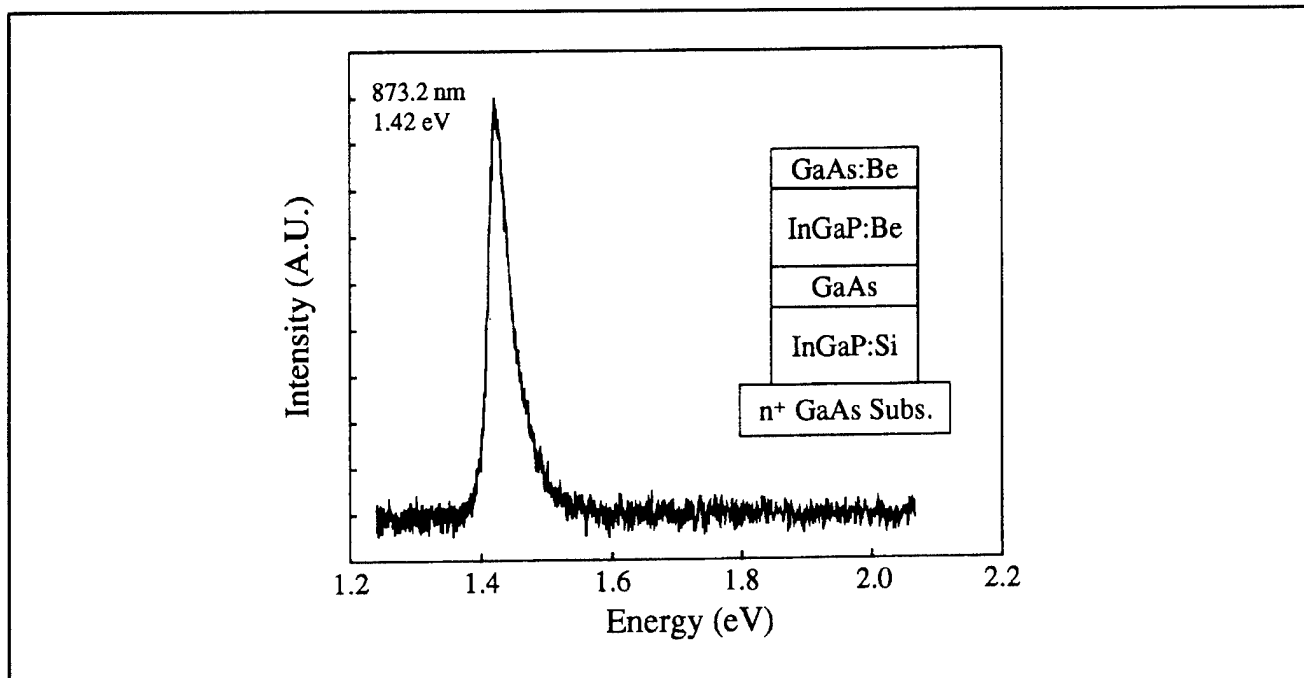


Figure 10. Electroluminescence from a InGaP/GaAs double heterostructure (inset shows a schematic) grown at 470°C. LEDs will be fabricated using this epitaxial structure.

investigation from the point of view of device fabrication, specifically for optical devices affecting 1.55 μm photons. Although the three-dimensional photonic bandgap structure has been simulated theoretically, the device fabrication is still in its infancy. Only the success in the fabrication of the one-dimensional structure will be described here.

A theoretical simulation of a semiconductor air bridge, containing holes that are placed periodically along the length of the bridge, shows that the electromagnetic radiation is confined within the air bridge in all three directions.⁹ Due to the periodicity of the holes (or dielectric scatterers) in the air bridge, the structure exhibits a photonic bandgap as a range of frequencies will not propagate within the bridge. The placement of a "defect", which locally disturbs the periodicity of the holes along the air bridge, creates a microcavity such that there is a high spatial concentration of a single electromagnetic mode. The Q factor of such a state has been calculated to exceed 13000.¹⁰ By adjusting the geometry of the system, the single mode of the microcavity can be placed within the photonic

bandgap of the air bridge and thus leads to the possibility of a semiconductor laser having a very low threshold current. Currently, initial prototypes of the semiconductor air bridges have been fabricated using Si/SiO₂ on Si substrates and GaAs/AlAs on GaAs substrates (figure 11). The thicknesses of each bridge was 0.5 μm . To create a semiconductor air bridge, the holes and the bridge are defined using reactive ion etching, and the material that is under the bridge is removed by selective wet chemical etching. The next generation of the one-dimensional photonic bandgap crystal will incorporate a waveguide leading to the air bridge in order to measure the transmission, and hence photonic bandgap, of the air bridges.

3.7.1 Publication

Villeneuve, P.R., S. Fan, J.D. Joannopoulos, K.Y. Lim, G.S. Petrich, L.A. Kolodziejski, and R. Reif. "Air-Bridge Microcavities." Submitted to *Phys. Rev. Lett.*

⁹ R.D. Meade, A. Devenyi, J.D. Joannopoulos, O.L. Alerhand, D.A. Smith, and K. Kash, "Novel Applications of Photonic Band Gap Materials: Low-loss Bends and High Q Cavities," *Appl. Phys. Lett.* 75: 4753-4755 (1994).

¹⁰ S. Fan, J.N. Winn, A. Devenyi, R.D. Mead, and J.D. Joannopoulos, "Guided and Defect Modes in Periodic Dielectric Waveguides," *J. Opt. Soc. Am. B*, forthcoming.

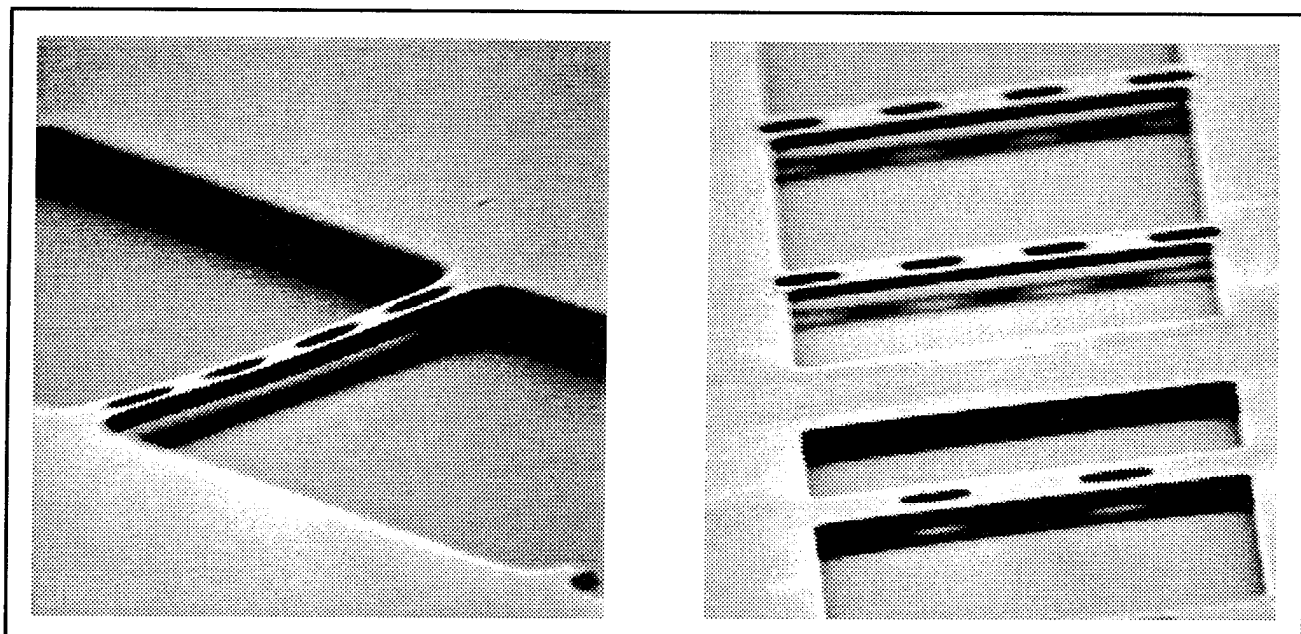


Figure 11. (left) SEM photograph of the Si bridge. The bridge has a length of 10 μm and a width of 4 μm . The holes are 2 μm in diameter and are separated by 3 μm from center to center. (right) SEM photograph of GaAs bridges. The bridges are 20 μm in length and range from 3.5 to 5.5 μm in width. The holes are all 2.5 μm in diameter and are separated from center to center by 7.5 μm (foreground) and 5 μm (background).

3.8 Heteroepitaxy of GaAs onto Corrugated Surfaces of Si

Sponsor

Joint Services Electronics Program
Contract DAAL03-92-C-0001
Grant DAAH04-95-1-0038

Project Staff

Professor Leslie A. Kolodziejski, Professor Henry I. Smith, Professor Carl V. Thompson, Dr. Gale S. Petrich, Sean M. Donovan

GaAs-based devices provide unique optoelectronic capabilities which are not available with Si-based devices. However, the processing technology for GaAs is not as mature as for Si VLSI processing technology. A natural step would be to combine the two device systems via monolithic integration, requiring the heteroepitaxial growth of GaAs onto Si substrates. Problems arise however from the 4.1 percent lattice constant mismatch and the large dif-

ference in thermal expansion coefficients occurring between GaAs and Si. Lattice constant and thermal expansion coefficient mismatch lead to the development of unacceptably high dislocation densities in the GaAs overlayer prohibiting the fabrication of optical devices. In earlier work by Professor Henry I. Smith and coworkers,¹¹ the growth of GaAs films on Si substrates, etched with a saw-tooth profile having a periodicity of 200 nm, resulted in a profound reduction of threading dislocations. A study is underway to determine the mechanism responsible for the reduction in dislocation density; this will result in the successful integration of GaAs and Si devices. Gas source molecular beam epitaxy is utilized for GaAs film growth on Si, where the high temperature *in situ* Si substrate cleaning step is avoided. This is essential for the monolithic integration of GaAs and Si devices. The study will also aid in the understanding of polar on non-polar epitaxy using GaAs-on-Si as a test structure. Current work is primarily focusing on establishing the optimal growth conditions for GSMBE of GaAs on Si substrates.

¹¹ K. Ismail, F. Legoues, N.H. Karam, J. Carter, and H.I. Smith, "High-quality GaAs on Sawtooth-Patterned Si Substrates," *Appl. Phys. Lett.* 59: 2418-2420 (1991).

Section 2 Quantum-Effect Devices

Chapter 1 Statistical Mechanics of Quantum Dots

Chapter 2 Artificial Atoms

Chapter 3 Coulomb Blockade in a Quantum Dot

Chapter 4 Superconducting and Quantum-Effect Devices

Chapter 5 Nanostructures Technology, Research, and Applications

Chapter 6 Single-Electron Spectroscopy

Chapter 1. Statistical Mechanics of Quantum Dots

Academic and Research Staff

Professor Boris L. Altshuler, Dr. Benjamin D. Simons, Dr. Nobuhiko Taniguchi

Graduate Students

Anton Andreev, Eduardo R. Mucciolo

Technical and Support Staff

Sarah Troutman

1.1 Project Description

Sponsor

Joint Services Electronics Program
Contract DAAL03-92-C-0001

In 1994, we concentrated our research on the dynamical properties of quantum dots. These closed systems which consist of a substantial but finite number of electrons usually demonstrate behavior that is called quantum chaos.¹ This behavior can be caused by disorder, the geometry of a quantum dot, or interactions between electrons. The phenomenon of quantum chaos was intensively studied by Berry for several years.² However, attention was concentrated for the most part on the statistics of energy spectra. It was found that these statistics are universal for systems with well developed chaos. Previously, we were interested in parametric spectra, in which exact energy levels are monitored as a function of an external tunable parameter, e.g., magnetic field. We studied the parametric spectral correlations and showed that these correlations are also universal, i.e., they depend only on the symmetries of the system and are the same for different systems and perturbations.

Our goal for 1994 was to extend the concept of universality, based on the phenomenon of quantum chaos, to the physically interesting and observable features of mesoscopic quantum objects. We found that, similar to spectral statistics, these features are determined by the relationship between the clas-

sical energy scale E_c and the quantum energy scale Δ , that is the mean level spacing.

We solved the fundamental problem of wave packet evolution within a chaotic quantum dot.³ Consider a particle that, originally at $t = 0$, is put at a certain point $r = 0$. At short times, the density distribution $\rho(t,r)$ demonstrates the usual ballistic and later (in a disordered dot) diffusion behavior.

At longer times, the density evolution depends on the symmetry of the system with respect to time inversion. If T -invariance is violated by a strong enough magnetic field, for example, the density distribution becomes nearly homogenous, at times $t_c \approx h/E_c$ (the time it takes a particle to get from one side of the dot to another side). However, the long time evolution turned out to be unexpectedly interesting: we found a remarkable evolution towards a state with increasing correlation with the original state. In other words, an echo appears. In 1991, Berry mentioned that the exact wave functions of a particle in a chaotic system $\Psi_v(r)$ are strongly inhomogenous and the correlation function $\langle |\Psi_v(0)|^2 \Psi_v(r)|^2 \rangle$ has a universal form.² For example, in two dimensions:

$$\langle |\Psi_v(0)|^2 \Psi_v(r)|^2 \rangle = C J_0(k|r|) \quad (1)$$

where $\langle \dots \rangle$ means ensemble and/or spectral averaging and $J_0(|r|)$ is a Bessel function that is known to decay very quickly for distances $|r|$ much bigger than the wavelength $1/k$. In terms of the wave packet evolution, this means that at $t = \infty$, density

¹ M.C. Gutzwiller, *Chaos in Classical and Quantum Mechanics* (New York: Springer Verlag, 1990).

² M.V. Berry, in *Chaos in Quantum Physics*, eds. M.-J. Giannoni, A. Voros, and J. Zinn-Justin (North Holland, Amsterdam, 1991), p. 251.

³ V.N. Prigodin, B.L. Altshuler, K.B. Efetov, and S. Iida, *Phys. Rev. Lett.* 72: 546 (1994).

distribution has a peak at $r = 0$: $\rho(\infty, r) = \langle |\Psi_v(0)|^2 \Psi_v(r)|^2 \rangle$.

We have not only computed the constant C, but also determined the dynamics of the density evolution. We found that at $t \gg t_c$, the density distribution has a form

$$\rho(t, r) = C(t) J_0(k|r|), \quad (2)$$

and the time dependance C(t) is determined by the Fourier transformed two-point spectral correlator:

$$C(t) = K(t) = \int \langle v(\varepsilon)v(\varepsilon + \omega) \rangle d\omega \quad (3)$$

Therefore, the evolution of the wave packet is determined by the spectral correlation, and the dynamical echo is a consequence of the spectral rigidity.

For T-invariant systems, the phenomenon is even more complex: there is a maximum in $\rho(t,r)$ at $r = 0$ even for $t < t_c$. This additional return probability is well known in the theory of weak localization. However, the echo takes place anyway and, if the spin-orbit interaction is substantially strong, the echo becomes even much more pronounced. Later, we analyzed the time dependence of the density distribution in several physically interesting cases: (1) for T-invariant systems, (2) in the cross-over regime, and (3) for a quantum dot with low conductance. We found that even in the latter case, when we do not yet know K(t) explicitly, we still can prove the validity of equation (3). We believe that the echo can manifest itself in a number of possible experimental situations.

We have also continued our work on quantum chaos in the band structure of complex crystals and superlattices. We have analyzed⁴ the *ab initio* band structure of silicon and the spectrum of the alloy AlGaAs. The Bloch quasimomenta act as in the Hamiltonian of a particle in a unit cell in close analogy to Aharonov-Bohm fluxes threading a torus. We found that the statistical properties of the band

structure obey the universal predictions derived from the theory of parametric quantum chaos. We have also analyzed the connection between the statistical properties and certain physical properties of a crystal with basic symmetries of the lattice.

We have started to study current fluctuations (noise) in a mesoscopic conductor using the non-equilibrium Keldysh diagram technique.⁵ We have derived a general expression for the fluctuations in the presence of a time dependent voltage V(t), valid for an arbitrary relation between voltage and temperature. Two limits are then treated: a pulse of voltage and a DC voltage. A pulse of voltage causes phase sensitive current fluctuations for which we derive microscopically an expression periodic in $\int V(t)dt$ with the period h/e . Applied to current fluctuations in Josephson circuits caused by phase slips, it gives an anomalous contribution to the noise with a logarithmic singularity near the critical current. In the DC case, we get a quantum to classical shot noise reduction factor of 1/3.

1.2 Publications

Altshuler, B.L., L.S. Levitov, and A.Y. Yakovets. "Non-equilibrium Noise in a Mesoscopic Conductor: Microscopic Analysis." *JETP Letters* 59: 857 (1994).

Mucciolo, E.R., R.B. Capaz, B.L. Altshuler, and J.D. Joannopoulos. "Manifestation of Quantum Chaos in Electronic Band Structures." *Phys. Rev. B* 50: 8245 (1994).

Prigodin, V.N., B.L. Altshuler, K.B. Efetov, and S. Iida. "Mesoscopic Dynamical Echo in Quantum Dots." *Phys. Rev. Lett.* 72: 546 (1994).

Thesis

Mucciolo, E.R. *Universal Correlations in the Quantum Spectra of Chaotic Systems in Exactly Solvable Many - Body Problems*. Ph.D. diss. Dept. of Physics, MIT, 1994.

⁴ E.R. Mucciolo, R.B. Capaz, B.L. Altshuler, and J.D. Joannopoulos, *Phys. Rev. B* 50: 8245 (1994).

⁵ B.L. Altshuler, L.S. Levitov, and A.Y. Yakovets, *JETP Letters* 59: 857 (1994).

Chapter 2. Artificial Atoms

Academic and Research Staff

Professor Marc A. Kastner, Dr. Olivier Klein

Visiting Scientists and Research Affiliates

Theodore M. Lyszczarz,¹ P. Mankiewich,² David C. Shaver,¹ Shalom Wind³

Graduate Students

David Abusch-Magder, David J. Goldhaber-Gordon, Nicole Y. Morgan

2.1 Goals and Objectives

Sponsors

Joint Services Electronics Program

Contract DAAL03-92-C-0001

Grant DAAH04-95-1-0038

National Science Foundation

Grant ECS 92-03427

When electrons are confined to a small particle of metal or a small region of semiconductor, both the energy and charge of the system are quantized. In this way such nanometer-sized systems behave like artificial atoms.⁴ The quantization of energy is familiar: The solutions of the Schrodinger equation in an isolated region have discrete energies. In some ways, however, the quantization of charge is more mysterious. We are quite comfortable with the idea that the charge of a collection of electrons is discrete. However, the charge in any small volume of a large sample of conductor is not discrete because the electronic wavefunctions are extended over the entire sample. Only when the states are localized is the charge quantized.

Artificial atoms have been constructed using metals and semiconductors, and they have been given a variety of names: single-electron-tunneling (SET)

transistor, quantum dot, single-electron transistor, and zero-dimensional electron gas. The physics of all these devices is the same, although the limits in which they operate may be quite different. The goal of our research is to better understand the physics of these devices in order to optimize their performance so that circuit design may commence.

The kind of artificial atom studied by our group is the single-electron transistor, illustrated in figure 1b.⁵ It consists of an inverted heterostructure: a degenerately doped substrate on which is grown a layer of AlGaAs and a layer of undoped GaAs. With source and drain contacts, this corresponds to a standard insulated-gate field-effect transistor. The strong electric field at the AlGaAs/GaAs interface caused by a voltage V_g on the lower gate confines electrons to the lowest quantum level for motion perpendicular to the surface at low temperature T , forming a two-dimensional electron gas (2DEG). The confinement is completed by a set of upper gate electrodes like those illustrated in the figure. In this case the tunnel barriers are introduced by constrictions in the electron channel defined by protrusions of the electrodes. With a lower-gate voltage applied, a droplet of electrons is confined in the potential well between the constrictions.

¹ MIT Lincoln Laboratory, Lexington, Massachusetts.

² AT&T Bell Laboratories, Short Hills, New Jersey.

³ IBM Corporation, Thomas J. Watson Research Laboratories, Yorktown Heights, New York.

⁴ M.A. Kastner, "Artificial Atoms," *Phys. Today* 46(1): 24: (1993).

⁵ U. Meirav, M.A. Kastner, and S.J. Wind, "Single-Electron Charging and Periodic Conductance Resonances in GaAs Nanostructures," *Phys. Rev. Lett.* 63: 1893 (1990).

2.2 Quantization of Energy and Charge

Figure 1a shows the conductance as a function of gate voltage for the single-electron transistor. The conductance is measured by reducing the drain-source voltage to less than kT/e , so that the response is Ohmic. We typically use $V_{ds} \sim 2\mu V$, corresponding to ~ 25 mK, near the base temperature of our dilution refrigerator. Of course, this means that the currents we measure are very small. The noise level seen in figure 1 corresponds to $\sim 10^{-15}$ amp. The conductance consists of sharp peaks that are roughly periodic in gate voltage. A calculation of the capacitance between the droplet of electrons and the gate⁶ shows that the voltage

between adjacent peaks or valleys is that necessary to add one electron to the droplet. At the low temperature of the experiment (electron temperature of ~ 50 mK) the peaks are very sharp so the peak-to-valley conductance ratio is larger than $\sim 10^3$ at low gate voltage.

One can understand the periodicity of the conductance peaks using the semiclassical Coulomb blockade model.⁷ The classical electrostatic energy stored in placing charge Q on the droplet is

$$E = QV + \frac{Q^2}{2C} \quad (1)$$

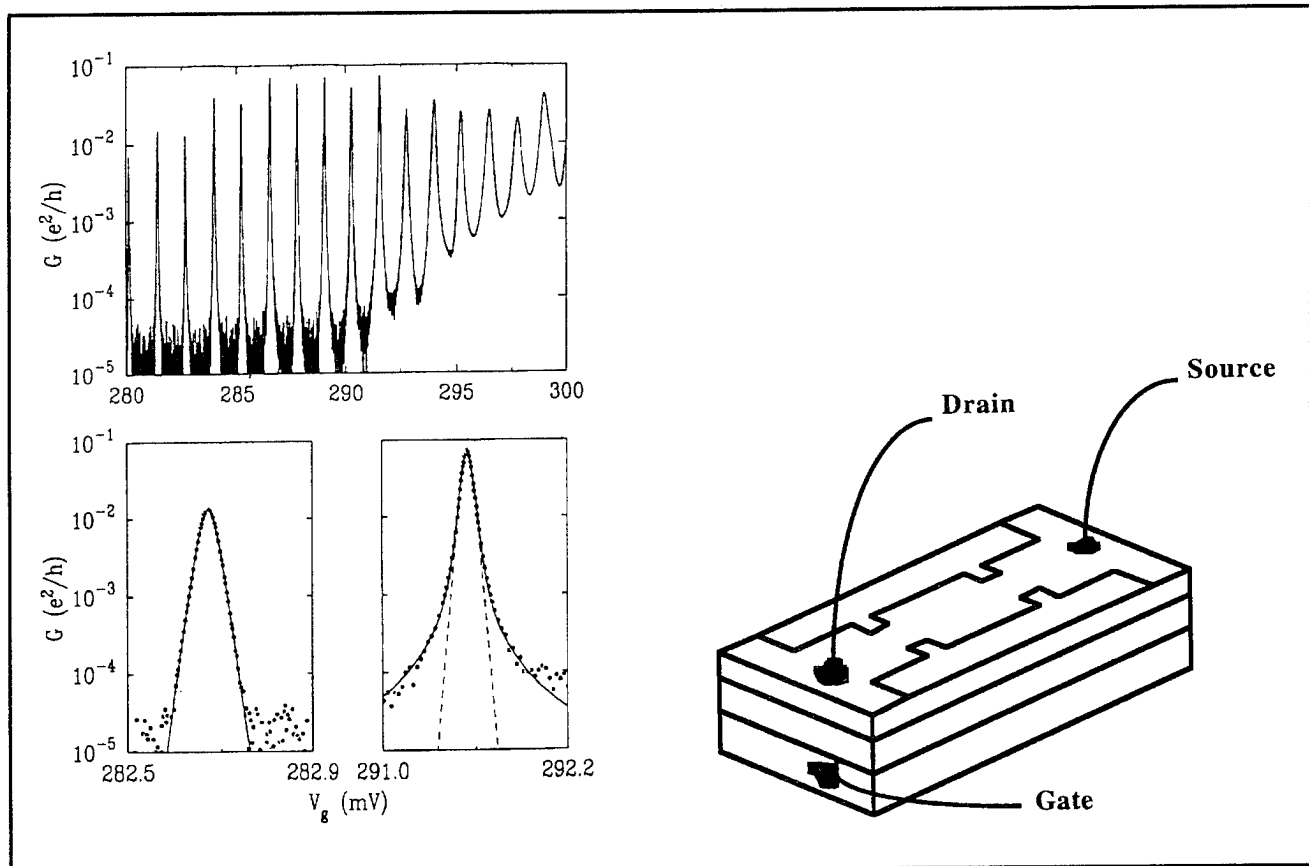


Figure 1. (a) Left: Conductance versus V_g showing broadening of levels with increasing V_g . Data was taken at magnetic field $B = 2.53$ T. The alternation of peak heights arises from the two spin states in the lowest Landau level. Bottom: Two of the peaks from the upper panel expanded to better illustrate their shapes. The lower V_g peak is well described by equation (4) and the higher V_g peak displays the Lorentzian tails as predicted by equation (4). (b) Schematic of device structure.

⁶ U. Meirav, M.A. Kastner, and S.J. Wind, "Single-Electron Charging and Periodic Conductance Resonances in GaAs Nanostructures," *Phys. Rev. Lett.* 63: 1893 (1990).

⁷ D.V. Averin and K.K. Likharev, "Single Electronic Correlated Transfer of Single Electrons and Cooper Pairs in Systems of Small Tunnel Junctions," in *Mesoscopic Phenomena in Solids*, eds. B.L. Altshuler, P.A. Lee, and R.A. Webb (Amsterdam: North-Holland, 1991). This is a comprehensive review of single-electron tunneling in metals.

The first term is the attractive interaction between the droplet and nearby conductors, and the second term is the repulsive interaction among the elements of charge on the droplet. C is the total capacitance of the droplet. If all electrode potentials except that of the gate are held constant, we can write $V = (C_g/C)V_g$ plus a constant. Equation (1) then shows that the energy as a function of Q is a parabola with minimum at $Q_0 = -C_g V_g$ (apart from a constant).

By varying V_g , we can choose any value of Q_0 . However, because the charge is quantized, only discrete values of the energy E are possible. When $Q_0 = -Ne$, for which an integer number N of electrons minimizes E , the Coulomb interaction results in the same energy difference $e^2/2C$ for increasing or decreasing N by one. In other words, there is a gap of size $e^2/2C$ for tunneling onto the artificial atom. For all values of Q_0 except $Q_0 = -(N + 1/2)e$, the energies for adding or subtracting an electron are not equal, but both are ≥ 0 . The gap is the same size but is shifted relative to the Fermi energy of the leads. Under these circumstances, no current can flow at zero temperature. However, if $Q_0 = -(N + 1/2)e$ the state with $Q = -Ne$ and that with $Q = -(N + 1)e$ are degenerate; the charge fluctuates between the two values even at zero temperature. Consequently, the energy gap in the tunneling spectrum disappears and current can flow. The peaks in conductance are, therefore, periodic, occurring whenever the average charge on the artificial atom is $Q_0 = -(N + 1/2)e$, spaced in gate voltage by e/C_g .

2.3 Spectroscopy of Artificial Atoms: The Three Energy Scales

The Coulomb blockade model accounts for charge quantization but ignores the quantization of energy resulting from the small size of the artificial atom. The confinement makes the energy spacing of levels in the atom relatively large especially at low energies. One can think of this spacing as roughly $\Delta E = (dN/dE)^{-1}$ where dN/dE is the density of states in the confined region. Because dN/dE increases with energy, ΔE decreases. If there are many elec-

trons in the atom, they fill up many levels, and the level spacing at the Fermi energy becomes small. The SET transistor has so many electrons that the level spectrum is usually thought of as continuous. However, the underlying discreteness of the level spectrum is essential for the observation of all single-electron phenomena, even those in the SET transistor.

The energy level spectrum can be measured directly by observing the tunneling current at fixed V_g as a function of the voltage (V_{ds}) between drain and source. Suppose we adjust V_g so that $Q_0 = -Ne$ and then begin to increase V_{ds} . The Fermi level in the source rises in proportion to V_{ds} relative to the drain, so it also rises relative to the energy levels of the artificial atom. Current begins to flow when the Fermi energy of the source is raised just above the first quantized energy level of the atom. As the Fermi energy is raised further, higher energy levels in the atom fall below the Fermi energy, and more current flows because there are additional channels for the electron to use for tunneling onto the artificial atom. Only one electron at a time can enter the atom, but the rate increases because there is more than one channel for the electron to use in tunneling onto the atom. Interestingly, if a level falls below E_F that has a large matrix element for tunneling into the atom but a small one for tunneling out, the current will decrease with increasing V_{ds} giving a negative differential conductance.⁸ We measure the energies of the levels by measuring the voltage at which the current increases (or decreases), or, equivalently, the voltage at which there is a peak (or valley) in the derivative of the current dI/dV_{ds} . Many beautiful tunneling spectra of this kind have been measured for quantum dots. We show one for our device in figure 2a. Similar level spectra have been reported by several groups.⁹

Increasing the gate voltage lowers all the energy levels in the atom by $-eV_g$, so that the entire tunneling spectrum shifts with V_g . This effect can be observed by plotting the values of V_{ds} at which peaks appear in dI/dV_{ds} , as is in figure 2b. One can see the gap in the tunneling spectrum shift lower with increasing V_g and then disappear at the charge-degeneracy point, just as predicted by the

⁸ J. Weis, R.J. Haug, K. von Klitzing, and K. Ploog, "Magnetotransport Investigations of a Quantum Dot with a Small Number of Electrons," *Physica B* 189: 111 (1993).

⁹ J. Weis, R.J. Haug, K. von Klitzing, and K. Ploog, "Magnetotransport Investigations of a Quantum Dot with a Small Number of Electrons," *Physica B* 189: 111 (1993); J. Weis, R.J. Haug, K. von Klitzing and K. Ploog, "Competing Channels in Single-Electron Tunneling through a Quantum Dot," *Phys. Rev. Lett.* 71: 4019 (1993); E.B. Foxman, P.L. McEuen, U. Meirav, N.S. Wingreen, Y. Meir, P.A. Belk, and S.J. Wind, "Effects of Quantum Levels on Transport Through a Coulomb Island," *Phys. Rev. B* 47: 10020 (1993); A.T. Johnson, L.P. Kouwenhoven, W. de Jong, N.C. van der Vaart, C.J.P.M. Harmans, and C.T. Foxon, "Zero-Dimensional States and Single-Electron Charging in Quantum Dots," *Phys. Rev. Lett.* 69: 1592 (1992).

Coulomb blockade model. One can also see the discrete energy levels of the artificial atom. For the range of V_{ds} shown in figure 2b, the voltage is only large enough to permit one extra electron to tunnel onto the atom. The discrete levels are the excited states of the atom with one extra electron or one extra hole. At still higher voltages (see figure 2c) we observe levels for adding two electrons and so forth. That is, a Coulomb staircase is seen with small steps superposed, corresponding to excited states of the artificial atom. The charge-degeneracy points are the values of V_g for which one of the energy levels of the artificial atom is degenerate with the Fermi energy in the leads when $V_{ds} = 0$, because only then can the charge of the atom fluctuate.

In the SET transistor the energies for adding electrons are equally spaced, by e^2/C , because the average electron-electron interaction completely determines the energy. For the quantum dot of Ashoori¹⁰ the energy spacings are large at low voltage, for which there are very few electrons in the artificial atom, but the spacings decrease with increasing number until they become approximately equally spaced. This happens because there is a large quantum mechanical confinement contribution to the energy for adding an electron at low number N of electrons, but the charging energy dominates the addition energy at high N .

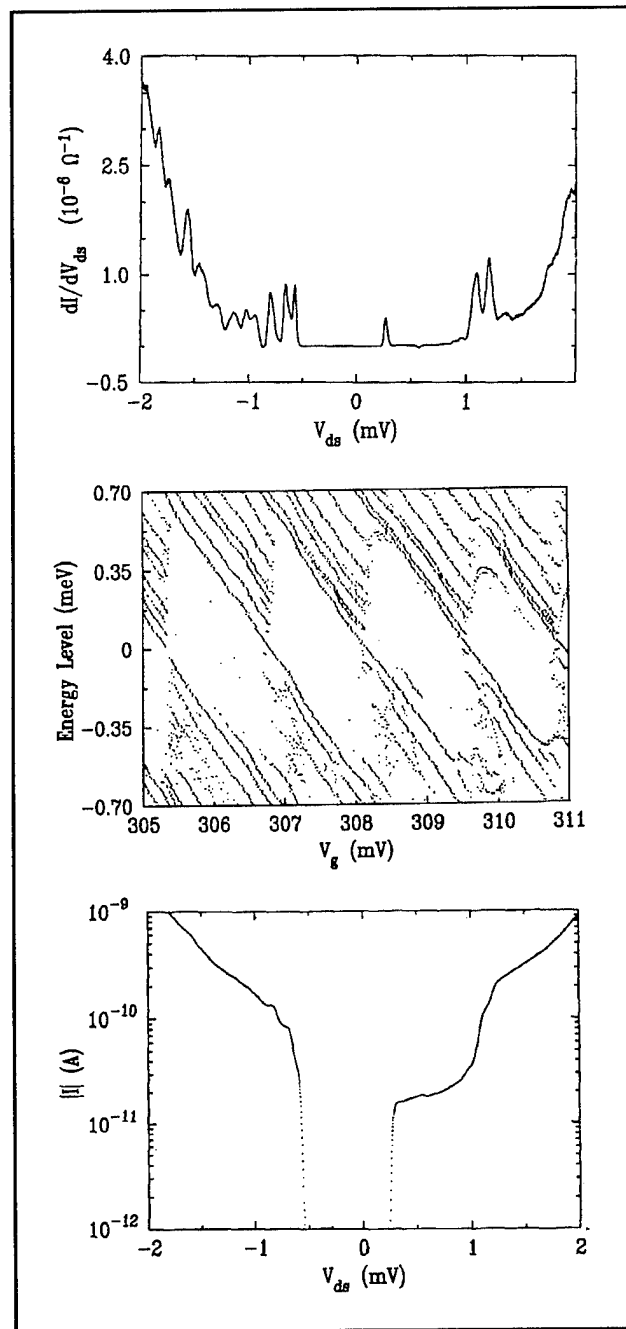


Figure 2. (a) Differential conductance at fixed V_g . The peaks and valleys correspond to V_{ds} at which the Fermi level in the leads is degenerate with the energy levels of the droplet of electrons. (b) Values of V_{ds} at which peaks and valleys are observed as a function of V_g . (c) Current as a function of V_{ds} found from integrating the data in figure 2a.

¹⁰ R.C. Ashoori, H.L. Stormer, J.S. Weiner, L.N. Pfeiffer, S.J. Pearton, K.W. Baldwin, and K.W. West, "Single-Electron Capacitance Spectroscopy of Discrete Quantum Levels," *Phys. Rev. Lett.* 68: 3088 (1992); R.C. Ashoori, H.L. Stormer, J.S. Weiner, L.N. Pfeiffer, S.J. Pearton, K.W. Baldwin, and K.W. West, "N-Electron Ground State Energies of a Quantum Dot in Magnetic Field," *Phys. Rev. Lett.* 71: 613 (1993).

In addition to the Coulomb interaction and the confinement energy, there is a third energy scale that is very important in understanding the behavior of artificial atoms. This is the width Γ of the energy levels resulting from tunneling between the artificial atom and the leads. Beenakker¹¹ suggested that the conductance near the charge degeneracy point should be given by that for resonant tunneling of non-interacting particles even though Coulomb interactions are obviously important. At zero temperature this single level conductance is

$$G_s = p \frac{e^2}{h} \frac{\Gamma_L \Gamma_R}{(E - E_o)^2 + \Gamma^2} \quad (2)$$

Here Γ_L and Γ_R are the tunneling rates (multiplied by h) through the left and right barriers, respectively, $\Gamma = (\Gamma_L + \Gamma_R)/2$, p is the level degeneracy, E is the energy at which the tunneling occurs, and E_o is the energy of the resonant level. At finite temperature the conductance is given by the convolution of $G_s(E)$ in equation (2) with the negative derivative of the Fermi-Dirac distribution function so the conductance is given by

$$G_s = p \frac{e^2}{h} \pi \frac{\Gamma_L \Gamma_R}{\Gamma^2} \int dE \frac{1}{kT} \frac{\Gamma^2}{(E - E_o)^2 + \Gamma^2} \operatorname{sech}^2 \left[\frac{E - \mu}{2kT} \right] \quad (3)$$

where μ is the chemical potential of the leads. Since the Lorentzian becomes a δ function in the limit $\Gamma \rightarrow 0$, G_s for narrow resonances is proportional to the derivative of the Fermi-Dirac function $(1/kT)\operatorname{sech}^2[(E-\mu)/2kT]$.

In our experiments, the electrochemical potential difference varies in proportion to the voltage V_g on the lower gate. In the limit $\Gamma \ll kT$, equation (2) reduces to

$$G_s = p \frac{e^2}{h} \pi \frac{\Gamma_L \Gamma_R}{\Gamma} \frac{1}{2kT} \operatorname{sech}^2 \left[\frac{E_o - \alpha eV_g}{2kT} \right] \quad (4)$$

where we have used $\mu = \alpha eV_g$, and $\alpha = U/e\Delta V_g$ is measured from the T dependence of the peak widths.¹² Meirav et al.¹³ showed that equation (4) is in excellent agreement with experimental shapes of conductance peaks at low V_g . An illustration of this is shown in the lower left panel of figure 1a. For higher V_g , the tails of the Lorentzian become apparent. However, over the entire range of V_g , equation (3) describes the conductance peaks very well. (See lower right panel of figure 1a.)

It is clear from this discussion that the tunneling measurements provide a spectroscopy of the energy levels of artificial atoms just as photoelectron spectroscopy provides a spectroscopy of the levels of natural atoms. In the case of tunneling the resolution of the spectroscopy is kT . When $kT < \Gamma$, one can probe the line shape of the levels. When $kT < \Delta E$, one can measure the level spacings. However, when $\Delta E < kT < U$, one can only measure the charging energy. The SET devices made of metals are always in the latter regime because ΔE and Γ are so small, whereas semiconductor devices may operate in any of the three regimes.

2.4 Criterion for Single-Electron Effects

It is well known that the condition for observation single-electron phenomena is that the conductance of the tunnel barriers must be less than the quantum of conductance e^2/h . However, it is not often made clear what this means on a microscopic level. It is usually argued that this criterion comes from the requirement that the charging time through the tunnel junction $R_f C$ be greater than the uncertainty time given by h/U . With $U = e^2/C$ this gives the correct criterion. However, it gives no insight into the underlying physics. To develop this insight, we must realize that the fundamental criterion for single-electron phenomena is that $\Delta E > \Gamma$. This is obviously the condition under which the energy of the droplet can be considered discrete. However, Thouless¹⁴ pointed out that it is also the condition for localization of charge on the droplet. Only when the charge is localized can there be a Coulomb gap in the tunneling spectrum. Thus single-electron

¹¹ C.W.J. Beenakker, "Theory of Coulomb-Blockade Oscillations in the Conductance of a Quantum," *Phys. Rev. B* 44: 1646 (1991).

¹² E.B. Foxman, P.L. McEuen, U. Meirav, N.S. Wingreen, Y. Meir, P.A. Belk, and S.J. Wind, "Effects of Quantum Levels on Transport Through a Coulomb Island," *Phys. Rev. B* 47: 10020 (1993).

¹³ U. Meirav, M.A. Kastner, and S.J. Wind, "Single-Electron Charging and Periodic Conductance Resonances in GaAs Nanostructures," *Phys. Rev. Lett.* 63: 1893 (1990).

¹⁴ D.J. Thouless, "Maximum Metallic Resistance in Thin Wires," *Phys. Rev. Lett.* 39: 1167 (1977).

effects can only be seen when $\Delta E > \Gamma$. Following Thouless, the current through the droplet is

$$I = \frac{e}{t} \frac{dN}{dE} eV_{ds} \quad (5)$$

where t is the time for an electron in a single quantum state to traverse the droplet, and $(dN/dE)eV_{ds}$ is the number of such current-carrying channels. Using $\Gamma = h/t$ and $dN/dE = 1/\Delta E$, we find that the condition $\Delta E > \Gamma$ is the same as $G < e^2/h$.

Foxman et al¹² presented data which demonstrate that the Coulomb charging energy disappears when G exceeds e^2/h . Their results are shown in figure 3. Fitting the peaks in the top panel with the form of equation (3) one extracts U and Γ for each one. In addition, using the data of figure 2 and similar data taken by reversing the source and drain, one can determine the separate capacitances between the droplet and each lead, C_r and C_l . By varying the voltages on the top gates, one observes a sequence of conductance peaks like those in the top panel of figure 3 from which one determines the capacitance between the top gates and the droplet, as well. Adding up all the capacitances, one can compute $e^2/2C$, where C is the total capacitance, and this agrees well with U determined from fitting the peaks with equation (3). One should note that in all these experiments we actually measure current not the charge on the droplet, so we are not actually measuring the capacitances. Instead, we are measuring the changes with voltage of the energy of the droplet relative to the leads.

One sees from figure 3 that U goes to zero at a critical gate voltage V_c . This happens because one of the tunnel-barrier capacitances (labeled C_r) diverges as $(1-V_g/V_c)^{-1}$. As one approaches V_c from below, Γ grows exponentially, as demonstrated in the second panel of figure 3. This is presumably because the tunnel barrier height is lowered by the gate voltage, and Γ is an exponential function of this height. In the absence of the magnetic field, one would expect $\ln \Gamma \sim \sqrt{(\phi - \mu)}$ where ϕ is the potential energy, but in a strong magnetic field, $\ln \Gamma \sim (\phi - \mu)$, as observed.¹⁵

Although Foxman et al did not appreciate this at the time of their experiment, it can all be understood in a simple way. As the gate voltage is increased, one of the barriers becomes transparent before the other because they are not identical and because their transmission varies exponentially with V_g . The

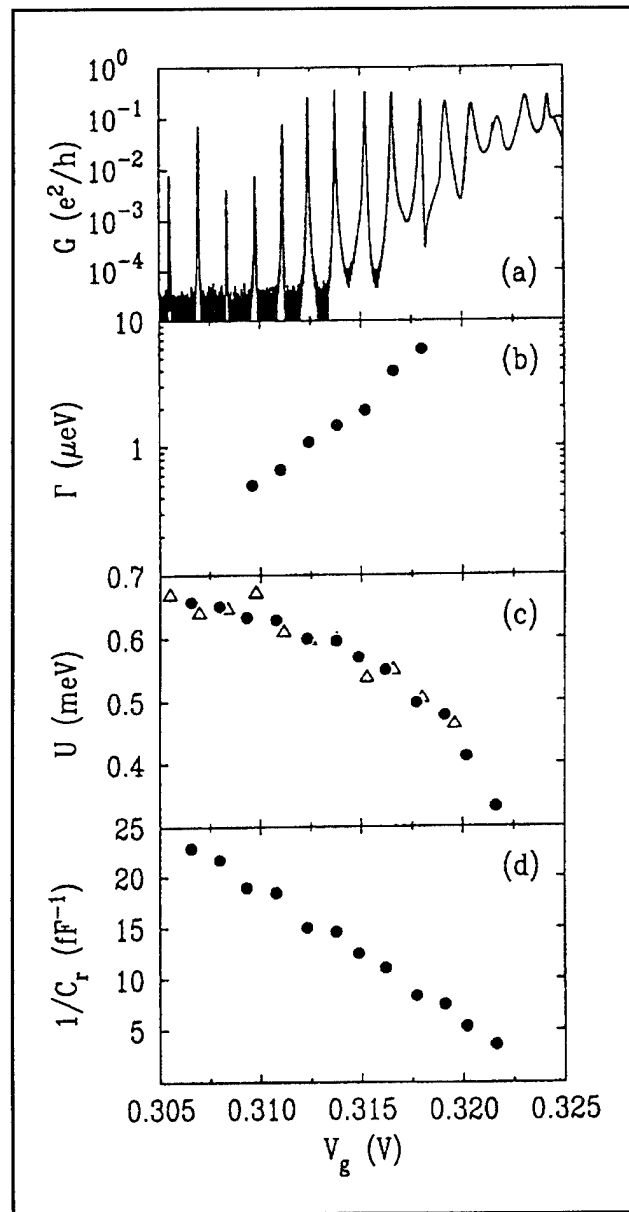


Figure 3. (a) Conductance versus gate voltage. (b) Full width at half-maximum of the Lorentzian component in each peak in (a) found by fitting equation (3). (c) Coulomb charging energy U determined (triangles) by fitting each peak with equation (3) using $\mu - \alpha eV_g$ and $\alpha = U/e\Delta V_g$, where ΔV_g is the spacing between peaks. Also shown is U determined (solid circles) by adding up all capacitances and using $U = e^2/2C$. (d) The reciprocal of the capacitance between the droplet of electrons and one of the leads, arbitrarily labeled the right.

localization length λ for the transparent barrier grows as $\sim (\phi - \mu)^{-1}$ and diverges at the critical voltage at which the height of the barrier above the

¹⁵ H.A. Fertig and B.I. Halperin, "Transmission Coefficient of an Electron Through a Saddle-Point Potential in a Magnetic Field," *Phys. Rev. B* 36: 7969 (1987).

Fermi energy goes to zero. The Coulomb energy associated with transfer of electrons across this barrier is $\sim e^2/\lambda$, which goes to zero at the critical gate voltage at which the localization length diverges. For the experiment of figure 3, V_c is about 0.325 V. Extrapolating G to V_c , one sees that it reaches ~ 50 eV at the critical point. This is just the average spacing between the levels ΔE extracted from the data of figure 2.

Thus, theory and experiment are in excellent agreement. The criterion for charge quantization and energy quantization are the same: the level spacing must be larger than the level width. This is true for metallic structures, like the SET transistor, as well. The condition $G < e^2/h$ guarantees that $\Delta E > \Gamma$ even though both quantities are smaller than kT , and therefore cannot be determined.

2.5 Crossover from Single to Multilevel Transport

At high enough temperatures, which is always the case for metallic single-electron devices, current is carried by many adjacent levels because $kT > \Delta E$. In this multilevel regime, the conductance is given by Kulik and Shekhter:¹⁶

$$G_m = \frac{e^2}{h} \frac{\rho}{4} \frac{\Gamma_L \Gamma_R}{\Gamma} \frac{\mu_c - \alpha e V_g}{kT} \operatorname{csch} \left[\frac{\mu_c - \alpha e V_g}{kT} \right] \quad (6)$$

where ρ is the density of levels (i.e., $1/\Delta E$) and μ_c is the chemical potential for which there is a charge degeneracy point for the artificial atom. That is, $\mu_c/\alpha e$ is the gate voltage at which the states with N and $N+1$ electrons have the same energy, the con-

dition for a conductance peak. To better than one percent, equation (6) is equivalent to

$$G_m = \frac{e^2}{h} \frac{\rho}{4} \frac{\Gamma_L \Gamma_R}{\Gamma} \operatorname{sech}^2 \left[\frac{\mu_c - \alpha e V_g}{2.5 kT} \right] \quad (7)$$

which has the same functional form as equation (4) for single level transport. However, the temperature dependencies are different. The peak height for the single level conductance is proportional to $1/T$ whereas for the multilevel conductance, it is temperature independent. The latter comes about because each level contributes a conductance that decreases as $1/T$, but the number of levels contributing increases as T . In addition to this difference in the T dependence of the peak height, the full width at half maximum of the peak is $3.5 kT$ for the single-level case but is $4.35 kT$ for the multilevel case.

These effects have been recently seen in our experiments.¹⁷ Figure 4 shows the temperature dependence of a single peak. Figure 4a shows the inverse of its amplitude as a function of T , which is proportional to T at low T as predicted by the single level form (equation 4). Above about 0.5 K the peak conductance becomes independent of temperature as predicted by the multilevel form (equation 6 or 7). The width of the peak also shows this crossover. The full width at half maximum is plotted as a function of T in figure 4b. The shallower line in the lower panel is the single-level prediction, $3.5 kT$, and the steeper line is the multilevel prediction, $4.35 kT$. This is dramatic evidence for the crossover from single-to-multilevel behavior and shows that the crossover occurs in a narrow range of T . The crossover temperature is expected to be $\sim \Delta E$, which gives $\Delta E \sim 40 \mu\text{eV}$. This is consistent with the level spacings measured by Foxman et al¹⁸ using source-drain tunneling spectroscopy (figure 2). As mentioned above, the SET devices made of metals are always in the multilevel regime because the level spacings are so small.

¹⁶ I.O. Kulik and R.I. Shekhter, "Kinetic Phenomena and Charge Discreteness Effects in Granulated Media," *Zh. Eksp. Teor. Fiz.* 68: 308 (1975), *Sov. Phys.-JETP* 41: 308 (1975).

¹⁷ E.B. Foxman, U. Meirav, P.L. McEuen, M.A. Kastner, O. Klein, P.A. Belk, D.M. Abusch, and S.J. Wind, "Crossover from Single-level to Multilevel Transport in Artificial Atoms," *Phys. Rev. B* 50: 14193 (1994).

¹⁸ E.B. Foxman, P.L. McEuen, U. Meirav, N.S. Wingreen, Y. Meir, P.A. Belk, and S.J. Wind, "Effects of Quantum Levels on Transport Through a Coulomb Island," *Phys. Rev. B* 47: 10020 (1993).

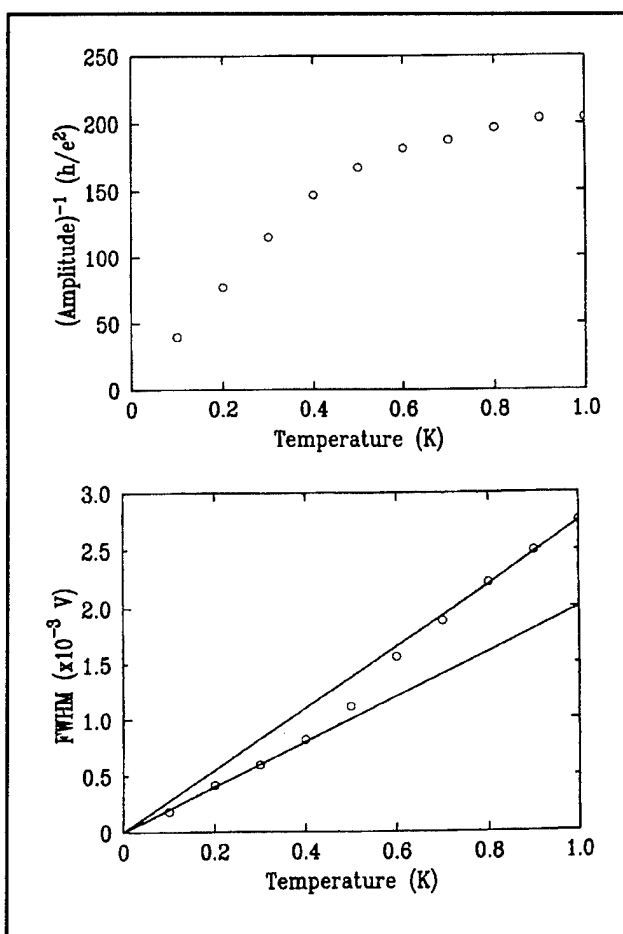


Figure 4. (a) Top: Height of one conductance peak as a function of temperature. The T^{-1} dependence indicates single-level transport. At higher T the conductance becomes constant indicative of multilevel transport. The crossover indicates that the level spacing ΔE is $\sim 40\mu\text{eV}$. (b) The crossover from single-level to multilevel transport is also indicated by the change in the proportionality between the width of the peak and T .

2.6 Ground State of the Artificial Atom in Strong Magnetic Fields

At zero magnetic field, the energy levels of our single-electron transistor appear to be approximately randomly spaced. This is presumably because the potential in which the electrons are confined is of sufficiently low symmetry that the eigenstates are in the regime of quantum chaos. Predictions have been made for the spacings of levels and their couplings Γ to the leads in this regime. However, we have not been able to test these properly so far because the temperature range in which we can probe one level at a time is very small. We expect this to become a major focus of our fundamental physics research on artificial atoms in the next few years when smaller atoms are constructed, for these will have larger level spacings, as discussed below.

At high magnetic fields, the level spacings become more regular. The strong field dominates the motion of the electrons, and only the parabolic component of the confining potential appears to be important. McEuen et al¹⁹ have tried to interpret results in this regime using a constant interaction model: One assumes a constant Coulomb charging energy, $e^2/2C$, for adding each new electron to the atom, and one assumes that once added the electrons do not interact with one another. While this model can explain some of the qualitative features of the experiments, it fails when quantitative comparisons are made.

The next step in modeling the system is to include the electron-electron interaction in a self-consistent but semi-classical (SC) way.²⁰ This SC model is similar to the Thomas-Fermi approximation and is the kind of modeling usually used for semiconductor devices. Until recently, we thought this was completely satisfactory. However, in the past year we learned how to test the SC model more stringently, and we found that it is also inadequate. One needs to include the exchange interaction between electrons in order to describe the energy spectrum properly. Next, we give a simple physical model that describes the effects of exchange and reviews our recent results.

¹⁹ P.L. McEuen, E.B. Foxman, U. Meirav, M.A. Kastner, Y. Meir, N.S. Wingreen, and S.J. Wind, "Transport Spectroscopy of a Coulomb Island in the Quantum Hall Regime," *Phys. Rev. Lett.* 66: 1926 (1991).

²⁰ P.L. McEuen, E.B. Foxman, J. Kinaret, U. Meirav, M.A. Kastner, N.S. Wingreen, and S.J. Wind, "Self-Consistent Addition Spectrum of a Coulomb Island in the Quantum Hall Regime," *Phys. Rev. B* 45: 11419 (1992).

First, consider the constant interaction model. From calculations²¹ as well as infrared studies,²² we know that the confining potential is approximately parabolic. For non-interacting electrons in a strong magnetic field and a parabolic potential the allowed single particle energies are given by

$$E_i = (n_i + 1)\hbar\omega_c + \frac{1}{2} m^* \omega_0^2 l_B^2 (m_i + 1) + g\mu_B B s_i \quad (8)$$

where $\omega_c = eB/m^*$ is the cyclotron frequency for effective mass m^* , ω_0 is the harmonic oscillator frequency from the parabolic confinement potential, n_i is the Landau level (LL) index for electron number i , l_B is the magnetic length defined below, m_i is the quantum number for the z-component of the orbital angular momentum, μ_B is the Bohr magneton, and s_i is the quantum number for the z-component of the spin angular momentum. The states for a given n_i and s_i can be thought of as orbits with centers at radii R_i given by

$$\pi R_i^2 B = (m_i + 1)\phi_0 = (m_i + 1)l_B^2 B, \quad (9)$$

each with an area containing one flux quantum $\phi_0 = hc/e$. The total energy of N electrons is found by summing up the single particle energies, given by equation (8) for the i th electron.

The largest term in the energy is $\hbar\omega_c$, so the energies of the higher LLs increase rapidly with increasing magnetic field. At the same time, l_B gets smaller so the confinement (second) term in equation (8) decreases for fixed m_i . As a result, electrons fall into successively lower LLs until all electrons are in the lowest LL ($n = 1$). Once this happens, ignoring the Zeeman (last) term in equation (8), the lowest energy state has all angular momentum states $m_i < N/2$ doubly occupied and all others empty if N is even. If N is odd, there is one unpaired spin in the state with $m_i = N/2 + 1$. The Zeeman term is not really zero so increasing the field further causes electrons with their spin antiparallel to the field (\downarrow) to, one at a time, flip their spins to become parallel to the field (\uparrow). The bare g-value in GaAs is very small (-0.44), so the total energy varies very slowly with B for non-interacting electrons once they all are in the lowest LL.

It turns out that the Coulomb interaction is much more important than the bare g-value in causing the spins to flip. As mentioned above, a peak in the conductance occurs when the electrochemical potential of the electron droplet $\mu + \alpha eV_g$ equals that of the leads. Thus, a measurement of the value of V_g at which the N th peak occurs is equivalent to measuring the chemical potential of the droplet with N electrons. When the magnetic field is increased, μ varies and displays a jump at fields for which there is a change in the electronic state of the droplet. Recall that the definition of μ is that it is the derivative of the free energy with respect to particle number. Thus a jump in μ indicates a change in slope of E vs. N for the ground state (GS), that is, a change in the GS.

Our experiment²³ measures very precisely the magnetic field B_n at which the n th jump in μ occurs, because at B_n there is a sharp minimum in the peak height. Figure 5 shows the peak position for one peak as a function of B ; a few of the peaks as a function of gate voltage are plotted in the inset. The change in behavior near 1.6 T signals the depopulation of all but the lowest orbital LL. We focus on the field regime above this, for which only the lowest orbital LL is occupied. For this region the values of B at which minima occur in the peak height are indicated by arrows. These are the fields at which electrons flip their spins from \downarrow to \uparrow .

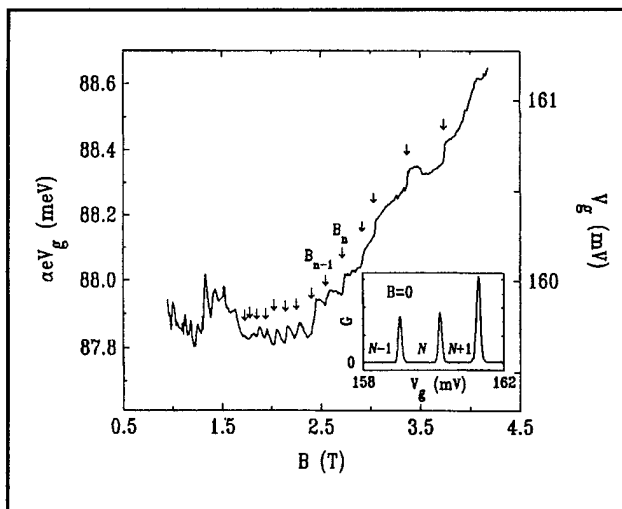


Figure 5. Peak position (multiplied by αe to convert to energy) as a function of magnetic field. Inset lower right shows peaks in conductance as a function of V_g .

²¹ A. Kumar, "Self-Consistent Calculations on Confined Electrons in Three-Dimensional Geometries," *Surf. Sci.* 263: 335 (1992).

²² U. Merkt, "Far-Infrared Spectroscopy of Quantum Dots," *Physica B* 189: 165 (1993).

²³ O. Klein, C. de C. Chamon, D. Tang, D.M. Abusch-Magder, S.-G. Wen, M.A. Kastner, and S.J. Wind, "Exchange Effects in an Artificial Atom at High Magnetic Fields," *Phys. Rev. Lett.*, forthcoming.

By taking differences between the B_n , we measure the increase in field necessary to flip one more spin. Therefore, the inverse of the field difference $\chi_n = (B_{n+1} - B_n)^{-1}$ can be thought of as the spin susceptibility of the droplet. Figure 6a shows the results of our measurement of this quantity, plotted versus B_n . Figure 6c shows the prediction of the constant interaction model (dashed line) and the SC model.²⁴ The SC calculation is much superior. The constant interaction model predicts values at least ten times too small and values that increase rather than decrease with B . The SC model predicts values of the correct magnitude which decrease with B , as observed. However, the SC model fails to predict the apparent divergence of χ_n at the field B_c . The SC model includes the electron-electron interaction as well as the Landau quantization, but it ignores exchange.

As seen in figure 6b, Hartree-Fock (HF), which includes exchange, provides a much better description of the data than does the SC model. It

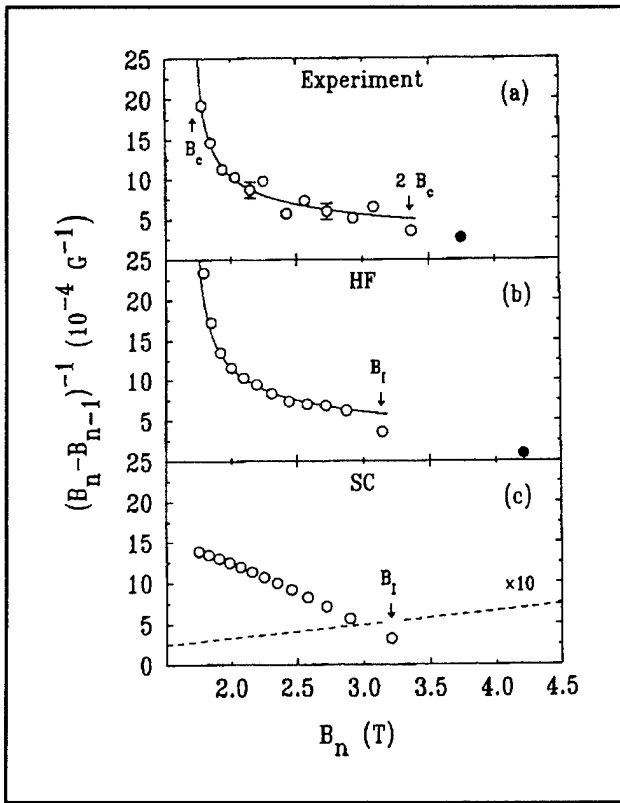


Figure 6. (a) Experimental measurement of χ_n . (b) Hartree-Fock calculation of χ_n . (c) Semiclassical (circles) and constant interaction (dashed line) calculations of χ_n .

predicts the divergence at B_c quantitatively. Fitting the data and the HF calculation to a power law gives the same exponent and the same prefactor, within the errors. This is dramatic evidence that exchange is important in determining the GS of the electron droplet.

To understand why exchange has this effect consider the states that are occupied when there are $N\uparrow$ up spins and $N\downarrow$ down spins. The effect of exchange is to reduce the Coulomb repulsion between electrons with parallel spins at small separations. This allows the confinement potential to force the electrons closer together than they would be with the Hartree (long range Coulomb) interaction alone. The result is that all states with $m_i < N\uparrow$ are occupied for spin up and all states with $m_i < N\downarrow$ are occupied for spin down. This gives a very different charge distribution $\rho(r)$ than the SC model. The SC charge density $\rho(r)$ is dome-like except near those values of r where the charge density is close to integer filling fractions $v = \phi_0\rho/B$. In these regions, ρ is constant for a range of r because of the incompressibility of the quantum Hall liquid. Sketches of the charge densities for the SC and HF calculations are shown in figure 7.

By summing the single particle energies, one finds that the total confinement energy associated with the HF density is

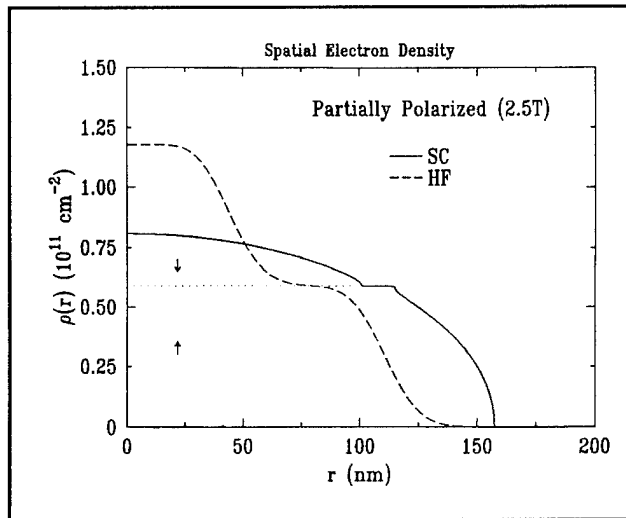


Figure 7. Semiclassical (solid line) and Hartree-Fock (dashed line) calculations of the charge density as a function of radius in the droplet. The density corresponding to one flux quantum per electron is shown by a dotted line separating spin down and spin up electrons.

²⁴ P.L. McEuen, E.B. Foxman, J. Kinaret, U. Meirav, M.A. Kastner, N.S. Wingreen, and S.J. Wind, "Self-Consistent Addition Spectrum of a Coulomb Island in the Quantum Hall Regime," *Phys. Rev. B* 45: 11419 (1992).

$$E_c = \frac{1}{2} m^* \omega_0^2 l_B^2 \{N\uparrow(N\uparrow+1) + N\downarrow(N\downarrow+1)\} = \frac{1}{2} m^* \omega_0^2 l_B^2 \{2S^2 + N^2/2 + N\} \quad (10)$$

where S is the total spin of the droplet $S = (N\uparrow - N\downarrow)/2$. To understand the physics, we treat S as a continuous variable even though it is actually discrete.

The confinement obviously favors the singlet state since E_c is a minimum for $S = 0$. However, the Coulomb interaction energy among the electrons is largest for the singlet because it has the largest density. We can not write a simple expression for the total Coulomb energy E_Q as we can for E_c . However, we know that it is a maximum for $S = 0$, because the singlet state keeps the electrons as close together as they can be. We also know that an expansion of the Coulomb energy as a polynomial in S will have only even powers because the Coulomb energy must be symmetric if we exchange up for down spins. Thus, the Coulomb energy for small S can be written

$$E_Q = \frac{e^2}{\epsilon l_B} [c_2 S^2 + c_4 S^4 + \dots] + \text{constant} \quad (11)$$

with the constant $c^2 < 0$. The prefactor $e^2/\epsilon l_B$ is the obvious scale for Coulomb interactions in a magnetic field because l_B is the distance between successive orbits. Ignoring the Zeeman energy because g is so small, we see that spins flip because, with increasing B at fixed S , E_c decreases as B^{-1} and E_Q increases as $B^{1/2}$ making the confinement less important than the Coulomb repulsion. In fact, were it not for the fourth order term in equation (11), all spins would flip at a single field B_c . By considering the balance of E_c and E_Q , one predicts that below the field B_c the singlet state is stable, but above B_c , the droplet acquires a spin which increases as $(B-B_c)^{1/2}$ or, equivalently, $X_n \sim (B-B_c)^{-1/2}$. The exponent we find from the fit of a power law to the data in figure 6a or the HF calculation in figure 6b is 0.4 ± 0.1 , within error of the prediction 0.5.

After the droplet is fully polarized at B_i , more transitions are observed. These are predicted qualitatively but not quantitatively by Hartree-Fock and probably therefore involve correlations.

2.7 Development of Process for Si Single-Electron Transistors

In the past six months, David Abusch-Magder, a graduate student in Physics, has made great progress in developing the fabrication process for single-electron transistors in Si. He has designed a class of devices using a double-gated MOSFET, which he will study to further illuminate both the physical and technological aspects of single electronics. The lower gate, set at a voltage below threshold, keeps most of the p-type surface insulating while the top gate inverts a small open region. The steps in this design were as follows:

Performed a literature search. There have been a very limited number of single electron transistors fabricated in silicon MOS systems. There is clearly a lack of knowledge about well controlled single-electron devices in material systems other than metals and GaAs.

Performed initial simulations to get an idea of the sort of device behavior expected. We have done initial simulations and have found software that will allow us to do more detailed work as the need arises. We have, however, decided that detailed simulations are less important than actually fabricating devices, and then using simulations as a tool to understand our measurements.

Designed a silicon process that is simple to carry out and is robust. We have done this making maximum use of existing technology and experience. Because of our device requirements we have chosen to make the device with a Cr lower metal gate. Since this is non-standard processing it has required additional process development.

Designed masks. We have attempted to design our masks to allow for a variety of physical measurements that might be interesting. We have also designed the masks so that a wide variety of lower gate metal patterns can be accommodated. This then allows the exploration of a large device space within the existing mask set and silicon process. We have also designed an optical mask level to pattern the lower metal gate which will allow us to build test devices to assess the impact of the process on the device parameters. Additionally, we have included redundancy in the mask to give a certain amount of fault tolerance.

Designed and wrote Scanning Electron Beam Lithography (SEBL) patterns on dummy substrates. Since the nanolithography on this project is very aggressive, it requires significant development work to obtain high quality patterns. We have written hundreds of different patterns at ten different exposure doses to obtain patterns that

will display interesting SET behavior. We have been forced to explore not only exposure and pattern variation, but also surface treatment of wafers, column charging effects, acceleration voltage, resist thickness, liftoff procedure and filament life cycle. Because of this work, we have successfully patterned lower gates with dimensions of 50 nm-100 nm. This is our most unique accomplishment so far.

Performed initial feasibility studies of our process. Before processing wafers we tested some key steps that are unique to our process to ensure that a process would be possible. Specifically, we investigated the deposition, patterning, and subsequent processing of our lower gate metal. We performed initial tests to liftoff nanolithographically patterned layers of Cr and trilayers of Cr-W-Cr. We also made sure that Low Temperature Chemical Vapor Deposition (LTCVD) of the oxide between the two gates and the subsequent rapid thermal annealing of these layers did not destroy the conductivity of the lower gate.

Designed and implemented an alignment scheme. We require a set of marks that allow both the optical lithography tool as well as the SEBL tool to align the wafer. These respective alignment schemes must be coordinated so all levels of the process are aligned with respect to each other. This had to be done taking subsequent processing into account to ensure that alignment marks do not get "buried".

Developed detailed process. This included specifying the process exactly, deciding exactly which machines will be used, and what recipes to follow for every detailed process step. This information then had to be entered into the clean room computerized environment. Several dry runs were necessary to work out minor bugs in the process. This has required significant work by Abusch-Magder in the clean room, both processing wafers and supervising the work of others, to make final decisions about contact hole etching, premetalization cleaning, and top gate metalization.

The following steps are in progress:

Assess process impact on device parameters. We are attempting to determine how different processes impact the device parameters. To that end, we have a lot of wafers all with different combinations of doping density, gate oxide thickness, rapid thermal anneal temperature cycle, contact hole etch recipe, and gate metalization. These wafers will then be tested to see how the device parameters vary. Among the device parameters we are examining are oxide charge, high temperature mobility, low temperature mobility, breakdown voltages of the insulating barriers that form on the contacts during processing, and inversion voltage thresholds.

Process wafers with single-electron devices. There are currently eight wafers with SEBL patterned lower metal gates that will be processed to completion in the next one to two months.

Bring device wafers to completion. This includes dicing and bonding devices. Future processing work includes: Fabricating another round of devices with different lower metal gate patterns to answer unresolved physical questions.

Finish process development for SEBL patterned wafers at 50 kV. Our SEBL has so far been done at 25 kV because the parameters at this voltage are known. On the other hand 50 kV gives a smaller spot size so smaller dimensions are possible. We have done initial work at 50 V, but have not finalized a process.

2.8 Publications

Foxman, E.B., U. Meirav, P.L. McEuen, M.A. Kastner, O. Klein, P.A. Belk, D.M. Abusch, and S.J. Wind. "Crossover from Single-Level to Multilevel Transport in Artificial Atoms." *Phys. Rev. B*. 50: 14193 (1994).

Klein, O., C. de C. Chamon, D. Tang, D.M. Abusch-Magder, S.-G. Wen, M.A. Kastner, and S.J. Wind. "Exchange Effects in an Artificial Atom at High Magnetic Fields." *Phys. Rev. Lett.* Forthcoming.

Chapter 3. Coulomb Blockade in a Quantum Dot

Academic and Research Staff

Professor Patrick A. Lee, Dr. Konstantin Matveev

Graduate Students

Dmitri Chklovskii

Technical and Support Staff

Imadiel Ariel

3.1 Project Description

Sponsor

Joint Services Electronics Program

Contract DAAH03-92-C-0001

Grant DAAH04-95-1-0038

Several years ago, Professor Kastner's group¹ discovered that the conductance through a quantum dot exhibits periodic oscillations as a function of gate voltage. These oscillations were interpreted as being due to the Coulomb blockade energy for adding an electron to the quantum dot. Most of the experimental and theoretical work dealt with the condition of strong blockade, where the electron states on the dot is coupled weakly to the states in the leads because the tunneling matrix element is small. However, it can be seen from the data that as the gate voltage is increased and the coupling between the dot and the leads becomes stronger, the sharp Coulomb blockade structures begin to merge and eventually become sinusoidal oscillations on top of a smooth background. The question then arises: what is the condition under which Coulomb blockade disappears as the coupling to the leads increases? Is there any signature remaining of the discrete quantization of charge as the dot becomes more open to the outside reservoir? This question was addressed by our research group in the past year.

Instead of tackling the transport problem, a slightly simpler problem was considered. The quantum dot is coupled to the outside reservoir via only a single lead, as shown in figure 1a. Furthermore, the lead is assumed to narrow adiabatically as shown in figure 1b, so that the electron state in the narrow region can be described by a single channel. In

this single terminal geometry, the conductance of the quantum dot cannot be measured. However, one can monitor the average charge Q on the dot as a function of gate voltage; i.e., one can measure the capacitance of the dot. Such experiments have

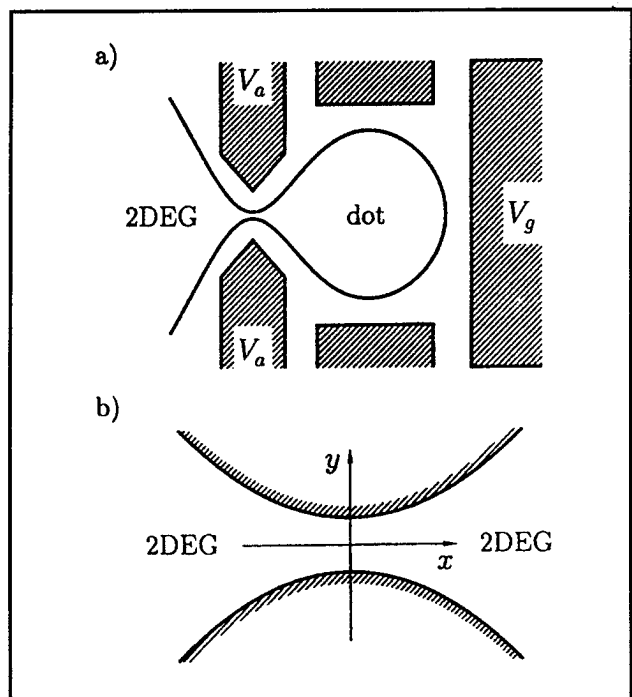


Figure 1. (a) Schematic view of a quantum dot connected to a bulk 2D electrode. The dot is formed by applying negative voltage to the gates (shaded). Solid line shows the boundary of the 2D electron gas (2DEG). Electrostatic conditions in the dot are controlled by the gate voltage V_g . Voltage V_a applied to the auxiliary gates controls the transmission coefficient τ through the constriction. (b) Constriction between two 2D regions. Inside the constriction the wave functions have 1D form which can be modeled by a single channel.

¹ M.A. Kastner, *Rev. Mod. Phys.* 64: 849 (1992).

been carried out by Professor Ashoori's group.² The coupling of the dot to the outside reservoir can be parametrized by the transmission coefficient T of the narrow lead. If $T=0$, the dot is completely isolated, and we expect perfect charge quantization, and Q should increase in steps as shown by the thick solid line in figure 2. If $T = 1$, the dot is fully open to the outside reservoir, and we expect no Coulomb blockade effect at all. Therefore, Q should be a simple linear function of the gate voltage, as shown by the thin solid line in figure 2. The question of interest is: what is the behavior of Q for intermediate T . The results are found to be the following:

1. If the electron is spin polarized, for instance, by an external magnetic field, the result is that for T slightly less than unity, the charge fluctuation can be described by a sinusoidal function. In this case, the Coulomb blockade washes out gradually as the coupling to the lead increases.
2. If the electron spin degeneracy is not lifted, a rather unexpected result is obtained. For any value of T between 0 and 1, it was found that Q as a function of gate voltage retains a non-analytic behavior at the point where Coulomb blockade occurs for the truly isolated dot. There is some residual memory of the blockade condition even when the dot is partially open to the outside reservoir. This surprising finding is related to rather subtle effects connected with the two channel Kondo problem, with the spin degeneracy playing the role of the two channels. In particular, the slope of the curve shown in figure 2, i.e., the capacitance, is predicted to show a logarithmic divergence whenever Q is a half integer.

In conclusion, the capacitance of a quantum dot coupled to the outside world is predicted to exhibit

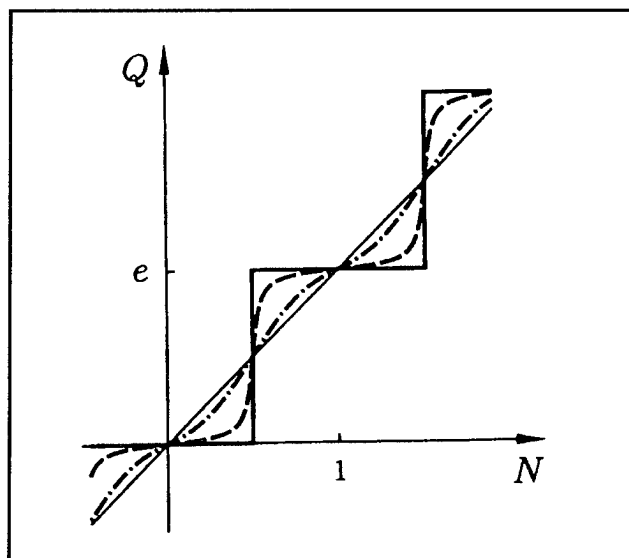


Figure 2. The average charge Q of the dot as a function of dimensionless gate voltage N at different values of transmission coefficient: $\tau = 0$ (solid line), $\tau \ll 1$ (dashed line), $1 - \tau \ll 1$ (dash-dotted line), and $\tau = 1$ (thin line).

quite different behavior depending on the presence or absence of a magnetic field. We are hopeful that in the future, this prediction can be tested by capacitance measurements of the kind carried out by Professor Ashoori's group.

3.2 Publications

Matveev, K.A. "Charge Fluctuations Under the Coulomb Blockade Conditions." *Physica B* 203: 404 (1994).

Matveev, K.A. "Coulomb Blockade at Almost Perfect Transmission." *Phys. Rev. B* 51: 1743 (1995).

² R.C. Ashoori et al., *Phys. Rev. Lett.* 68: 3088 (1992).

Chapter 4. Superconducting and Quantum-Effect Devices

Academic and Research Staff

Professor Terry P. Orlando

Visiting Scientists and Research Affiliates

Dr. Herre S.J. van der Zant

Graduate Students

David Berman, David J. Carter, Janet A. Cutro, Amy E. Duwel, James J. Hugunin, Arvind Kumar, Laurence H. Lee, Derek S. Linden, Joel R. Phillips, Enrique Trías

Undergraduate Students

Robert D. Bock, Roger A.M. Receveur, Vjekoslav Svilan

Technical and Support Staff

Charmaine A. Cudjoe-Flanders, Angela R. Odoardi

4.1 Simulations of Vortices in Arrays of Josephson Junctions

Sponsor

National Science Foundation
Fellowship MIP 88-58764

Project Staff

Enrique Trías, Robert D. Bock, Professor Terry P. Orlando, Joel R. Phillips, Dr. Herre S.J. van der Zant, Professor Jacob K. White

Vortices play a central role in determining the static and dynamic properties of two-dimensional (2D) superconductors. Artificially fabricated networks of superconducting islands weakly coupled by Josephson junctions are model systems to study the behavior of vortices. Studies of vortices in Josephson junction arrays generally neglect the magnetic fields induced by currents flowing in the array, i.e., it is assumed that the penetration depth for flux λ is much larger than the size of the array. With the present SNAP technology, all niobium arrays have been made with λ of the order of the cell size, therefore, effect of induced fields must be considered for an accurate description of these systems.

We use numerical simulation to investigate how a variety of vortex static properties are affected by

finite penetration depth λ , and we calculate for the first time the self-consistent current and magnetic fields from a vortex in a 2D array. We find that in order to calculate the correct current and field distributions, the full 3D behavior of the magnetic fields must be accounted for by including nearly all mutual inductance terms. However, to calculate the energy barrier for cell to cell vortex motion—which was first shown by Lobb, Abraham, and Tinkham (LAT)¹ to be $0.2 E_J$, where E_J is the Josephson coupling energy—it is sufficient to include only self- and nearest-neighbor inductances. The LAT calculation neglected induced magnetic fields. We show that induced fields may increase the energy barrier substantially above $0.2 E_J$. Our calculations also show that (1) the thermodynamic lower critical field of the array is enhanced when the computation self-consistently accounts for induced magnetic fields, and (2) by using only a self-inductance term to model the induced fields, the lower critical field is overestimated.

Measurements and numerical studies of the self-field effects in arrays of Josephson junctions have been performed. For two-dimensional arrays, we find that the mutual inductive couplings among all the cells of the array must be included to correctly model the current and magnetic field distributions; whereas, for one-dimensional arrays of parallel junctions, these static properties can be modeled well by just including the nearest neighbor cou-

¹ C.J. Lobb, D.W. Abraham, and M. Tinkham, "Theoretical Interpretation of Resistive Transition Data from Arrays of Superconducting Weak Lines," *Phys. Rev. B* 27: 150-157 (1983).

plings. The lower critical field and the energy barrier for depinning are found to increase as the self-inductance becomes more important, and we verify these numerical results with measurements on both one- and two-dimensional arrays of niobium junctions. We have also simulated and measured some dynamical properties of arrays. For example, measurements of the Fiske modes and Eck peaks in one-dimensional arrays allow measuring the self and mutual inductances directly. Likewise, current-voltage characteristics of two-dimensional arrays show that the flux-flow resistance increases as the self-field effects become more important, reflecting the decrease of the effective mass of the vortex.

4.2 Superconducting Transmission Lines

Sponsor

Advanced Research Projects Agency/
Consortium for Superconducting Electronics
Contract MDA972-90-C-0021

Project Staff

Laurence H. Lee, Professor Jacob K. White, Professor Terry P. Orlando, in collaboration with W.G. Lyons²

A full-wave spectral-domain volume-integral-equation method has been developed to analyze various configurations of superconducting transmission lines: microstrip lines, striplines, coplanar strips, and coplanar waveguides. In the formulation, a spectral-domain Green's function for isotropic, layered media is used to set up an integral equation for the electric field inside the superconducting strips. Galerkin's method with roof-top basis functions is employed to solve for the complex propagation constant and current distribution. The characteristic impedance of the structures is then obtained from transmission line theory. This method rigorously accounts for the anisotropy and the finite thickness of the superconducting films, yielding accurate characterization for the loss and kinetic effect of the superconductors. However, this technique is computationally inefficient.

To implement an efficient method, an equivalent surface impedance is used to transform the superconducting strip with finite thickness to an infinitely thin strip. This equivalent surface impedance

accounts for the loss and kinetic inductance of the superconductors. An empirical formula for the current distribution in a thin superconducting film is determined for the derivation of the equivalent surface impedance. To include effects of anisotropic substrates, a 2D dyadic Green's function for anisotropic, layered media is used to formulate an integral equation for the surface current. Galerkin's method with entire-domain basis functions is used to solve for the complex propagation constant and the surface current. The characteristic impedance is then calculated using the power-current definition. This method has been used to analyze superconducting single and coupled microstrip lines on anisotropic substrates.

A closed-form expression was found for the current distribution in an isolated strip made from a superconducting thin film with thickness less than a few penetration depths. This equation gives a good approximation within certain limits for the resistance and inductance per unit length of superconducting striplines and microstrip lines. Both the ac resistance of an isolated superconducting strip and the resistance per unit length of a superconducting stripline calculated using this closed-form expression agree well with the numerical results generated by the modified Weeks' method. It is now possible to use this expression along with the integral equation method to develop an efficient full-wave method for analyzing superconducting planar transmission lines.

4.3 Discrete Superconducting Vortex Flow Transistors

Sponsor

Advanced Research Projects Agency/
Consortium for Superconducting Electronics
Contract MDA972-90-C-0021

Project Staff

Dr. Herre S.J. van der Zant, Professor Terry P. Orlando, in collaboration with Dr. K.A. Delin³

Vortex flow transistors (VFT) are the focus of renewed interest since a discrete flux flow device made of weak links in a high-temperature film demonstrated promising results. Current gains higher than one, transresistances of the order of 10Ω , a maximum output voltage of about 20 mV, and

² MIT Lincoln Laboratory, Lexington, Massachusetts.

³ Conductus, Sunnyvale, California.

speeds of the order of 50 ps were obtained. Flux-flow devices were proposed more than ten years ago and were fabricated in a long continuous Josephson junction. There are two versions of a VFT in long Josephson junctions; one is a device made of a long overdamped junction (the McCumber parameter $\beta_c < 1$) and the other is made with an underdamped junction ($\beta_c > 1$). The disadvantage of long Josephson junctions is that the output resistance is low (much smaller than 1 Ω) and that the output voltage is generally much smaller than 1 mV. Moreover, it is difficult to manipulate the parameters and improve the response time of the device. Discrete vortex flow transistors (DVPT) overcome these difficulties.

We have fabricated discrete overdamped vortex flow transistors (DVFTs) made of short niobium Josephson tunnel junctions connected in parallel. The results of our DVFT were compared with the high- T_c devices and long continuous Josephson junctions. We have also done model calculations on our DVFT which are in good agreement with our experimental results. We calculated the current gain, transresistance, output voltage, and output resistance. Our model is also applicable to other 1D discrete systems and can also be used to model long Josephson junctions. Our analysis shows that when disregarding the lower temperatures and voltage levels in low- T_c materials, DVFTs made of niobium tunnel junctions can perform at the level comparable to the present high- T_c flux flow devices.

4.4 Fiske Modes in One-Dimensional Parallel Josephson-junction Arrays

Sponsor

National Science Foundation
Grant DMR 91-08748

Project Staff

David Berman, Dr. Herre S.J. van der Zant, Professor Terry P. Orlando, in collaboration with Dr. K.A. Delin³

We have performed measurements on one-dimensional (1D) arrays of underdamped Josephson junctions connected in parallel by superconducting wires which in a magnetic field show resonances in the current-voltage characteristics. From analytical calculations, we find that the position of the steps is determined by the dispersion relation $\omega(k)$ of a 1D discrete, linear transmission line, where the Josephson junction has been replaced by the capacitor and the resistance of the junction. When nearest-neighbor inductances are accounted for, the model agrees well with the

measured positions of the steps. Numerical calculations of the full dynamics with inclusion of inductances between all cells support our model. As an example of a system with more complicated dispersion, we have measured 1D arrays with two different junctions per primitive cell. The measured dispersion relation shows an acoustic and an optical branch in agreement with numerical simulations of the full dynamics.

4.5 Novel Mesoscopic Superconducting Devices

Sponsors

National Science Foundation
Fellowship Program
U.S. Air Force - Office of Scientific Research
Grant F49620-92-J-0064

Project Staff

Professor Dimitri A. Antoniadis, James J. Hugunin, Professor Terry P. Orlando, Professor Henry I. Smith

Superconductor/semiconductor contacts are fabricated between V_3Si and Si by a solid-phase reaction between SiO_2 and V. Auger spectroscopy is used to confirm the presence of the V_3Si phase, the sheet resistance versus temperature of the device is measured to determine a superconducting transition temperature of 14 K.

The electrical properties of the V_3Si/Si interface are examined for cases where the V_3Si is in both normal and superconducting states. The first two measurements are performed at room temperature and are used to investigate the two forms of transport for normal electrons, either through or over a Schottky barrier. The second set of measurements are performed between 17 K and 0.3 K and are used to examine the properties of this interface as the superconducting energy gap increases in the V_3Si . Each of these three experiments shows a Schottky barrier height of about 0.16 eV for the V_3Si/Si interface. In addition, the low temperature measurements confirm that this interface is that of a superconductor/semiconductor.

There are two anomalies in this experiment. First, the current flow through the contacts is approximately 10^6 times smaller than that expected for contacts of the given area, indicating some flaw in the fabrication process. Second, low temperature measurements reveal unexpected structure near 0.5 meV. It is speculated that this is related to the presence of a superconducting phase of another vanadium compound.

4.6 Single Charging Effects and Tunneling in Quantum Dot Nanostructures

Sponsor

U.S. Air Force - Office of Scientific Research
Grant F49620-92-J-0064

Project Staff

Professor Dimitri A. Antoniadis, Martin Burkhardt, David J. Carter, Arvind Kumar, Professor Terry P. Orlando, Professor Henry I. Smith

Quantum-effect devices, whose feature size is comparable to the Fermi wave-length (about 50 nm in a typical inversion layer), have great potential in novel electronics applications because of their nonlinear characteristics. Such tunneling devices were fabricated using x-ray lithography and measured at cryogenic temperatures. The devices were fabricated on modulation doped AlGaAs/GaAs substrates. After mesa etch and deposition of ohmic contacts, x-ray lithography was used to put down the gate patterns. The finished device had minimum line widths below 70 nm.

This work focuses on the study of GaAs quantum dot devices in which an electron gas is electrostatically confined to a small conducting island. The device dimensions are sufficiently small that striking effects due to the capacitive charging of the island by a *single* electron can be observed in the transistor characteristics, leading to a *periodic* dependence of the current on gate voltage. In particular, we study a quantum dot structure in which a novel gate geometry allows the island to be contacted by three electron reservoirs. When the dot charge is well-confined, periodic conductance oscillations due to Coulomb charging are observed in-phase with each other at two of the leads in response to small excitation voltage at the third. As the tunnel barriers are made softer by changing the gate voltage, a strikingly different phenomenon is observed: conductance peaks at the two output leads evolve from perfect *correlation* to perfect *anti-correlation* with each other. Two simple models of transport in the weakly blockaded regime are presented as possible explanations.

4.7 One-dimensional Parallel Josephson-junction Arrays as a Tool for Diagnostics

Sponsor

Advanced Research Projects Agency/
Consortium for Superconducting Electronics
Contract MDA972-90-C-0021

Project Staff

A.W. Kleinsasser,⁴ Professor Terry P. Orlando, Roger A.M. Receveur, Dr. Herre S.J. van der Zant

We propose and demonstrate the use of underdamped, one-dimensional parallel arrays of Josephson junctions as a tool for circuit diagnostics. By measuring the Fiske modes and the critical current in a magnetic field, we determined the self- and nearest-neighbor inductances as well as the capacitances of single junctions. We have used this technique to find the capacitance of Nb-Al₂O_x-Nb junctions for critical current densities of 0.3 - 20 kA/cm². We find that the specific capacitance increases by about a factor of 2 over this range. This increase has important consequences for the design of single-flux-quantum circuits and SQUIDs. Measurement of the junction capacitance for critical current densities of 100 kA/cm² is possible, but requires submicrometer junctions with dimensions of the order of 0.3 μm.

4.8 Nonlinear Dynamics of Discrete Josephson Rings

Sponsor

National Science Foundation
Grant DMR 94-02020

Project Staff

Professor Terry P. Orlando, Steven H. Strogatz, Dr. Herre S.J. van der Zant, Shinya Watanabe

We have studied the dynamics of circular one-dimensional arrays of underdamped Josephson junctions connected in parallel. In these Josephson rings, a single vortex can be trapped and studied experimentally without the complications caused by reflections off boundaries. We find that a propagating vortex can become phase-locked to linear waves excited in its wake. In the *I/V* curve, resonant steps are observed indicative of this phase-

⁴ IBM Corporation, Thomas J. Watson Research Center, Yorktown Heights, New York.

locking. Their position is well predicted by theory and, numerical simulations indicate that, at least in principle, an infinite number of these steps is possible. Resonant steps also occur in the I/V curves for higher voltages in the return path of the subgap region. These resonant steps have a completely different origin. They occur at voltages where the periodic whirling solution destabilizes itself by parametrically exciting the linear modes of the system. Only $N/2$ of these steps are possible, with N the number of junctions in the ring. Despite the presence of linear modes, our numerical studies show that a single propagating vortex can be viewed for a certain range of parameters as a particle with a long mean free path. This almost free vortex propagation makes discrete Josephson rings ideal systems for further quantum vortex experiments.

4.9 Discrete Underdamped Vortex Flow Devices

Sponsor

Advanced Research Projects Agency/
Consortium for Superconducting Electronics
Contract MDA972-90-C-0021

Project Staff

Amy E. Duwel, Professor Terry P. Orlando, Dr.
Herre S.J. van der Zant

Parallel arrays of Josephson junctions behave, in many ways, like long, continuous junctions. Both structures may be used as superconducting circuit elements, such as transistors, oscillators, phase shifters, and amplifiers. These systems also serve as valuable models for high-temperature superconducting devices.

Vortex flow devices consisting of discrete arrays of underdamped Josephson junctions have been fabricated and measured. These devices and their long, continuous junction counterparts are based on the ability to magnetically control the Eck voltage in an underdamped system. We find that both transistor and oscillator parameters are improved by placing the arrays above a superconducting ground plane and by connecting two arrays in series. We developed models for the device behavior which numerically account for the measured parameters. Our models also suggest that junctions with smaller capacitances will further improve the device parameters.

4.10 Publications

- Berman, D., H.S.J. van der Zant, T.P. Orlando, and K.A. Delin. "Discrete Superconducting Vortex Flow Transistors." *IEEE Trans. Appl. Superconduct.* 4: 161-168 (1994).
- Bock, R.D., J.R. Phillips, H.S.J. van der Zant, and T.P. Orlando. "Influence of Induced Magnetic Fields on the Static Properties of One-Dimensional Parallel Josephson-junction Arrays." *Phys. Rev. B* 49: 10009-10012 (1994).
- José, J.V., G. Ramirex-Santigo, and H.S.J. van der Zant. "Critical Exponents of Frustrated Josephson-junction Arrays." *Physica B* 194-196: 1671-1672 (1994).
- Linden, D.S., T.P. Orlando, and W.G. Lyons. "Modified Two-Fluid Model for Superconductor Surface Impedance Calculation." *IEEE Trans. Appl. Superconduct.* 4: 136 (1994).
- Phillips, J.R., H.S.J. van der Zant, and T.P. Orlando. "Dynamics of Row-switched States in Josephson-junction Arrays." *Phys. Rev. B* 50: 9380-9386 (1994).
- Phillips, J.R., H.S.J. van der Zant, and T.P. Orlando. "Numerical Study of Self-field Effects on Dynamics of Josephson-junction Arrays." *Physica B* 194-196: 1777-1779 (1994).
- Phillips, J.R., H.S.J. van der Zant, T.P. Orlando, and E. Trías. "Self-field Effects in Two-Dimensional Nb Josephson-junction Arrays." *IEEE Trans. Appl. Superconduct.* Forthcoming.
- Phillips, J.R., H.S.J. van der Zant, J. White, and T.P. Orlando. "Influence of Induced Magnetic Fields on Shapiro Steps in Josephson Junction Arrays." *Phys. Rev. B* 50: 9387-9396 (1994).
- Phillips, J.R., H.S.J. van der Zant, J. White, and T.P. Orlando. "Influence of Induced Magnetic Fields on the Static Properties of Josephson-junction Arrays." *Phys. Rev. B* 47: 5219-5229 (1993).
- van der Zant, H.S.J., D. Berman, T.P. Orlando, and K.A. Delin. "Fiske Modes in One-Dimensional Parallel Josephson-junction Arrays." *Phys. Rev. B* 49: 12945-12952 (1994).
- van der Zant, H.S.J., K.A. Delin, R.D. Bock, D. Berman, and T.P. Orlando. "Resonance Modes in One-dimensional Parallel Arrays of Josephson Junctions." *Physica B* 194-196: 1779-1780 (1994).

van der Zant, H.S.J., F.C. Fritschy, T.P. Orlando, and J.E. Mooij. "Massive Vortices in Under-damped Josephson-Junction Arrays." In *Tunneling Phenomena in High and Low T_c Superconductors*. Eds. A. di Chira and M. Russo. Singapore: World Scientific, 1993.

van der Zant, H.S.J., F.C. Fritschy, T.P. Orlando, and J.E. Mooij. "Vortex Dynamics in 2D Under-damped, Classical Josephson-Junction Arrays." *Phys. Rev. B* 47: 295-304 (1993).

van der Zant, H.S.J., and T.P. Orlando. "Eck Peak in Underdamped Discrete Superconducting Vortex Flow Devices." *J. Appl. Phys.* 76: 7606-7612 (1994).

van der Zant, H.S.J., T.P. Orlando, and A.W. Kleinsasser. "One-dimensional Parallel Josephson-junction Arrays as a Tool for Circuit Diagnostics." *IEEE Trans. Appl. Superconduct.* Forthcoming.

van der Zant, H.S.J., T.P. Orlando, S. Watanabe, and S.H. Strogatz. "Kink Propagation in a Highly Discrete System: Observation of Phase Locking to Linear Waves." *Phys. Rev. Lett.* 74: 174-177 (1995).

van der Zant, H.S.J., T.P. Orlando, S. Watanabe, and S.H. Strogatz. "Vortex Propagation in Discrete Josephson Rings." *Proceedings of the ICTP Workshop on Quantum Dynamics of Submicron Structures*, Trieste, Italy, June 13 - July 1, 1994.

van der Zant, H.S.J., T.P. Orlando, S. Watanabe, and S.H. Strogatz. "Vortices Trapped in Discrete Josephson Rings." *Physica B* 203: 490-496 (1994); *Proceedings of NATO ARW Conference*

on *Mesoscopic Superconductivity*, Karlsruhe, Germany, May 24-27, 1994.

van der Zant, H.S.J., R.A.M. Receveur, T.P. Orlando, and A.W. Kleinsasser. "One-dimensional Parallel Josephson-junction Arrays as a Tool for Diagnostics." *Appl. Phys. Lett.* 65: 2102-2104 (1994).

van der Zant, H.S.J., E.H. Visscher, D.R. Curd, T.P. Orlando, and K.A. Delin. "Vortex Dynamics in One-Dimensional Parallel Arrays of Under-damped Josephson-Junctions." *IEEE Trans. Appl. Superconduct.* 3: 2658-2661 (1993).

van der Zant, H.S.J., M.N. Webster, J. Romijn, and J.E. Mooij. "Vortices in Two-dimensional Superconducting Weakly Coupled Wire Networks." *Phys. Rev. B* 50: 340-350 (1994).

Watanabe, S., S.H. Strogatz, H.S.J. van der Zant, and T.P. Orlando. "Whirling Modes and Parametric Instabilities in the Discrete Sine-Gordon Equation: Experimental Tests in Josephson Rings." *Phys. Rev. Lett.* 74: 379-382 (1995).

4.10.1 Theses

Berman, D. *Discrete Superconducting Vortex Flow Transistors*. S.M. thesis. Dept. of Electr. Eng. and Comput. Sci., MIT, 1994.

Hugunin, J.J. *The Superconductor/Semiconductor Interface of V_3Si and Si*. S.M. thesis. Dept. of Electr. Eng. and Comput. Sci., MIT, 1994.

Kumar, A. *Single Electron Charging Effects in Quantum Dot Nanostructures*. Ph.D. diss. Dept. of Electr. Eng. and Comput. Sci., MIT, 1994.

Chapter 5. Nanostructures Technology, Research and Applications

Academic and Research Staff

Professor Henry I. Smith, Dr. Mark L. Schattenburg, Richard J. Aucoin, James M. Carter, Robert C. Fleming, Euclid E. Moon, Scott E. Silverman

Visiting Scientists and Research Affiliates

Patrick N. Everett

Graduate Students

Martin Burkhardt, David J. Carter, Jay N. Damask, Sean M. Donovan, Juan Ferrera, Nitin Gupta, Scott D. Hector, Hang Hu, James J. Hugunin, Arvind Kumar, Huiying Li, Akbar A. Moolji, Thomas E. Murphy, Gabrielle M. Owen, Timothy A. Savas, Satyen Shah, Vincent V. Wong, Isabel Y. Yang, Anto Yasaka

Undergraduate Students

Brian M. Smith

Technical and Support Staff

Mark K. Mondol, Edward Murphy, Jeanne M. Porter, Robert D. Sisson, Michael J. Weinberg

5.1 NanoStructures Laboratory

The NanoStructures Laboratory (NSL) at MIT develops techniques for fabricating surface structures of integrated circuits (IC) with feature sizes in the range from nanometers to micrometers, and uses these structures in a variety of research projects. The NSL includes facilities for lithography (photo, interferometric, electron beam, ion beam, and x-ray), etching (chemical, plasma and reactive-ion), liftoff, electroplating, sputter deposition, and e-beam evaporation. Much of the equipment and nearly all of the methods utilized in the NSL are developed in-house. Generally, commercial IC processing equipment cannot achieve the resolution needed for nanofabrication, and it lacks the required flexibility. The research projects fall into four major categories: (1) development of submicron and nanometer fabrication technology; (2) short-channel semiconductor devices, quantum-effect electronics, and optoelectronics; (3) periodic structures for x-ray optics, spectroscopy, atomic interferometry and nanometer metrology; (4) crystalline films on nonlattice-matching substrates.

5.2 Scanning Electron Beam Lithography

Sponsors

Joint Services Electronics Program
Contract DAAL03-92-C-0001
Grant DAAH04-95-1-0038

Semiconductor Research Corporation
Contract 94-MJ-550

Project Staff

Scott E. Silverman, Juan Ferrera, Professor Henry I. Smith

Figure 1 is a photograph of the scanning electron beam lithography (SEBL) system (VS-PL) located in Room 38-185 at MIT. This instrument was donated from IBM in November 1993. It is an experimental system based on many years of IBM technology development of SEBL. In 1994, a novel pattern generator was fabricated and installed on the system. The pattern generator is based on RISC parallel processor technology, enabling the generation of arbitrary shapes, including curved geometries.

The VS-PL system is the cornerstone of a newly established facility for high performance electron-beam lithography. The goals of the new facility are (1) to provide the MIT research community with an in-house SEBL capability for writing directly on

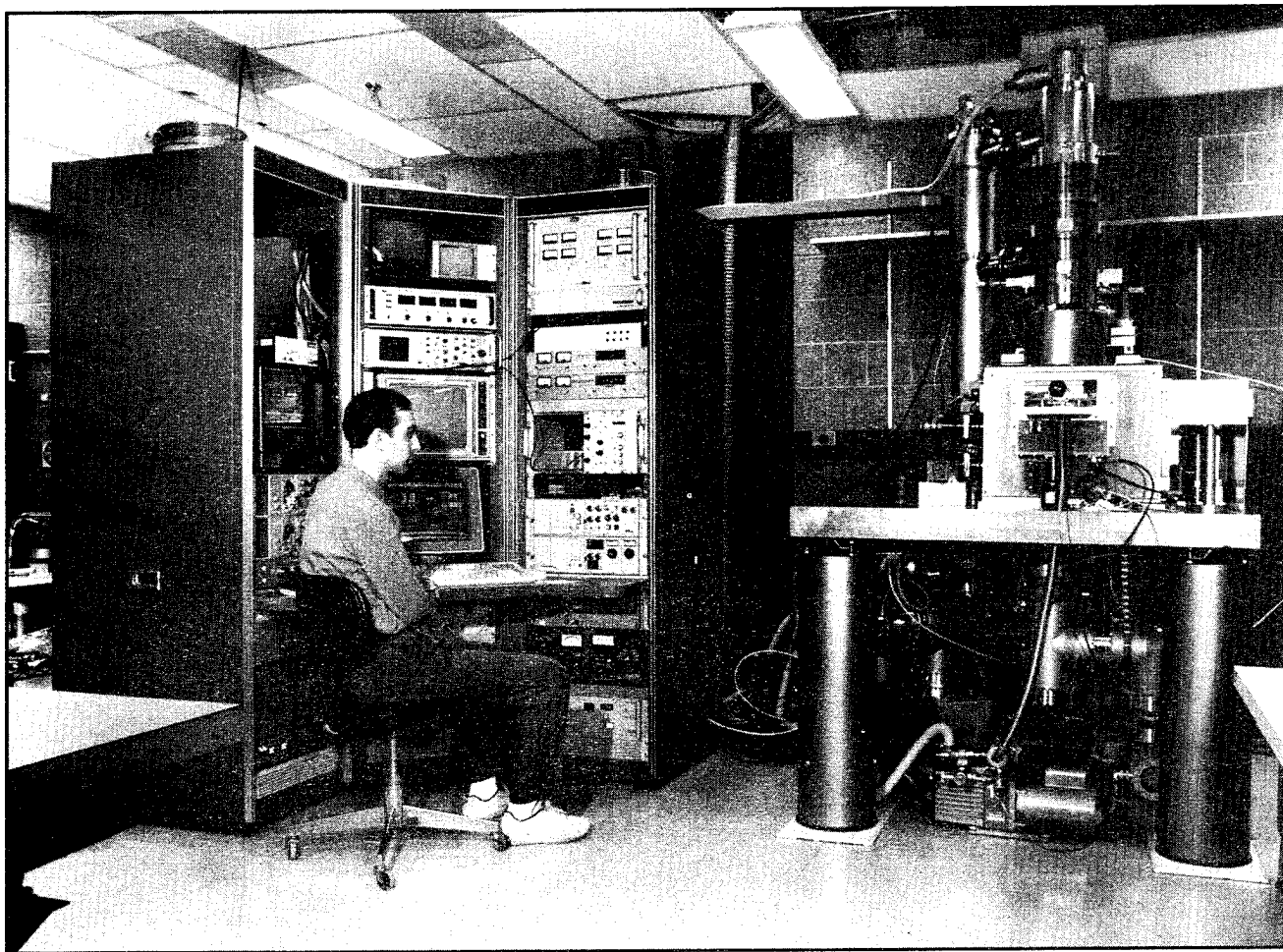


Figure 1. Photograph of the new VS-PL scanning-electron-beam lithography system, obtained as a donation from IBM in November 1993. The operator is Research Engineer Scott E. Silverman. (Photo by John F. Cook)

experimental device substrates; (2) to advance the state-of-the-art in SEBL, particularly with regard to pattern placement accuracy and long-range spatial-phase coherence; and (3) to pattern x-ray nanolithography masks for in-house use. Our approach to improved pattern placement accuracy is based on a new technique, invented at MIT, called spatial-phase locking. It is expected that the new SEBL facility will concentrate on sub-100 nm electronic and quantum-effect devices, and opto-electronic devices such as DFB lasers and channel-dropping filters for wavelength-division multiplexing in optical communication systems.

5.3 Spatial-Phase-Locked Electron-Beam Lithography

Sponsors

Joint Services Electronics Program
Contract DAAL03-92-C-0001
Grant DAAH04-95-1-0038

National Science Foundation
Grant ECS 94-07078
Semiconductor Research Corporation
Contract 94-MJ-550
U.S. Army Research Office
Contract DAAL03-92-G-0291

Project Staff

Juan Ferrera, Scott E. Silverman, Vincent V. Wong,
James M. Carter, Professor Henry I. Smith

It is well known that scanning-electron-beam lithography can write extremely fine lines, ~10 nm in thin PMMA and ~1 nm in AlF₃. However, because writing fields in electron-beam lithography are quite small (~ 10⁴ beam steps), large-area patterns must be created by stitching together the small fields, using a laser interferometer to provide X-Y positioning information. However, it is often overlooked that, due to instability, drift, and a variety of other problems, the precision with which this can be done is much poorer than the resolution. Typically,

stitching errors of 30 to 100 nm are observed at field boundaries.

To solve this problem, we are developing a technology called spatial-phase-locked electron-beam lithography (SPLEBL), which will provide pattern placement accuracy and precision finer than the resolution. The basic idea behind SPLEBL is to create on the substrate a fiducial grid and conduct all e-beam lithography with reference to it. The fiducial grid is produced by interferometric lithography to ensure long-range spatial-phase coherence. We are investigating two modes of implementation, the global fiducial grid and the segmented grid. In the latter approach, the grid is transferred onto the substrate only in small regions ($2 \times 2 \mu\text{m}$ square) at the corners of each e-beam scan field. Spatial-frequency-domain techniques

are used to achieve sub-pixel alignment and scaling. In the latter approach the fiducial grid is transparent to the exposing e-beam and covers the entire top of the resist film. By collecting the emitted secondary electrons, a computer will keep track of the e-beam position at all times and correct for any drift or spurious displacement.

In order to demonstrate the efficacy of SPLEBL, x-ray masks for optical filters were fabricated in collaboration with IBM's Thomas J. Watson Research Center. These classes of devices have linewidths of ~ 100 nm and span many fields of the e-beam lithography system. They require field stitching errors of ~ 1 nm for highest performance. Figure 2 illustrates the repeatability of spatial-phase locking using the VS-6 e-beam lithography system at IBM Yorktown Heights.

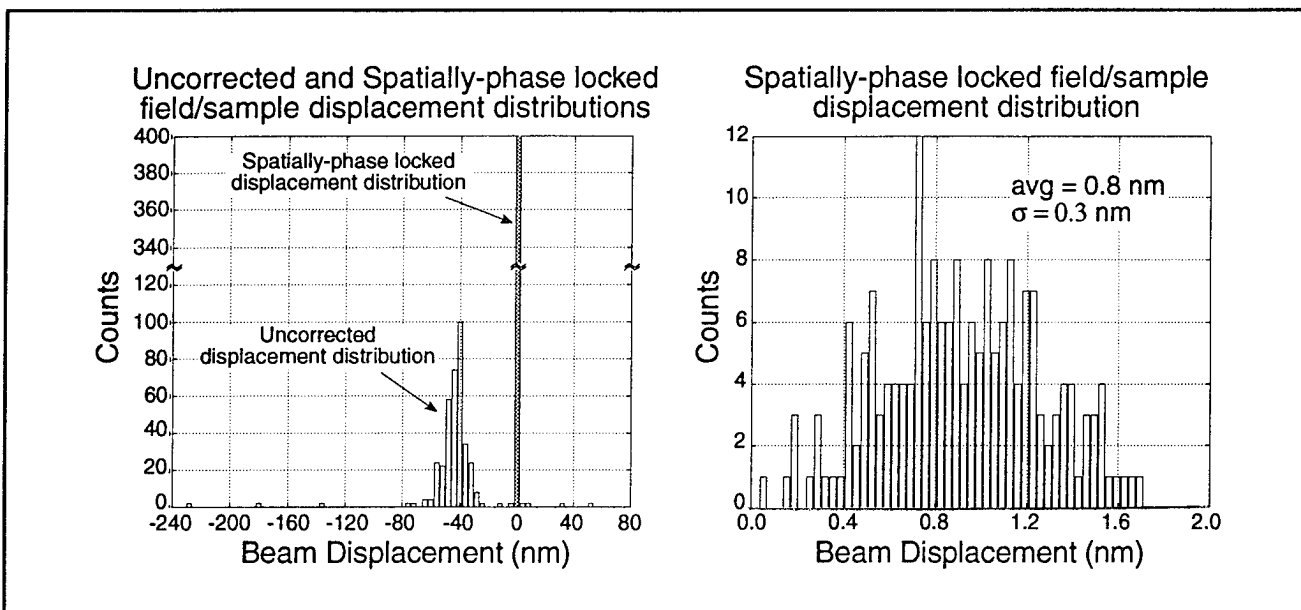


Figure 2. Histogram illustrating the repeatability of spatial-phase locking, and, for comparison, e-beam placement precision without spatial-phase locking. The right panel is a magnified display of the spatial-phase locking results, showing a mean displacement of 0.8 nm and a standard deviation of 0.3 nm. With spatial-phase locking, field-stitching errors below 1 nm appear feasible, an improvement of nearly 2 orders-of-magnitude over conventional technology.

5.4 X-Ray Nanolithography

Sponsors

Advanced Research Projects Agency/

Naval Air Systems Command
Contract N00019-92-K-0021

Joint Services Electronics Program
Contract DAAL03-92-C-0001
Grant DAAH04-95-1-0038

Project Staff

James M. Carter, Scott D. Hector, Euclid E. Moon, Gabrielle M. Owen, Mark L. Schattenburg, Vincent V. Wong, Isabel Y. Yang, Professor Henry I. Smith

For several years, we have been developing the tools and methods of x-ray nanolithography (i.e., sub-100 nm features). We have explored the theoretical and practical limitations and endeavored to make its various components (e.g., mask making, resists, electroplating, sources, alignment, etc.) reliable and "user friendly". Because of the critical importance of the x-ray mask technology, we discuss this separately in section 5.5.

Our sources for x-ray nanolithography are simple, low-cost electron-bombardment targets, typically Cu_L ($\lambda = 1.32$ nm), separated by a 1.4 μm -thick SiN_x vacuum windows from helium-filled exposure chambers. In the future, we hope to replace the CuL sources with higher flux plasma-based x-ray sources.

For most applications that require multiple mask alignment, we currently use a simple microscope-based system which provides about 0.3 μm superposition precision. We are also developing a high precision mask alignment system (see section 5.6) that should provide overlay approaching 1 nm.

In earlier research, we showed that for x-ray wavelengths longer than ~ 0.8 nm, the range of the photoelectron emitted when an x-ray photon is absorbed in resist does not limit the resolution. Down to feature sizes ~ 20 nm, diffraction is the major concern. By means of accurate electromagnetic calculations, taking into account the vectorial character of the electromagnetic field and the dielectric properties of the absorber, we have shown that when source spatial coherence is optimized, diffraction does not limit resolution as severely as had been predicted by simple Fresnel diffraction calculations. Figure 3 plots the maximum mask-to-sample gap G versus minimum feature size W for two values of the parameter α which connects gap and feature size: $G = \alpha W^2/\lambda$. Modeling and experiment verify that α can be between 1 and 1.5 while retaining good process latitude.

For gaps below 10 μm , the mask and substrate must be optically flat (see section 5.5) and dust particles must be detected and eliminated. To accomplish this, we use a jet of frozen CO₂ micropellets impinging on the substrate or mask at a low angle. The pellets knock off adhering dust particles while leaving no residue, and the CO₂ gas also tends to remove thin layers of organic contamination.

For the linewidth range from 70 to 20 nm, mask-substrate gaps must be below 5 μm . This is not a problem in a research setting, but may be unacceptable for manufacturing. For this reason, we have investigated the feasibility of using arrays of zone plates for projection imaging with x rays of either 4.5 nm or about 1.0 nm wavelength.

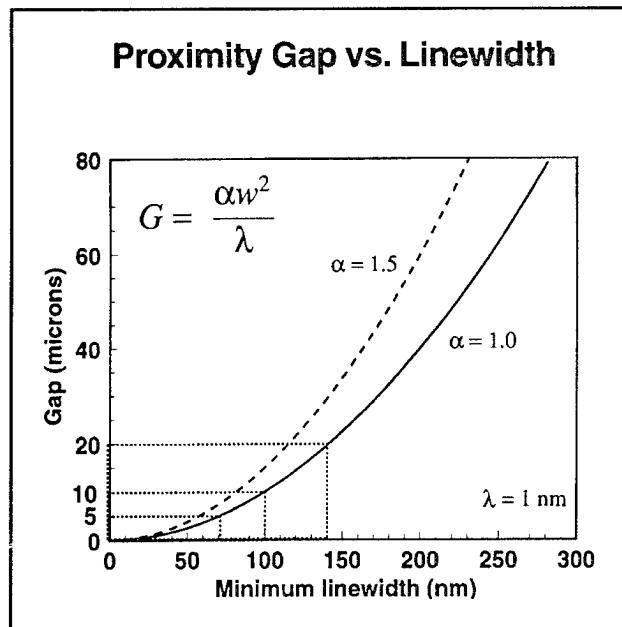


Figure 3. Plot of maximum mask-sample gap G versus minimum feature size W for two values of the parameter α .

5.5 Improved Mask Technology for X-Ray Lithography

Sponsors

Advanced Research Projects Agency/
Naval Air Systems Command
Contract N00019-92-K-0021
Joint Services Electronics Program
Contract DAAL03-92-C-0001
Grant DAAH04-95-1-0038

Project Staff

Martin Burkhardt, James M. Carter, Juan Ferrera, Scott D. Hector, Huiying Li, Mark K. Mondol, Edward Murphy, Gabrielle M. Owen, Mark L. Schattenburg, Vincent V. Wong, Isabel Y. Yang, Professor Henry I. Smith

At feature sizes of 100 nm and below the mask-to-sample gap G must be less than ~ 10 μm . We have developed a mask configuration compatible with this requirement in which the mask membrane is flat to less than 250 nm. We continue to make incremental improvements in this technology as illustrated in figure 4. A novel, low-gradient furnace was developed to achieve such high levels of mask flatness.

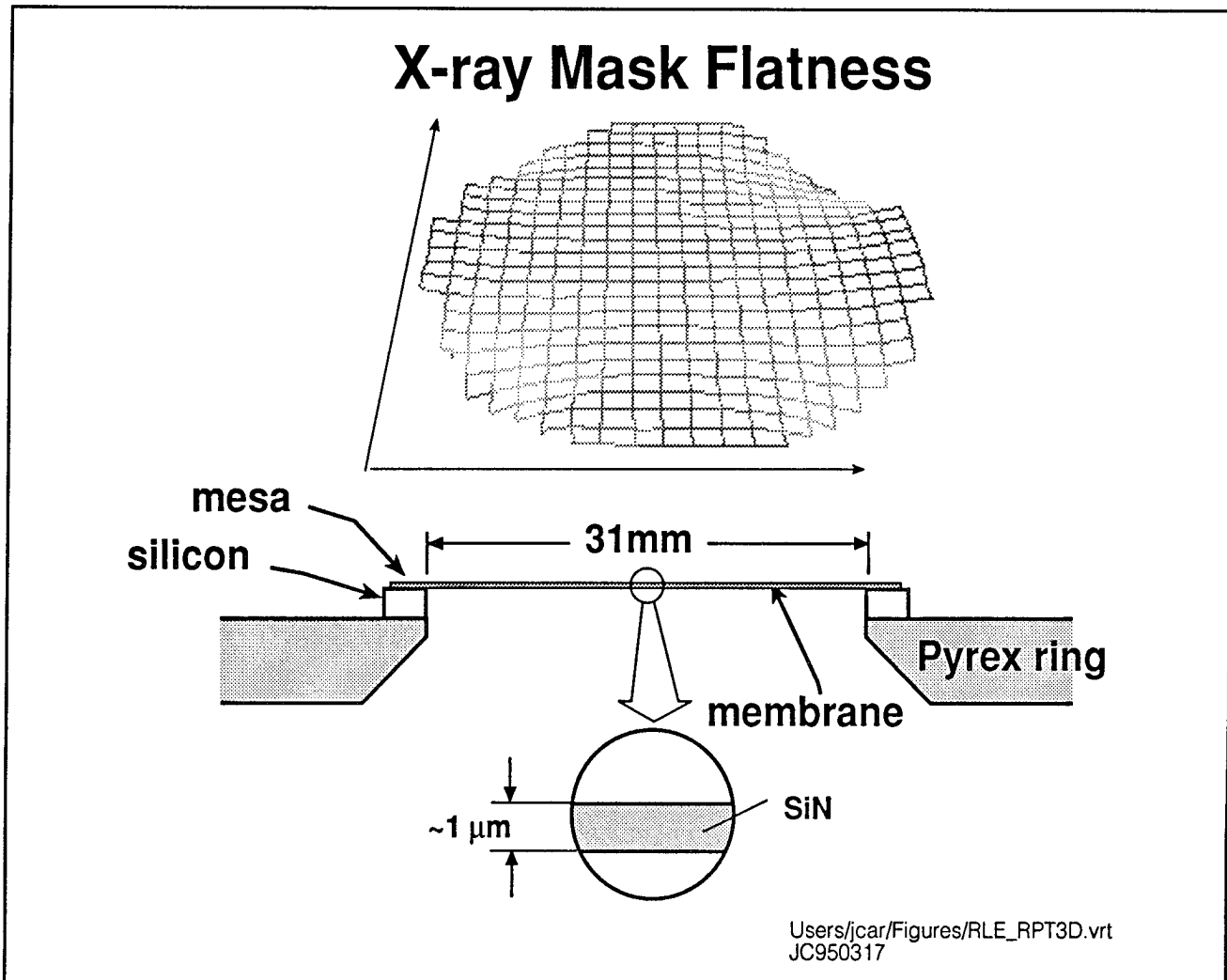


Figure 4. Schematic of mesa-style x-ray mask combined with a plot of mask flatness for a 31 mm-diameter Si_N_x membrane. Stress at the Si-Pyrex interface causes some twisting. However, the membrane is tensile and flat to within 200 nm.

Our mask technology is based on low-stress, Si-rich silicon nitride, SiN_x. This material is produced in the IC Laboratory at MIT in a vertical LPCVD reactor. The resulting films are clean and uniform, and x-ray mask membranes made from them are extremely robust. These mask membranes can be cleaned and processed in conventional stations. Radiation hardness remains a problem at dose levels corresponding to production (i.e., millions of exposures) but is quite suitable for the purpose of research material.

For absorber patterns, we use both gold, Au, and tungsten, W. Both can be obtained with near-zero

stress (i.e., $< 10^7$ MPa), which implies that pattern distortion should be negligible (i.e., $< 1 \text{ nm}$). The gold is electroplated onto the membrane after resist exposure and development using a specially designed apparatus. The W is sputter deposited and patterned by reactive-ion etching. During sputter deposition, the plasma environment leads to a nonuniform temperature distribution, which, in turn, causes nonuniform stress. In order to ensure uniform W stress over an entire membrane, a He-backside temperature-homogenization apparatus is used. This produces stress that is uniform to within our measurement error of ± 5 MPa (figure 5).

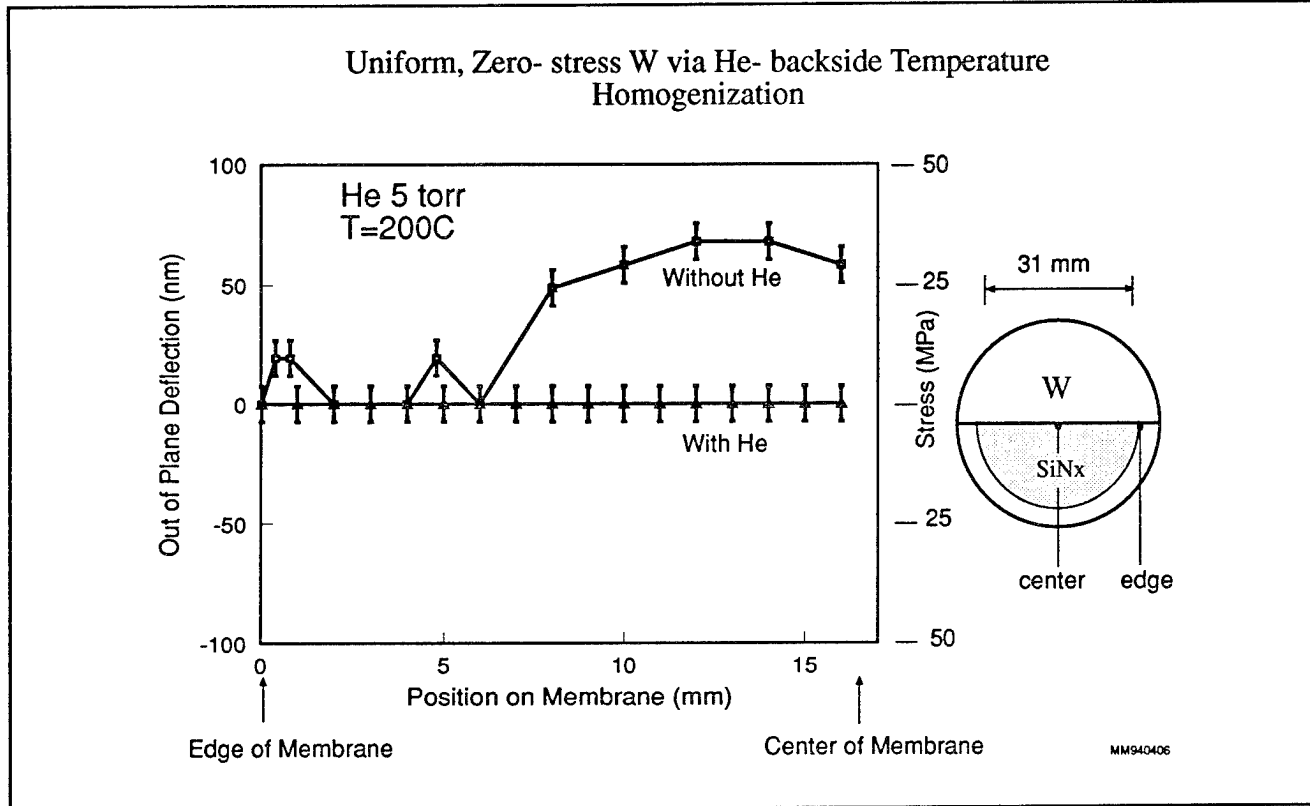


Figure 5. Plot of out-of-plane deflection (left ordinate) and stress (right ordinate) versus radial position for 300 nm-thick W, sputter deposited at 200°C onto a SiNx x-ray mask membrane, with and without He backside temperature homogenization. A uniform zero stress is achieved with He, whereas stress is nonuniform without the He.

The He Pressure on the backside of the membrane for heat transfer also enables us to monitor the stress by measuring the change in the bulge of the membrane during W deposition. With this *in situ* scheme, we hope to achieve a stress in the neighborhood of 5×10^6 MPa, with good repeatability.

Patterning of x-ray masks is done by interferometric lithography for periodic structures, but for patterns of arbitrary geometry, it is done by e-beam lithography, either in the MIT e-beam facility or in collaboration with NRL or IBM. We use CAD tools at MIT and convert the data into formats compatible with the e-beam exposure systems. Data is shipped to NRL or IBM by electronic network. After e-beam exposure, masks are shipped back to MIT by express mail where development and Au electroplating are carried out. This collaboration has already demonstrated that patterning x-ray masks by e-beam can be done remotely, and, by

implication, that university researchers with limited facilities can have access to nanolithography via x ray alone and do not need to own or even visit an e-beam lithography facility.

Figure 6 illustrates the sequence followed in most cases. The master mask written by e-beam lithography is replicated into a daughter mask of opposite "polarity". This daughter mask is then replicated onto a GaAs device substrate.

For etching W absorber patterns on x-ray masks, a reactive-ion-etching process is required, which puts considerable power into the membrane substrate. Since membranes have very low thermal mass and conductivity, we use He-backside cooling in a reactive ion etcher. Membranes can be cooled to below -20°C. At such low temperatures the isotropic etching component is suppressed leading to highly directional etching.

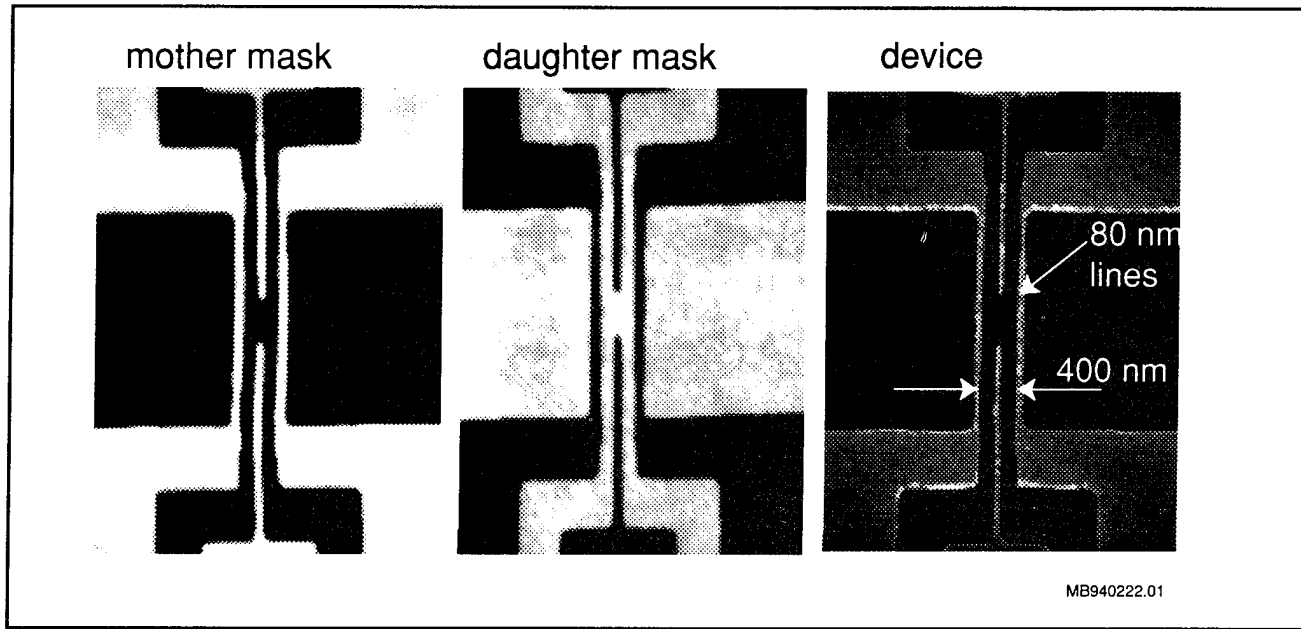


Figure 6. Masks used to fabricate a quantum tunneling device by x-ray nanolithography. (a) A "mother" mask is first written by e-beam lithography at the Naval Research Laboratory, and electroplated in Au at MIT. (b) This mask is then replicated onto a second x-ray mask to produce a "daughter" of opposite polarity, and electroplated to 200 nm Au thickness. The final device on a GaAs substrate is produced by lift-off of Al following x-ray exposure and development.

5.6 A High-Precision Mask Alignment System

Sponsors

Advanced Research Projects Agency/
Naval Air Systems Command
Contract N00019-92-K-0021
Joint Services Electronics Program
Contract DAAL03-92-C-0001
Grant DAAH04-95-1-0038

Project Staff

Euclid E. Moon, Patrick N. Everett, Professor Henry I. Smith

In order for any lithographic technique to be of general utility, a compatible alignment technique must also be provided. The technique must be capable of superposition precision that is a small fraction of the minimum feature size. Previously, we demonstrated a new scheme for aligning x-ray masks to substrates that was based on the principle of on-axis interference from gratings on the mask and substrate that differ in spatial period (e.g., p_1 on mask, p_2 on the substrate). The interference pattern was compared in spatial phase to a fixed

fiducial on the mask using a CCD camera and frequency domain image analysis. An alignment standard deviation of 6 nm was achieved. The goal of the present work is threefold: first, to improve the superposition precision by an order of magnitude; second, to fully automate the alignment process; and third, to make the system compatible with industrial x-ray lithography sources and steppers. In order to improve the superposition precision, a new alignment mark was designed that consists of two adjacent gratings on the mask (p_1 and p_2) facing two complementary gratings on the substrate (p_2 and p_1). The resulting on-axis interference pattern consists of two sets of fringes of the same spatial period which move in opposite directions. By matching them in spatial phase, one achieves alignment. We believe that in conjunction with a CCD and appropriate image processing, a superposition precision below 1 nm can be achieved.

The alignment system under development is shown in figure 7. It incorporates a large-travel closed-loop wafer stage that can accept eight-inch wafers and a six-axis mask stage which uses closed-loop piezos to achieve subnanometer positioning. All stages are under unified computer control.

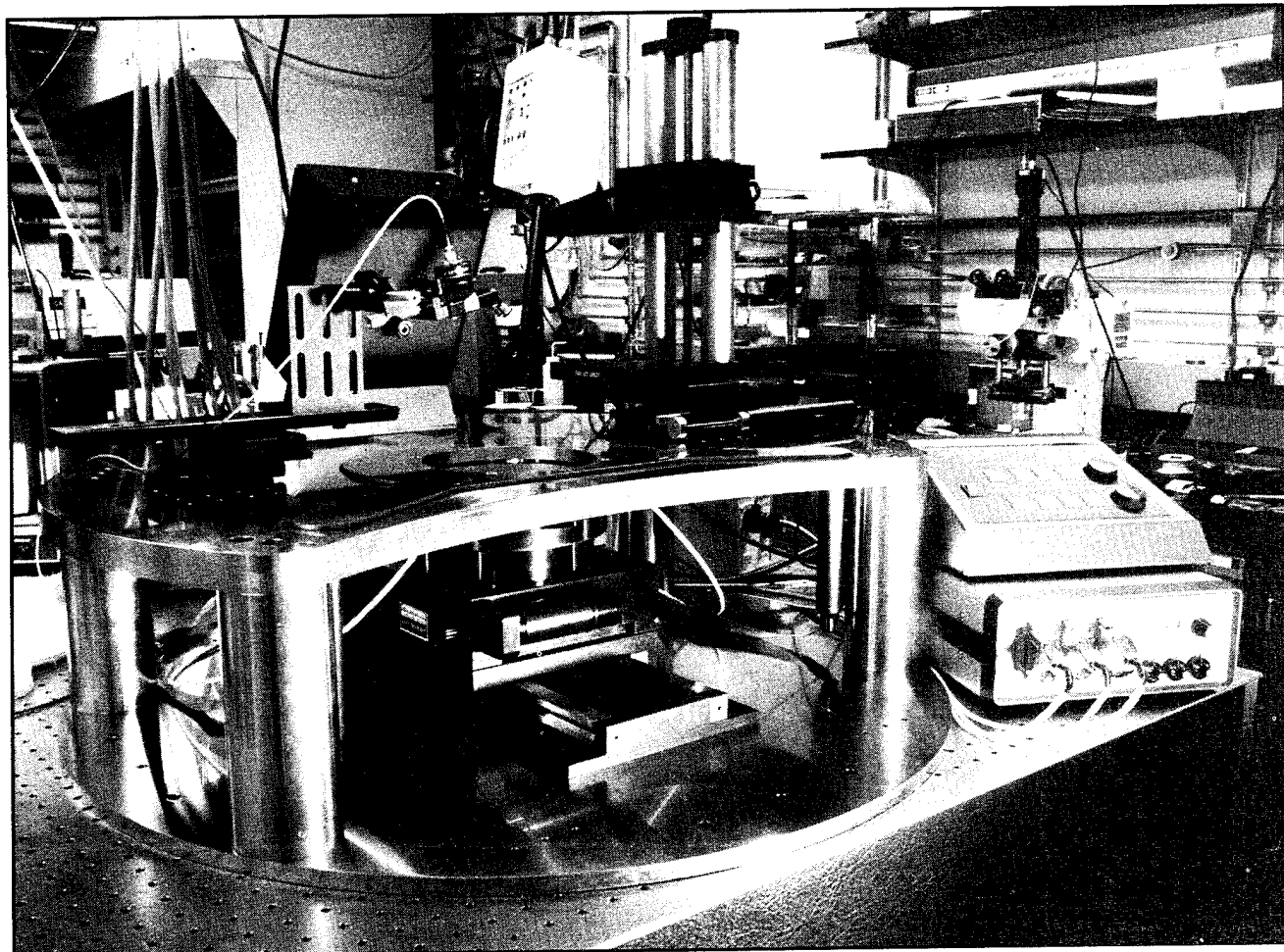


Figure 7. Photograph of the x-ray mask alignment system under development. The six-axis mask stage, which can accept up to eight-inch wafers, is controlled by closed-loop piezos. Light beams are brought in from the side onto grating type alignment marks. Alignment is determined by interpreting the resulting back diffracted fringe pattern. The system should be capable of nanometer alignment. The x-ray source, not shown, is located above the staging. (Photo by John F. Cook)

A collimated, polychromatic laser beam is diffracted by a pair of gratings on the mask and wafer. The gratings are arranged so that counterpropagating interference patterns are imaged with a compact microscope and CCD in an off-axis configuration, as shown in figure 8. The microscope can be positioned in a variety of ways, depending on the type of alignment mark in use. In all cases, the microscope is positioned out of the way of the x-ray beam. This configuration is compatible with industrial practice. A further advantage of the off-axis setup is that the reflected component of the incident

beam is not part of the alignment signal. This dramatically increases the contrast of the image, which, in turn, yields higher accuracy and faster phase detection.

For any alignment scheme to be useful in VLSI manufacturing, it must be highly accurate and insensitive to overayers on the wafer, such as resist, SiO_2 , or polysilicon. We have demonstrated that due to the symmetric combination of the diffracted orders in the interference pattern, the relative and absolute phase of the alignment fringes are unaffected by dielectric overayers.

**Perspective View of Back-Diffracted Orders
in Interferometric Imaging Alignment**

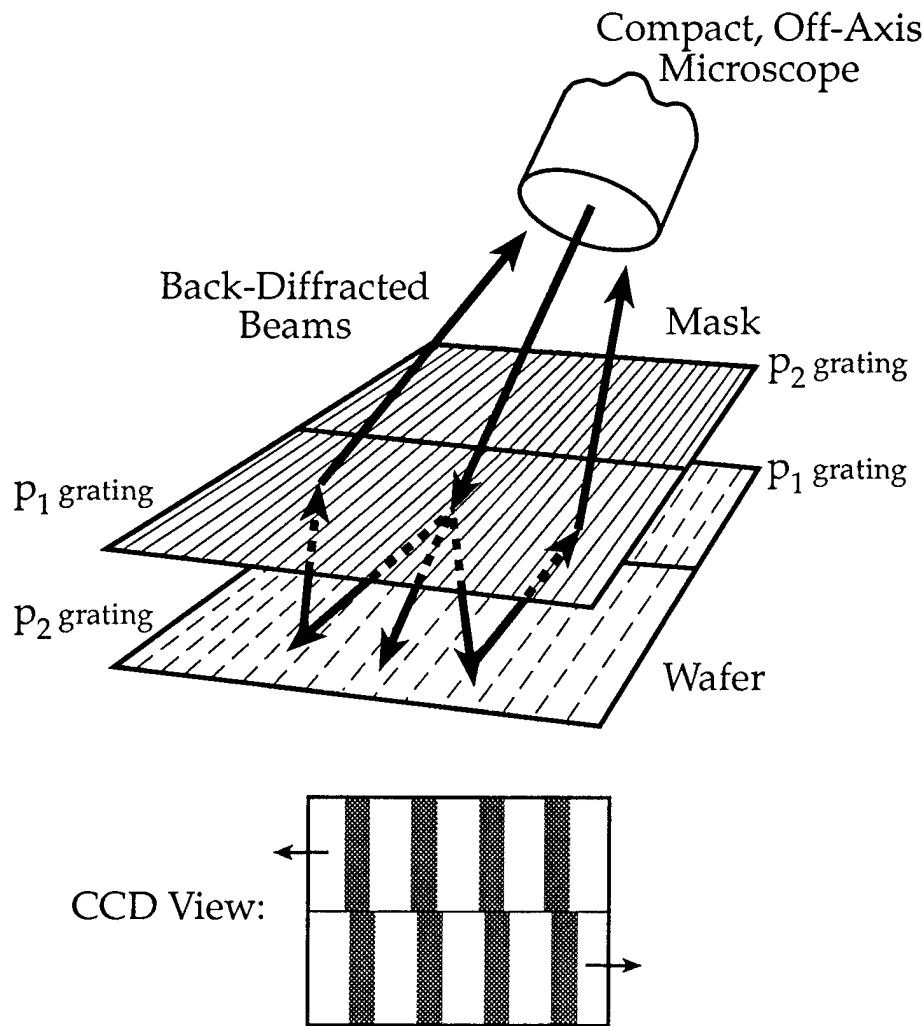


Figure 8. Schematic of the principle of the interferometric imaging alignment scheme showing the grating pairs and the beams back diffracted into the alignment microscope.

5.7 Interferometric Lithography

Sponsors

Joint Services Electronics Program
Contract DAAL03-92-C-0001
Grant DAAH04-95-1-0038

National Aeronautics and Space Administration
Contract NAS8-36748
Grant NAGW-2003

Project Staff

James M. Carter, Juan Ferrera, Robert C. Fleming,
Timothy A. Savas, Dr. Mark L. Schattenburg,
Satyen Shah, Professor Henry I. Smith

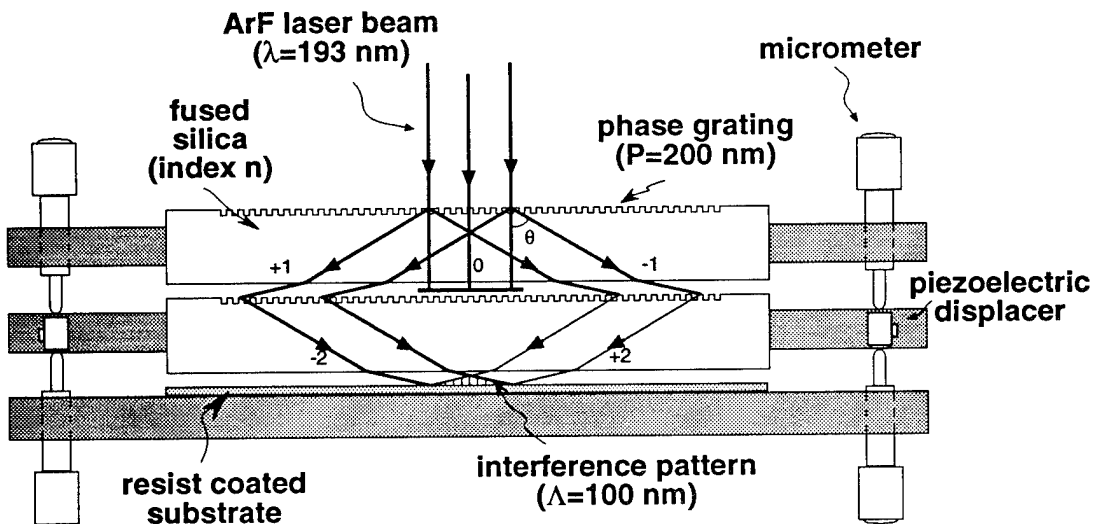
Interferometric (also called holographic) lithography schemes are preferred for the fabrication of periodic and quasi-periodic patterns that must be spatially coherent over large areas, and free of phase errors. For spatial periods down to 200 nm an argon ion laser is used in a Mach-Zender configuration, with a unique fringe-locking feedback system. This

produces large area (10 cm diameter) gratings with long-range spatial-phase coherence, free of phase errors or detectable distortion. The fringe locking ensures reproducibility of exposure. A multiple exposure moiré technique is used to verify freedom from distortion.

For spatial periods below 200 nm, light sources with wavelengths below 200 nm must be used. Such sources have limited temporal coherence, and thus one is forced to employ an achromatic scheme such as shown in figure 9. The source is an ArF

laser (193 nm wavelength). A collimating lens and a slit scanning system are interposed between the source and the interferometer in order to achieve reasonable depth-of-focus. We also use a white light interference principle to ensure that the gap between the two quartz plates is equal to the gap between the second plate and the substrate. Using this system, gratings of 100 nm period (nominally 50 nm lines and spaces) are obtained in PMMA on top of a specially designed antireflection coating. As shown in figure 10, such patterning is successfully transferred into Si_3N_4 .

Achromatic Holographic Lithography

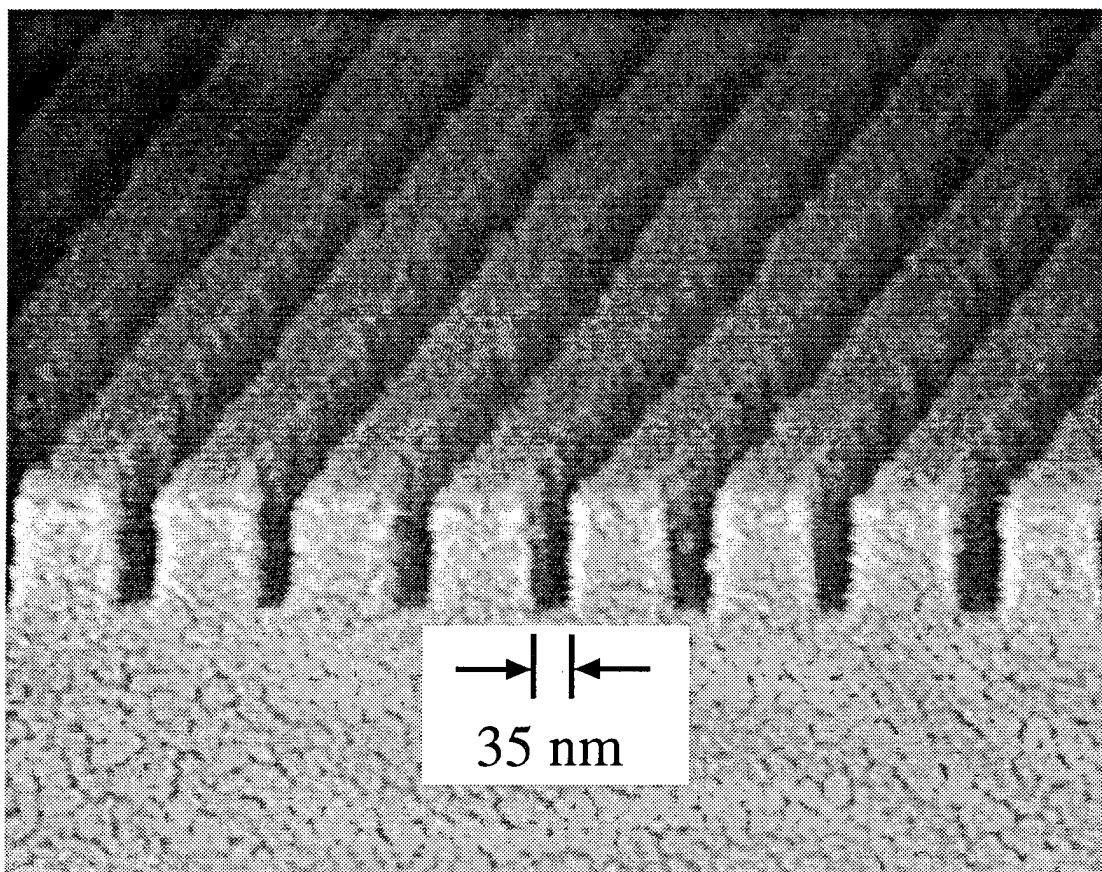


$$\sin\theta = \lambda/(nP),$$

$$\Lambda = \lambda/(2n \sin\theta)$$

$$\Lambda = P/2$$

Figure 9. Achromatic interferometric lithography (AIL) configuration.



100 nm-Period Grating in Si_3N_4 on Si

Figure 10. Scanning electron micrograph of a 100 nm period grating, exposed in PMMA on top of a specially designed antireflection coating, and transferred into Si_3N_4 by reactive ion etching.

5.8 Ion-Beam Lithography

Sponsor

Joint Services Electronics Program
Contract DAAL03-92-C-0001
Grant DAAH04-95-1-0038

Project Staff

Scott E. Silverman, Anto Yasaka, Professor Henry I. Smith

Focused-ion-beam (FIB) systems are potentially useful as nanolithography tools because of the near absence of backscattering, which is a significant problem in electron-beam lithography, especially on high-atomic-number substrates. We currently work with Si^{+} and Be^{++} ions and have demonstrated 50

nm lines and spaces. We are investigating the feasibility of combining spatial-phase-locking with FIB lithography. This could prove to be the superior technology for making x-ray nanolithography masks based on W absorbers, at linewidths below 70 nm.

5.9 High-Performance Self-aligned Sub-100 nm MOSFETs Using X-ray Lithography

Sponsors

Advanced Research Projects Agency/
Naval Air Systems Command
Contract N00019-92-K-0021
IBM Corporation
Contract 1622

Joint Services Electronics Program
Contract DAAL03-92-C-0001
Grant DAAH04-95-1-0038

Project Staff

Isabel Y. Yang, Keith Jackson, James M. Carter,
Juan Ferrera, Scott E. Silverman, Vincent V. Wong,
Professor Dimitri A. Antoniadis, Professor Henry I.
Smith

We have fabricated sub-0.1 μm N-channel MOSFET devices on bulk Si using x-ray lithography. Extremely well controlled short-channel

effects were achieved through appropriate channel and source/drain engineering. Figure 11 shows the device schematic. The retrograde channel doping profile was accomplished using shallow indium and deep boron implants. The source/drain halo extensions were formed using a low-energy arsenic implant with indium preamorphization and counter-doping. The self-aligned polysilicon gates were fabricated using x-ray nanolithography and an anisotropic etching process. The aligned microgap x-ray exposures were carried out using mesa-etched SiN_x x-ray masks with Au absorber pattern. Figure 12 shows the I-V characteristics of an 85 nm channel length MOSFET.

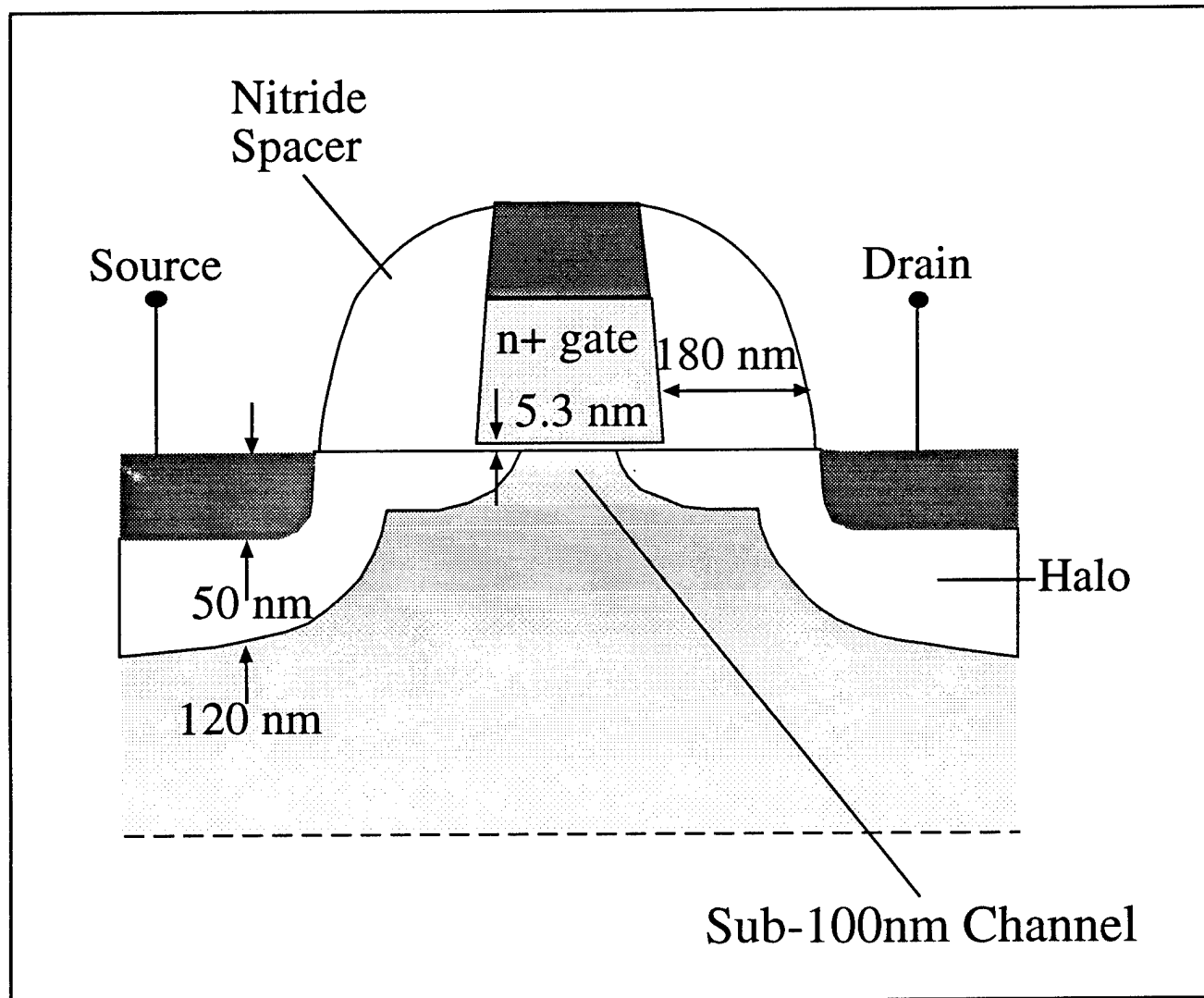


Figure 11. Schematic of 0.1 μm channel-length self-aligned NMOSFET.

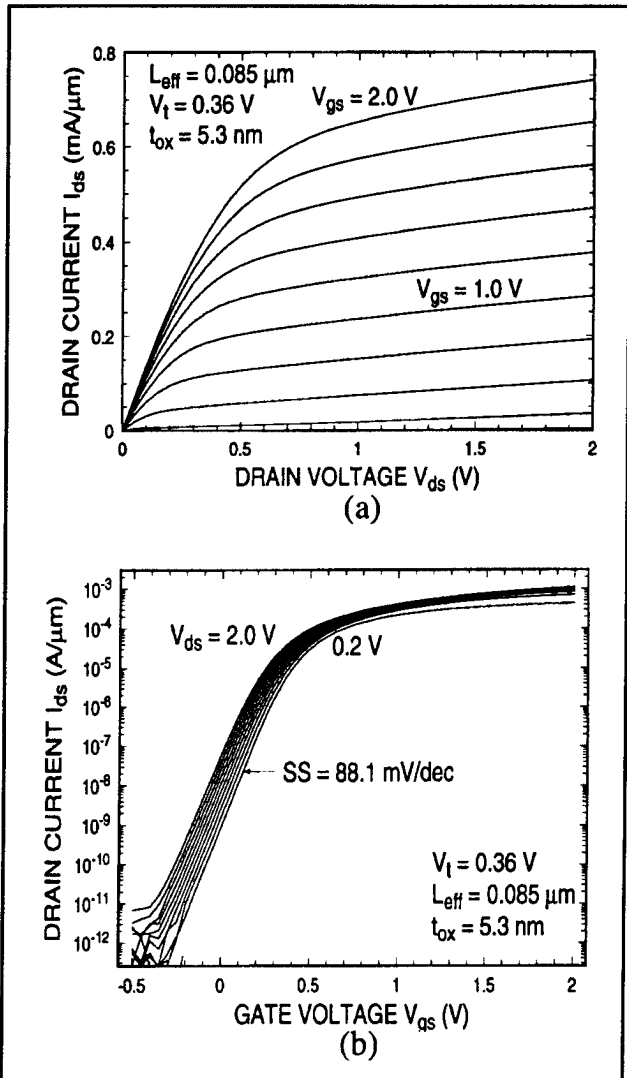
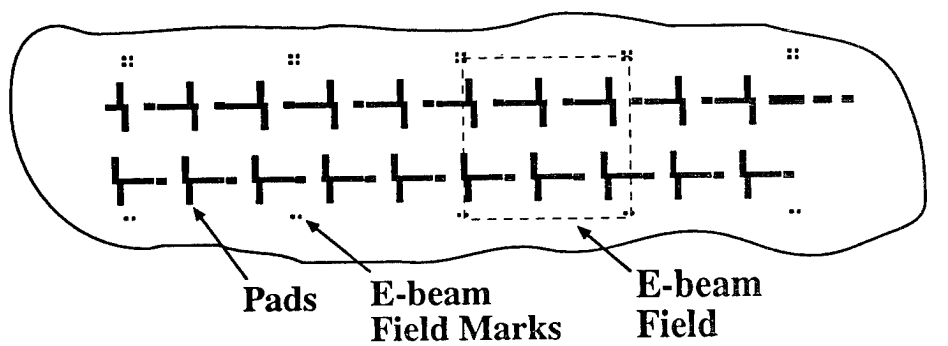
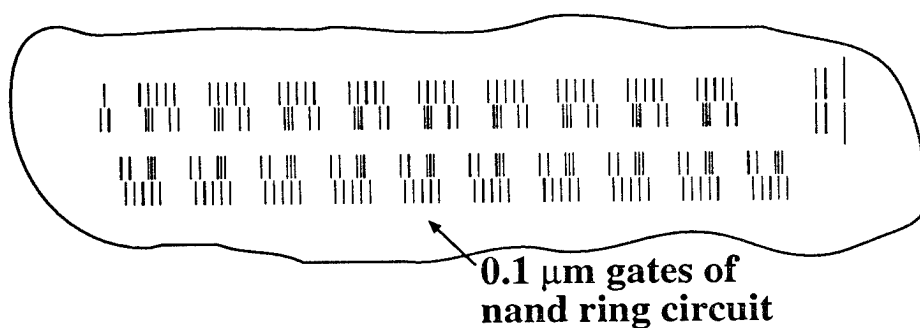


Figure 12. I-V characteristics of an 85 nm-channel-length NMOSFET.

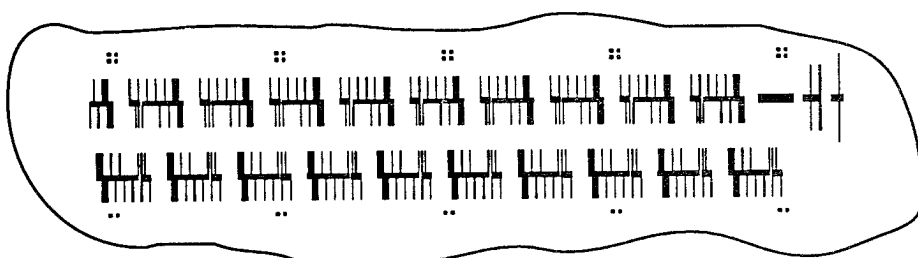
Our current work involves the extension of this technology to a full CMOS line on bulk as well as on SOI substrates. Two different device structures are explored on the SOI substrates. One is the conventional structure on SOI, and the other is the double-gated structure with a deep submicron dimension top gate and a wider bottom gate. Our first effort is to get a fundamental understanding of these devices in DC; i.e., short channel effects, drain-induced barrier lowering (DIBL), coupling of the backgate to the front gate, etc. Currently, the backgate is defined by ion implantation through the top using optically exposed thick resist as the mask. The top gate is then aligned over this bottom gate via x-ray lithography. The technology issue here is the mixing and matching of the optical stepper to the e-beam tool which writes the patterns on the x-ray masks. We have developed a technique to do this matching that also saves e-beam writing time. Figure 13 shows this process in which the coarse patterns, e.g., pads and e-beam field alignment marks, are first transferred onto a chrome coated quartz wafer using the optical stepper. The pattern is then transferred into chrome by a wet etch. A one-to-one pattern transfer of the coarse features onto the x-ray mask is then done using proximity 240 nm UV exposure. The coarse patterns and the field alignment marks are then plated up in Au and sent to the e-beam for fine pattern writing. The final patterns on the mask will have coarse features patterned by UV proximity printing and fine features written by e-beam lithography, as depicted in figure 13(c).



(a)



(b)



(c)

Figure 13. Sketch of a small portion of the chip showing: (a) a pattern of coarse features (pads) transferred onto the x-ray mask by deep UV lithography; (b) fine features written by e-beam lithography; (c) composite of fine and coarse features on the x-ray mask. The pattern is a nand ring circuit.

5.10 Fabrication of T-gate Devices using X-ray Lithography

Sponsor

U.S. Army Research Office
Grant DAAH04-94-G-0377

Project Staff

Nitin Gupta, Professor Henry I. Smith

Monolithic microwave integrated circuits (MMICs) have potential applications in automobile navigation, collision-avoidance, and personal wireless communication systems. High-speed MODFET devices require very short gate lengths, while preserving low resistance. Large gate widths are required for high current drive. To meet these conflicting demands, so-called "T-gate" and "gamma-gate" processes are used in which the base of the gate is very short (~100 nm) while the upper part is large and overlaps the short base, similar to a mushroom, or the letters T or Γ . Such structures are readily achieved using direct-write electron-beam lithography (EBL). However, this technology is expensive, slow, and unlikely to meet future production volume needs. For these reasons, we are developing a process for fabricating T-gates using x-ray lithography.

Previously, we reported on a tri-level PMMA-based process for fabricating T-gate devices using x-ray lithography. Recently, we have pursued a more robust process, offering the advantages of throughput as well as large process latitude. SAL-601, a commercially available negative chemically-amplified resist, is used. In order to maintain a large process latitude the time and temperature of the baking steps used in the fabrication are tightly controlled by means of vacuum-chucked hotplates, with the temperature monitored using thermocouple junctions integrated into a Si wafer. The result is a stable, robust process.

The fabrication sequence is shown in figure 14. The first layer defines the footprint of the gate, the critical parameter for a field-effect device. After developing this fine-linewidth feature, the resist is baked to increase the degree of cross-linking, thereby making the resist insoluble in its own casting solvent. A second layer of SAL-601 or ordinary photoresist is spun on and used to define the upper portion of the gate. This may be aligned symmetrically to the lower feature, or shifted to

achieve the Γ -gates used in high-end microwave devices. Following development, metal is evaporated and liftoff completed. Results are shown in figure 15.

There are a number of interesting directions that may be followed once a high latitude process is established. For manufacturable MMIC systems, both MESFETs and HEMTs are required for low-noise and power applications. Initially, relatively simple GaAs MESFETs will be studied, followed by GaAs and InP HEMTs of varying degrees of complexity. Further studies could include low-temperature-grown GaAs MESFETs for high breakdown voltages, self-aligned devices, or gate materials other than Au, such as W.

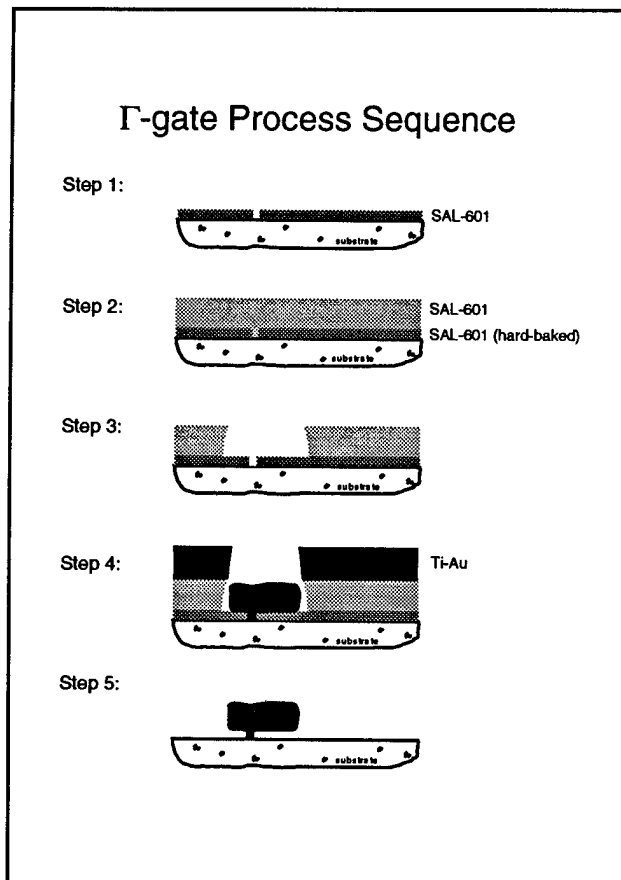


Figure 14. Depiction of the steps of the T-gate process: (1) chemically amplified resist is applied and exposed using x-ray lithography, (2) the exposed resist is hard-baked and a second layer of resist applied, (3) the second layer is exposed using either UV or x-ray lithography, (4) metal is deposited, typically Ti/Au, (5) liftoff, i.e., the resist is removed.

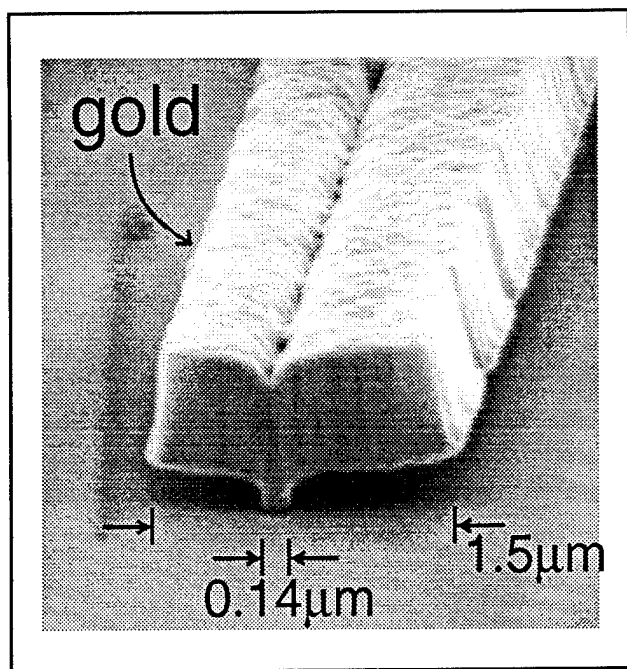


Figure 15. Scanning-electron micrograph of a T-gate obtained by the process depicted in figure 14.

5.11 Studies of Coulomb Charging Effects and Tunneling in Semiconductor Nanostructures

Sponsors

Joint Services Electronics Program

Contract DAAL03-92-C-0001

Grant DAAH04-95-1-0038

U.S. Air Force - Office of Scientific Research

Grant F-49-620-92-J-0064

Project Staff

Martin Burkhardt, David J. Carter, Professor Dimitri A. Antoniadis, Michael R. Melloch,¹ Professor Terry P. Orlando, Professor Henry I. Smith

Quantum-effect devices, whose minimum feature sizes are comparable to the Fermi wavelength (about 50 nm in a typical inversion layer), have promising potential in novel electronics applications. Quantum-dot devices have drawn particular attention.

In such devices an electron gas is confined electrostatically in all three dimensions, forming a small "island" of electrons ~100 nm, bounded on all sides by potential walls. This small electron "island" resembles an atom in that there can be only an integer number of electrons, and these electrons can occupy only certain discrete energy levels. If two dots are coupled, a structure resembling a molecule is obtained. The conductance of the dot, when connected to leads through tunneling barriers, exhibits strong oscillations as the voltage of the gate is varied. Each successive conductance maximum corresponds to the addition of a single electron to the dot. At temperatures in the mK range, the conductance decreases by orders of magnitude between adjacent conductance maxima because there is a large energy cost for an electron in the lead to enter the dot. This energy cost can be removed by changing the gate voltage, resulting in the observed periodic dependence of the conductance on gate voltage. This depends on how fast the chemical potential within the dots is changed for a change in gate voltage. For two arbitrary dot sizes and very low temperature, the conditions for conductance through the dots are arbitrary, and conductance events are expected to be stochastic.

A quantum dot device that provides control over the size of the dot was fabricated and measured in various biasing situations. Figure 16 shows an SEM micrograph of the device, and a schematic of the biasing configurations. A two-dimensional electron gas (2DEG) is formed at the interface of a GaAs/AlGaAs heterostructure approximately 55 nm below the sample surface. A negative voltage applied to Schottky gates at the surface depletes the 2DEG below, forming the quantum dot. With this structure it is possible to produce dots of 200, 400 or 600 nm length. The 200 and 400 nm dots can be biased simultaneously, producing a coupled dot system. The conductances are measured at 300 mK and plotted for these four cases in figure 17. The change in gate voltage necessary to add one electron to a quantum dot depends on the magnitude of the coupling capacitance between the dot and the gate. Accordingly, the distance between conductance peaks becomes very large for very small dots and small capacitances.

¹ Purdue University, West Lafayette, Indiana.

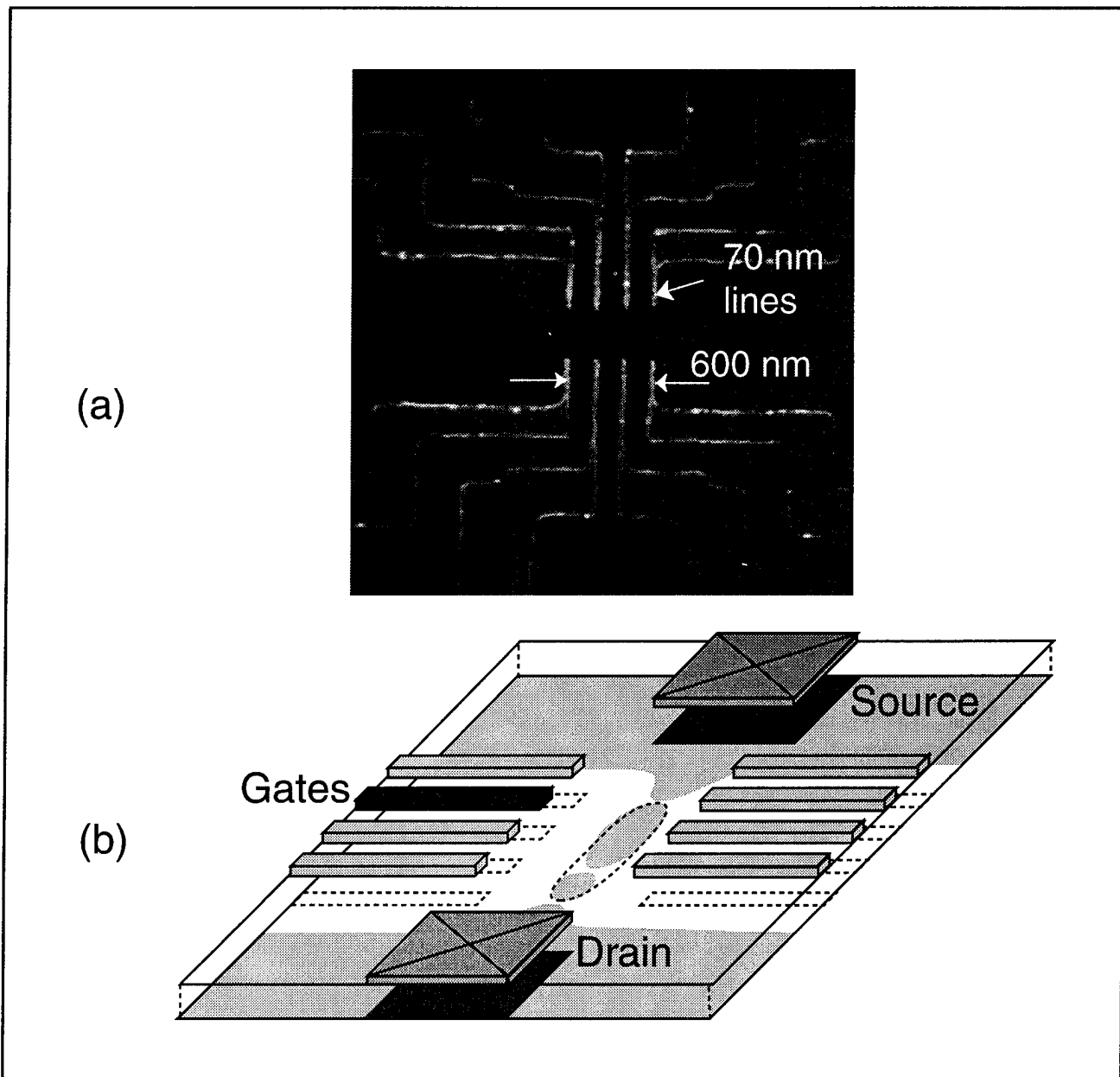


Figure 16. (a) Variable sized quantum-dot device made using x-ray nanolithography. (b) The device can be biased to achieve several different dot-sizes. The center-to-center distance between tunneling barriers can be set to 200, 400, or 600 nm. Alternatively, the biasing can produce two coupled quantum dots in series.

For two quantum dots in series, the conductance peaks are sparse for very negative gate voltages because the small dot suppresses conduction. For less negative voltages, the conductance maxima are spread due to the opening of the tunneling bar-

riers, and the smaller dot becomes conducting between the peaks, similar to the small dot measured by itself. In this case, we observe a modulation of the long periodicity of the small dot and the short periodicity of the larger dot.

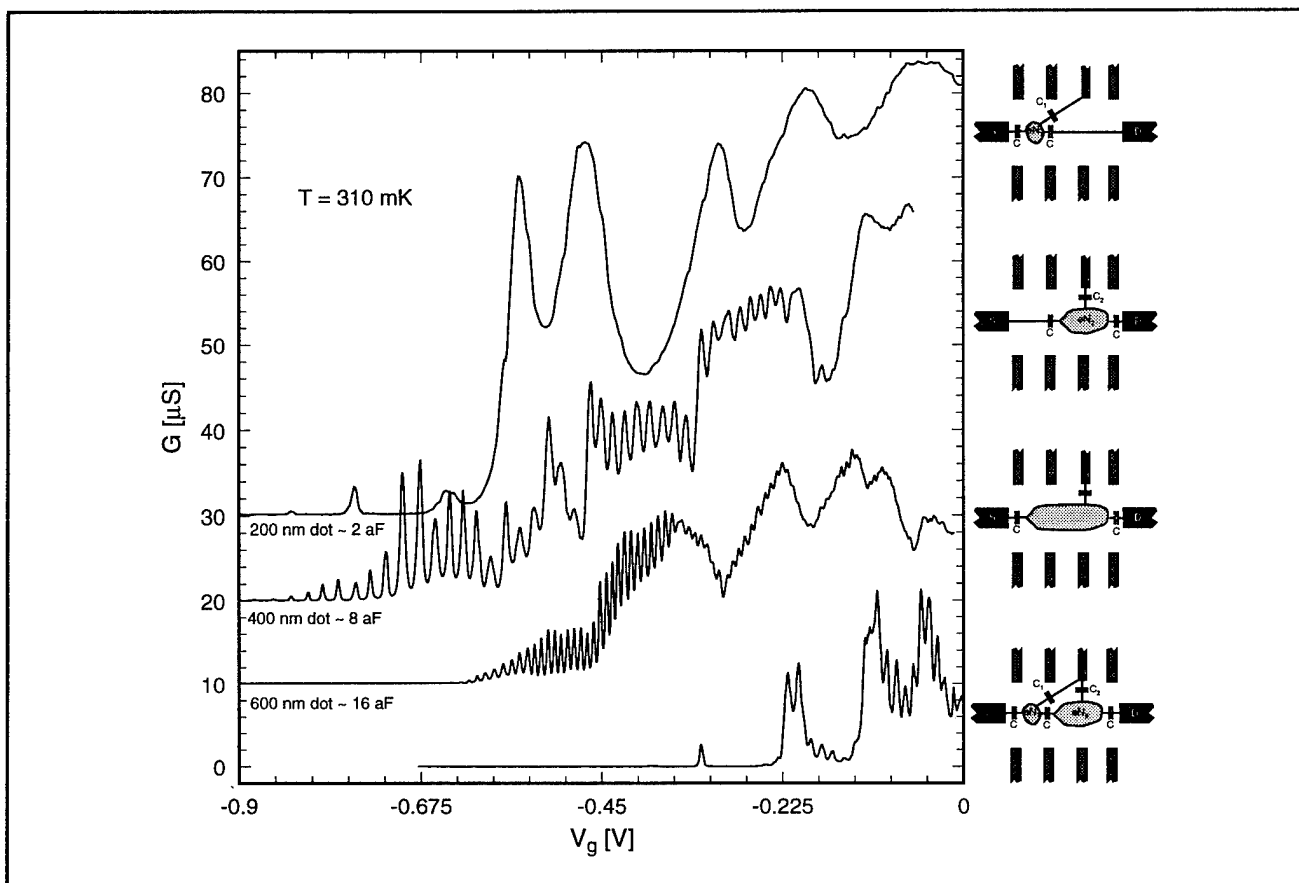


Figure 17. Conductance as a function of gate voltage for three different quantum-dot sizes and for a double dot system. The distinct peaks correspond to adding a single electron to a dot.

5.12 Superconductor/Semiconductor Interface of V_3Si and Si

Sponsor

Joint Services Electronics Program
Contract DAAL03-92-C-0001
Grant DAAH04-95-1-0038

Project Staff

James J. Hugunin, Professor Dimitri A. Antoniadis,
Professor Terry P. Orlando, Professor Henry I.
Smith

Superconductor/semiconductor contacts are fabricated between V_3Si and Si by a solid-phase reaction between SiO_2 and V. Auger spectroscopy is used to confirm the presence of the V_3Si phase, and the sheet resistance versus temperature of the device is measured to determine a superconducting transition temperature of 14 K.

The electrical properties of the $\text{V}_3\text{Si}/\text{Si}$ interface are examined for cases where the V_3Si is in both

normal and superconducting states. The first two measurements are performed at room temperature and investigate the two forms of transport for normal electrons, either through or over a Schottky barrier. The second set of measurements are performed between 17 K and 0.3 K and examine the properties of this interface as the superconducting energy gap increases in the V_3Si . Each of these three experiments shows a Schottky barrier height of about 0.16 eV for the $\text{V}_3\text{Si}/\text{Si}$ interface. In addition, the low temperature measurements confirm that this interface is that of a superconductor/semiconductor.

There are two anomalies in this experiment. First, the current flow through the contacts is approximately 10^6 times smaller than that expected for contacts of the given area, indicating some flaw in the fabrication process. Second, low temperature measurements reveal unexpected structure near 0.5 meV. It is speculated that this is related to the presence of a superconducting phase of another vanadium compound.

5.13 Laterally-Coupled Distributed-Feedback Lasers Fabricated by X-Ray Lithography

Sponsors

Joint Services Electronics Program
 Contract DAAL03-92-C-0001
 Grant DAAH04-95-1-0038
 U.S. Army Research Office
 Contract DAAL03-92-G-0291

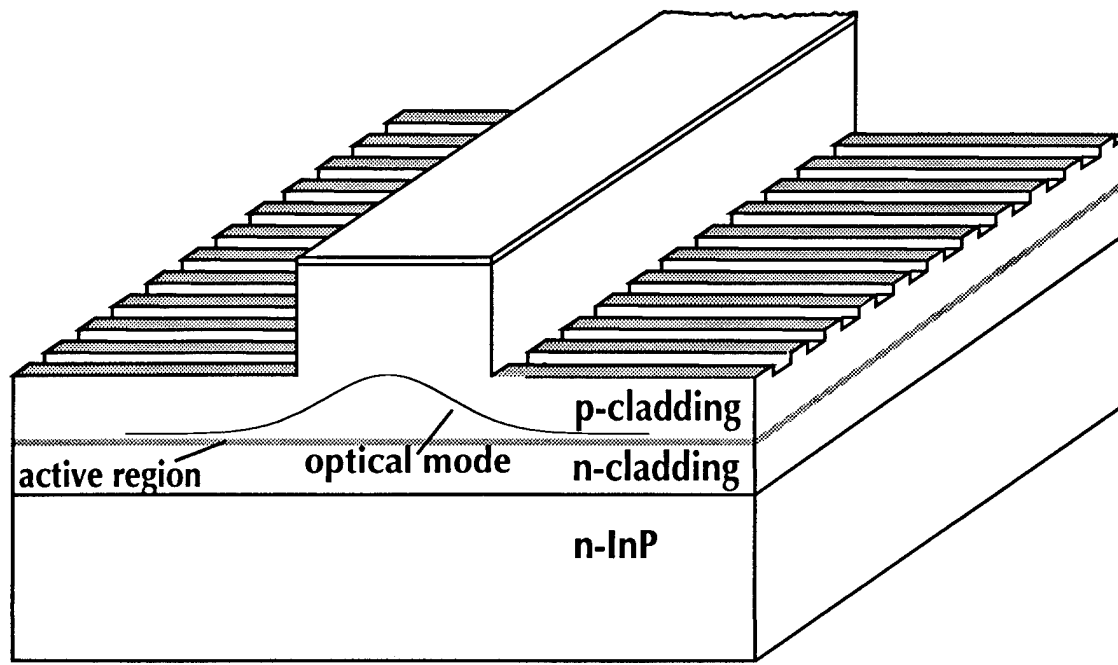
Project Staff

Vincent V. Wong, James M. Carter, Juan Ferrera,
 Professor Clifton G. Fonstad, Jr., Professor Henry I.
 Smith

Distributed feedback (DFB) lasers are essential components in future wavelength-division-multiplexed systems. These systems require transmitters that are tunable, that oscillate in a single longitudinal mode with narrow linewidths, and that are integrable with electronic circuitry such as detectors and field-effect transistors. In the fabrication of a typical DFB laser, an epitaxial regrowth step is carried out on top of the grating, a process that is often of low yield. In particular, because of etch back, the coupling constant after epi-growth can be difficult to predict. Figure 18 illustrates a

novel laterally-coupled DFB laser structure in which gratings are etched on both sides of the ridge waveguide. This structure eliminates the need for regrowth, and maximizes the utility of ridge-waveguide devices, which are much simpler to fabricate. Furthermore, the materials growth, grating fabrication and waveguide fabrication are decoupled, which should increase device yield.

We are working in collaboration with Lasertron, a commercial semiconductor-laser vendor in Burlington, Massachusetts, to fabricate both the first-order quarter-wave-shifted (QWS) and second-order uniform DFB lasers. First-order QWS-DFB lasers are attractive because they emit a single, well defined wavelength whereas uniform first-order DFB lasers can oscillate in one of two degenerate modes. In second-order uniform DFB lasers, the above degeneracy is broken by mode discrimination through radiation loss normal to the surface. Presently, we are working to better understand this phenomenon. The current view is that the discrimination arises from interference between the radiating waves. That is, on one side of the stopband these waves interfere destructively, while on the other side of the stopband they interfere constructively. The lasing wavelength emerges on the side on which the destructive interference occurs because of the lower radiation losses.



VW940228.03.ai

Figure 18. Schematic of a laterally-coupled distributed feedback laser.

To achieve laser action in the laterally-coupled DFB structure (figure 18) as well as reliable control of coupling from device-to-device, the lateral gratings should run right up to the ridge sidewall. Figure 19 shows the dependence of the coupling κ on the proximity δ of a first-order lateral grating ($\Lambda \sim 235$ nm) to the ridge sidewall of a 1.1 μm -high ridge waveguide laser structure for grating duty cycles (DC) of 0.5, 0.6, and 0.7. The ridge width and grating depth are 2.0 μm and 200 nm, respectively. As expected, the coupling decreases as the lateral gratings move away from the ridge sidewall. This decrease is attributable to the decreased overlap between the optical field and the grating. For reasonable values of κ ($\sim 20 \text{ cm}^{-1}$), the lateral gratings must be within 100 nm of the ridge sidewall. Lateral gratings that reside closer to the ridge sidewall also relax the tolerance on the grating duty cycle.

For deep-ridge waveguides, spun-on resist tends to build up significantly next to the sidewall, which at thicknesses greater than 1 μm presents a problem even for x-ray lithography. We are developing a process that uses ion implantation to eliminate such highly nonuniform resist thickness variations. By controlling the energy of the ion species one can

tailor the depth these ions penetrate a film, which in our case is PMMA. The proposed process is as follows. First, a thick planarizing layer of PMMA is spun onto the substrate containing the deep-ridge waveguides (i.e., 1.5 to 2 μm deep). Next, the substrate is implanted. The accelerating voltages are chosen so ions penetrate a certain depth into the PMMA, and the dose of the implantation is chosen so that enough energy is delivered to the PMMA film to cause chain scissioning. After development, a thin layer (~ 500 nm) of PMMA is left behind. This layer will have fairly uniform thickness up to the edge of the ridge sidewall, which alleviates the problem of varying x-ray absorption. Furthermore, it is equally applicable in cases where electron-beam lithography is performed over such deep topography.

Figure 20 shows experimental results from three separate phosphorous implantations into 1.5 μm -thick layers of PMMA. As expected, the depth removed can be tailored with accelerating voltage. Furthermore, negligible development occurs after 30 s, which implies precise depth control. Presently, we are collaborating with researchers at Genus, Inc., of Newburyport, Massachusetts, in developing this process.

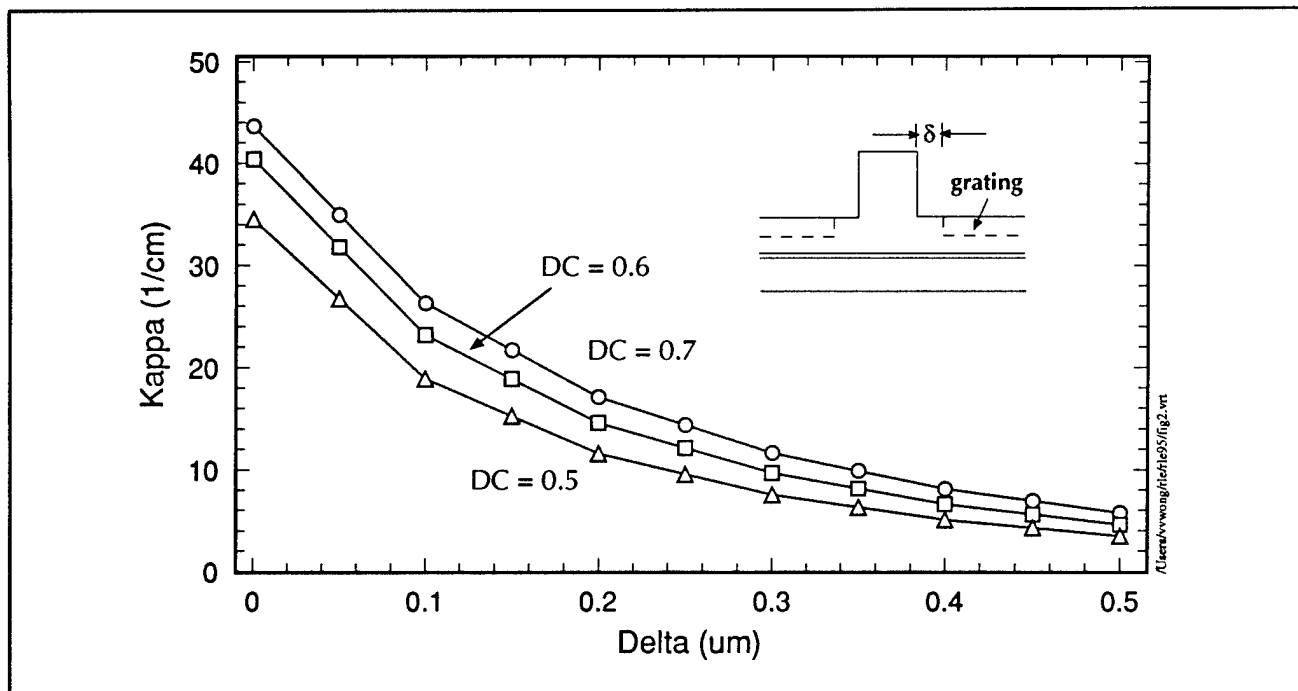


Figure 19. Coupling coefficient κ versus proximity δ of lateral grating to the ridge sidewall for a 1.1 micron-high ridge waveguide and grating duty cycles of 0.5, 0.6 and 0.7. The ridge width and grating depth are 2.0 microns and 0.2 microns, respectively.

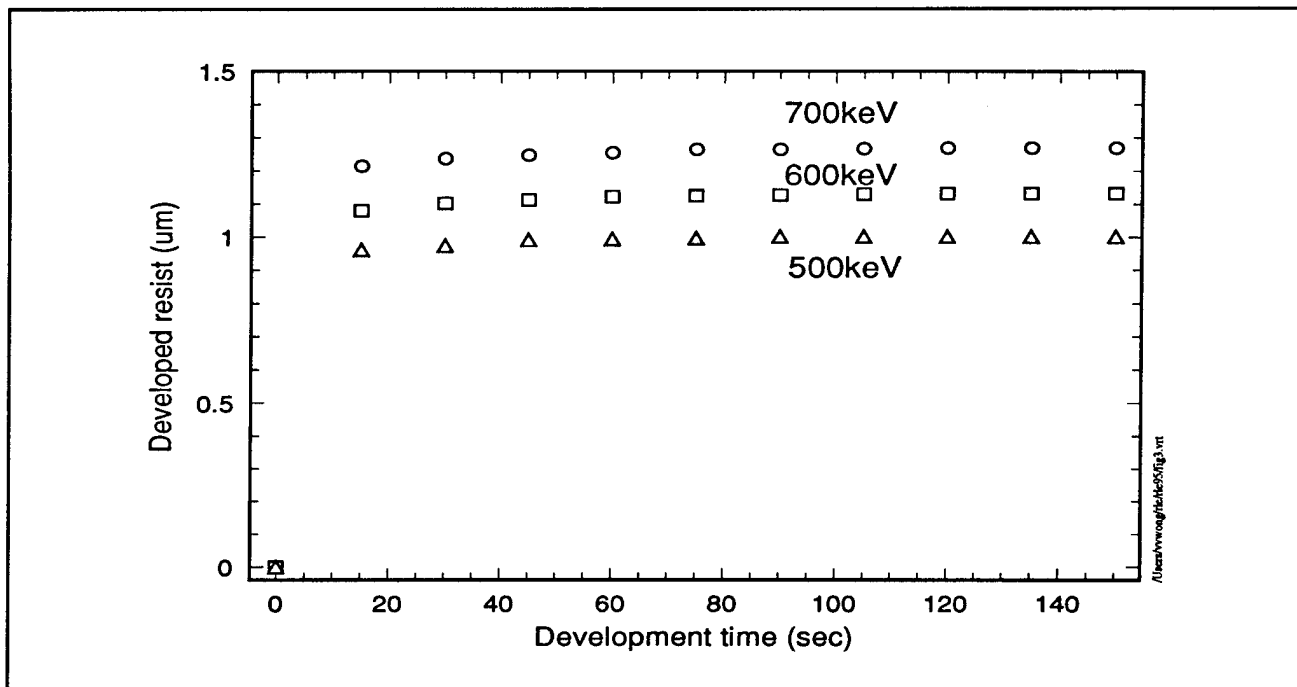


Figure 20. Plot of developed resist versus development time for three Phosphorous (P+) implantations into PMMA at energies of 500, 600, and 700 keV. The dose in all cases was 10^{13} cm^{-2} .

5.14 Combined Spatial-Phase-Locked Electron-Beam, X-ray, and Optical Lithography for Channel-Dropping Filters

Sponsor

Joint Services Electronics Program
Contract DAAL03-92-C-0001
Grant DAAH04-95-1-0038

Project Staff

Jay N. Damask, Juan Ferrera, Vincent V. Wong,
Professor Hermann A. Haus, Professor Henry I.
Smith

The integrated resonant channel-dropping filter (figure 21) was first proposed by Professor Hermann A. Haus in 1991 for use in wavelength-division multiplexed (WDM) fiberoptic communication systems. The function of the filter is to spatially separate, or "drop", just one channel from a WDM bit stream without terminating or otherwise disturbing the remaining channels. The WDM bit stream is carried along the center rib waveguide. Only that channel, or wavelength band, that excites the side-coupled quarter-wave shifted distributed Bragg reflector resonators is removed from the bus to the leftmost waveguide. The remaining channels travel through undisturbed.

As the first step towards demonstrating an integrated resonant channel-dropping filter we have fabricated highly coherent, high-Q, quarter-wave shifted distributed-feedback reflector (QWS-DBR) resonators in silicon-dioxide/silicon-nitride/silicon-dioxide (figure 22) and investigated their transmission characteristics. The grating patterns were written on an x-ray mask using spatial-phase-locked electron-beam lithography and transferred to the rib waveguides using x-ray nanolithography. With the first test chip we studied the grating strength, filter finesse, radiation loss, and spectral response as a function of grating length, depth, and width. A grating strength of 75 cm^{-1} , corresponding to a 3.6 nm-wide stopband, a maximum Q of 50,000, and a device-to-device resonant-location-repeatability of $\leq 0.05 \text{ nm}$ were demonstrated.

The selection of grating period and waveguide dimensional parameters for the in-line resonator in figure 22 were determined prior to fabrication by calculating the grating strength and effective index across a parameter space that spanned waveguide width and etch depth, given a set of core and cladding film thicknesses. Figure 23 maps contours of constant grating strength and period as a function of waveguide width and etch depth. A rib width of $2 \mu\text{m}$ and depth of $0.2 \mu\text{m}$ is expected to give a grating strength of 100 cm^{-1} and a center Bragg wavelength of 1550 nm for a 511 nm grating period.

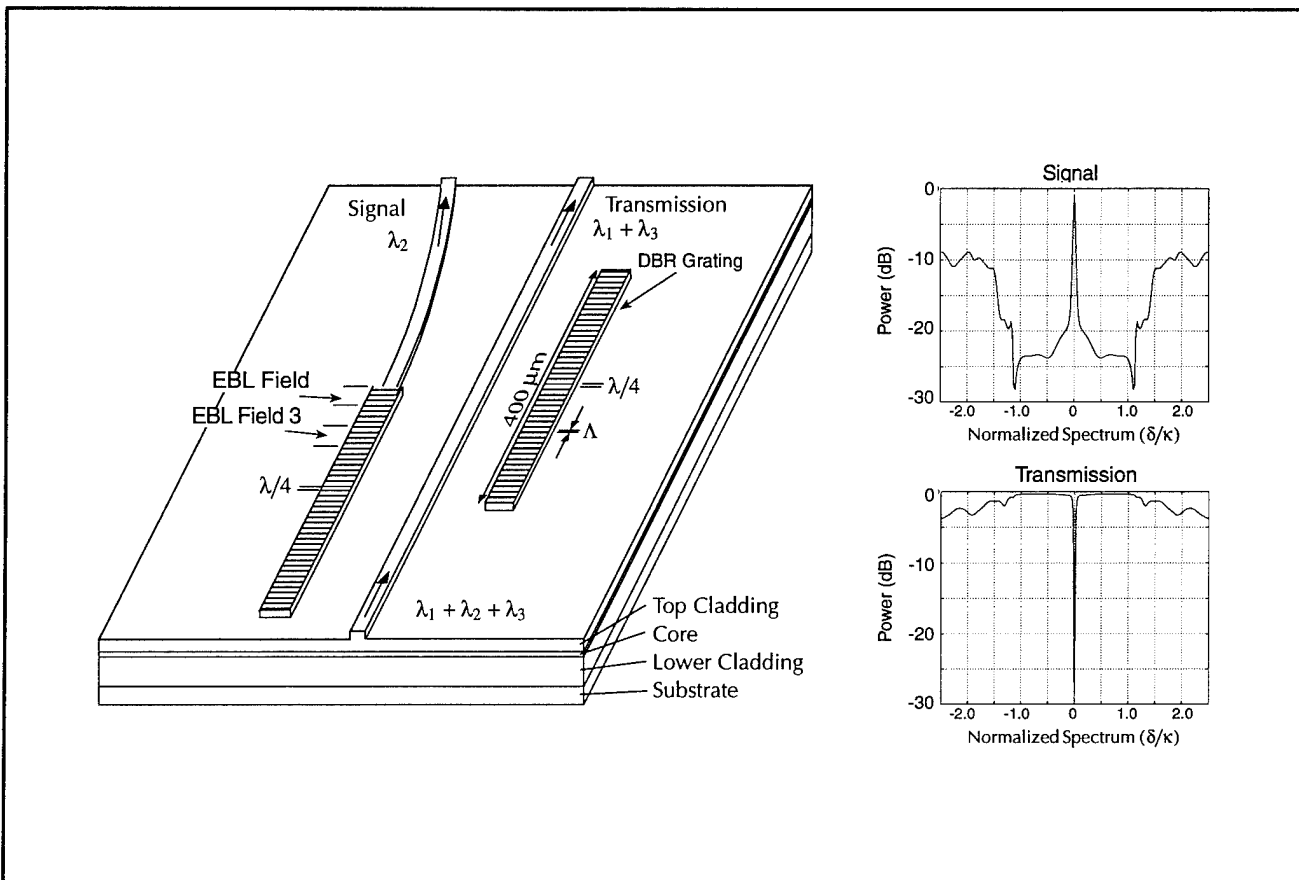


Figure 21. Schematic of the integrated resonant channel dropping filter (CDF).

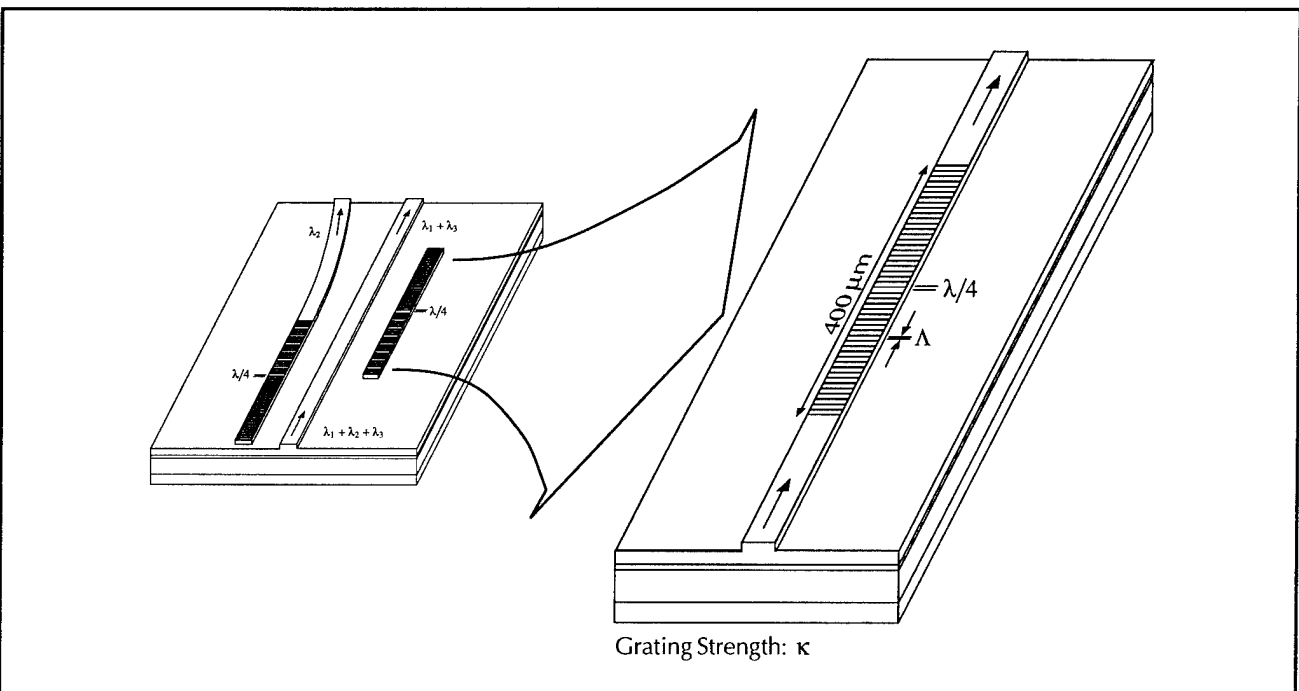


Figure 22. Left: The integrated resonant channel-dropping filter. Right: The key element of the filter, the quarter-wave shifted distributed Bragg resonator.

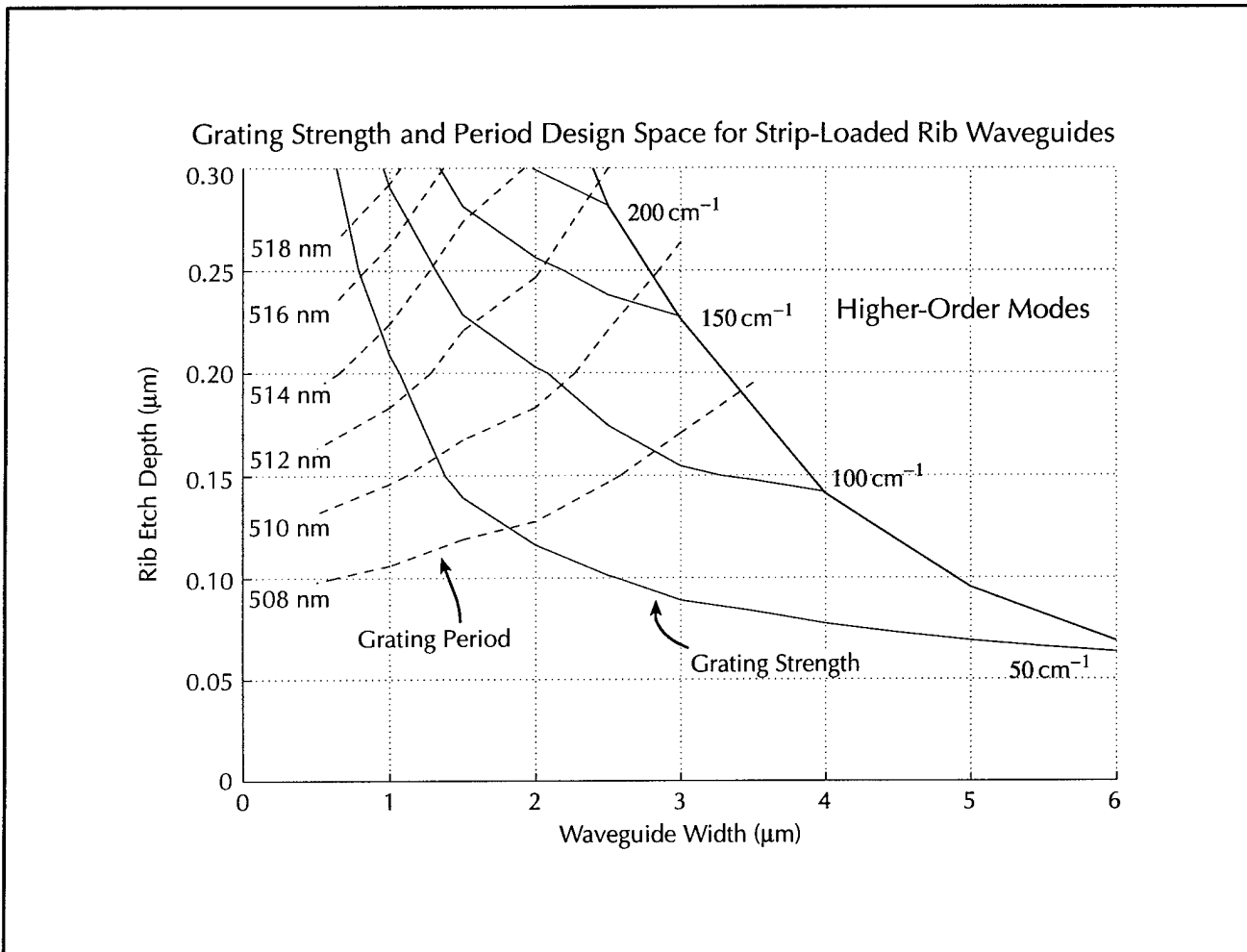


Figure 23. Design study of grating strength and grating period for a Bragg grating etched on top of a rib waveguide to a depth of one-half the rib etch depth. The Bragg wavelength is 1550 nm.

In order to achieve grating period control and arbitrary quarter-wave shift placement, the grating corrugation patterns must be produced by electron-beam lithography (EBL). However, in order for an EBL field to be sufficiently free of distortion and have small enough inter-pixel distance for the channel-dropping filter, the EBL field cannot be larger than about 100 μm . Since the grating lengths required by the channel-dropping filter extend beyond one EBL field, the grating patterns must be composed by stitching together several adjacent EBL fields. It has been calculated using a stochastic model that the standard deviation of EBL field placement precision must be better than 12 nm for a 511 nm period grating to have better than a

90 percent chance of writing a resonator with a linewidth broadening of ≤ 10 percent and an offset of the spectral location less than one-quarter of the stopband width. Such high-coherence requirements demand the use of spatial-phase-locked e-beam lithography, which has demonstrated a field placement precision of $\sigma \leq 2$ nm.

The grating patterns are written on an x-ray mask for subsequent transfer to the rib waveguides. A self-aligned method is used to localize the grating patterns to the top of the rib waveguides and to simplify the alignment procedure. The devices were die-saw cut at a 6 degree angle with respect to the waveguide perpendicular axis and the facets were polished.

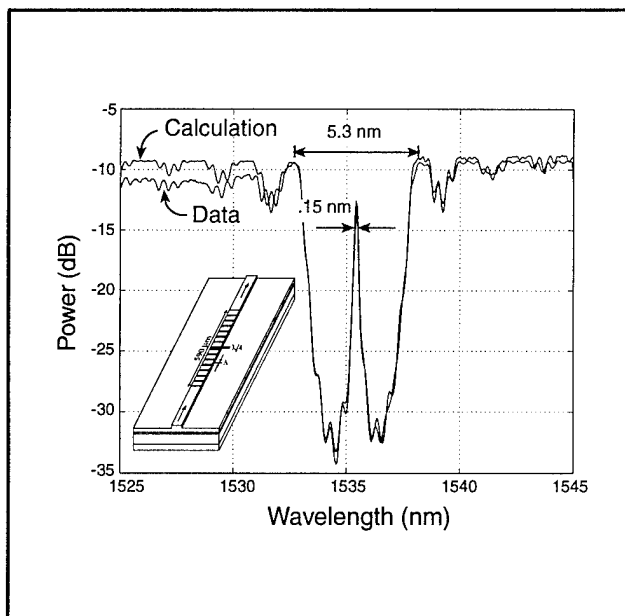


Figure 24. Overlay of measured and calculated transmission response of a $590\ \mu\text{m}$ long, 9-e-beam-field resonator. The modulation fringes are due to Fabry-Perot effects. The resonance linewidth and stopband width are $0.15\ \text{nm}$ and $5.3\ \text{nm}$, respectively. The deviation between the data and calculation on the blue side of the spectrum is due to grating-induced radiation loss.

Figure 24 shows an overlay of the transmission response of a QWS-DBR resonator with a full calculation of the expected response. The modulation fringes, present in the data and included in the calculation, are due to the Fabry-Perot cavity established between the grating end that faces the front facet and the front facet itself. Note that the resonance is very well centered within the stopband. The degree to which the resonance is centered is strongly dependent on the magnitude of the stitching errors between fields.

Figure 25 (inset) shows the resonance offset as measured on twelve resonators of different κL products and grating periods. The resonance deviations from center are within ± 1 percent of the stopband width. It is estimated from this data that the stitching errors along the gratings are $\sigma \leq 4\ \text{nm}$, or $\leq \lambda/250$. These gratings are the most highly coherent e-beam-written Bragg gratings reported to date.

Figure 26 shows the transmission spectrum of five $513\ \text{nm}$ -period resonators 5, 7, 9, 11, and 13 e-beam fields long. The resonance location of each device is $1535.4\ \text{nm}$. The Q-value ranges from 3,000 to 50,000 while the in-band baseline level is measurement limited.

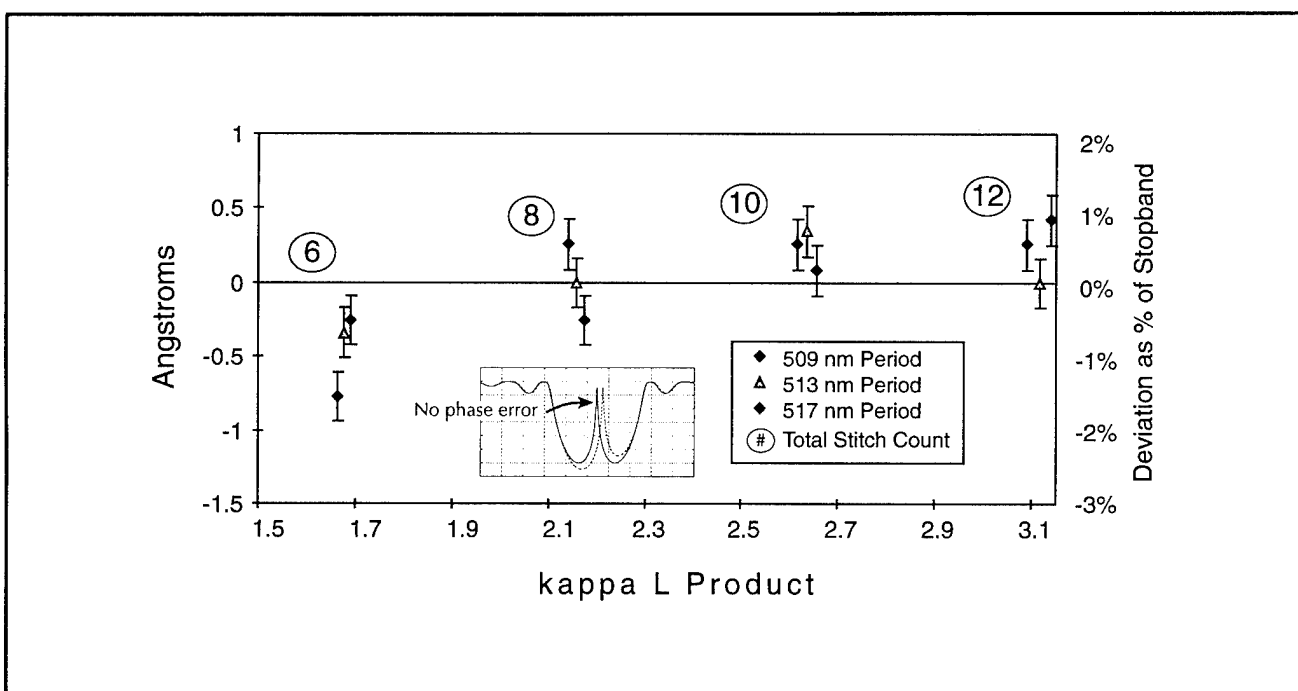


Figure 25. Measured resonance deviation from center of stopband for twelve devices with different periods and grating lengths. A 1 percent deviation corresponds to $\delta/\kappa = 0.02$. Inset shows the effect of a large stitching error (dashed) on the location of the resonance within the stopband.

Five High-Q Quarter-Wave Shifted Resonators Centered at 1535.4 nm

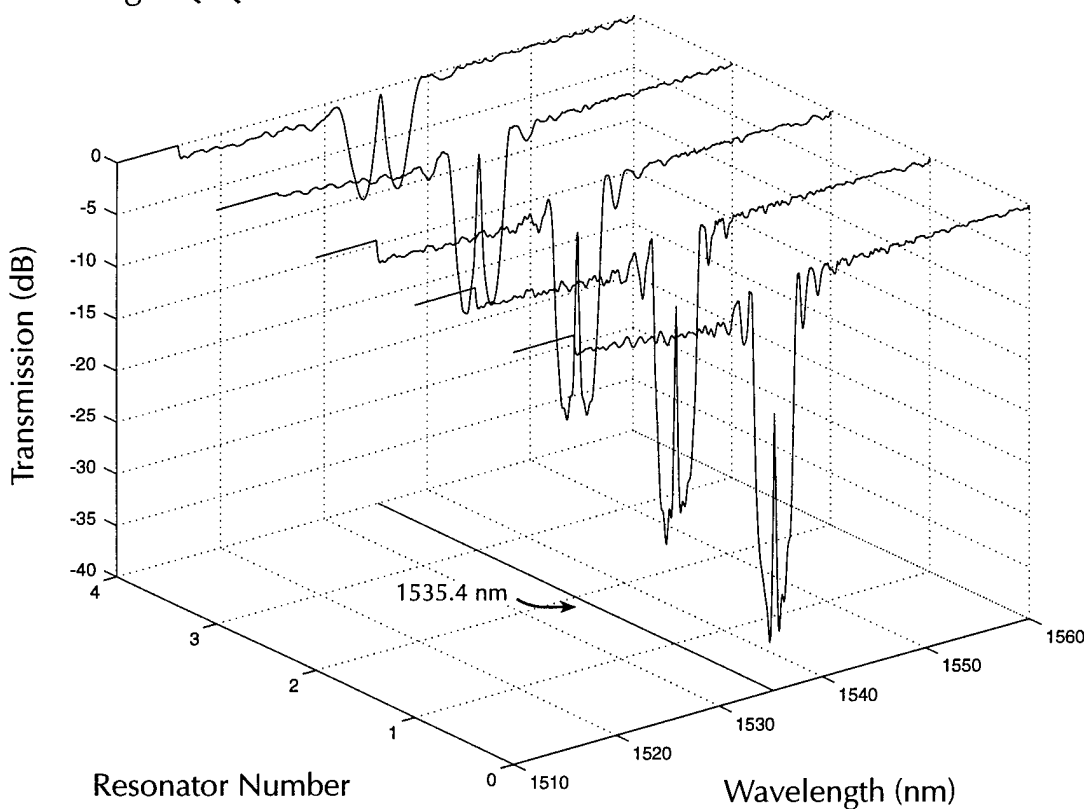


Figure 26. Five quarter-wave-shifted Bragg resonators 5, 7, 9, 11, and 13 EBL fields long, with 128 grating corrugations per field. The resonance location deviates by less than 0.05 nm from device to device.

5.15 High-Dispersion, High-Efficiency Transmission Gratings for Astrophysical X-ray Spectroscopy

Sponsor

National Aeronautics and Space Administration
Contract NAS8-36748
Grant NAGW-2003

Project Staff

Richard J. Aucoin, Robert C. Fleming, Dr. Mark L. Schattenburg, Professor Claude R. Canizares, Professor Henry I. Smith

Through a collaboration between the Center for Space Research (CSR) and the NanoStructures Laboratory (NSL), transmission gratings are provided for the Advanced X-ray Astrophysics Facility (AXAF) x-ray telescope, scheduled for launch on the NASA Space Shuttle in 1998. Many hundreds of large area, gold transmission gratings of 200 nm and 400 nm periods are required. In order to

achieve spectrometer performance goals, the gratings must have very low distortion. The gratings will provide high resolution x-ray spectroscopy of astrophysical sources in the 100 eV to 10 keV band.

The need for high grating quality and an aggressive production schedule demand the development of a robust, high-yield manufacturing process. We have adopted a scheme involving interference lithography with tri-level resist, followed by cryogenic reactive-ion etching and gold electroplating. A chemical etching step then yields membrane-supported gratings suitable for space use. The gratings undergo extensive testing before being released for use in the spectrometer.

A new cleanroom fabrication facility (the Space Microstructures Laboratory) on the 4th floor of Building 37 (adjacent to the Gordon Stanley Brown Building), has been constructed in order to fabricate the AXAF gratings. The proximity of the new lab to the MTL proper has allowed the lab to share many MTL services, such as DI, as well as process

water, nitrogen, process vacuum, and waste drains. The laboratory space includes 1700 sq-ft of Class 100 and associated support areas. A large complement of new equipment has been purchased and installed, and production of flight gratings is underway.

5.16 Submicrometer-Period Transmission Gratings for X-ray and Atom-Beam Spectroscopy and Interferometry

Sponsors

Joint Services Electronics Program

Contract DAAL03-92-C-0001

Grant DAAH04-95-1-0038

National Aeronautics and Space Administration

Contract NAS8-36748

Grant NAGW-2003

Project Staff

James M. Carter, Jeanne M. Porter, Timothy A. Savas, Dr. Mark L. Schattenburg, Satyen Shah, Professor Henry I. Smith

Transmission gratings with periods of 100-1000 nm are finding increasing utility in applications such as x-ray, vacuum-ultraviolet, and atom-beam spectroscopy and interferometry. Over 20 laboratories around the world depend on MIT-supplied gratings in their work. For x-ray and VUV spectroscopy, gratings are made of gold and have periods of 100-1000 nm, and thicknesses ranging from 100-1000 nm. They are most commonly used for spectroscopy of the x-ray emission from high-temperature plasmas. Transmission gratings are supported on thin ($1 \mu\text{m}$) polyimide membranes or made self-supporting ("free standing") by the addition of crossing struts (mesh). (For short x-ray wavelengths membrane support is desired, while for the long wavelengths a mesh support is preferred in order to increase efficiency.) Fabrication is performed by interferometric lithography combined with reactive-ion etching and electroplating. Progress in this area tends to focus on improving the yield and flexibility of the fabrication procedures.

Another application is the diffraction of neutral atom and molecular beams by mesh supported gratings. Lithographic and etching procedures have been developed for fabricating free-standing gratings in thin silicon nitride (SiN_x) supported in a Si frame. Figure 27 shows a free-standing 100 nm-period grating in 100 nm-thick silicon nitride.

We have recently established a collaboration with the Max Planck Institute in Goettingen Germany, in which they will utilize our gratings of 200 and 100 nm period (see section 5.7) in diffraction and interferometer experiments using He atom beams. In addition, free-standing zone plates for use in atom focusing experiments will also be fabricated in SiN_x .

5.17 GaAs Epitaxy on Sawtooth-Patterned Silicon

Sponsor

Joint Services Electronics Program

Contract DAAL03-92-C-0001

Grant DAAH04-95-1-0038

Project Staff

Sean M. Donovan, Dr. Khalid Ismail,² Professor Leslie A. Kolodziejski, Professor Henry I. Smith, Professor Carl V. Thompson

The growth of GaAs on Si offers the possibility of combining high-speed and optoelectronic GaAs devices with Si integrated-circuit technology. Ordinarily, the 4.1 percent mismatch between the two materials leads to high dislocation densities. However, it has been shown here at MIT that when GaAs is grown on sawtooth-patterned Si substrates the dislocation density is less than $10^5/\text{cm}^2$, orders of magnitude lower than in GaAs films grown on planar Si substrates. We investigate this effect both for its potential of greatly improving the quality of GaAs on Si and as a model for understanding the mechanism of dislocation reduction. Oriented gratings of 200 nm period are fabricated in Si_3N_4 on (100) Si substrates using holographic lithography. Anisotropic etching in KOH is then used to produce sawtooth-profile gratings in the Si. Then these serve as substrates for GaAs growth by gas source MBE.

² Professor, Cairo University, Cairo, Egypt.

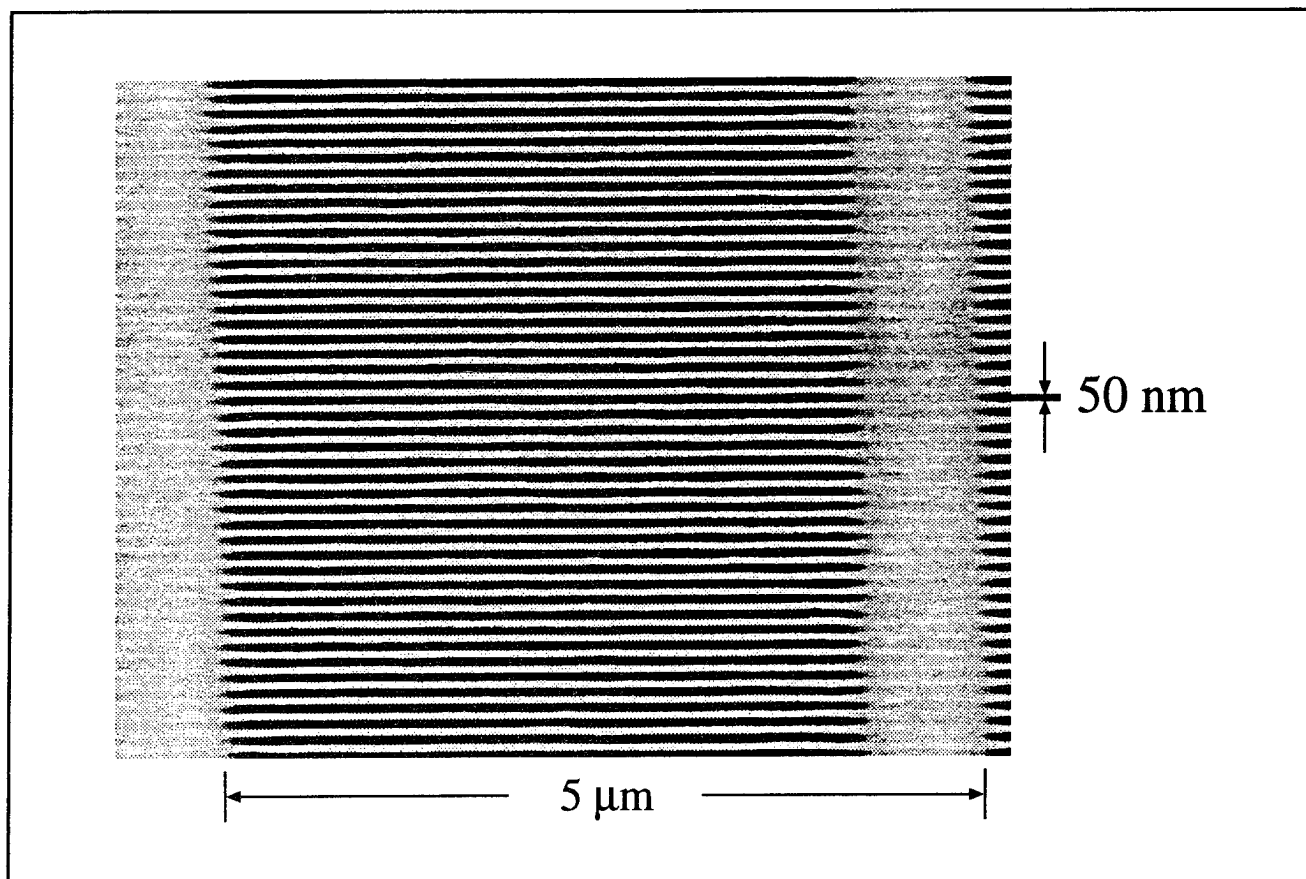


Figure 27. Scanning electron micrograph of a portion of a free-standing 100 nm-period grating in a silicon nitride membrane of area 200 μm by 5 mm.

5.18 Publications

5.18.1 Journal Articles

Bozler, C.O., C.T. Harris, S. Rabe, D.D. Rathman, W.D. Goodhue, M.A. Hollis, and H.I. Smith. "Arrays of Gated Field-Emitter Cones Having 0.32 μm Tip-to-Tip Spacings." *J. Vac. Sci. Technol. B* 12: 629-632 (1994).

Burkhardt, M., H.I. Smith, D.A. Antoniadis, T.P. Orlando, M.R. Melloch, K.W. Rhee, and M.C. Peckerar. "Fabrication Using X-ray Nanolithography and Measurement of Coulomb Blockade in a Variable-Sized Quantum Dot." *J. Vac. Sci. Technol. B* 12: 3611-3613 (1994).

Grayson, M., D.C. Tsui, M. Shayegan, K. Hirakawa, R.A. Ghanbari and H.I. Smith, "Far Infrared Emission from Hot Quasi-One Dimensional Quantum Wires in GaAs." Submitted to *Appl. Phys. Lett.*

Guo, J.Z.Y., G.K. Celler, J.R. Maldonado, and S.D. Hector. "Wavelength Dependence of Exposure

Window and Resist Profile in X-Ray Lithography." *J. Vac. Sci. Technol. B* 12: 4044-4050 (1994).

Hector, S.D., H.I. Smith, N. Gupta, and M.L. Schattenburg. "Optimizing Synchrotron-Based X-ray Lithography for 0.1 μm Lithography." *Microelectron. Eng.* 23: 203-206 (1994).

Hector, S.D., V.V. Wong, H.I. Smith, M.A. McCord, A. Wagner, and K.W. Rhee. "Printability of sub-150 nm features in X-ray Lithography: Theory and Experiments." *J. Vac. Sci. Technol. B* 12: 3965-3969 (1994).

Hu, H., J.B. Jacobs, J.E. Chung, and D.A. Antoniadis. "The Correlation between Gate Current and Substrate Current in 0.1 μm NMOSFETs." *IEEE Electron Dev. Lett.* 11: 418 (1994).

Mondol, M., H. Li, G. Owen, and H.I. Smith. "Uniform-Stress Tungsten on X-ray Mask Membranes via He-Backside Temperature Homogenization." *J. Vac. Sci. Technol. B* 12: 4024-4027 (1994).

Wong, V.V., J. Ferrera, J. Damask, J. Carter, E. Moon, H.A. Haus, H.I. Smith, and S. Rishton. "Spatial-Phase Locked E-Beam Lithography and X-ray Lithography for Fabricating First-Order Gratings on Rib Waveguides." *J. Vac. Sci. Technol. B* 12: 3741-3745 (1994).

Yang, I.Y., H. Hu, L.T. Su, V.V. Wong, M. Burkhardt, E. Moon, J. Carter, D.A. Antoniadis, H.I. Smith, K.W. Rhee, and W. Chu. "High Performance Self-Aligned Sub-100 nm MOSFETs Using X-ray Lithography." *J. Vac. Sci. Technol. B* 12: 4051-4054 (1994).

Zhao, Y., D.C. Tsui, M.B. Santos, M. Shayegan, R.A. Ghanbari, D.A. Antoniadis, H.I. Smith, and K. Kempa. "Mode Softening in the Far Infrared Excitation of Quantum Wire Arrays." *Phys. Rev. B* 48: 5249-5255 (1993).

5.18.2 Conference Proceedings

Burkhardt, M., H.I. Smith, D.A. Antoniadis, T.P. Orlando, M.R. Melloch, K.W. Rhee, and M.C. Peckerar. "Gap Control in the Fabrication of Quantum-Effect Devices Using X-Ray Nanolithography." *Micro- and Nano-Engineering (MNE)*, Davos, Switzerland, September 26-29, 1994.

Damask, J.N., J. Ferrera, V.V. Wong, H.I. Smith, and H.A. Haus. "Limitations and Solutions for the Use of Integrated 1/4-Shifted Distributed Bragg Resonators in Wavelength-Division Multiplexing Applications." International Symposium on Integrated Optics, Lindau, Germany, April 13-14, 1994; *Nanofabrication Technologies and Device Integration*. Ed. Wolfgang Karthe. SPIE 2213: 137-151 (1994).

Hu, H., L.T. Su, I.Y. Yang, D.A. Antoniadis, and H.I. Smith. "Channel and Source/Drain Engineering in High-Performance Sub-0.1 μm NMOSFETs using X-ray Lithography." *Symposium on VLSI Technology, Digest of Technical Papers*, Honolulu, Hawaii, June 7-9, 1994, pp. 17-18. (IEEE cat. No. 94CH3433-0, JSAP cat. No. AP 941211).

Schattenburg, M.L., R.J. Aucoin, R.C. Fleming, I. Plotnik, J. Porter and H.I. Smith. "Fabrication of High Energy X-Ray Transmission Gratings for AXAF." Submitted to SPIE Proceedings 2280, EUV, X-ray and Gamma-Ray Instrumentation for

Astronomy V, San Diego, California, July 24-29, 1994.

Smith, H.I., and M.L. Schattenburg. "X-ray Nanolithography: Limits, and Application to Sub-100 nm Manufacturing." Presented at the NATO Workshop on Nanolithography, Rome, Italy, April 6-8, 1993; In *Nanolithography: A Borderland between STM, EB, IB, and X-Ray Lithographies*. Eds. M. Gentili, et al. Netherlands: Kluwer Academic Publishers, 1994, pp. 103-119.

5.18.3 Theses

Ferrera, J. *Highly Coherent Gratings for Optoelectronics: An Application of Spatial-Phase-Locked Electron Beam Lithography*. B.S. and M.S. thesis. Dept. of Electr. Eng. and Comput. Sci., MIT, 1994.

Hector, S.D. *Optimization of Image Formation in X-Ray Lithography Using Rigorous Electromagnetic Theory and Experiments*. Ph.D. diss. Dept. of Electr. Eng. and Comput. Sci., MIT, 1994.

Hu, H. *Experimental Study of Electron Velocity Overshoot in Silicon Inversion Layers*. Ph.D. diss. Dept. of Physics, MIT, 1994.

Kumar, A. *Single Electron Charging Effects in Quantum Dot Nanostructures*. Ph.D. diss. Dept. of Electr. Eng. and Comput. Sci., MIT, 1994.

Li, H. *Temperature Homogenization with Tungsten Absorber on X-Ray Mask*. B.S. and M.S. thesis. Dept. of Electr. Eng. and Comput. Sci., MIT, 1994.

Owen, G.M. *Optical and Mechanical Characterization of Thin Membranes for X-Ray Lithography*. S.M. thesis. Dept. of Electr. Eng. and Comput. Sci., MIT, 1994.

5.18.4 Books

Smith, H.I. "Microlithography." In *Encyclopedia of Applied Physics*. 10: 281-295. New York: VCH Publishers, 1994. In collaboration with the American Institute of Physics, the German Physical Society, the Japan Society of Applied Physics, and the Physical Society of Japan.

Chapter 6. Single-Electron Spectroscopy

Academic and Research Staff

Professor Raymond C. Ashoori

Visiting Scientists and Research Affiliates

Dr. Albert Folch¹

Graduate Students

David Berman, Mikhail G. Brodsky, Ho Bun Chan, Sven Heemeyer

Undergraduate Students

Ilia Sokolinski

6.1 Goals and Objectives

Three years ago, we developed single-electron capacitance spectroscopy (SECS). This is a technique for measuring the quantum energy levels of nanoscale objects such as quantum dots, single impurity atoms, and localized electronic states in a semiconductor. The resolution of the method is limited only by the sample temperature, and objects containing as few as one electron may be probed. We intend to develop this type of single-electron spectroscopy into a general tool for studying nanostructured materials.

In the simplest version of SECS, we position the small object of interest between the two plates of a "tunnel capacitor". Electrons may tunnel between the object and the "bottom" plate, while a large barrier forbids tunneling to the "top" plate. By adjusting the voltage applied across the plates, single electrons are caused to tunnel onto and off the object. Once the electron tunnels onto the object, image charge is induced onto the top plate. By building a high electron mobility transistor (HEMT) directly onto the "chip" containing the sample, we demonstrated that we could detect and precisely measure this image charge.

In addition to applying a DC bias across the tunnel capacitor, we prompt single electrons to tunnel back and forth between the object and the bottom plate using an AC voltage. We then synchronously detect signals due to electronic tunneling. Peaks appear in the response at those particular positions in DC bias at which a quantum state in the object is

energy resonant with the chemical potential in the bottom plate. A simple geometric scale factor converts the DC bias scale into an energy scale for the object to allow a quantitative energy level spectroscopy. In essence, we measure the ground state energy levels of a system containing a specifiable number N of electrons as a function of an extrinsic parameter (e.g., magnetic field). The resolution of this technique is limited only by the sample temperature (typically 300 mK).

We are developing SECS into a tool for the characterization of many types of electronic structures. We have used it to measure spectra from *single* impurity atoms and a wide variety of traps. Now we are enhancing the technique by: (1) increasing its frequency response so that times for electrons to occupy and leave single traps can be characterized over a wide range; (2) adding a scanning capability so that the precise positions, shapes, and sizes of traps may be identified along with the determination of their energy spectra; and (3) creating more sensitive detectors in order to characterize samples much more rapidly.

Since the arrival of Professor Ashoori at MIT in 1993, much of our work has been directed largely toward the setup of our low temperature laboratory and developing tools for sample preparation. In this regard, we have completed installation of a top-loading dilution refrigerator with a 16 Tesla integral magnet, a helium-3 refrigerator, an electron beam lithography system, and a scanning tunneling microscope controller.

¹ Postdoctoral associate, Department of Chemistry, MIT.

6.2 Traps Created by Disorder and Impurities in Semiconductor Structures

Sponsors

Joint Services Electronics Program

Contract DAAL03-92-C-0001

Grant DAAH04-95-1-0038

National Science Foundation

Young Investigator Award

Packard Foundation

U.S. Navy - Office of Naval Research

Project Staff

Ho Bun Chan, David Berman, Professor Raymond C. Ashoori

One system that we have studied in detail is a circular disk of electrons 1 mm in diameter and contained within a GaAs quantum well. We empty this disk and begin adding electrons to it. The first few electrons enter localized states of this disk. Observation of the magnetic field evolution of these energy levels allows a characterization of the type of minimum which localizes the electron as well as the lateral extent (localization length) of quantum levels. We find that some of the states are localized on minima of the disorder potential while others are located on *single* impurity atoms. At higher filling, the sample behaves as a disk of two-dimensional electron gas (2DEG), with Landau level structure evident in magnetic field.

We intend to exploit samples of this type as a laboratory to study systems of localized electrons, and much work remains. For instance, although the first electrons in the disk are in spatially separate localized states, they interact electro-statically. These interactions create correlations between the electron additions that are of principal interest in studying the Coulomb gap. Our experiment can thus directly measure the density of states within the Coulomb gap. As the disk is filled, near the metal-insulator transition these correlations should evolve into the Coulomb blockade with nearly periodic electron additions in gate bias. Our ability to monitor this evolution together with direct measurements of the localization length of quantum states will provide an unprecedented view of the metal-insulator transition. Although all electronic states in two-dimensions are thought to be localized, the localization length increases smoothly with chemical potential. The sample displays metallic conduction when the localization length grows to become equal to the sample size. In magnetic field, this picture changes radically with the localization length of electronic states thought to oscillate as the chemical potential is swept through the Landau level

structure. This picture is central to theories of the quantum Hall effect. Our direct probe of localization lengths of electronic states can provide a key test of these ideas.

6.3 Artificial Atoms

Sponsors

Joint Services Electronics Program

Contract DAAL03-92-C-0001

Grant DAAH04-95-1-0038

National Science Foundation

Young Investigator Award

Packard Foundation

U.S. Navy - Office of Naval Research

Project Staff

Ho Bun Chan, David Berman, Mikhail Brodsky, Professor Raymond C. Ashoori

We have created another sample in which electrons accumulate at a single potential minimum defined by gating. This sample behaves as a true "quantum dot" or an artificial atom. We have measured the ground state energies of this system in magnetic field with electronic population from 0-50. The most apparent new physics arises with only two electrons in the dot. We observe an exchange induced singlet-triplet crossing of the two-electron state as the magnetic field is increased beyond 1.5 Tesla. This is the first instance in which a two-electron singlet-triplet crossing has been observed; for He atoms it takes place at fields of >400,000 Tesla. Understanding our results for a dot containing three or more electrons becomes quite complicated, requiring intensive computer modeling. However, with more than 10 electrons the system begins to approximate a very small 2DEG. Features, related to the quantum Hall effect, arise when the dot encloses integer numbers of electrons per flux quantum threading the dot. At higher fields, we see features suggestive of the fractional quantum Hall effect in both the energetics and tunneling rates of electrons.

A central topic in quantum dot physics is the role of the electron-electron interaction in modifying a dot's electronic level structure. Single-particle-like states exist in the limit of very small dots, while level structure is dominated by the electron-electron interaction in larger dots. Since the confinement potential in semiconductor quantum dots can be controlled at will, there exists a continuum of physics that we may explore. We plan a detailed examination of quantum dots in different size regimes.

6.4 Spatially Resolved Charge Sensing

Sponsors

Joint Services Electronics Program
 Contract DAAL03-92-C-0001
 Grant DAAH04-95-1-0038
 U.S. Navy - Office of Naval Research

Project Staff

Sven Heemeyer, Dr. Albert Folch, Professor
 Raymond C. Ashoori

We are presently developing methods for adding spatial resolution to our charge sensitive measurements. We are constructing a charge sensitive scanning tunneling microscope (STM) for low temperature studies.

As a first step, we have recently completed building a room temperature STM. This STM is a "walker" design. Its chief advantages are that it allows large lateral range of motion in observations of the surface of a sample, and no mechanical linkages to the sample are required. Figure 1 presents room temperature data of a gold $\langle 111 \rangle$ surface. The lateral dimensions are 100 Angstroms, and the observed steps are about 50 Angstroms high.

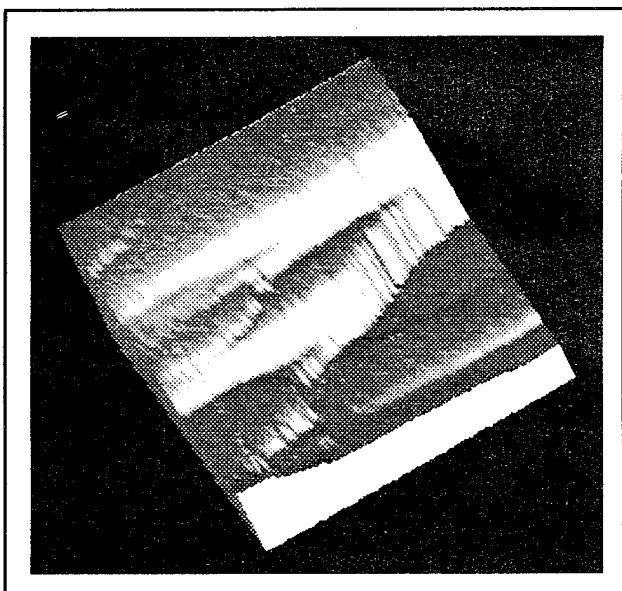


Figure 1. Scanning tunneling microscope image of a Au $\langle 111 \rangle$ surface taken with our home-built scanning tunneling microscope. The lateral dimensions are 100 Angstroms, and the terraces are 50 Angstroms tall.

We are presently constructing a low temperature STM. It will operate inside our helium-3 refrigerator at a temperature of 0.3 K.

6.5 Single-Electron Transistors for Spectroscopy

Sponsors

Joint Services Electronics Program
 Contract DAAL03-92-C-0001
 Grant DAAH04-95-1-0038
 National Science Foundation
 Young Investigator Award
 U.S. Navy - Office of Naval Research

Project Staff

David Berman, Professor Raymond C. Ashoori

We are developing single-electron transistors to improve the sensitivity of SECS. Invented about five years ago, much interest has been focused on the study of the physics of the devices themselves. With further development, these transistors hold promise for being the most sensitive electrometers available. Calculations indicate that they could provide one or two more orders of magnitude improvement in charge sensitivity over our present HEMTs. Such sensitivity will greatly enhance SECS and will make feasible a number of experiments that are presently impractical.

We have converted an existing JEOL 6400 scanning electron microscope for use in electron beam writing. Using this system and the processing facilities of the Center for Materials Science and Engineering, we have recently created our first single-electron transistors fabricated from aluminum and aluminum oxide. We are presently attempting to integrate these devices onto semiconductor structures.

6.6 Publication

Ashoori, R.C., H.L. Stormer, J.S. Weiner, L.N. Pfeiffer, K.W. Baldwin, and K.W. West. "Energy Levels of an Artificial Atom Probed with Single-Electron Capacitance Spectroscopy." *Surf. Sci.* 305: 558-565 (1994).

Section 3 Optics and Devices

Chapter 1 Optics and Quantum Electronics

Chapter 2 Optical Propagation and Communication

Chapter 3 High-Frequency (> 100 GHz) and High-Speed
(< 1 ps) Electronic Devices

Chapter 1. Optics and Quantum Electronics

Academic and Research Staff

Professor Hermann A. Haus, Professor Erich P. Ippen, Professor James G. Fujimoto, Professor Peter L. Hagelstein, Dr. Brett E. Bouma, Dr. Joseph A. Izatt

Visiting Scientists and Research Affiliates

Dr. Mark E. Brezinski,¹ Dr. Charles P. Lin, Dr. Brent E. Little, Dr. Shu Namiki, Dr. Matasaka Shirasaki

Graduate Students

Laura E. Adams, Susan Bach, Keren Bergman, Igor P. Bilinsky, Luc Boivin, Stephen A. Boppart, Jerry C. Chen, Jay N. Damask, Ali M. Darwish, Christopher R. Doerr, David J. Dougherty, Siegfried B. Fleischer, Marc Fleury, Boris Golubovic, James G. Goodberlet, Michael R. Hee, Charles T. Hultgren, David J. Jones, Sumanth Kaushik, Mohammed J. Khan, Farzana I. Khatri, Gadi Lenz, Martin H. Muendel, John D. Moores, Lynn E. Nelson, Malini Ramaswamy-Paye, Timothy A. Savas, Chi-Kuang Sun, Kohichi R. Tamura, Guillermo J. Tearney, Constantine Tziligakis, Morrison Ulman, William S. Wong

Undergraduate Students

Leo Chun, Charles Yu

Technical and Support Staff

Mary C. Aldridge, Donna L. Gale, Cynthia Y. Kopf

1.1 Fiber Ring Lasers

Sponsors

Charles S. Draper Laboratories
Contract DL-H-467138

Joint Services Electronics Program
Contract DAAL03-92-C-0001
Grant DAAH04-95-1-0038

U.S. Air Force - Office of Scientific Research
Contract F49620-91-C-0091

Project Staff

Professor Hermann A. Haus, Professor Erich P. Ippen, Christopher R. Doerr, Lynn E. Nelson, Kohichi R. Tamura

Several new fiber ring laser systems have been developed over the past few years in the Optics and Devices Group of RLE. The simplicity of design of these systems allows for modifications that lead to outstanding performance characteristics.

The laser consists of an erbium doped fiber and an undoped fiber forming a ring. The net dispersion (group velocity as a function of frequency) can be adjusted through proper choice of the two fiber segments. Polarizers and quarter wave plates control the polarization of the mode circulating in the ring. The polarizers can be realized entirely with fiber components. An isolator assures propagation in one direction around the ring (see figure 1). By proper adjustment of the polarizers, the self-phase modulation of the two polarizations of the mode circulating in the ring is transformed into amplitude modulation such as to spontaneously form pulses in the ring by injection locking of the modes of the ring resonator (modelocking). Pulses are formed when higher intensities experience less loss than lower intensities. We call this mechanism additive pulse modelocking (APM), and this acronym is now accepted in the literature as the descriptor of this form of modelocking.² The ring delivers pulses of the order of 400 fs duration at the round-trip rate of 40 MHz. We have studied the wavelength tuning

¹ Massachusetts General Hospital, Boston, Massachusetts.

² H.A. Haus, E.P. Ippen, and K. Tamura, "Additive Pulse Modelocking in Fiber Lasers," *IEEE J. Quant. Electron.* 30: 200-208 (1994).

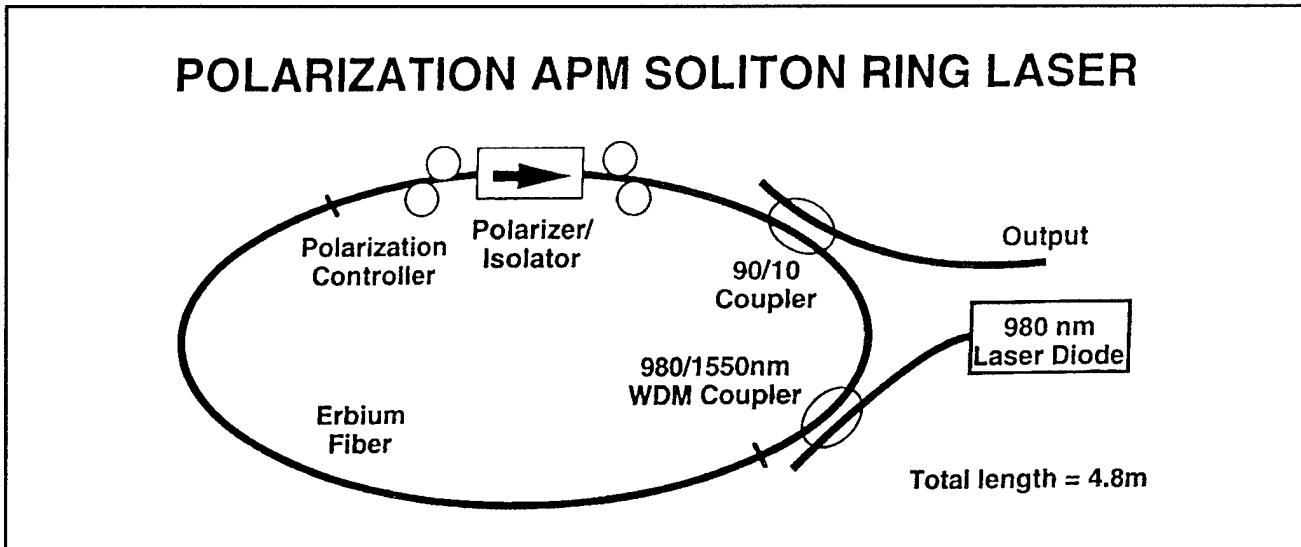


Figure 1. Schematic of Additive Pulse Modelocked ring laser.

and filtering characteristics of this laser³ and developed optimization criteria.⁴ Last year, with proper adjustment of the fiber dispersion, we were able to produce pulses as short as 69 fs.⁵ The system has been copied by a group at Bell Laboratories for their use. We are currently in the process of working with Clark MXZ to commercialize these systems.

As mentioned in the introduction, the simplicity of the system permits modifications for the realization of different operating characteristics. For many purposes it is desirable to generate pulses at much higher rates than 40 MHz. This can be accomplished with a modulator in the ring, yet not without further precautions. Indeed, a modulator by itself produces pulse trains of very poor pulse-to-pulse stability, because the gain relaxation time is of the order of a millisecond, and there is no mechanism to regulate the energy from pulse to pulse. Last year, we reported operation of a harmonically modelocked system operating at 1 GHz, using a modified APM mechanism, used to stabilize the energy from pulse to pulse.⁶ Instead of providing

decreasing loss for increasing intensity, the APM mechanism was reversed by a change of the polarization controllers to limit peak intensities. In this way, we obtained stable pulse-streams at 1 GHz, the highest frequency accessible with our modulator. MIT Lincoln Laboratory has copied our system and, with their 20 GHz modulator, produced stable pulse streams at this much higher repetition rate.

The modelocked ring laser described above delivers pulses of width according to the formula for active modelocking, dictated by the magnitude of the modulator drive which is limited. In the 1 GHz system just described, the pulse widths are 15 ps. In an attempt to generate shorter pulses at a high repetition rate, Chris Doerr, a graduate student, discovered asynchronous modelocking, a new principle of modelocking fiber ring lasers.⁷ A phase modulator is used instead of the amplitude modulator described before. The modelocking drive of 1 GHz is detuned by about 15 kHz from the frequency synchronous with a harmonic of the round-trip frequency. The pulses are now 1 ps long and

³ K. Tamura, L.E. Nelson, H.A. Haus, and E.P. Ippen, "Soliton versus Non-soliton Operation of Fiber Ring Lasers," *Appl. Phys. Lett.* 62: 149-151 (1993); K. Tamura, C.R. Doerr, L. Nelson, H.A. Haus, and E.P. Ippen, "Technique for Obtaining High-energy Ultrashort Pulses from an Additive-pulse Mode-locked Erbium-doped Fiber Ring Laser," *Opt. Lett.* 19: 46-48 (1994); K. Tamura, C.R. Doerr, H.A. Haus, and E.P. Ippen, "Soliton Fiber Ring Laser Stabilization and Tuning with a Broad Intracavity Filter," *IEEE Photon. Technol. Lett.* 6: 697-699 (1994).

⁴ K. Tamura, E.P. Ippen, and H.A. Haus, "Optimization of Filtering in Soliton Fiber Lasers," *Photon. Technol. Lett.* 6 (1994).

⁵ H.A. Haus, K. Tamura, L.E. Nelson, and E.P. Ippen, "Stretched Pulse Additive Pulse Modelocking of Fiber Lasers," *IEEE J. Quant. Electron.* 31: 591-592 (1994).

⁶ C.R. Doerr, H.A. Haus, E.P. Ippen, M. Shirasaki, and K. Tamura, "Additive-Pulse Limiting," *Opt. Lett.* 19: 31-33 (1994).

⁷ C.R. Doerr, H.A. Haus, and E.P. Ippen, "Asynchronous Soliton Modelocking," *Opt. Lett.* 19: 1958-1960 (1994).

travel around the loop at their own rate. The modelocking drive serves the purpose of starting the system and of arranging the pulses equidistantly around the loop by refreshing the pulse stream every time it becomes synchronous with the modelocking drive. Because phase modulation is used, instead of amplitude modulation, the pulses do not experience modulator induced loss when they drift out of alignment with the modelocking drive. The APM action in the loop is responsible for the shortening of the pulse to 1 ps.

This is an entirely new principle of modelocking made possible by the pulse-forming capabilities of the fiber loop. The APM mechanism of the fiber loop provides the short pulse widths. The limiting of the APM mechanism provides the stability for the pulse-to-pulse energy. If any conventional modelocked system were detuned in the same way, modelocked operation would simply cease. We believe that this asynchronous modelocking principle is applicable to all systems with their own passive pulse-shaping mechanism (e.g., Kerr Lens Modelocking) if harmonic modelocking with short pulse widths is sought.

In the upcoming year, we shall explore the asynchronous modelocking principle for its potential use in optical storage rings (see section 1.2).

1.2 Fiber Storage Ring

Sponsors

Charles S. Draper Laboratories
Contract DL-H-467138

U.S. Air Force - Office of Scientific Research
Contract F49620-91-C-0091

Project Staff

Professor Hermann A. Haus, Professor Erich P. Ippen, Christopher R. Doerr, David J. Jones, John D. Moores, William S. Wong

In a theoretical paper published in 1992,⁸ we proposed that a fiber loop with gain, filter, and an amplitude modulator could maintain a stream of

pulses separated by empty intervals (ones and zeros), in spite of the spontaneous emission noise associated with gain. In this way, a fiber ring could act as a storage ring of a bit-stream of optical pulses. This year, we demonstrated the storage principle with an experimental fiber ring containing 66 bits at a 1 GHz rate.⁹

The system consists of two rings; one serves as the pulse pattern generator, the other as the storage ring. The pulse pattern generator is simply a ring laser with a modelocking element which, starting from noise, reaches a steady state with pulses in some of the time slots and "zeros" in other slots. Figure 2 (top) shows such a bit pattern. The "zeros" turn out to be pulses as well, but of much lower peak amplitude. Through the LiNbO₃ switch this pattern is injected into the storage ring. Figure 2 (bottom) shows the pattern in the ring. The "zeros" have been improved so that they are now pulses of much lower amplitude than the "ones." The storage was on a time scale of hours (as long as the gain was maintained). We have addressed the stability and timing issue theoretically,¹⁰ and MIT Lincoln Laboratory, interested in high bit-rate optical storage, has built a storage ring according to the same design and an 18 Gb/s bit-stream was stored. No physical principle prevents the upscaling of this storage to bit-rates of 100 Gb/s, if 100 GHz modulators become available.

In the upcoming year, we will determine various means for loading and unloading the storage ring. Also, we will explore the possibility of asynchronous phase modulation for storage application. If operation with an asynchronous modulation is feasible, then loading and unloading of bit-packets would be greatly facilitated.

1.3 Long-Distance Fiber Communications

Sponsors

MIT Lincoln Laboratory
National Science Foundation
Grant ECS 90-12787

⁸ H.A. Haus and A. Mecozzi, "Long-Term Storage of a Bit Stream of Solitons," *Opt. Lett.* 17: 1500-1502 (1992).

⁹ C.R. Doerr, W.S. Wong, H.A. Haus, and E.P. Ippen, "Additive-Pulse Mode Locking/Limiting Storage Ring," in *Conference on Lasers and Electro-Optics*, OSA Technical Digest Series, vol. 8 (Washington, D.C.: Optical Society of America, 1994), pp. CPD12-1/27 - CPD12-2/28; C.R. Doerr, W.S. Wong, H.A. Haus, and E.P. Ippen, "Additive-Pulse Mode Locking/Limiting Storage Ring," *Opt. Lett.* 19(21): 1747-1749 (1994).

¹⁰ J.D. Moores, W.S. Wong, and H.A. Haus, "Stability and Timing Maintenance in Soliton Transmission and Storage Rings," *Opt. Comm.* 113: 153-175 (1994).

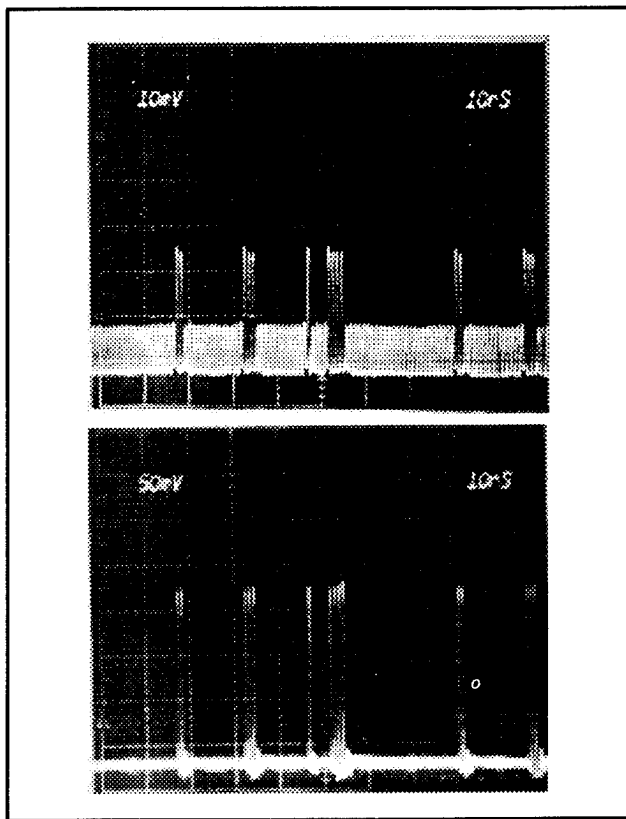


Figure 2. Example of loading. (Top) Oscilloscope trace of a bit pattern in ring number 1 (started from noise); (bottom) Oscilloscope trace of a bit pattern in ring number 2 after being loaded from ring number 1 using a 90 ns electrical gate. Horizontal scale is 10 ns/div.

Project Staff

Professor Hermann A. Haus, Farzana I. Khatri, John D. Moores, William S. Wong

We have continued to develop analytical theory and to simulate soliton propagation on the computer. In particular, we concentrated on the long-range interaction effects between solitons. When a soliton is perturbed nonadiabatically by gain, lumped filters, or loss segments, it sheds continuum. The continuum spreads away from the perturbed soliton and hits neighboring solitons. This continuum is not orthogonal to the neighboring soliton and shifts its frequency and position. These shifts are very small. However, if they are frequent enough, they can cause bit-errors.

We have developed an analytical theory for these interactions which we checked against computer

simulations finding satisfactory agreement. While these effects are not large enough to cause increased bit-error rates in transoceanic transmission at the projected rates of 5 to 10 Gb/s, they could become more severe for higher bit-rates and are likely to have been observed in loop experiments conducted by Dr. Linn Mollenauer at AT&T Bell Laboratories over distances of 20,000 km or more. In his experiments, anomalous errors were attributed to piezo-optic effects produced by the solitons, but it is likely that these continuum interactions also contributed to the bit-error rate. We intend to compare our theory with past and future experiments at AT&T Bell Laboratories.

1.4 Squeezing

Sponsors

Charles S. Draper Laboratories
Contract DL-H-467138
Fujitsu Laboratories
National Science Foundation
Grant ECS 90-12787

Project Staff

Professor Hermann A. Haus, Professor Erich P. Ippen, Keren Bergman, Luc Boivin, Christopher R. Doerr, Dr. Matasaka Shirasaki

The purpose of squeezing optical radiation is to provide means for interferometric measurements with reduced noise, at noise levels less than shot noise. We are continuing our successful experiments in squeezing. Our present aim is to improve the shot noise reduction, which is currently 5.1 dB.¹¹ This will be done by Luc Boivin with a system under construction which uses a high repetition rate Ti:Sapphire laser. By moving into this wavelength range, we may utilize fibers with large positive dispersion and detectors of higher quantum efficiency than for detectors at 1.3 μm wavelength. The dispersion-free fiber at 1.3 μm produced squeezing with gaussian pulses that maintained their gaussian shape throughout. In homodyne detection, the phase of the local oscillator does not align with the phase of maximum squeezing across the pulse profile. In simplest terms, a square pulse would not suffer from this drawback, realizing the full noise reduction over its entire width. Since square pulses are difficult to generate without incurring excessive power loss, we have explored theoretically the

¹¹ K. Bergman, H.A. Haus, E.P. Ippen, and M. Shirasaki, "Squeezing in a Fiber Interferometer with a Gigahertz Pump," *Opt. Lett.* 19: 290-292 (1994).

squeezing in a fiber with built-in pulse shaping.¹² A positively dispersive fiber, starting with a gaussian pulse, can produce better shot noise reduction than a pulse in a zero-dispersion fiber.

The high repetition rate modelocked Ti:Sapphire is of a new design pioneered by Professor James G. Fujimoto and his student Malini Ramaswamy-Paye. The repetition rate of the pulses in a squeezing experiment must be 1 GHz or higher to avoid convolution of the guided acoustic wave brillouin scattering noise into the low frequency detection window. Theoretical work on quantum noise also continues to provide new insight.¹³

1.5 Optical Channel Dropping Filters

Sponsors

National Center for Integrated Photonics

National Science Foundation

Grant ECS 90-12787

Project Staff

Professor Hermann A. Haus, Professor Leslie A. Kolodziejksi, Professor Henry I. Smith, Jerry C. Chen, Jay N. Damask, Juan Ferrera, Mohammed J. Khan, Vincent V. Wong

We have begun to fabricate quarter-wave shifted distributed feedback (DFB) resonators in silica on Si using e-beam lithography. In order to produce gratings of reproducible quality, it was necessary to reduce the stitching error between e-beam fields to less than five nanometers. This has been accomplished by a new technique developed by Professor Henry I. Smith and his students, the spatial-phase-locked e-beam lithography described elsewhere in this report. The measured response of an in-line quarter wave shifted DBR resonator is shown in figure 3a, and a schematic of the resonator is shown in figure 3b. A theoretically predicted response is superimposed, and is almost indistin-

guishable from the measured response over the stopband of the grating. The fringes are due to a Fabry-Perot effect between the imperfectly matched waveguide input and the front of the grating. This artifact can be removed by AR coatings of the facets. On the short-wavelength side of the grating, the loss due to radiation into the substrate is clearly discernible.

The next step is to fabricate resonators side-coupled to a "signal" waveguide. For acceptable performance, the grating waveguide and the "signal" waveguide must be synchronous. Because the two waveguides are subjected to different processing steps, synchronism is not easily accomplished. Jay N. Damask has made extensive studies of the synchronism requirement and the fabrication steps required to achieve synchronism with a sufficient degree of accuracy.¹⁴

Other possibilities for channel dropping filter design have been explored theoretically. In collaboration with Professor John D. Joannopoulos of the Physics Department, we have started to explore the use of photonic bandgap structures for filter applications. Photonic bandgap structures have large reflections per cell, and thus a wide bandgap. With such structures, it would be possible to cover the entire bandwidth of erbium amplifiers (40 nm). Further, a single resonator becomes only a few wavelengths long. Thus, through coupling of such resonators, compact optical filters with sophisticated response characteristic could be constructed. One serious problem that must be overcome in such structures is the loss via radiation into the substrate. Computer simulations by Jerry C. Chen and some analytic modeling predict (radiation-loss) Qs as high as 20,000.¹⁵

Active filters (containing gain) have very interesting properties of their own. Spurious resonances can be suppressed much more effectively with active filter design than with passive ones. Further, the filters can be tuned by changes in reflection, rather than index. Since reflection is varied much more

¹² C.R. Doerr, M. Shirasaki, and F.I. Khatri, "Simulation of Pulsed Squeezing in Optical Fiber with Chromatic Dispersion," *J. Opt. Soc. Am. B* 11: 143-149 (1994).

¹³ H.A. Haus, "From Classical to Quantum Noise," submitted to *J. Opt. Soc. Am. B* (based on Frederic Ives Medal lecture); L. Boivin, F.X. Kärtner, and H.A. Haus, "Analytical Solution to the Quantum Field Theory of Self-phase Modulation with a Finite Response Time," *Phys. Rev. Lett.* 73: 240-243 (1994); F.X. Kärtner, D.J. Dougherty, H.A. Haus, and E.P. Ippen, "Raman Noise and Soliton Squeezing," *J. Opt. Soc. Am. B* 11: 1267-1276 (1994); M. Shirasaki, I. Lyubomirsky, and H.A. Haus, "Noise Analysis of Mach-Zehnder Squeezer for Nonclassical Input State," *J. Opt. Soc. Am. B* 11: 857-863 (1994); J.K. Bounds and H.A. Haus, "Quantum Noise of Raman Amplification," *Quant. Opt.* 6: 79-85 (1994).

¹⁴ J.N. Damask, J. Ferrara, V.V. Wong, H.I. Smith, and H.A. Haus, *Proc. SPIE* 2213: 137 (1994).

¹⁵ J.C. Chen, H.A. Haus, J.N. Winn, and J.D. Joannopoulos, "Wide Stop Band Optical Filters from Photonic Band Gap Air Bridges," in *Guided-Wave Optoelectronics: Device Characterization, Analysis, and Design* (New York: Plenum Press), forthcoming.

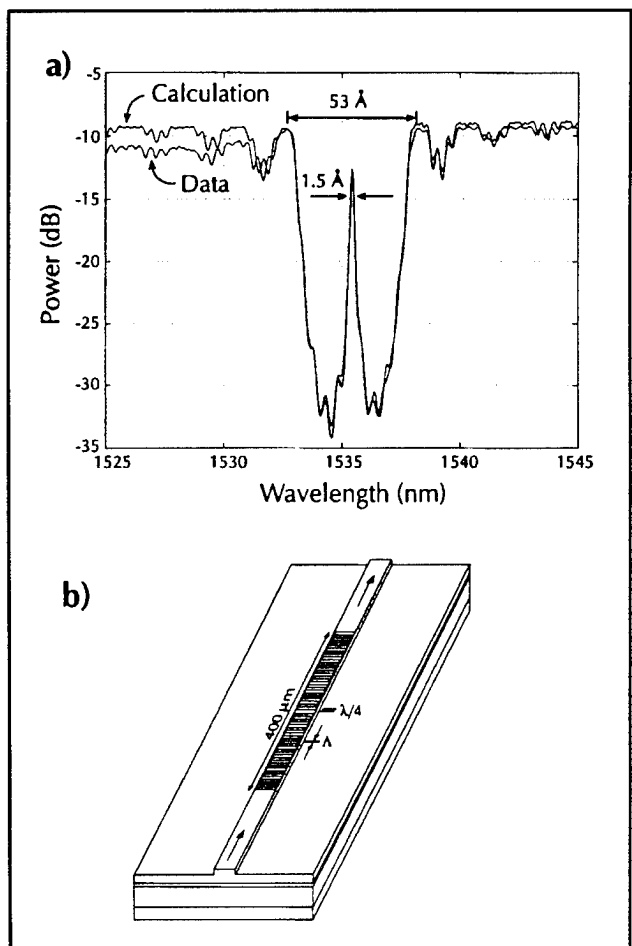


Figure 3. (a) Overlay of calculated and measured response of an in-line quarter wave shifted DBR resonator. (b) Schematic of device.

easily than the index, wider tuning ranges are possible. We have made extensive studies of such active DFB filter structures.

1.6 Overdriven Additive Pulse Modelocking

Sponsors

Joint Services Electronics Program
Contract DAAL03-92-C-0001
Grant DAAH04-95-1-0038

U.S. Air Force - Office of Scientific Research
Contract F49620-91-C-0091

Project Staff

Professor Erich P. Ippen, Professor Hermann A. Haus, Gadi Lenz, Farzana I. Khatri, John D. Moores

Overdriven additive pulse modelocking (APM) is a recent technique for passively modelocking solid state and all-fiber lasers. The principle behind APM involves splitting a pulse into two pulses which accumulate differential phase profiles. One pulse is sent through a nonlinear medium and accumulates an intensity-dependent phase profile. The pulses are then interferometrically superimposed so that they add constructively at the peak and destructively in the wings. This produces a shorter pulse. This artificial fast saturable absorber action can be achieved in a single-cavity (via a Mach-Zehnder interferometer or interference of two polarizations) or a coupled-cavity arrangement. In the NaCl:OH⁻ laser system, we use a coupled-cavity scheme with a gain medium in the main cavity and a nonlinear fiber in the auxiliary cavity.

Recently, we have observed "overdriven" operation of our NaCl:OH⁻ APM laser¹⁶ in which the laser operates very stably, producing short pulses with very high, nonlinear phase shifts in the auxiliary fiber. This mode of operation is difficult to analyze with our conventional APM theory which assumes small nonlinear phase shifts in the fiber. In order to understand this mode of operation, we developed a new analytical theory which looks at this overdriven case.¹⁷ In this theory, we propose that filtering provided by bulk optical elements in the laser allows the laser to operate with these large nonlinear phase shifts. Our theory takes the usual Master Equation of APM and treats the operation of the auxiliary cavity with a new operator. Furthermore, we use Gaussian-shaped pulses as an approximate solution in order to simplify the mathematics. Using this theory along with numerical simulations, we obtain results which are in good agreement with experimental results.

Another feature of this overdriven system is a hysteretic behavior we observed which was uncharacteristic of conventional APM systems. We observed a direction-dependence of the laser operation depending on if the auxiliary cavity length was lengthened or shortened. While the cavity length is lengthened, ordinary APM behavior occurs. Pulsing

¹⁶ G. Lenz, J. Paye, F.I. Khatri, J.D. Moores, H.A. Haus, and E.P. Ippen, "Recent Developments in Additive Pulse Modelocking of Solid State Lasers," invited paper UOE/SSL1.4, IEEE Lasers and Electro-Optics Society 1993 Annual Meeting, San Jose, California, November 1993.

¹⁷ F.I. Khatri, G. Lenz, J.D. Moores, H.A. Haus, and E.P. Ippen, "Extension of Coupled-Cavity Additive Pulse Mode-Locked Laser Theory," *Opt. Comm.* 110: 131-136 (1994).

is intermittent, corresponding to each wavelength of detuning. However, when the cavity is shortened, pulsing begins and persists over several wavelengths. In addition, the output pulses experience a spectral red-shift as their intensity increases. We have proposed an explanation for this behavior which is based upon the saturation of the artificial fast saturable absorber action.¹⁸ The explanation involves the nonlinear gain curve for a self-limited additive pulse modelocked laser¹⁹ and will be described in detail in a forthcoming publication.

1.7 A Broadband-Tunable Femtosecond Source for 1.55 μm Diagnostics

Sponsors

Joint Services Electronics Program

Contract DAAL03-92-C-0001

Grant DAAH04-95-1-0038

National Center for Integrated Photonics

U.S. Air Force - Office of Scientific Research

Contract F49620-91-C-0091

Project Staff

Professor Erich P. Ippen, Gadi Lenz, Kohichi R. Tamura

Modern lightwave communication systems use carrier wavelengths around 1.55 μm because optical fibers have minimum losses and can be tailored to have negligible dispersion in this spectral region. Since all-optical systems are desirable, other communication system components need to operate around this wavelength as well. These include semiconductor laser diodes, detectors, optical amplifiers, and modulators. The characteristics of these components depend strongly on the material they are made of, the structure of the device, and the wavelength at which they are used. The probe lasers used for diagnostics need to be

able to resolve ultrafast transient behavior, and be broadly tunable around 1.55 μm .

Fiber lasers have recently emerged as new sources in this spectral region. Ultrashort pulses can be obtained from these lasers by a passive modelocking technique known as stretched-pulse additive pulse modelocking (SP-APM). We have demonstrated that when pumped with a high power master oscillator power amplifier (MOPA) diode, this SP-APM laser can produce pulse energies up to 2.25 nJ in highly-chirped 1.5 ps pulses, which may then be compressed to less than 90 fs duration and more than 1.5 nJ per pulse.²⁰ In this mode of operation we have also found that the laser exhibits extremely low amplitude noise (less than 0.1 percent from 0 to 200 KHz), making this an excellent source for pump-probe measurements and also a seeding source for an optical amplifier.

Although these pulse energies are suitable for a variety of experiments, for many applications higher pulse energies are required. In collaboration with W. Gellerman of the University of Utah, we have built an optical amplifier for the purpose of reaching these energies.²¹ We have achieved a gain of $> 10^4$ yielding $\sim 10 \mu\text{J}$ pulses using this system. Our amplifier uses a 2-cm-long piece of KCl:Ti⁺ crystal as the gain medium, which is pumped by a Q-switched Nd:YAG at a rate of 1 KHz. To match the pump repetition rate, we have set up a synchronized electro-optic pulse selection system which selects single pulses at the 1 KHz rate from the 40 MHz output pulse train of the SP-APM fiber laser. The amplified pulse passes through the amplifier only twice resulting in excellent beam quality. The amplified pulse has been compressed to 250 fs. With further optimization, we expect to achieve even more energy per pulse and shorter pulses. These energies will allow continuum generation and make possible new time resolved spectroscopy experiments. These experiments will yield new information on the basic physics of optical devices.

¹⁸ G. Lenz, J.D. Moores, F.I. Khatri, E.P. Ippen, and H.A. Haus, "Hysteresis in Highly Overdriven Additive Pulse Modelocked Laser Systems," Paper SS5.4, IEEE Lasers and Electro-Optics Society 1994 Annual Meeting, Boston, Massachusetts, November 1994.

¹⁹ F.I. Khatri, J.D. Moores, G. Lenz, and H.A. Haus, "Models for Self-Limited Additive Pulse Mode-Locking," *Opt. Comm.* 114: 447-452 (1995).

²⁰ K. Tamura, C.R. Doerr, L. Nelson, H.A. Haus, and E.P. Ippen, "Technique for Obtaining High-energy Ultrashort Pulses from an Additive-pulse Mode-locked Erbium-doped Fiber Ring Laser," *Opt. Lett.* 19: 46-48 (1994).

²¹ G. Lenz, W. Gellerman, E.P. Ippen, and K.R. Tamura, "Stretched-Pulse Mode-Locked Er-Doped Fiber Laser Amplified by KCl:Ti⁺ Color-Center Crystals," Conference on Lasers and Electro-Optics/Quantum Electronics and Laser Science, Baltimore, Maryland, May 21-26, 1995, paper CWI3.

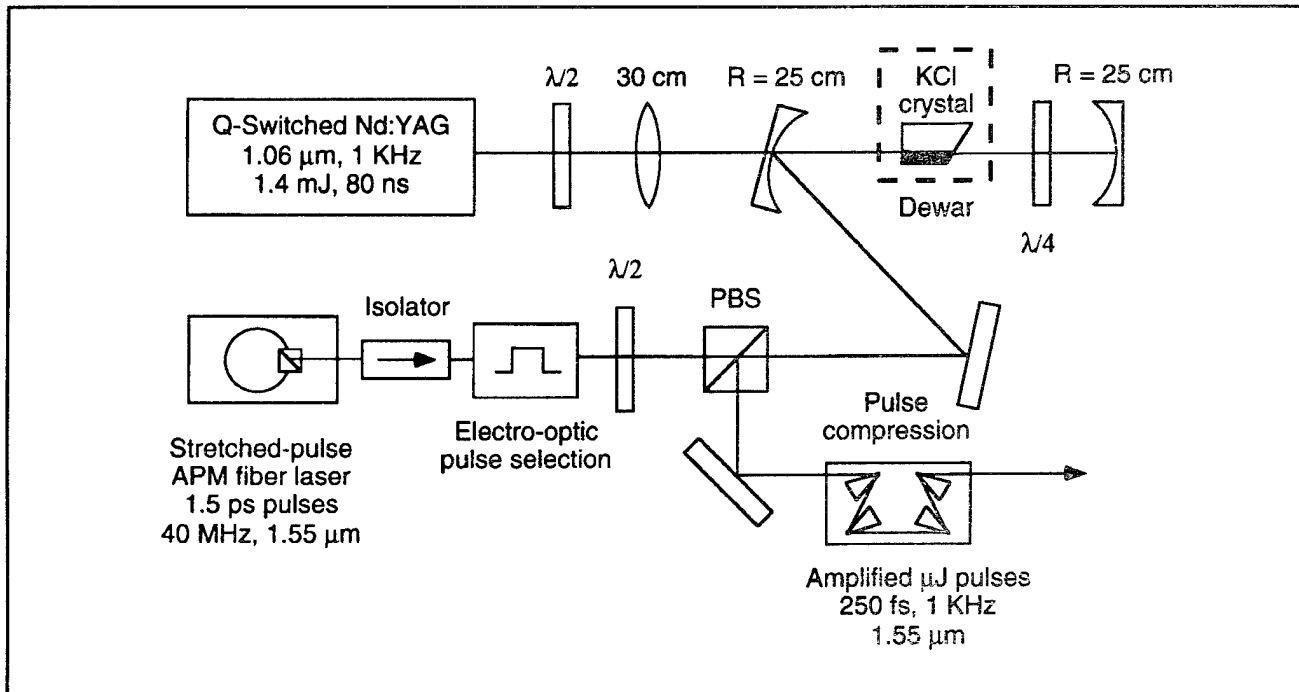


Figure 4. Experimental setup of amplified fiber laser.

1.8 Ultrafast Nonlinearities in Active Semiconductors

Sponsors

Joint Services Electronics Program
Contract DAAL03-92-C-0001
Grant DAAH04-95-1-0038

National Center for Integrated Photonics
U.S. Air Force - Office of Scientific Research
Contract F49620-91-C-0091

Project Staff

Professor Erich P. Ippen, David J. Dougherty,
Charles T. Hultgren, Gadi Lenz

We have continued our investigation of nonlinear optics and ultrafast dynamics in semiconductor optical amplifiers (SOAs).²² The active nature of these devices makes it possible to bias them electronically to produce optical gain or eliminate unwanted long-lived nonlinear components associated with carrier density dynamics. The injected carriers also introduce novel optical nonlinearities

that affect ultrashort-pulse propagation in amplifiers and may potentially be used for controlling one optical pulse with another.

Measurements of gain and index of refraction dynamics have been performed by femtosecond pump-probes over a wide range of photon energy in AlGaAs SOAs.²³ Our broadly-tunable femtosecond Ti:sapphire laser makes it possible to study these nonlinearities throughout the gain region and below band, as well as near the transparency point that has been investigated in detail before. Using a time-division interferometer (TDI), we have performed pump-probe of both the optically-induced transmission dynamics and the index of refraction dynamics. Below band, the transmission dynamics are dominated by the instantaneously responding two-photon absorption that is essentially independent of wavelength and bias current. The index dynamics, however, exhibit a fast, negative dynamic with a bandgap resonant component that varies by more than a factor of ten with bias current and wavelength, in agreement with recent theory.²⁴ There is also a slower dynamic that provides proof

²² K.L. Hall, G. Lenz, A.M. Darwish, and E.P. Ippen, "Subpicosecond Gain and Index Nonlinearities in InGaAsP Diode Lasers," *Opt. Comm.* 111: 589-612 (1994).

²³ C.T. Hultgren, *Femtosecond Nonlinearities in AlGaAs Diode Laser Amplifiers*, Ph.D. diss., Dept. of Electr. Eng. and Comput. Sci., MIT, 1994.

²⁴ M. Sheik-Bahae and E.W. Van Stryland, "Ultrafast Nonlinearities in Semiconductor Laser Amplifiers," *Phys. Rev.* 50: 14171-8 (1994).

of nonequilibrium carrier heating. It is characterized by a 100 fs risetime related to Fermi equilibration and a 1.1 psec relaxation determined by the carrier-lattice energy exchange rate in this material. In above-band also, we have observed large variations of gain and index nonlinearity with bias current. Stimulated emission contributes to either carrier heating or cooling depending upon wavelength, and wavelength-varying gain couples ultrafast index changes to transmission dynamics. The results of all these studies can now be used to improve modeling of ultrafast device characteristics. The strength of the observed nonlinearities, and their dependence on controllable device parameters, make them interesting also for all-optical pulse control and switching applications.

In collaboration with J. Wiesenfeld, M.A. Newkirk, U. Koren, and R.M. Jopson of AT&T Bell Labs, we have begun a new set of studies on SOAs fabricated to have polarization insensitive gain. This polarization insensitivity is achieved by alternating compressive and tensile strained quantum wells in the active region.

Because of polarization selection rules, the compressive wells provide gain only for light polarized in the plane of the wells (TE), while tensile wells provide gain mainly to light polarized perpendicular (TM). The resulting small signal gain is made polarization independent, but the nonlinear dynamics are not necessarily so. By using a heterodyne pump-probe scheme developed in our lab,²⁵ we are able to investigate these dynamics with any combination of TE or TM pump and probe pulses. Varying the relative polarization between pump and probe changes the measurement sensitivity to processes occurring in different wells. For example, when the pump is TM polarized and the probe TE, the pump will induce interband transitions primarily in the tensile wells and the probe will monitor population in the compressive wells. Thus, we may investigate inter-well transport as well as intra-well relaxation. Preliminary experiments have revealed some subpicosecond anisotropy in the dynamic gain response.²⁶ Future work will quantify these results and provide information about their dependence on quantum-well dimension and other device parameters.

1.9 Nonlinear Interactions of Continuous and Pulsed Light in Optical Fibers

Sponsors

Joint Services Electronics Program

Contract DAAL03-92-C-0001

Grant DAAH04-95-1-0038

U.S. Air Force - Office of Scientific Research

Contract F49620-91-C-0091

Project Staff

Professor Erich P. Ippen, David J. Dougherty

Because of their short duration, modelocked pulses have a broad spectrum. An ultrashort pulse system can be useful in nonlinear spectroscopy for this feature alone without considering its time resolving capability.

We have used the wide spectrum available from self-phase modulated 100 fs pulses from a Titanium-Sapphire laser to accurately and directly measure the Raman gain spectrum of glass optical fibers. The pulses were counter-propagated through 700 meters of fiber against light from a continuous laser whose frequency lay in the middle of the pulses' spectrum. The CW laser modulated the different wavelength components of the pulse train via stimulated Raman scattering. By measuring this modulation spectrum with a spectrometer at the fiber output, we were able to extract the full Raman gain spectrum from 13 THz down to approximately 100 GHz. This approach is much simpler than measuring the gain spectrum point by point with a CW tunable probe laser.

Of course, modelocked pulses are not completely equivalent to a bright broad band incoherent source. The definite relationship between the time and frequency characteristics of the pulses permits observation of new effects which would not occur in nonlinear gain measurements of this type using incoherent light.²⁷ An effect of this type was discovered in our Raman gain experiment. The left hand plot in the figure shows the measured Raman gain

²⁵ K.L. Hall, G. Lenz, E.P. Ippen, and G. Raybon, "Heterodyne Pump-Probe Technique for Time-Domain Studies of Optical Nonlinearities in Waveguides," *Opt. Lett.* 17: 874-876 (1992).

²⁶ G. Lenz, E.P. Ippen, J.M. Wiesenfeld, M.A. Newkirk, U. Koren, and R.M. Jopson, "Anisotropy in the Ultrafast Nonlinear Response of Semiconductor Optical Amplifiers with Polarization Insensitive Gain," *Proceedings of CLEO '95, Optical Society of America*, forthcoming.

²⁷ D.J. Dougherty, F.X. Kärtner, H.A. Haus, and E.P. Ippen, *Opt. Lett.* 22: 276 (1994).

spectrum at small detuning for several lengths of fiber. The curve at positive Stokes detuning is the Raman gain which decreases towards zero detuning where it is masked by scattered pump light and the Brillouin gain peak at 20 GHz. At negative detuning the mirror image anti-Stokes raman spectrum is seen with an oscillatory signal superimposed.

These oscillations are a direct result of the connected time and frequency structure of the strongly chirped probe pulses. The chirp on the pulses due to the positive group velocity dispersion (GVD) of glass at 800 nm means that the red frequency components of the pulse travel ahead of the blue components. This implies that at a fixed point in the fiber, the Stokes gain of the probe occurs before the anti-Stokes gain. An excitation left in the glass by the Stokes frequencies can potentially effect the propagation of the anti-Stokes frequencies. For the highly damped Raman modes, no excitation is left behind. However, the central portion of the probe at the lowest frequencies can beat with the pump field to drive sound waves in the glass which result in Brillouin scattering of the backward traveling pump into the direction of the probe. This extra field impresses a time-dependent phase shift on the co-propagating anti-Stokes side of the probe through interference terms in the Kerr effect. The chirp causes this oscillatory phase modulation waveform in the time domain to appear directly in the spectral domain because different frequency components travel with different delays behind the center frequency. If the chirp were constant down the fiber, the spectral oscillations would extend over the

entire anti-Stokes side of the probe. However, GVD stretches the duration of the probe pulse continuously and most of the oscillations are washed out. Results for several fiber lengths shown in figure 5 show the modulation extending further with shorter fibers. Calculations shown in the right hand plot of the effect of this Kerr phase shift on the probe's spectrum including effects of GVD wash out agree well with experimental results.

A thermal white light source probe would not reveal this coupling mechanism in its spectrum. Although this phenomena was a nuisance for our Raman experiment, use of such a chirped probe was fortuitous for detecting the effect itself, which would appear more subtly in other situations. For instance, a train of solitons propagating against a CW background will shed these Brillouin wake fields the same as in our experiment. The consequence in this case will be merely a phase or frequency shift on the trailing pulses' spectrum rather than pronounced oscillations. This may contribute excess timing jitter in communications applications or may be judiciously used to cancel soliton self-frequency shift. In analog CW communication systems operating at power levels near the Brillouin threshold, these phase modulations could result in excess noise at channel frequencies detuned much greater than the Brillouin linewidth from the carrier. While these specific ideas are being pursued with further experiments, a more important result of this study is that small amounts of Brillouin scattering can cause observable indirect effects in certain short-pulse, broad-bandwidth applications where its direct effects can be safely neglected.

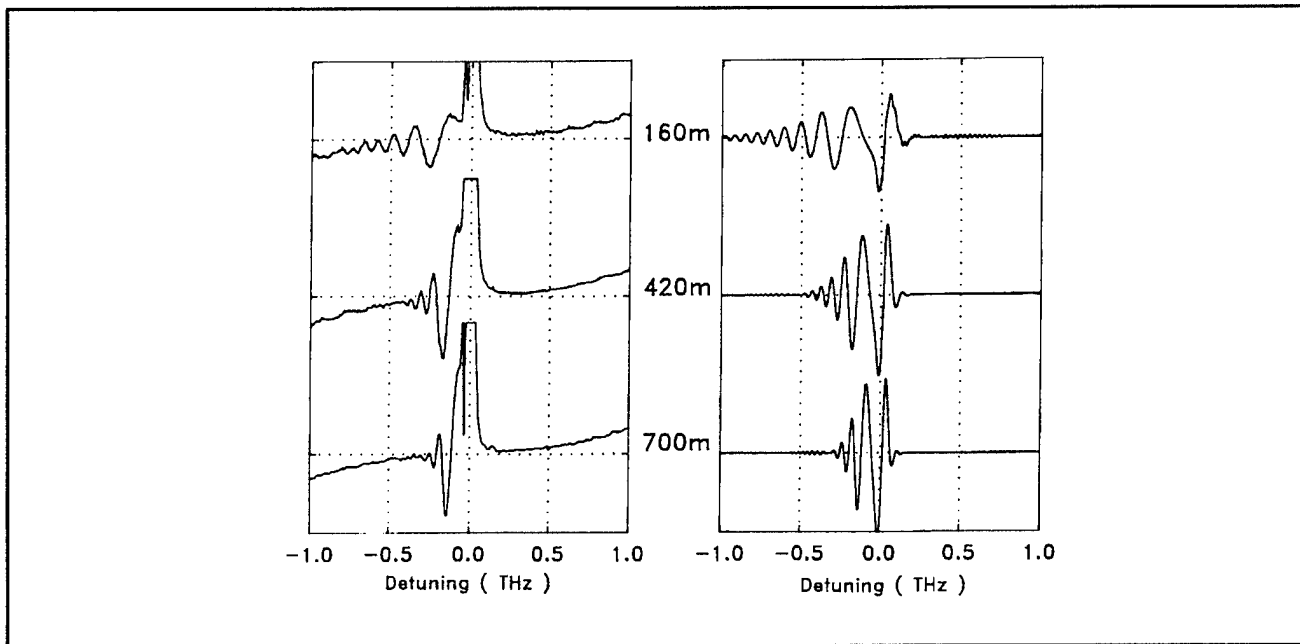


Figure 5. Observed and calculated spectral oscillations for several fiber lengths.

1.10 Intensity Autocorrelation of Light Sources for Fiber Optical Gyroscopes

Sponsors

Honeywell Technology Center
 Joint Services Electronics Program
 Contract DAAL03-92-C-0001
 Grant DAAH04-95-1-0038

Project Staff

Professor Erich P. Ippen, David J. Dougherty,
 Siegfried B. Fleischer

The statistics of the light used for fiber optical gyroscopes (FOG) have a considerable effect on the rotation rate error.²⁸ This artifact is caused by the optical Kerr effect (n_2) of the fiber. The intensity dependent nonreciprocal phase shift has components due to self-phase modulation (SPM) and cross phase modulation (XPM) for both counter propagating beams in the Sagnac loop. The relative contributions from SPM and XPM depend on the intensity statistics of the light source. In order to cancel the Kerr effect both, the SPM and XPM have to be made equal. Then, the rotation rate error vanishes even for coupling ratios that differ from the ideal 50 percent.²⁹ This requires that the variance of the intensity fluctuations be $\sqrt{2}$ times the average intensity.

Theory predicts that the light emitted from a light emitting diode (LED) is Poisson, and the nonreciprocal phase shift cancels for such a source. For a practical gyroscope, one either uses a super luminecent diode or a laser diode driven below threshold. Both these devices also give, at least theoretically, vanishing rotation rate error. In practice, however, both sources are very sensitive to backreflections, which can affect the source statistics, and thus overcompensate for the rotation rate error.

To investigate intensity fluctuation properties of these sources under various conditions applicable to a commercial gyroscope, an intensity autocorrelator based on second harmonic generation was built. This autocorrelator resembles the experimental setup used to measure the pulse width of ultrafast optical pulses by means of a

background-free collinear autocorrelation. The light emitted from the diode is split into two parts and, after propagating through two distinct paths with adjustable difference, focused into an SHG crystal. The measured SHG intensity is proportional to the second-order coherence function of the light.

To preserve the light statistics, care was taken to balance the dispersion between both beams and to ensure upconversion of the whole spectrum. Because of the large bandwidth of the source a, very thin and broadband doubling crystal was selected (100 μm BBO). This results in a very low (10^{-9}) SHG conversion efficiency for the incoherent, low-power sources, and a photon counting detection system was needed.

The measured second-order coherence functions agree with what is predicted for a chaotic source with the given spectrum (first order coherence function). The contrast ratios of the intensity autocorrelations; however, differ in various ways from those expected. We believe that these deviations are mostly due to artifacts of the different measurement geometries. A contrast ratio $G^{(2)}(0)/G^{(2)}(\infty) = 1.93$ was obtained using type II phasematching in the BBO crystal. This is close enough to the value 2.0 expected from Poisson statistics to provide confidence that the light of these sources can be chaotic. Reduction of backscatter turned out to be very critical. How residual backreflections into the diode affect the measured statistics of the light is currently being investigated.

1.11 Wavelength Shifting by Four-Wave Mixing in Passive Semiconductor Waveguides

Sponsors

Joint Services Electronics Program
 Contract DAAL03-92-C-0001
 Grant DAAH04-95-1-0038
 National Center for Integrated Photonics
 U.S. Air Force - Office of Scientific Research
 Contract F49620-91-C-0091

Project Staff

Professor Erich P. Ippen, Ali M. Darwish, Gadi Lenz

²⁸ S. Ezekiel, J.L. Davis, and R.W. Hellwarth, "Non-Reciprocal Errors Sources," *Fiber-Optic Rotation Sensors and Related Technologies* 332 (1982).

²⁹ R.A. Bergh, B. Culshaw, C.C. Cutler, H.C. Lefere, and H.J. Shaw, "Source Statistics and the Kerr Effect in Fiber-Optic Gyroscopes," *Opt. Lett.* 7: 563 (1982).

To investigate devices for wavelength-division-multiplexed (WDM) optical network applications, we are performing all-optical, wavelength-shifting experiments in semiconductor waveguides at 1.55 μm , in collaboration with H.Q. Le, J.P. Donnelly, S.H. Groves and Eric A. Swanson of Lincoln Laboratory. The wavelength-shifting is accomplished by non-degenerate four-wave mixing (FWM) which uses optical beams at two different input wavelengths (signal-in and pump) to generate output at a third wavelength (signal-out). Since the mixing process depends upon instantaneous field products, there is no response-time limit in the time domain. Instead, the nonlinearity response time of the medium manifests itself as variation of conversion efficiency with magnitude of the wavelength shift. To investigate the possibility of obtaining a relatively flat conversion efficiency over a wide detuning range, we are studying InGaAsP/InP passive waveguides. We have performed both cw experiments and picosecond pulse experiments at 1.55 μm wavelengths, with tunable, synchronized F-center lasers, to evaluate variations of efficiency with pump wavelength (below band), the effects of phase matching on shifts as large as 130 nm (17 THz), and the limitations on conversion imposed by two-photon absorption. Our data allows us to extract quantitative values for waveguide loss, group-velocity dispersion, and both the real and imaginary parts of $\chi^{(3)}$. Two-photon absorption, strictly a liability in nonlinear index switching, can actually enhance FWM conversion efficiency to some extent. We have analyzed this theoretically and quantified it experimentally.³⁰ In a 7.5-mm-long passive InGaAsP single quantum well waveguide, we have achieved a conversion efficiency for picosecond pulses of -11 dB for a wavelength shift of 20 nm. In a waveguide with an effective mode area of $3 \times 10^{-3} \text{ cm}^2$, this requires a pump pulse energy of 10 nJ in 10 ps. The waveguide structures are fabricated at Lincoln Laboratory. Future plans call for optimizing design of the waveguide

shifters using multiple quantum wells and incorporating a p-n junction for carrier sweep-out.

1.12 Ultrashort Pulse Generation in Solid State Lasers

Sponsors

Joint Services Electronics Program

Contract DAAL03-92-C-0001

Grant DAAH-04-95-1-0038

U.S. Air Force - Office of Scientific Research

Contract F49620-91-C-0091

U.S. Navy - Office of Naval Research (MFEL)

Contract N00014-94-1-0717

Project Staff

Dr. Brett E. Bouma, Malini Ramaswamy-Paye, Dr. Joseph A. Izatt, Professor James G. Fujimoto, Dr. Jeffrey Russell,³¹ Dr. Raymond Sierra,³¹ Professor Ursula Keller³²

1.12.1 Compact Ultrashort Pulse Sources

Compact ultrashort pulse sources are of fundamental importance for advances in signal processing, high speed communications, and the investigation of ultrafast nonlinear processes in semiconductor devices and materials. Generally, these sources must be technologically simple, robust and cost effective. While solid state gain media are well suited to meet these criteria, their relatively low gain cross-sections have required the use of fast saturable absorption for modelocking. During the last few years significant advances have been made in the development of fast saturable absorbers utilizing the electronic Kerr effect. Kerr lens modelocking (KLM),³³ in fact, has allowed the generation of the shortest pulses ever produced directly from a laser oscillator.³⁴ A theoretical understanding of Kerr effect modelocking has been

³⁰ A.M. Darwish, G. Lenz, E.P. Ippen, H.Q. Le, J.P. Donnelly, S.H. Groves, and E.A. Swanson, "Frequency Conversion in Passive InGaAsP/InP Waveguides," *OSA Technical Digest, QELS '95*, Optical Society of America, paper QThJ2, 1995.

³¹ Candela Laser Corporation, Wayland, Massachusetts.

³² Swiss Federal Institute of Technology, Zürich, Switzerland.

³³ D.K. Negus, L. Spinelli, N. Goldblatt, and G. Feuget, "Sub-100 fs Pulse Generation by Kerr Lens Modelocking in Ti:Al₂O₃," *Technical Digest of the Topical Meeting on Advanced Solid State Lasers* (Washington, D.C.: Optical Society of America, 1991), postdeadline paper.

³⁴ J. Zhou, G. Taft, C.-P. Huang, M.M. Murnane, H.C. Kapteyn, and I.P. Christov, "Pulse Evolution in a Broad-Band Ti:sapphire laser," *Opt. Lett.* 19: 1149 (1994).

developed by Professors Eric P. Ippen and Hermann A. Haus in conjunction with our group.³⁵

In the past year, we have applied our theoretical model of KLM to facilitate optimization of modelocking performance and to allow the extension of this simple pulse forming mechanism to novel resonator geometries. Two Ti:Al₂O₃ KLM lasers in our laboratory, currently producing pulses of ~10 fs duration, are direct results of the accuracy of our modeling.

Chirp-free ultrashort pulses are produced in KLM as a result of a self-focusing nonlinearity in the presence of soliton-like pulse shaping arising from self-phase modulation and net negative intracavity group-velocity dispersion (GVD). Negative GVD is most commonly achieved in KLM lasers by use of an intracavity prism pair; however, this places constraints on laser geometry and size. To date, KLM lasers have almost exclusively used a folded X- or Z-cavity geometry with the prism pair in one arm of the laser. Repetition rates have not exceeded the 100 MHz range.

This past year, we have developed a novel and compact dispersion-compensation technique and laser geometry for KLM in solid-state lasers.³⁶ This design provides built-in and easily adjustable GVD as a direct consequence of the resonator geometry, eliminating the need for prism pairs. We have produced 111 fs pulse durations at a repetition rate of 1 GHz and 54 fs pulses at 385 MHz. The demonstrated geometry has important implications for compact, all-solid-state, femtosecond laser technology, especially because it can readily be extended to the modelocking of diode-pumped lasers.

1.12.2 Cavity Dumped Ultrashort Pulse Lasers

Femtosecond laser systems have been widely applied for the study of ultrafast phenomena in physics, chemistry, and biology. An optimum laser source for these studies should have a short pulse duration, wavelength tunability, sufficient pulse energy to permit the investigation of nonlinear effects and sufficient repetition rate to permit the use of averaging techniques for high sensitivity detection. Finally, the laser system should be simple, cost effective, and robust.

The advent of the femtosecond Kerr lens modelocked (KLM) Ti:Al₂O₃ laser was an important advance in ultrafast optics. The peak power at the output of modelocked Ti:Al₂O₃ laser sources can be in the range of 0.2 MW, significantly higher than that of modelocked dye lasers. However, for studies of nonlinear phenomena, higher peak powers are often necessary. Several amplification techniques have recently been developed to extend the range of available pulse energies from Ti:Al₂O₃ sources. Regenerative as well as multipass amplifiers with Nd:YAG and Nd:YLF pump lasers have been demonstrated up to a few kilohertz repetition rates.³⁷ More recently, argon laser pumped Ti:Al₂O₃ amplifiers have produced microjoule energies at repetition rates as high as 450 kHz.³⁸ However, the requirement of multiple stages and/or multiple pump lasers makes these oscillator plus amplifier systems complex and relatively expensive. Lastly, the repetition rate of many of these sources is low enough to limit detection sensitivity for ultrafast measurements.

A superior alternative to these laser systems, demonstrated by our group, is cavity dumping of a KLM Ti:Al₂O₃ oscillator.³⁹ This technique allows the generation of 50 fs pulses with pulse energies as high as 100 nJ at variable repetition rates as high as 0.95 MHz. The limitation on the energy currently available from this source arises because of mul-

³⁵ H.A. Haus, J.G. Fujimoto, and E.P. Ippen, "Structures for Additive Pulse Modelocking," *J. Opt. Soc. Am. B* 8: 2068 (1991); H.A. Haus, J.G. Fujimoto, and E.P. Ippen, "Analytic Theory of Additive Pulse and Kerr Lens Mode Locking," *IEEE J. Quant. Electron.* 28: 2086 (1992).

³⁶ M. Ramaswamy-Paye and J.G. Fujimoto, "Compact Dispersion-Compensating Geometry for Kerr-Lens Mode-Locked Femtosecond Lasers," *Opt. Lett.* 19: 1756 (1994).

³⁷ K. Wynne, G.D. Reid, and R.M. Hochstrasser, "Regenerative Amplification of 30 fs Pulses in Ti:Sapphire at 5 kHz," *Opt. Lett.* 19: 895 (1994).

³⁸ T.B. Norris, "Femtosecond Pulse Amplification at 250 kHz with a Ti:Sapphire Regenerative Amplifier and Application to Continuum Generation," *Opt. Lett.* 17: 1009 (1992).

³⁹ M. Ramaswamy, M. Ulman, J. Paye, and J.G. Fujimoto, "Cavity-Dumped Femtosecond Kerr-Lens Mode-Locked Ti:Al₂O₃ Laser," *Opt. Lett.* 18: 1822 (1993).

tiple pulse instabilities that occur at high pulse energies as a result of saturation of the KLM saturable absorber action. Decreasing the output coupling of this laser increases the cavity Q but does not enhance the dumped energies since it reduces the pump level at which multiple pulse instabilities occur. We are currently testing techniques such as defocusing the beam within the gain crystal and implementing other dumping mechanisms that do not require a focused beam so that the KLM nonlinearity can be decreased and the instability threshold, thereby, increased.

1.12.3 Flashlamp Pumped Modelocked Ti:Al₂O₃ Laser

Nearly all modellocked Ti:Al₂O₃ lasers to date have been cw modellocked systems with relatively low pulse energies. Short pulse energies in the range of microjoules to millijoules can be generated using regenerative and multipass amplifier systems. While these techniques achieve excellent performance, they are relatively costly and complex. Simple affordable sources of wavelength tunable, picosecond, high power laser pulses are relevant to applications such as frequency doubling, optical parametric oscillators, materials processing, laser surgery, and picosecond ultrafast nonlinear spectroscopy.

This past year, we have demonstrated a high performance, all solid-state, modellocked flashlamp pumped Ti:Al₂O₃ laser by combining active acousto-optic modulation and fast saturable absorber action from a low temperature multiple quantum well.⁴⁰ This laser has produced pulses as short as 4.5 ps with peak powers exceeding 4 MW at a repetition rate of 10 Hz. The flashlamp pumped Ti:Al₂O₃ laser is a simple, economical, high peak power laser source which can be an attractive alternative technology to conventional oscillator-amplifier approaches. In addition, the development of new techniques for modelocking flashlamp pumped

lasers can be generalized to a broad class of new solid state laser materials currently being developed.

1.13 Ultrafast Phenomena in Materials and Devices

Sponsors

Joint Services Electronics Program

Contract DAAL03-92-C-0001

Grant DAAH-04-95-1-0038

U.S. Air Force - Office of Scientific Research

Contract F49620-91-C-0091

U.S. Navy - Office of Naval Research (MFEL)

Grant N00014-91-J-1956

Project Staff

Igor P. Bilinsky, Boris Golubovic, Morrison Ulman, Malini Ramaswamy-Paye, Chi-Kuang Sun, Dr. Brett E. Bouma, Professor Erich P. Ippen, Professor James G. Fujimoto, Professor Christopher Stanton⁴¹

1.13.1 Carrier Dynamics in InGaAs Strained Layer Diodes

Nonlinear gain and transient carrier dynamics in diode lasers play important roles in laser line width, modulation bandwidth, amplification, and short pulse generation. Femtosecond, multiple wavelength pump-probe measurements of nonlinear gain dynamics were performed in InGaAs/InGaAsP strained-layer multiple-quantum-well (MQW) amplifiers.⁴² These studies have shown that non-equilibrium carrier temperature effects play a dominant role in nonlinear gain dynamics. Previous studies⁴³ have shown that free carrier absorption dominates carrier heating process. A number of experimental techniques were used to study carrier dynamics in waveguide devices such as bias lead

⁴⁰ B. Bouma, A. Gouveia-Neto, J.A. Izatt, J. Russell, R. Sierra, U. Keller, and J.G. Fujimoto, "Hybrid Mode Locking of a Flash-Lamp-Pumped Ti:Al₂O₃ Laser," *Opt. Lett.* 19: 1858 (1994).

⁴¹ University of Florida, Gainesville, Florida.

⁴² M.S. Stix, M.P. Kesler, and E.P. Ippen, "Observations of Subpicosecond Dynamics in GaAlAs Laser Diodes," *Appl. Phys. Lett.* 48: 1722 (1986).

⁴³ C.T. Hultgren, D.J. Dougherty, and E.P. Ippen, "Above- and Below-Band Femtosecond Nonlinearities in Active AlGaAs Waveguides," *Appl. Phys. Lett.* 61: 2767 (1992).

monitoring,⁴⁴ time domain interferometry,⁴⁵ and heterodyne detection.⁴⁶ These techniques, however, are based on conventional, single-wavelength pump-probe geometry. To our knowledge, preceding this work, no multiple wavelength gain and transient carrier dynamics measurements were reported.

The measurements were performed using a new heterodyne multiple wavelength pump-probe technique. A modelocked Ti:Al₂O₃ laser output spectrum was coupled into an optical fiber for self-phase modulation spectral broadening. The light coming out of the fiber was split into the pump and probe beams. Two separate spectral windowing assemblies allowed for independent frequency, pulselwidth, and polarization selection of both pump and probe pulses. Since this technique utilizes a collinear geometry, it is of particular interest for studies of guided wave optical devices. Moreover, this technique can be applied to both measurements of gain and index dynamics. The demonstrated technique represents a powerful tool for investigating device dynamics since it allows for performing temporal as well as spectral studies in a single experimental set-up.⁴⁷

The devices investigated were InGaAs/AlGaAs graded-index separate confinement heterostructure SQW ridge waveguide diode lasers. The devices used were fabricated in collaboration with investigators at the MIT Lincoln Laboratory. The epitaxial growth of nonlattice-matched materials, strained layer quantum well devices provide an added degree of freedom to band structure engineering and optic and optoelectronic device research. High power, high efficiency, long lifetime, and low threshold current density semiconductor lasers have been achieved in the laboratory by InGaAs strained layer devices in the past few years.

Studies of the femtosecond gain dynamics were performed using the multiple-wavelength pump-

probe technique. We were able to map the femtosecond gain dynamics at a range of wavelengths for a fixed excitation pulse. The transient measurements showed a pump-induced transmission decrease in both the gain and loss regions. Around zero time delay, a sharp transmission decrease was observed with a spectral peak around the pump wavelength and a time-resolution-limited recovery. This transient may be attributed to a combination of two-photon absorption, spectral hole burning, and coherent artifacts. Shortly after the pump pulse, a thermalized carrier distribution with higher temperature and lower concentration is established. Gain depletion throughout the investigated spectral region was observed. For time delays longer than 1 ps, the gain partially recovers as the temperature reaches equilibrium with the lattice. The residual gain changes are produced by the decrease in the carrier population and recover on a much longer time scale.

Under conditions of high carrier concentrations, with the pump wavelength close to the bottom of the gain region, strong spectral hole burning effects were observed. Moreover, an additional blue shift of the spectral hole with respect to the pump wavelength was observed.⁴⁸ At lower carrier concentrations with the pump close to the transparency point, spectral hole burning effects were much weaker without any spectral shifts. This new information is important to understanding gain dynamics and its implication on high speed optical device performance such as cross-talk effects, short pulse amplification, and high speed modulation behavior.

In collaboration with theoretical physicists at the University of Florida, Gainesville, a detailed theoretical model for the gain dynamics for the measured device is being developed. This aids in the full understanding of the obtained experimental results and may aid future device design. The theoretical

⁴⁴ K.L. Hall, E.P. Ippen, and G. Eisenstein, "Bias-Leading Monitoring of Ultrafast Nonlinearities in InGaAsP Diode Laser Amplifiers," *Appl. Phys. Lett.* 57: 129 (1990).

⁴⁵ M.J. LaGasse, K.K. Anderson, C.A. Wang, H.A. Haus, and J.G. Fujimoto, "Femtosecond All-Optical Switching in AlGaAs Waveguides using a Time Division Interferometer," *Appl. Phys. Lett.* 54: 2068 (1989).

⁴⁶ K.L. Hall, G. Lenz, E.P. Ippen, U. Koren, and G. Raybon, "Carrier Heating and Spectral Hole Burning in Strained-Layer Quantum Well Laser Amplifiers at 1.5 μm ," *Appl. Phys. Lett.* 61: 2512 (1992).

⁴⁷ C.-K. Sun, B. Golubovic, J.G. Fujimoto, H.K. Choi, and C.A. Wang, "Heterodyne Nondegenerate Pump-Probe Measurement Technique for Guided Wave Devices," *Opt. Lett.* 20: 210-212 (1995).

⁴⁸ C.-K. Sun, B. Golubovic, H.K. Choi, C.A. Wang, and J.G. Fujimoto, "Femtosecond Investigations of Spectral Hole Burning in Semiconductor Lasers," *App. Phys. Lett.*, forthcoming.

work is an extension of previous collaborations,⁴⁹ and preliminary results show close agreement with experimental data obtained.

1.13.2 Nonequilibrium Electron Dynamics in Metals

Studies of interactions between free carriers and their environment constitute one of the major problems of solid state physics. This has been addressed directly in the time domain employing femtosecond techniques, both in semiconductor and metals. Of particular interest in the case of metals is the display of very high electron density whose behavior can be modeled on a relatively simple basis. In previous experiments,⁵⁰ it was demonstrated that it is possible to create and probe transient nonequilibrium electron populations using ultrashort laser pulses. In these experiments, it was assumed that electron-electron interactions were sufficiently fast to thermalize the electron gas on the order of, or shorter, than the pulse pump duration. This assumption was made even though some deviations from the instantaneous response were observed.⁵¹ More recent investigations using transient photoemission have demonstrated the existence of non-Fermi electron distribution with thermalization times as long as 600 fs.⁵² These results were observed in gold foil for large changes of the electron temperature (of the order of 400° K) with a limited time resolution. Similar conclusions were drawn at lower laser fluence by analyzing the temperature dependence of the optically measured electron-photon interaction time in gold and silver.⁵³

Femtoscond studies of electron thermalization in metals were conducted using transient thermomod-

ulation transmissivity and reflectivity. Studies were performed using a tunable multiple-wavelength femtosecond pump-probe technique in optically thin gold films in the low perturbation limit. An infra-red (IR) pump beam was used to heat the electron distribution and changes in electron distribution and electron temperature were measured with a visible probe beam at the *d* band to Fermi-surface transition.⁵⁴ These studies show that the subpicosecond optical response of gold is dominated by delayed thermalization of the electron gas. This effect is particularly important far off the spectral peak of the reflectivity or transmissivity changes, thus permitting a direct and sensitive access to the internal thermalization of the electron gas.

Measurements using a high stability, high repetition rate, and tunable, modelocked Ti:Al₂O₃ laser, show evidence for non-Fermi electron distribution. This distribution was measured to have an electron thermalization time of the order of 500 fs and an electron-lattice cooling time of 1 ps, independent of laser fluence in the range of 2.5 mJ/cm². At energies close to the Fermi surface, longer thermalization timer ~1-2 ps were observed. These results are in agreement with a more sophisticated model based on calculations of the electron-thermalization dynamics by numerical solutions of the Boltzman equations.⁵⁵ This model quantitatively describes the measured transient optical response during the full thermalization time of the electron gas to be of the order of 1.5 ps. Finally, the theoretical and experimental techniques developed in this study can form the basis for investigating and understanding nonthermal electronic effects in a wide range of materials.

⁴⁹ G.D. Sanders, C.-K. Sun, J.G. Fujimoto, H.K. Choi, C.A. Wang, and C.J. Stanton, "Carrier Gain Dynamics in InGaAs/AlGaAs Strained-Layer Single-Quantum-Well Diode Lasers: Comparison of Theory and Experiment," submitted to *Phys. Rev. B*.

⁵⁰ G.L. Eesley, "Observation of Nonequilibrium Electron Heating in Copper," *Phys. Rev. Lett.* 51: 2140 (1983).

⁵¹ H.E. Elsayed-Ali, T.B. Norris, M.A. Pessot, and G.A. Mourou, "Time-Resolved Observation of Electron-Phonon Relaxation in Copper," *Phys. Rev. Lett.* 58: 1212 (1987).

⁵² R.W. Schoenlein, W.Z. Lin, J.G. Fujimoto, and G.L. Eesley, "Femtosecond Studies of Nonequilibrium Electronic Process in Metals," *Phys. Rev. Lett.* 58: 1680 (1987).

⁵³ W.S. Fann, R. Storz, H.W.K. Tom, and J. Bokor, "Direct Measurement of Nonequilibrium Electron Energy Distributions in Subpicosecond Laser-Heated Gold Films," *Phys. Rev. Lett.* 68: 2834 (1992).

⁵⁴ C.-K. Sun, F. Vallée, L.H. Acioli, E.P. Ippen, and J.G. Fujimoto, "Femtosecond-Tunable Measurement of Electron Thermalization in Gold," *Phys. Rev. B* 50: 337 (1994).

⁵⁵ C.-K. Sun, F. Vallée, L. Acioli, E.P. Ippen, J.G. Fujimoto, "Femtosecond Investigation of Electron Thermalization in Gold," *Phys. Rev. B* 48: 12365 (1993).

1.13.3 Time Gated Scanning Tunneling Microscopy

Since the invention of the scanning tunneling microscope (STM) in 1982, scanning tunneling microscopy has become a well established technique that allows us to study surfaces with very high spatial resolution down to atomic dimensions. However, the temporal resolution of a conventional STM is limited to microseconds. Today, femtosecond laser technology enables measurement of the highest time resolution possible of solid state phenomena. However, the spatial resolution is limited to microns by a laser spot size. A combination of STM with ultrafast time resolution of femtosecond lasers would enable us to develop an instrument capable of performing surface measurements highly localized in both spatial and temporal domain. Recently, a number of approaches to this problem have been taken.⁵⁶

In an STM, a sharp metal tip is positioned a few angstroms away from the surface under investigation. An electrical bias is applied between the tip and the surface. When the tip is close to the surface, a small tunneling current will flow from the tip to the surface. The size of this current depends exponentially on the distance between the tip and the sample. If we heat an electron distribution with a laser pulse, we would expect the tunneling of heated carriers to be different from that of a cold equilibrium distribution.

In our experiment, a Pt-Ir tip is positioned above an Au surface. Amplified femtosecond laser pulses are applied to the tip-sample junction of an STM and the effect of the laser pulses on the tunneling current is monitored. Several effects contribute to the laser induced tunneling current. They include three-photon photoionization and carrier heating, which in turn leads to thermally assisted

photoionization and thermally assisted tunneling.⁵⁷ Time resolution is achieved by splitting a laser pulse into two pulses of equal energy and varying time delay between them. As a result, a femtosecond interferometric cross correlation is obtained. We have investigated the dependence of different components of the laser assisted tunneling current on a number of parameters including laser intensity and polarization and the STM tip-sample bias voltage.

1.14 Laser Medicine

Sponsors

National Institutes of Health
Grant NIH-5-R01-GM35459-09

U.S. Air Force - Office of Scientific Research
Grant F49620-93-1-0301

U.S. Navy - Office of Naval Research (MFEL)
Contract N00014-94-1-0717

Project Staff

Stephen A. Boppart, Michael R. Hee, Dr. Charles P. Lin, Guillermo J. Tearney, Dr. Brett E. Bouma, Dr. Joseph A. Izatt, Professor James G. Fujimoto, Eric A. Swanson,⁵⁸ Dr. Mark E. Brezinski, Dr. Reginald Birngruber,⁵⁹ Dr. Cynthia A. Toth,⁶⁰ Dr. Clarence P. Cain, Gary D. Noojin,⁶¹ Dr. W.P. Roach, Dr. Cheryl D. DiCarlo⁶²

1.15 Optical Coherence Tomography Technology

Optical coherence tomography (OCT) is a new technique that uses low coherence interferometry to gate out multiply scattered photons, and in the single scattering limit, is equivalent to time-of-flight

⁵⁶ D.M. Bloom, A.S. Hou, and F. Ho, "Brave New Nanoworld: Probing the Realm of Ultrafast, Ultrasmall Electronics," *Ultrafast Phenomena*, Vol. 7, 1994 OSA Technical Digest Series (Washington, D.C.: Optical Society of America, 1994), pp. 298-300; S. Weiss, D. Botkin, D.F. Ogletree, M. Salmeron, and D.S. Chemla, "Advances in Ultrafast Scanning Probe Microscopy," *Ultrafast Phenomena*, Vol. 7, OSA Technical Digest Series (Washington, D.C.: Optical Society of America, 1994), pp. 301-303.

⁵⁷ G. Gerber, F. Sattler, S. Vogler, J.Y. Grand, P. Leiderer, R. Möller, "Femtosecond Time-Resolution in Scanning Tunneling Microscopy," *Ultrafast Phenomena*, Vol. 7, 1994 OSA Technical Digest Series (Washington, D.C.: Optical Society of America, 1994), p. 254.

⁵⁸ MIT Lincoln Laboratory, Lexington, Massachusetts.

⁵⁹ Medizinisches Laserzentrum, Lubeck, Germany.

⁶⁰ Duke University Eye Center, Durham, North Carolina.

⁶¹ TASC, San Antonio, Texas.

⁶² Armstrong Laboratory, Brooks Air Force Base, Texas.

imaging.⁶³ OCT is analogous to ultrasound B mode imaging except that it uses an infrared light source and low coherence interferometry to perform micron resolution ranging and imaging. For an interferometric signal to be detected, the optical pathlengths of the object and reference beam must be matched to within the coherence length of the source. Since multiply scattered photons from the object have travelled different optical pathlengths than the reference beam, multiple scattering effects are minimized in the OCT image.

An OCT system that accommodates multiple sources has been constructed. The source is coupled into a single mode fiber optic Michelson interferometer. The OCT system obtains tissue axial reflectance by varying the reference arm length and digitizing the magnitude of the demodulated interference envelope. A cross-sectional image is produced by recording axial reflectance profiles while the object beam or the tissue specimen is scanned laterally. After acquisition, the reflectance images can be displayed using false color or gray scale lookup tables chosen to enhance visualization of tissue microstructure.

The axial resolution of OCT images is determined by the coherence length of the source. When using a superluminescent diode (SLD) as the optical input, an axial resolution of less than 20 μm is achieved. This resolution is 10 times greater than the resolution obtained using conventional ultrasound, MRI, or CT. In addition, an axial resolution of 4 μm has recently been demonstrated using a modelocked Kerr lens Ti:Al₂O₃ source. Another advantage of OCT over other imaging modalities is its high detection sensitivity. Because OCT uses heterodyne detection in conjunction with other noise reduction techniques, a sensitivity of 110 dB is possible for detection of reflectance within the tissue.

This work is an ongoing collaboration with researchers at MIT, the Optical Communications Group at MIT Lincoln Laboratories, New England Eye Center of the Tufts University School of Medicine, Massachusetts General Hospital Cardiology Department, Pathology Department, and the Wellman Laboratories of Photomedicine. Lincoln Laboratories has provided much of the OCT tech-

nology and equipment for use in ophthalmic and multiply scattering tissue studies. The New England Eye Center is currently performing clinical trials using an OCT system adapted to a slit lamp for anterior and posterior diagnosis of a wide array of ophthalmic diseases. Massachusetts General Hospital has been instrumental in providing the tissue samples and pathology for research aimed at evaluating the potential for OCT to perform micron level "optical biopsies" in multiply scattering human tissue.

1.15.1 Optical Coherence Tomography for Ophthalmic Diagnosis

In collaboration with investigators at the New England Eye Center of the Tufts University Medical School, we have been investigating OCT as a new ophthalmic imaging instrument in the anterior and posterior eye. In comparison to existing ophthalmic imaging techniques such as ultrasound and scanning laser ophthalmoscopy, OCT is non-contact and has higher (10 μm) longitudinal resolution. A high-sensitivity fiber-optic OCT instrument has been constructed and is interfaced to a standard slit-lamp biomicroscope for clinical use.⁶⁴ The probe beam is coincident with the observation path of the slit-lamp permitting visualization of the scanning pattern on the anterior chamber or fundus simultaneously with biomicroscopic observation. Computer control and data acquisition allow fine positioning and orientation of the scan in the eye and digitization of the tomographic images. A real-time display of the scan in progress is available on a computer monitor, which is updated every 2.5 s. Computer algorithms have been developed for image analysis and restoration.

In the anterior eye, OCT is potentially useful for the highly accurate biometry of large scale ocular structures, and the evaluation of pathologies of the cornea, iris, and lens.⁶³ Preliminary tomograms have been obtained in patients with band keratopathy, keratitis, corneal edema, iridocorneal adhesions, and cataracts. The non-contact, high-resolution cross-sectional view provided by OCT is also promising for the intraoperative and post-operative evaluation of keratorefractive surgeries. As an example, we have used OCT to quantitate

⁶³ J.A. Izatt, M.R. Hee, E.A. Swanson, D. Huang, C.P. Lin, J.S. Schuman, C.A. Puliafito, and J.G. Fujimoto, "Micron-Scale Resolution Imaging of the Anterior Eye *in Vivo* with Optical Coherence Tomography," *Arch. Ophthalmol.* 112: 1584 (1994).

⁶⁴ J.A. Izatt, M.R. Hee, E.A. Swanson, D. Huang, C.P. Lin, J.S. Schuman, C.A. Puliafito, and J.G. Fujimoto, "Micron-Scale Resolution Imaging of the Anterior Eye *in vivo* with Optical Coherence Tomography," *Arch. Ophthalmol.* 112: 1584 (1994); M.R. Hee, J.A. Izatt, E.A. Swanson, D. Huang, J.S. Schuman, C.P. Lin, C.A. Puliafito, and J.G. Fujimoto, "Optical Coherence Tomography of the Human Retina," *Arch. Ophthalmol.*, forthcoming.

the changes in corneal edema and curvature following laser thermokeratoplasty (LTK) surgery in a rabbit model. Dynamic information on the cellular healing process is also available from sequential OCT images of a single lesion obtained over a period of several weeks. These tomograms clearly document the extent of the lesion, changes in lesion morphology with time, and provide a non-invasive, *in vivo* alternative to histopathology.

Micron-scale axial resolution is particularly important for the early diagnosis and monitoring of degenerative retinal diseases. We have examined over 600 patients at the New England Eye Center with a variety of diseases of the macula⁶⁵ and optic nerve,⁶⁶ including macular hole, retinal detachment, macular edema, age-related macular degeneration, and glaucoma. OCT images have been correlated with conventional clinical examination, fluorescein angiography, and visual field testing.

The diagnosis of macular holes, a common cause of progressive central vision loss, can be difficult. Lesions that ophthalmoscopically resemble various stages of macular hole development include lamellar holes, macular cysts, foveal detachments of the neurosensory retina or pigment epithelium, and epiretinal membranes and macular pseudo-holes. OCT can effectively distinguish these pathologies in cross-section.⁶⁷ OCT can also stage idiopathic macular holes which may be important in evaluating surgical intervention. Vitreomacular traction has been implicated in the pathogenesis of hole formation. The high resolution of OCT is helpful in assessing the vitreoretinal interface which is useful for evaluating the risk of hole formation, especially in the fellow eyes of patients with a unilateral macular hole. Quantitative information may be directly extracted from the OCT tomograms, including the diameter of the hole, and the extent of surrounding subretinal fluid accumulation. The high-resolution obtained in the tomographs suggests that OCT may be a useful method of precisely monitoring hole progression, or recovery after surgery.

Macular edema is commonly associated with diabetic retinopathy, retinal vein occlusion, uveitis, and cataract extraction. Although fluorescein angiography is highly sensitive for the qualitative detection of fluid leakage which causes macular edema, measurements of retinal thickening may correlate better with areas of retinal dysfunction than the amount of fluorescein leakage. OCT provides high longitudinal resolution cross-sectional images of retinal structure and direct measurements of retinal thickness are possible from the tomographs. OCT images obtained in patients with cystoid macular edema closely correspond to known histopathology.⁶⁸ Measurements of retinal thickness at the same location in tomographs acquired longitudinally over time provide an objective means of tracking the development or resolution of fluid accumulation. Unlike conventional slit-lamp observation or fluorescein angiography, these measurements enable the objective monitoring of disease progression or resolution with a single, permanently recorded number. For example, OCT is useful in quantitatively monitoring retinal thickness changes before and after focal laser photocoagulation treatment for macular edema. In patients with diabetes mellitus, measurements of retinal thickness with OCT in the central fovea correlate with best corrected visual acuity. In a preliminary study, a simple linear regression provided a good fit (adjusted R² = 0.78) between foveal thickness and visual acuity. In this study, OCT was also more sensitive compared to slit-lamp biomicroscopy to small changes in retinal thickness. These results suggest that OCT is promising as a sensitive diagnostic for macular thickening, the major treatable cause of vision loss in diabetic retinopathy.

OCT also offers an objective test for the quantitative evaluation of patients with central serous chorioretinopathy, a common cause of reduced vision among middle-aged men. Longitudinal examinations with OCT are able to track the resolution of the sensory retinal detachment in this

⁶⁵ C.A. Puliafito, M.R. Hee, C.P. Lin, E. Reichel, J.S. Schuman, J.S. Duker, J.A. Izatt, E.A. Swanson, and J.G. Fujimoto, "Imaging of Macular Diseases with Optical Coherence Tomography (OCT)," *Ophthalmol.*, forthcoming.

⁶⁶ J.S. Schuman, M.R. Hee, C.A. Puliafito, C. Wong, T. Pedut-Kloizman, C.P. Lin, E. Hertzmark, J.A. Izatt, E.A. Swanson, and J.G. Fujimoto, "Quantification of Nerve Fiber Layer Thickness in Normal and Glaucomatous Eyes Using Optical Coherence Tomography: A Pilot Study," *Arch. Ophthalmol.*, forthcoming.

⁶⁷ M.R. Hee, C.A. Puliafito, C. Wong, J.S. Duker, E. Reichel, J.S. Schuman, E.A. Swanson, and J.G. Fujimoto, "Optical Coherence Tomography (OCT) of Macular Holes," *Ophthalmol.*, forthcoming.

⁶⁸ M.R. Hee, C.A. Puliafito, C. Wong, J.S. Duker, E. Reichel, B.K. Rutledge, J.S. Schuman, E.A. Swanson, and J.G. Fujimoto, "Quantitative Assessment of Macular Edema with Optical Coherence Tomography (OCT)," submitted to *Arch. Ophthalmol.*

disease with more sensitivity than slit-lamp biomicroscopy.⁶⁹

Clinical imaging of the optic nerve with OCT is directly relevant to the early diagnosis of glaucoma, the third leading cause of blindness in the U.S. Unlike tonometry, visual field testing, or optic nerve head appearance, OCT images of peripapillary nerve fiber layer thickness may be able to provide an objective early indicator of glaucoma onset. In preliminary studies, OCT images have been correlated with visual field testing and fundus photography in a cross-section of patients.⁶⁶ Areas of retinal nerve fiber layer thinning correlate with regions of visual field loss, and the severity of thinning is indicative of the stage of glaucoma. Taken together, these studies suggest that OCT is a promising diagnostic tool in clinical ophthalmology.

1.15.2 In vivo Imaging of Laser-Induced Retinal Lesions Using OCT

An understanding of laser-tissue interaction in the eye is relevant both to laser surgery as well as to establishing standards for laser eye safety. Previous studies which establish laser retinal injury thresholds have been based primarily on ophthalmoscopic or fluorescein angiographic examination of the retina.⁷⁰ Histopathology provides direct measurement of the morphology and ultrastructural changes which accompany retinal laser injury.⁷¹ However, this technique requires that a specimen be obtained for microscopic examination.

During the past year, we have taken a new approach to investigating laser retinal injury using optical coherence tomography (OCT). OCT is a new imaging technique which utilizes fiber optic based low-coherence interferometry along with a super luminescent diode laser source to provide micron scale cross-sectional tomographic images of retinal structure. In contrast to conventional histopathology techniques, OCT is noninvasive; there-

fore, it is possible to image laser induced retinal lesions at different time intervals ranging from immediately after laser exposure to several days. This provides a direct tomographic measurement of the formation and healing response to laser retinal exposure.

Comparative OCT studies were performed at Brooks Air Force Base, Texas, using cw argon, nanosecond, picosecond, and femtosecond laser-induced lesions. Histopathology was acquired at selected time points for comparisons with OCT images. By combining sequentially acquired images, a time-lapse movie illustrating lesion evolution was produced. Additionally, images acquired spatially across the retinal surface, and later assembled, enabled the visualization of the three-dimensional structure of an optic disk.

These studies are the first *in vivo* microstructural measurements which document the formation and healing response of retinal laser exposure, provide improved visualization of retinal structure, and have important implications for ophthalmic laser surgery as well as establishing laser retinal injury standards.

1.15.3 Noninvasive OCT Imaging for Cataract Evaluation

Clinically, the primary means for cataract evaluation is by slit-lamp examination. Although this provides a reasonably adequate view of the lens, the grading of cataract formation is based upon a subjective grading system used by the clinician. A more quantitative means of evaluating the lens is by Scheimpflug imaging. The Scheimpflug camera and anterior eye segment analysis system provide a small margin of error (3-9 percent), but the examiner using this device must be very experienced in order to reproduce clinically viable data.⁷² In addition, the instrument is not available to most clinicians.

The use of OCT to image cataracts provides quantitative data of optical reflectance within the lens. Previously in our laboratory, we have imaged

⁶⁹ M.R. Hee, C.A. Puliafito, C. Wong, J.S. Duker, E. Reichel, J.S. Schuman, E.A. Swanson, and J.G. Fujimoto, "Optical Coherence Tomography (OCT) of Central Serous Chorioretinopathy," *Am. J. Ophthalmol.*, forthcoming.

⁷⁰ R. Birngruber, V.-P. Gabel, and F. Hillenkamp, "Threshold Criteria and Derivation of Safe Levels for Laser Radiation," in *Current Concepts in Ergophthalmology*, eds. B. Tengroth, D. Epstein, A. Anseth, A. Hedin, A.H. Keeney, M.J. Roper-Hall, and D.H. Sliney (The Hague, The Netherlands: 1978).

⁷¹ B. Lorentz, "Morphologic Changes of Chorioretinal Argon Laser Burns during the First Hour Post Exposure," *Lasers Life Sci.* 2: 207 (1988).

⁷² Y. Sakamoto and K. Sasaki, "Accuracy of Biometrical Data Obtained from the NIDEK EAS-1000," *Ophthalmic Res.* 26 (suppl. 1): 26 (1994).

bovine lenses *in vitro* using OCT after cold-induced cataracts were formed.⁶³ This year, we completed the first *in vivo* study using OCT to image lenticular cataracts in a colony of geriatric rhesus monkeys with historically documented radiation-induced cataracts.⁷³ The documented cataract grading of this colony was accomplished using the subjective grading system and provides complete descriptions of the cataracts that were imaged. Detailed images were produced from 18 subjects with cataracts ranging in grade from 0 to 3. Nuclear, cortical, and subcapsular opacities were clearly imaged in the anesthetized subjects. Each image was produced from an average of three scans with each scan taking 20 s to complete. Movement artifacts were subsequently removed through image processing on a computer. Faster image acquisition will be necessary before images can be obtained in human subjects.

Cataracts with increasingly dense opacities revealed under slit-lamp examination correlate well with the increasing optical reflectance detected with OCT. In addition, OCT was able to detect opacities previously hidden posterior to nuclear opacities. When OCT images were acquired prior to slit-lamp examination, images provided direction toward visually confirming the opacities that were extremely subtle and would have been missed otherwise. These early results suggest that OCT can be readily utilized as a noninvasive means of quantitatively grading cataracts and identifying opacities not easily observed during standard slit-lamp examination.

1.15.4 OCT Enhanced Confocal Microscopy

The axial and lateral resolution of cross-sectional OCT images is increased by combining OCT with confocal microscopy.⁷⁴ For OCT enhanced confocal microscopy, the reference arm length is matched to the focus of the high numerical aperture objective illuminating the sample. The sample is scanned axially and laterally through the focus of the objective, and the interferometric signal is detected at every scan position.

OCT enhanced confocal microscopy narrows the system point spread function (PSF) of the confocal

microscope by multiplying the PSF defined by the coherence envelope with that of the confocal system. Also, coherent detection limits the multiple scattering contribution to the resultant confocal image. Both improvements enable OCT enhanced confocal microscopy to provide higher resolution and greater contrast than standard confocal microscopy.⁷⁴

The OCT enhanced confocal microscope consists of broad bandwidth superluminescent diode centered at 850 nm. The coherence length of the source is approximately 20 nm. The source is coupled into a single mode fiber-optic Michelson interferometer. The fiber is modulated at 20 KHz with a piezoelectric transducer, and the interference signal is detected using a lock-in amplifier. The heterodyne detection of the OCT enhanced confocal system provides a signal-to-noise ratio in excess of 110 dB. The sample arm objective has a high magnification ranging from 40 to 100 times, and numerical aperture ranging from 0.85 to 1.3. The pinhole of the OCT enhanced confocal system is the aperture of the single mode fiber of the object arm. The image is formed from the magnitude of the interferometric signal detected as the sample is raster scanned through the focus. The total image scan time ranges from 5 to 15 minutes.

OCT enhanced confocal microscopy has been used to image microscopic features of *in vitro* skin lesions. Images obtained from the OCT enhanced confocal microscopy system show cellular morphology up to 200 μm deep. The OCT enhanced confocal images also allow visualization of the dermoepidermal junction and dermal structures. The ability of OCT enhanced confocal microscopy to image cellular and architectural morphology of skin validates the use of this approach for obtaining high resolution optical biopsies.

1.15.5 Optical Biopsy

A cross-sectional optical imaging device for performing noninvasive "optical biopsies" in human tissue would greatly improve the quality of medical care. The optical biopsy might be done by cross-sectional imaging of backscattered reflectance from architectural and cellular structures within tissue.

⁷³ A.B. Cox et al., "Progress in the Extrapolation of Radiation Cataractogenesis Data Across Longer-Lived Mammalian Species," in *Biological Effects and Physics of Solar and Galactic Cosmic Radiation*, Part A, eds. C.E. Swenberg et al. (New York: Plenum Press, 1993).

⁷⁴ J.M. Schmitt, A. Knutel, A. Gandjbakche, and R.F. Bonner, "Optical Characterization of Dense Tissues using Low-Coherence Interferometry," *SPIE* 1889: 197 (1993); J.A. Izatt, M.R. Hee, and G.M. Owen, "Optical Coherence Microscopy in Scattering Media," *Opt. Lett.* 19: 590 (1993).

Cross-sectional reflectance images could have functional as well as structural significance if the wavelengths were selected around absorption maxima of endogenous chromophores that are physiologically significant, e.g., hemoglobin. Measuring spatially localized reflectance in tissue is complicated by multiple scattering, however. Optical coherence tomography (OCT) is a new technique that uses low coherence interferometry to gate out multiply scattered photons and produce cross-sectional reflectance images.

An OCT system that accommodates multiple sources has been constructed. The source is coupled into a single mode optic based Michelson interferometer. Tissue axial reflectance is obtained by varying the reference arm length and digitizing the magnitude of the demodulated interference envelope. A cross-sectional image is produced by recording axial reflectance profiles while the tissue specimen is scanned laterally.

Clinically relevant OCT images of pathologic *in vitro* human tissue have been obtained using superluminescent diodes at two different wavelengths, 850 and 1300 nm. For both wavelengths, the system has an axial resolution of approximately 20 μm , object arm power of 100 μW , and a signal-to-noise ratio (SNR) of 100 dB. Reflectance images of coronary artery and aortic atherosclerotic plaques demonstrate a clear delineation between cardiac muscle, fatty plaque, and fibrous tissue. Architectural morphology of normal and pathologic *in vitro* human tissue specimens, including skin, lung, respiratory tract, gastrointestinal tract, bone, and cartilage have also been imaged. OCT imaging at 1300 nm has been found to be superior to 850 nm because of increased penetration depth. The variation in penetration is likely due to the decreased attenuation from tissue scattering and absorption at 1300 nm.⁷⁵

A wavelength tunable modelocked Kerr lens modellocked Ti:Al₂O₃ laser has been constructed for coupling into the OCT system. Ultra high axial resolution (<4 μm) OCT images from aortic atherosclerotic plaques and other human tissues have been acquired using the Ti:Al₂O₃ laser. Our studies show that ultra high resolution OCT images obtained using the Ti:Al₂O₃ laser are superior to images produced by the SLD based systems.

The Ti:Al₂O₃ laser allows samples to be illuminated by more than 50 mW of optical power distributed

over the wide spectral range of 750-875 nm. The ultra high resolution OCT system has greater resolution than the SLD based systems because of the large spectral bandwidth, and accompanying shorter coherence length of the Ti:Al₂O₃ laser. In addition to providing a large dynamic range (115 dB), the high power of this source permits rapid image acquisition. The wavelength tunability of the Ti:Al₂O₃ laser also has applications for performing research on the optical properties of tissue. Future studies will be conducted using this laser to perform OCT spectroscopy of human tissue.

Our lab has demonstrated the use of OCT for noninvasive diagnostic imaging of human tissue. OCT images at 1300 nm contain more diagnostic information because of increased penetration depth. The high resolution of the Ti:Al₂O₃ OCT system outperforms SLD based systems for imaging tissue architectural morphology. These studies suggest that OCT and ultra high resolution OCT will become important tools for performing noninvasive "optical biopsies" in the future.

1.16 EUV Laser Studies

Sponsor

MIT Lincoln Laboratory
Contract BX-5098

Project Staff

Professor Peter L. Hagelstein, James G. Goodberlet, Timothy A. Savas, Marc Fleury, Martin H. Muendel, Sumanth Kaushik

In previous RLE reports, we have described our progress toward the development of small scale EUV lasers at MIT. In this report, we provide a brief overview of results and goals.

Our basic approach is to ionize the surface of a solid flat target with a pump laser pulse (about 1 J in 60 ps) in-line focus to produce a hot low-density plasma. The plasma length is up to about 1 cm, the laser focus is about 30 microns, and the low-density plasmas of interest for EUV laser studies are formed from 100 to 500 μ above the target surface. In the collisional scheme, direct collisional excitation of the ground state of the Ni-like ions produces a population inversion between the excited state n=4 levels; we have observed amplifi-

⁷⁵ J.M. Schmitt, A. Knutte, A. Gandjbakche, and R.F. Bonner, "Optical Characterization of Dense Tissues using Low-Coherence Interferometry," *SPIE* 1889: 197 (1993); J.M. Schmitt, A. Knutte, M. Yadlowsky, and M.A. Eckhaus, "Optical Coherence Tomography of a Dense Tissue: Statistics of Attenuation and Backscattering," *Phys. Med. Biol.* 39: 1705 (1994).

cation on the 4d-4p transition in Ni-like Nb at 204 Å. In the recombination scheme, a population inversion is produced when electrons recombine onto ions in a cooling plasma; we have observed amplification of the 3d-2p transition in H-like B at 262 Å.

Considerable development of our system during the past year has given us a new capability for short pulse and long pulse operation; we have further developed our diagnostics, improving sensitivity using a microchannel plate imaged onto film.

Preliminary experiments using the new system indicate that recombination experiments appear to achieve better ionization with longer pulses. The collisional schemes have been predicted to work better with shorter pulses at high intensity, but this has not yet been tested. There is reason to believe that the use of short pulses for these schemes will produce an underionized plasma. New experiments to clarify these issues are ongoing.⁷⁶

1.16.1 Pulse Compression System

The electron collisional EUV laser schemes are pumped more efficiently the hotter the electron distribution; consequently, an increase in the pump intensity will result in an increased electron temperature. One approach to this is to employ a larger pump laser capable of a higher pump power; this

approach has been demonstrated to work at laser facilities that can deliver more energy than ours by a factor of 1000. We decided instead to pursue the use of a higher intensity pump pulse which we obtained by implementing a pulse compression scheme into our pump laser system.

The compression system is shown in figure 6. The system employs chirped-pulse amplification, based upon bulk glass self-phase modulation, to generate shorter pump pulses at higher peak power. In order to increase the pulse bandwidth, the amplified oscillator pulse of 60 ps is focused into bulk SF6 glass, $n_2 = 9 \times 10^{13}$ esu in a double pass optical arrangement. The spectrally broadened pulse is temporally stretched with a grating pair pulse stretcher to 120 psec, limited by the nonlinear phase modulation of the glass. The stretcher consists of two 1800 lines/mm gratings separated by three meters and an inverting lens pair; the beam makes two passes through the stretcher.

The 120 ps pulse is amplified by passing through the zig-zag slab power amplifier, and then shortened to 20 ps by a second 1800 lines/mm grating pair compressor. The compressor gratings are used 8° off Littrow and separated by seven meters; the transmission efficiency of system from slab amplifier to target was measured to be 67 percent. We are presently able to pump at 800 mJ with 20

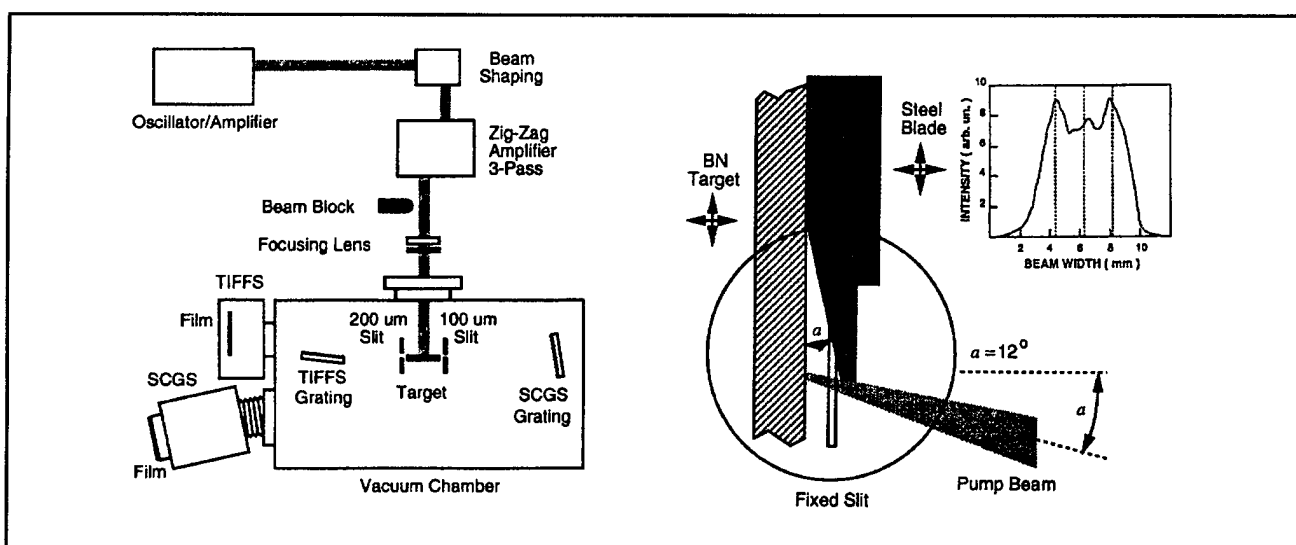


Figure 6. (a) The MIT table-top x-ray laser system. Time integrated flat field spectrometer (TIFFS). Streaked concave grating spectrometer (SCGS). (b) Target and blade arrangement used for H-like recombination laser. Insert: Transverse intensity profile of pump-laser beam.

⁷⁶ P.L. Hagelstein, J. Goodberlet, M. Muendel, T. Savas, M. Fleury, S. Basu, and S. Kaushik, "Recent Progress in Table-Top Lasers at MIT," *Proceedings of the International Symposium on X-ray Lasers*, Williamsburg, Virginia, June 1994; J. Goodberlet, T. Savas, S. Basu, M. Muendel, S. Kaushik, M. Fleury, and P.L. Hagelstein, "Recent Experiments with the MIT Table-Top X-ray Laser System," *Proceedings QELS*, Quebec, 1994.

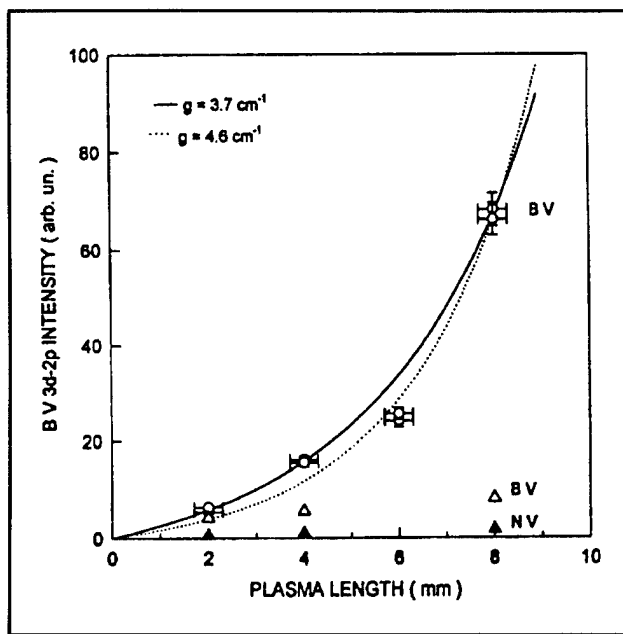


Figure 7. Line intensities, recorded with the SCGS, for several plasma lengths. 400 μm above the target surface, the B V 3d-2p line, shown as circles, exhibited amplification. 250 μm above the surface, the B V line showed optically thick behavior and the N V 3s-2p line showed linear growth.

ps pulses, and 1.5 J with 120 ps pulses; increasing the bandwidth further (which is planned for the near future) will allow us to pump with 1.5 J at 15 ps, and 3 J at 220 ps.

1.16.2 Short-Pulse Versus Long-Pulse Plasma Heating

While it is expected theoretically that pumping with a higher intensity will produce an increased coronal electron temperature, this effect can be mitigated to some degree by an increased PdV cooling rate. Use of an intense short pulse should produce higher gain in the collisional scheme, as long as Ni-like ions are present when the intense pulse arrives. There has been concern as to whether a short intense pulse can produce the proper conditions for EUV lasing.

Experiments were carried out to examine the response of the coronal plasma to laser pulses of different intensities. Carbon and boron plasmas were studied comparing 20 ps and 120 ps single pulse irradiation at constant energy; carbon plasmas were studied at 1 mm and 4 mm length, and boron plasmas were studied at 8 mm. The experiments indicated stronger 2p-1s and 3d-2p emission at 120 ps, and stronger H-like to He-like K-shell emission, apparently consistent with the production of a hotter coronal plasma at the longer pulse length.

If the electron temperature goes down more rapidly by PdV cooling in the case of short-pulse pumping, then the use of two-pulse irradiation should reduce the PdV cooling during the second pulse since the plasma is pre-expanded. The results of the two-pulse measurements in a carbon plasma showed an improvement in the short-pulse emission, but the long-pulse irradiation results in a "hotter" spectra. Experiments to explore plasma heating in calcium plasmas are ongoing (Ne-like calcium is an EUV laser candidate that may be within our range).

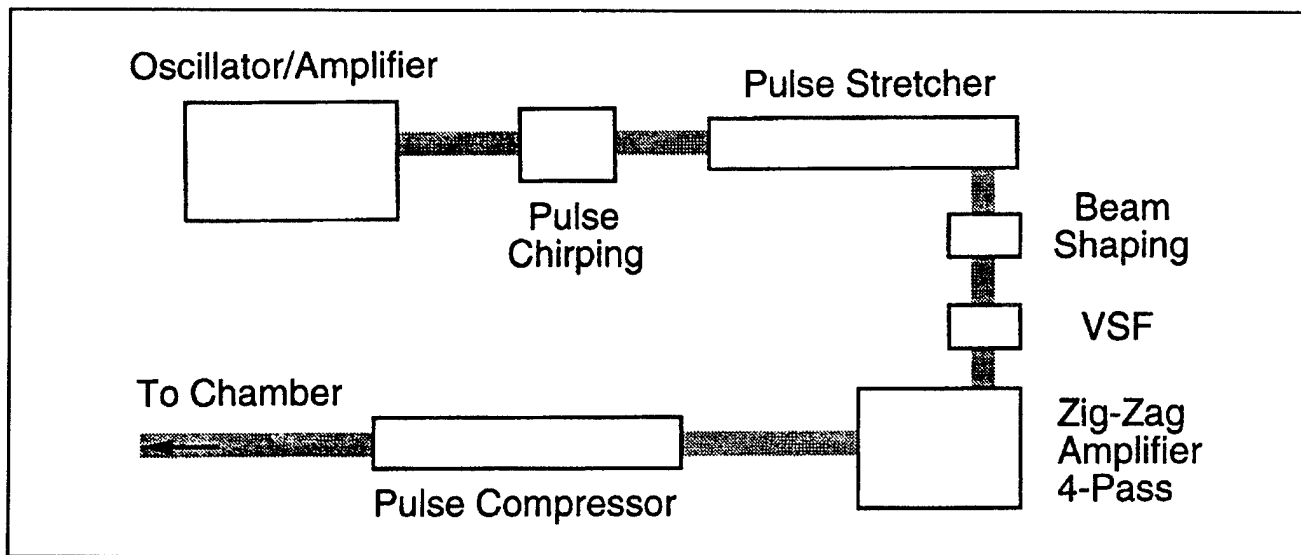


Figure 8. The upgraded pump-laser system. Chirped pulse amplification has been on the pump-laser system. The pulse is chirped in bulk SF₆ glass, and is stretched and compressed with two grating pairs. VSF: Vacuum spatial filter.

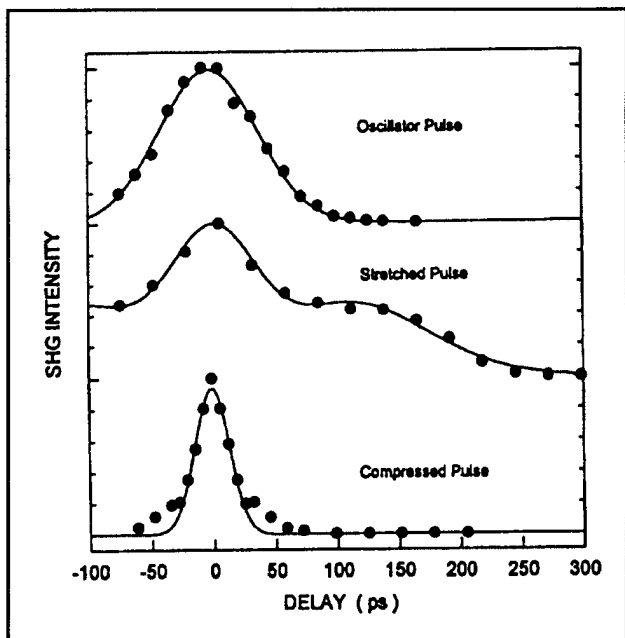


Figure 9. Second harmonic generation pulse measurements. The oscillator pulse, stretched pulse and compressed pulse durations were found to be 62 ps, \sim 120 ps, and 20 ps, respectively.

1.16.3 EUV Diagnostics Upgrades

As described in previous reports, we have fielded two EUV diagnostics. The primary spectrometer diagnostic has used a nearly stigmatic concave spherical grating at near normal incidence to image onto an x-ray streak camera. The secondary spectrometer has used a flat-field variable spacing Harada grating that has imaged onto a microchannel plate or directly onto film. Experience with both diagnostics has indicated that our experiments would be accelerated and improved by some modifications, which are described below.

The use of the Harada grating spectrometer has provided important x-ray spectra below 100 Å, but as implemented, a break in the vacuum was required to recover film. An insert was designed, built, and implemented in order to speed this up by an order of magnitude. The use of a microchannel plate detector at the Harada image plane will allow us to extend this range to 450 Å, to relay the image out of the vacuum chamber, while retaining spatial information. The Harada spectrometer has the potential to detect beam formation that would allow single shot gain analysis.

We have implemented a microchannel plate detector at the image plane of the concave grating spectrometer for time-integrated imaging. This has resulted in a doubling of the available spectral range; it has increased the sensitivity of the diag-

nostic and extended our spectral range: we can now measure from 140 Å to 420 Å. A set of experiments can now be recorded on a single piece of film, increasing the shot rate and reducing film costs. The film response can be avoided now by capturing the microchannel plate image with a CCD array. The spectrometer now gives us spatial information about the plasma emission; the H-like boron 3d-2p emission is observed to be localized within a $200 \times 400 \mu$ region above the target. The cooling of the plasma by blades placed in the coronal region is now readily apparent in the 2D images.

1.16.4 Shallow-angle Pumping Experiments

While side-pumped EUV lasers have been demonstrated at a number of laboratories and have also played an important role in the development of the field of short wavelength lasers, side-pumped plasma targets have not produced particularly efficient EUV lasers. The highest conversion efficiencies observed so far are 10^{-5} , as determined by the ratio of output energy to input laser pump energy.

An improvement in overall efficiency is expected through the use of end-pumping in pre-expanded plasmas. Much of the inefficiency of current short wavelength lasers occurs because: (1) high density plasma is heated and not used; (2) much of the absorbed energy goes into accelerating plasma; (3) in some target arrangements, the absorbed energy is not large. In the next section, we discuss further our efforts to develop a low density end-pumped gaseous laser.

We pursued shallow-angle pumping of slab targets as a possible route to more efficient EUV lasers. The basic idea is that a beam incident at shallow angle is turned at low density, so that only low density plasma is heated. While most of the beam is not absorbed, it can in principle be used again by refocusing. In order to obtain a profile suitable for EUV laser experiments, a prepulse is required.

In a preliminary set of experiments, shallow-angle pumping was attempted in H-like B coronal plasmas. We were able to produce a line focus by transverse irradiation and then bring a second beam in at glancing angle to heat the pre-formed coronal plasma. As the constraints on relative alignment were rather stringent, it was important to prove that the shallow angle beam in fact hit the plasma region. Observations of the shallow-angle beam emerging from the plasma showed that the coronal plasma refracted the incident beam, in some cases causing beam break-up.

One potential advantage of shallow angle pumping is the increase in pump intensity that occurs. In

these experiments, a pump intensity of 3×10^{13} Watts/cm² was demonstrated, as compared to a transverse pump intensity of 10^{13} Watts/cm². In these experiments, the Harada grating spectrometer was used with film, and the x-ray lines below 60 Å were monitored.

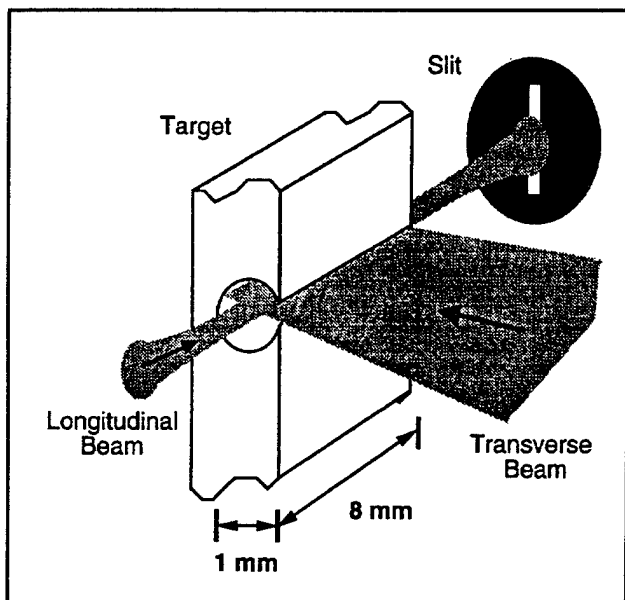


Figure 10. New pumping arrangement. Transverse- and longitudinal-pumping was implemented with a new target geometry. The solid BN target was designed to counter effects of beam refraction.

1.17 Collisional and Recombination Schemes at Longer Wavelength

Sponsor

MIT Lincoln Laboratory
Contract BX-5098

Project Staff

Professor Peter L. Hagelstein, James G. Goodberlet, Timothy A. Savas, Marc Fleury, Martin H. Muendel, Sumanth Kaushik

Experiments on small scale systems have recently achieved some successes at other laboratories. Midorikawa and coworkers claim to have seen significant gain in H-like Li near 135 Å, in a recombining plasma created by optical field ionization from an intense femtosecond pulse.⁷⁷ Rocca and colleagues have recently obtained up to seven gain lengths in Ne-like argon at 469 Å in capillary discharge experiments⁷⁸ and the Stanford group has recently obtained 11 gain lengths gain in Pd-like Xe at 418 Å, using optical field ionization with a circularly polarized femtosecond pulse.⁷⁹

So far, we have explored the Ni-like collisional scheme in Nb at 204 Å,⁸⁰ and the H-like recombination scheme in B at 262 Å.⁸¹ The peak gain in these experiments corresponds to 2.2 and 3.0 gain lengths as interpreted conservatively using the Linford formula. The Linford formula assumes an angular resolving diagnostic, while our diagnostic was angle-integrating; correcting for this effect would lead to about 3 and 4 gain lengths in the two sets of experiments.

Recently, we have been considering different strategies in order to improve on the total number of gain lengths. We have modified our system to be able to use shorter pulses in order to achieve a higher intensity (and thus higher temperatures) in the collisional schemes. Using longer pulses appears to help the recombination schemes. The recombination scheme takes advantage of a blade⁸² to improve cooling; we experimented with many different blade configurations. Some exploratory end-pumped and shallow-angle pumped experiments were done, primarily with the boron recombination scheme.

⁷⁷ Y. Nagata, K. Midorikawa, S. Kubodera, M. Obara, H. Tashiro, and K. Toyoda, "Soft X-ray Amplification of the Lyman- α Transition by Optical Field-induced Ionization," *Phys. Rev. Lett.* 71: 3774 (1993).

⁷⁸ J.J. Rocca, V. Shlyaptsev, F.G. Tomasel, O.D. Cortazar, D. Hartshorn, and J.L.A. Chilla, "Demonstration of a Discharge Pumped Table-Top Soft-X-ray Laser," *Phys. Rev. Lett.* 73: 2192 (1994).

⁷⁹ B.E. Lemoff, G.Y. Yin, C.L. Gordon III, C.P.J. Barty, and S.E. Harris, submitted to *Phys. Rev. Lett.*

⁸⁰ S. Basu, P.L. Hagelstein, J.G. Goodberlet, M.H. Muendel, and S. Kaushik, "Amplification in Ni-like Nb at 204.2 Å Pumped by a Table-top Laser," *Appl. Phys. B* 57: 303 (1993).

⁸¹ J. Goodberlet, S. Basu, M.H. Muendel, S. Kaushik, T. Savas, M. Fleury, and P.L. Hagelstein, *J. Opt. Soc. Am. B*, forthcoming.

⁸² D. Kim, C.H. Skinner, G. Umesh, and S. Suckewer, "Gain Measurements at 18.22 nm in C VI Generated by a Glass Laser," *Opt. Lett.* 14: 665 (1989).

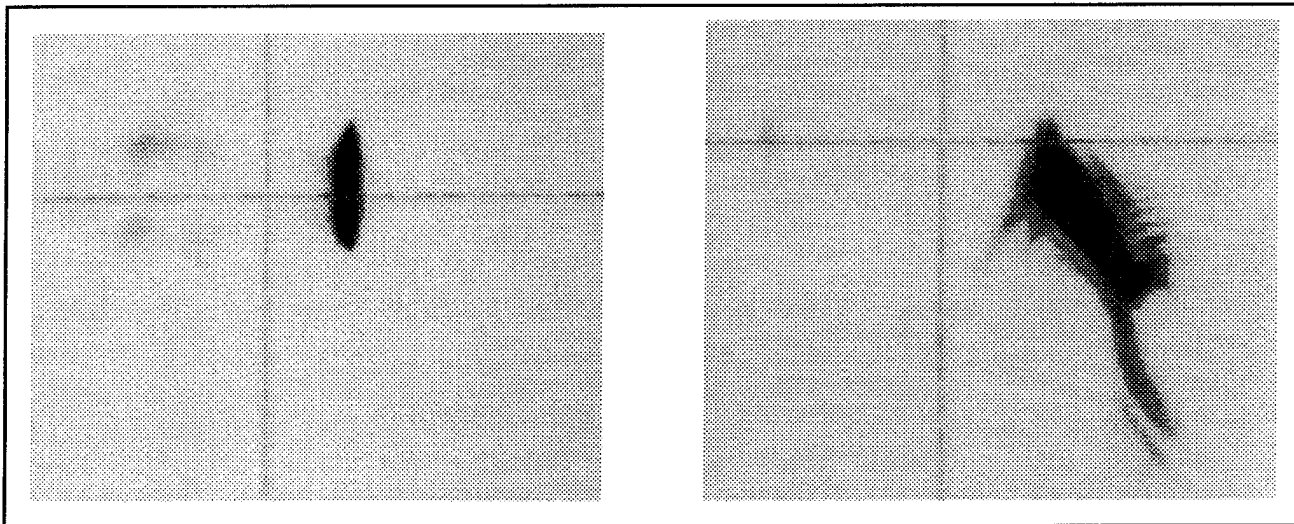


Figure 11. (left) Burn pattern of the longitudinal beam only. (right) Burn pattern of the longitudinal beam when the transverse beam is allowed to preform the plasma. Beam break-up, due to the plasma, is evident.

Longer wavelength schemes should require less pump power. Consequently, we have been considering different classes of schemes at longer wavelength. As our best results to date have been in the recombination scheme, we consider extensions of this scheme in other sequences first. In table 1 we show recombination schemes in the various alkali-isoelectronic sequences with predicted pump intensities that are less than the pump power for H-like B. While the Li-like scheme has been studied for many years (primarily Li-like Al), only recently has some work been reported in the Na-like scheme; no work has been reported in Cu-like ions yet.

It is expected that these recombination schemes will suffer from radiation trapping. Perhaps coincidentally, it has been found to be very difficult to obtain a large gain length product on these transitions in other ions. There exists a class of recombination schemes which would not be expected to suffer such a large trapping effect. Schemes that are available at our pump intensities are listed in table 2. High gain was observed in Li-like S on such a transition.

Table 1. Accessible recombination schemes. λ is the laser wavelength, ΔE is the ionization energy of the ground state electron, I_{est} is the predicted incident pump intensity.

Sequence	Element	Transi-tion	λ (Å)	ΔE (eV)	$I_{\text{est}} \left(\frac{\text{W}}{\text{cm}^2} \right)$
H-like	B	3d-2p	262	340	1.2×10^{13}
Li-like	F	4f-3d	382	167	4.1×10^{12}
Na-like	Ca	5g-4f	402	151	3.6×10^{12}
Na-like	Ti	5g-4f	279	218	6.2×10^{12}
Cu-like	Mo	6h-5g	380	167	4.1×10^{12}

Table 2. Accessible Untrapped Recombination Schemes.

Sequence	Ele-ment	Transi-tion	λ (Å)	ΔE (eV)	$I_{\text{est}} \left(\frac{\text{W}}{\text{cm}^2} \right)$
Li-like	Mg	5g-4f	404	340	1.2×10^{13}
Na-like	Cr	6h-5g	380	296	9.8×10^{12}
Cu-like	Pd	7i-6h	382	275	8.8×10^{12}

Collisional excitation schemes at longer wavelength are also of interest, especially given the recent results in Ne-like A by Rocca and coworkers. While the density and temperature required for argon match our plasmas rather well, it is not easy to use argon in our experiments. As the odd Z versions of the scheme have substantially reduced gain due to hyperfine broadening, the next available scheme is Ne-like Ca. According to the intensity requirements, calcium may be out of our reach. Some preliminary experiments with Ca have been done,

but no gain has been seen. The Ni-like schemes at longer wavelength require a lower pump intensity, but the gain is predicted to be correspondingly lower (due to operation at lower electron density). Our previous efforts at pumping Ni-like Zr were hindered also by the presence of strong emission due to oxygen contamination. Also of interest are higher Z collisional schemes, like the Pd-like ions (demonstrated at Stanford) and the Nd-like ions. While the Nd-like ions that are accessible are unlikely to produce gain, due to a poor ratio of radiative decay rates, it is probable that the Pr-like ions near Z=80 would show gain.

Table 3. Accessible Collisional Schemes.					
Sequence	Element	Transi-tion	λ (Å)	ΔE (eV)	$I_{est} \left(\frac{W}{cm^2} \right)$
Ne-like	Ca	3p-3s	390	405	1.6×10^{13}
Ni-like	Sr	4d-4p	267	195	5.2×10^{12}
Ni-like	Y	4d-4p	242	222	6.4×10^{12}
Ni-like	Zr	4d-4p	221	250	7.6×10^{12}
Pd-like	La	5d-5p	304	~200	$\sim 5.5 \times 10^{12}$

1.18 Toward a Novel End-Pumped EUV Laser

Sponsor

MIT Lincoln Laboratory
Contract BX-5098

Project Staff

Marc Fleury, Professor Peter L. Hagelstein, James G. Goodberlet, Martin H. Muendel

Most laser-driven short wavelength lasers that have been studied make use of plasmas that are created from solid surfaces or thin films by pumping from the side. The efficiencies that have been obtained using this approach have been low; the best efficiencies reported to date have been on the order of 10^{-5} for side pumping.

There are many reasons for this. Ablation from a solid surface leads to heating of unwanted high density plasma, large conduction losses, and signif-

icant hydrodynamic losses. Laser-heating of thin foils leads to similar losses, but also leads to very a low absorption efficiency when the foil has expanded to low density.

Many of these problems can be overcome through the use of end-pumping of a pre-expanded low density plasma. The end-pumped beam will be absorbed efficiently in passing through a long low density plasma, as long as it can stay within the plasma. If the plasma is pre-expanded, the hydrodynamic losses will be minimized. The use of a low density plasma increases the efficiency of the population kinetics. Such systems have the potential to reach an efficiency of on the order of 10^{-2} . Successful implementations of low energy femtosecond EUV laser pumping schemes have to date been all end-pumped lasers.

Recently, Milchberg and coworkers have demonstrated a plasma channel that works as an optical fiber for pump radiation.⁸³ This is important since the ionization of the plasma typically results in defocusing and beam break-up. Milchberg et al. used a transmitting axicon to create a plasma channel, and then demonstrated stable beam propagation within the channel.

The length of the channel in this work was limited by the high power requirements for channel formation. We have proposed to employ a reflecting tube to refocus the light from the axicon in order to obtain a longer channel.⁸⁴ This is illustrated in figure 12.

This design is the combination of an axicon (conical part) and a tube; it can be thought of as an 'optical funnel'. The axicon focuses a collimated beam down to a line on its axis and the tube refocuses this line again and again down its length. This scheme is exact since from the side-view it can be seen that the axicon focuses down to its center and the tube re-focuses on the same point translated. The dimensions are such that each re-focus matches the end of the previous one thereby creating a continuous line focus.

The constraints on this piece are quite stringent. The surface quality must be as good as those of mirrors for high powered lasers. The constraints on the figure of the piece are dictated by the necessity to have a tight focus on axis and a straight line by exact refocusing. That is to say that the piece

⁸³ C.G. Durfee III and H. Milchberg. "Light Pipe for High Intensity Laser Pulses," *Phys. Rev. Lett.* 71: 2409 (1993).

⁸⁴ P.L. Hagelstein, J. Goodberlet, M. Muendel, T. Savas, M. Fleury, S. Basu, and S. Kaushik, "Recent Progress in Table-Top Lasers at MIT," *Proceedings of the International Symposium on X-ray Lasers*, Williamsburg, June 1994.

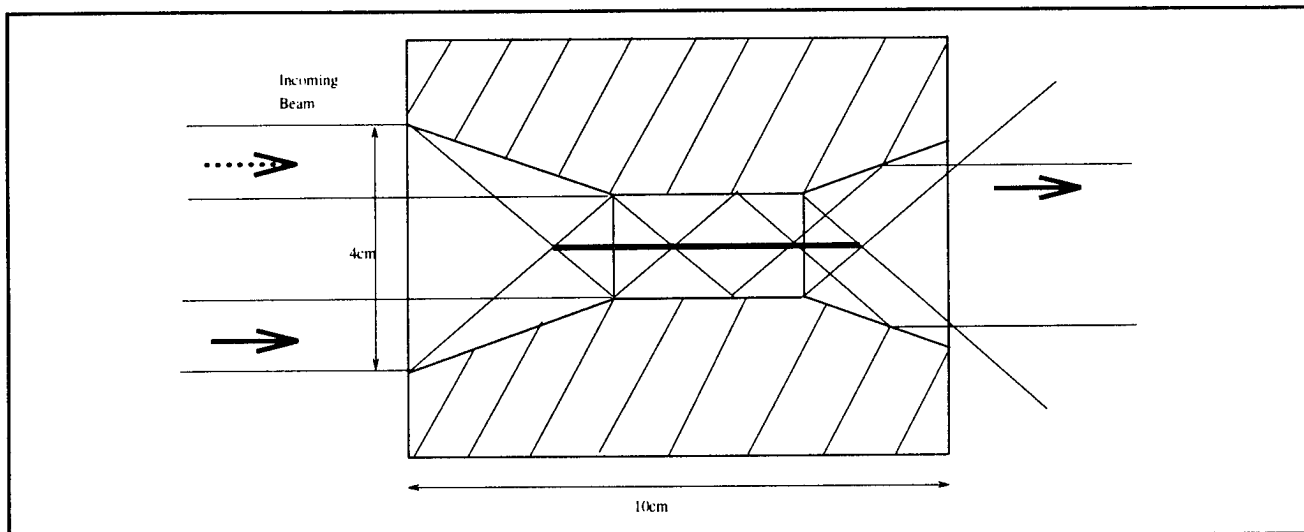


Figure 12. Axicon and tube design of an EUV laser.

needs μm -precision over 20 cm. These optics can be fabricated using hard diamond-turning of OFHC copper, a technology developed over the last 10 years. A mock version of this mirror in brass has been machined and polished here at MIT (figure 13).

We have studied the focusing properties of the mock-up axicon and tube. Refocusing has been demonstrated over a length of 20 cm. On center, an amplification factor of 1200 in a diameter of 80 μm has been recently measured by scanning the intensity profile.

1.19 Photon Operators and Photon Configuration-Space Equations

Project Staff

Professor Peter L. Hagelstein

In a number of recent publications on pulse propagation in fibers, the description of the radiation field has been cast in terms of second quantized photon operators. This is unusual, since quantum radiation theory is usually cast in terms of field operators (\hat{E} , \hat{H} , or \hat{A} operators), and most problems are worked out in terms of these field operators.



Figure 13. Scattering of He-Ne light from condensation at the focus of the mock-up axion and tube.

The photon operators are quite interesting for several reasons. One can compute the field distributions, the energy distribution and the photon distribution; if you do, you will find the photon distribution does not coincide with the energy distribution. A gedanken box could be constructed inside of which a photon is localized; it would be found that the associated fields extend outside of the box. Another gedanken box could be constructed to contain the electric and magnetic fields associated with a photon; yet it can be shown that the associated photon will not be localized within that same box.

Interactions of photons and matter are mediated in QED through the vector potential operator. Written in terms of the vector potential operator, the inter-

action is local; written in terms of the photon field operator, the interaction is fundamentally nonlocal.

QED is a quantum field theory, and as such is cast in terms of field theory operators that are second quantized (they are written in terms of operators that create or destroy photons or electrons). Historically, there has been a considerable computational advantage if a configuration space (first quantization) model is available. An example of this is in atomic structure calculations; the underlying model is QED (a field theory in second quantization), but numerical computations are usually done with the relativistic Hartree-Fock equations which are configuration space equations.

One advantage of studying the photon field operators and their dynamics is that the methods used to obtain configuration space equations from the field theory require a description of the problem in terms of the photon operators. We have recently applied these methods to the second quantized linear response photon Hamiltonian and have derived configuration space equations for photons.⁸⁵ Such equations might be termed "Maxwell-Fock" equations, and the single photon equations are very closely related to Maxwell's equations.

For example, the Maxwell-Fock equations for two photons in a dielectric medium would be written in the form:

$$\begin{aligned} \varepsilon_{aa}\phi_a(r_1) = & \alpha_1 \cdot \mathbf{c} p_1 \phi_a(r_1) + \int U(r_1, s_1) \phi_a(s_1) d^3 s_1 - \varepsilon_{ab} \phi_b(r_1) \\ & + \iiint \phi_b(r_2) V(r_1, r_2, s_1, s_2) [\phi_a(s_1) \phi_b(s_2) + \phi_b(s_1) \phi_a(s_2)] d^3 r_2 d^3 s_1 d^3 s_2 \end{aligned}$$

In this equation, the orbitals ϕ are 6×1 column vectors, corresponding roughly to three electric field pieces on top of three magnetic field pieces. The $\alpha \cdot \mathbf{c} p$ term is a spin-1 analog of the Dirac kinetic energy term; it can be written out in terms of two curls. The dielectric response of the medium is contained in the U terms, and the medium nonlinearity is contained in the photon-photon interaction terms containing V .

In free-space, the 1-photon configuration space equations are mathematically equivalent to Maxwell equations. In the photon equivalent of the Furry picture, the resulting 1-photon configuration space equations are again equivalent to Maxwell's equations in a dielectric medium (which apparently may be nonlocal). The 1-photon results establish the cleanest connection between QED and classical Maxwell equations and under certain restrictions permit Maxwell's equations to be interpreted directly as quantum mechanical equations.

The photon-photon interactions are nonlocal. Photons interact with matter through fields, whose distributions do not correspond to the photon dis-

tributions; this results in a nonlocal photon-photon interaction. In a nonlinear medium, the interaction can be attractive, and photons can bind together to form pulses. In first quantization, these pulses are mathematically similar to nuclei. A nucleus has a center of mass, and the nucleons are correlated within fermis of the center of mass. The nuclear center of mass travels through space freely in the absence of potentials; the relative coordinates are used to develop the nuclear states. Analogously, in a nonlinear optical medium, the photonic center of mass will propagate freely in the absence of a spatially varying dielectric medium, and the relative coordinates may be used to build up the photonic internal states.

Interference effects are known for many-particle systems. The center of mass coordinate of atoms can exhibit interference in a two-slit type of experiment. This interference will be preserved as long as the internal state is not altered. Analogously, it would be expected that the photonic center of mass coordinate should be able to exhibit interference effects, as long as the internal photonic state is not altered. This effect is presently unknown exper-

⁸⁵ P.L. Hagelstein, "Many-Photon Configuration Space Equations," submitted to *Phys. Rev. A*.

imentally. It would be quite interesting, as the center of mass momentum would be approximately the sum of all the individual photon momenta individually; consequently, the wavelength of the center of mass would be of the order of λ/N , where N is the number of photons. The resulting interference pattern would differ from normal one photon interference patterns.

This new effect is predicted to occur in nonlinear optical media under specialized conditions; it has never been observed and may prove to be difficult to observe. If it can be observed, the effect would be very sensitive to perturbations of the optical material, might serve as a new interferometric optical materials diagnostic, and might have other applications as well. We had examined these pulses initially for their potential to serve as the basis of an optical quantum computer.

In any event, we must be able to observe the effect for it to have any applications. In the future, our interest will be toward understanding the new correlated states predicted by this theory and under what conditions the states can be observed.

1.20 Neutron Hopping

Sponsors

Electric Power Research Institute
Contract RP3170-25
ENECO

Project Staff

Professor Peter L. Hagelstein, Sumanth Kaushik

Electrons are known to hop in solid crystalline materials. Models for electron hopping in ordered and disordered solids have been studied for several decades. Over a wide range of materials and conditions, quantitative models are available that can explain experimental observations. We have recently adapted one such model to the problem of neutron hopping in crystals and have found that a neutron analog to electron hopping should occur.⁸⁶

The existence of a neutron hopping effect is not accepted by many, largely because neutrons are so deeply bound, and because the neutron orbitals are so closely localized around their parent nucleus. If these reasons were not sufficient, then there is the absence of experimental observations of effects that could be attributed to a neutron hopping effect.

Electrons hop due to a first order Coulombic coupling of electron orbitals at a site with orbitals at neighboring sites. Since bound neutron orbitals do not extend to neighboring sites, there is no analogous first order coupling. Nevertheless, there does exist a strong-force mediated coupling between bound neutrons and continuum neutrons, which leads to a weak second-order coupling between bound neutron orbitals at different sites. Brillouin's Theorem would force this coupling to be zero in a fixed core Hartree-Fock approximation. But nucleon-nucleon correlation is very strong in nuclei, so that strong core relaxation effects are present that lead to large residual coupling matrix elements.

This interaction can be described mathematically in terms of a neutron mixed valence Hamiltonian⁸⁷

$$\begin{aligned} \hat{H} = & \sum_{k, \sigma} \varepsilon_k \hat{c}_{k, \sigma}^\dagger \hat{c}_{k, \sigma} + \sum_{i, \sigma} \varepsilon_i \hat{d}_{i, \sigma}^\dagger \hat{d}_{i, \sigma} + \frac{1}{2} U \sum_{i, \sigma} \hat{n}_{i, \sigma} \hat{n}_{i, -\sigma} \\ & + \frac{1}{\sqrt{N}} \sum_{i, k, \sigma} [V_k e^{-ik \cdot R_i} \hat{c}_{k, \sigma}^\dagger \hat{d}_{i, \sigma} + V_k^* e^{ik \cdot R_i} \hat{d}_{i, \sigma}^\dagger \hat{c}_{k, \sigma}] \end{aligned}$$

⁸⁶ P.L. Hagelstein and S. Kaushik, "Neutron Transfer Reactions," *Proceedings of ICCF4*, Maui, Hawaii, December, 1993; S. Kaushik and P.L. Hagelstein, "A Mixed Valence Model for Second Order Mixing of Neutron Orbitals in a Lattice," *Bull. Am. Phys. Soc.* 40: 317 (1995); P.L. Hagelstein and S. Kaushik, "Possibility of Neutron Hopping in Crystalline Silicon," submitted to *Phys. Rev. B*.

⁸⁷ P.L. Hagelstein and S. Kaushik, "Neutron Transfer Reactions," *Proceedings of ICCF4*, Maui, Hawaii, December, 1993; P.L. Hagelstein and S. Kaushik, "Possibility of Neutron Hopping in Crystalline Silicon," submitted to *Phys. Rev. B*.

This equation is mathematically closely related to the periodic Anderson model, but the underlying physics is very different. The Anderson model was developed to describe localized states embedded in a continuum; the neutron valence levels are separated from the continuum by several MeV.

We have analyzed this model in the case of a thermal silicon lattice. The results of this analysis indicate that a weak neutron hopping effect is present at high temperature.⁸⁸ The basic effect comes about through interaction of the bound neutron orbitals with free Bragg orbitals in the zero-phonon exchange limit. The different Bragg orbitals destructively interfere, and so the effect is maximized through reducing the number of Bragg orbitals that participate. As phonons are exchanged more readily at high temperature, the neutron recoil couples to fewer Bragg states at high temperature. There is no analog of this for electrons (since electrons are so light), and we recover an unusual coherence effect that is predicted to improve with increasing temperature.

The silicon lattice has a diamond structure, which is composed of two interpenetrating fcc sublattices. Virtual neutrons originating from one sublattice are predicted to be resonantly Bragg scattered by the other sublattice and delocalized. This leads to a finite site-to-site coupling, which results in a weak temperature-dependent band shift (predicted to be too weak to be observable). The delocalization of the neutron orbitals leads to the possibility of neutron capture at other sites. In natural silicon, this effect would lead to gamma emission at 2.1 MeV due to neutrons originating from ²⁹Si being absorbed by ²⁹Si, at a rate that is too slow to be observable.

The effect is predicted to be stronger for lighter nuclei with outer s-wave valence neutrons, or for strongly driven phonon fields. Phonons exchange through recoil more readily when phonons are already present; this effect is enhanced when a very large number of phonons are in a few modes. Consequently, we anticipate that second order gamma emission at 2.1 MeV should be more readily observable in a driven silicon lattice. Calculations of this effect are in progress.

1.21 Possible Phonon Laser Driven by Exothermic Desorption

Sponsor

Electric Power Research Institute
Contract RP3170-25

Project Staff

Professor Peter L. Hagelstein

We have been interested for some time in the transfer of energy from a lattice to atoms and electrons within the lattice. As is well-known, there are two fundamental modes of energy transfer: energy may be exchanged through (1) the creation and destruction of phonons; and (2) the frequency-shifting of phonons present in the lattice. Energy exchange by frequency shifting in molecular physics is known as the Duschinsky effect; in lattices it has no special name, but the effect is present in the Mossbauer effect (it determines the underlying shape of the Mossbauer pip), it is the basis of Huang-Rhys factors, and it appears elsewhere in condensed matter physics.

We are interested in this energy exchange mechanism because it has the potential to lead to anomalously large energy transfer. The total energy transfer ΔE is⁸⁹

$$\Delta E = N\hbar\delta\omega$$

where N is the number of phonons present and where $\delta\omega$ is the phonon mode frequency shift. In the case of vacancy impurity phonon modes occurring in a phonon band gap, and separated by a band gap, the frequency shift can be a few meV. Either through the development of a phonon laser, or through stimulated Brillouin scattering, the number of phonons N can be made to be very large. An total energy shift greater than a few eV would be considered to be anomalous. The effect would be observable through the detection of fast ions or electrons produced at very high rates if the anomalous energy transfer process becomes allowed.

One approach to developing a large modal phonon density N is to generate an optical phonon laser. Phonon lasers have been demonstrated previously

⁸⁸ S. Kaushik and P.L. Hagelstein, "A Mixed Valence Model for Second Order Mixing of Neutron Orbitals in a Lattice," *Bull. Am. Phys. Soc.* 40: 317 (1995); P.L. Hagelstein and S. Kaushik, "Possibility of Neutron Hopping in Crystalline Silicon," submitted to *Phys. Rev. B*.

⁸⁹ P.L. Hagelstein, "Possible Mossbauer Effect in Neutron Capture," *Hyperfine Interact.* 92: 1059 (1994); P.L. Hagelstein, "Lattice-Induced Atomic and Nuclear Reactions," *Fusion Tech.* 26: 491 (1994).

at frequencies up to 0.87 THz. One of the most interesting demonstrations came about through the optical pumping of Cr ions in ruby by Hu (1980),⁹⁰ in which saturation of the phonon laser was claimed. To demonstrate anomalous energy transfer, phonon lasing of optical phonons may be required, which implies the development of phonon lasers at frequencies higher by factors of 5-20. Our application requires the use of materials with a phonon band gap, and an optical pumping scheme implies the use of a transparent crystal. This could be accomplished in LiH, or other transparent hydrides.

One potential difficulty associated with the proposed anomalous energy transfer mechanism discussed above concerns phonon loss. At low temperature, the lifetimes of phonons tend to be relatively long, and may be measured in units of a thousand cycles of oscillation. At room temperature or higher, the loss is much greater (the lifetime can be on the order of ten cycles), and it may be problematic to arrange for a coherent motion of a large number of atoms. This effect would rather drastically limit the maximum total energy transfer possible. However, if phonon gain is present, then the effect of phonon loss can be countered, and a large energy transfer may again be possible. Phonon gain may be more important in this problem than simply giving a large N.

We have recently considered exothermic desorption in metal hydrides as a candidate for driving surface phonon gain at high frequency.⁹¹ A Hamiltonian that is appropriate for a metal hydride and gas system is:

$$\hat{H} = \hat{H}_{\text{MeH}} + \hat{H}_{\text{ph}} + \hat{H}_{\text{gas}} + \hat{H}_{\text{int}}$$

Hydrogen that is inside the metal is described by \hat{H}_{MeH} , which is of the form

$$\hat{H}_{\text{HeH}} = \sum_i \varepsilon_i \hat{b}_i^\dagger \hat{b}_i + \sum_{i,j} t_{ij} \hat{b}_i^\dagger \hat{b}_j$$

This includes the internal energy and hydrogen diffusion. Hydrogen molecules in the gas at low pressure are described by

$$\hat{H}_{\text{gas}} = \sum_k \varepsilon_k \hat{c}_k^\dagger \hat{c}_k$$

which includes the binding and kinetic energy. The phonons are assumed to be harmonic

$$\hat{H}_{\text{ph}} = \sum_{q\sigma} \hbar \omega_{q\sigma} \hat{a}_{q\sigma}^\dagger \hat{a}_{q\sigma}$$

Hydrogen in the metal can desorb to make molecular hydrogen; this is described by

$$\hat{H}_{\text{int}} = \sum_i \sum_k [V_{ijk}(\hat{a}) \hat{c}_k^\dagger \hat{b}_i \hat{b}_j + V_{ijk}^*(\hat{a}) \hat{b}_i^\dagger \hat{b}_j \hat{c}_k]$$

This model is a generalization of the model of Gortel and coworkers.⁹²

In the event that the desorption is exothermic (see figure 14), and if the interaction potential V is expanded to first order in the phonon operators \hat{a} , then the resulting model is equivalent to models used to describe lasers. The molecular hydrogen is not stable at the metal surface, which guarantees a population inversion whenever the ambient gas pressure is below the equilibrium pressure. As a phonon laser, this system is the analog of the optical excimer laser.

⁹⁰ P. Hu, "Stimulated Emission of 29 cm⁻¹ Phonons in Ruby," *Phys. Rev. Lett.* 44: 417 (1980).

⁹¹ P.L. Hagelstein, "Lattice-Induced Atomic and Nuclear Reactions," *Fusion Tech.* 26: 491 (1994); P.L. Hagelstein, "Proposed Novel Optical Phonon Laser Pumped by Exothermic Desorption," *Bull. Am. Phys. Soc.* 40: 808 (1995).

⁹² Z.W. Gortel, H.J. Kreutzer, and D. Spaner, "Quantum Statistical Theory of Flash Desorption," *J. Chem. Phys.* 72: 234 (1980).

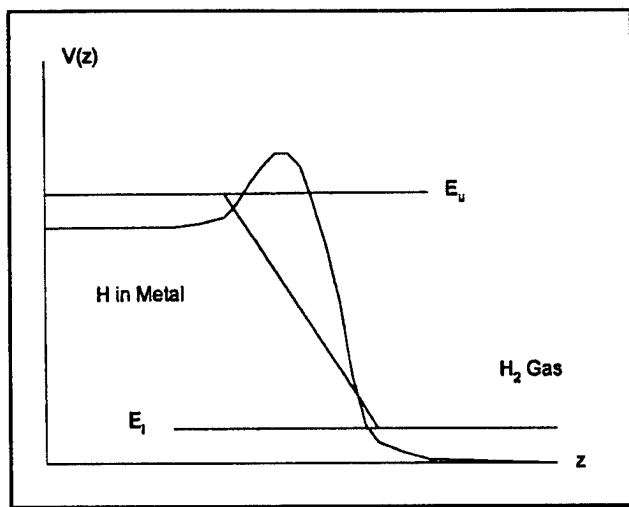


Figure 14. Schematic of potential for exothermic desorption.

Many metal hydrides become exothermic desorbers at high loading. For example, PdH is an endothermic desorber below a loading of about 0.9, and is an exothermic desorber at higher loadings. This is illustrated below in figure 15.

Because the theoretical gain for this system will be very high when gain exceeds loss, this phonon laser will be limited by the reaction kinetics and hydrogen diffusion. The gain criterion can be established immediately from the condition that the number of phonons generated must exceed the number of phonons destroyed per unit time. Assuming a highly excited surface phonon mode, we find the condition

$$\bar{n}J_{\text{des}}A > \frac{N}{\tau}$$

where J_{des} is the desorption flux, \bar{n} is the mean number of phonons generated per desorption event, A is the area of the phonon mode, τ is the phonon lifetime, and N is the number of phonons in the mode (which must be on the order of 1 per atom at the surface in order to dominate over thermal effects). In metal hydrides at room temperature, the losses are very great, and phonon lifetime is on the order of 1 ps.

Consequently, the desorption flux must be very large. A desorption flux in the neighborhood of $10^{28} \text{ cm}^2/\text{sec}$ appears to be the minimum flux required to produce optical phonon gain. This is

not a sustainable flux, as it is impossible to develop an equivalent inward flux. Moreover, it cannot even be sustained by ordinary diffusion mechanisms.

We know that palladium can be loaded into the exothermic regime by either electrochemical or by ion bombardment techniques. In the electrochemical experiments, this is accomplished by developing a blocking layer that passes incoming ions, but blocks the outward gas flow. If this blocking layer were removed transiently on a very short (ns) timescale, then unhindered desorption would occur explosively. During such an explosive desorption event, a large desorption flux will be developed—whether it is sufficiently great to drive an optical phonon laser is presently unknown. A mechanism that causes hydrogen near the surface to be forced out at very high rates is required for large coherent phonon fields to build up.

In the case of impurity (for example, vacancy) optical phonon modes, the density of impurities is lower, and consequently the required desorption flux is lower by the dilution factor. In this case, desorption fluxes in the range of $10^{25}\text{--}10^{26} \text{ H}_2/\text{cm}^2 \text{ sec}$ are required, which is sustainable over nanosecond time-scales.

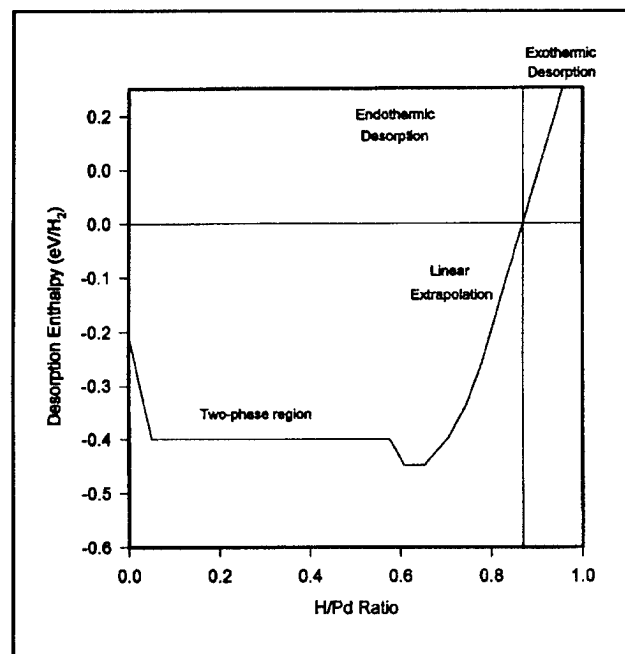


Figure 15. Relative internal potential energy for hydrogen in Pd as a function of loading.

Chapter 2. Optical Propagation and Communication

Academic and Research Staff

Professor Jeffrey H. Shapiro, Dr. Robert H. Rediker, Dr. Ngai C. Wong

Visiting Scientists and Research Affiliates

Dr. Lance G. Joneckis¹

Graduate Students

Jeffrey K. Bounds, L. Reginald Brothers, Irene Fung, Donald R. Greer, Bobby Y. Lai, Dicky Lee, Elliott J. Mason, Phillip T. Nee, Steven G. Patterson, Asif Shakeel

2.1 Introduction

The central theme of our programs has been to advance the understanding of optical and quasi-optical communication, radar, and sensing systems. Broadly speaking, this has entailed: (1) developing system-analytic models for important optical propagation, detection, and communication scenarios; (2) using these models to derive the fundamental limits on system performance; and (3) identifying and establishing through experimentation the feasibility of techniques and devices which can be used to approach these performance limits.

2.2 Nonlinear and Quantum Optics

Sponsor

Maryland Procurement Office
Contract MDA 904-93-C4169
Contract MDA 903-94-C6071

Project Staff

Professor Jeffrey H. Shapiro, Dr. Ngai C. Wong, Dr. Lance G. Joneckis, Jeffrey K. Bounds, Elliott J. Mason, Phillip T. Nee, Steven G. Patterson, Asif Shakeel

2.2.1 Quantum Optical Tap

An optical parametric amplifier (OPA) is a nearly ideal nonresonant generator of nonclassical light: its signal and idler beams exhibit quantum entanglement which can be sensed as sub-shot-noise photon correlation or as a sub-shot-noise quadrature squeezing. It has been suggested that a gain-saturated OPA can provide a new route to nonclassical light-beam generation,² without recourse to joint signal/idler measurements. In particular, it may be possible to preserve the input large-signal signal-to-noise ratio (SNR) of the amplified channel in such an arrangement. Thus, a quantum optical tap for binary-phase-shift-keying (BPSK) could then be developed: such a tap would incur neither signal strength nor SNR degradation in either of its output channels, i.e., its signal and tap output ports.

As a prelude to demonstrating the preceding quantum optical tap concept, we have set up an ultralow loss optical parametric oscillator (OPO) for study of quantum noise correlation. High quality mirrors and a potassium titanyl phosphate (KTP) crystal have permitted stable cw operation of the OPO with a threshold of 30 mW. Another KTP OPO with a longer crystal and a two-piece lower-loss design has been found to have a threshold of 20 mW. It is expected that the KTP OPOs should yield an intensity correlation between the signal and idler outputs of 90 percent and allow us to study the mean-field characteristics, gain saturation, and quantum-noise spectra of an injection-seeded OPA.³

¹ Laboratory for Physical Sciences, College Park, Maryland.

² N.C. Wong, "Squeezed Amplification in a Nondegenerate Parametric Amplifier," *Opt. Lett.* 16(21): 1698-1700 (1991).

³ K.-X. Sun, *Classical and Quantized Fields in Optical Parametric Interactions*, Ph.D. diss., Dept. of Physics, MIT, 1993.

We have begun an experiment to resonantly generate the second harmonic of a 500-mW 1.06 μm YAG laser. The goal is to obtain stable cw operation and a high conversion efficiency of 60-80 percent in the second-harmonic generation. If successful, this arrangement will serve as a compact, low-noise pump source for KTP OPOs. Moreover, for degenerate OPO operation, the YAG laser can be used as the local oscillator for homodyne detection of quadrature-noise squeezing.

2.2.2 Quasi-Phase Matched Nonlinear Optics

We have initiated a study of quasi-phase matching (QPM)⁴ in lithium niobate with the goal of fabricating QPM nonlinear optical devices that can be operated at any user specified wavelength, such as in the 1.5 μm optical communication window. Nonlinear optical devices that are fabricated using QPM are potentially useful in many applications, such as optical frequency conversion and amplification for optical communication networks. By employing the electric field poling technique,⁵ we have successfully obtained domain reversal in a bulk 250- μm -thick lithium niobate sample. To achieve QPM it is necessary to obtain a periodic grating pattern of regular and domain reversed material in lithium niobate with a grating period of 5-15 μm maintained over a length of 1 cm. We are in the process of fabricating domain-reversed material in a periodic grating pattern.

2.2.3 Squeezed-State Generation in Optical Fiber

In theoretical work, we have been establishing the limits on squeezed-state generation in optical fiber. Recently, we have shown that the Raman noise which accompanies the noninstantaneous Kerr effect sets a new limit on the degree of quadrature-noise squeezing that can be obtained from continuous-wave four-wave mixing in optical fiber.⁶

For pulsed squeezed-state generation in fiber, we have shown that local-oscillator (LO) pulse compression is the key to observing the full squeezing generated when the nonlinear interaction is pumped by a transform-limited Gaussian pulse.⁷ We are now working on the theory of optimal LO selection for quadrature-noise measurements of arbitrary spatio-temporal quantum states.

2.2.4 Quantum Phase Measurements

Recently, a great deal of attention has been given to the phase problem for a single-mode quantum field. Previously, we showed that there are significant physical differences—with potentially important practical consequences—that emerge if the focus in phase-based quantum communication and precision measurement is shifted from single-mode fields to two-mode fields.⁸ In particular, with a two-mode field it is possible to achieve perfect (i.e., zero error probability) K-ary phase-based digital communication at a root-mean-square (rms) photon number of $K/2$. This same rms photon number is also sufficient for a phase-based precision measurement of a c-number phase shift whose observation error is guaranteed to be no more than $\pm \pi/K$. The capabilities of these schemes for phase-based digital communication and precision measurement are radically different from those of their single-mode counterparts. Indeed, in single-mode phase-based communication it is impossible to achieve zero error probability at finite average photon number. Likewise, a single-mode phase measurement at finite average photon number cannot realize probability-one confinement of the measurement error to any proper subinterval of $(-\pi, \pi]$.

The two-mode phase measurement scheme referenced above relies on generating an entangled state, and the use of a quantum measurement which is the two-mode generalization of the Susskind-Glogower probability operator measure. As yet, there are no explicit approaches available for realizing either of these abstractions. In our

⁴ M.M. Fejer, G.A. Magel, D.H. Jundt, and R.L. Byer, "Quasi-Phase-Matched Second Harmonic Generation: Tuning and Tolerances," *IEEE J. Quantum Electron.* 28(11): 2631-2654 (1992).

⁵ M. Yamada, N. Nada, M. Saitoh, and K. Watanabe, "First-Order Quasi-Phase Matched LiNbO₃ Waveguide Periodically Poled by Applying an External Field for Efficient Blue Second-Harmonic Generation," *Appl. Phys. Lett.* 62(5): 435-436 (1993).

⁶ J.H. Shapiro and L. Boivin, "Raman-Noise Limit on Squeezing Continuous Wave Four-Wave Mixing," *Opt. Lett.*, forthcoming.

⁷ L.G. Joneckis and J.H. Shapiro, "Enhanced Fiber Squeezing via Local-Oscillator Pulse Compression," *Proceedings of Nonlinear Optics: Materials, Fundamentals and Applications*, Waikaloa, Hawaii, July 24-29, 1994.

⁸ J.H. Shapiro, "Phase Conjugate Quantum Communication with Zero-Error Probability at Finite Average Photon Number," *Phys. Script.* T48: 105-112 (1993).

present program, however, we have relieved the measurement part of this realization burden. Specifically, we have shown that zero error probability phase-based digital communication and $\pm \pi/K$ accuracy phase-based precision measurement can be accomplished—at an average photon number of approximately $K\sqrt{3/2}$ —via optical heterodyne detection.⁹ Again, an appropriate two-mode entangled state is needed for which a generation technique is currently being sought.

2.2.5 Publications

Joneckis, L.G., and J.H. Shapiro. "Enhanced Fiber Squeezing via Local-Oscillator Pulse Compression." *Proceedings of Nonlinear Optics: Materials, Fundamentals and Applications*, Waikaloa, Hawaii, July 24-29, 1994.

Shapiro, J.H. "An Eclectic Tour of Quantum Optical Communications." Invited paper presented at the 1994 Annual Meeting of the Optical Society of America, Dallas, Texas, October 2-7, 1994.

Shapiro, J.H. "Phase Conjugate Quantum Communication with Optical Heterodyne Detection." *Opt. Lett.* Forthcoming.

Shapiro, J.H., and L. Boivin. "Raman-Noise Limit on Squeezing continuous Wave Four-Wave Mixing." *Opt. Lett.* Forthcoming.

Shapiro, J.H., and K.-X. Sun. "Semiclassical versus Quantum Behavior in Fourth-Order Interference." *Proceedings of Nonlinear Optics: Materials, Fundamentals and Applications*, Waikaloa, Hawaii, July 24-29, 1994.

Shapiro, J.H., and K.-X. Sun. "Semiclassical versus Quantum Behavior in Fourth-Order Interference." *J. Opt. Soc. Am. B* 11(6): 1130-1141 (1994).

2.3 Multiresolution Laser Radar Range Profiling

Sponsor

U.S. Air Force - Office of Scientific Research
Grant F49620-93-1-0604

Project Staff

Professor Jeffrey H. Shapiro, Irene Fung, Donald R. Greer

This effort is part of a collaboration on automatic target detection and recognition, with Professors Alan S. Willsky (from MIT's Laboratory for Information and Decision Systems) and W. Eric L. Grimson (from MIT's Artificial Intelligence Laboratory) and their students. The unifying theme of the collaboration is the use of multiresolution (wavelet) methods at every stage—from sensor front-end processing, through feature extraction, to the object recognition module—in an overall system. Our own activity centers on the application of multiresolution techniques to laser radars. Previously, we have studied maximum-likelihood (ML) estimation for planar range-profiling with a laser radar.¹⁰ The importance of the ML approach lies in its ability to suppress the range anomalies caused by laser speckle. The practicality of the ML approach derives from the utility of the expectation-maximization (EM) algorithm for this problem. In the current program, we have shown that the same EM approach can be applied, at any desired wavelet scale, to perform ML profiling. Using the Haar wavelet basis, we have demonstrated the use of this technique on simulated laser-radar range data.¹¹ In this study, we have established an efficient, weight-based stopping rule for terminating the coarse-to-fine progression of multiresolution ML estimation. We are presently working on improving the computational efficiency of our ML/EM approach so that this technique can be applied to real laser-radar test bed data from the Opto-Radar Systems Group at MIT Lincoln Laboratory.

⁹ J.H. Shapiro, "Phase Conjugate Quantum Communication with Optical Heterodyne Detection." *Opt. Lett.*, forthcoming.

¹⁰ T.J. Green, Jr., and J.H. Shapiro, "Maximum-Likelihood Laser Radar Range Profiling with the Expectation-Maximization Algorithm," *Opt. Eng.* 31(11) 2343-2354 (1992)

¹¹ I. Fung and J.H. Shapiro, "Multiresolution Laser Radar Range Profiling with the Expectation-Maximization Algorithm," *Proceedings of the Joint ATR Systems and Technology Conference IV*, Monterey, California, November 14-18, 1994.

2.3.1 Publications

Fung, I. *Multiresolution Laser Radar Range Profiling with the Expectation-Maximization Algorithm*. S.M. thesis. Dept. of Electr. Eng. and Comput. Sci., MIT, 1994.

Fung, I., and J.H. Shapiro. "Multiresolution Laser Radar Range Profiling with the Expectation-Maximization Algorithm." *Proceedings of the Joint ATR Systems and Technology Conference IV*, Monterey, California, November 14-18, 1994.

2.4 Optical Frequency Division and Synthesis

Sponsors

MIT Lincoln Laboratory
Advanced Concepts Program
Contract CX-16335
U.S. Army Research Office
Grant DAAH04-93-G-0399
Grant DAAH04-93-G-0187

Project Staff

Dr. Ngai C. Wong, L. Reginald Brothers, Bobby Y. Lai, Dicky Lee

Frequency division and synthesis in the optical domain play an important role in modern optical precision measurements, optical frequency standards, and coherent optical communication. The focus of this program is to study the feasibility of establishing an optical frequency counter based on a parallel network of phase-locked optical parametric oscillators (OPOs). It includes the development of a number of enabling technologies, such as wideband optical frequency comb (OFC) generation,¹² tunable cw OPOs,¹³ and techniques for operating a parallel network of OPOs. An OPO-based optical frequency counter can be operated to measure, compare, and synthesize frequencies from optical to microwave, with high precision and accuracy.

2.4.1 Terahertz Optical Frequency Comb Generation

In order to facilitate difference-frequency measurements in the terahertz range, we have developed an optical frequency comb (OFC) generator based on an efficient electro-optic phase modulator design. By incorporating a microwave waveguide resonator structure in a LiNbO₃ electro-optic modulator, the phase velocities of the microwave and optical fields can be matched to maximize the electro-optic modulation at a user-specified microwave frequency. The modulation is further enhanced by placing the modulator inside an optical cavity that is resonant for the input optical beam and the generated sidebands. For 1 W of microwave power at 17 GHz, we have obtained an optical frequency comb with a 3-THz span.¹²

We have investigated the effects of small microwave frequency detuning on the OFC spectrum. Without detuning a symmetric spectrum is obtained and the span of 3 THz is entirely limited by the dispersion of the lithium niobate crystal. By detuning +2.3 MHz, we have observed an asymmetric spectrum, expanding towards the shorter wavelengths and contracting from the longer wavelengths because the detuning brings the shorter wavelengths into resonance and the longer wavelengths out of resonance. The one-sided span toward the shorter wavelengths is found to be 2.3 THz. Further detuning returns the spectrum to a symmetric shape but with a much smaller span. By using positive and negative detuning it is therefore possible to extend the OFC spectrum to a span of 4.6 THz. We are presently working on compensating the dispersion in order to extend the spectrum span to 10 THz or more.

2.4.2 Tunable Optical Parametric Oscillator

Optical parametric generation has been well known for producing tunable radiation over a broad spectral range. This has been realized in pulsed OPOs but not in cw OPOs. The doubly-resonant condition in cw operation, in which both the signal and idler waves are resonant with the cavity, prevents continuous frequency tuning. A singly resonant cw OPO can be tuned continuously, but at the expense of a much higher threshold power. We have developed a novel dual-cavity configuration that retains the

¹² L.R. Brothers, D. Lee, and N.C. Wong, "Terahertz Optical Frequency Comb Generation and Phase Locking of Optical Parametric Oscillator at 665 GHz," *Opt. Lett.* 19(4): 245-247 (1994).

¹³ D. Lee and N.C. Wong, "Tunable Optical Frequency Division using a Phase-Locked Optical Parametric Oscillator," *Opt. Lett.* 17(1): 13-15 (1992).

low-threshold capability of an ordinary doubly-resonant system, and at the same time is capable of continuous tuning. By employing two separate cavities to resonate the signal and idler waves independently, the output frequencies become continuously tunable. Experimentally, we have observed a tuning range of 1 GHz, which is 100 times more than a single-cavity OPO. Theoretically, the tuning range is limited only by the phase-matching bandwidth of the nonlinear crystal, which is about 50-100 GHz for KTP.

We have discovered that the limiting factors for the tuning range are the weak pump resonance and the resonant leakage between the two cavities. As the OPO is tuned, the weak resonance of the pump field reduces the circulating pump intensity to a level below the threshold, thus effectively limiting the tuning range. Leakage of the signal and idler waves is caused by the imperfect coating of the polarizing beam splitter that is used to separate the signal and idler beams. Resonant leakage occurs when the idler cavity is resonant with the leaked signal field, which effectively leads to a lossy signal cavity, and vice versa. Lossy cavities increase the threshold and hence limit the tuning range. We are in the process of minimizing their effects by utilizing the angle walkoff of KTP to separate the two beams, thus eliminating the polarizing beam and improving the tuning range.

2.4.3 Three-Wave Mixing in CTA

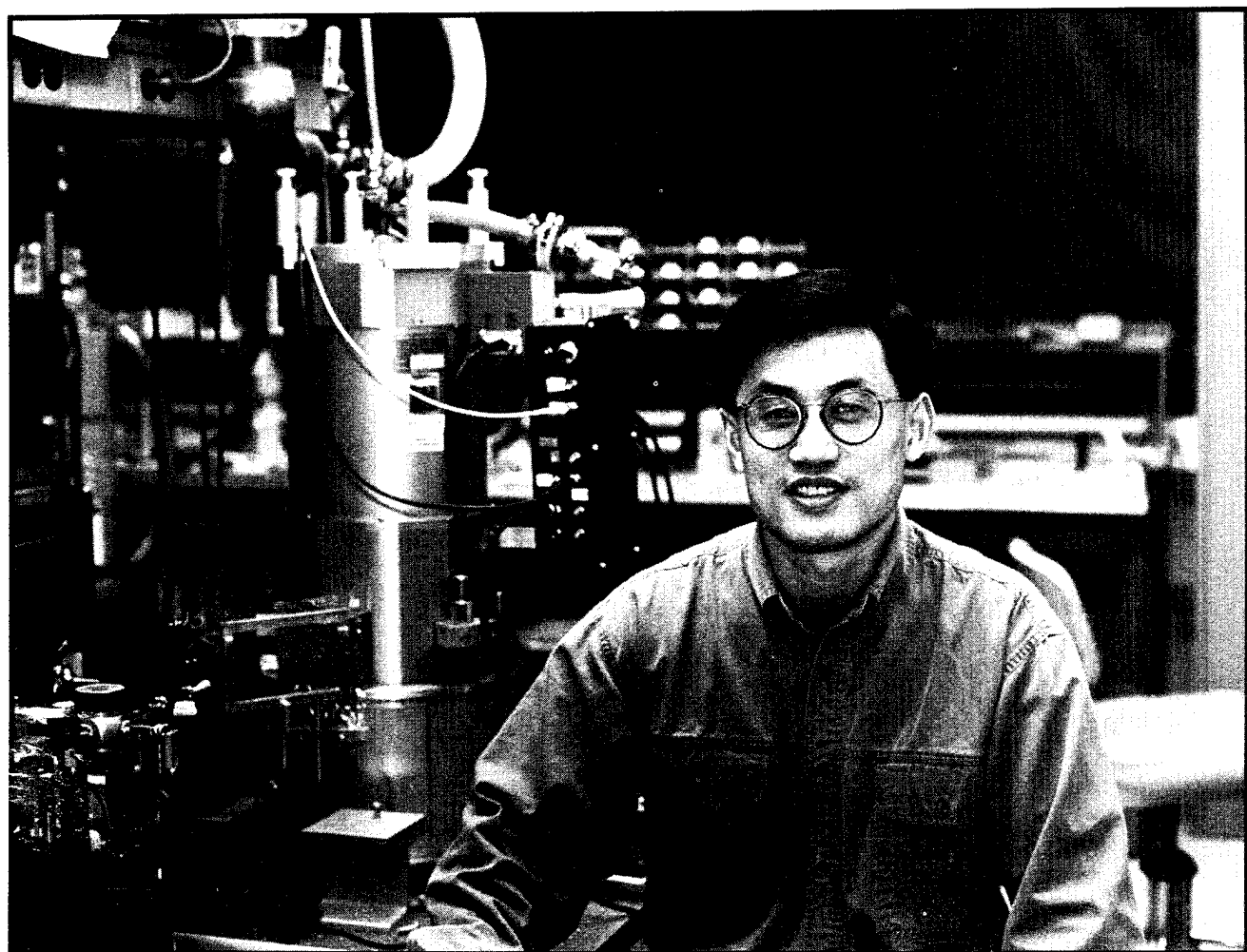
It is potentially useful to have a tunable source at $1.5 \mu\text{m}$ for optical communications. We have used a new nonlinear optical crystal, cesium titanyl arsenate (CTA), to generate tunable radiation by three-wave difference-frequency mixing.¹⁴ By using a krypton ion laser at 531 nm as the pump and a tunable Ti:sapphire laser as the input signal, we have generated $1 \mu\text{W}$ of tunable radiation from 1567 nm to 1653 nm. The use of a resonant cavity for frequency mixing has yielded an output power of

$\sim 100 \mu\text{W}$. We have also determined that the CTA phase-matching angle for generating a 3-to-1 OPO frequency divider pumped at 532 nm is $\theta = 90^\circ$, $\phi = 48^\circ$. We have not observed parametric oscillation due to the quality of the crystal. We are presently investigating the use of other nonlinear crystals with better crystal quality such as lithium borate for demonstrating a 3-to-1 OPO.

2.4.4 Publications

- Brothers, L.R., D. Lee, and N.C. Wong. "Terahertz Optical Frequency Comb Generation and Phase Locking of Optical Parametric Oscillator at 665 GHz." *Opt. Lett.* 19(4): 245-247 (1994).
- Lee, D., and N.C. Wong. "Tuning Characteristics of a cw Dual-Cavity KTP Optical Parametric Oscillator." Paper presented at the Conference on Lasers and Electro-Optics, Anaheim, California, May 8-13, 1994.
- Wong, N.C., and D. Lee. "Frequency Tuning and Phase Locking of an Ultrastable Doubly Resonant Optical Parametric Oscillator." Paper presented at the Advanced Solid-State lasers Topical Meeting, Salt Lake City, Utah, February 7-10, 1994.
- Wong, N.C., D. Lee, and L.R. Brothers. "Cw Phase-Locked Optical Parametric Oscillator as a Tunable Source for Terahertz Radiation." *Proceedings of the SPIE Nonlinear Optics for High-Speed Electronics*, Los Angeles, California, January 25, 1994.
- Wong, N.C., D. Lee, L.R. Brothers, and B. Lai. "Optical Frequency Measurement and Synthesis using Nonlinear Optical Techniques." Invited paper presented at the Conference on Lasers and Electro-Optics, Anaheim, California, May 8-13, 1994.

¹⁴ B.Y.F. Lai, *A Tunable Light Source at $1.6 \mu\text{m}$ by Difference-Frequency Mixing in Cesium Titanyl Arsenate*, S.M. thesis, Dept. of Electr. Eng. and Comput. Sci., MIT, 1995.



Professor Qing Hu (Photo by John F. Cook)

Chapter 3. High-Frequency (>100 GHz) and High-Speed (<1 ps) Electronic Devices

Academic and Research Staff

Professor Qing Hu, Dr. Gerhard de Lange, Dr. Simon Verghese

Visiting Scientists and Research Affiliates

Dr. Thomas Schäpers

Graduate Students

James Ernstmeyer, Brian R. Jacobson, Ilya Lyubomirsky, Arifur Rahman, Farhan Rana, Rolf A. Wyss, Bin Xu, Noah D. Zamdmer

3.1 Introduction

Millimeter wave and far-infrared frequencies ($f > 100$ GHz) remain one of the most underdeveloped frequency ranges, even though there are a great number of potential applications in remote sensing, spectroscopy, plasma diagnostics, and communications. This is because the millimeter wave and far-infrared frequency range falls between two other frequency ranges in which conventional semiconductor devices are usually operated, the microwave frequency range and the near-infrared and optical frequency range. Semiconductor devices which utilize the classical diffusive transport of electrons, such as diodes and transistors, have a high frequency limit. This limit is set by the time electrons take to travel a certain distance. Currently, electron mobility and the smallest feature size which can be fabricated by lithography limit the frequency range to below several hundred GHz. Semiconductor devices based on quantum mechanical interband transitions, however, are limited to frequencies higher than those corresponding to the semiconductor energy gap, which is higher than 10 THz for most bulk semiconductors. Therefore, a large gap exists from 100 GHz to 10 THz in which very few devices are available.

Semiconductor quantum-effect devices (which can be loosely termed "artificial atoms"), including both vertically grown quantum-well structures and laterally confined mesoscopic devices, are human-made quantum mechanical systems in which the energy levels can be chosen by changing the size of the device. Typically, the frequency corresponding to the intersubband transitions is in the millimeter-wave to THz range ($\Delta E \sim 1\text{-}4$ meV) for the lateral quantum-effective devices, and above one THz for the vertical quantum wells. It is therefore appealing to develop ultrahigh-frequency devices, such as radiation detectors and mixers,

and THz lasers utilizing the intersubband transitions in these devices. Furthermore, the study of the interaction between photons (with energies comparable to the intersubband spacings) and the quantum-effect devices (artificial atoms) is analogous to optical spectroscopy in atomic physics. Naturally, this study will literally shine "new light" on these novel devices and new information will be obtained that could not be extracted from dc transport measurements. It is also clear that devices with THz characteristic frequencies will have picosecond speed response. Such ultrahigh-speed devices could be useful in easing the electronic "bottleneck" in the current fiber optical communication systems, in which only a small fraction of the 20-THz bandwidth of optical fibers are utilized because of the slow speed of electronic devices.

In addition to new physical concepts, novel technologies must also be developed to meet the challenges at these high frequencies. Conventional mechanically machined horn antennas integrated with waveguide cavities have been the workhorse at microwave and millimeter-wave frequencies since they were first implemented more than 50 years ago during World War II. Very high antenna gain and essentially perfect antenna efficiency can be achieved using these structures. However, they are expensive, bulky, and incompatible with arrays. In order to overcome these problems, there have been new developments in micromachining to fabricate the horn antenna structures. In these structures, the active elements and their planar antennas are fabricated on a free-standing thin (~ 1 micron) SiN membrane, which is suspended over a silicon pyramidal horn that is formed by anisotropic etching, or micromachining. The side walls of this micromachined structure can then be coated with Au to form a horn antenna. Compared to conventional waveguide horn antennas, this novel micromachined structure has several major advantages. It is easier

to fabricate fine three-dimensional structures by using photolithography. Horn antennas with micron precision can be easily defined and inexpensively mass produced. It is made on Si or GaAs wafers and compatible with thin-film technology. Thus, active elements, such as RF and IF amplifiers, mixers and video detectors, local oscillators, and post-detection signal processors, can be integrated monolithically with the antenna structures to form monolithic transmitter/receiver systems. It is lightweight and compact. The most attractive feature of the micromachined structure is that focal-plane arrays can be fabricated easily on a single wafer, as illustrated in figure 1b. Such systems will yield a significantly improved spatial resolution in remote sensing, and a much greater antenna gain when implemented with phased-arrays.

In our group, we are systematically investigating physical and engineering issues that are relevant to high-frequency and high-speed devices. Specifically, we are working on micromachined millimeter- and submillimeter-wave devices, far-infrared and picosecond time-resolved transport studies of lateral quantum-effect devices, and development of far-infrared lasers, photodetectors, and optical parametric amplifiers using multiple quantum-well structures.

3.2 Micromachined Millimeter-wave Devices

Sponsors

Advanced Research Projects Agency
Contract MDA972-90-C-0021
National Aeronautics and Space Administration
Grant NAG2-693
Contract 959705

Project Staff

Gerhard de Lange, Brian R. Jacobson, Arifur Rahman, Professor Qing Hu, in collaboration with Dr. Rich Ralston and Group 86 at MIT Lincoln Laboratory

3.2.1 Micromachined Millimeter-wave SIS Receivers

SIS (superconductor-insulator-superconductor) heterodyne receivers have been demonstrated to be the most sensitive receivers throughout 30-840 GHz frequency range. The challenge now in the SIS receiver technology is to extend their operating frequency into the THz range and to develop focal-plane arrays in order to improve the efficiency of

data acquisition. To achieve these goals, we are currently developing a novel scheme to couple the millimeter-wave and infrared signals to the superconducting devices by using a micromachined horn antenna and a planar antenna supported by a thin (~ 1 micron) membrane, as shown in figure 1a. As stated in the introduction, this novel micromachined antenna structure can be produced with a high precision using photolithography, and it can be utilized in focal-plane arrays, as shown in figure 1b.

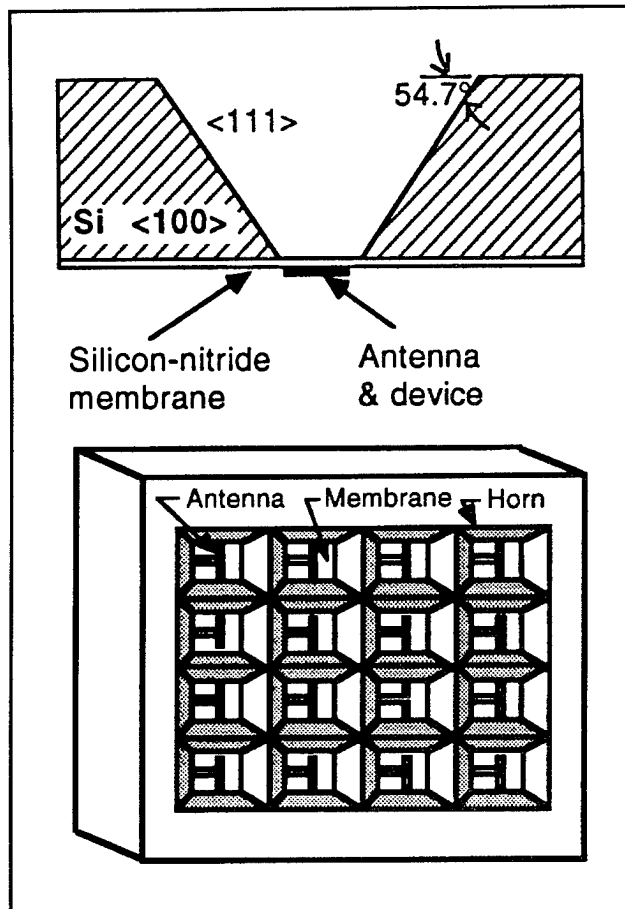


Figure 1. (a) Example of a micromachined horn antenna structure that is made by anisotropically etching a $<100>$ silicon wafer; (b) Schematic of a focal-plane array on a single wafer made using micromachining.

Following our initial success in fabricating high-quality high-current-density SIS junctions on free-standing SiN membranes, we have further improved our micromachining techniques for whole-wafer fabrication, higher yield, and better quality side walls that are critical for the antenna performance. Recently, we have constructed and tested a W-band (75-110 GHz) micromachined SIS receiver. Figure 2 shows the pumped and unpumped I-V characteristics of an SIS receiver in a micromachined antenna structure. It also shows the response to a hot (the curved marked as 300 K)

and a cold (at 77 K) blackbody radiator at the intermediate frequency (IF). The 4-dB difference between the two curves corresponds to a double-sideband (DSB) receiver noise temperature of 70 K (without any corrections). By using SIS junctions with higher current densities or by using integrated tuning elements to tune out the junction capacitance at the operating frequencies, we are confident that we can reduce the noise temperature by at least another factor of two, which will be comparable to the best results achieved from conventional waveguide SIS receivers.

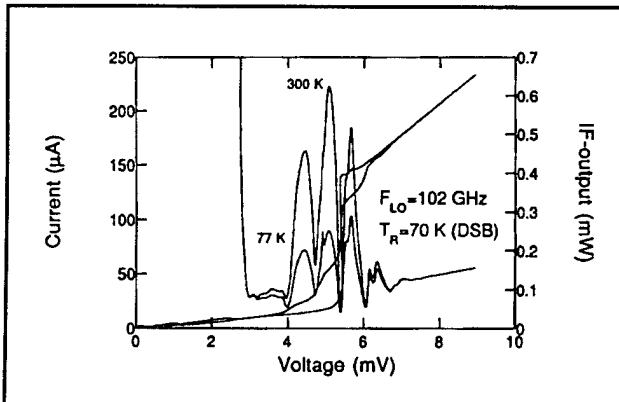


Figure 2. Pumped and unpumped I-V characteristics of an SIS device in a micromachined antenna structure. The curve marked 300 K corresponds to the IF response when a hot (300 K) blackbody radiator is placed in front of the receiver, while the curve marked 77 K is with a cold load.

We have measured the mixer performance over the whole W-band (75-110 GHz). The lowest noise temperature occurs at 102 GHz (the system was designed for 95 GHz), and the 3-dB bandwidth is approximately 15 percent, which is comparable to those of fix-tuned waveguide receivers. This achievement has given us confidence that the micromachined antenna structure is a competitive alternative to the conventional waveguide systems.

3.2.2 Micromachined Room-temperature Millimeter-wave Sensors

Due to a millimeter-wave's (especially around the 94-GHz atmospheric window) great penetration in foggy, dusty, and smoky environments, and to its much better spatial resolutions compared to the longer wavelengths at microwave frequencies, sensitive room-temperature millimeter-wave devices are very useful in imaging and object identification and tracking. They are important for both military and commercial applications, such as motor vehicle col-

lision avoidance radars. Based on our recent remarkable success in the development of micro-machined SIS receivers, we are currently developing the most sensitive room-temperature millimeter-wave sensors using the micromachining technology.

We plan to use microbolometers (whose dimension is approximately several microns, as shown in figure 3) in our micromachined systems. Microbolometers are easy to make (in fact, they are much easier to make than the superconducting tunnel junctions in our current systems), robust, and sensitive. In addition, our micromachined millimeter-wave structure is ideal for bolometric detectors in such a way that the thin SiN membrane provides a natural thermal isolation that a sensitive bolometer requires.

The dominating noise source in bolometric detectors is the 1/f noise associate with the resistive element (which is usually made out of semimetal materials, such as Bi, to achieve a high resistance value for impedance matching). Recently, it was discovered in the field of superconducting electronics that a commonly used superconducting material, Nb, has an order of magnitude lower level of 1/f noise (at room-temperature) than Bi while still provides sufficiently high resistivity for impedance matching. Assume we operate the microbolometers above the 1/f noise frequency region and use low-noise on-chip amplifiers, the NEP (noise equivalent power) of the microbolometers is limited by the temperature fluctuation, i.e., the phonon noise. Using realistic parameters for thermal conductance, a room-temperature Nb microbolometer can achieve an NEP of $6 \times 10^{12} \text{ W}/(\text{Hz})^{1/2}$. This is more than one order of magnitude lower than that of pyroelectric detectors, which are the commonly used room-temperature millimeter-wave sensors. This level of reduction in NEP will significantly improve the sensitivity of the detectors and reduce the required integration time by at least a factor of one hundred for the same signal/noise ratio.

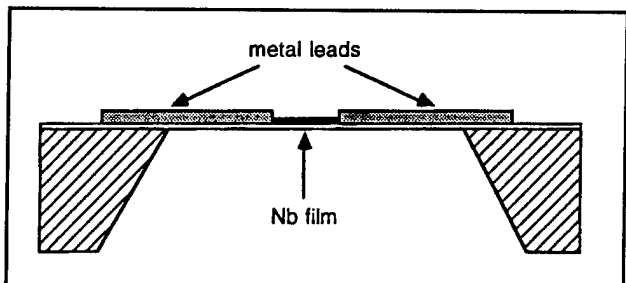


Figure 3. Schematic of a microbolometer supported by a thin membrane, which provides a good thermal insulation.

3.3 Far-infrared and Picosecond Time-resolved Transport Studies of Quantum-effect Devices

3.3.1 Far-infrared Studies of Antenna-coupled Quantum Point Contacts

Sponsor

National Science Foundation/MRSEC
Grant DMR 94-00334

Project Staff

Rolf A. Wyss, Professor Qing Hu, in collaboration with Professor Jesús A. del Alamo, Dr. Michael R. Melloch,¹ Michael J. Rooks²

Quantum transport has been one of the most active fields in solid-state physics in recent years. Advances in material preparation have made quantum phenomena profound in electron transport for many semiconductor quantum devices such as quantum point contacts, quantum dots, quantum wires, quantum wells, superlattices, etc. In clean samples and at low temperatures, electrons can travel through the whole sample without suffering phase-destructive scattering. Extensive work has been done to study various features of such phase-coherent quantum transport. However, most of the experiments reported so far are limited to dc transport measurements and far-infrared spectroscopy measurements.

It is well known in the field of superconducting tunneling that photons can assist the tunneling process, provided the tunneling is elastic. In a broad sense, elastic tunneling is a phase-coherent quantum transport process in a classically forbidden region. Therefore, all the results of photon-assisted tunneling can be applied to the study of photon-assisted quantum transport in semiconductor devices. This will provide a new dimension to study the exciting quantum transport phenomena. Novel long-wavelength optoelectronic devices may also emerge from this research.

In this project, we intend to study the interaction between far-infrared photons and ballistic electrons in quantum point contact devices, whose schematic is shown in figure 4a.

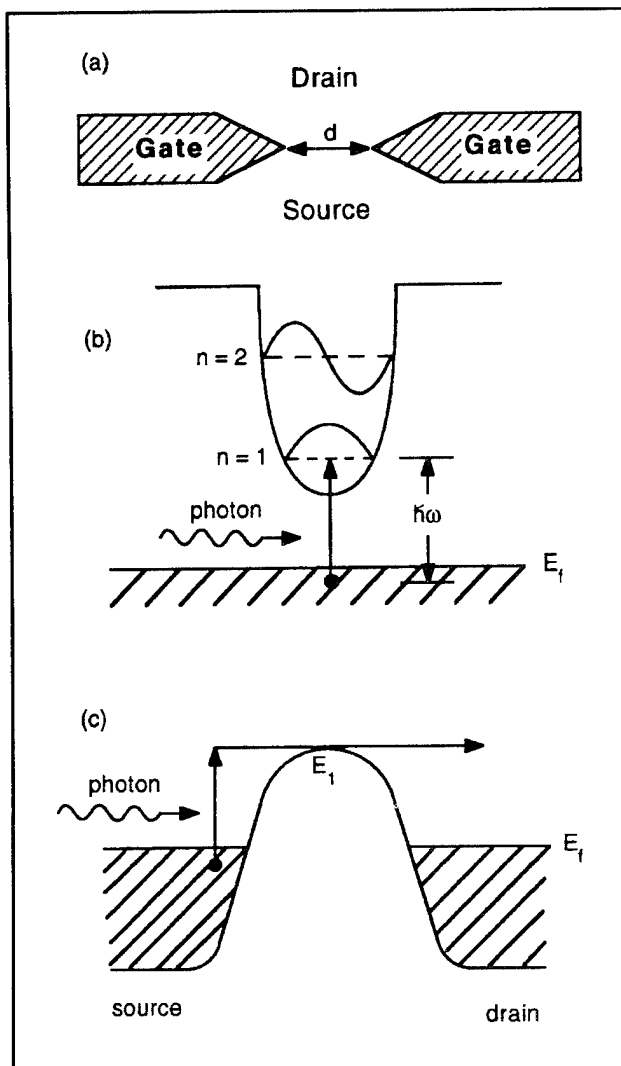


Figure 4. (a) Schematic of a quantum point contact. (b) and (c) Illustration of photon-assisted over-the-barrier quantum transport.

We have fabricated several antenna-coupled quantum point contact devices using a combination of optical and electron-beam lithography. The dc transport measurement of the drain/source transport showed high quality of the devices. Under coherent far-infrared radiation at 285 GHz, a pronounced photon-induced drain/source current is produced throughout the gate voltage range in which the device exhibits the behavior of a one-dimensional electron system. This photon-induced current is attributed to a bolometric effect as described in the previous report.

¹ Purdue University, West Lafayette, Indiana.

² Cornell National Nanofabrication Facility, Ithaca, New York.

In addition to the photoconductive effect, we have recently discovered a pronounced photovoltaic effect in several antenna-coupled quantum point contacts irradiated from 280 GHz to 2.5 THz. Figure 5a shows the drain/source current of an irradiated quantum point contact without external drain/source bias. This induced current tracks the subband structure in a very regular manner that is similar to the transconductance of the device measured without radiation. We have identified this photovoltaic effect as a result of thermopower due to an asymmetric heating of the source and drain. This analysis is supported by an experimental evidence that by shifting the focal spot of the radiation, we can reverse the polarity of the photon-induced current, as shown in figure 5b.

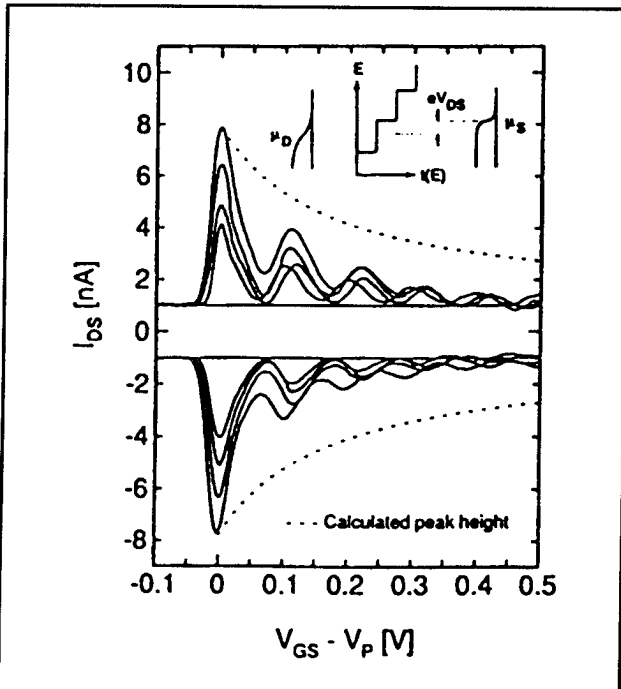


Figure 5. Measured photocurrents (at zero bias voltage) at different radiation power levels. (a) Positive currents correspond to beaming toward the source region, while (b) negative currents correspond to beaming toward the drain region.

By comparing the measured thermopower signals with theoretical predictions based on ballistic transport in one-dimensional systems, we have discovered that it is essential to include the electronic thermal conductance between the source and drain in order to account for the rapid decrease of the thermopower signals at higher subbands. The measured and calculated results (including this

thermal conductance) are plotted in figure 6, which shows an excellent agreement.

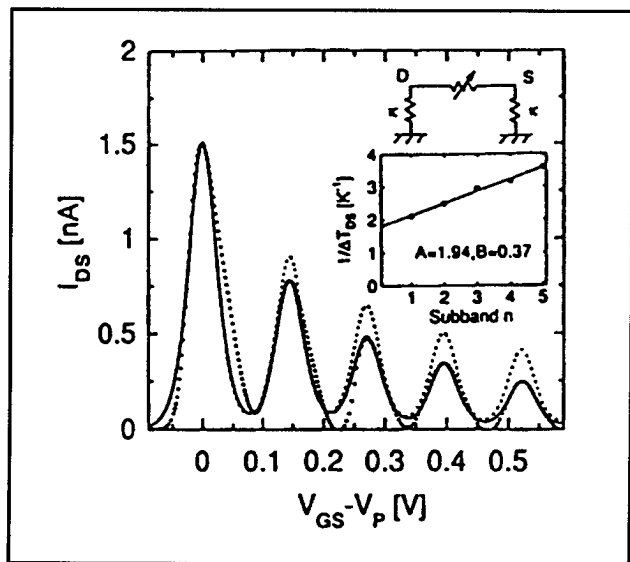


Figure 6. Radiation-induced thermal current versus gate voltage (•) shown together with calculated curves including the drain/source thermal conductance illustrated in the inset (—), and excluding that conductance (....). The inset shows the deduced temperature difference between the drain and source at different subband thresholds.

3.3.2 Direct Simulation of Photon-assisted Transport

Sponsor

National Science Foundation/MRSEC
Grant DMR 94-00334

Project Staff

Professor Qing Hu, in collaboration with Kou Yakubo,³ Shechao Feng³

We have proposed and theoretically investigated photon-assisted transport in quantum point contact devices. In essence, the process of photon-assisted transport is strictly analogous to the photoemission phenomenon in metals, which intrigued Einstein to propose the famous $E = \hbar\omega$ relationship. Following this analogy, we should expect an irradiated quantum point contact to exhibit photon-induced steps in the I_{DS} - V_{GS} curves, with the step width proportional to the photon energy. In spite of the intuitively plausible picture and the straightforward

³ University of California at Los Angeles, Los Angeles, California.

analogy with the photoemission phenomenon, experimental investigations have failed to provide evidence for photon-assisted transport. We have carried out extensive measurements over a broad frequency range from 90 GHz to 2.5 THz (corresponding to $\hbar\omega = 0.3 - 10$ meV), with the radiation electric field polarization both along and perpendicular to the drain/source conductance path, which have yielded nothing but bolometric signals. It is natural to ask why such a simple process (which is analogous to so many well-established phenomena, such as photoemission in metals, photo-ionization of atoms, photon-excited bound-to-extended-state transitions in quantum-well structures, and photon-assisted tunneling in superconducting tunnel junctions) has not been observed in quantum-point-contact devices.

In this work, we solve time-dependent Schrödinger's equation numerically in order to investigate what conditions could produce a pronounced effect of photon-assisted transport. Our main finding is that the selection rule, which is the mathematical statement of the momentum conservation of the electron/photon systems, determines whether the electron transport is adiabatic or photon-excited. Mathematically, to achieve an appreciable photon-excited transition probability, the dipole-moment integration must be truncated to a region that is not much greater than the coherence length $1/\Delta k$, where Δk is equal to the momentum difference between the electrons before and after photon absorption/emission. This truncation can be achieved experimentally by either a localized electron state or a localized photon-field profile. Physically, this spatial localization of the electron or photon field provides the momentum spread that is necessary for the momentum conservation in the photon excitation process. Figure 7a shows a wave function (in k -space) in the presence of an ac field. The main peak at $k = 0$ corresponds to the wave function in a free space without radiation. The satellite peaks correspond to photon absorptions. Figure 7b shows the amplitudes of these peaks as functions of the ac-field spatial width. Clearly, photon-excitation process decreases dramatically as the ac-field spatial confinement loosens.

Our simulation study indicates that the selection rule requires a spatially confined ac field if the photon-excited transition is between two extended electronic states, such as the case for quantum-point-contact devices. This can be achieved by bringing the antenna terminals very close to the central region. Photon excitation can also be

achieved by using double- or multiple-barrier structures to create quasibound electronic states. The spatially localized nature of these quasibound states provide the momentum change for the photon-assisted process. This understanding has been demonstrated experimentally in the observations of photon-assisted tunneling in quantum dots and photon-assisted transport in dual-gate devices.

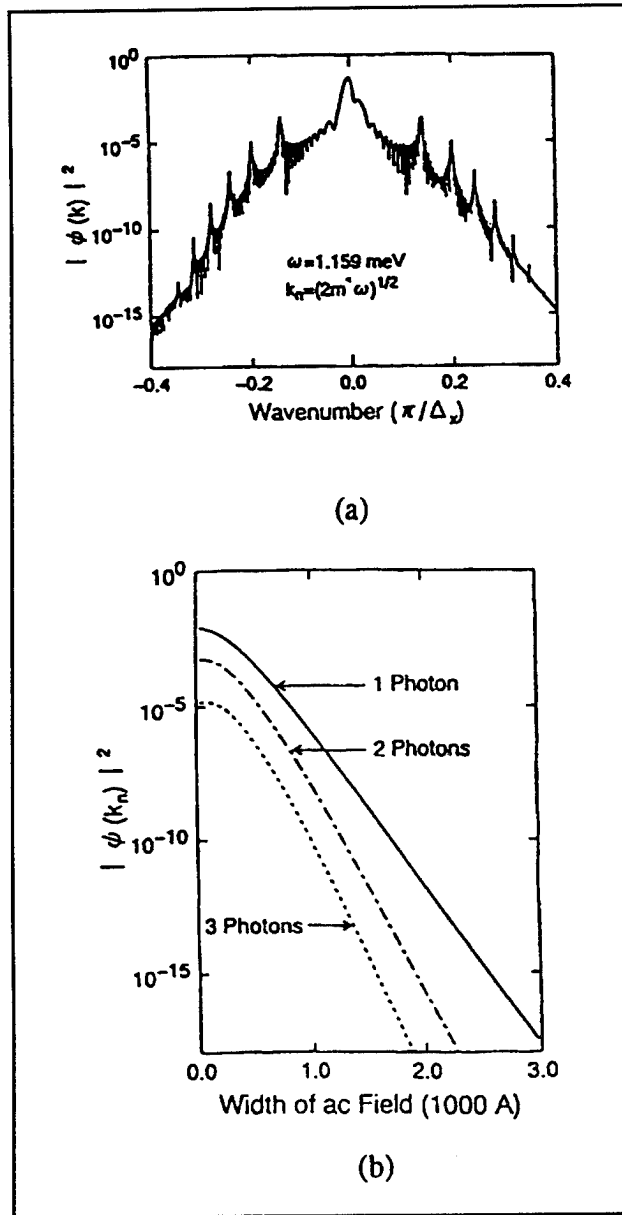


Figure 7. (a) Square of a wave function of free electrons (in k -space) under the irradiation of an ac field. The satellite peaks correspond to photon absorption (on the right of the main peak) and emission (on the left). (b) Values of photon-excited states as functions of the width of the ac field.

3.3.3 Photon-assisted Transport in Lateral Dual-gate Devices

Sponsors

MIT Lincoln Laboratory
 Advanced Concept Program
 Contract BX-5464
 MIT Research Laboratory of Electronics
 Postdoctoral Fellowship
 National Science Foundation/MRSEC
 Grant DMR 94-00334

Project Staff

Dr. Simon Verghese, Rolf A. Wyss, Dr. Thomas Schäpers

As our direct simulation study of photon-assisted transport indicates, photon absorption requires a momentum transfer of $\Delta k \sim m^* \omega / \hbar k$, for an electron of mass m^* with a wavevector $\sim k_i$ to absorb a photon with $k \sim 0$. This momentum transfer can be achieved either by localizing the photon field to within the coherence length $1/\Delta k$, or by localizing the electron wavefunctions. The devices described here supplies Δk by mainly localizing the electron wavefunction in one dimension that is parallel to the photon's polarization. Similar scheme has been successfully implemented in infrared ($\lambda \sim 10\mu\text{m}$) photon detectors using vertically grown quantum-well structures. These devices absorb photons when a 1D-localized electrons in a bound state is excited into the continuum. To maintain a steady-state operation, the depleted electrons in the quantum wells are supplied by thermionic electrons from the emitter over the barriers. In our case, the depleted electrons are supplied by tunneling injection from the source. Consequently, the eigenstates are quasibound states with lifetimes much greater than the modulation period of the ac field.

An SEM picture of an antenna-coupled dual-gate device is shown in figure 8, along with a side view of the device, a self-consistently calculated dc potential profile in the drain/source direction, and the transmission coefficient $T(\epsilon)$ through such a structure. The peaks in the transmission coefficient correspond to the energy levels of the quasibound states, while the peak widths correspond to their lifetimes. In the presence of an ac field, photon-assisted transport (due to quasibound state to con-

tinuum transitions) can be modeled by an effective transmission coefficient $T_{\omega}(\epsilon)$, whose main peaks correspond to the original $T(\epsilon)$ and the sidebands correspond to photon absorption or emission, as shown in figure 9a. Photon-induced current can be calculated in this model by taking the difference between the current calculated using $T_{\omega}(\epsilon)$ and $T(\epsilon)$.

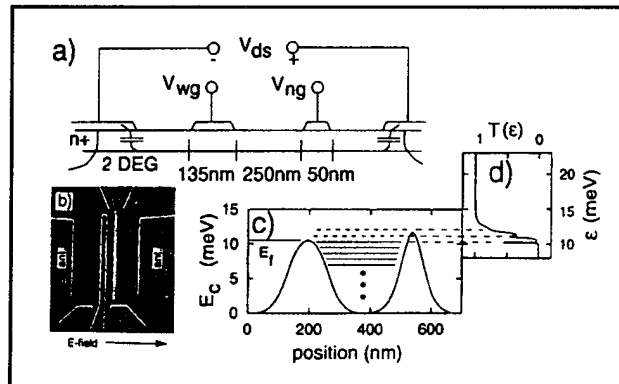


Figure 8. (a) Side view of a dual-gate device. (b) SEM picture of the device. (c) Self-consistently calculated dc potential profile for the device. (d) Transmission coefficient as a function of the energy.

Figures 9b and 9c show the measured radiation-induced current as functions of the drain/source bias voltage V_{ds} (curves labeled (i)). The two sets of curves are taken with radiation frequencies at 90 GHz (in 9b) and 270 GHz (in 9c). The radiation power level at both frequencies is approximately the same. It is clear that the two sets of curves exhibit distinctively different features at the two radiation frequencies. The ones at 90 GHz show much sharper modulations of the radiation-induced current, while the ones at 270 GHz have much smoother features, which is due to the overlap of photon subbands at this high frequency, as illustrated in figure 9a. This frequency-dependent feature is the strongest evidence that the radiation-induced current is a photonic effect that depends on the energy of an individual photon. The curves labeled (ii) in figure 9b and 9c are calculated photocurrent based on the model of photon-assisted transport. They agree with the experimental results quite well. In comparison, the calculated radiation-induced current based on a bolometric model (labeled (iv)) is frequency independent and cannot explain the experimental results taken at 270 GHz.

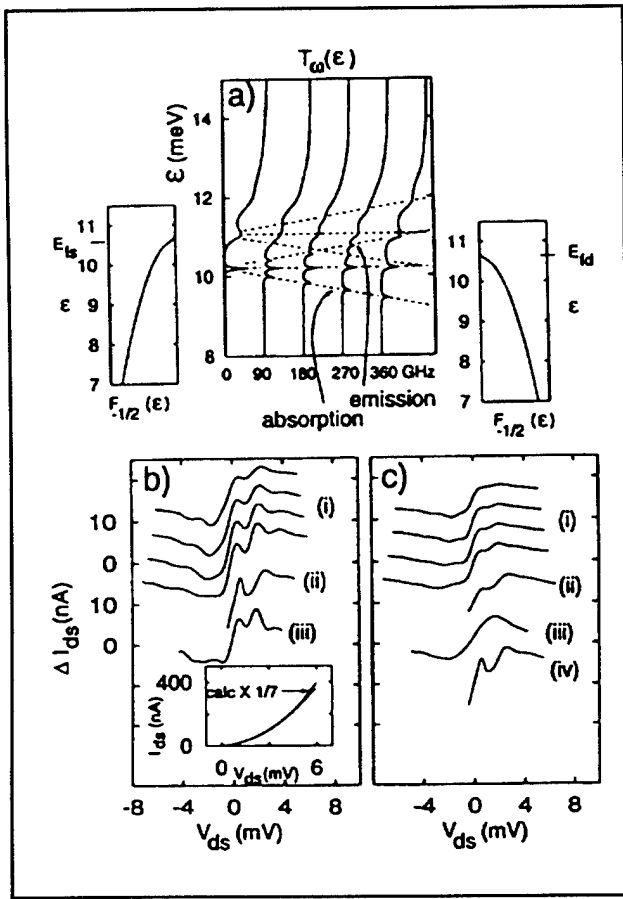


Figure 9. (a) Effective transmission coefficient that includes the effect of photon absorptions and emissions. (b) and (c) Curves (i): measured radiation-induced current at 90 GHz (b) and 270 GHz (c). Curves (ii): calculated radiation-induced current based on the model of photon-assisted transport. Curve (iv): calculated radiation-induced current based on heating model.

3.3.4 Subpicosecond Dynamical Studies of Quantum-effect Devices

Sponsors

MIT Lincoln Laboratory
Advanced Concept Program
Contract BX-5464
National Science Foundation/MRSEC
Grant DMR 94-00334

Project Staff

Dr. Simon Verghese, Noah D. Zamdmer, Professor Qing Hu, in collaboration with Dr. Elliot Brown,⁴ Dr. Michael R. Melloch⁵

The modern solid-state physics and electrical engineering communities are witnessing a trend where electronic devices are becoming smaller and speeds are becoming faster. This is driven by modern society's insatiable appetite for the increased capacity of information processing and transmission. As a result, the smallest feature size of state-of-the-art devices has reached several hundred angstroms. At this length scale, the intersubband spacing and the Coulomb interaction energy are in the millielectrovolt range, corresponding to THz frequencies. In a related project (see previous sections), we have studied transport properties of antenna-coupled quantum-effect devices under coherent far-infrared radiation whose frequencies are comparable to the intersubband spacing. In this project, we are carrying out transport studies in time domain by using subpicosecond electrical pulses generated by Auston switches to study the dynamical processes of electrons in quantum-effect structures.

Although our work in frequency domain has yielded new information about quantum-effect devices, a complementary approach is to study the response of the quantum devices in time-resolved fashion by using a pump-and-probe method with a pulsed laser. A 100-fs laser pulse contains frequency components up to 10 THz, which should enable us to perform spectroscopic studies on quantum devices over a broad frequency range that covers all the interesting energy levels, namely the intersubband transition and Coulomb interaction energies. Furthermore (and perhaps the most attractive feature of the time-domain studies), the time-resolved studies can reveal information that frequency-domain studies cannot reveal, namely the time scale of transport process in quantum devices. This is one of the basic issues in determining the potential applications of the quantum devices.

We are pursuing two types of measurements in this project. The first one involves a far-infrared spectrometer pumped by a mode-locked Ti:Sapphire laser which we have constructed recently, as shown in figure 10. In this set up, two antenna-coupled Auston switches are pumped by a Ti:Al₂O₃ pulsed laser. The THz electrical pulses are

⁴ MIT Lincoln Laboratory, Lexington, Massachusetts.

⁵ Purdue University, West Lafayette, Indiana.

launched into free space and then combined by a beam splitter. The combined beam is a superposition of two coherent subpicosecond electrical pulses whose relative time delay can be varied. These combined pulses will then be focused onto an antenna-coupled quantum device and generate a dc electrical current in the device through the photon-assisted transport/tunneling process. Effectively, the generated electrical current is proportional to the time autocorrelation function of the whole system, whose Fourier transform will give the frequency response of the system. This measure-

ment is essentially the same as that using a conventional far-infrared Fourier transform spectrometer (FTS), which uses a Hg-arc lamp as its source. There are several major advantages of the pulsed laser system, however. First, its source is much brighter than that of the FTS so that far-infrared nonlinear spectroscopy can be performed. Second, the short duration of the laser pulses minimizes the heating effect and thus enhances the relative strength of the photon-assisted quantum process.

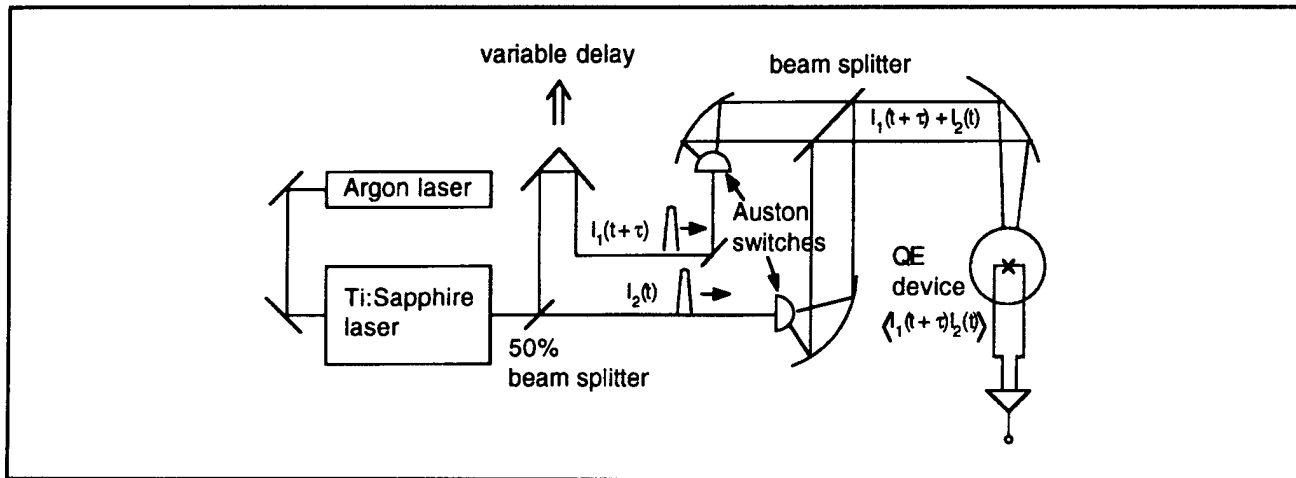


Figure 10. Schematic of an interferometer pumped by a pulsed Ti:Sapphire laser.

The second type of experiment involves a pump-and-probe method, by integrating two Auston switches monolithically with the quantum-effect devices, as shown in figure 11. One switch will be used to apply a short electric pulse on the input, and the second one will be used to probe the output electrical current in a time-resolved fashion. This scheme differs from the first one in that the pump and probe beams are focused on different

spots. In this way, we can measure the time scale of the transport process from the input to the output, as well as the spectroscopic information of the system. In order to achieve a high speed from the Auston switches, lattice-matched low-temperature-grown (LTG) GaAs materials will be used which have subpicosecond recombination time.

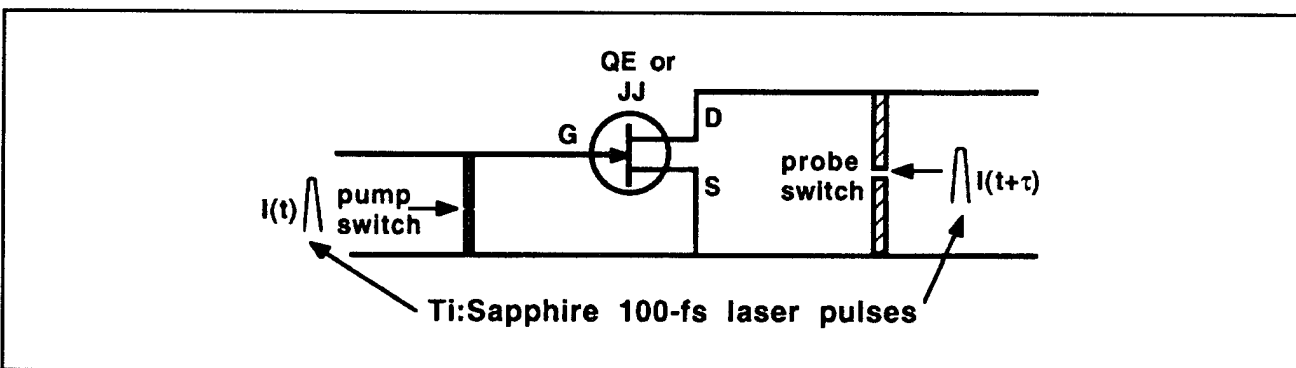


Figure 11. Schematic of a three-terminal (QE or Josephson) device pumped by a subpicosecond electrical pulse at the input, and the induced output current can be time-resolved by another time-delayed probe beam.

3.4 Intersubband Transitions in Coupled Double Quantum-well (DQW) Structures

Coupled DQWs are simply voltage tunable two-level or multi-level systems. Therefore, under specific bias conditions for carefully designed and fabricated DQWs, the devices can generate far-infrared radiation (when the initial state is higher than the final state), detect far-infrared radiation (when the initial state is lower than the final state), or perform nonlinear optical functions such as parametric amplifications.

3.4.1 Far-infrared Lasers and Detectors Using DQW Structures

Sponsors

Rome Air Force Laboratory
Graduate Fellowship
U.S. Army Research Office
Grant DAAL03-92-G-0251

Project Staff

James Ernstmeyer, Bin Xu, Jurgen H. Smet, Professor Qing Hu, in collaboration with Dr. Michael R. Melloch⁶

The schematic of a single DQW structure is shown in figure 12a. The conduction band profile, subband structures, and carrier densities are calculated self-consistently from Schrödinger and Poisson equations, after typical five iterations. Figure 12b shows the transmission coefficient through such a structure, whose peaks correspond to the subband

levels in (a). Clearly, the intersubband energy difference $E_2 - E_1$ (corresponding to the radiation frequency) can be tuned by a bias voltage between the emitter and collector. The most important parameter that determines the radiation properties (due to the $1 \rightarrow 2$ intersubband transition) of this DQW structure is the dipole moment $\langle 1|z|2 \rangle$, or equivalently, the oscillator strength f_{12} , which is the ratio of the quantum mechanical radiative decay rate over that of a classical Hertzian dipole at the same frequency.

By using a tight-binding model to calculate the eigenenergy levels of the coupled DQW device, we can obtain the expression for the energy of the two lowest levels,

$$E_{2,1} = E_0 \pm \sqrt{(\Delta_0/2)^2 + (eV/2)^2},$$

where the field-induced energy splitting $\Delta = |E_2 - E_1| = \sqrt{(\Delta_0)^2 + (eV)^2}$. Δ as a function of the bias voltage V is shown in figure 13. The energy splitting takes the minimum value Δ_0 at the anti-crossing point, above which the energy of the state that is mainly localized in the left well becomes higher than that of the state that is mainly localized in the right well. Since the state mainly localized in the left well couples strongly to the emitter (which always has a higher Fermi energy than the collector), and is therefore the initial state that is filled with electrons, figure 13 indicates that the relative energy difference between the initial and final states (not only the amplitude but also the sign) can be tuned by the bias voltage. Consequently, the same DQW structure can be used as both a detector and an emitter. As a detector, the initial state lies below the final one; while as an emitter, the initial state lies above the final one.

⁶ Purdue University, West Lafayette, Indiana.

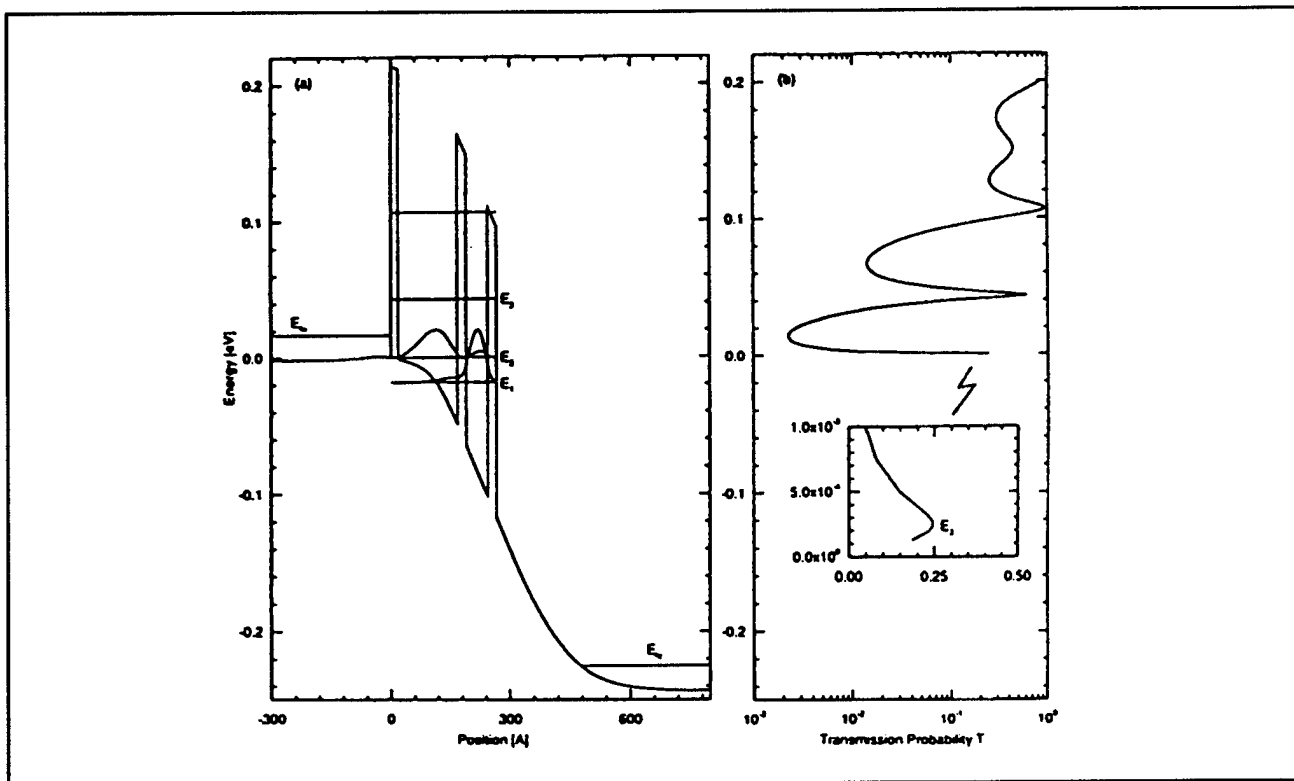


Figure 12. (a) Conduction band profile and the square of wavefunctions at a bias voltage of 240 mV for a typical DQW structure. The wider emitter well (on the left) is to ensure that a large carrier density can be achieved at a desired intersubband spacing $E_2 - E_1$. (b) Transmission coefficient $T(E)$ as a function of the electron incident energy. The peak positions in $T(E)$ correspond to the subband levels in (a). The resonance widths in $T(E)$ determine the escape lifetimes.

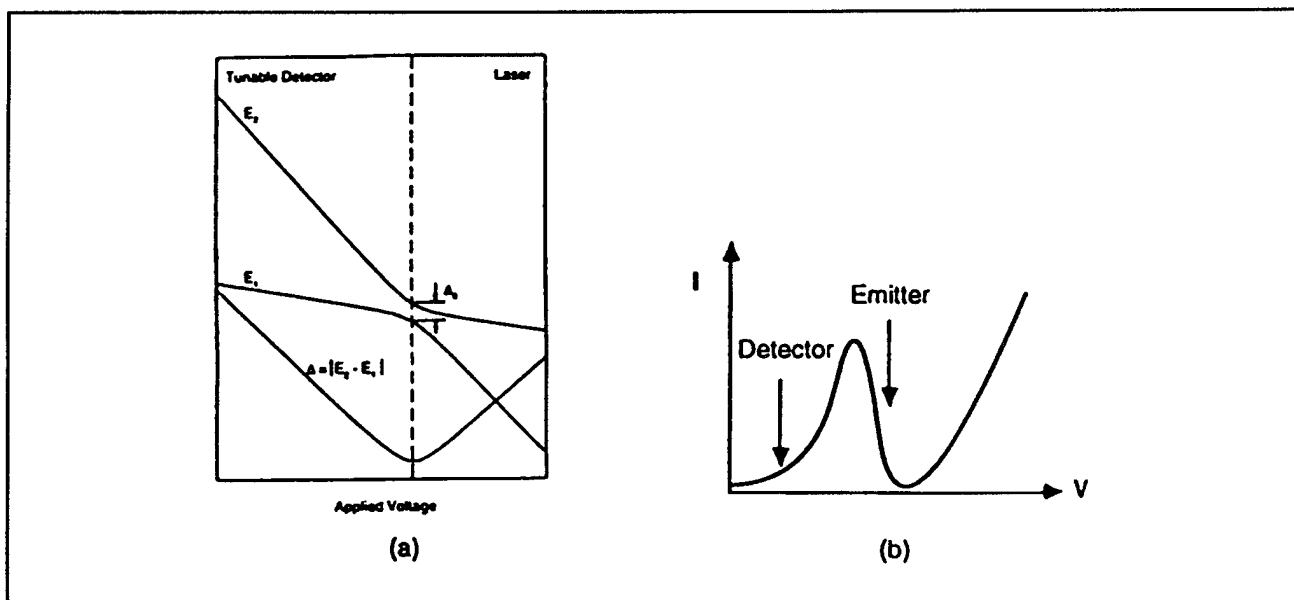


Figure 13. Left: Energy level diagram as a function of applied voltage, which exhibits an anticrossing with a gap Δ_0 . At low voltages the device can be used as a tunable detector, as indicated in the figure on the right, and beyond the anticrossing it functions as a field-tunable emitter.

We have performed a thorough analysis on the radiation properties of the coupled DQW structures. In figure 14, the oscillator strength, which is mainly determined by the dipole moment between the two states, is plotted as a function of the photon energy. Clearly, for experimentally achievable values of the anticrossing gap, for example, $\Delta_0 = 4$ meV (corresponding to a 20-Å thick Al_{0.24}Ga_{0.76}As middle barrier in the GaAs/AlGaAs DQW structures), the oscillator strength is close to 0.2, making the DQW an efficient radiator. Using the free-carrier plasmas in a heavily doped emitter and collector for mode confinement, we have calculated the required inverted population density Δn at

the lasing threshold, which are plotted in figure 14 for different values of Δ_0 . It appears that $\Delta n \sim 10^{13}/\text{cm}^2$ in the THz frequency range for $\Delta_0 = 4$ meV. But using many identical DQW modules connected in series, we can reduce this threshold density by a factor of N , which is the number of modules. Using 100 DQW modules, the threshold carrier density will be approximately $10^{11}/\text{cm}^2$. At this density, the dominating nonradiative relaxation mechanism is electron-electron scattering, which is estimated to have a relaxation time on the order of 20 picoseconds. Consequently, lasing threshold can be reached at $e\Delta n/\tau \sim 1\text{kA}/\text{cm}^2$ current density, which is quite feasible.

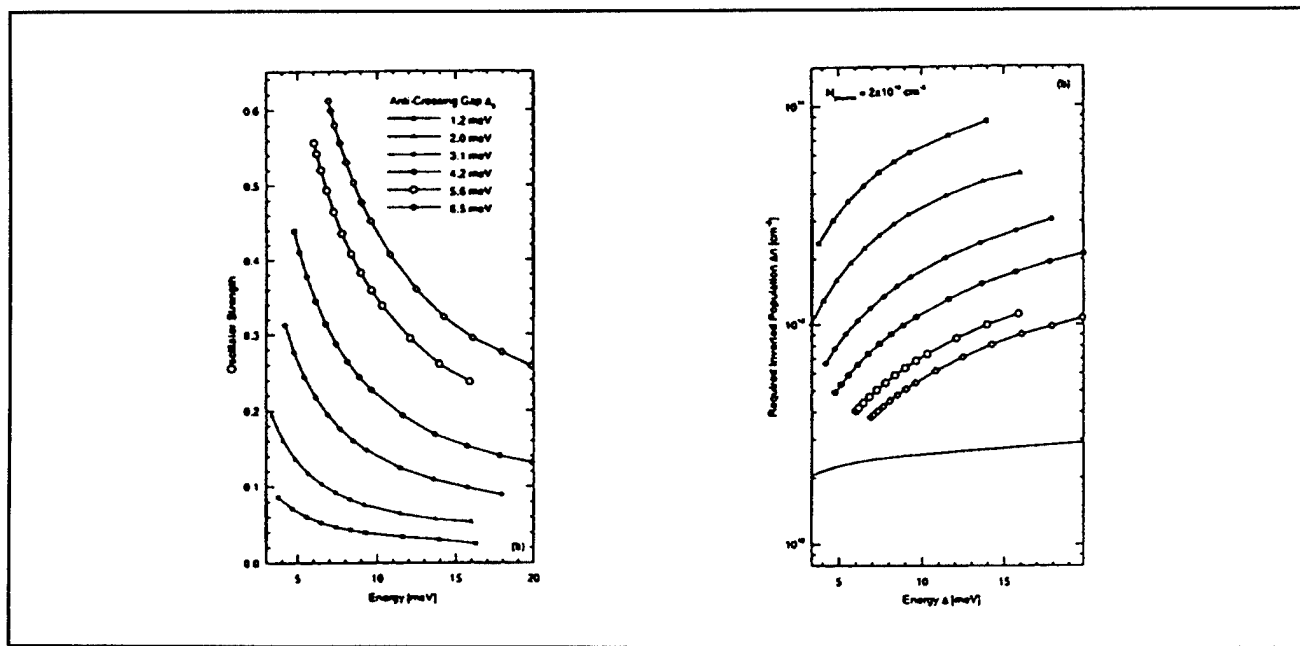


Figure 14. Left: Oscillator strengths for the intersubband transition as a function of the photon energy and with the anticrossing gap as a parameter. Right: Threshold inverted population density required to overcome plasma confinement losses.

3.4.2 Magnetotunneling Spectroscopy of DQW Structures

Sponsor

U.S. Army Research Office
Grant DAAL03-92-G-0251

Project Staff

Jurgen H. Smet, Professor Qing Hu, in collaboration with Professor Clifton G. Fonstad, Jr.

One of the major difficulties in achieving far-infrared lasing in DQW devices is the fast nonradiative relaxation rate (~ 20 picosecond) compared to the slow radiative relaxation process (~ 1 microsecond). The nonradiative relaxation processes are

so fast because the subbands in a quantum well have continuum states for all the possible transverse momentum values (perpendicular to the growth direction), instead of discrete energy levels. Thus, the conservation of energy and transverse momentum can be simultaneously satisfied for these processes. Similar to the concept employed to confine plasmas in a tokamak, several groups have proposed the use of magnetic fields to reduce the dimensionality of the electron system in order to suppress nonradiative relaxation processes. Under a strong field along the growth direction, the transverse motion of electrons will be confined in cyclotron orbits and their energy spectrum will be quantized at Landau levels. This magnetic field-induced transverse confinement, along with the longitudinal confinement provided by the quantum-well structures, will effectively reduce the dimensionality

of the electron system to that of a zero-dimensional system, similar to that of quantum-dot systems. Consequently, the detrimental nonradiative relaxation processes will be significantly reduced. In this scheme, the applied longitudinal magnetic field will not affect transport in that direction or the dipole moment associated with the transition between two subbands. Therefore, the field will not have any adverse effect on the radiative process, and thus will substantially increase the radiation efficiency $\eta = T_{\text{nonrad}}/T_{\text{spon}}$.

Motivated by the magnetic suppression effect, we have performed extensive tunneling studies of DQWs in strong magnetic fields with both a longitudinal and transverse component. This study, called *magnetotunneling spectroscopy*, is a very powerful spectroscopic tool to measure the subband levels and in-plane energy-momentum dispersion (crucial information for any intersubband devices) with much greater accuracy than a dc tunneling study alone would yield. In the previous report, we have shown current oscillations as a function of a longitudinal magnetic field. This magnetooscillation is analogous to de Haas-Shubnikov oscillation, whose period in $1/B$ gives accurate measurements of the intersubband energy levels. In this work, we have extended the magnetotunneling spectroscopy to include a transverse magnetic field.

Under a transverse or in-plane magnetic field (with the field perpendicular to the current-flow direction), as well as a longitudinal one, electrons will acquire momentum in the transverse direction while traversing the MQW structures. Thus, the conservation of transverse momentum is no longer valid. Consequently, the applied transverse field broadens the resonant peaks in the tunneling I-V characteristics, and shifts the position of the resonances to higher bias voltage, as shown in figure 15.

Using this method, we can perform spectroscopy in the I-V curve region, where it has a negative dynamic resistance (NDR) that otherwise would be inaccessible, due to the instability associated with the NDR. This information is crucial for laser operations, since the NDR region corresponds to the initial state with a higher energy than the final state, which is the normal operating condition for lasers. Figure 16 shows the I-V curve and the energy levels of a DQW device measured from magnetotunneling spectroscopy. The energy levels in the NDR region

(represented by the open circles) are measured with an in-plane magnetic field applied.

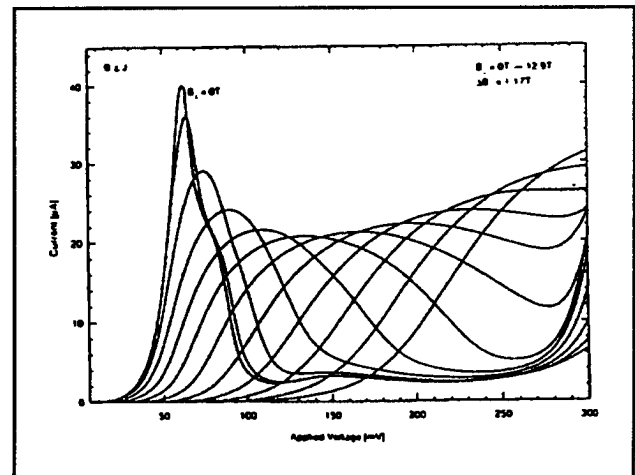


Figure 15. I-V tunneling characteristics near resonance of a DQW device with an in-plane field varying from 0 T to 12.9 T in steps of 1.17 T.

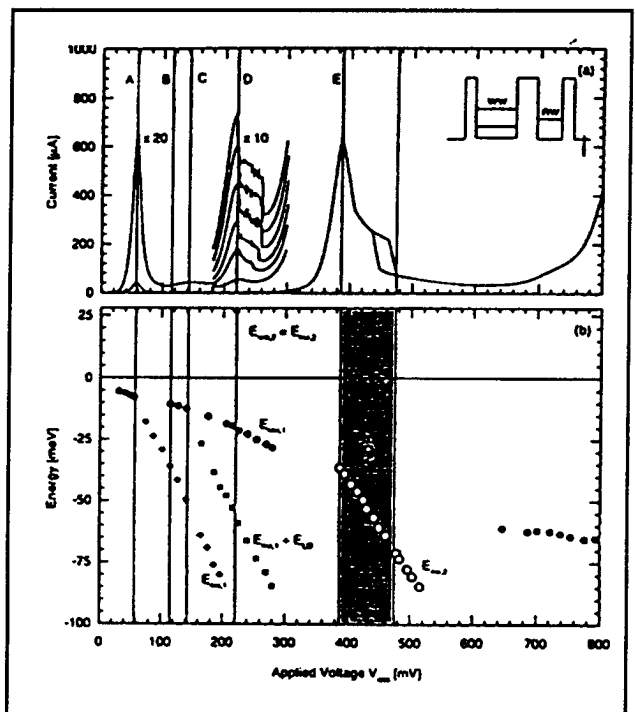


Figure 16. (a) I-V characteristic and (b) the subband energies as functions of the bias voltage at 4.2 K. The quasi-Fermi level in the emitter well is used as the energy reference (i.e., $E_{\text{FE}} = 0$). The open-circle data in the negative dynamic region (NDR) was obtained by applying an in-plane field to broaden the resonance peak.

3.4.3 Far-infrared Optical Parametric Amplifiers Using DQWs

Sponsors

Hertz Foundation Fellowship
U.S. Army Research Office/ASSERT
Grant DAADH04-94-G-0167

Project Staff

Ilya Lyubomirsky, Professor Qing Hu, in collaboration with Dr. Michael R. Melloch⁷

It is well known in the field of nonlinear optics that the nonlinear susceptibility $\chi^{(2)}$ is large near a reso-

nant frequency for a system that is lack of inversion symmetry. Such a large $\chi^{(2)}$ has been widely used in second harmonic generation, second frequency generation, and parametric amplification at optical and near-infrared frequencies, where coherent sources at pump frequencies are available. As far as its optical properties are concerned, a quantum-well device acts like a giant atom, whose resonant frequencies are in the mid- to far-infrared frequencies. Naturally, if we design a QW structure such that it has resonances at mid-infrared frequency ($\lambda \sim 10$ microns) and far-infrared frequencies, we can use widely available CO₂ lasers as a pump source to parametrically generate far-infrared radiations. This nonlinear photon conversion process is illustrated in figure 17a.

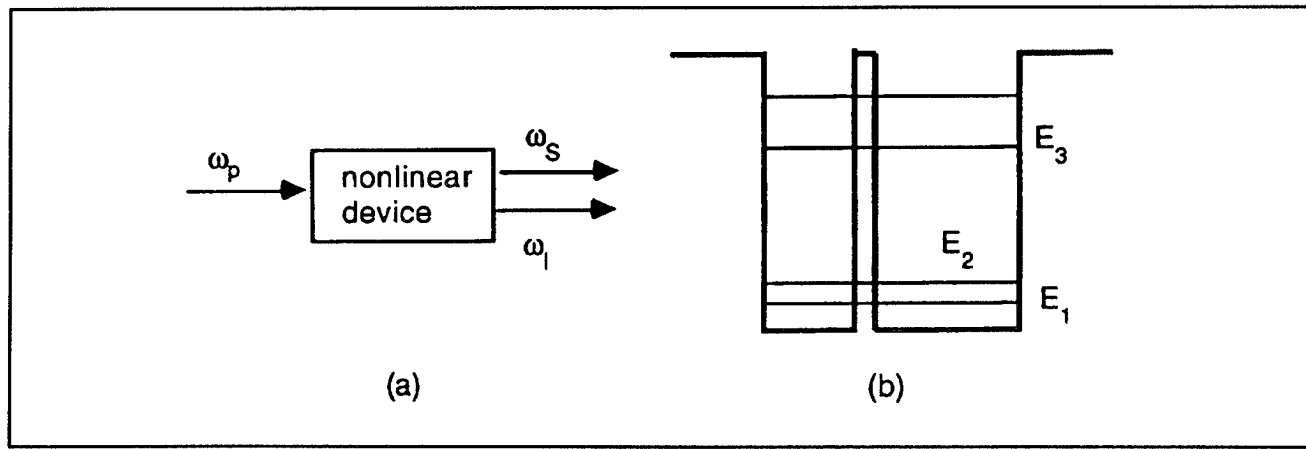


Figure 17. (a) Illustration of parametric amplification process, which converts a photon with a frequency ω_p into two photons with frequencies ω_i and ω_s , with $\omega_i + \omega_s = \omega_p$; (b) An asymmetric DQW structure that could produce a large $\chi^{(2)}$ at mid- and far-infrared frequencies.

However, a single quantum well has inversion symmetry, and therefore has a vanishing $\chi^{(2)}$. This problem can be solved easily by using a coupled DQW structure with an asymmetric well widths, as shown in figure 17b. In this structure, the energy differences between level 3 and level 1 and 2 are close to 120 meV (corresponding to a wavelength of 10 microns). These intersubband transition energies correspond to the pump and idler frequencies. The energy difference between level 1 and 2 is approximately 10 meV, corresponding to the far-infrared signal frequency. The nonlinear susceptibility $\chi^{(2)}$ is proportional to the product of three dipole moments, $\langle z_{12} \rangle \langle z_{13} \rangle \langle z_{23} \rangle$. By careful

designing, each dipole moment can be as large as several 10 Å, which is at least one order of magnitude larger than that for optical transitions in atomic systems. Using the doubly resonant structure shown in figure 17b, we estimate $\chi^{(2)}$ to be as large as 10^{-6} m/V, which is four orders of magnitude larger than the value for bulk GaAs materials. This extraordinarily large $\chi^{(2)}$ can be used for efficient parametric amplifications. The challenging issue of phase-matching can be solved by using Stark effect (changing the resonant conditions by applying a bias voltage) to diminish $\chi^{(2)}$ beyond the coherence length.

⁷ Purdue University, West Lafayette, Indiana.

3.4.4 Millimeter-wave, THz, and Subpicosecond Facilities

Professor Hu's laboratory is equipped with various millimeter-wave and infrared sources which can generate coherent and incoherent radiation from 75 GHz up to 30 THz. These include: Gunn oscillators at W-band frequencies (75-11 GHz); a frequency doubler, tripler, and quadrupler using Schottky diodes at 200, 300, and 400 GHz; an optically pumped far-infrared laser which generates coherent radiation from 245 GHz to 8 THz; and an infrared Fourier transform spectrometer which is capable in performing linear spectroscopy from 45 GHz to 30 THz and beyond. This laboratory is also equipped with various cryogenic millimeter-wave and infrared detectors. These include: Si composite bolometers InSb hot-electron bolometers, SIS (superconductor-insulator-superconductor) receivers, and high T_c Josephson detectors. Recently, with the support from AT&T, a mode-locked Ti:sapphire laser that can generate optical pulses as short as 70 femtosecond was purchased and installed.

3.5 Publications

3.5.1 Journal Articles

de Lange, G., B.R. Jacobson, and Q. Hu. "Micro-machined Millimeter-wave SIS Mixers." *IEEE Trans. Supercond.* Forthcoming.

Gupta, R., Q. Hu, D. Terpstra, G.J. Gerritsma, and H. Rogalla. "A Noise Study of a High-T_c Josephson Junction under Near-millimeter-wave Irradiation." *Appl. Phys. Lett.* 64: 927 (1994).

Hu, Q., R.A. Wyss, C.C. Eugster, J.A. del Alamo, and S. Feng. "Far-infrared Study of an Antenna-coupled Quantum Point Contact." In *Quantum Well Intersubband Transition Physics and Devices*. Eds. H.C. Liu, B.F. Levine, and J.Y. Andersson. Boston: Kluwer Academic, 1994, p. 553.

Smet, J.H., C.G. Fonstad, and Q. Hu. "Intrawell and Interwell Intersubband Transitions in Multiple Quantum Wells." Submitted to *J. Appl. Phys.*

Smet, J. H., C.G. Fonstad, and Q. Hu. "Magnetotunneling Spectroscopy with both In-plane and Longitudinal Fields." Submitted to *Phys. Rev. B*.

Verghese, S., R.A. Wyss, T. Schäpers, A. Förster, M.J. Rooks, and Q. Hu. "Photon-assisted Trans-

port through Quantized Energy States in a Lateral Dual-Gate Device." Submitted to *Phys. Rev. Lett.*

Wyss, R.A., C.C. Eugster, J.A. del Alamo, Q. Hu, M.J. Rooks, and M.R. Melloch. "Far-infrared Radiation-induced Thermopower in a Quantum Point Contact." *Appl. Phys. Lett.* 66: 1144 (1995).

Yakubo, K., S. Feng, and Q. Hu. "Direct Simulation of Photon-assisted Quantum Transport." Submitted to *Phys. Rev. B*

3.5.2 Conference Presentations

de Lange, G., B.R. Jacobson, and Q. Hu. "Micro-machined Millimeter-wave SIS Mixers." Presented at 1994 Applied Superconductivity Conference, Boston, Massachusetts, 1994.

Hu, Q., J.H. Smet, and C.G. Fonstad. "Terahertz Lasers Using Quantum-well Structures." Presented at the SPIE International Symposium, OE/LASE '94, Los Angeles, January 25, 1994. (invited)

Hu, Q., R. Gupta, D. Terpstra, G.J. Gerritsma, and H. Rogalla. "Response of High-T_c Ramp-type Josephson Junctions to Near-millimeter-wave Radiation." Presented at the SPIE International Symposium, OE/LASE '94, Los Angeles, January 26, 1994. (invited)

Schäpers, T., R.A. Wyss, Q. Hu, M. Krueger, A. Förster, A. van der Hecht, and H. Lueth. "Far-infrared Studies of Planar Resonant Tunneling Field Effect Transistors." Presented at the American Physical Society Meeting, Pittsburgh, Pennsylvania, 1994; *Bull. Amer. Phys. Soc.* 39: 352 (1994).

Verghese, S., R.A. Wyss, T. Schäpers, Q. Hu, E.R. Brown, K.A. McIntosh, and M.R. Melloch. "Broad-band Far-infrared Spectroscopy of Mesoscopic Devices." Presented at the American Physical Society Meeting, Pittsburgh, Pennsylvania, 1994; *Bull. Amer. Phys. Soc.* 39: 352 (1994).

Wyss, R.A., C.C. Eugster, J. del Alamo, Q. Hu, M.J. Rooks, and M.R. Melloch. "Far-infrared Radiation-induced Thermopower in an Antenna-coupled Quantum Point Contact." Presented at the American Physical Society Meeting, Pittsburgh, Pennsylvania, 1994; *Bull. Amer. Phys. Soc.* 39: 352 (1994).

3.5.3 Theses

Jacobson, B.R. *A Micromachined SIS Mixer.* S.M. thesis. Dept. of Electr. Eng. and Comput. Sci., MIT, 1994.

Smet, J.H. *Intrawell and Interwell Intersubband Transitions in Single and Multiple Quantum Well Heterostructures.* Ph.D. diss. Dept. of Electr. Eng. and Comput. Sci., MIT, 1994.

Section 4 Surfaces and Interfaces

Chapter 1 Synchrotron X-Ray Studies of Surface Disordering

Chapter 2 Semiconductor Surface Studies

Chapter 3 Step Structures and Epitaxy on Semiconductor Surfaces

Chapter 1. Synchrotron X-ray Studies of Surface Disordering

Academic and Research Staff

Professor Robert J. Birgeneau, Dr. Barry Wells

Graduate Students

Monte J. Ramstad, Michael J. Young

Technical and Support Staff

Debra L. Harring

1.1 Introduction

Sponsor

Joint Services Electronics Program
Contract DAAL03-92-C-0001
Grant DAAH04-95-1-0038

In this research program, we use modern x-ray scattering techniques to study structures and phase transitions in thin films and on surfaces. We have two principal experimental facilities, one at MIT and the other at the National Synchrotron Light Source at Brookhaven National Laboratory. At MIT, we have four high-resolution computer-controlled x-ray spectrometers. The angular resolution can be made as fine as 1.8 seconds of arc, which enables us to probe the development of order from distances of the order of the x-ray wavelength, 1 Å, up to 30,000 Å. The sample temperature can be varied between 2 K and 500 K with a relative accuracy of 2×10^{-3} K. At the National Synchrotron Light Source, in collaboration with IBM, we have three fully instrumented beam lines. Two of these beam lines allow us to make studies with photons varying in energy between 3 and 12 keV; the third has a fixed energy of 17 keV. These facilities make possible high-resolution scattering experiments with a flux more than three orders of magnitude larger than that of a rotating anode x-ray generator. In collaboration with Professor Simon G.J. Mochrie, we have designed, built, and commissioned a second-generation x-ray surface facility which is extremely versatile, allowing a wide range of surface scattering experiments.

Our basic scientific objective is to understand the morphologies and microscopic structures of simple semiconductor and metal surfaces at high temperatures. Possible phase changes include surface roughening, surface reconstruction, melting, amorphization, and dilution.

Semiconductor surfaces exhibit rich structural and morphological behavior in both equilibrium and non-

equilibrium but steady state conditions. Equilibrium structures and phase transitions of high-symmetry facets are often closely related to important models in two-dimensional statistical mechanics. The physics of stepped (vicinal) surfaces, even in equilibrium, is subtle and poorly understood. For example, stepped surfaces should always be rough because of the freedom of the steps to wander. Step structures and spacing should be profoundly affected by any nearby high-symmetry surface reconstruction. Their association bears on issues of faceting and equilibrium crystal shapes. The steps themselves may exhibit phase transitions that involve dislocations and/or bunching in the step lattice as well as step-height changes; changes in the morphology, especially those involving vacancy aggregates, should be strongly affected by nearby steps.

Semiconductor surface physics involves fundamental issues in statistical mechanics that are important to a broad spectrum of other problems. Furthermore, elucidating the factors that control the morphology and perfection of vicinal semiconductor surfaces can be expected to lead to improved electronic device processing, and ultimately improve semiconductor device performance and lifetime.

1.2 Stability of Vicinal Si(111) Surfaces Under Sublimation and Electromigration

Two types of morphological instabilities due either to a surface reconstruction or to a current effect during resistive heating have been observed on vicinal Si(111). The first is a longitudinal instability in the step spacing, which causes the surface to separate into bands of high step density and (111) facets of low step density. Step bands are formed during the 7x7 reconstruction as the vicinal surface is removed from the equilibrium crystal shape. Step bands are also formed during DC heating for one direction of current where the destabilizing current direction depends on temperature. The

second is a transverse instability in the step profile, which causes a rippling of the surface morphology. Surface rippling is observed for one direction of DC current independent of temperature. An exception to this occurs if step pairs of opposite inclination are generated on large (111) facets due to rapid sublimation. Then, since steps with opposite inclination form ripples for opposite current directions, the rippling instability may occur for both current directions. The concurrence of step bands and surface rippling is manifested by rippled step bands and flat (111) terraces. A common property of the current dependent instabilities is that the fluctuations are damped by reversing the current direction. Using a DC current to heat a sample resistively can cause the formation of step bands or can smooth the surface depending on the direction of the current. Likewise, the transverse fluctuations in the step profiles may be damped or smoothed by a DC current.

A combination of diffraction and imaging techniques has been used to study these morphological changes. X-ray diffraction studies have been carried out in the MIT UHV chamber at Brookhaven National Laboratory using the X20 x-ray beamline. Laser diffraction studies have been carried out in our new optical chamber at MIT. Optical microscopy and atomic force microscopy studies have been carried out using CMSE central facilities.

1.2.1 Non-equilibrium Behavior Accompanying the 1x1 - 7x7 Transition

On a vicinal Si(111) surface miscut toward $\langle 11\bar{2} \rangle$ with negative current heating, the 7x7 reconstruction causes a homogeneous step density to separate into step bands. During this transformation, the x-ray diffraction peak from the homogeneous step density disappeared over a 2°C temperature range. Not only does this provide strong evidence that the transition is first order, but it also indicates that the surface temperature is very uniform. A signature of a first order transition is the existence of a meta-stable phase. A meta-stable homogeneous phase was observed by comparing cooling and heating data through the transition. At the spinodal temperature, the meta-stability vanishes and spontaneous step bunching occurs. The spinodal temperature measured during cooling was about 4°C below the transition temperature measured during heating. Another signature of a first order transition is nucleation and coarsening. Characterizing these aspects requires studies of time dependence. Using x-rays, the average sizes of the (111) terraces and step bunches were measured as a function of time and temperature for surfaces quenched from the homogeneous phase to

below the transition temperature. The sizes follow a power law in time, t^η , where η increases from 0.1 to 0.5 as the temperature increases toward T_s . Below the spinodal temperature, the steps remain relatively well-ordered and the order increases over time. Above the spinodal temperature, the steps become disordered as the (111) terraces undergo coarsening. To avoid the decomposition time dependence and access the equilibrium crystal shape, the transition was studied by heating through transition.

The 7x7 reconstruction driven phase separation was also studied for positive current. Reversing current direction from negative to positive at 900°C causes a homogeneous step density to undergo step bunching and step rippling. The step rippling occurs first. After a certain amount of rippling occurs, step bunching begins. The time required for step bunching to appear depends on the initial degree of order of the steps. Reversing the current direction from negative to positive below T_c causes the steps to become disordered and the step bunches to wander. This is evident in the broadening of the step and (111) terrace x-ray diffraction peaks in both of the surface plane directions. We conclude that the current drive step bunching and step rippling occur both above and below T_c for positive current. However, they occur much more slowly and on larger length scales than the reconstruction-driven step bunching. The behavior through the transition of a surface initially in a homogenous state but heated with positive current is similar to that of a surface heated with negative current. However, as time progresses, the degree of large length scale step bunching and step rippling above T_c increases. Since the current driven step bunching and step rippling occur both above and below T_c , it is difficult to access the equilibrium crystal shape with positive current.

1.2.2 High Temperature Current - Dependent Morphologies

The dynamics of the instabilities between 1000°C and 1300°C were studied using x-rays by reversing the current direction while maintaining a constant temperature. Below 1250°C, switching the current to positive caused step bands to unbunch and step rippling to occur. In the early stage, the steps unbunch and a homogeneous phase is formed. After obtaining a certain amount of order, the steps begin to ripple. Switching to negative current causes the rippled steps to transform to step bunches. First, an unripped homogeneous phase is formed, then step bunching occurs. The rate of these transformations increases with temperature.

However, the time dependence has not yet been fully analyzed.

Above 1250°C, reversing current direction causes transformation between a homogeneous phase at negative current and rippled step bunches for positive current. Initially, x-ray diffraction from the rippled step bunches shows a sharp (111) facet peak. The step diffraction peak, however, is too weak to measure due to the disorder of the steps. When the current direction is reversed, steps leave the step bunches creating a low step density on the (111) facets which gradually increases to the homogeneous phase density. The width of the diffraction peak from the low density regions broadens as the step density increases. After unbunching, which occurs rapidly, a slow step ordering process begins. The shape of the step peak is Lorenzian in the <110> direction and Gaussian in the <112> direction. The width is initially about three times broader in the <112> direction than in the <110> direction. The peak width sharpens in time according to a power law where $\eta = 0.77$ in the transverse direction and $\eta = 0.62$ in the longitudinal direction. Upon switching the current direction to positive, the

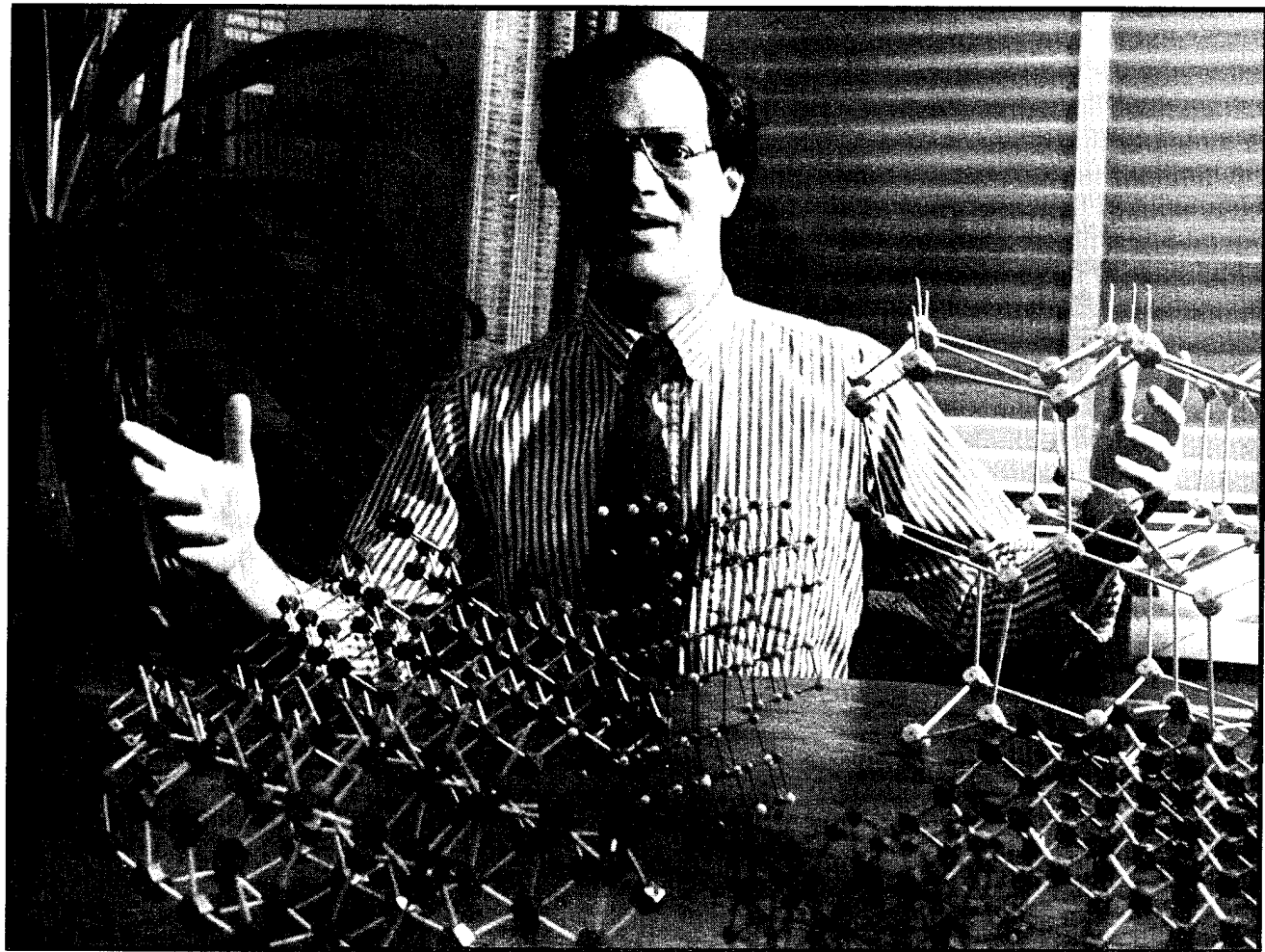
step bunching occurs by the rapid growth of (111) facets with simultaneous rapid increase of the step density in the step bunches. This occurs so rapidly that it is difficult to observe in real-time.

Manifestly, the phenomenological behavior is very rich. We are continuing our empirical studies of these novel phenomena. We are also trying to develop basic theoretical models involving sublimation from steps and electromigration of surface Si atoms.

1.3 Publications

Abernathy, D.L., S. Song, K.I. Blum, R.J. Birgeneau, and S.G.J. Mochrie. "Chiral Melting of the Si(113) (3x1) Reconstruction." *Phys. Rev. B* 49: 2691 (1994).

Nuttall, W.J., D.Y. Noh, B.O. Wells, and R.J. Birgeneau. "Synchrotron X-ray Scattering Study of the Pressure Melting of Near-monolayer Xenon on Single Crystal Graphite at 140K." *Surf. Sci.* 307-309: 768 (1994).



Professor John D. Joannopoulos (Photo by John F. Cook)

Chapter 2. Semiconductor Surface Studies

Academic and Research Staff

Professor John D. Joannopoulos, Professor Tomas A. Arias, Dr. Karl Brommer

Graduate Students

Rodrigo B. Capaz, Kyeongjae Cho

Technical and Support Staff

Imadiel Ariel

2.1 Introduction

Sponsor

Joint Services Electronics Program

Contract DAAL03-92-C-0001

Grant DAAH04-95-1-0038

Understanding the properties of surfaces of solids and the interactions of atoms and molecules with surfaces is extremely important both from the technological and academic points of view. The advent of ultrahigh vacuum technology has made microscopic studies of well-characterized surface systems possible. The way atoms move to reduce the energy of the surface, the number of layers of atoms involved in this reduction, the electronic and vibrational states that result from this movement, and the final symmetry of the surface layer are all of utmost importance in arriving at a fundamental and microscopic understanding of the nature of clean surfaces, chemisorption processes, and the initial stages of interface formation.

The theoretical problems associated with these systems are quite complex. However, we are currently at the forefront of solving the properties of real surface systems. In particular, we are continuing our efforts to develop new techniques for calculating the total ground-state energy of a surface system from "first principles," so that we can provide accurate theoretical predictions of surface geometries and behavior. Our efforts in this program have concentrated in the areas of surface growth, surface reconstruction geometries, structural phase transitions, and chemisorption.

2.2 Chemisorption

In this section we discuss an *ab initio* theoretical investigation of the electronic surface states and the reactivity of the Si(111)-(7x7) surface reconstruction. The Si(111)-(7x7) reconstruction has a

rich and complex chemistry because it contains a diverse set of dangling bonds. This surface is a challenge for studying surface reactions, because a single atomic species reconstructs into a large (7x7) unit cell containing nineteen dangling bonds. The nineteen dangling bonds in the unit cell define nineteen different reactive sites, each on a silicon atom. Seven are unique, with the other twelve related by symmetry. It is difficult and challenging to rationalize the dramatic differences in reactivity among the different sites on the surface. While this reconstruction has been studied for thirty years, it is only with the use of massively parallel computers that realistic *ab initio* studies of its electronic structure are tractable. In particular, we used the *ab initio* molecular dynamics scheme that we have developed at MIT for calculating the electronic states and computing the relaxed positions of the ions.

The relaxed positions of atoms in the 7x7 unit cell are plotted in figure 1. A top view of the surface with the unit cell outlined with dotted lines is shown in figure 1a. In this figure, all unique dangling

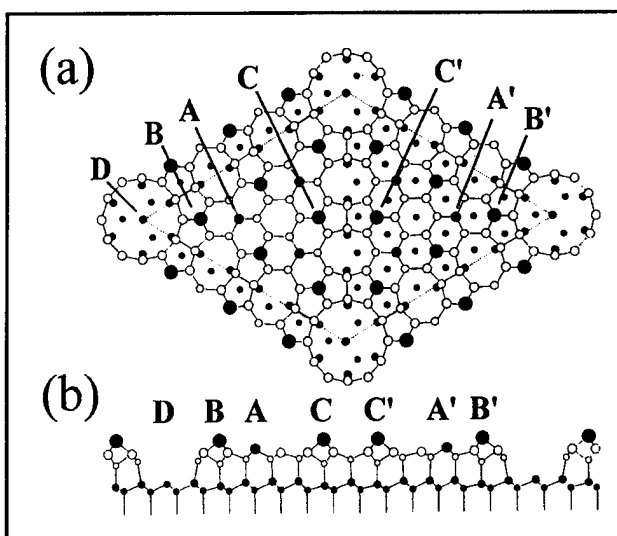


Figure 1. Si(111)-(7x7) surface dangling bond sites.

bonds are labeled with capital letters. The faulted and unfaulted rest atoms, denoted by shaded circles labeled A and A' respectively, sit on the top surface bilayers. There are a total of six rest atoms, three on each side of the unit cell. The large black circles labeled B, B', C and C' denote adatoms sitting on the top of the first surface bilayer. The six adatoms on each side of the unit cell form triangles. Adatoms at the faulted and unfaulted triangle corners B and B' are chemically distinct from adatoms at the triangle centers C and C'. The relative heights of the surface atoms are plotted in figure 1b, showing a side view through the long diagonal of the cell. It can be seen that the rest atoms with the dangling bonds are buckled slightly upward from the positions of other first-layer atoms. In the side view, the depth of the large hole at each corner of the cell is also apparent. Inside this corner hole sits the nineteenth dangling bond site, labeled D.

Surface chemisorption will depend on a variety of factors, especially electronic effects dictating the existence and magnitude and activation barriers, as well as dissipative channels for the energy of incident reactants, steric constraints, and surface diffusion. The close similarity of different dangling bonds sites on the complex Si(111)-(7x7) surface reconstruction means that most of the common chemisorption factors are virtually identical among the different sites. To determine reactivity we construct a theory that is based on two parameters describing the electronic surface states: the global electronegativity, and the local softness.

The definition of local softness introduced by Yang and Parr for metals was extended to systems with a gap to obtain regional softness for the Si(111)-(7x7) surface reconstruction. Two different classes of regional softness are calculated, one related to the nucleophilic (acceptor) capacity, and the other related to the electrophilic (acceptor) capacity of the surface. Accordingly, an order can be assigned for the nucleophilic and electrophilic nature of the seven dangling bonds of the surface. From this analysis of regional softness, a general qualitative behavior for the reactivity of this surface reconstruction can emerge.

For our application, we are interested in determining the possible differences in reactivity between the seven types of dangling bonds in the system. To do this we defined a regional reactivity index associated with a local region of the surface through spatial integration of the local softness

$$S_i = \int_{\Omega_i} s(r) dr,$$

where Ω_i is the local volume surrounding the dangling bond i . As an extension of the physical meaning of $s(r)$ we interpret S_i as the measure of the ability of the dangling bond i to perform charge transfer. Extrapolating from Politzer, we choose the name *charge capacity* for this property. Thus, differences in charge transfer capabilities among the different dangling bonds will be determined entirely through S_i .

Our calculations of the charge capacity, S_i , are exhibited in figure 2. An analysis of the values in this figure shows that the donor and acceptor capacities follow the order displayed in table 1. Table 2 summarizes the differences in charge capacity between faulted and unfaulted halves of the unit cell.

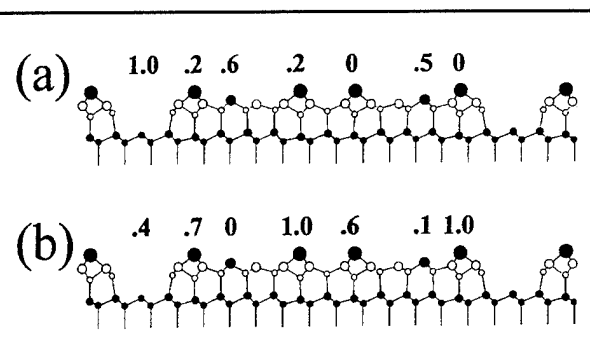


Figure 2. Charge capacity of each unique dangling bond on the 7x7 surface for (a) electrophilic and (b) nucleophilic reactants.

Table 1. Charge capacity order for different sites on the Si(111)-(7x7) reconstruction

Surface donor capacity	Corner hole > rest atoms > adatoms
Surface acceptor capacity	Adatoms > corner hole > rest atoms

Table 2. Differences in charge capacity between faulted and unfaulted halves

As a donor	Faulted rest atoms > unfaulted rest atoms
As an acceptor	Faulted center adatoms > unfaulted center adatom Unfaulted corner adatoms > faulted corner adatom

General reactivity patterns. According to table 1, electrophilic attaching groups interact with the surface in the following order: corner hole > rest atom > adatoms. The corner hole and rest atom

reactivities are strong, while the adatom reactivity is relatively weak. The nucleophilic groups interact with the surface mainly through the adatoms, to a lesser extent with corner holes, and most weakly with the rest atoms. Among the seven different dangling bonds the corner holes is unique in exhibiting a strongly active site for electrophilic reactants as well as exhibiting some reactivity for nucleophilic reactants. Adatoms are more selective towards nucleophiles. While rest atoms are strongly reactive toward electrophilic species, the rest atoms are weakly reactive toward nucleophilic species.

We now consider the effects of the stacking fault in the reactivity of the Si(111)-(7x7) reconstruction. With respect to donor capacity, there is a clear distinction between reactivity at faulted and unfaulted halves as shown in table 2. Electrophiles should prefer to interact with the faulted half of the surface, and in particular with the faulted rest atoms. With respect to acceptor capacity, there does not appear as strong a selectivity for one half or the other since preferred reactive sites are found on both sides to the unit cell. If a donor (nucleophile) reacts with the faulted half, the interaction will be primarily with the faulted center adatom. If the unfaulted half is selected, the interaction is generally with the unfaulted corner adatom.

Reactions preserving reconstruction. To illustrate the utility of the present approach, we will use it to analyze some experimental reactivity patterns of the Si(111)-(7x7) reconstruction. In particular, table 3 displays the reactivity patterns for some attacking compounds which maintain the reconstruction. The experimental information was obtained using infrared spectroscopic techniques by Chabal and by scanning tunneling microscopy (STM) by Avouris and colleagues. To classify the reactants as donors or acceptors, we used an electronegativity criterion. If the difference in electronegativity between the surface and the reactant is negative, then the reactant is the acceptor and the surface the donor. If the difference is positive, the roles are reversed. Table 4 shows these differences for a series of compounds. Electronegativities for the reactants were taken from Pearson's estimations. The surface electronegativity is the work function, 4.8 eV.

Interaction with hydrogen. According to table 4, H can be classified as an acceptor species with respect to the surface. Hydrogen is one of the most electronegative of the neutral reactants listed in this table. From table 4 it is clear that the corner hole atoms are the most reactive sites in this case, and this is in complete agreement with the experiments of Chabal et al. summarized in table 3.

Table 3. Experimental studies of chemical reactivity of the Si(111)-(7x7) reconstruction

Reactant	Method	Reactivity
H	Spectroscopy	The most active site is the corner hole atom
Pd, Ag, Li	STM	The faulted half is preferred and reactants are believed to bond primarily to rest atoms and center adatoms
NH ₃ , H ₂ O, PH ₃	STM	Rest atoms > center adatoms > corner adatoms

Interaction with Pd, Ag, and Li. According to table 4, these metal atoms are electron donors with respect to the surface. Thus, our theoretical calculations suggest that they should interact primarily with adatoms and specifically with faulted center adatoms. This is again consistent with the experimental evidence summarized in table 3.

Interaction with NH₃, H₂O, and PH₃. These molecules dissociate on the surface into anions OH⁻, (NH₂)⁻, and (PH₂)⁻ and the cation H⁺. From table 4, all of the dissociation products except the proton are donors. The proton is clearly a strong acceptor. By assuming that the dissociation process takes place in the initial step of the reaction without inducing large changes in the chemical potential of the surface, we determine the order of preferential reactivity as corner hole atoms, then rest atoms, and last adatoms. Table 3 shows that the predicted reactivity order of rest atoms and adatoms agrees with experimental STM data. Our calculations also predict that the corner hole site is the most reactive. This remains to be detected experimentally, but may be difficult due to the depth of the corner hole below the adatom and rest atom layers.

Interaction with O₂. From table 4, the O₂ molecule is an electron acceptor with respect to the Si surface. Therefore, it should prefer to interact with the faulted half of the unit cell. Our calculations predict that the corner hole is the preferred reaction site, followed by rest atoms and adatoms. The preference for the faulted half agrees with STM experiments. Room temperature experiments have shown that O₂ is a molecular precursor which then dissociates and reacts preferentially with corner adatoms compared to center adatoms. While the regional softness of the isolated Si surface explains the preference for the faulted half by the molecular precursor, the presence of O₂ on the surface changes the local softness sufficiently to require

recomputation of local softness to analyze reactivity after dissociation.

Table 4. Relative electronegativity of reactants

Reactant	Electronegativity difference (eV)
Li	1.8
Ag	0.4
Pd	0.3
PH ₃	0.7
H	-2.4
NH ₃	2.2
H ₂ O	1.7
<i>Radicals (anions)</i>	
NH ₂	-1.3
OH	-2.7
PH ₂	-0.7
<i>Acceptors</i>	
As	-0.5
Au	-1.0
Pt	-0.8
Metal cations	<0.0
Halogen atoms	<0.0
BF ₃	-1.4
H ₂	-1.9
O ₂	-1.5
<i>Donors</i>	
Ga	1.6
Pb	0.9
Al	1.6
Ti	1.3
Alkaline Metals	>0.0

Predicted interactions. Based on the success of our reactivity analysis as demonstrated in the preceding example, we attempt to predict the reactivity associated with a number of atoms and molecules that yet remain to be studied. By using Pearson's

electronegativity tables and the work function of the surface, we can classify a great variety of atoms and molecules as donors or acceptors with respect to the Si(111)-(7x7) reconstruction. Selected examples are presented in table 5 including predictions of possible reaction patterns. These examples were chosen to illustrate the interaction of both acceptors and donors with the surface, including both hard and soft chemical reactants. The predictions assume non dissociative interactions and that surface reconstruction is maintained.

Table 5. Theoretical predictions of the chemical reactivity of the Si(111)-(7x7) reconstruction

Reactant	Reactivity
Acceptors: As, Au, Pt, metal cations, halogens, BF ₃ , H ₂	Corner hole > rest atoms > adatoms Faulted rest atom > unfaulted rest atom
Donors: Ga, Pb, Al, Ti, Ca, alkaline metals	Adatoms > corner holes > rest atoms Faulted center adatoms > faulted corner adatoms

2.3 Cross-sectional Scanning Tunneling Microscopy

Scanning tunneling microscopy (STM) provides an image of the structure of a surface at atomic resolution. This STM image is generated by an electron tunneling between the STM tip and a surface atom under the tip as a result of the overlap between the tip and surface wave functions. Consequently, the tip and the surface may in certain cases interact significantly during the process of an STM measurement. The conventional theories of STM, however, are based on a first order perturbation approximation which does not include the tip-surface interaction. STM images are then interpreted simply as a convolution of the tip wave function and the surface wave function. Although this interpretation is a very useful approximation for many applications, there may exist systems for which the tip-surface interaction and the surface dynamics play a crucial role in the STM measurement process.

In this section we describe *ab initio* total energy pseudopotential calculations to demonstrate that the Si(100) surface is an example of a system for which STM does not provide a direct mapping of

the surface atomic structure and that a conventional interpretation of the STM images is not appropriate. Typically, a room temperature STM image of the Si(100) surface shows the majority of dimers in what appear to be unbuckled, symmetric configurations. Such configurations are in disagreement with the theoretical predictions of buckled, asymmetric dimer configurations. One might expect that this discrepancy could reasonably be resolved by arguing that thermal fluctuations in the asymmetric dimer configurations will create an averaged or "symmetric" image. Such thermal fluctuations have been predicted to be present on the surface in the absence of a tip. In the presence of a tip, however, we propose that a different mechanism is operational. Specifically, we demonstrate that the tip-surface interactions are significant enough to flip and bind an asymmetric dimer to the tip. As the tip is then moved along the surface, dimers are flipped tracking the tip and create what appears to be a symmetric image in the scan.

In our calculations, we allowed the tip to vary in the range 4.5 to 5.2 Å above the atoms in the outermost surface layer. As shown in figure 3 even for the shortest tip-surface distance of 4.5 Å, the surface is not greatly perturbed by the presence of the tip, and no new bonds are formed between them. Nevertheless, as we discuss in the next section, there is enough interaction between tip and surface to significantly alter the dynamics of the surface dimers.



Figure 3. This plot shows a cross section of the total charge density of the tip-surface system with the tip directly above an upper dimer atom. The buckling angle of the dimer, the position of the apex tip atom, and the charge density distributions of the tip and the dimer are not significantly changed by the tip-surface interaction, but the interaction energy is significant. (-0.57 eV).

Interaction energies. The tip-surface interaction energy is calculated by combining three separately

calculated energies: $E(\text{tip})$, $E(\text{surface})$, and $E(\text{tip+surface})$. The results of our calculations for a tip restricted to lie directly above a surface atom are summarized in figure 4. For the configuration shown on the left panel, the tip lies 5.2 Å above the lower dimer atom, and the interaction energy is -0.37 eV. The panel at the center of the figure refers to a symmetric dimer configuration that corresponds to the "saddle point" or static barrier configuration for flipping the buckled dimer. In the absence of the tip, the barrier is calculated to be 0.08 eV in good agreement with 0.09 eV as obtained by Dabrowski and Scheffler. In the presence of the tip, the barrier for an *up flip* of the buckled dimer is found to be 0.1 eV. The opposite barrier, corresponding to a down flip of the buckled dimer is obtained from the right panel of figure 4 and is found to be 0.3 eV. Note that the interaction energy in the latter case is correspondingly large at -0.57 eV and the distance between tip and dimer atom is 4.5 Å.

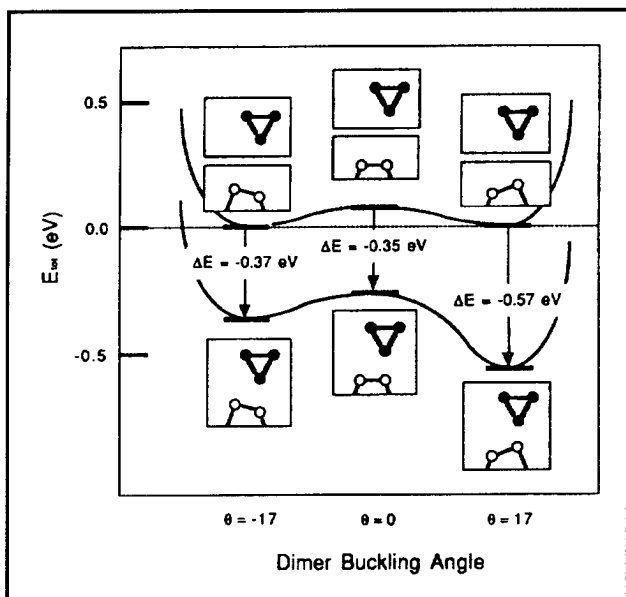


Figure 4. Total energy (in eV) of a tip-surface system as a function of surface-dimer buckling angle. The tip (shown schematically as a triangle with filled circles) is situated directly above a surface-dimer atom (open circles). The results at and above the horizontal dashed line correspond to $E(\text{tip}) + E(\text{surface})$. Note that the barrier for flipping from one asymmetric dimer configuration to the other is about 0.08 eV. The panels below the dashed line correspond to the fully interacting tip-surface system. In this case the horizontal bars correspond to $E(\text{tip} + \text{surface})$. Note that the barriers for up flip and down flip are 0.1 and 0.3 eV, respectively.

Implications. For a given value of energy barrier E_b , the average time that a dimer spends in one asymmetric configuration before flipping to the other is simply

$$\tau_b = 10^{-13} e^{E_b/k_B T},$$

where the phonon frequency is estimated to be 10^{13} sec $^{-1}$. During an STM measurement, an STM tip typically stays 2×10^{-3} sec = t_{STM} above a surface atom, and therefore the relative values of τ_b and t_{STM} will determine the nature of the STM image. In the *absence of interactions* between the STM tip and the surface, a buckled dimer is in a symmetric potential well as shown in the upper curve of figure 4, and the energy barrier for flipping (0.08-0.09 eV) is small enough that at room temperature the dimer can flip up and down very frequently ($\tau_b = 2 \times 10^{-12}$ sec). This would lead to a symmetric STM image that is the average of up-flip and down-flop configurations.

In the presence of interactions between the STM tip and surface, a buckled dimer is in an asymmetric potential well as shown in the lower curve of figure 4 and τ_b is different for the down-flip and the up-flip configurations. At room temperature, τ_b 's are short enough ($\tau_{down} = 5 \times 10^{-12}$ sec and $\tau_{up} = 1.3 \times 10^{-8}$ sec) that, in principle, the dimer can flip up and down freely, and thermal equilibrium between two local energy minima of the asymmetric potential is reached during the STM imaging time. Therefore, the dimer spends different amounts of time in each local energy minimum, and the ratio of the times is given by the Boltzmann factor of the difference of two local minimum energies (4×10^{-4}). Consequently, the dimer stays in the up-flip configuration except for intermittent rapid round trips to the down-flip configuration. For all practical purposes, therefore, one is always measuring a dimer in the up-flip position as the tip moves along the surface. The resulting image is then deceptively that of a "symmetric" dimer.

2.4 Publications

Arias, T., and J.D. Joannopoulos. "Electron Trapping and Impurity Segregation at Grain Boundaries." *Phys. Rev. B* 49: 4525 (1994).

Arias, T., and J.D. Joannopoulos. "Ab-initio Theory of Dislocation Interactions." *Phys. Rev. Lett.* 73: 680 (1994).

Brommer, K., M. Calvan, A. Dal Pino, and J.D. Joannopoulos. "Theory of Adorption of Atoms and Molecules on Si(111)-(7x7)." *Sur. Sci.* 314: 57 (1994).

Capaz, R., A. Dal Pino, and J.D. Joannopoulos. "Identification of the Migration Path of Interstitial Carbon in Si." *Phys. Rev. B* 50: 7439 (1994).

Cho, K., and J.D. Joannopoulos. "The Devilish World of Surfaces." *Proceedings of the Teraflop Computer Conference*, Baton Rouge, 1994.

Devenyi, A., K. Cho, T. Arias, and J.D. Joannopoulos. "Adaptive Riemannian Metric for All-Electron Calculations." *Phys. Rev. B* 49: 13373 (1994).

Fan, S., A. Devenyi, R. Meade, and J.D. Joannopoulos. "Guided Modes in Periodic Dielectric Materials." *J. Opt. Soc. Am.* (1995) in press.

Fan, S., P. Villeneuve, R. Meade, and J.D. Joannopoulos. "Design of 3D Photonic Crystals at Submicron Lengthscales." *Appl. Phys. Lett.* 65: 1466 (1994).

Joannopoulos, J.D., "Ab-initio Statistical Mechanics." *Proceedings of the QTRM Conference*, Berkeley, California, 1994.

Larrabee, J., V. Baisley, R. Huffman, R. Meade, and J.D. Joannopoulos. "Detectivity of a UB-B Photodiode." *Proceedings of the SPIE Conference*, San Diego, California, 1994.

Meade, R., A. Devenyi, J.D. Joannopoulos, O. Alerhand, D. Smith, and K. Kash. "Novel Applications of Photonic Band Gap Materials." *J. Appl. Phys.* 75: 4753 (1994).

Mucciolo, E., R. Capas, B. Altshuler, and J.D. Joannopoulos. "Manifestation of Quantum Chaos in Electronic Band Structures." *Phys. Rev. B* 50: 8254 (1994).

Winn, J., R. Meade, and J.D. Joannopoulos. "Two Dimensional Photonic Band Gap Materials." *J. Opt.* 41: 257 (1994).

Chapter 3. Step Structures and Epitaxy on Semiconductor Surfaces

Academic and Research Staff

Professor Simon G.J. Mochrie

Graduate Students

Seungheon Song, Mirang Yoon

3.1 Introduction

Sponsor

Joint Services Electronics Program
Contract DAAL03-92-C-0001
Grant DAAH04-95-1-0038

Surface morphology is key to a number of technologically important processes, including, for example, corrosion, catalysis and epitaxial growth. A striking change in the morphology of a crystal surface occurs at a *faceting transformation*, in which an initially uniform surface separates into regions with different surface orientations. An example of a surface that has undergone thermodynamic faceting is illustrated in figure 1, which shows an atomic force microscopy (AFM) image of a stepped Si(113) surface, misoriented from the [113] direction by 2.1° towards [001]. As may be seen, the surface morphology consists of grooves, each of which is in fact comprised of a (113) and a (114) facet. In general, the morphology for a given temperature and macroscopic misorientation may be specified by means of an *orientational phase diagram*, which is analogous to the phase diagram of a fluid, with the surface orientation (or step density) corresponding to the particle density.¹ In this context, faceting is a first-order phase transformation, and the image seen in figure 1 represents phase coexistence between (113) and (114) facets, which are distinct orientational phases.²

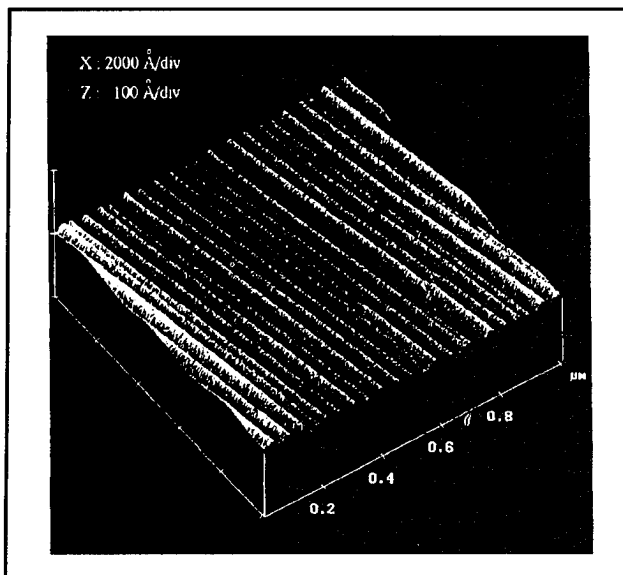


Figure 1. Grey-scale *ex situ* atomic force microscopy image of a stepped Si(113) surface misoriented by 2.1° toward [001] after annealing at 900 K. The sides of each groove are formed of a (113) facet and (114) facet. Note that the vertical scale is much exaggerated compared to the horizontal scales.

In addition to scientific motivations for studying faceting, an understanding of faceting may eventually allow for the introduction of simple processing strategies for tailoring surface morphology to suit technological needs. For example, recently it has been shown within the MIT JSEP program that the use of silicon substrates with a three-dimensionally grooved morphology decreases the dislocation

¹ R.J. Phaneuf and E.D. Williams, *Phys. Rev. Lett.* 58: 2563 (1987); E.D. Williams and N.C. Bartelt, *Sci.* 251: 393 (1991); J.C. Heyraud, J.J. Metois, and J.M. Bermond, *J. Cryst. Growth* 98: 355 (1989); P. Nozieres, *J. Phys. France* 50: 2541 (1989); G.M. Watson, D. Gibbs, D.M. Zehner, M. Yoon, and S.G.J. Mochrie, *Phys. Rev. Lett.* 71: 3166 (1993); M. Yoon, S.G.J. Mochrie, D.M. Zehner, K.G. Huang, and D. Gibbs, *Phys. Rev. B* 49: 16702 (1994); J.S. Ozcomert, W.W. Pai, N. Bartelt, and J.E. Reutt-Robey, *Phys. Rev. Lett.* 72: 258 (1994).

² C. Rottman and M. Wortis, *Phys. Rev. B* 29: 328 (1984); C. Jayaprakash and W.F. Saam, *Phys. Rev. B* 30: 3916 (1984); C. Jayaprakash, C. Rottman, and W.F. Saam, *Phys. Rev. B* 30: 6549 (1984); C. Rottman, M. Wortis, J.C. Heyraud, and J.J. Metois, *Phys. Rev. Lett.* 52: 1009 (1984).

density of epitaxially grown GaAs films.³ One may also suppose that surfaces, like that shown in figure 1, might be suitable templates for the growth of quantum wires or nano-crystal arrays.

Over the last one-year period, the goal of our JSEP research has been to elucidate and understand the orientational phase diagram of certain surfaces of silicon—namely stepped Si(113) surfaces—and also to understand the kinetics of the faceting process. To this end, we have carried out a comprehensive x-ray scattering study of stepped Si(113) surfaces as a function of the sample temperature and misorientation angle, which is equivalent to the step density. We have also studied the evolution of surface morphology following a temperature jump (quench) from a temperature where the surface is uniformly stepped to a temperature where it is faceted. Our experiments were performed at the National Synchrotron Light Source (NSLS) with MIT-IBM beamlines at X20 and NSLS beamlines at X25. For these experiments, we used our ultra-high-vacuum apparatus for surface x-ray scattering. Important new insight into the mechanism of faceting has emerged from these studies.⁴

3.2 Phase Behavior of Stepped Si(113) Surfaces

For fluids, at the appropriate conditions of temperature and density, attractive interactions between the constituent particles of the fluid lead to the condensation of a liquid phase in coexistence with a vapor. It is natural then to expect that for attractive interactions between steps, "step condensation"—that is faceting—might occur. Prior to our experiments, such a possibility had been predicted theoretically, but not observed. In the case of a fluid, special interest attaches to the critical point, in part, because of the dramatic variation of fluid properties that occurs nearby, and, in part,

because the critical exponents that characterize this behavior are universal. Just as a near-critical fluid exhibits critical opalescence, so might a surface with mutually attracting steps show critical step fluctuations that are manifest as a divergent surface roughness. Such a step critical behavior seems remarkable, but nevertheless was observed and characterized in our recent experiments.

Specifically, we studied stepped Si surfaces miscut away from the [113] direction towards [001].⁵ The phase diagram deduced from our measurements is shown in figure 2. The solid lines indicate phase boundaries; while the solid circles and squares represent mesoscopic surface orientations measured for samples with macroscopic misorientations of 2.1° and 3.7°, respectively. The (113) orientation, located at zero misorientation angle, is a stable phase for all temperatures studied.⁶

Above 1223 K and at non-zero misorientation angles, there occurs a one-phase region of the phase diagram, in which the surface is uniformly stepped. We infer that the transformation versus orientation between the stepped phase and the (113) facet occurs smoothly and continuously above 1223 K.⁷ In this region, we find strongly temperature-dependent diffuse scattering, which may indeed be identified as critical scattering, and is the result of an increase in step fluctuations with decreasing temperature. Figure 3 highlights the step critical scattering for several temperatures above 1223 K on a log-log scale versus κ . (κ is the component of the scattering wave-vector parallel to the surface.) The lineshape for $\kappa < 0.005$ is determined by the resolution. However, the scattering that appears for $\kappa > 0.005$ is the step critical scattering of interest. The inset illustrates that the surface stiffness (\tilde{y}), which is inversely proportional¹⁸ to the intensity of this critical scattering varies as a power-law versus reduced temperature with respect to a spinodal line: $\tilde{y} = \tilde{y}_0 t_s^\lambda$, with $\lambda = 0.76 \pm 0.2$, $\tilde{y} = (56 \pm 20) k_B T_c^{-2}$, and $t_s = (T - T_s(\theta)) / T_s(\theta)$.

³ L.A. Kolodziejksi, H.I. Smith, and C.V. Thompson, *RLE Progress Report* 136: 88 (1993).

⁴ S. Song and S.G.J. Mochrie, *Phys. Rev. Lett.* 73: 995 (1994); S. Song, S.G.J. Mochrie, and G.B. Stephenson, in preparation (1995).

⁵ S. Song and S.G.J. Mochrie, *Phys. Rev. Lett.* 73: 995 (1994); S. Song and S.G.J. Mochrie, *Phys. Rev. B* (forthcoming).

⁶ D.L. Abernathy, *An X-ray Scattering Study of the Si(113) Surface: Structure and Phase Behavior*, Ph.D. diss., Dept. of Phys., MIT, 1993.

⁷ C. Rottman and M. Wortis, *Phys. Rev. B* 29: 328 (1984); C. Jayaprakash and W.F. Saam, *Phys. Rev. B* 30: 3916 (1984); C. Jayaprakash, C. Rottman, and W.F. Saam, *Phys. Rev. B* 30: 6549 (1984); C. Rottman, M. Wortis, J.C. Heyraud, and J.J. Metois, *Phys. Rev. Lett.* 52: 1009 (1984).

⁸ A. Braslau, M. Deutsch, P.S. Pershan, A.H. Weiss, J. Als-Nielsen, and J. Bohr, *Phys. Rev. Lett.* 54: 114 (1985); M. Sanyal, S.K. Sinha, K.G. Huang, and B.M. Ocko, *Phys. Rev. Lett.* 66: 628 (1991).

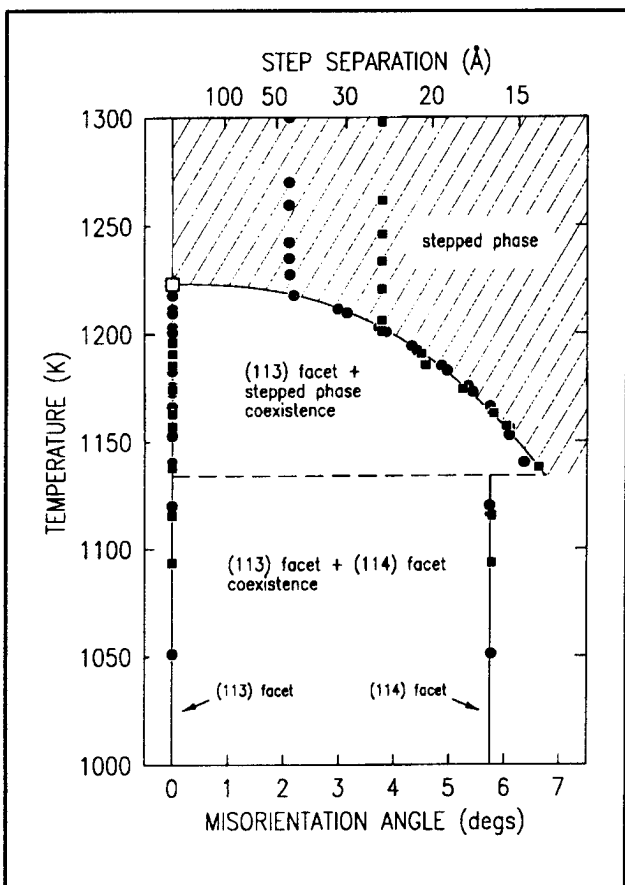


Figure 2. Orientational phase diagram of stepped Si(113) surfaces misoriented towards [001] versus temperature and misorientation angle. The one-phase region is hatched; two-phase regions are unhatched solid lines are phase boundaries. The dashed line corresponds to the triple point. Solid circles and solid squares show the mesoscopic misorientations measured for samples with macroscopic misorientations of 2.1° and 3.7° , respectively.

The step critical scattering anticipates a faceting transformation at which the surface transforms from a homogeneous phase of uniform orientation into coexisting phases with different orientations. Between 1223 and 1130 K, there is a two-phase region, so that the transformation versus orientation between the stepped phase and the (113) facet is first-order. The range of angles forbidden to the stepped phase (θ) may also be described as a power-law versus reduced temperature (shown as a solid line in figure 2): $\theta = \theta_0 t^\beta$, with $\beta = 0.42 \pm 0.10$,

$\theta_0 = 21 \pm 6^\circ$, and $t = (T_t - T)/T_t$, with $T_t = 1223$ K. The point in a phase diagram that separates a line of continuous transformations from a line of first-order transformation is a *tricritical point*. Thus, the point at $T_t = 1223$ K and zero misorientation angle is a tricritical point (open square in figure 2). To our knowledge, the present example is the first experimental observation of a tricritical point in an orientational phase diagram.

Finally, below a triple point temperature of $T_3 = 1130 \pm 10$ K (dashed line in figure 2), coexistence between the (113) facet and the (114) facet, which lies 5.7° from the [113] direction, replaces coexistence between the (113) facet and the stepped phase.

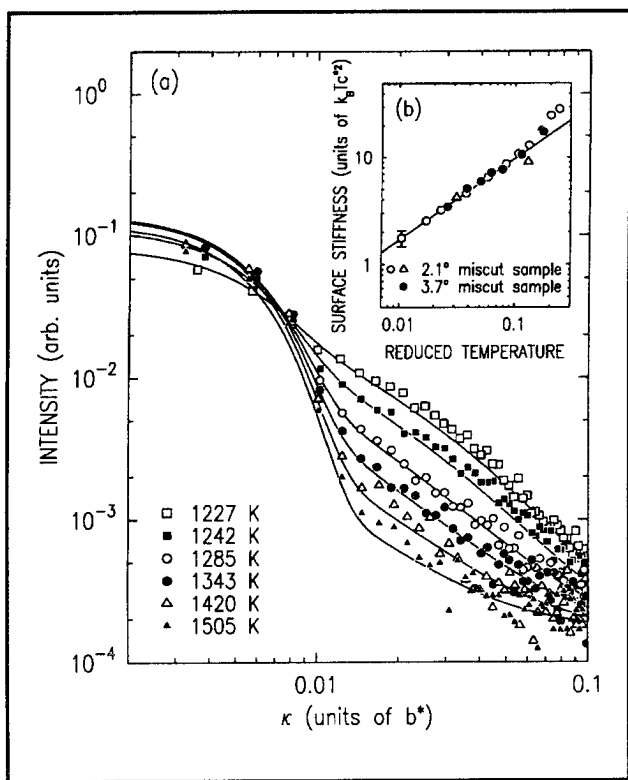


Figure 3. Log-log plot of the scattered intensity vs. κ for the 2.1° miscut sample at $L = 2$ for several temperatures in the one-phase region. Solid lines are a model lineshape based on the capillary mode model for surface roughness. The inset shows that the surface stiffness, deduced from fits to the model lineshape, varies as a power law versus reduced temperature.

3.3 Faceting Kinetics of Stepped Si(113) Surfaces: Self-Assembled Nano-Scale Gratings

Most recently, we have studied the behavior following a quench from the uniformly stepped phase (hatched in figure 2) into the coexistence region (unhatched in figure 2), using time-resolved x-ray scattering techniques.⁹ The kinetics of phase separation is a topic of considerable and growing interest.¹⁰ After a quench, domains of the low-temperature phase first form and then "coarsen," becoming larger and larger with time. It is generally expected that the coarsening process exhibits *dynamic scaling*, so that the system at a time t is characterized by a single time-dependent length which grows as a power law versus time, i.e., $L \sim t^\phi$. Analogous to critical behavior, the value of ϕ and of other exponents is expected to be characteristic of the kinetic universality class in question, which itself depends on the dimensionality of space, the symmetry of the order parameter, and the applicable conservation laws. Most systems studied to date correspond to a scalar order parameter for which $\phi = 1/2$ or $1/3$ for a conserved or a non-conserved order parameter, respectively.

Figure 4 shows the intensity versus the wavevector transfer parallel to the surface, obtained at several times up to 1200 seconds, using a linear detector following a quench of a 2.1° misoriented sample from a temperature of 1240 K in the one-phase region to a temperature of 1173 K in the two-phase region.¹¹ The intense peak at zero wavevector (figure 4a) corresponds to specular reflection. Evidently, following the quench the specular peak decreases in intensity as a result of the increasing surface roughness. By 1200 seconds after the quench, the specular peak has decreased by a factor of approximately two.

The peaks symmetrically located about the specular peak (figure 4b) constitute the first-order diffraction scattering from the "grating" of figure 1. It is evident that with increasing time, these peaks grow in intensity, shift to smaller wavevector, and become narrower. This behavior is reminiscent of that observed at small angles when a binary alloy or binary fluid is quenched into the coexistence

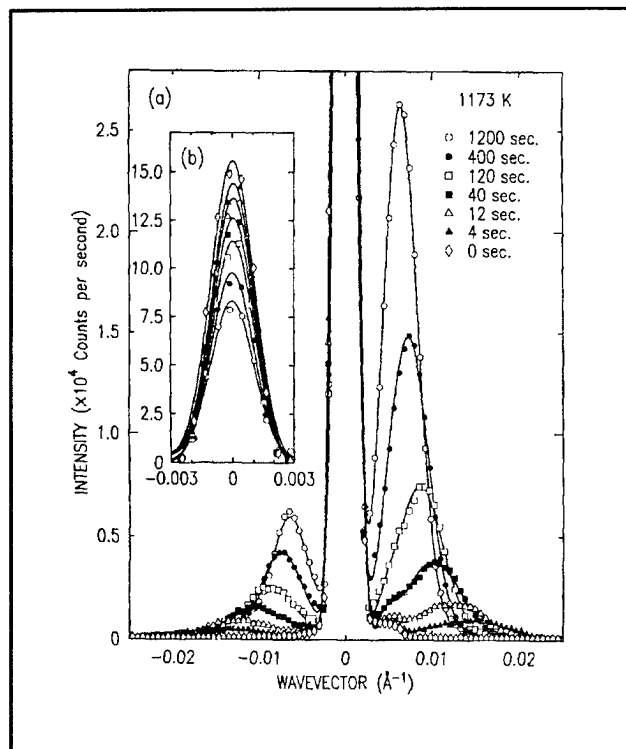


Figure 4. Scattering versus temperature for stepped Si(113) surface at several different times up to 1200 seconds following a quench from 1240 to 1173 K.

region. In that case, the small angle scattering originates in the correlated domain structure of the phase separation mixture. Similarly, the scattering of figure 4 is a result of finite-sized (113) facets in coexistence with densely stepped regions. The peak shift to smaller wavevectors corresponds to an increase in the separation and size of these domains with increasing time. Further quenching to room temperature allows us to freeze in any groove rise between 400 and 1500 Å. Detailed fitting reveals that the peak width decreases approximately proportionately to the peak position. This is particularly interesting in view of the facts that the system in question is two-dimensional and corresponds to a kinetic universality class that has not previously been investigated experimentally. Of additional special interest is that the exponent ϕ for the facet coarsening process takes the value $\phi = 0.1625 \pm 0.015$, which is very different from $1/3$ or $1/2$.

⁹ G.B. Stephenson, *Nucl. Instr. Meth. Phys. Res.* A266: 447 (1988).

¹⁰ J.D. Gunton, M.S. Miguel, and P.S. Sahni in *Phase Transitions and Critical Phenomena* Vol. 8, eds. C. Domb and J. L. Lebowitz (Academic Press, New York, 1983); S.N. Majumdar, D.A. Huse, and B.D. Lubachevsky, *Phys. Rev. Lett.* 73: 182 (1994).

¹¹ S. Song, S.G.J. Mochrie, and G.B. Stephenson, in preparation (1995).

3.4 Publications

Abernathy, D.L., S. Song, K.I. Blum, R.J. Birgeneau, and S.G.J. Mochrie. "Chiral Melting of the Si(113) (3 X 1) Reconstruction." *Phys. Rev. B* 49: 2691 (1994).

Song, S., and S.G.J. Mochrie. "Attractive Interactions Between Steps, Tricriticality and Faceting in the Orientational Phase Diagram of Silicon Surfaces Between (113) and (114)." *Phys. Rev. B.* Forthcoming.

Song, S., and S.G.J. Mochrie. "Tricriticality in the Orientational Phase Diagram of Stepped Si(113) Surfaces." *Phys. Rev. Lett.* 73: 995 (1994).

Part II Applied Physics

Section 1 Atomic, Molecular and Optical Physics

Section 2 Plasma Physics

Section 3 Electromagnetics

Section 4 Radio Astronomy

Section 1 Atomic, Molecular and Optical Physics

Chapter 1 Quantum Optics and Photonics

Chapter 2 Basic Atomic Physics

Chapter 1. Quantum Optics and Photonics

Academic and Research Staff

Professor Shaoul Ezekiel, Dr. Selim M. Shahriar, Dr. Stephen P. Smith

Visiting Scientists and Research Affiliates

Dr. Philip R. Hemmer,¹ Dr. Mara G. Prentiss,² John D. Kierstead¹

Graduate Students

John J. Donoghue,³ Daniel Katz,² Juliet Mervis²

Undergraduate Students

Arthur Chu²

1.1 Distributed Fiberoptic Sensor for Quench Detection in Superconducting Tokamak Magnets

Sponsor

MIT Plasma Fusion Center

The next generation of magnetic confinement fusion machines (tokamaks) will use superconducting rather than conventional magnets for confining and heating plasmas. These magnets can be longer than a kilometer and typically cooled using a forced flow of liquid helium through the conduit which surrounds the superconducting cable. The detection of a quench, i.e., a section of the magnet going normal, is important since any increase in heat in an area caused by an undetected quench could result in permanent magnet damage. Thus, a quick and reliable way of detecting such quenches is very valuable.

Conventional methods for quench detection in superconducting magnets, such as voltage taps or monitoring the helium flow in the conduit, have various limitations. For example, voltage taps can have poor signal-to-noise ratio due to inductive

pickup, while helium flow changes caused by a quench can be slow, depending on the location of the quench and the length of the magnet.

One novel method for detecting quenches in such a magnet is to include an optical fiber with the superconducting cable inside the conduit.⁴ Since the optical fiber is in close contact with the cable, any increase in heat in an area of the cable also causes heating of the fiber, which can be detected interferometrically.

Figure 1 shows a simplified schematic diagram of a fiberoptic quench detector. Light from an optical source is coupled along a single mode optical fiber and is then sent into two fiber arms using the directional coupler (labeled C1 in the figure). One of these arms, the sense arm, is co-wound with the superconducting cable, and the other arm, the reference arm, is held at a constant temperature. Light from these two arms is recombined using a second directional coupler (C2) to form a Mach-Zehnder interferometer. As the sense arm is heated, its optical length increases, and a series of fringes are observed at the output of the interferometer. By counting the number and the direction of these fringes, the change in the integrated temperature along the fiber can be found.

¹ Rome Laboratory, Hanscom Air Force Base, Bedford, Massachusetts.

² Professor, Harvard University, Cambridge, Massachusetts.

³ Tufts University, Medford, Massachusetts.

⁴ S. Pourrahimi, W.C. Guss, J.V. Minervini, D.B. Montgomery, N.T. Pierce, J.H. Schultz, S.P. Smith, and S. Ezekiel, "US Contributions to the Development and Calibration of Quench Detectors for the ITER QUELL," *Proceedings of the Applied Superconductivity Conference*, Boston, Massachusetts, October 17-20, 1994.

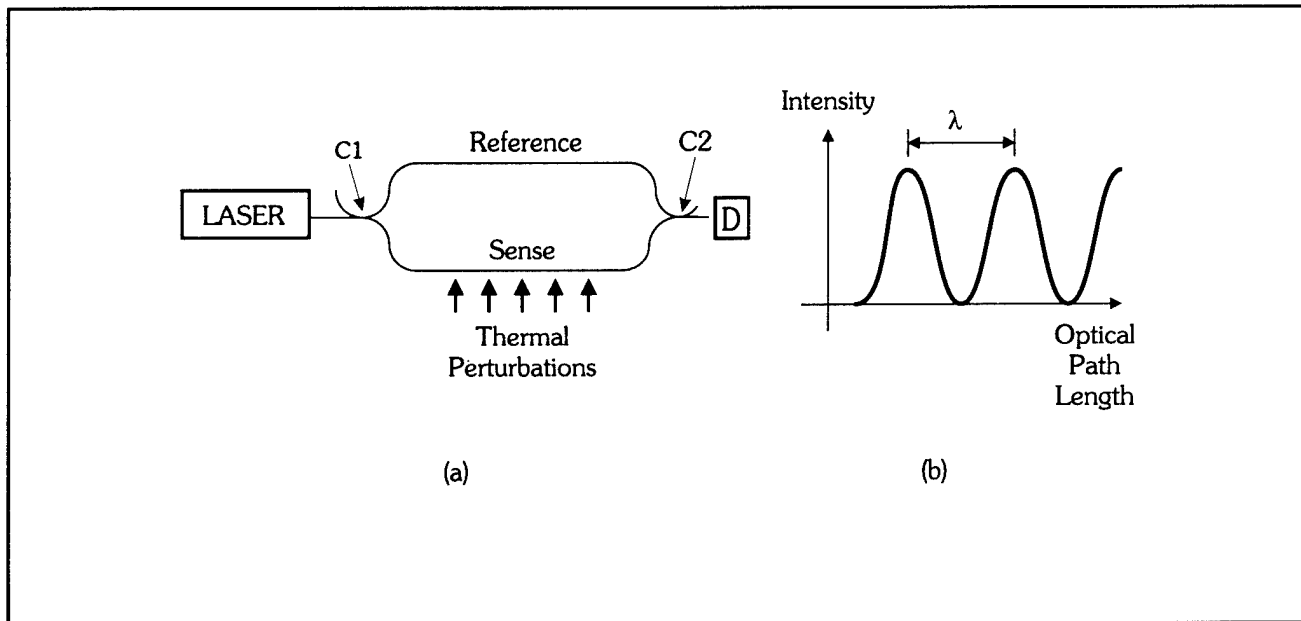


Figure 1.

Initial tests of this fiber interferometer using short lengths of superconducting wire have demonstrated that quenches can be easily observed even at liquid helium temperatures. Figure 2 shows one example of the data, where initially there is no perturbation to the optical fiber, and very little drift is observed in the fringe count. When a current is introduced into the superconducting wire, as indicated by the slight rise in the voltage across the wire (due to ohmic losses in the leads), very little change is observed in the fringe count. However, when the superconductor is quenched, using a current pulse applied to a heater wrapped around a short section of the superconducting wire, a large rise in the voltage across the superconductor is observed, and the fringe count rises dramatically. Finally, when the current is stopped in the superconducting wire, the fringe count abruptly drops to near its pre-quench level.

There are a number of issues with this sensor that still need to be investigated including reduction of the sensitivity of the optical fibers to changes in cable strain, survival of the optical fibers through the manufacturing of the superconducting cable, and extraction of the fibers from the magnets.

Preparations are currently underway to test this quench detection scheme and a number of others in a 100 meter superconducting cable. This test is part of ITER, an international scientific collaboration on fusion research between the United States, Japan, the European Union, and the Russian Federation. This test cable will be manufactured in Japan with sensors provided by the United States. The tests will be carried out in Switzerland.

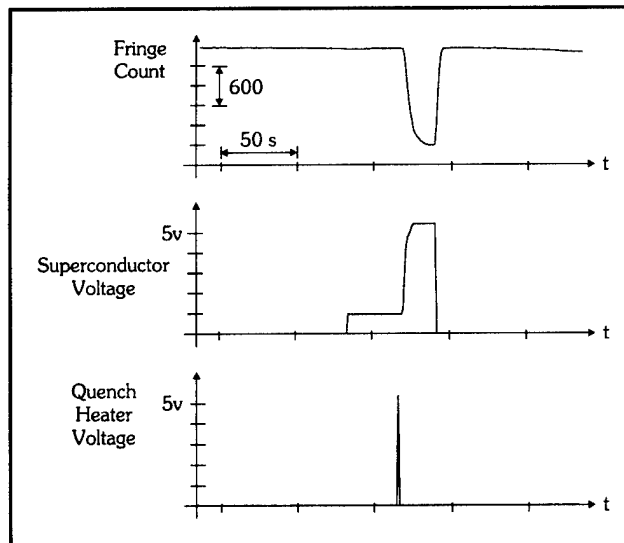


Figure 2.

1.2 Measurement of Liquid Helium Flow in Superconducting Tokamak Magnets

Sponsor

MIT Plasma Fusion Center

The accurate measurement of liquid helium flow is important in a number of experiments and applications involving superconducting magnets. Conventional measurement techniques such as venturis or orifice plates have a number of drawbacks including a small dynamic range, constriction of the flow,

poor bidirectional response, and poor transient response.

A new optical technique is being investigated for the measurement of the liquid helium flows. This technique has the advantages of a very large dynamic range, high accuracy, inherent bidirectionality, virtually no constriction or disruption of the flow and, in contrast with laser Doppler velocimetry, does not require a seeded flow.

This flow measurement technique is based on the change in the speed of light in a moving medium, referred to as Fresnel drag.⁵ The relativistic calculation gives the speed of light in a moving medium, c_m , as:

$$c_m = \frac{c_0/n + v}{1 + v/nc_0} \approx \frac{c_0}{n} + \left(1 - \frac{1}{n^2}\right)v$$

where c_0 is the speed of light in vacuum, n is the index of refraction of the medium, and v is the velocity of the flow along the direction of light propagation. Thus, for a 1 m/s flow in liquid helium the fractional optical path length change, $\Delta L/L$, resulting from this change in the speed of light is only about 2×10^{-10} .

One method for measuring this small effect uses a Sagnac interferometer (shown in figure 3).⁶ Light from a source is coupled into a single mode optical fiber and then is split into two beams by a fiber coupler C and the beams are then sent in opposite directions around a fiber ring. The beams are then recombined using the same coupler C and the resulting intensity is measured using detector D. However, in contrast with either a Michelson or Mach-Zehnder interferometer, since both beams travel along the same path, any change in optical path length, for example due to fiber temperature or strain changes, is the same for both beams so that the effect is reciprocal, and results in no change in the output intensity. Only effects which are non-reciprocal, i.e., different for the two directions of propagation, will result in a change in the output intensity.

Fresnel drag, as discussed above, is one such non-reciprocal effect. As shown schematically in figure 4, the light in the clockwise (CW) direction experiences a copropagating flow while the light in the counterclockwise (CCW) direction experiences a

counterpropagating flow. Thus, the flow will cause a difference in the optical path length for the two beams, resulting in a phase shift between the two beams. Figure 5 shows an example of how this system could be implemented with only minimal disruption of the flow. In this case, the interferometer will measure the component of the flow along the direction of light propagation.

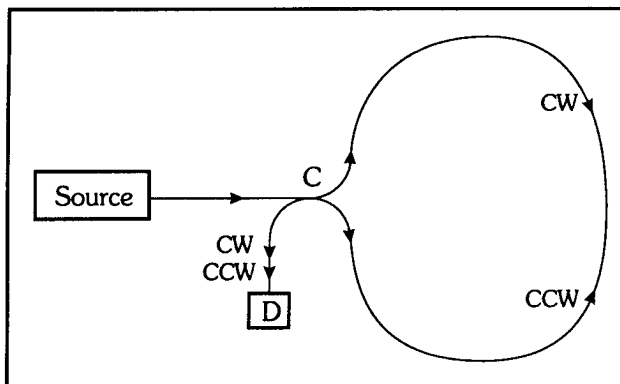


Figure 3.

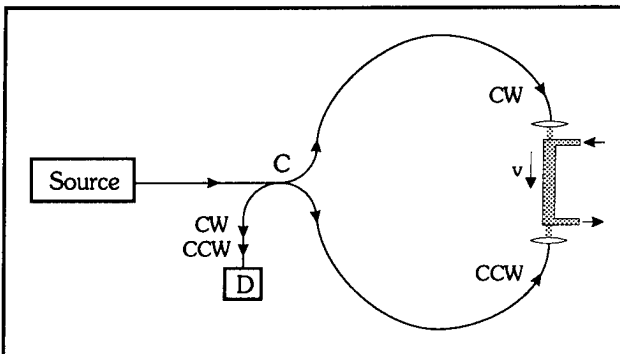


Figure 4.

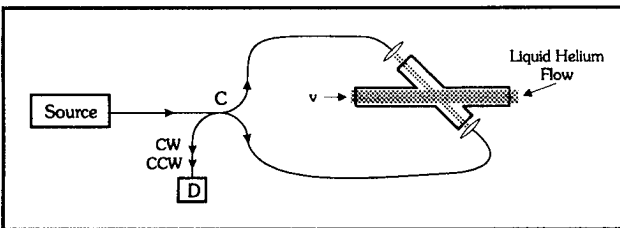


Figure 5.

Initial calculations indicate that this technique could be used for liquid helium flows on the order of 1 m/s with very small or negligible perturbation to the

⁵ R.T. de Carvalho and J. Blake, "Slow-flow Measurements and Fluid Dynamics Analysis Using Fresnel Drag Effect," *Appl. Opt.* 33: 6073-6077 (1994); G.A. Sanders and S. Ezekiel, "Measurement of Fresnel Drag in Moving Media Using a Ring-resonator Technique," *J. Opt. Soc. Am. B* 5: 674-678 (1988).

⁶ J.L. Davis and S. Ezekiel, "Closed-loop, Low-noise Fiber-optic Rotation Sensor," *Opt. Lett.* 6: 505-508 (1981).

flow. In addition, the sensor is inherently bidirectional, virtually immune to electro-magnetic interference, and insensitive to temperature and mechanical perturbations. It also has a very high dynamic range and a very low sensitivity to magnetic fields. Experiments are currently underway to study this type of flow meter using several cryogenic liquids.

1.3 Efficient, Low-Intensity Optical Phase Conjugation using Coherent Population Trapping in Sodium

Sponsor

U.S. Air Force - Electronic Systems Division
Contract F19628-92-K-0013

We have observed optical phase conjugate gain (>50) in sodium vapor using low intensity pump lasers (1 W/cm^2), with a response time on the order of 1 μsec .⁷ We have experimentally identified coherent population trapping (CPT) as the phase conjugate mechanism. We have also developed a theoretical model which supports these observations by showing that coherent population trapping can write large amplitude, nonlinear optical gratings at laser intensities well below those needed to saturate the optical transitions.

Four-wave mixing and optical phase conjugation (OPC) have long been known to have potential applications to optical image amplification, processing and aberration correction. However, widespread application of these techniques has so far been limited because of the slow response and/or low efficiency of existing nonlinear optical materials at laser intensities achievable with compact cw lasers. For example, previous work in sodium vapor shows fast response,⁸ but phase conjugate gain is observed only at high pump intensities (in the range of 100 W/cm^2).⁹ We have demonstrated high efficiency OPC in sodium for pump intensities near 1 W/cm^2 , with a response time on the order of 1 μsec . If sodium were replaced by rubidium or cesium, a similar performance could be achieved at

intensities accessible with cw diode lasers, opening the possibility of the development of portable, high speed, four-wave mixing devices.

To see how CPT can be used to perform OPC, consider the four-level double Λ system of figure 6a in the traditional phase conjugation geometry of figure 6b. The two Λ subsystems are assumed to be separate. For simplicity, consider only the case where F and S saturate the two-photon transition and B and C are weak. The Λ subsystem involving F and S and the states $|a\rangle$, $|b\rangle$, and $|e\rangle$ gets optically pumped into a transparent superposition of the ground states. This corresponds to a purely sinusoidal grating in the phase of the ground state coherence. The important property of this grating is that it can be saturated at optical intensities well below those needed to saturate the individual optical transitions.

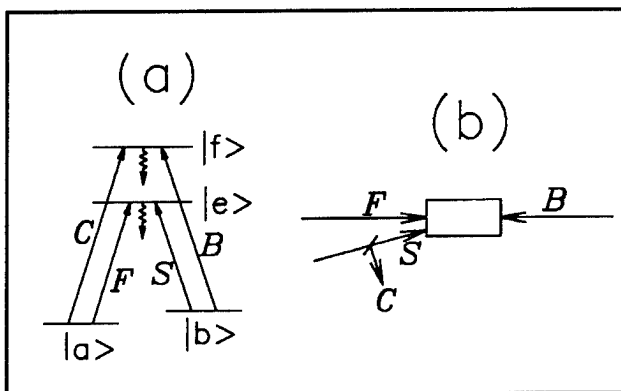


Figure 6. (a) Schematic of four-level double Λ system.
(b) Corresponding four wave mixing geometry.

To produce the conjugate beam C, the read beam B scatters off of the grating formed by F and S. For the special case where all lasers are resonant with the excited states, the conjugate wave amplitude C only increases until the four-level closed-loop transparency condition is approached. After this, B and C propagate as though the medium were transparent. In the more general case, for example, off resonant lasers and strong forward and backward pumps F and B, preliminary calculations show that high gain is possible. In the case of a pure three-

⁷ P.R. Hemmer, M.S. Shahriar, D.P. Katz, J. Donoghue, P. Kumar, and M. Cronin-Golomb, "Efficient Low-Intensity Optical Phase Conjugation Based on Coherent Population Trapping in Sodium," *Opt. Lett.* 20: 982 (1995).

⁸ C.J. Gaeta, J.F. Lam, and R.C. Lind, *Opt. Lett.* 14: 245 (1989).

⁹ M. Vallet, M. Pinard, and G. Grynberg, *Opt. Comm.* 81: 403 (1991); J.R.R. Leite, P. Simoneau, D. Bloch, S. Le Boiteux, and M. Ducloy, *Europhys. Lett.* 2: 747 (1986).

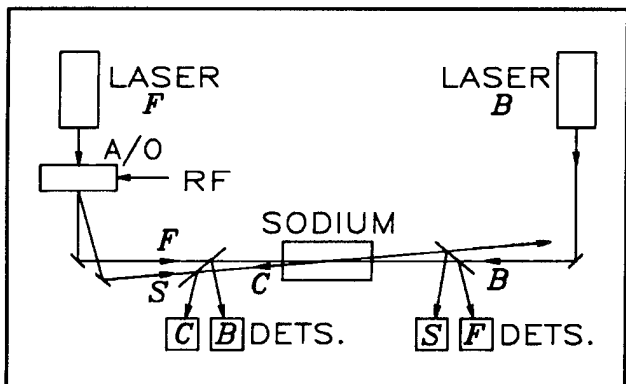


Figure 7. Schematic of experimental setup. Laser beam S is derived from F with an acoustic optic modulator (A/O), driven with a stable rf source.

level system, this scheme still works as long as B and S are nondegenerate.¹⁰

The experimental apparatus used to perform OPC using CPT is schematically shown in figure 7. The sodium vapor cell is a heat pipe oven operated at about 200° C with 5 mtorr of He buffer gas and a variable interaction length of 6 to 12 cm which is magnetically shielded to better than 100 mGauss. Two ring dye lasers generate the forward and backward pumps F and B, as shown. Both lasers are tuned approximately to the D1 transition. The signal beam S is derived from F using an acousto-optic modulator (A/O) configured for upshifting and driven with an rf signal of 1.77 GHz having about 1 kHz frequency jitter. This ensures that the laser jitters of F and S are correlated as required for efficient CPT.¹¹ Laser beams F and S typically enter the active medium with a 4 mrad angular separation. In addition, the backward pump B is also aligned about 3 mrad away from counterpropagating with F in a direction perpendicular to the F and S plane. This prevents optical feedback of one laser into the other while maintaining the Bragg angle. Typical spot sizes in the cell are about 1.6 mm FWHM for B, 1.0 mm for F, and 1.0 mm for S. Pump intensities (F and B) are in the range of 1 W/cm². All of the beams are detected in transmission through the cell. Finally, the frequency reference is provided by an atomic beam (not shown).

Figure 8a shows a scan of the conjugate gain R (reflected power/input signal power) and transmitted signal gain T as a function of the frequency of the

forward pump laser F. Note that the frequency of laser S is also scanned since S is generated from F with the A/O. As shown, high gains are observed, both in reflection and transmission. Here, the peak conjugate gain of 55 occurs when F is blue detuned about 200 MHz from the $F=2 \leftrightarrow F'=2$ transition frequency, S is upshifted from F by 1774 MHz, and B is red detuned about 600 MHz from the $F=1 \leftrightarrow F'=2$ transition. For this data, the optical intensity of the forward and backward pumps F and B are 1.2 and 0.5 W/cm², respectively, and the signal beam S has an intensity of 3.5 mW/cm². This data shows a factor of 16 increase in reflectivity over previous sodium vapor experiments at about 1 percent of the pump intensity. For this data, the shortest interaction length of 6 cm is used. Using a longer interaction length of 12 cm and higher pump intensities (5 W/cm²), conjugate reflectivities well above 100 are observed (not shown). The response time is measured by switching the rf signal to the A/O and monitoring the phase conjugate reflection. We find that the response time is no slower than 1.4 μ sec, the measurement being limited by the speed of the rf switching electronics.

Figure 8b shows a scan of the conjugate gain R as a function of the frequency detuning of S relative to F, obtained by scanning the rf frequency applied to the A/O (see figure 7) while compensating for alignment changes. All other conditions correspond to the peak gain in figure 6a. The observed difference frequency width of the gain is about 2.3 MHz (centered near 1774 MHz), which is to be compared with the 10 MHz natural linewidth of sodium. This subnatural rf frequency linewidth provides evidence of Raman CPT.¹² Frequency measurements of the conjugate beam C show that it is downshifted from the backward pump B by 1774 MHz. When B and C are combined on a fast photodiode, a narrow 2 kHz beat note is observed (near the 1 kHz rf linewidth), even though beams F and B are derived from independent lasers, each having about 50 MHz absolute frequency jitter. This narrow beat is evidence of the closed-loop model.

In summary, we have observed high-phase conjugate gain ($R > 50$) in sodium vapor at low pump intensities (~ 1 W/cm²), with a fast response time (~ 1 μ sec). Raman coherent population trapping has been experimentally identified as the physical basis of the conjugate generation process. This excellent

¹⁰ M.S. Shahriar, P.R. Hemmer, J. Donoghue, M. Cronin-Golomb, and P. Kumar, *OSA Annual Meeting Technical Digest* (Washington, D.C.: Optical Society of America, 1992), v. 23, p. 127.

¹¹ J.E. Thomas, P.R. Hemmer, S. Ezekiel, C.C. Leiby, Jr., R.H. Picard, and C.R. Willis, *Phys. Rev. Lett.* 48: 867 (1982).

¹² M. Poelker and P. Kumar, *Opt. Lett.* 17: 399 (1992).

performance opens the possibility of developing practical, portable, high-gain optical signal processing devices, based on optical phase conjugation or four-wave mixing.

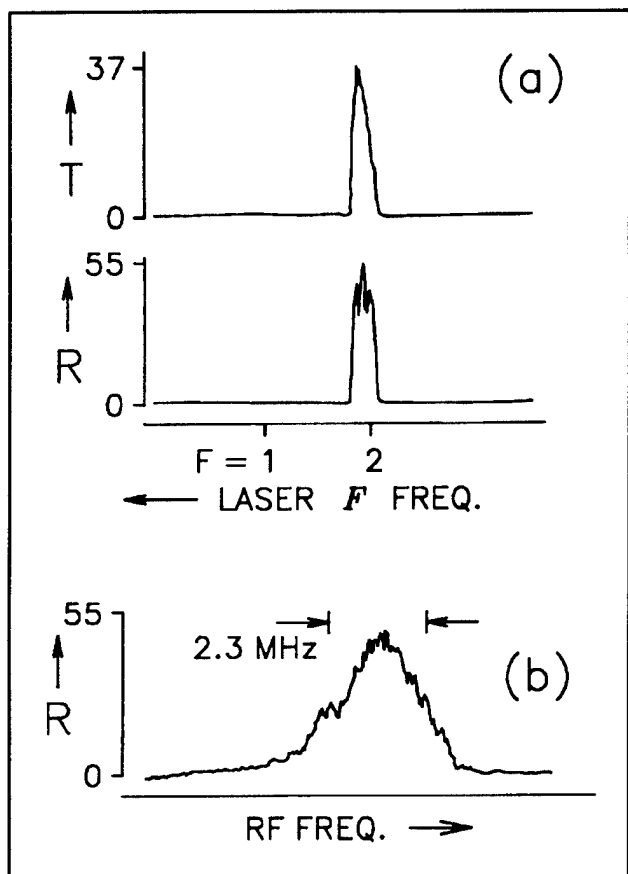


Figure 8. (a) Signal gain T and phase conjugate gain R versus laser F frequency. The frequency scale is labeled by the transition frequencies corresponding to the $F=1$ and $F=2$ ground state hyperfine components. (b) Phase conjugate gain R versus rf frequency driving the acousto-optic modulator.

1.4 Highly Selective Nonspatial-Filters Using Porous Matrix Based Thick Holograms

Sponsor

Ballistic Missile Defense Organization
Grant NG0921-94-C-0101

We have developed a novel technique for laser beam cleanup, the nonspatial filter,¹³ which is based on the Bragg selectivity of thick holograms. This technique eliminates the need for laser beam focusing, which is the source of many of the alignment instabilities and laser power limitations of spatial filters. Standard holographic materials are not suitable for this application because differential shrinkage during processing limits the maximum Bragg angle selectivity attainable. We have developed a new technology which eliminates this problem. Preliminary results show an angular selectivity of less than one milliradian.

For practically any application, the laser beam should be as clean as possible. Currently, this is accomplished by spatial filtering.¹⁴ There are two types of spatial filters in widespread use. The most common is the so-called "pinhole" filter, which consists of a lens with a pinhole in the focal plane. For more demanding applications, the pinhole is replaced by a single-mode optical fiber. One major problem with both the pinhole and fiber spatial filters is their requirement for matching a tightly focused laser beam to a small target. Moreover, both pinhole and fiber spatial filters are problematic when used with high-power lasers. In the case of pinhole spatial filters, a focused high-power laser can machine its own pinhole (of nonoptimal size). For this reason, spatial filters for high-power lasers are often aligned with the power turned down. However, if the pinhole position is inadvertently shifted during high-power operation, the hole-burning problem returns. The situation is worse for fiber spatial filters, since even a moderate intensity laser beam can produce nonlinear optical interactions when focused into the small optical fiber core, for example Brillouin and Raman scattering and refractive index changes due to increases in heating.

To solve the numerous problems inherent in spatial filters, we have developed nonspatial filtering. The basic idea of nonspatial filtering is similar to that of spatial filtering. Specifically, note first that a laser beam with arbitrary spatial variations in intensity can be expressed as linear combinations of plane waves (or some other basis functions). In spatial filters, a Fourier transform lens is used to convert angle into position in order to separate the spatial components. In contrast, nonspatial filtering is done directly on the laser beam angle. A filter

¹³ J.E. Ludman, J. Riccobono, J. Caulfield, J. Fournier, I. Semenova, N. Reinhard, P.R. Hemmer, and M.S. Shahriar, "Porous Matrix Holography for Non-Spatial Filtering of Lasers," *Proceedings of the IEEE Symposium on Electronic Imaging: Science and Technology*, San Jose, California, 1995.

¹⁴ E. Hecht and A. Zajac, *Optics* (Reading, Massachusetts: Addison-Wesley, 1975).

element is inserted in the laser beam path to selectively deflect light waves propagating at a particular angle, throwing away the unwanted light (as does the spatial filter). In particular, we use a thick hologram as the filter element. The Bragg selectivity of such a hologram guarantees that only waves propagating at a particular angle (the Bragg angle) get deflected. Two-dimensional filtering can be achieved by using two such holograms.

We consider here the special case in which nothing is absorbed, and where only the phase of the wave gets modulated, due to the presence of index modulation. For a monochromatic hologram with a grating periodicity of Λ , the angle of incidence, θ_B for perfectly phase matched Bragg diffraction is given by $\sin(\theta_B) = \lambda/2n\Lambda$, where λ is the wavelength of incident light, and n is the average index of refraction of the hologram.¹⁵ The diffraction efficiency, η , for TE polarization, is then given by $\eta = \sin^2\{\pi n_1 d/\lambda \cos(\theta)\}$. Here, n_1 is the amplitude of the sinusoidal index modulation, and d is the thickness of the hologram. For TM polarization, the effective value of the index modulation is reduced by a factor of $\cos(2\theta)$. The smallest value of n_1 for which maximum diffraction can be obtained thus varies inversely with the thickness and is very small for a thick hologram.

The angular selectivity (FWHM) is given by $\Delta\theta \approx \Lambda/d$. Thus, in order to maximize the angular selectivity, one has to choose as small a wavelength as possible for writing the hologram and make the hologram as thick as possible. Both of these factors are of course limited by practical considerations. For example, residual loss may limit the maximum usable thickness.

Standard holographic materials are not suitable for this application because differential shrinkage during holographic processing limits the maximum Bragg angle selectivity attainable by affecting the Bragg angle in a nonuniform manner. Differential shrinkage occurs because processing usually requires the addition or removal of molecules through the surface of the material, thus leading to shrinkage, which depends on the distance from the surface of the material. What is needed is a holographic structure with negligible differential shrinkage. The technology we have developed is based on the use of a rigid porous substrate material, porous glass. An active light sensitive material such as holographic photopolymer is loaded into

the rigid host structure. The size of the pores is much smaller than the optical wavelength, and the index of modulation is small.

We made a thick hologram using porous glass, which contains Boron, Sodium, and about 70 percent SiO_2 (before being rendered porous). The light sensitive material used is a holographic photopolymer.¹⁶ The average pore diameter is about 300 Å. The hologram was recorded using a wavelength of 488 nm, resulting in about 2000 lines/mm. The thickness of the hologram is about 0.7 mm. The hologram was found to be most transparent (96 percent) at 1500 nm, a wavelength of particular interest in fiberoptic communications. The transparency drops on either side of this wavelength. For example, at 1900 nm the transparency is about 50 percent, while at 540 nm it is about 70 percent.

We tested the performance of this hologram using a He-Ne laser. At this wavelength (632.8 nm), the transparency is close to 75 percent. To measure angular selectivity, we mounted the hologram on a rotation stage and measured the diffracted power as a function of the incidence angle. We found an angular selectivity of about 0.8 milliradian, which is close to the theoretically expected value of about 0.7 milliradian. This small difference may be attributed to the finite resolution of the rotation stage, as well as the finite divergence of the test beam.

To demonstrate nonspatial filtering in one dimension, we used a Gaussian beam from a He-Ne laser as the input beam. In order to compare the transmitted beam profile with that of the diffracted beam, we did not add any index matching fluid so that the transmitted and diffracted beams could be of comparable intensity. The profiles of the transmitted (top) beam and the diffracted (bottom) are shown in figure 9. The image was taken with a CCD camera and recorded on a video tape. A frame grabber was then used to digitize the image. As can be seen clearly, the beam has the same width in the horizontal direction but is much narrower in the vertical direction (the direction of diffraction). Thus, the beam has been cleaned in the vertical direction but not in the horizontal direction. Figure 10 shows the horizontal (top) and vertical (bottom) cross section of the diffracted beam. As can be seen, the width (FWHM) in the vertical direction is about one-fifth of the width in the horizontal direc-

¹⁵ H. Kogelnik, "Coupled Wave Theory for Thick Hologram Gratings," *Bell Sys. Tech. J.* 48: 2909-2947 (1969).

¹⁶ D.H. Whitney and R.T. Ingwall, "The Fabrication and Properties of Composite Holograms Recorded in DMP-128 Photopolymer," *Proc. SPIE* 1213: 18 (1990).

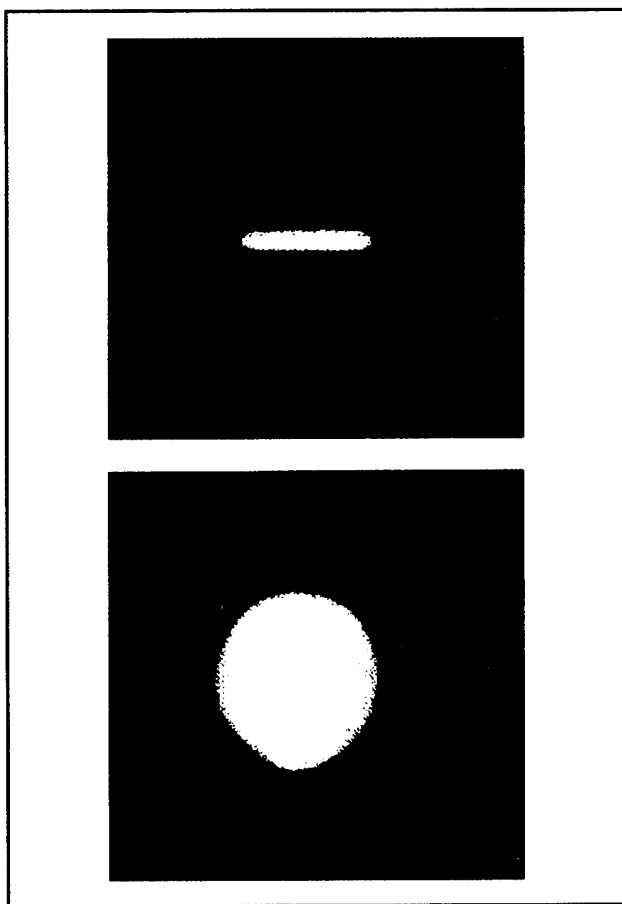


Figure 9. Profiles of the transmitted (top) and diffracted (bottom) spots through the one-dimensional thick hologram.

tion, with a residual divergence of about 0.8 milliradian.

To summarize, we have demonstrated nonspatial filtering with a thick hologram made in a porous glass host. We have demonstrated an angular selectivity of about 0.8 milliradian, which is in close agreement with theoretical predictions. Future work will include demonstration of nonspatial filtering in two dimensions, further enhancement of angular selectivity, and reduction in absorption. The thick holograms we have developed may also be of use for other applications, such as holographic optical data storage, spectroscopy, and intracavity laser mode selection.

1.5 Cache Memory using Optically Induced Spin Echo

Sponsor

U.S. Air Force - Electronic Systems Division
Contract F19628-92-K-0013

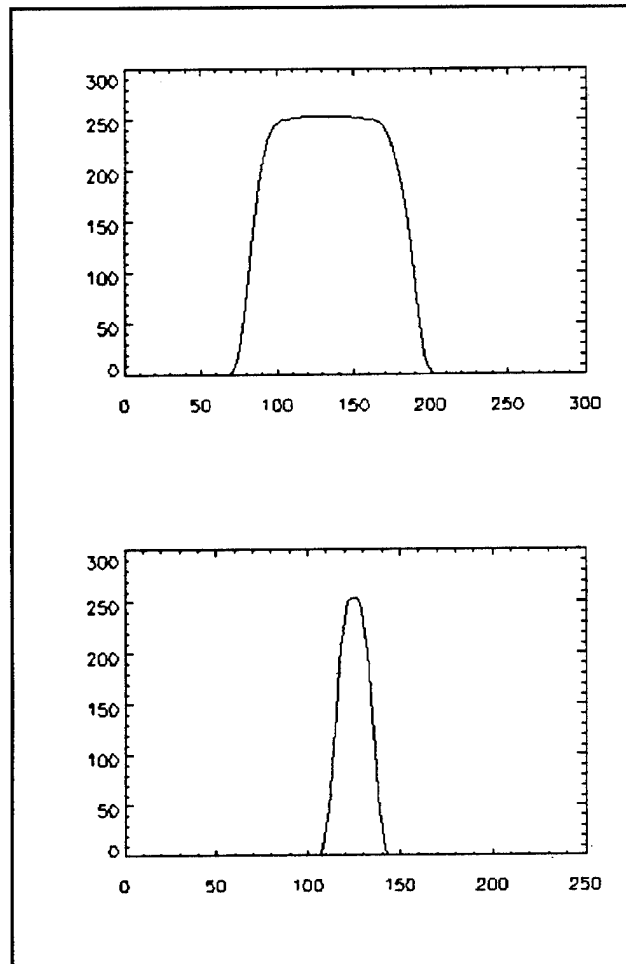


Figure 10. Horizontal (top) and vertical (bottom) cross sections of the diffracted beam, demonstrating an angular selectivity of 0.8 mrad.

Optical computers and neural networks require the ability to store, process, and interconnect high-resolution 2D (and 3D) optical data entering at high frame rates. Currently, high-speed 2D images can be stored (for later readout and processing at slower rates) using high-speed video cameras. Commercially available cameras can store 30 frames at 1 MHz or 8 frames at 10 MHz, and effectively act as optical cache memories. To store 3D images, high-speed holographic techniques can be used. Holographic cinematography can store 4000 medium-resolution holograms at 300 kHz frame rates or 40 high-resolution holograms at 20 kHz frame rates. Optical spectral hole-burning materials can be used to both store and process 2D and 3D optical images at high frame rates. So far, optical photon echoes have been used to perform medium-resolution pattern recognition at a 30 MHz frame

rate,¹⁷ and to store 1600 optical data bits (at a single spatial location) with a 40 MHz frame rate.¹⁸

Optical spectral hole burning has limitations, however. For example, slow readout for interfacing to optoelectronic devices would require a gated detection scheme and multiple reads of the entire memory contents. While 10 read cycles at a single point has not been found to significantly degrade the stored data, the 1000 read cycles required to separately read 1000 images would be expected to cause image degradation, especially for high-resolution data. Also, although data storage times for stimulated optical echoes can exceed hours,¹⁹ the total duration of the input optical data stream cannot be longer than 1 msec. This limits the number of images that can be stored at frame rates slower than 10 MHz. Even to achieve this maximum 1 msec duration, a very stable laser is needed so that the laser will remain approximately phase-coherent. Finally, there are potential limitations due to the low readout efficiency (about 10^{-5} of the input image strength).¹⁸

We have designed a high-speed optical cache memory²⁰ which should have similar performance to optical echo memories (i.e., capability of storing 1000 successive holographic images at frame rates up to 10 MHz), but without many of their limitations. For example, slow readout should be possible without multiple reads (and hence partial erasure) of each image. This memory should also be capable of storing optical data streams of duration much longer than 1 msec without the need for maintaining absolute laser phase coherence (i.e., noisy lasers can be used). Finally, theoretical efficiencies are higher than for optical spectral hole burning.

This design is based on our recent demonstration of the ability of Raman coherent population trapping to store and recall optical temporal and phase information using spin echoes (in a sodium atomic beam).²¹ In this experiment, two optical data pulses are used as input, each pulse consisting of two-frequency Raman-resonant laser light. Both of these Raman optical pulses create spin coherences via Raman population trapping.²² The population trapping process also allows for these spin coherences to interfere, thereby storing the temporal/phase information. Any technique applicable to spin echoes can be used to rephase the spin coherences, for example an rf π -pulse or an off-resonance Raman π -pulse. The rephased spin coherences are then detected optically using a two-frequency Raman resonant probe. The spin echo leads to an experimentally observed decrease or increase in probe absorption, depending on the relative optical phase.²¹

Slow readout of the stored optical images can be achieved by noting that the maximum input/output data rate in a spin-echo memory is determined by the magnitude of the inhomogeneous broadening of the rf spin-transition. Since most spin-echo materials have small intrinsic inhomogeneous broadening (about 1 - 10 kHz), their speed is determined primarily by the strength of an applied magnetic field gradient. For example, a 2 kGauss/cm magnetic field gradient and a 5 kHz/Gauss magnetic Zeeman shift should permit an input data rate of 10 MHz over a 1 cm sample of spin-echo material. However, reducing the magnetic field gradient to 2 Gauss/cm gives a 10 kHz output data rate. This is illustrated in figure 11.

¹⁷ X.A. Shen and R. Kachru, "High-speed Pattern Recognition by Using Stimulated Echoes," *Opt. Lett.* 17: 520 (1992).

¹⁸ Y.S. Bai and R. Kachru, "Coherent Time-domain Data Storage with a Spread Spectrum Generated by Random Biphasic Shifting," *Opt. Lett.* 18: 1189 (1993).

¹⁹ M. Mitsunaga, R. Yano, and N. Uesugi, "Time- and Frequency-domain Hybrid Optical Echo Memory: 1.6-kbit Data Storage in Eu³⁺:Y₂SiO₅," *Opt. Lett.* 16: 1890 (1991).

²⁰ M.S. Shahriar, P.R. Hemmer, and M.K. Kim, "Five Dimensional Optical Data Storage," submitted to *Opt. Comm.*

²¹ P.R. Hemmer, M.S. Shahriar, M.K. Kim, K.Z. Cheng, and J. Kierstead, "Time Domain Optical Data Storage using Raman Coherent Population Trapping," *Opt. Lett.* 19, 296 (1994).

²² M.S. Shahriar and P.R. Hemmer, "Direct Excitation of Microwave-spin Dressed States Using a Laser-excited Resonance Raman Interaction," *Phys. Rev. Lett.* 65: 1865 (1990).

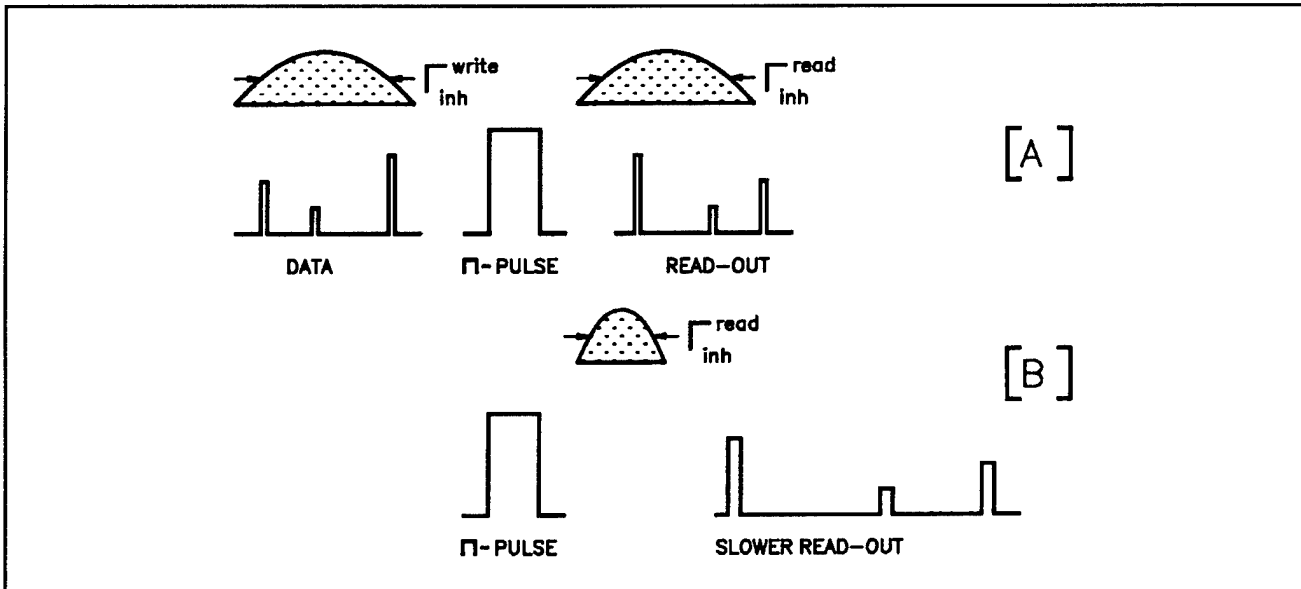


Figure 11. Schematic illustration of the variable speed read-out of spin echo: (a) Data stream stored, time-reversed, and read at a high speed using a large spin inhomogeneous broadening, created by a magnetic field gradient; (b) Slower read-out if the inhomogeneous broadening is reduced during rephasing.

The duration of the input data stream is not limited by the optical coherence lifetime, but by the spin coherence lifetime which can be much longer than the 1 msec limit for optical echoes. For example, in Eu³⁺:Y₂SiO₅ crystal at 2 K, the spin population lifetime can exceed hours and spectral diffusion is also very small. Thus, it is reasonable to expect that spin coherence lifetimes on the order of seconds or longer should be possible. Moreover, since Raman coherent population trapping is not very sensitive to correlated laser frequency jitter, the laser stability requirement can be greatly relaxed if, for example, laser field 2 is generated from field 1 with acousto-optic or electro-optic devices.

To summarize, we have designed a novel high-speed optical cache memory which is capable of storing about 1000 successive holographic images at frame rates up to 10 MHz and allows a much slower read-out. Experiment is in progress using a dye laser and a Eu³⁺:Y₂SiO₅ crystal cryogenically cooled to superfluid He temperature to demonstrate this memory.

1.6 Doppler Cooling in Traveling Wave Velocity Selective Coherent Population Trapping

Sponsor

U.S. Navy - Office of Naval Research
Grant N0014-91-J-1808

Recently, there has been increasing interest in cooling atoms to ultralow temperatures for potential applications to spectroscopy, improved atomic clocks, and observation of quantum collective effects such as Bose-Einstein condensation. One promising candidate is a system of Λ type atoms excited by two counterpropagating traveling waves. It has been shown previously that such a system cools to a temperature far below the recoil limit. However, velocity selective coherent population trapping (VSCPT), occurs via random walks in momentum space and therefore is extremely slow. This makes it nearly impossible to achieve sub-recoil cooling in three dimensions. What is needed is to provide additional frictional forces that coexist with this process. However, theoretical calculations showed that no such frictional force exists in this system for any choice of parameters.²³

²³ A. Aspect, E. Arimondo, R. Kaiser, N. Vansteenkiste, and C. Cohen-Tannoudji, *Phys. Rev. Lett.* 61: 826 (1988).

We have found that this theoretical prediction was incorrect,²⁴ and have identified conditions under which a frictional cooling force exists. In a semi-classical view, this force is found to exist in the transient regime of the optical Bloch equations. However, we have also shown that this frictional cooling is actually continuous when a fully quantized model is used. This additional cooling force is expected to accelerate the process of VSCPT enough to achieve a sub-recoil temperature in three dimensions.

Figure 12 illustrates the physical origin of this cooling force. Consider the case where, in the lab frame, both fields are equally detuned to the red, and the atom is moving opposite to the σ_- polarized beam at a velocity v . In the atom's rest frame, the σ_- beam is tuned closer to the resonance, while the σ_+ beam is tuned farther away from resonance. It turns out, however, that even under this broken symmetry there is no semiclassical friction force in the steady state. We have interpreted this result physically using cascaded adiabatic following arguments. The steady state coherence is such that the expectation value of the force operator identically vanishes.

However, in the transient regime, more photons are absorbed (and randomly remitted) from the σ_- beam than the other one. Therefore, the atom

experiences cooling until the steady state is reached. This is illustrated in figure 13. For parameters of experimental interest, this transient process lasts about as long as the time scale for the polarization gradient cooling. The cooling coefficient is comparable to that of conventional Doppler cooling for a two level atom.

This semi-classical result, however, is not valid when the atoms become so cold that the de Broglie wavelength becomes comparable to the laser wavelength. Therefore, it is necessary to examine this process in a model in which the atom's position and linear momentum are fully quantized. We performed this calculation and found that the cooling takes place even in the model. More important, the model predicts that this additional cooling process is not transient, but is continuous. Therefore, VSCPT under the condition of red detuning is expected to be significantly more efficient.

To summarize, we have found that, contrary to previous assertions, frictional cooling force does exist in traveling wave VSCPT if the beams are red detuned. This may prove useful in enhancing the rate of VSCPT in three dimensions. Experimental work is in progress for using this effect, as well as the alternative method of standing wave VSCPT, to achieve subrecoil cooling in three dimensions, using 87 Rb atoms and semiconductor lasers.

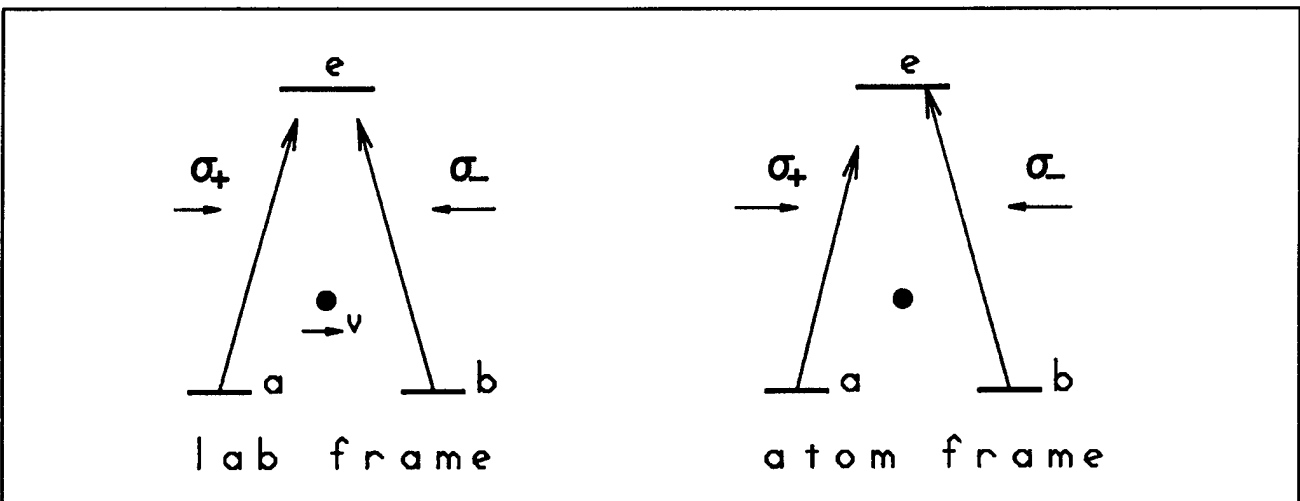


Figure 12. Physical origin of the transient cooling force in traveling wave VSCPT for red detuning.

²⁴ M.S. Shahriar, M.G. Prentiss, and P.R. Hemmer, "Transient Heating and Cooling in Travelling Wave Velocity Selective Coherent Population Trapping," *OSA Annual Meeting Technical Digest*, (Washington, D.C.: Optical Society of America, 1994), v. 25, p. 159.

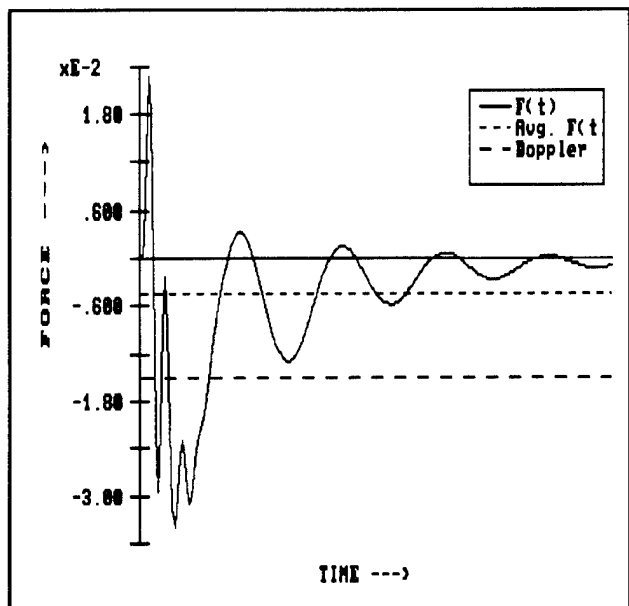


Figure 13. Illustration of the duration and magnitude of the transient cooling force for traveling wave VSCPT under red detuning. The force is in units of $\hbar k/\Gamma$, and time duration is $80 \Gamma^{-1}$. In the fully quantized model, this cooling is seen to be continuous.

1.7 Near-perfect Squeezing in a Folded Three-Level System

Sponsor

U.S. Air Force - Electronic Systems Divisions
Contract F19628-92-K-0013

In many applications involving lasers, the ultimate accuracy of measurement is limited fundamentally by the shot noise. The shot noise is a consequence of the quantum nature of light, and results from the Heisenberg uncertainty principle. The output of a conventional laser is the coherent state, which closely resembles a classical electromagnetic field. However, the strength of the electric field amplitude, for example, can not be measured precisely. In particular, the two quadratures of the sinusoidally oscillating field are conjugate quantum variables, and the product of the variance for the two quadratures is limited by Planck's constant.

The uncertainty in one quadrant, however, may be arbitrarily small, provided the uncertainty in the other quadrant is allowed to grow correspondingly larger. Phase sensitive detection of the quadrant with the reduced variance thus may be used to perform measurements below the shot noise limit. Fields that have suppressed variance in one quadrature are called squeezed states and can be generated via multi-wave mixing processes in a nonlinear medium.

To date, the best material for generating squeezed states have been crystals with χ_2 type nonlinearity. However, this medium is inappropriate for applications involving detection of very weak images because phase matching constraints severely limit the spatial bandwidths of image squeezing.²⁵ What is needed is a material with χ_3 type nonlinearity, which yields perfect phase matching for any configuration, which in turn implies very large spatial bandwidth for image squeezing. One such material is a two-level atom. The noise from spontaneous emission strongly degrades squeezing in such a system, however.

We have performed calculations showing that near perfect squeezing can be achieved if a Λ system is used instead of a two level system.²⁶ This system possesses strong χ_3 type nonlinearity, but does not have problems of noise from spontaneous emission. This is because Raman type strong gain can be generated via ground states coherence, without much optical coherence. Figure 14 illustrates the field configuration to be used for observing this squeezing. Here, F and B are the forward and backward pumps, respectively, in a phase-conjugate geometry, S is the probe, and C is the conjugate. When mixed with the local oscillator, a superposition of the signal and conjugate beams yields quadrature squeezing in a configuration similar to the one used by Slusher et al. for a two level system.²⁷ Note that unlike other predictions,²⁸ this system does not assume a nonzero decay rate of the ground states and can be easily realized for example, using a $j=1 \leftrightarrow j'=1$ transition.

To summarize, we have found that near perfect squeezing can be achieved in a χ_3 phase matched

²⁵ P. Kumar and M.I. Kolobov, "Degenerate Four-wave Mixing as a Source for Spatially-broadband Squeezed Light," *Opt. Comm.* 104: 374 (1994).

²⁶ M.S. Shahriar, P.R. Hemmer, and P. Kumar, "Detailed Theory of Near-perfect Squeezing Using an Ideal Λ System," to be submitted to *Phys. Rev. A*.

²⁷ R.E. Slusher, L.W. Hollberg, B. Yurke, J.C. Mertz, and J.F. Valley, *Phys. Rev. Lett.* 55, 2409 (1985).

²⁸ C.M. Savage and D.F. Walls, "Squeezing Via Two-photon Transitions," *Phys. Rev A* 33: 3282 (1986).

four wave mixing geometry using a pure Λ system. Experimental work is under progress to observe this effect in sodium using dye lasers, and in rubidium using semiconductor lasers. Twin beams generated this way may help improve the signal to noise ratio in the large angle atomic beam splitter demonstrated by us.²⁹

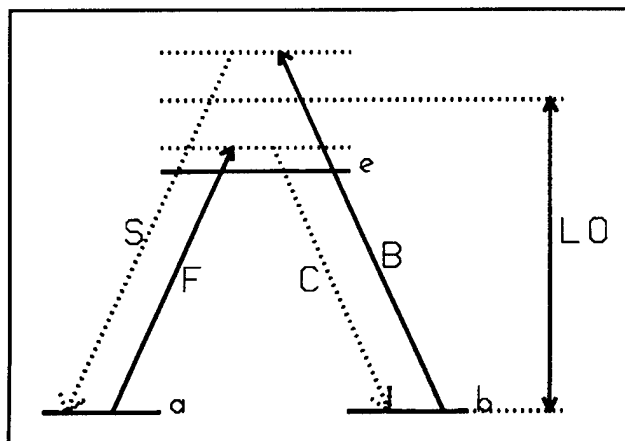
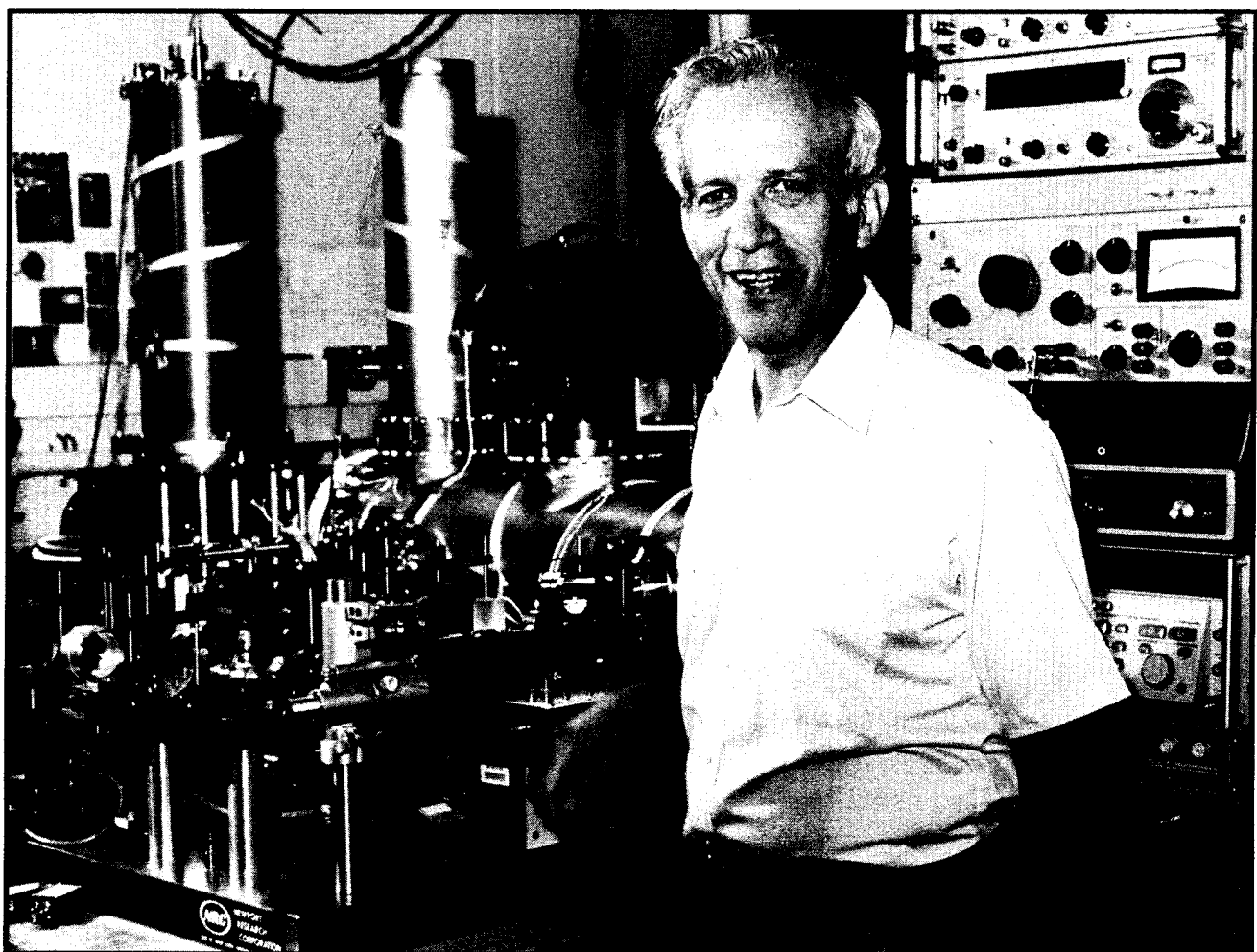


Figure 14. Schematic illustration of the level structure and optical fields to be used in generation of squeezed states via four wave mixing, using a Λ system. F: forward pump, B: backward pump, S: probe, C: conjugate, LO: local oscillator.

²⁹ K. Johnson, A. Chu, T. Lynn, K. Barggren, M.S. Shahriar, and M. Prentiss, "Demonstration of a Non-magnetic Blazed Grating Atomic Beam Splitter," *Opt. Lett.*, forthcoming.



Professor Daniel Kleppner, Associate Director of the Research Laboratory of Electronics (Photo by John F. Cook)

Chapter 2. Basic Atomic Physics

Academic and Research Staff

Professor Daniel Kleppner, Professor David E. Pritchard, Professor Wolfgang Ketterle

Visiting Scientists and Research Affiliates

Dr. Theodore W. Ducas,¹ Dr. Alan L. Lenef, Dr. Fred L. Palmer, Dr. H. Jörg Schmiedmayer

Graduate Students

Michael R. Andrews, Michael P. Bradley, Michael S. Chapman, Michael W. Courtney, Kendall B. Davis, Frank DiFilippo, Joel C. DeVries, Troy D. Hammond, Jeffrey R. Holley, Hong Jiao, Robert I. Lutwak, Marc-O. Mewes, Richard A. Rubenstein, Edward T. Smith, Neal W. Spellmeyer

Undergraduate Students

Ilya Entin, Philip M. Hinz, Wan Y. Morshidi, Amrit R. Pant, Szymon M. Rusinkiewicz, Abraham D. Stroock, Bridget E. Tannian, Stanley H. Thompson, John J. Wuu, Peter S. Yesley

Technical and Support Staff

Carol A. Costa

2.1 Studies in Quantum Chaos: High Resolution Periodic Orbit Spectroscopy

Sponsors

Joint Services Electronics Program
Contract DAAL03-92-C-0001
Grant DAAH04-95-1-0038

National Science Foundation
Grant PHY 92-21489

U.S. Navy - Office of Naval Research
Grant N00014-90-J-1322

Project Staff

Michael W. Courtney, Hong Jiao, Neal W. Spellmeyer, Professor Daniel Kleppner

Our understanding of Rydberg atoms in strong fields has been advanced by high resolution spectroscopy, the development of efficient quantum calculations for atoms in electric and magnetic fields, and theoretical advances in classical dynamics. The principal motivation for this work is to understand atomic systems under external perturbations that are comparable to the unperturbed energy and in which the classical motion may be irregular. Rydberg atoms are central to this research because their atomic fields are comparable to the field strengths available in the laboratory. In addition,

with the important exception of the hydrogen atom in an electric field, the classical counterparts of these systems all undergo a transition from order to chaos. Consequently, Rydberg atoms in applied fields provide a natural testing ground for studying the connections between quantum mechanics and classical chaos.

In the semiclassical limit, periodic orbit theory provides a unifying principle for relating a quantum spectrum to the periodic orbits of the corresponding classical system. According to periodic orbit theory, each periodic orbit produces a sinusoidal modulation in the density of states. Quantum mechanically, a spherical wave sent out from the origin will recur (overlap with the original outgoing wave) at times corresponding to the periods of the periodic orbits of the classical system. The magnitude of this overlap gives the strength of the modulation of the spectrum.

In our laboratory, we have studied lithium in an electric field, a system that displays a transition from order to core-induced chaos. In contrast, the classical dynamics of hydrogen in an electric field is always orderly. Its Hamiltonian

$$H = \frac{1}{2} p^2 - \frac{1}{r} + Fz$$

¹ Physics Department, Wellesley College, Wellesley, Massachusetts.

can be rescaled using the substitutions $r = F^{-1/2}\tilde{r}$ and $p = F^{1/4}p$. Because the scaled Hamiltonian

$$\tilde{H} = \frac{1}{2} \tilde{p}^2 - \frac{1}{\tilde{r}} + \tilde{z}$$

does not depend explicitly on the field, the classical dynamics depends only on the scaled energy $\varepsilon = EF^{-1/2}$, not on E and F separately. This classical scaling is exact for hydrogen and a good approximation for lithium.

The scaled action of a particular closed orbit, $\tilde{S}_k = F^{-1/4}S_k$, depends only on ε . If the spectrum is recorded while the field and the energy are varied simultaneously to keep ε constant, the classical dynamics remains the same. This approach has been applied to several systems,² but we have extended it to a higher resolution than previously possible.

An orbit's scaled action and recurrence strength can be obtained directly from the Fourier transform of the spectrum. This Fourier transform is called the *recurrence spectrum* because each peak is located at the scaled action of a periodic orbit. The height of a peak is proportional to that orbit's recurrence strength. We have applied this approach to the lithium Stark spectrum. To model the atomic core potential of lithium, we have added to the hydrogenic Hamiltonian a short range potential, chosen to give the proper quantum defects. Within these constraints a variety of model potentials yields essentially the same classical behavior. In particular, as the scaled energy is increased, lithium shows a transition from regular to chaotic motion at about $\varepsilon = -16$.

We have carried out laser spectroscopy on an atomic beam of lithium in an applied electric field. The atomic beam passes through holes in the centers of a pair of electric field plates. Between the field plates, one laser (735 nm) excites the $2S \rightarrow 3S$ two-photon transition, and a second laser (610 nm), polarized parallel to the external field, excites

Rydberg states. These states are field ionized and ions are detected by a channeltron. The error in scanning the laser to maintain constant scaled energy is 0.002 cm^{-1} ; the fractional error in the electric field is 0.3 percent.

To verify our methods, the experimental recurrence spectrum at $\varepsilon = -3.0$ is compared with a recurrence spectrum obtained from quantum computations in figure 1.³ Agreement is generally good, although there are some small discrepancies that we believe arise from experimental noise and neglect of the continuum in the computations. Closed orbits parallel to the field play an important role in the spectrum. These form two classes: "uphill" orbits, directed toward the cathode, and the "downhill" orbits, directed toward the anode. For $\varepsilon = -3.0$, the first return of the uphill orbit has a scaled action of 0.3915, and the first return of the downhill orbit has a scaled action of 0.4285. As a result, the recurrence spectrum should have peaks at 0.3915 n and 0.4285 n. In figure 2, most of the prominent peaks for scaled action less than 10 are identified as corresponding to repetitions of the parallel orbits. For high action, the parallel orbits continue to display a strong signature in the spectrum. We have identified recurrences near the 100th return of the uphill parallel orbit (figure 3). This illustrates the power of closed-orbit theory to associate spectral features with long-period orbits.⁴

Gao and Delos⁵ recently examined closed orbits and recurrences for single electron atoms in electric fields. At high energy (positive energy regime), only one closed orbit, parallel to the field and extending from the nucleus to the classical turning point, exists. The spectrum contains a fundamental Fourier component from this orbit plus harmonics and its repetitions. As the energy is decreased, new orbits are predicted to spring into existence by an orderly sequence of bifurcations. At each bifurcation, a new frequency component is added to the spectrum. To study these bifurcation processes near the ionization limit of lithium in an electric field, we have performed scaled-energy spectroscopy on $m=0$ states of lithium for scaled energy between $\varepsilon =$

² A. Holle, J. Main, G. Wiebusch, H. Rottke, and K.H. Welge, *Phys. Rev. Lett.* 61(13): 161 (1988); T. van der Veldt, W. Vassen, and W. Hogervorst, *Europhys. Lett.* 21: 9 (1993); U. Eichmann, K. Richter, D. Wintgen, and W. Sander, *Phys. Rev. Lett.* 61: 2438 (1988).

³ M.L. Zimmermann, M.G. Littman, M.M. Kash, and D. Kleppner, "Stark Structure of the Rydberg States of Alkalimetal Atoms," *Phys. Rev. A* 20: 2251 (1979).

⁴ M. Courtney, H. Jiao, N. Spellmeyer, and D. Kleppner, "Long-Period Orbits in the Stark Spectrum of Lithium," *Phys. Rev. Lett.* 73: 1340 (1994).

⁵ J. Gao and J.B. Delos, "Resonances and Recurrences in the Absorption Spectrum of an Atom in an Electric Field," *Phys. Rev. A* 49: 869 (1994).

$\epsilon = -2.1$ and $\varepsilon = -0.37$. A map of the recurrence spectra is shown in figure 4. We observe small recurrences corresponding to repetitions of the parallel orbit, and large recurrences near bifurcations. The large bifurcation peaks are labeled with the fractions, m/l , used to designate the newly created orbits. These orbits are displayed in figure 4. Our

experimental study reveals that the bifurcation of classical trajectories dominates the spectrum, and bifurcation theory provides a natural way of understanding the evolution of the spectrum from a broad continuum above the ionization limit to a quasi-discrete spectrum below the ionization limit.⁶

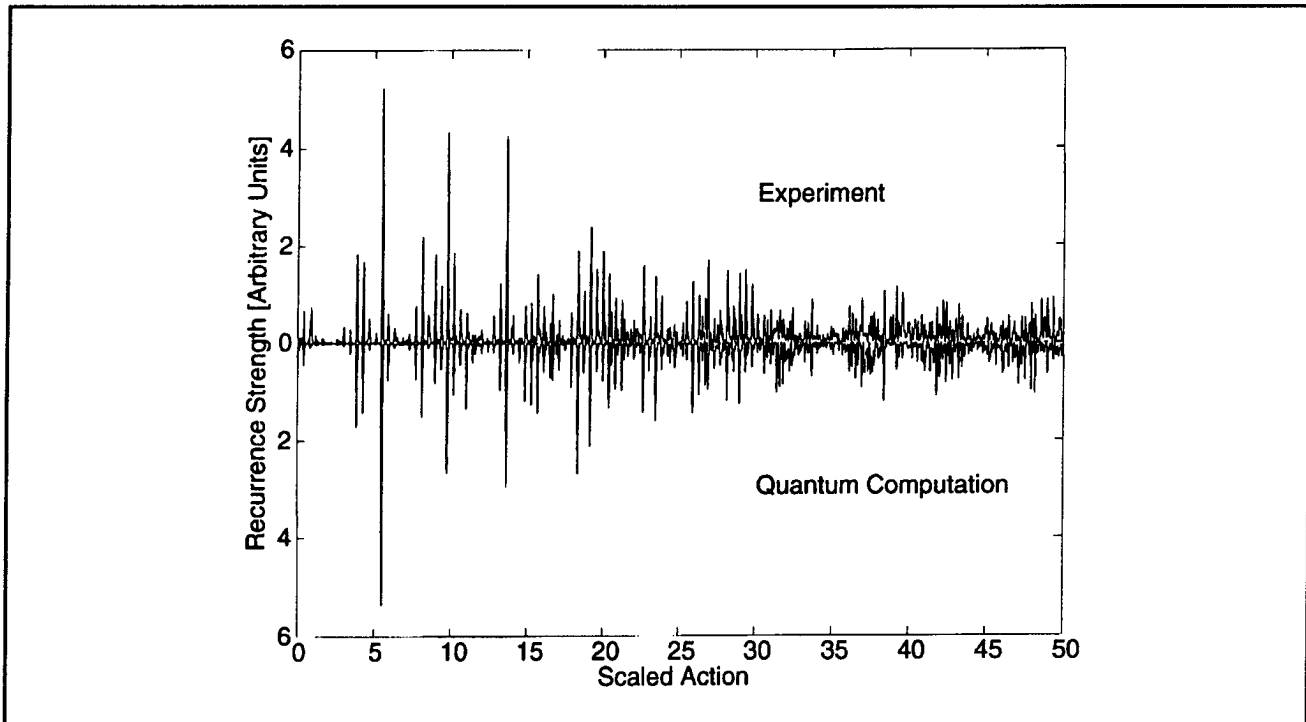


Figure 1. Lithium recurrence spectrum for $\epsilon = -3.0$. A mirror plot is used for comparison of the experimental spectrum (top) with the results of a quantum computation (bottom). The computed spectrum has been normalized to provide comparable heights.

2.1.1 Publications

Courtney, M., H. Jiao, N. Spellmeyer, and D. Kleppner. "Quantum Chaos and Rydberg Atoms in Strong Fields." *Drexel Conference Proceedings*. Forthcoming.

Courtney, M., N. Spellmeyer, H. Jiao, and D. Kleppner. "Classical, Semiclassical, and Quantum Dynamics in the Lithium Stark System." *Phys. Rev. A*. Forthcoming.

Courtney, M., and D. Kleppner. "Core-Induced Chaos in Diamagnetic Lithium." *Phys. Rev. A*. Forthcoming.

Courtney, M., H. Jiao, N. Spellmeyer, D. Kleppner, J. Gao, and J.B. Delos. "Closed Orbit Bifurcations in Continuum Stark Spectra." *Phys. Rev. Lett.* 74: 1538 (1995).

Courtney, M., H. Jiao, N. Spellmeyer, and D. Kleppner. "Long-period Orbits in the Stark Spectrum of Lithium." *Phys. Rev. Lett.* 73: 1340 (1994).

2.1.2 Theses

Courtney, M. *Rydberg Atoms in Strong Fields: A Testing Ground for Quantum Chaos*. Ph.D. diss., Dept. of Physics, MIT, 1994.

⁶ M. Courtney, H. Jiao, N. Spellmeyer, and D. Kleppner, "Closed Orbit Bifurcations in Continuum Stark Spectra," *Phys. Rev. Lett.* 74: 1538 (1995); M. Courtney, *Rydberg Atoms in Strong Fields: A Testing Ground for Quantum Chaos*, Ph.D. diss., Dept. of Phys., MIT, 1995.

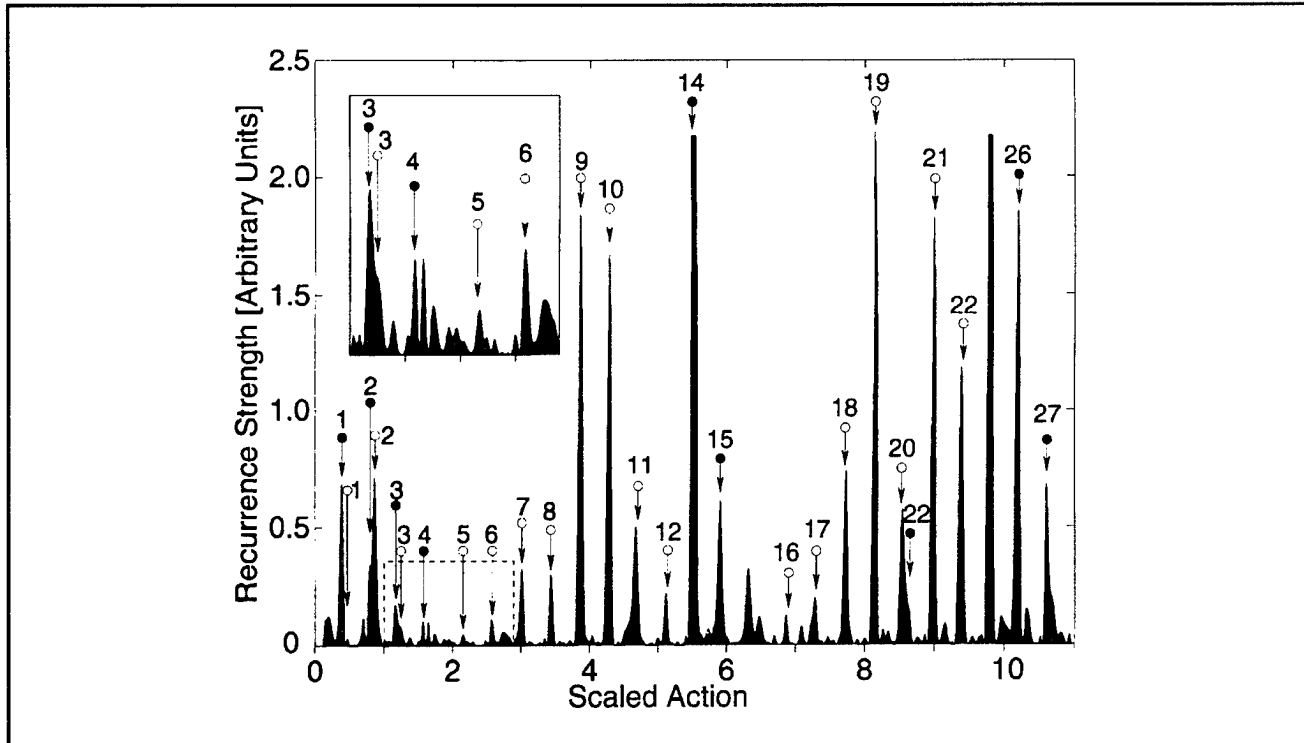


Figure 2. Blowup of experimental data in figure 1. Recurrences corresponding to the parallel orbits are marked with arrows. Filled circles: uphill orbits. Open circles: downhill orbits. The number specifies the number of repetitions of the primitive orbit. The truncated peak at scaled action of 5.5 has strength 5.2. The truncated peak at scaled action of 9.8 has strength 4.3. The inset shows detail near scaled action of 2.

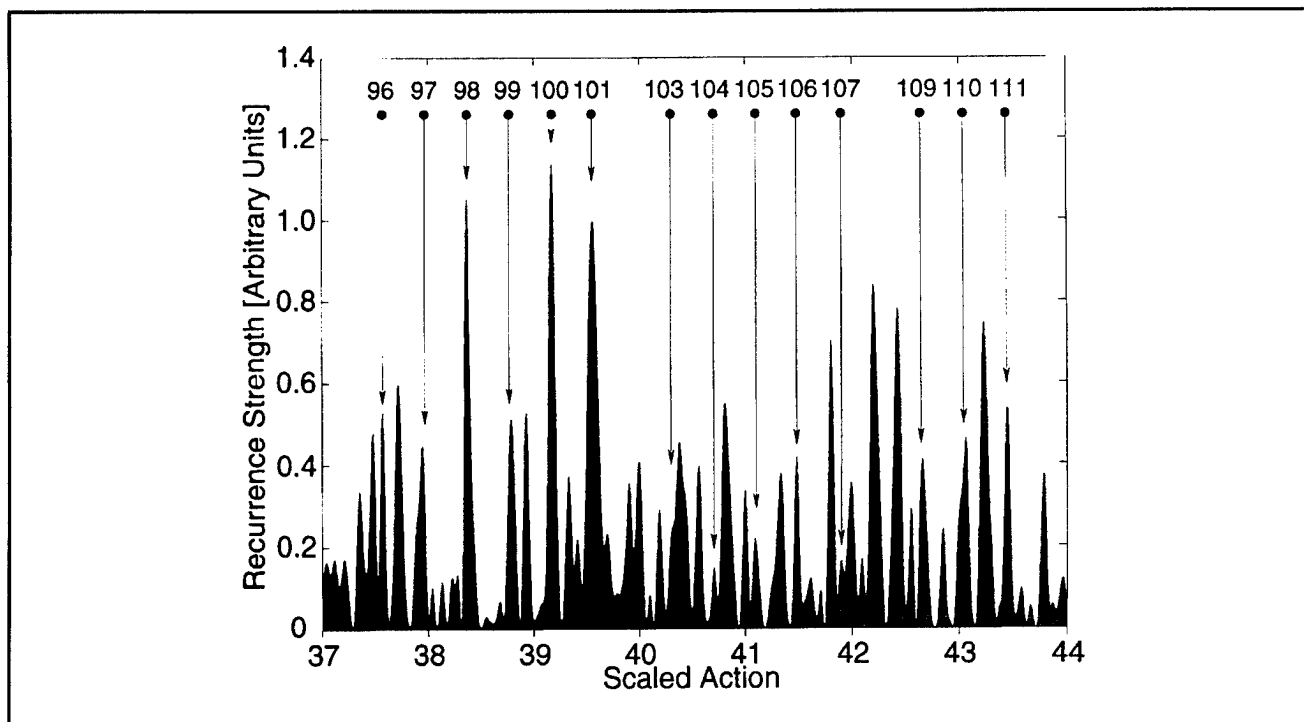


Figure 3. Blowup of figure 1 at large action. Peaks identified with uphill parallel orbits are marked with arrows, as in figure 2.

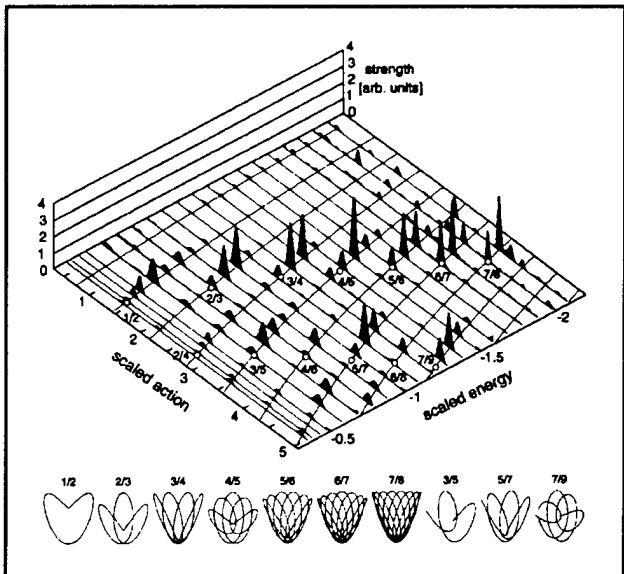


Figure 4. The curves in the horizontal plane represent the scaled action of the parallel orbit and its repetitions as a function of scaled energy. Locations of bifurcations are marked with small open circles. New orbits created in bifurcations have almost the same action as the corresponding return of the parallel orbit. Measured recurrence strengths are shown in the z direction. Recurrences are especially strong at scaled energies slightly lower than bifurcations. Orbits created by bifurcation of the parallel orbit are shown along the bottom. The 2/4, 4/6 and 6/8 orbits are repetitions of the 1/2, 2/3 and 3/4 orbits respectively, so their shapes are identical.

2.2 Determination of the Rydberg Frequency

Sponsor

Joint Services Electronics Program
Contract DAAL03-92-C-0001
Grant DAAH04-95-1-0038

National Science Foundation
Grant PHY 92-21489

Project Staff

Joel C. DeVries, Dr. Theodore W. Ducas, Jeffrey R. Holley, Robert I. Lutwak, Professor Daniel Kleppner

The Rydberg constant, R_{∞} , relates the atomic unit of distance to laboratory units. It is a so-called fundamental constant, and recent advances in laser optical spectroscopy have made it possible to measure it with accuracy approaching 2 parts in

10^{11} .⁷ The Rydberg frequency, cR_{∞} , relates the atomic unit of frequency to laboratory units. Although the speed of light c is an exactly defined quantity, the relation between the Rydberg constant and the Rydberg frequency is not merely formal: the precision with which a frequency can be measured is limited in principle to the precision of atomic clocks, which currently exceeds 1 part in 10^{14} and is expected to grow even larger. In contrast, wavelength metrology appears to have reached its limit of precision, somewhat less than 1 part in 10^{11} .

To make full use of the precision of lasers and modern laser spectroscopy, and for applications in communications, control, and metrology, general techniques for measuring the frequency of light need to be developed. As part of this effort, we propose to help establish a new optical frequency standard by measuring the Rydberg frequency.

Our approach involves measuring the frequency of transitions in atomic hydrogen at wavelengths long enough for the frequency to be measured directly by an atomic clock. The experiment employs a highly excited "Rydberg" state of atomic hydrogen, $n=29$, and involves measuring transitions to nearby states at frequencies of approximately 256 GHz. This signal is generated coherently from a frequency standard based on an atomic clock.

The goals of our experiment are three-fold: First is the reevaluation of R_{∞} itself, providing an independent check, in a different regime, of other evaluations based on optical wavelength metrology. Second is the measurement of the ground state Lamb shift. Because our measurements involve high angular momentum states for which the Lamb shift is extremely small, our results may be compared with optical measurements of transitions between low-lying states to yield an improved measurement of the Lamb shift. Third is to provide a frequency calibration of the spectrum of hydrogen, enabling the creation of a comprehensive frequency standard extending from the radio-frequency regime to the ultra-violet.

Our experiment employs an atomic beam configuration to reduce Doppler and collisional perturbations. Atomic hydrogen is excited to the low angular momentum $n=29$, $m=0$ state by two-photon step-wise absorption from a pulsed laser source. The excited atoms are then transferred to the longer lived $n=29$, $m=28$ "circular" state by absorption of

⁷ T. Andreea et al., "Absolute Frequency Measurement of the Hydrogen 1S-2S Transition and a New Value of the Rydberg Constant," *Phys. Rev. Lett.* 69(13): 1923-1926 (1992); F. Nez et al., "Precise Frequency Measurement of the 2S-8S/8D Transitions in Atomic Hydrogen: New Determination of the Rydberg Constant," *Phys. Rev. Lett.* 69(16): 2326-2329 (1992).

circularly polarized radio-frequency radiation.⁸ The atoms enter a region of uniform electric field in which the frequency of the transition ($n=29, m=28 \rightarrow n=30, m=29$) is measured by the method of separated oscillatory fields. The final state distribution is analyzed by electric field ionization. The resonance signal appears as a transfer of atoms from the $n=29$ state to the $n=30$ state as the millimeter-wave frequency is tuned across the transition.

Figure 5 illustrates the apparatus. Atomic hydrogen or deuterium is produced by dissociating H₂ or D₂ in a radio-frequency discharge. The beam is cooled by collisions in a cryogenic thermalizing channel in order to slow the beam and thereby increase the interaction time. The atoms enter the circular state

production region, where they are excited from the 1s ground state, through the 2p state, to the $n=29, m=0$ state by two-photon stepwise excitation. The laser excitation is performed in an electric field to provide selective population of a particular $n=29, m=0$ level. The electric field is then rapidly reduced to an intermediate value as the atoms pass through the center of a circle of four antennas. The antennas are fed by a 2 GHz RF source with a 90° phase delay between adjacent pairs. The circularly polarized field drives the atoms into the $m=28$ circular state through the stepwise absorption of 28 photons. A detector in the circular state production region monitors the efficiency of the optical excitation and angular momentum transfer processes.

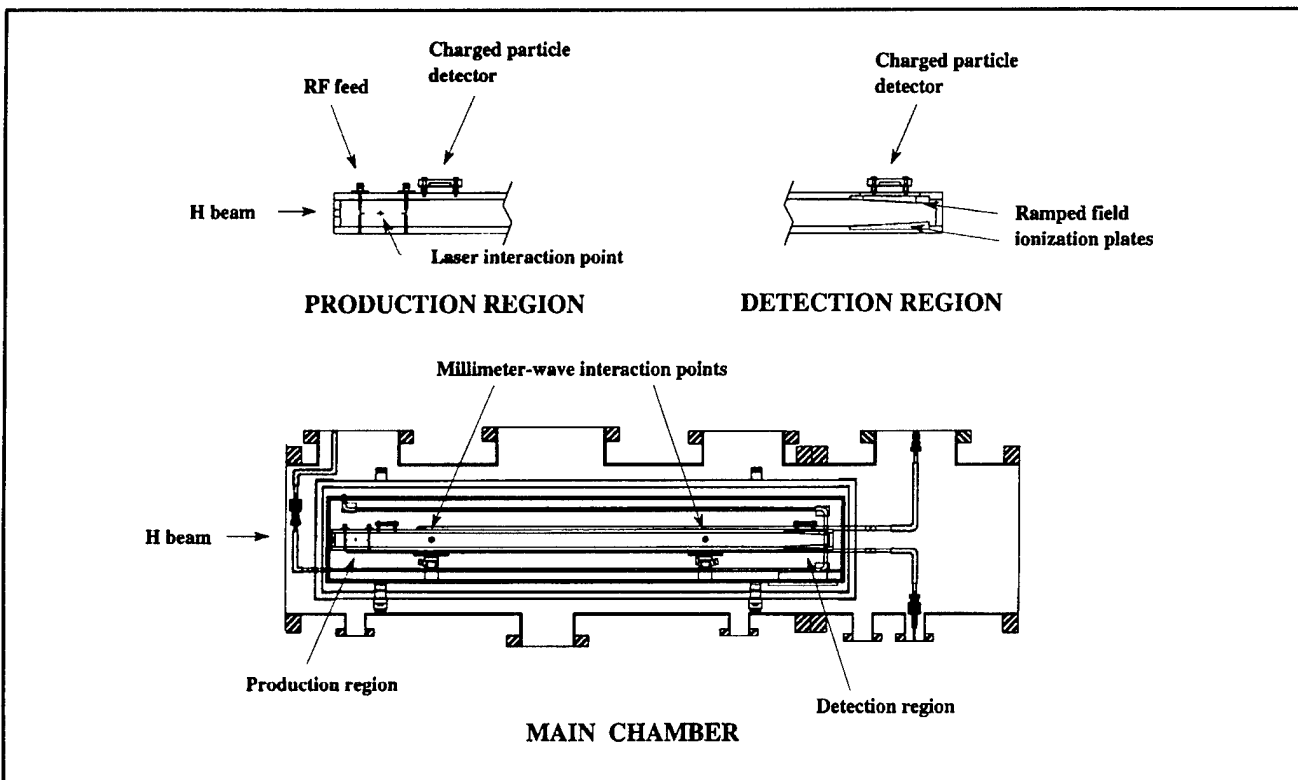


Figure 5. Main chamber of the atomic beam apparatus, with close-ups of the production region and the detection region.

After the atoms are prepared in the $n=29$ circular state, the beam enters the millimeter-wave interaction region. Because Rydberg atoms interact strongly with external fields, accurate measurement of the energy level structure requires careful control of the interaction environment. Thermal radiation is reduced by cooling the interaction region to ~ 10 K with a liquid helium flow system. The ambient mag-

netic field is reduced by a double-wall high-permeability shield. A small electric field, which defines the quantization axis of the atoms, is applied with high uniformity by field plates above and below the atomic beam. The millimeter-waves intersect the atomic beam at two locations separated by 50 cm. The millimeter-wave optical

⁸ R. Hulet and D. Kleppner, "Rydberg Atoms in 'Circular' States," *Phys. Rev. Lett.* 51(16): 1430-1433 (1983).

system was described in a previous *Progress Report*.

The state distribution of the atoms emerging from the interaction region is analyzed by a state-selective electric field ionization detector. Within the detector, the atoms enter a region of increasing electric field produced by a symmetric pair of ramped plates held at constant potential. Atoms in different states ionized at different fields, and the charged nuclei are detected at different positions. The signals from individual atoms are time resolved. Because the source is pulsed, this allows contributions to the resonance pattern from each velocity class to be analyzed individually, providing a valuable measure of possible systematic errors.

Preliminary Ramsey interference data was presented in a previous *Progress Report*. The signal-to-noise ratio was too low to achieve the desired accuracy, but having demonstrated the feasibility of the method, we set about building a second-generation version of the apparatus designed to improve the signal-to-noise ratio by several orders of magnitude. We are nearing the end of this construction phase of the experiment.

The past year has been devoted to three major efforts: perfecting a new method of populating the initial circular state, building a new atomic beam interaction region and cooling system, and building a new high duty-cycle laser system.

Our original method of producing circular states used a magnetic field, which required that the production region be outside the magnetically shielded interaction region. We believe that this geometry introduced radiation leaks that significantly reduced our signal-to-noise ratio. The new circularization method described above does not require a magnetic field, and the production region is now located inside the magnetic shields.

Early during the past year, we finished testing the new technique, using a mock-up of the new production region. Field ionization signals indicate efficient transfer to the circular state (see figure 6). In the course of diagnosing the circular state production efficiency, we have found that our electric field ionization data agrees with exact numerical calculations. However, it differs significantly from a previously accepted semi-empirical formula which was found to be in good agreement with experiments using alkali metal atoms.⁹ We are currently preparing a paper on the production of circular states in hydrogen.

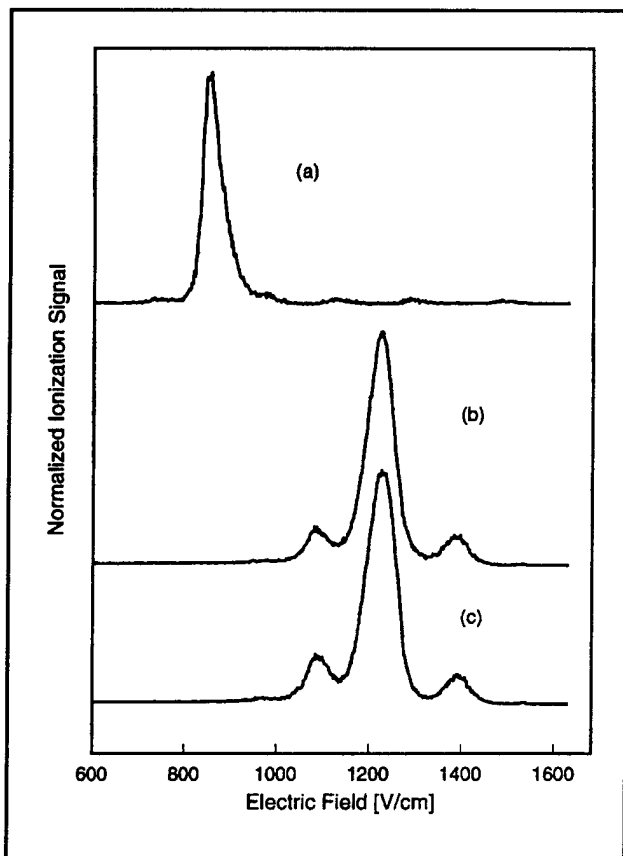


Figure 6. Production of "circular" states by absorption of circularly polarized 2 GHz radio-frequency radiation. The initial state, which ionizes at relatively low electric field (850 V/cm), is shown in (a). The two circular states are shown in (b) and (c). The characteristic ionization signal of the circular state appears at roughly 1220 V/cm.

By incorporating the production region into the magnetically shielded interaction region, it has been possible to consolidate the production, interaction, and detection regions into a monolithic helium temperature enclosure. We have completed much of this structure, including new field plates, liquid nitrogen temperature radiation shield, magnetic shields, and a precision supporting frame. We have also assembled a new helium flow system that should greatly reduce our liquid helium consumption rate, allowing longer data collection runs.

Finally, we are constructing a new ultraviolet dye laser system. Our original system was pumped with a YAG laser operating at 10 Hz. Since the transit time of even our slowest atoms is a few milliseconds, the duty cycle of the experiment was unnecessarily low. The new laser system, built

⁹ R.J. Damburg and V.V. Kolosov, "A Hydrogen Atom in a Uniform Electric Field III," *J. Phys. B.* 12(16): 2637-2643 (1979).

around an excimer pump laser, will run at 120 Hz. We are building our own tunable single-mode UV dye lasers to replace the yellow dye lasers used in the previous scheme. A pulsed wavemeter will allow calibration of the laser frequencies, which is an important advantage in setting up since there are no convenient atomic or molecular references at the wavelength of the UV dye lasers. With the completion of the laser system, we expect to begin taking data soon.

2.3 Precision Mass Spectrometry of Ions

Sponsors

Joint Services Electronics Program

Contract DAAL03-92-C-0001

Grant DAAH04-95-1-0038

National Science Foundation

Grant PHY 92-22768

Project Staff

Michael P. Bradley, Dr. Frank DiFilippo, Dr. Fred L. Palmer, Szymon M. Rusinkiewicz, Professor David E. Pritchard

In 1994, we published a table of ten atomic masses important for metrology or the determination of fundamental constants.¹⁰ The accuracy of the masses in the table, typically 10^{-10} , represents one to three orders of magnitude improvement over previously accepted values. In addition, a wide variety of self-consistency checks allowed us to virtually eliminate the possibility of unknown systematic errors. This capability has allowed us to contribute to several important experiments in both fundamental and applied physics, including:

- Recalibration of the current x-ray wavelength standard by weighing the energy differences associated with the neutron capture gamma rays of ^{14}N , which are widely used as calibration lines.
- Determination of the atomic weight of ^{28}Si , part of a program to replace the "artifact" kilogram mass standard by a crystal of pure silicon, in effect creating an atomic standard of mass.
- Determination of the molar Planck constant $N_A\hbar$, by weighing γ -rays whose wavelength is to be accurately determined by a NIST group;

this will also provide an independent determination of the fine structure constant.

In the fall of 1994, we made several important improvements to the stability and versatility of our mass spectrometer culminating in the demonstration of a technique for dramatically improving the accuracy of our mass comparisons by comparing two simultaneously trapped ions (to eliminate the problems due to field drift). In addition, we have demonstrated a squeezing technique to reduce the influence of thermal noise on the measurements. These advances led to another dramatic improvement in mass resolution that would allow:

- Determination of excitation and binding energies of atomic and molecular ions by weighing the small decrease in energy, $\Delta m = E_{\text{bind}}/c^2$. (We must reach our ultimate goal of a few $\times 10^{-12}$ to make this a generally useful technique.);
- Measurement of the ^3H - ^3He mass difference, important in ongoing experiments to determine the electron neutrino rest mass;
- Improvement of some traditional applications of mass spectrometry resulting from our orders of magnitude improvement in both accuracy and sensitivity; and
- Determination of the molar Planck constant $N_A\hbar$, by measuring the atomic mass and recoil velocity of an atom that has absorbed photons of known wavelength.

Our experimental approach is to measure ion cyclotron resonance on a single molecular or atomic ion in a Penning trap, a highly uniform magnetic field in which confinement along the magnetic field lines is provided by much weaker electric fields. We monitor the ion's axial oscillation by detecting the currents induced in the trap electrodes using ultrasensitive superconducting electronics developed for this application.¹¹ This work in trapping and precision resonance draws on techniques developed by Hans Dehmelt at the University of Washington and Norman Ramsey at Harvard University, for which they shared the 1989 Nobel Prize.

We have developed techniques for driving, cooling, and measuring the frequencies of all three normal modes of ion motion in a Penning trap. Thus we can manipulate the ion position reproducibly to

¹⁰ F. DiFilippo, V. Natarajan, K. Boyce, and D. E. Pritchard, *Phys. Rev. Lett.* 73: 1481 (1994).

¹¹ R. Weisskoff, G. Lafyatis, K. Boyce, E. Cornell, R. Flanagan, Jr., and D.E. Pritchard, *J. Appl. Phys.* 63: 4599 (1988).

within 30 microns of the center of the trap, correcting for electrostatic shifts in the cyclotron frequency to great accuracy. We use a π -pulse method to coherently swap the phase and action of the cyclotron and axial modes.¹² Therefore, although we detect only the axial motion directly, we can determine cyclotron frequency by measuring the phase accumulated in the cyclotron motion in a known time interval. We have implemented a new signal processing algorithm to improve our phase estimation by a factor of 2-3. We can measure the phase of the cyclotron motion to within 10 degrees, leading to a precision of 10^{-10} for a one minute measurement. Our entire ion-making process is fully automated, and the computer can cycle from an empty trap to having a cooled single ion in about three minutes under optimal conditions.

Careful shimming of the electric and magnetic fields allows us to keep our systematic errors well below 5×10^{-11} , but unfortunately, the typical statistical fluctuation in our magnetic field between measurements is 2.4×10^{-10} . Thus, even with the ability to achieve ~ 20 alternate loadings of two different ions in one night, our overall accuracy is at best 8×10^{-11} (see figure 7). We have found that the distribution of field variation is not Gaussian, but rather has too many outlying points. This has led us to use robust statistical analysis of field fluctuations; in particular a generalization of least squares fitting called "M-estimates" in which outlying points are deweighted in a manner determined by the observed excess number of outliers. This has eliminated arbitrary decisions about dropping "bad points" from our data sets and has increased the stability of our fits.

We have performed a wide variety of stringent checks for systematic errors. In fact, every mass in the table has been obtained from at least two independent sets of mass ratios. Several of the checks employ our new technique for comparison of non-doublets, pairs of ions whose nominal mass to charge ratios are unequal. This technique represents a significant advance in precision mass spectrometry since it allows us to obtain absolute masses by direct comparison to carbon, which is defined to have an atomic mass of exactly 12. It also provides an absolute check of our accuracy by allowing measurements that should verify known ratios such as N_2^+ and Ar^+/Ar^{++} . We have compared CD_3^+ and CD_3^{++} to C to obtain two independent determinations of the atomic weight of deuterium. The results are consistent with the values for the

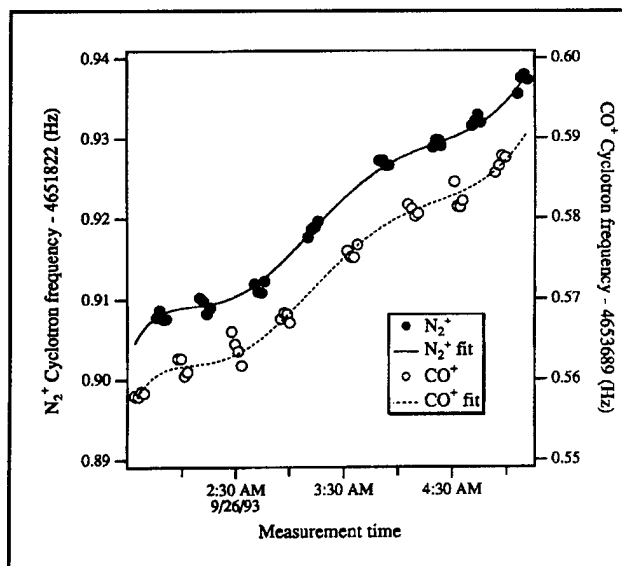


Figure 7. Cyclotron frequency as a function of time for alternate N_2^+ and CO^+ ions in our Penning trap. The frequencies are obtained after a 50s integration of cyclotron phase (see text). The solid line is a polynomial fit to the drift in the field common to both ions.

hydrogen masses we obtained from conventional doublet measurements. These carefully determined hydrogen and deuterium masses determine the mass of any organic compound composed of C, D, and H. The organic ions can in turn be used in doublet comparisons with many different ions. We have used this approach to obtain the absolute masses of several light atoms—H, D, N, O, Ne, Ar—to at least an order of magnitude better than the current standard mass table (see table 1).

An extensive series of quantitative systematic checks of our results using only doublet ratios was also performed. These include repeated checks of identical ratios (some interspaced by a significant reduction of our field inhomogeneities), checks of circular ratios (e.g., A/B, B/C, and C/A), and checks of related ratios (e.g., CO/N_2^+ and CO_2/N_2O). The consistency of all these checks practically guarantees that our errors are within the quoted limits.

Our newly rebuilt apparatus features improved stability of the trapping fields, a new and more efficient system for the ejection of unwanted ions, and most importantly, provisions for the excitation and detection of two different ions trapped at the same time. These improvements form the basis for an order of magnitude improvement in accuracy which will be achieved by simultaneous measurements on two ions to eliminate the problem of field fluctu-

¹² E.A. Cornell, R.M. Weisskoff, K. Boyce, and D.E. Pritchard, *Phys. Rev. A* 41: 312 (1992).

ations, and by using squeezing techniques to reduce thermal noise. We have expanded our previous theoretical understanding¹³ of two ion dynamics to include the effects of minute imperfections in the trapping fields, and demonstrated the capability of this technique to reduce the effects of field fluctuations (figure 8). If this works as planned, the primary source of measurement noise will be the special relativistic mass shift due to thermal fluctuations in cyclotron amplitude. We

have proposed several methods of classical squeezing with parametric drives to reduce amplitude fluctuations,¹⁴ and demonstrated the simplest of these,¹⁵ reducing thermal noise by about a factor of two. We have also built an external ion source and associated optics with which we plan to produce and select ions and guide them into the trap, thereby extending the types of ions we can measure.

Table 1. Atomic mass table. The center column lists the atomic masses determined from our experiment, and the right column lists the accepted atomic masses from the 1983 evaluation. For the purpose of comparison, zeros have been added to the numbers in the right column so that the number of digits are equal.

Atom	Mass (amu)	Accepted values (amu)
¹ H	1.007 825 031 6 (5)	1.007 825 035 0 (120)
ⁿ	1.008 664 923 5 (23)	1.008 664 919 0 (140)
² H	2.014 101 777 9 (5)	2.014 101 779 0 (240)
¹³ C	13.003 354 838 1 (10)	13.003 354 826 0 (170)
¹⁴ N	14.003 074 004 0 (12)	14.003 074 002 0 (260)
¹⁵ N	15.000 108 897 7 (11)	15.000 108 970 0 (400)
¹⁶ O	15.994 914 619 5 (21)	15.994 914 630 0 (500)
²⁰ Ne	19.992 440 175 4 (23)	19.992 435 600 0 (22000)
²⁸ Si	27.976 926 532 4 (20)	27.976 927 100 0 (7000)
⁴⁰ Ar	39.962 383 122 0 (33)	39.962 383 700 0 (14000)

2.3.1 Publications

DiFilippo, F., V. Natarajan, K. Boyce, and D.E. Pritchard. "Accurate Masses for Fundamental Metrology." *Phys. Rev. Lett.* 73: 1481 (1994).

DiFilippo, F., V. Natarajan, M. Bradley, F. Palmer, and D.E. Pritchard. "Accurate Atomic Mass Measurements from Penning Trap Mass Comparisons of Individual Ions." *Physica Scripta*. Forthcoming.

DiFilippo, F., V. Natarajan, M. Bradley, F. Palmer, and D.E. Pritchard. "Accurate Atomic Mass Measurements from Penning Trap Mass Comparisons of Individual Ions," *Proceedings of the Fourteenth International Conference on Atomic Physics*, Boulder, Colorado, July 31-August 5, 1994. Forthcoming.

Natarajan, V., F. DiFilippo, and D.E. Pritchard. "Squeezed States of Classical Motion in a Penning Trap." Submitted to *Phys. Rev. Lett.*

¹³ E.A. Cornell, K. Boyce, D.L.K. Fygenson, and D.E. Pritchard, *Phys. Rev. A* 45: 3049 (1992).

¹⁴ F. DiFilippo, V. Natarajan, K. Boyce, and D.E. Pritchard, *Phys. Rev. Lett.* 68: 2859 (1992).

¹⁵ V. Natarajan, F. DiFilippo, and D.E. Pritchard, "Classical Squeezing of a Oscillator for Sub-thermal Noise Operation," *Phys. Rev. Lett.* 74(15): 2855 (1995).

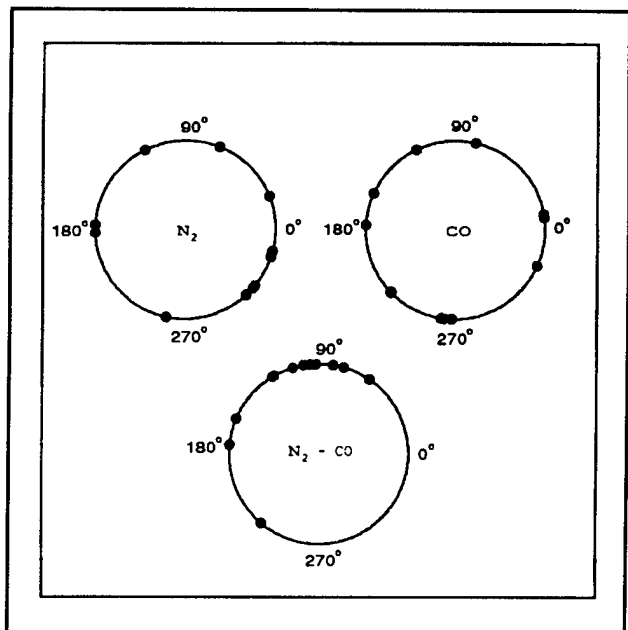


Figure 8. Each dot represents one measured cyclotron phase of simultaneously trapped single N₂ and CO⁺ ions 16 seconds after excitation. Daytime field fluctuations have virtually randomized the phases of the individual ions but the phase difference between the two remains well defined.

2.3.2 Thesis

DiFilippo, F. *Precise Atomic Masses for Determining Fundamental Constants*. Ph.D diss., Dept. of Physics, MIT, 1994.

2.4 Atom Interferometry

Sponsors

Joint Services Electronics Program

Contract DAAL03-92-C-0001

Grant DAAH04-95-1-0038

U.S. Army - Office of Scientific Research

Grant DAAL03-92-G-0229

Grant DAAL01-92-6-0197

U.S. Navy - Office of Naval Research

Grant N00014-89-J-1207

Project Staff

Michael S. Chapman, Troy D. Hammond,¹⁶ Dr. Alan L. Lenef, Amrit R. Pant, Richard A. Rubenstein, Dr.

H. Jörg Schmiedmayer,¹⁷ Edward T. Smith,¹⁶ Bridget E. Tannian, Professor David E. Pritchard

The recent development of atom interferometers, in which atom or molecule de Broglie waves are coherently split, physically separated, and subsequently recombined to produce fringes represents a revolution in atomic physics. Atom interferometers give us the ability to measure accurately interactions that displace the phase or energy of the particles in one arm of the interferometer. This in turn allows us to make new qualitative measurements in atomic and molecular physics, fundamental tests of quantum mechanics, especially in areas involving atom-light interactions, and to measure acceleration and rotation in new ways.

- Atom interferometers permit completely new precision measurements of ground state properties of atoms and molecules. Important applications include precision measurements of atomic polarizabilities to test atomic structure models, measuring both molecular polarizability tensor components, and determining long range forces that are important in cold collisions and Bose-Einstein condensation.
- Atom interferometers have important applications to fundamental measurements in quantum mechanics. These include measurements of topological and geometric phases, loss of coherence to a reservoir, quantum measurement, and investigations of multi-particle interferometry and entanglement.
- The large mass and low velocities of atoms makes atom interferometers especially sensitive to inertial effects like acceleration and rotation. They have a potential sensitivity to rotations that is $\sim 10^{10}$ greater than an optical interferometer of the same area.
- Atom interferometers may have significant application to condensed matter physics, including measurement of atom-surface interactions and lithography using coherently manipulated fringe patterns that are directly deposited onto substrates.

Our group has been a pioneer in the area of atom optics and atom interferometry, demonstrating the first nanofabricated diffraction gratings for atoms and using them to study atomic Talbot re-imaging of grating patterns, an effect that may have impor-

¹⁶ Partially supported by a National Science Foundation Fellowship.

¹⁷ Partial support from the Universitaet Innsbruck; partial support from an APART Fellowship of the Austrian Academy of Sciences.

tant lithographic applications.¹⁸ We used these gratings to make the first atom interferometer in which the atom waves traverse physically separated paths. We have pioneered the scientific applications of atom interferometers by using this instrument to make accurate measurements of atomic polarizability,¹⁹ and the first measurements of the index of refraction of gas for incident matter waves traversing a gas.²⁰ We have made a molecular interferometer, demonstrating that complex particles with a large number of populated internal states can exhibit high contrast interference.²¹

During 1994, we performed atom interferometer experiments to test fundamental concepts of coherence in quantum interference and began an experiment to investigate the very high intrinsic sensitivity of atom interferometers to acceleration and rotation. In 1995, we have also completed and submitted several major papers, some of which are already in press. These include papers on atomic polar-

izability, index of refraction of matter waves, near field imaging (atomic Talbot effect), molecule optics and interferometry, and a proposed new velocity selection scheme for precision measurements.

The key element in our interferometer (figure 9) is the set of three matched transmission diffraction gratings with a 200 nm period that we fabricated at the National Nanofabrication Facility (NNF) at Cornell University using a process that we developed there. One of the important contributions this year has been the development of an alignment process to eliminate edge discontinuities or "stitches" between the adjacent $50 \mu\text{m}^2$ fields when writing large patterns. This has produced our most coherent gratings to date, resulting in a measured fringe contrast of nearly 45 percent. We also produced new 140 and 160 nm period grating sets, together with new non-magnetic silicon nitride collimating slits.

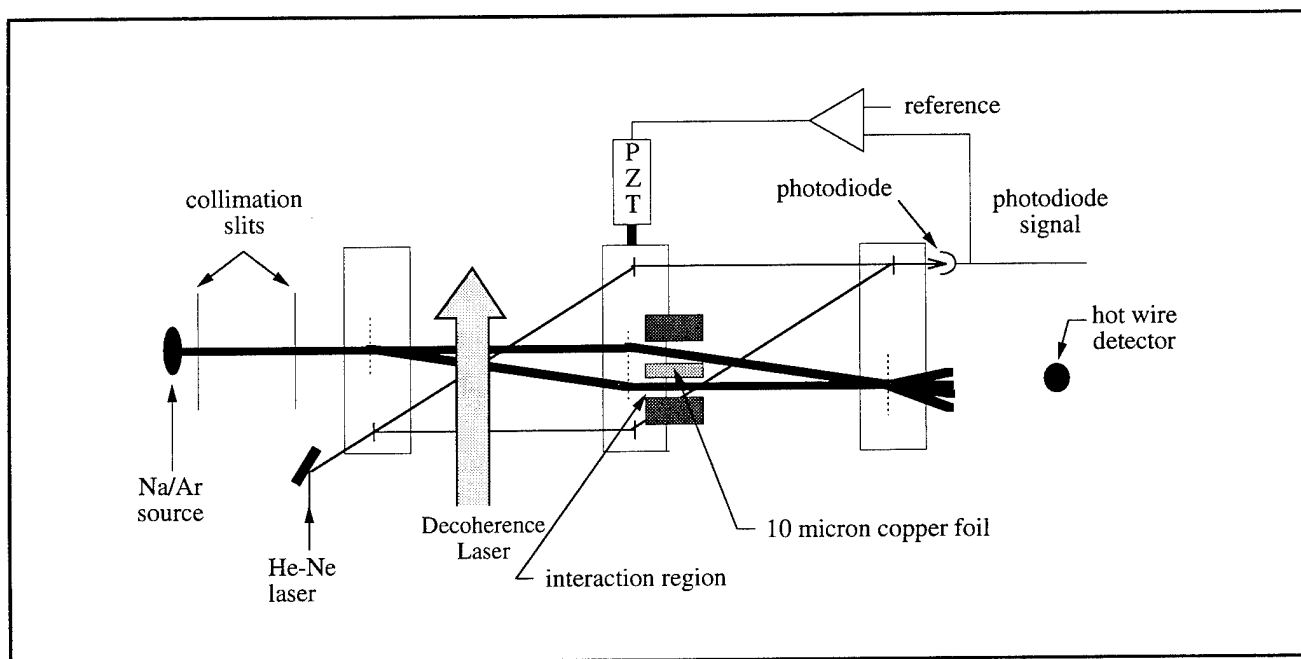


Figure 9. Schematic of our interferometer and interaction region. Vertical dashed lines are 200 nm period diffraction gratings. The interaction region used in measurements of fundamental phases and atomic and molecular properties is inserted between the atom waves. A focused laser applies π -pulses to scatter photons in decoherence and re-coherence experiments. Scattering of photons produces a phase shift in each de Broglie wave path that depends upon separation of de Broglie waves.

¹⁸ M.S. Chapman et al., "Near Field Imaging of Atom Diffraction Gratings: the Atomic Talbot Effect," *Phys. Rev. A* 51: R14 (1994).

¹⁹ C.R. Ekstrom, J. Schmiedmayer, M.S. Chapman, T.D. Hammond, and D.E. Pritchard, "Measurement of the Electric Polarizability of Sodium with an Atom Interferometer," submitted to *Phys. Rev. A*.

²⁰ J. Schmiedmayer, M.S. Chapman, C.R. Ekstrom, T.D. Hammond, S. Wehinger, and D.E. Pritchard, "Index of Refraction of Various Gases for Sodium Matter Waves," *Phys. Rev. Lett.* 74: 1043 (1995).

²¹ M.S. Chapman et al., "Optics and Interferometry with Molecules," *Phys. Rev. Lett.*, forthcoming.

2.4.1 Quantum Interference and Coherence

We integrated a dye laser into our apparatus to investigate photon-atom interactions in the interferometer and to polarize the atom beam by optical pumping techniques. This permitted us to investigate the loss of coherence or "decoherence" between the two separated de Broglie wave components when resonant single photons are scattered in the interferometer (figure 9). The fringe contrast and phase shift are measured as a function of separation between the two paths. We found that fringe contrast decreases significantly when the separation exceeds about $\lambda_{\text{photon}}/4$, in accordance with the expectations of Bohr's complementarity principle. However, contrast at larger separations also exhibits strong revivals (figure 10), as predicted by our theory.²²

In recent theoretical and experimental investigations of spontaneous emission from interfering atom de Broglie waves,²³ coherence loss can be naturally interpreted as a smearing or "diffusion" of the atom fringes by the random photon recoil kicks. One of the important implications of our experiment is that contrast loss in our interferometer clearly arises from an averaging over phase differences imparted to the two interfering de Broglie waves by the scattering photon, rather than displacements of the scattered atom by the photon recoil.

We modified our decoherence experiment to take advantage of the correlation or entanglement between scattered photons and the phase difference imparted to the de Broglie waves. By using highly collimated beams and a narrow slit in front of the detector, we could select only atoms that scattered photons within a limited range of photon recoil momenta. For these atoms, we find that the fringe contrast persists over significantly larger path separations than in our "decoherence" experiment (figure 10). We call this a "recoherence" experiment. It explicitly shows, for the first time, that resonantly scattering a photon from an atom does not irreversibly destroy the atomic coherence.

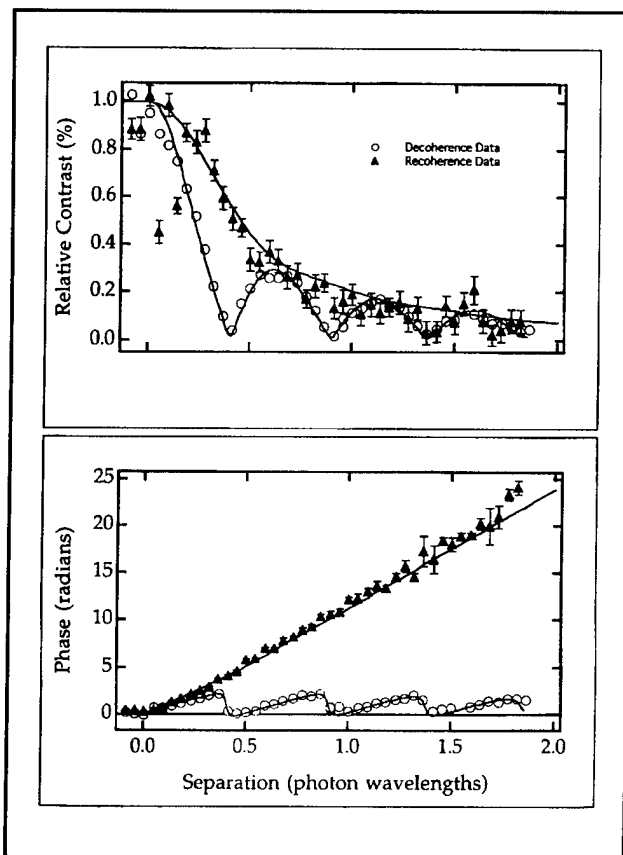


Figure 10. Results of light scattering experiment. (upper plot) Contrast versus separation between de Broglie wave components in optical wavelengths. Decoherence data (circles) shows fringe contrast decreasing rapidly but with revivals. Recoherence data (triangles) shows a more gradual decrease in fringe contrast from sub-photon recoil momentum resolved detection of atoms. (lower plot) Phase versus separation between de Broglie wave components in optical wavelengths for decoherence data (circles) and recoherence data (triangles).

2.4.2 Inertial Effects

Phase shifts that arise from the path length differences in interfering de Broglie waves in accelerating frames have been discussed by many authors in both non-relativistic and relativistic contexts.²⁴ Recently, we have obtained preliminary results in which we measured rotations of our interferometer at rotation speeds of about one earth rate (7.3×10^{-5} rads/sec) (figure 11). This is about three-orders of magnitude more sensitive than pre-

²² M.S. Chapman et al., "Loss of Coherence by a Single Scattering Event," to be submitted.

²³ T. Pfau, S. Späler, C. Kurtsiefer, C.R. Ekstrom, and J. Mlynek, "Loss of Spatial Coherence by a Single Spontaneous Emission," *Phys. Rev. Lett.* 29: 1223 (1994); D.F. Walls in "Laser Manipulation of Atoms and Ions," Varenna, 1991, E. Arimondo, E.D. Phillips and F. Strumia, (North Holland: Amsterdam, 1992).

²⁴ J. Anandan, *Phys. Rev. Lett.* 48: 1660 (1982).

vious measurements of rotation using atom interferometry and shows the promise of using atom interferometers for inertial navigation systems. We expect to be able to measure rotations to less than 5×10^{-4} earth rates with one hour of integration time and demonstrate accuracies below one percent at higher rotation rates. This is close to the

performance of the best commercial laser gyroscopes. Improvements in our current nanofabrication technology to make 1 cm^2 gratings coupled with slower, high flux, effusive cesium beams should lead to much greater detectivities ($\sim 10^{-7}\text{-}10^{-8}$ earth rates for one hour integration).

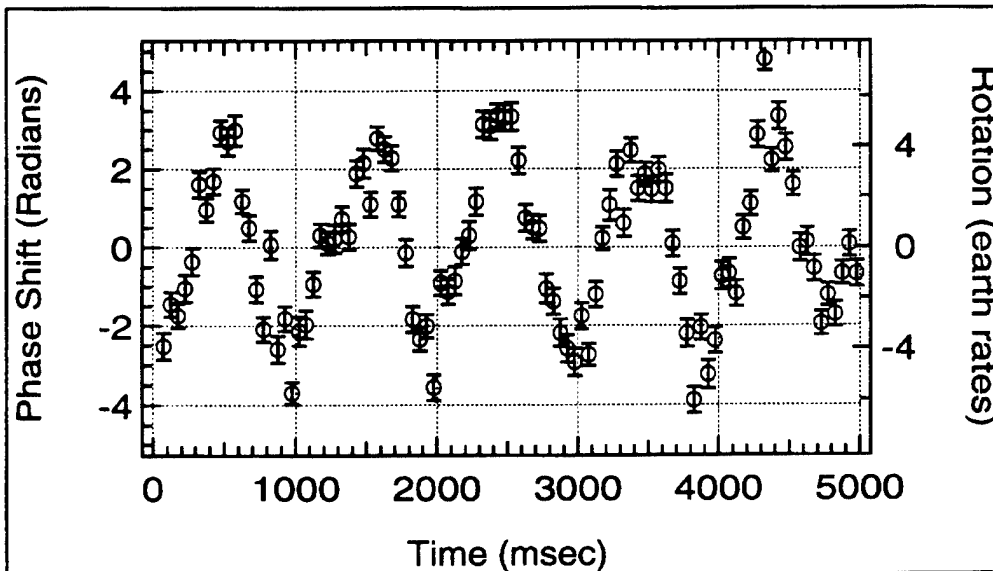


Figure 11. Experimental data showing measured phase versus time for a sinusoidal rotating excitation at approximately 1 Hz. The corresponding estimated rotation rates are shown in units of earth rates (7.3×10^{-5} rad/sec).

2.4.3 New Precision Measurements

In order to improve the precision of atom and molecular interferometry measurements, we have proposed a promising high-flux velocity selection technique that will permit the application of large phase shifts without loss of fringe contrast due to the velocity dependence of the phase for most applied potentials. In this approach, which we call "velocity multiplexing," a potential is applied such that the phase shifts of atoms in the peaks of a multi-peaked velocity distribution are exact integral multiples of 2π . Thus, interference patterns from each of the velocity peaks add constructively to produce high fringe contrast at very large applied phase shifts. This technique appears capable of measurements with less than 0.1 percent errors.

In future experiments, we plan to perform precision measurements of the Aharonov-Casher (AC) phase and Berry's phase using our separated beam interferometer. We will be able to achieve up to 1 radian AC phase shift in our interferometer, significantly greater than in previous experiments that use much weaker neutron spins. This will allow us

to study the predicted dependence on the dipole orientation for the first time. With further modifications to our interaction region to introduce spatially varying magnetic fields, we will also investigate the geometric or Berry's phase.

2.4.4 Publications

Chapman, M.S., C.R. Ekstrom, T.D. Hammond, R. Rubenstein, J. Schmiedmayer, S. Wehinger, and D.E. Pritchard. "Optics and Interferometry with Molecules." Submitted to *Phys. Rev. Lett.*

Chapman, M.S., C.R. Ekstrom, T.D. Hammond, J. Schmiedmayer, B.E. Tannian, S. Wehinger, and D.E. Pritchard. "Near Field Imaging of Atom Diffraction Gratings: the Atomic Talbot Effect." *Phys. Rev. A* 51: R14 (1995).

Ekstrom, C.R., J. Schmiedmayer, M.S. Chapman, T.D. Hammond, and D.E. Pritchard. "Measurement of the Electric Polarizability of Sodium with an Atom Interferometer." Submitted to *Phys. Rev. A*.

Hammond, T.D., D.E. Pritchard, M.S. Chapman, A. Lenef, and J. Schmiedmayer. "Multiplex Velocity Selection for Precision Matter Wave Interferometry." *App. Phys. B.* Forthcoming.

Pritchard, D.E. "Atom Interferometer." *Proceedings of the 13th International Conference on Atomic Physics.* Eds. T.W. Hansch, H. Walther, and B. Neizert. New York: American Institute of Physics, 1993.

Pritchard, D.E., M.S. Chapman, C.R. Ekstrom, T.D. Hammond, J. Schmiedmayer, A. Lenef, R. Rubenstein, and S. Wehinger. "Interferometry with Atoms and Molecules." In *Fundamental Problems in Quantum Theory.* Proceedings of the New York Academy of Sciences, Baltimore, Maryland, June 18-22, 1994. Forthcoming.

Pritchard, D.E., C.R. Ekstrom, J. Schmiedmayer, M.S. Chapman, and T.D. Hammond. "Atom Interferometry." *Proceedings of the Eleventh International Conference on Laser Spectroscopy,* June 13-18, 1993. Eds. L.A. Bloomfield, T.F. Gallagher, and D.J. Larson. New York: American Institute of Physics, 1993.

Pritchard, D.E., T.D. Hammond, J. Schmiedmayer, C.R. Ekstrom, and M.S. Chapman. *Proceedings of the Conference on Quantum Interferometry,* Trieste, Italy, March 2-5, 1993. Eds. F. DeMartini, A. Zeilinger, and G. Denardo. Singapore: World Scientific, 1993.

Schmiedmayer, J., M.S. Chapman, C.R. Ekstrom, T.D. Hammond, S. Wehinger, and D.E. Pritchard. "Index of Refraction of Various Gases for Sodium Matter Waves" *Phys. Rev. Lett.* Forthcoming.

Schmiedmayer, J., C.R. Ekstrom, M.S. Chapman, T.D. Hammond, and D.E. Pritchard. "Atom Interferometry." *Proceedings of the Seminar on Fundamentals of Quantum Optics III,* Kuhtai, Austria, 1993. Ed. F. Ehlotzky. Berlin: Springer-Verlag, 1993.

Schmiedmayer, J., C.R. Ekstrom, M.S. Chapman, T.D. Hammond, S. Wehinger, and D.E. Pritchard. "Magnetic Coherences in Atom Interferometry." *J. Phys. II (France)* 4: 2029 (1994).

2.4.5 Thesis

Tannian, B. *Near Field Imaging of Atomic Diffraction Gratings: The Atomic Talbot Effect.* B.S. thesis. Dept. of Physics, MIT, 1994.

2.5 Cooling and Trapping Neutral Atoms

Sponsors

Alfred P. Sloan Foundation
 Joint Services Electronics Program
 Contract DAAL03-92-C-0001
 Grant DAAH04-95-1-0038
 U.S. Navy - Office of Naval Research
 Grant N00014-90-J-1642
 Grant N00014-94-1-0807

Project Staff

Professor Wolfgang Ketterle, Michael R. Andrews, Kendall B. Davis, Marc-O. Mewes, Ilya Entin, Phillip M. Hinz, Everest W. Huang, Wan Y. Morshidi, Stanley H. Thompson, John J. Wuu, Peter S. Yesley

2.5.1 Introduction and Summary

Cooling and trapping of neutral atoms offers exciting new possibilities. Many are related to the fact that the deBroglie wavelength increases with decreasing temperature T as $1/\sqrt{T}$. When the deBroglie wavelength is comparable to atomic dimensions (range of the interaction potential) collisions can no longer be treated classically. They are dominated by weak long-range interactions. Since the collision duration for slow atoms greatly exceeds the radiative decay time, stimulated and spontaneous radiative transitions can take place during the collision. Slow collisions are therefore fundamentally different from the fast collisions which have been studied so far, and they are becoming an exciting new field of atomic physics. Dramatic effects are expected for even colder temperatures and higher densities, when the deBroglie wavelength becomes comparable to the interatomic spacing. In this case, the "atomic waves overlap" and a novel type of highly correlated quantum matter is predicted, but has not yet been observed. In the case of bosonic atoms, one expects the formation of a Bose condensate, a macroscopic population of a single quantum state,²⁵ and phenomena

²⁵ K. Huang, *Statistical Mechanics*, 2nd ed. (Wiley: New York, 1987).

similar to superconductivity or superfluidity; fermions would form a highly correlated Fermi sea.

Such strongly correlated atoms are predicted to exhibit unusual behavior both in their interaction with light and in collisions. Furthermore, such samples of atoms have potential applications in the field of atom optics, such as in the creation of microscopic structures by direct-write lithography or in atom microscopy. Structures as small as 65 nm were obtained recently by laser-focused atomic deposition,²⁶ mainly limited by the transverse collimation and the thermal velocity spread of the atomic beam. Improvements by an order of magnitude should be possible. With coherent atoms, one could realize the ultimate resolution in focusing atoms which is analogous to the diffraction limit in optics. A Bose condensate would also find application in metrology, improving frequency standards and atom interferometry. Cesium clocks using microkelvin atoms might improve the accuracy of the current frequency standard by two orders of magnitude.²⁷ Nanokelvin atoms will offer additional improvements.

Despite the rapid progress in laser cooling over the last few years, the conditions necessary to observe degenerate quantum gasses have not yet been achieved. This is related to the fact that temperatures well below the recoil-limit are necessary (i.e., kinetic energies should be much less than the recoil energy due to the emission of a single photon). Although optical sub-recoil cooling is possible, it has severe limitations due to collisions of excited atoms and absorption of scattered light.

Our approach is to use evaporative cooling which does not involve light and therefore has no recoil limit to overcome. The cooling is accomplished by selectively removing atoms with the highest energy from the trap and then allowing the rest of the sample to rethermalize through elastic collisions. Unfortunately, this method requires high initial densities which, until recently, could only be prepared by cryogenic methods applicable solely to atomic hydrogen.²⁸ By using a combination of different cooling and trapping techniques involving lasers and magnetic fields, we can now obtain high initial density and observe evaporative cooling. This closes the gap between optical cooling at relatively

low density and collisional cooling. It frees evaporative cooling from the restrictions of a cryogenic environment by using laser cooling as the precooling stage. In our initial experiments, the temperature was reduced by a factor of twelve and the phase space density increased by more than two orders of magnitude.²⁹ We are optimistic that experimental improvements will result in even colder temperatures in the near future. These results and other projects will now be described in greater detail.

2.5.2 Magnetic Trapping of Sodium Atoms

We have captured more than 10^{10} atoms in a dark light trap and transferred them into a magnetic trap. Initial atomic densities in the magnetic trap were 10^{11} atoms cm^{-3} . Much higher atomic densities have been obtained by subsequent adiabatic compression. A slow increase of the magnetic field gradient to 1000 G/cm resulted in ten times higher densities at five times higher temperatures. Although there is no gain in phase space density, adiabatic compression resulted in a substantial speedup of evaporative cooling due to an increase in the elastic collision rate by a factor of twenty. The thermalization time in the compressed cloud was only 50 ms, much shorter than the lifetime of the sample which was 30 seconds, due to the residual pressure of $5 \cdot 10^{-11}$ mbar.

2.5.3 Elastic Cross Section of Ultracold Sodium Atoms

The driving process for evaporative cooling is elastic collisions. Although the interaction potential between two sodium atoms at long range is fairly well known (van der Waals potential), the low temperature elastic cross section cannot be accurately predicted. The reason is that only one partial wave (s-wave) contributes to the scattering of sodium atoms below 1 mK. Depending on the scattering phase shift, the zero-temperature cross section varies between zero and infinity. The phase shift depends critically on the binding energy of the last bound vibrational level and is very sensitive to fine details of the interaction potential.

²⁶ J.J. McClelland, R.E. Scholten, E.C. Palm, and R.C. Celotta, *Sci.* 262: 877 (1993).

²⁷ K. Gibble and S. Chu, *Metrologia* 29: 201 (1992).

²⁸ N. Masuhara et al., *Phys. Rev. Lett.* 61: 935 (1988).

²⁹ K.B. Davis, M.-O. Mewes, M.A. Joffe, M.R. Andrews, and W. Ketterle, submitted to *Phys. Rev. Lett.*

We were able to deduce the elastic collision cross section by observing the thermalization of an atom cloud. For this, a non-thermal distribution was prepared by temporarily displacing the trap center along the symmetry axis resulting in an elongated cloud. Using absorption imaging, the relaxation of this anisotropic energy distribution was observed by recording the shape of the cloud as a function of time.³⁰ In principle, equilibration might happen due to the ergodic evolution of orbits in the trap independent of collisions. However, this effect was ruled out by showing that the equilibration time depended linearly on density.

From the thermalization time, we derived the elastic cross section $\sigma = 6.0 \pm 3.0 \text{ cm}^{-2}$. The measurement was performed at $200 \mu\text{K}$, well below the temperature (1 mK) at which one expects d-wave contributions or a temperature dependence of the s-wave cross section. We can therefore deduce the scattering length $a = \pm(92 \pm 25) a_0$ using the relation $\sigma = 8\pi a^2$. Recently, accurate calculations of the scattering length of cold sodium atoms have been performed. For sodium atoms in the $F = 1, m_F = -1$ state result was $56 a_0 < a < 154 a_0$ and, for an alternative choice of potentials $-36 a_0 < a < 154 a_0$.³¹ Thus, those calculations could not rule out negative values of the scattering length which would result in an unstable Bose condensate. Our experimental result, together with the theoretical prediction, show that sodium in the $F = 1, m_F = -1$ state has a large positive scattering length and is therefore an ideal choice for the pursuit of Bose Einstein condensation in alkali atoms.

2.5.4 Rf Induced Evaporative Cooling of Atoms

We want to reach the nK regime using evaporative cooling. Evaporative cooling is accomplished by repetitively removing the high energy "tail" of the thermal distribution of atoms in the trap.³² The remaining atoms then cool collisionally as the high energy "tail" is repopulated. The essential condition

for evaporative cooling is that the collision rate is sufficiently high for many collisions to occur within the lifetime of the atoms in the trap. In addition to high initial density and long trapping times, evaporative cooling requires a method for selectively removing hot atoms from the trap. In rf induced evaporation, atoms are spinflipped to an untrapped state when they are in resonance with an applied rf field.³³ Since this resonance frequency is a function of magnetic field B , atoms are selectively removed at a specific value of B . In the case of transitions between magnetic sublevels m_F , the resonance frequency is $\omega_r = |g| \mu_B B / \hbar$, where g is the g-factor and μ_B the Bohr magneton. Since the trapping potential is given by $m_F g \mu_B B(r)$, only atoms which have a total energy $E > \hbar \omega_r |m_F|$ will evaporate; or in other words, application of rf radiation of frequency ω_r creates a trap "lip" with a height of $\hbar \omega_r |m_F|$. An advantage is that the "lip" exists over a large surface rather than a small saddle point region of the trap.³⁴

We observed temperature reduction by a factor of 12 and a simultaneous increase in density by a factor of 3.5 resulting in an increase in phase space density by a factor of 140. Evaporation was performed in such a way that the elastic collision rate, which is proportional to density times velocity, increased during evaporation. We are therefore already in the regime where evaporative cooling is self-accelerating. Indeed, one expects "run-away" evaporation when the number of collisions during a trapping time exceeds 25.³⁵ With an estimated collision rate of 50/s in the compressed cloud, we exceed this value by about a factor of 60. The cloud after evaporation had a temperature of $80 \mu\text{K}$ and a density of $2 \cdot 10^{12} \text{ cm}^{-3}$. This phase space density is $2 \cdot 10^4$ times smaller than required for Bose-Einstein condensation.

The current limitation of our evaporative cooling is an increased trap loss for small atom clouds. For the coldest temperatures achieved, the trapping time decreases from 30 s to a few seconds. This is probably due to Majorana flops, non-adiabatic transitions to an untrapped state which happen near

³⁰ C.R. Monroe, E.A. Cornell, C.A. Sackett, C.J. Myatt, and C.E. Wieman, *Phys. Rev. Lett.* 70: 414 (1993).

³¹ A.J. Moerdijk and B.J. Verhaar, *Phys. Rev. Lett.* 73: 518 (1994).

³² H.F. Hess, *Phys. Rev. B* 34: 3476 (1986).

³³ D.E. Pritchard, K. Helmerson, and A.G. Martin, "Proceedings of the 11th International Conference on Atomic Physics 11," in *Atomic Physics*, eds. S. Haroche, J.C. Gay, and G. Grynberg (Singapore: World Scientific, 1989) p. 179.

³⁴ N. Masuhara et al., *Phys. Rev. Lett.* 61: 935 (1988).

³⁵ K.B. Davis, M.-O. Mewes, and W. Ketterle, *Appl. Phys. B* 60: 155 (1995).

the center of the trap where the magnetic field vanishes.³⁶ Further progress should be possible after transferring the atoms into a trap with a different field geometry which does not have zero magnetic field in the center.

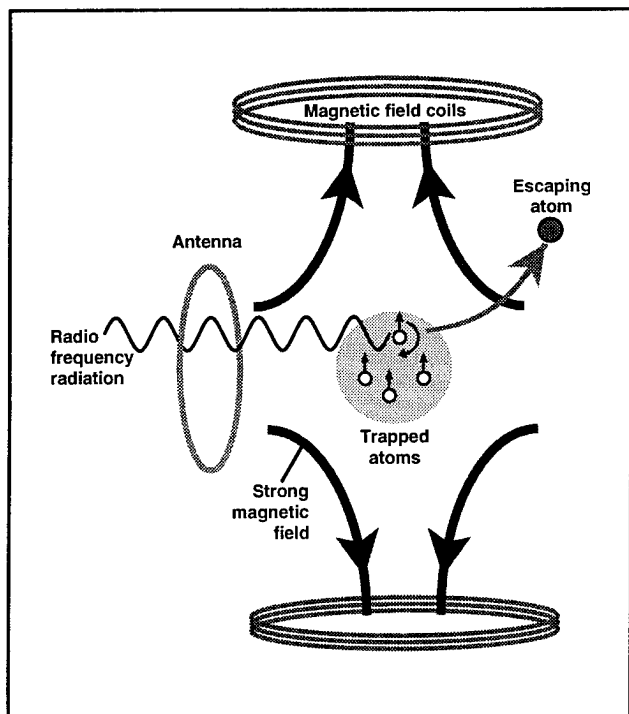


Figure 12. Experimental setup for forced evaporation. Neutral atoms are magnetically trapped. Radio-frequency radiation is tuned into resonance with the most energetic atoms in the thermal distribution. These atoms are spin-flipped to an untrapped state and ejected from the trap. The temperature of the remaining atoms is reduced by collisional thermalization.

2.5.5 An Analytical Model for Evaporative Cooling

In a recent theoretical paper, we describe an analytical model for evaporative cooling.³⁷ By simulating evaporation as a discrete process, we could predict the time dependence of all important parameters

such as temperature, density, and elastic collision rate. By incorporating trap loss due to background gas collisions into our model, we predicted the threshold conditions for "run-away" evaporation. This is characterized by an increase in the thermalization rate during the cooling process. This model has proven to be valuable in understanding the experimental results.

2.5.6 Lithium Experiment

In addition to the sodium experiment, we are currently working on an intense source of cold lithium atoms. The long term goal is to observe quantum-statistical effects in a fermionic system (⁶Li) in direct comparison with a bosonic system (⁷Li). During the last year, two dye lasers were set up providing tunable single-mode light at 671 nm, the wavelength of the Li D-line. In order to lock the lasers to a Doppler free resonance, a lithium vapor cell and a phase modulator driven by a resonant transformer were built.

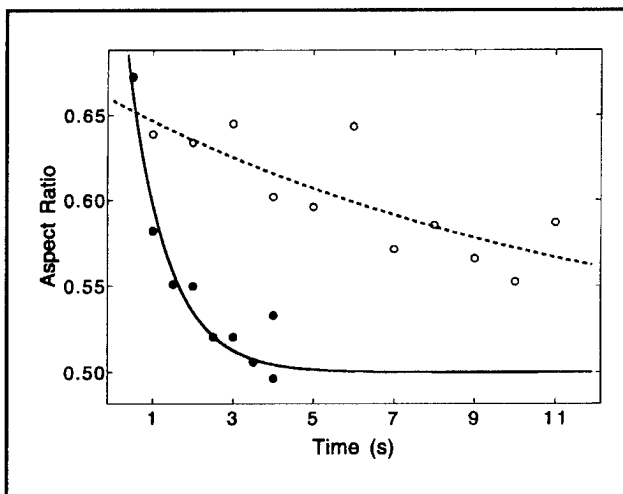


Figure 13. Thermal relaxation of an atom cloud after one-dimensional heating. The figure shows the aspect ratio of the cloud versus time for two different initial densities (solid circles: $5 \cdot 10^{10} \text{ cm}^{-3}$, open circles: $4 \cdot 10^9 \text{ cm}^{-3}$). The lines represent simple exponential fits with time constants of 1.0 s and 13 s, respectively.

³⁶ T.H. Bergeman, P. McNicholl, J. Kycia, H. Metcalf, and N.L. Balazs, *J. Opt. Soc. Am. B* 6: 2249 (1989).

³⁷ K.B. Davis, M.-O. Mewes, and W. Ketterle, *Appl. Phys. B* 60: 155 (1995).

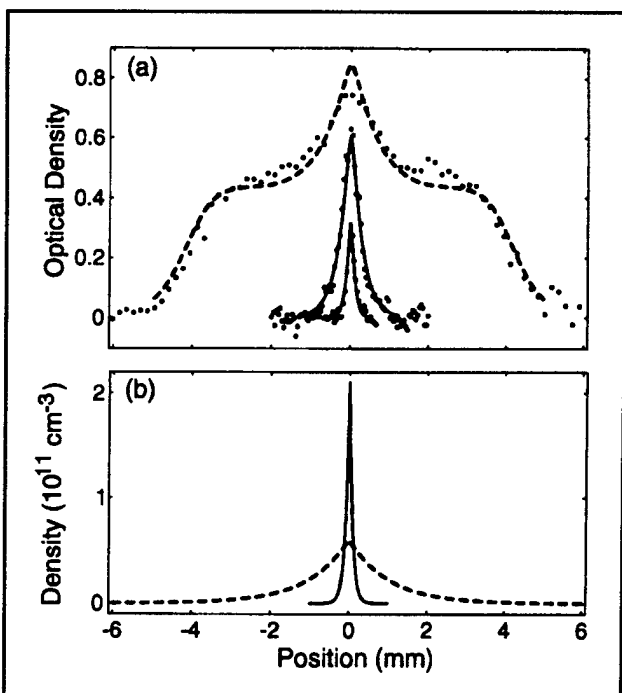


Figure 14. Optical density (a) and density (b) before and after evaporative cooling. The initial temperature was reduced by a factor of twelve. At the same time, the density increased, despite the loss in the number of trapped atoms.

2.5.7 Publications

Davis, K.B., M.-O. Mewes, M.A. Joffe, M.R. Andrews, and W. Ketterle. "Evaporative Cooling of Sodium Atoms." Submitted to *Phys. Rev. Lett.*

Davis, K.B., M.-O. Mewes, and W. Ketterle. "An Analytical Model for Evaporative Cooling of Atoms." *Appl. Phys. B* 60: 155 (1995).

2.5.8 Published Conference Papers

Davis, K.B., M.-O. Mewes, M.A. Andrews, and W. Ketterle. "Transfer of Laser-cooled Atoms into a Magnetic Trap." OSA Annual Meeting, Dallas, Texas, 1994, Program p. 135, Abstract WPP3.

Davis, K.B., M.-O. Mewes, M.A. Joffe, and W. Ketterle. "Evaporative Cooling of Sodium Atoms." 14th International Conference on Atomic Physics (ICAP), Boulder, Colorado, 1994, Book of Abstracts, Paper 1M-3.

Ketterle, W. "Cooling and Trapping of Neutral Atoms." The Future of Spectroscopy: From Astronomy to Biology, Quebec, Canada, September 1994, *National Research Council Canada, Book of Abstracts*, p. 34.

Ketterle, W., K.B. Davis, M.A. Joffe, M.-O. Mewes, and D.E. Pritchard. "Dark Cold Atoms at High Densities." International Quantum Electronics Conference (IQEC), Anaheim, California, 1994. *1994 Technical Digest Series*, Vol. 9. Washington, D.C.: Optical Society of America, 1994, p. 236.

Mewes, M.-O., K.B. Davis, P. Yesley, M.A. Joffe, D.E. Pritchard, and W. Ketterle. "A Spin-flip Zeeman Slower for the Production of Intense Slow Sodium Beams." OSA Annual Meeting, Dallas, Texas, 1994, Abstract WPP4, Program p. 135.

2.5.9 Thesis

Morshidi, W.Y. *Frequency Modulation Spectroscopy for Frequency Stabilization of Dye-laser*. B.S. thesis. Dept. of Phys., MIT, 1994.

Section 2 Plasma Physics

Chapter 1 Plasma Dynamics

Chapter 1. Plasma Dynamics

Academic and Research Staff

Professor George Bekefi, Professor Abraham Bers, Professor Bruno Coppi, Professor Jonathan S. Wurtele, Dr. Chiping Chen, Dr. Stefano Migliuolo, Dr. Abhay K. Ram, Dr. Linda E. Sugiyama, Ivan Mastovsky

Visiting Scientists and Research Affiliates

Dr. Giuseppe Bertin, Francesca Bombarda, Franco Carpignano, Dr. Carson C. Chow,¹ Dr. Paolo Detragiache, Dr. Vladimir Fuchs,² Dr. Eli Jerby,³ Andrew J. Kerman, George M. Svolos, Dr. Jiri Ullschmied,⁴ Dr. Ian Wilson,⁵ Dr. Walter Wuensch⁶

Graduate Students

Abdulaziz Al-Jalal, James C. Blastos, Palmyra E. Catravas, Kai P. Chan, William S. Daughton, Darin R. Ernst, Wen Hu, Gregory E. Penn, Darren M. Pierre, Caterina Riconda, Todd H. Rider, Suraj D. Salihu, Steven D. Schultz, Gennady Shvets, Richard E. Stoner, Luigi Vacca, Pavel S. Volfbeyn

Undergraduate Students

Beth L. Chen, David Sisson

Technical and Support Staff

Felicia G. Brady, Catherine Lorusso,⁶ Laura von Bosau, Miriam Weiner

1.1 Relativistic Electron Beams

Sponsors

U.S. Air Force - Office of Scientific Research
Grant F49620-93-1-0108

U.S. Army - Harry Diamond Laboratories
Contract DAAL02-89-K-0084
Contract DAAL02-92-K-0037

U.S. Department of Energy
Grant DE-FG02-91ER-40648

U.S. Navy - Office of Naval Research
Grant N00014-90-J-4130

Project Staff

Professor George Bekefi, Professor Jonathan S. Wurtele, Ivan Mastovsky, Dr. Chiping Chen, Dr. Eli Jerby, Dr. Jiri Ullschmied, Dr. Ian Wilson, Dr. Walter

Wuensch, Abdulaziz Al-Jalal, James C. Blastos, Palmyra E. Catravas, Wen Hu, Gennady Shvets, Richard E. Stoner, Pavel S. Volfbeyn, Beth L. Chen, David Sisson

1.1.1 A 70-Period High-Precision Microwiggler for Free-Electron Lasers

Reducing the size and cost of visible and UV wavelength FEL systems is necessary to make them practical sources of radiation. The use of a short-period (1-10 mm) microwiggler magnet permits the generation of higher frequency radiation because the device is more compact than one employing wigglers of the usual period (typically 3-10 cm).

Microwiggler design and construction poses some very serious engineering challenges. Mechanical tolerances of a given value become increasingly

¹ Boston University, Boston, Massachusetts.

² Centre Canadien de Fusion Magnétique (CCFM), Quebec, Canada.

³ Tel Aviv University, Faculty of Engineering, Tel Aviv 69978, Israel.

⁴ Institute of Plasma Physics, Czechoslovak Academy of Sciences, P.O. Box 17, 18211 Prague 8, Czechoslovakia.

⁵ CERN, SL-RFL, CH-1211, Geneva 23, Switzerland.

⁶ Deceased, March 18, 1995.

large in the fractional sense as the size is reduced, leading to a corresponding increase in fractional field errors. Also, wiggler field strength falls off exponentially as the ratio of the separation between wiggler halves (the "gap") to the wiggler period increases. Therefore, maintaining a gap adequate to pass an electron beam (a few mm) while reducing the wiggler period results in significant field magnitude reduction unless corrective measures are taken.

Despite these difficulties, numerous groups have investigated short-period wigglers. A variety of techniques have been proposed and studied; some of these are: samarium-cobalt permanent magnet grooved slabs,⁷ ferromagnetic core stacks with interleaved copper sheets,⁸ high current pulsed-wire designs,⁹ electromagnetic helical microwigglers,¹⁰ staggered ferromagnetic core arrays immersed in a solenoidal field,¹¹ superconducting ferromagnetic core designs,¹² and hybrid samarium cobalt and iron microwigglers.¹³ A common characteristic of most of these approaches is to control and minimize field errors by means of precise fabrication while dealing with steering errors (imparting of net transverse momentum to an electron beam) and deflection (imparting a net transverse displacement to an electron beam) with internal or external trim coils (note: Tecimer and Elias¹³ used poleface shim tuning). These measures, while successfully employed in full-sized wigglers, have met with

varying degrees of success in most of the above mentioned designs, yielding errors of order several percent RMS spread in the amplitudes of the wiggler field peaks, as well as uncompensated end effects (notable exceptions being Benzvi et al.,¹² having attained field errors of order 0.28 percent, and Tecimer and Elias¹³ having achieved 0.2 percent; see table 1).

In contrast, we have constructed a 70-period planar microwiggler, having period 8.8 mm, which employs extensive tuning to accomplish field error reduction. Each half-period is independently adjustable, permitting great control over the amplitude profile. Also, we have developed a coil/ferrocore geometry permitting pulsed operation at high peak field amplitudes (4.2 kG) at experimentally useful repetition rates (> 1/2 Hz). The design is an outgrowth of our earlier work.¹⁴

We used amplitudes tuning to produce a 70-period microwiggler with 0.12 percent RMS spread in the peak amplitudes, the lowest value we are aware of in a sub-cm-period wiggler.

The microwiggler is a 70-period device with an 8.8 mm period and a 4.2 mm gap, consisting of 280 electromagnets held by a precisely formed aluminum matrix. Figure 1 illustrates the geometry of the microwiggler (and the coordinate axes used to describe the wiggler geometry).

⁷ I. Kimel and R. Elias, "Micro-undulator Fields," *Nucl. Instr. Meth.* A296: 611-618 (1990); G. Ramian, L. Elias, and I. Kimel, "Micro-undulator FELs," *Nucl. Instr. Meth.* A250: 125-133 (1986).

⁸ J.H. Booske, W.W. Destler, Z. Segalov, D.J. Radack, E.T. Rosenbury, J. Rodgers, T.M. Antonsen, Jr., V.L. Granatstein, and I.D. Mayergoyz, "Propagation of Wiggler Focused Relativistic Sheet Electron Beams," *J. Appl. Phys.* 64(1): 6-11 (1988).

⁹ R.W. Warren, D.W. Feldman, D. Preston, "High-field Pulsed Microwigglers," *Nucl. Instr. Meth.* A296: 558-562 (1990).

¹⁰ N. Ohigashi, K. Mima, T. Tsunawaki, S. Ishii, M. Ikeda, K. Imasaki, M. Fujita, S. Kuruma, A. Murai, C. Yamanaka, and S. Nakai, "Development of an Electromagnetic Helical Microwiggler," *Nucl. Inst. Meth.* A341: 426-430 (1994); J. Vetrovec, "Design of a High-field Taperable Helical Wiggler," *Nucl. Instr. Meth.* A296: 563-567 (1990).

¹¹ Y.C. Huang, H.C. Wang, R.H. Pantell, J. Feinstein, and J. Harris, "Performance Characterization of a Far-infrared, Staggered Wiggler," *Nucl. Instr. Meth.* A341: 431-435 (1994).

¹² I. Ben-Zvi, R. Fornow, J. Gallardo, G. Ingold, W. Sampson, and M. Woodle, "Performance of a Superconducting, High Field Subcentimeter Undulator," *Nucl. Instr. Meth.* A318: 781-788 (1992).

¹³ M. Tecimer and L.R. Elias, "Hybrid Microundulator Designs for the CREOL Compact cw-FEL," *Nucl. Inst. Meth.* A341: ABS126-ABS127 (1994).

¹⁴ R. Stoner, S.-C. Chen, and G. Beketi, "A Planar Electromagnet Microwiggler for Free Electron Lasers," *IEEE Trans. Plasma Sci.* 18(3): 387-391 (1990).

GROUP	TECHNOLOGY AND STATUS	#PER.	λ_w/mm G/mm	B_w/kG	PEAK RMS ERROR	POLE INT. ERROR
Stoner <i>et. al.</i> MIT	Pulsed ferrocold electromagnet; operational	70	8.8/4.2	4.2	0.12%	0.18%
Huang <i>et. al.</i> Stanford	Staggered ferrocold array in solenoid; test	50	10.0/2.0	10.8	1.2%	Not reported
Warren and Fortgang LANL	Permanent magnet; operational	73	13.6/1.5	6.5	0.3%	Not reported
Tecimer and Elias CREOL	Hybrid; test	62	8/Not reported	1.0	0.2%	0.6%
Ben-zvi <i>et. al.</i> BNL	Superconducting ferrocold electromagnet; test	20	8.8/4.4	>5.5	0.29%	0.36%

Table 1. Comparison of some short-period wigglers.

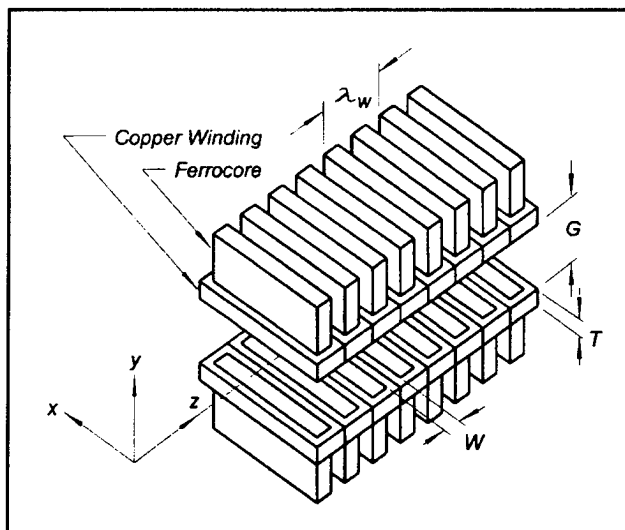


Figure 1. Microwiggler geometry. Coordinate axes are shown. Current flow in adjacent coils have opposite handedness, while current flow in cross-gap pairs have the same handedness. Parameter values: $\lambda_w = 8.8 \text{ mm}$, $G = 4.2 \text{ mm}$, $T = 3.1 \text{ mm}$, $W = 2.3 \text{ mm}$. Note that the gap shown is larger than in the actual design.

Figure 2 is a photograph of the microwiggler. Each electromagnet is formed from wire wound on a core consisting of six Microsil laminations of dimension $12.7 \times 25.4 \times 0.35 \text{ mm}$ (29 gauge). Microsil was chosen in favor of more exotic materials (like vanadium permendur) because of its extremely low cost and ready availability, and its very small hysteresis and remnant fields. A very high degree of uniformity was achieved in the thickness of the laminated cores: the thicknesses of all 280 cores lay within a range between 2.101-2.106 mm. This precision was attained by sorting 2000 individual laminates according to thickness and then selecting sets of laminates having the proper total thickness. Figure 3 shows an individual electromagnet, which was hand wound with 50 turns of 32 AWG Formex wire.

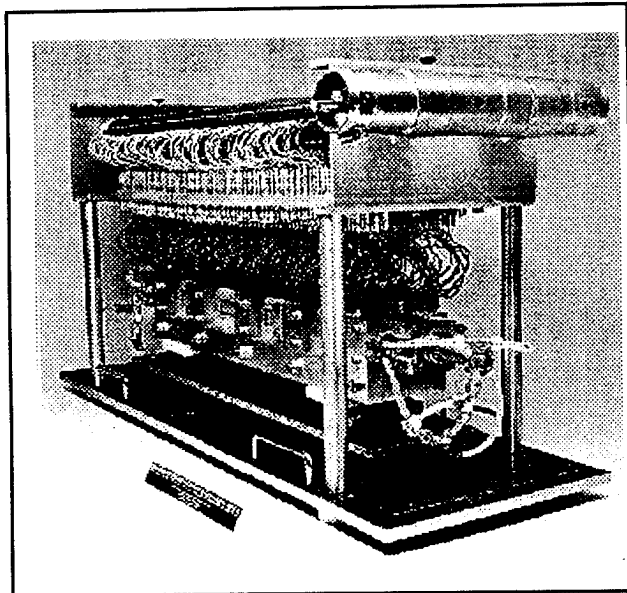


Figure 2. The Microwiggler. The high-current busswork (top) delivers 12 kA in 0.5 ms pulses, which is distributed by the current distribution network. Current is delivered to each of the 280 coils by a 22 AWG twisted pair.

The individual coils are placed in two aluminum holder pieces to form a wiggler configuration. Each holder consists of a bar fashioned from aluminum jig-plate stock with 140 slots cut perpendicular to the longitudinal axis of the bar: each slot accommodates an individual electromagnet. The two aluminum holder pieces lie on each side of the wiggler gap and are aligned by a pin-and-socket arrangement at each end of the holders.

The coil holders were manufactured with precision. Neither the width nor the cumulative (axial) positional error of any of the 140 coil holder slots in each holder exceeds 0.01 mm. The gap separation is determined by the aluminum holders. Figure 4 is a section drawing showing the assembly of the wiggler halves, drift tube, etc. The rectangular electron drift tube consists of a 75-cm length of 0.25-mm thick wall stainless steel K_a band waveguide with stainless mini-CONFLAT flanges braised onto each end. Longitudinal slots cut into each end of the magnet holders secure the drift tube position. The transverse position of the drift tube is also very well-fixed by the polefaces; this is crucial because the pickup coil probe for magnetic field measurements takes its position via a slip fit inside the drift tube. Measurement of the relative height of each of the 280 polefaces shows that the highest polefaces are randomly distributed through the wiggler and that they fix the transverse (y) position of the drift tube to better than 20 microns. Drift tube wall thickness variations thus yield as much (or more) drift tube position error as poleface height variations.

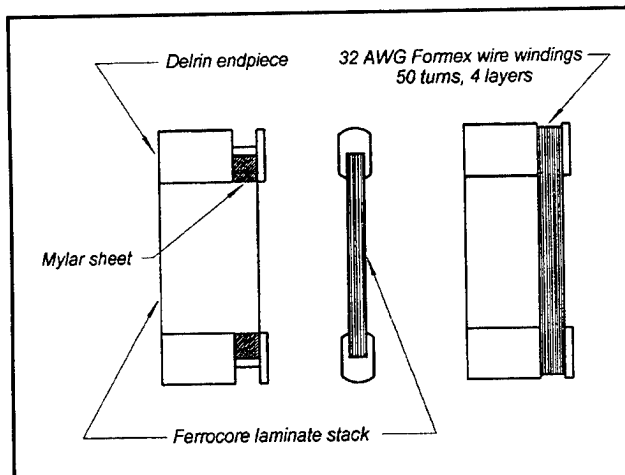


Figure 3. An individual electromagnet. The side view on the left shows a core without windings to better illustrate the structure of the core/endpiece assembly. The mylar sheet is indispensable: in tests, fully half of the coils made without it were electrically shorted to the core, a catastrophic failure rate.

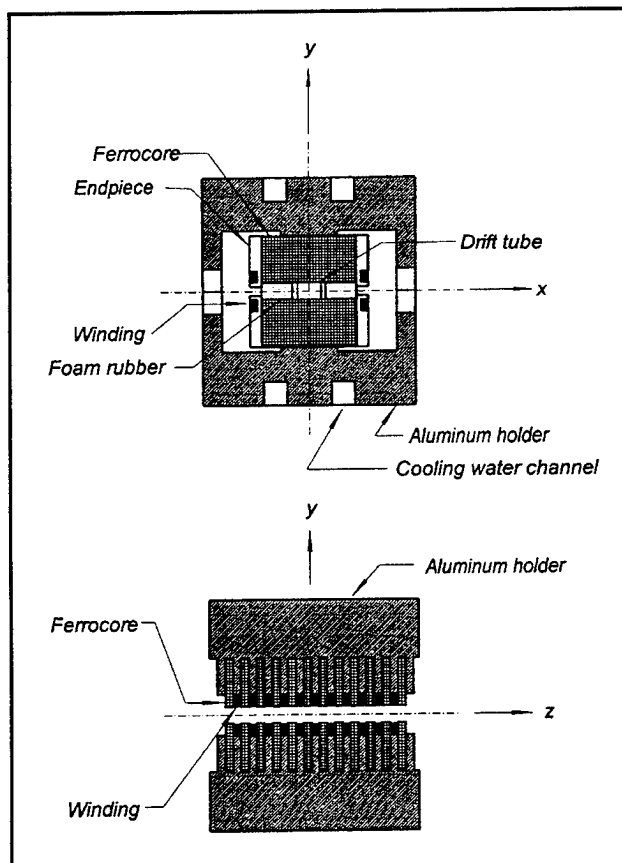


Figure 4. Wiggler assembly section drawings: (a) shows how the holders, coils, and drift tube are assembled. (b) illustrates the installation of the coils into the aluminum holders.

Two electromagnets facing across-gap from one another comprise a half-period and are connected in parallel to a ground and the current source through a tuning resistor. Figure 5 illustrates this arrangement schematically. The wiggler circuit consists of 140 half-period pairs, connected in parallel to the current source. Tuning is accomplished by means of variable resistors. They consist of 22 AWG manganin wires with their lengths varied to

adjust their resistances. Tuning the microwiggler therefore consisted of adjusting the value of 140 resistors in a resistive current divider network. Care was taken to energize the microwiggler with pulses of long duration (880 μ s) compared to the (L/R) time of the microwiggler (about 60 μ s) to ensure that the impedance of the various half-period circuit elements remained primarily resistive.

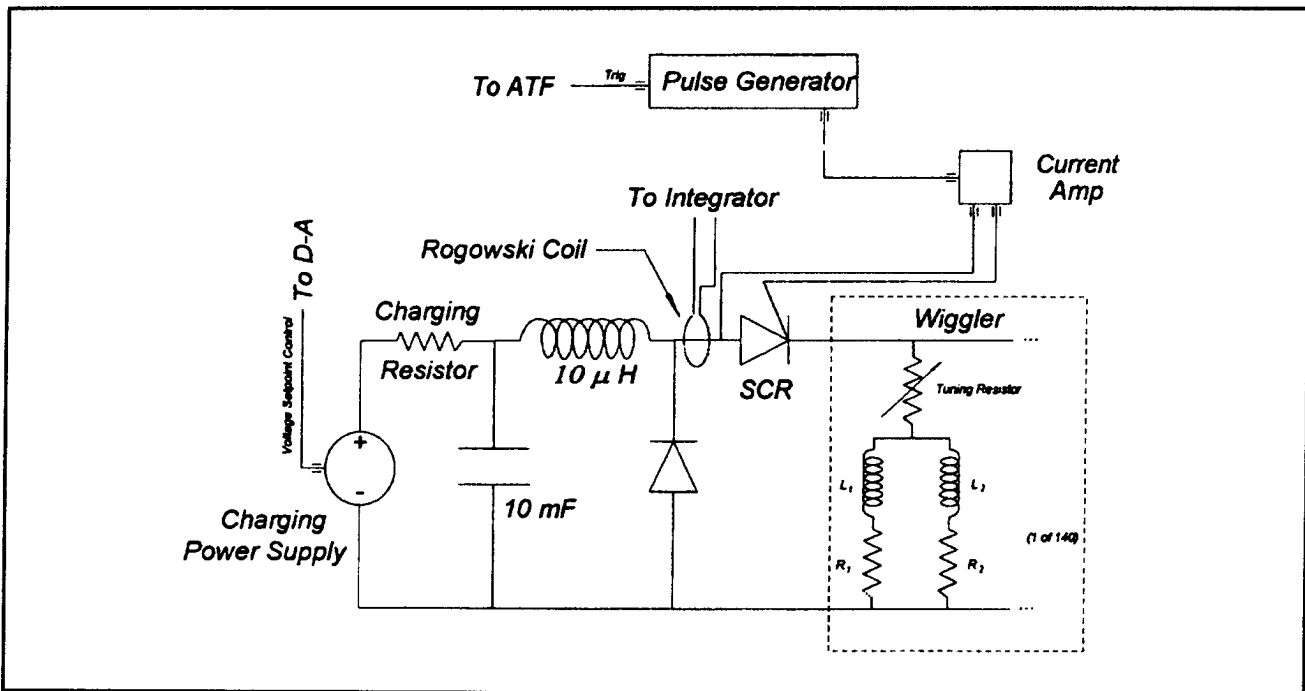


Figure 5. Schematic of the pulsed power supply for the microwiggler.

The measured peak amplitudes of our microwiggler are plotted in figure 6, as a function of peak number, before and after tuning. Two peaks at each end are tapered for minimal beam steering and deflection. A zero-steering POISSON model was generated, and the amplitudes obtained therefrom were tuned into the ends of the microwiggler. For these and all other measurements described in this section (the saturation data excepted), the microwiggler was operated at a repetition rate of 1/2 Hz and energized with underdamped half-sine waves of half-period 880 μ s. The mean field amplitude was 4.2 kG.

In conclusion, we have constructed and operated a ferromagnetic-core based electromagnetic wiggler having 70 periods of 8.8 mm and a gap of 4.2 mm, producing an on-axis wiggler field of 4.2 kG in 0.5-ms pulses at a repetition rate of 0.5 Hz. We claim that the field produced has the smallest RMS spread in the peak amplitudes, 0.12 percent, and the smallest spread in the pole integrals, 0.18 percent, of any sub-cm-period wiggler yet reported. We have performed an extensive battery of measurements to support this claim. Our microwiggler is presently being used in a visible- and UV-wavelength FEL oscillator experiment at the Accelerator Test Facility, Brookhaven National Laboratory.

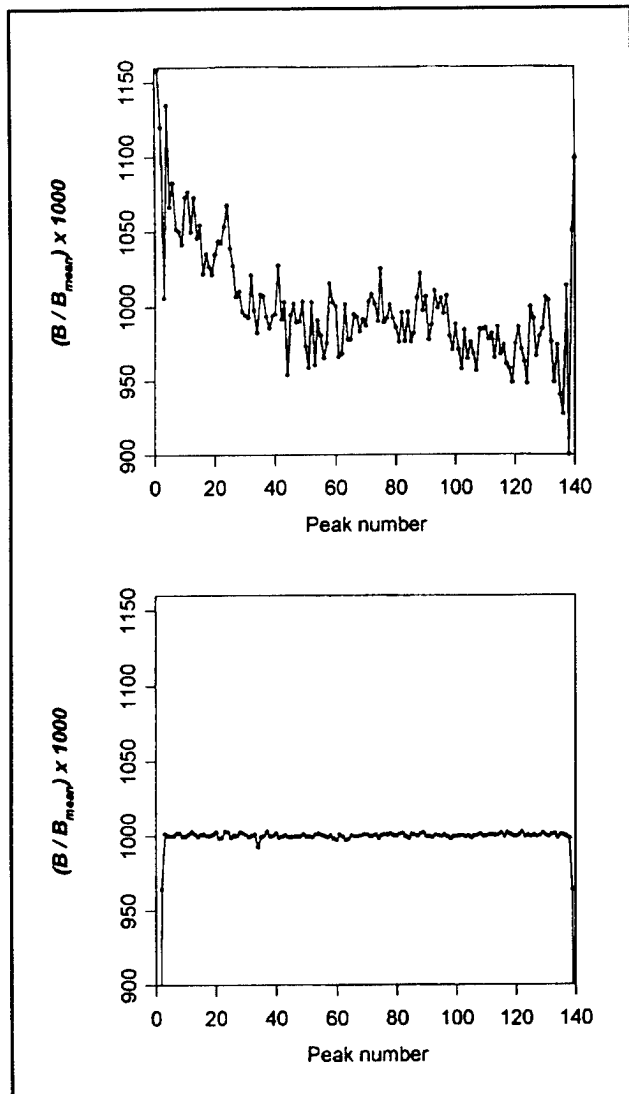


Figure 6. (a) Untuned and (b) tuned peak amplitude profiles of the microwiggler. The ranges and scales of the two plots are identical; clearly, tuning has greatly reduced peak amplitude variations. The tuned profile also shows the tapering of the end peaks.

1.1.2 Publications

Journal Articles

Bekefi, G., B. Chen, M.E. Conde, I. Mastovsky, K. Ricci, C.J. Taylor, and P. Volfbeyn. "Observations of Frequency Chirping and Phase of a Free Electron Laser Amplifier." *Nucl. Inst. Meth.* A341: 119-123 (1994).

Jerby, E., G. Bekefi, and A. Shahadi. "Observation of Chirping in a Traveling-Wave Cyclotron Maser Experiment." *Nucl. Inst. Meth.* A341: 115-118 (1994).

Jerby, E., A. Shahadi, V. Grinberg, V. Dikhtiar, M. Sheinin, E. Agmon, H. Golombek, V. Trebic, M. Bensal, and G. Bekefi. "Cyclotron Maser Oscillator Experiments in a Periodically Loaded Waveguide." *IEEE J. Quantum Electron.* Forthcoming.

Stoner, R., and G. Bekefi. "A 70-Period High-Precision Microwiggler for Free Electron Lasers." *IEEE J. Quantum Electron.* Forthcoming.

Volfbeyn, P., K. Ricci, B. Chen, and G. Bekefi. "Measurement of the Temporal and Spatial Phase Variations of a Pulsed Free Electron Laser Amplifier." *IEEE Trans. Plasma Sci.* 22(5): 659-665 (1994).

Theses

Blastos, J.C. *The Spectral Analysis of the Spontaneous Emission of MIT's 8.8 mm, Room Temperature, Pulsed Free Electron Laser Microwiggler.* S.M. thesis, Dept. of Phys., MIT, 1994.

Catravas, P.E. *MIT 3.3 GHz Relativistic Klystron Amplifier: Experimental Study of Input Cavity and Beam Characteristics.* S.M. thesis. Dept. of Electr. Eng. and Comput. Sci., MIT, 1994.

Chen, B.L.-J. *Experimental Studies of a CERN-CLIC 32.98 GHz High Gradient RF Accelerating Structure Driven by a Free Electron Laser Amplifier.* B.S. thesis. Dept. of Phys., MIT, 1994.

Hu, W. *Generation of Coherent High-Power Microwave Radiation with Relativistic Electron Beams.* S.M. thesis. Dept. of Phys., MIT, 1994.

Shvets, G. *Interaction of Intense Lasers with Plasmas.* Ph.D. diss., Dept. of Phys., MIT, 1994.

Sisson, D.L. *Magnetic Field in a Tunable Microwiggler.* B.S. thesis. Dept. of Phys., MIT, 1994.

Stoner, R.E. *Radiation from Relativistic Electron Beams in Periodic Structures.* Ph.D. diss. Dept. of Phys., MIT, 1994.

Volfbeyn, P.S. *Measurements of the Temporal and Spatial Phase Variations of a 33 GHz Pulsed Free Electron Laser Amplifier and Application to RF Acceleration.* S.M. thesis, Dept. of Phys., MIT, 1994.

1.2 Plasma Wave Interactions—RF Heating and Current Generation

Sponsors

National Science Foundation
 Contract ECS 94-42438
 U.S. Department of Energy
 Grant DE-FG02-91-ER-54109

Project Staff

Professor Abraham Bers, Dr. Abhay K. Ram, Dr. Carson C. Chow, Dr. Vladimir Fuchs, Kai P. Chan, Steven D. Schultz, Luigi Vacca

The research work of this group is concerned with studies on the electrodynamics of plasmas. Attention is directed toward understanding the nonlinear dynamics of plasmas driven by high-frequency electromagnetic fields (such as in RF heating and current drive of magnetically confined plasmas, or as in laser-plasma interactions), and the generation and propagation of unstable radiations from laser-plasma interactions and anisotropic electron distributions in space and astrophysical plasmas.

In the following, we report on our continuing studies to determine the conditions for optimizing power mode conversion of fast Alfvén waves to ion-Bernstein waves. These studies form the basis for using ion-Bernstein waves as a means of enhancing current drive efficiency in advanced tokamak scenarios.¹⁵ The second report is on some initial progress in understanding the effect of RF waves on the bootstrap current in a tokamak. The third report gives some of the recent results on the orbits of energetic ions interacting with RF waves in the ion cyclotron range of frequencies. These calculations are the basis of our studies to determine the RF-induced transport of energetic ions.

1.2.1 Mode Conversion of Fast Alfvén Waves to Ion-Bernstein Waves

Sponsor

U.S. Department of Energy
 Grant DE-FG02-91-ER-54109

In tokamak plasmas heated by waves in the ion-cyclotron range of frequencies (ICRF), the power is carried from the antenna into the center of the plasma by fast Alfvén waves (FAW). Near the ion-ion hybrid resonance inside the plasma, the FAW can couple to ion-Bernstein waves (IBW). These IBWs interact effectively with electrons and can lead to electron heating¹⁶ or, in the presence of lower-hybrid current drive (LHCD), enhance the current drive efficiency.¹⁷ The latter case explained observations on JET of the enhancement in LHCD efficiency in the presence of ICRF heating. The observed conditions required for this enhancement also are the conditions for which a fraction of the incoming power can be mode-converted to IBWs. This was discussed in the previous *RLE Progress Report*.¹⁵

Our previous results¹⁷ have shown that the IBWs propagate short distances away from the mode conversion region before they are damped on electrons. Thus, by moving the mode conversion region in a plasma, one can control the spatial location where the IBWs transfer their energy and momentum to the electrons. We have also found that the electron diffusion coefficient in the presence of IBWs is significantly larger than in the presence of FAWs.¹⁵ Recent experiments on TFTR have shown substantial electron heating near the mode conversion region. Furthermore, the region heating changes with a change of the location of the mode conversion region. From these observations, it has been concluded that the heating is due to mode converted IBWs. It has also been observed on TFTR that the directionality of the FAW spectrum is maintained by the IBWs after mode conversion. Currents were generated in the plasma near the mode conversion region when an

¹⁵ A. Bers, A.K. Ram, C.C. Chow, V. Fuchs, K.P. Chan, S.D. Schultz, and L. Vacca, "Plasma Wave Interactions—RF Heating and Current Generation," *RLE Progress Report* 136: 237-249 (1993).

¹⁶ A.K. Ram and A. Bers, *Phys. Fluids* B3: 1059 (1991).

¹⁷ A.K. Ram, A. Bers, S.D. Schultz, and V. Fuchs, "Interaction of Ion-Bernstein Waves with Electrons," *Bull. Am. Phys. Soc.* 39: 1626 (1994); A.K. Ram, A. Bers, S.D. Schultz, and V. Fuchs, "Enhanced Current Drive with Lower-Hybrid and Ion-Bernstein Waves," *Proceedings of the 15th International Conference on Plasma Physics and Controlled Nuclear Fusion Research (IAEA)*, Seville, Spain, September 26 - October 1, 1994, forthcoming; A.K. Ram, A. Bers, V. Fuchs, and S.D. Schultz, "Current Drive by the Combination of Lower Hybrid and ICRF Waves," *Proceedings of the 21st European Physical Society Conference on Controlled Fusion and Plasma Physics*, Montpellier, France, 3: 1134-1137 (1994); A.K. Ram, A. Bers, V. Fuchs, and S.D. Schultz, "Enhancing Lower Hybrid Current Drive with ICRF Waves," *Proceedings of the International Sherwood Fusion Theory Conference*, Dallas, Texas, March 14-16, 1994, paper 1C49.

asymmetric FAW spectrum was launched by the antenna. This indicates that IBWs could also be used for current drive. Since ICRF-generated heating and current drive is expected to play an important role in the future tokamaks (TPX and ITER), we have been examining the possible use of mode converted IBWs in advanced tokamak scenarios.

There are three important issues that need to be studied so that we can determine the importance of IBWs in advanced tokamak scenarios. The first issue is to determine the fraction of the incident FAW power that can be coupled to IBWs and the conditions for which the mode converted power can be maximized. The second issue is to determine the trajectories of the IBWs after mode conversion and the spatial location where the IBWs will interact with the electrons. The third and final issue is to determine the effectiveness of this interaction. In particular, for the case of current drive by IBWs, we need to know the efficiency of current drive by IBWs. Here we report on some of the recent progress we have made towards determining the conditions for optimizing the mode conversion to IBWs.

For efficient mode conversion of the ICRF-FAW power to IBWs, the fundamental ion cyclotron layers should be near the edge or outside the plasma, and the ion-ion hybrid resonance (IHR) layer should be in the central region of the plasma. In the simplest, one-dimensional (equatorial plane) description of the FAW, the local cold-plasma dispersion relation is:

$$n_{\perp}^2 = \frac{(L - n_{\parallel}^2)(R - n_{\parallel}^2)}{S - n_{\parallel}^2} \quad (1)$$

where $n_{\perp} = ck_{\perp}/\omega$, $n_{\parallel} = ck_{\parallel}/\omega$, c is the speed of light, k_{\parallel} is the component of the wave vector along the toroidal magnetic field, k_{\perp} is the component of the wave vector perpendicular to the toroidal magnetic field, ω is the ICRF frequency, and S , R , L are the usual Stix tensor elements. $R = n_{\parallel}^2$ gives the positions of the right-hand cutoffs (RHC). There are usually two such cutoffs: one on the low magnetic field side (LFS) near the antenna, and another on the high magnetic field side (HFS) near the inside edge of the plasma. The positions where $L = n_{\parallel}^2$

and $S = n_{\parallel}^2$ correspond to the left-hand cutoff (LHC) and IHR, respectively. Usually, the LHC and the IHR are close to each other and define the Budden-type cutoff-resonance pair. In the vicinity of this region, local analysis leading to (1) breaks down and the propagation of FAWs is described by a differential equation:

$$\frac{d^2 E_y}{dx^2} + Q(x)E_y = 0 \quad (2)$$

where E_y is the normalized (poloidal) component of the electric field, x is the normalized spatial coordinate along the equatorial plane, and $Q(x)$ is the potential function,¹⁸ which for a cold plasma is equal to the right-hand side of (1). The Budden-type analysis of the mode conversion process only includes the LHC and the IHR. For such a cutoff-resonance pair we can express $Q(x)$ in a simple form:

$$Q(x) = \gamma - \frac{\beta}{x} \quad (3)$$

where γ and β are chosen to fit the right-hand side of (1) near the IHR and LHC. (In this model the IHR is located at $x = 0$ and the LHC is located at $x = \beta/\gamma$.) The solution to (2) with the model potential given in (3) can be written in terms of the Whittaker functions.¹⁹ An asymptotic analysis of the Whittaker functions will completely determine the scattering parameters. From such an analysis, it has been found²⁰ that the power transmission coefficient is:

$$T_B = e^{-\pi\eta} \text{ where } \eta = \frac{\beta}{\sqrt{\gamma}}. \quad (4)$$

The power reflection and power mode conversion coefficients are, respectively,

$$R_B = T_B(1 - 2T_B) \text{ and } C_B = T_B(1 - T_B). \quad (5)$$

Thus, the maximum power mode conversion coefficient can be only 25 percent, i.e., from the Budden-type analysis of the mode conversion process, under ideal circumstances, a maximum of 25 percent of the incoming FAW power can be converted to IBWs.

¹⁸ C.N. Lashmore-Davies, V. Fuchs, G. Francis, A.K. Ram, A. Bers, and L. Gauthier, *Phys. Fluids* 31: 1614 (1988).

¹⁹ M. Abramowitz and I.A. Stegun, *Handbook of Mathematical Functions* (New York: Dover Publications, 1972).

²⁰ K.G. Budden, *The Propagation of Radio Waves* (Cambridge, Massachusetts: Cambridge University Press, 1985), pp. 596-602.

However, the Budden potential (3) does not account for the reflection of the FAW at the HFS-RHC. This can significantly modify the mode conversion results obtained from the Budden potential. An easy way to see the effect of the HFS-RHC is as follows. We assume that the potential function is still represented by the Budden potential (3). However, we impose an additional condition: we assume that the wave incident from the low field side ($x > 0$), after passing through the LHC-IHR cutoff-resonance pair, is completely reflected at some point $x = x_R$ ($x_R < 0$) where x_R is the location of the HFS-RHC. Clearly, in this case the transmission coefficient is zero, since the waves do not propagate for $x < x_R$. Thus, we only have a power reflection coefficient and a power mode conversion coefficient. The general solution, in terms of the Whittaker functions, is given by:

$$R = \left| \frac{e^{i\sqrt{\gamma}x} e^{\pi\eta/4} |2\sqrt{\gamma}x|^{-i\eta/2} \left\{ 1 - e^{-i(\pi+\phi)} \frac{2\pi i e^{\pi\eta/2}}{\Gamma(-i\eta/2)\Gamma(1-i\eta/2)} \right\}^2}{e^{-i(\pi+\phi)} e^{-i\sqrt{\gamma}x} |2\sqrt{\gamma}x|^{-i\eta/2} e^{3\pi\eta/4}} \right|. \quad (8)$$

Using the properties of the Gamma function,¹⁹ it can be shown that:

$$\begin{aligned} R(\eta, \phi) &= (1 - T_B)^2 + T_B^2 - 2T_B(1 - T_B)\cos(\phi + 2\psi) \\ &= 1 - 4T_B(1 - T_B)\cos^2\left(\frac{\phi}{2} + \psi\right) \end{aligned} \quad (9)$$

where T_B is given in (4), and ψ is the phase of $\Gamma(-i\eta/2)$. Then the power-mode conversion coefficient is:

$$C(\eta, \phi) = 4T_B(1 - T_B)\cos^2\left(\frac{\phi}{2} + \psi\right). \quad (10)$$

The maximum power mode conversion coefficient can now be 100 percent provided $T_B = 1/2$ and the $\phi/2 + \psi$ is an integer multiple of π . Thus, the effect of a high-field side reflection in the Budden problem can significantly alter the power mode conversion coefficient. In figure 7 we have plotted contours of constant $C(\eta, \phi)$ as functions of ϕ and η . These contours are periodic in ϕ modulo 2π . From this figure, it is clear that the maximum value of C is critically dependent on η —the distance between the left-hand cutoff and the ion-hybrid resonance.

$$E_y(x) = c_1 W_{\kappa, \mu}(z) + c_2 W_{-\kappa, \mu}(-z) \quad (6)$$

where c_1 and c_2 are arbitrary constants that depend on the boundary conditions, and

$$z = -2i\sqrt{\gamma}x, \quad \kappa = -\frac{i}{2} \frac{\beta}{\sqrt{\gamma}} = -\frac{i}{2}\eta, \quad \mu = \frac{1}{2}. \quad (7)$$

For $x \rightarrow -\infty$, $W_{\kappa, \mu}(z)$ represents an incoming (towards $x = 0$) wave while $W_{-\kappa, \mu}(-z)$ represents an outgoing wave. If we assume that there is no damping of the wave between the resonance and the high-field cutoff, then c_1 and c_2 differ by at most an arbitrary phase. Let us assume that $c_2 = c_1 \exp\{-i(\pi + \phi)\}$. Then, using the asymptotic properties of the Whittaker functions for $x \rightarrow \infty$, the power reflection coefficient is:

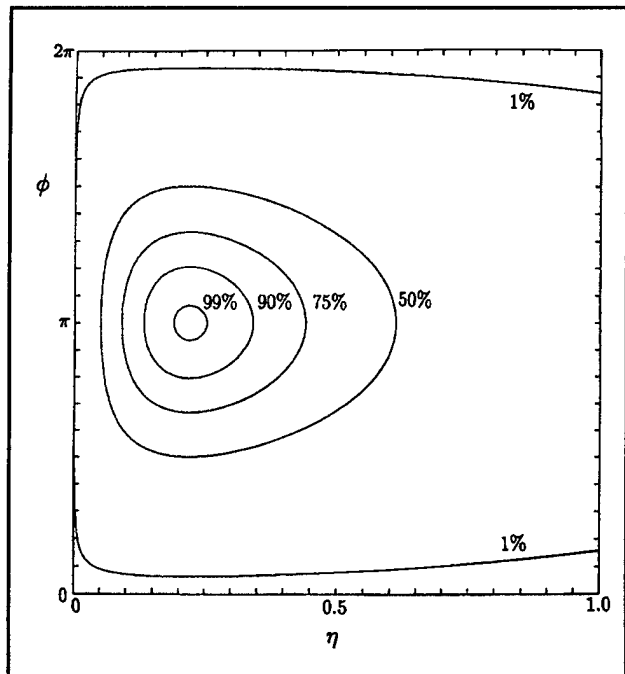


Figure 7. Theoretical contours of percent power mode converted in the (ϕ, η) plane; the figure is 2π -periodic in ϕ . These are contours of maximum possible power mode conversion coefficient. For large conversion (small reflections) the range of η 's is relatively narrow.

For example, for $\eta > 0.3$ it is not possible to get 100 percent mode conversion regardless of the choice of the phase ϕ .

The physics leading to this enhanced mode conversion due to the HFS-RHC is similar to the behavior of a transmission line coupled to a dissipative resonator: complete absorption results when the incident FAW is critically coupled to the resonator formed by the LHC-IHR-RHC plasma system; the HFS-RHC adjusts the resonator while the LHC-IHR adjusts the coupling.

Studies are presently underway to determine the dependence of ϕ on plasma parameters. Recently, we have used the phase-integral technique²¹ to find ϕ . We are also applying our results to determine the optimum mode conversion regimes in Alcator C-MOD, Tore Supra, and TPX.

1.2.2 Enhancement of the Bootstrap Current in Tokamaks Using RF Waves

Sponsors

Magnetic Fusion Science Fellowship Program
 National Science Foundation
 Grant ECS 94-42438
 U.S. Department of Energy
 Grant DE-FG02-91-ER-54109

In advanced steady-state tokamak scenarios, a substantial fraction of the necessary plasma current will be provided by the bootstrap current. The use of radio frequency waves to generate the remainder of this current is a practical idea in steady state tokamaks. We have been studying the interaction of RF waves with the neoclassical bootstrap current.

The bootstrap current was initially predicted by the neoclassical theory of transport in toroidally shaped plasmas.²² If we consider a plasma in the shape of a cylindrical torus, as shown in figure 8, then the confinement of this plasma by a magnetic field results in a gradient of plasma pressure inwards along the minor radius. The diffusion of particles against this gradient drives a current in the toroidal (ϕ) direction.

In a tokamak, the toroidal magnetic field is inversely proportional to the major radius R . There is also a

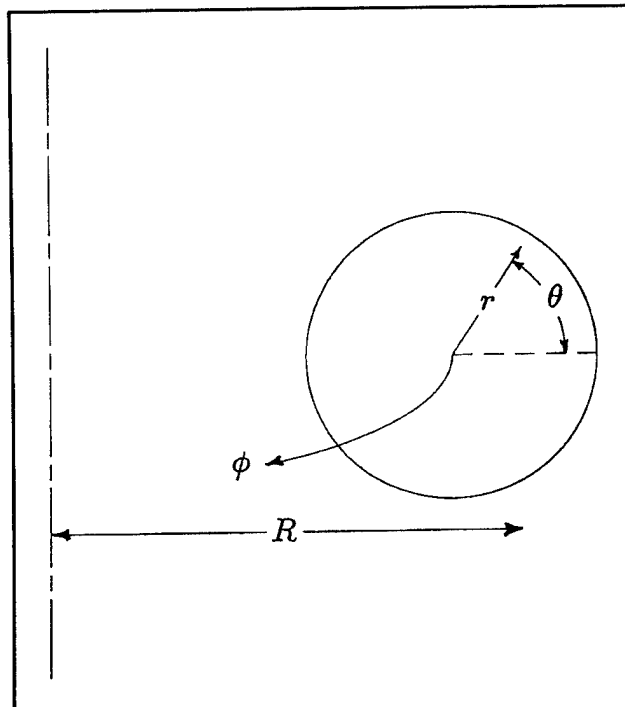


Figure 8. Toroidal coordinate system.

magnetic field in the poloidal direction, and this causes a small fraction of particles to become trapped in a magnetic well. These trapped particles are limited to the region where θ is less than a critical trapping angle θ_c , and they also have a small drift in the radial direction caused by the inhomogeneity and the curvature of the magnetic field. The orbits followed by the trapped particles are known as banana orbits. Figure 9 shows two of these orbits, labeled A and B, projected onto a poloidal cross section. The two orbits each pass through the same point X, but in opposite directions. A decrease in plasma density with increasing r means that there will be more particles on orbit A than on orbit B. Thus at point X, there will be a net current of trapped particles in both the poloidal and toroidal directions. Quantitatively, this current has a value

$$J_{||} \sim \left(\frac{r}{R} \right)^{3/2} \frac{1}{B_\theta} \frac{dp}{dr} .$$

Neoclassical theory shows that this current will be enhanced by a factor of R/r due to collisions which transfer momentum from trapped particles to passing particles. This gives the bootstrap current.

²¹ V. Fuchs, A.K. Ram, S.D. Schultz, A. Bers, and C.N. Lashmore-Davies, "Mode Conversion and Electron Damping of the Fast Alfvén Wave in a Tokamak at the Ion-Ion Hybrid Frequency," *Physics of Plasmas*, forthcoming.

²² M.N. Rosenbluth, R.D. Hazeltine, and F.L. Hinton, *Phys. Fluids* 13: 116 (1972).

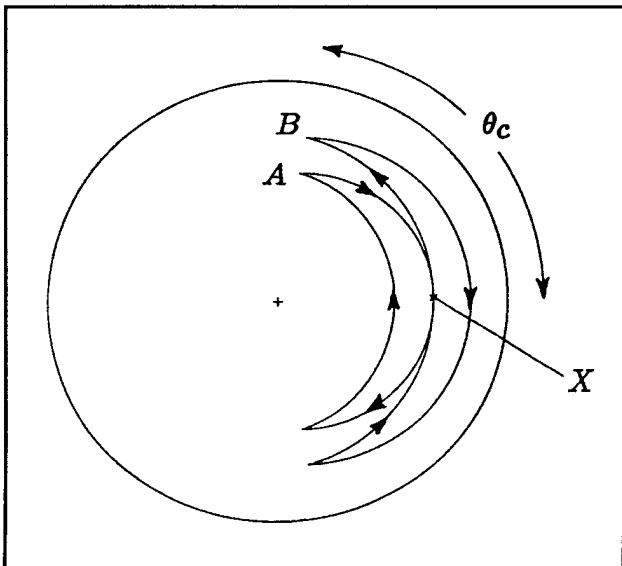


Figure 9. Poloidal cross section showing trapped particle orbits.

RF waves, used to drive a current, interact primarily with those electrons which move in resonance with the phase velocity of the waves. In this particular resonant region of velocity space, the diffusion of electrons can be modeled by a quasilinear operator.²³ In the absence of the bootstrap current, it is the balance of this quasilinear diffusion with collisions which gives the steady-state distribution of electrons in velocity space. Usually RF waves interact with tail electrons; however, they can be used to modify the bulk distribution.

The steady-state distribution function f of electrons is assumed to be averaged over the magnetic gyromotion, and, for an axisymmetric tokamak, is independent of the toroidal angle ϕ . Under these assumptions, f can be written as a function of the guiding center coordinates r and θ and two constants of the motion, the electron's energy E and magnetic moment μ . Then f will satisfy the steady-state form of the drift kinetic equation (DKE)

$$v_{\parallel} \frac{B_{\theta}}{B} \frac{1}{r} \frac{\partial f}{\partial \theta} + v_{Dr} \frac{\partial f}{\partial r} = C(f) + Q(f). \quad (1)$$

In terms of the coordinates (E, μ, r, θ) , the parallel velocity is given by

$$v_{\parallel}(E, \mu, r, \theta; \sigma) = \sigma \left\{ \frac{2}{m} [E - \mu B(r, \theta)] \right\}^{1/2} \quad (2)$$

where $\sigma = v_{\parallel}/|v_{\parallel}| = +1$ or -1 , and the radial drift velocity is

$$v_{Dr}(E, \mu, r, \theta) = \frac{m}{eB_0} \frac{v_{\parallel}}{r} \frac{\partial}{\partial \theta} (hv_{\parallel}), \quad (3)$$

where $h = R/R_0 = 1 + (r/R_0)\cos\theta$. The current is found by taking the first-order velocity space moment of f , $J_{\parallel} = -e \int d^3v v_{\parallel} f$.

The DKE (1) is a partial differential equation in four dimensions, which makes finding a general solution for $f(E, \mu, r, \theta)$ complicated. One way to reduce the number of dimensions is to average over one bounce orbit in θ . This bounce average is defined as

$$\{A\} = \int \frac{d\theta}{v_{\parallel}} A / \int \frac{d\theta}{v_{\parallel}} \quad (4)$$

where the integral is taken from $\theta = -\pi$ to $+\pi$ for passing particles and from $\theta = -\theta_c$ to θ_c for trapped particles.

An approximate solution for f can be obtained by expanding in terms of two small parameters. The first of these expansion parameters is the ratio of the width of a banana orbit to the tokamak's minor radius, $\Delta_b/a = \delta \ll 1$. The second parameter is the ratio of the electron collision frequency (as evaluated in the collision operator C) to the frequency of bounce orbits, $\nu_e/\omega_b = \hat{\nu} \ll 1$. Expanding in these parameters, $f = f_0^{(0)} + \delta f_1^{(0)} + \hat{\nu} f_0^{(1)} + \delta \hat{\nu} f_1^{(1)} + \dots$. Substituting this into (1) and equating terms of the same order, we get

$$v_{\parallel} \frac{B_{\theta}}{B} \frac{1}{r} \frac{\partial f_0^{(0)}}{\partial \theta} = 0 \quad (5)$$

$$v_{\parallel} \frac{B_{\theta}}{B} \frac{1}{r} \frac{\partial f_0^{(1)}}{\partial \theta} = C(f_0^{(0)}) + Q(f_0^{(0)}) \quad (6)$$

$$v_{\parallel} \frac{B_{\theta}}{B} \frac{1}{r} \frac{\partial f_1^{(0)}}{\partial \theta} = -v_{Dr} \frac{\partial f_0^{(0)}}{\partial r} \quad (7)$$

$$v_{\parallel} \frac{B_{\theta}}{B} \frac{1}{r} \frac{\partial f_1^{(1)}}{\partial \theta} = C(f_1^{(0)}) + Q(f_1^{(0)}) - v_{Dr} \frac{\partial f_0^{(1)}}{\partial r}. \quad (8)$$

²³ C.F. Kennel and F. Engelmann, *Phys. Fluids* 9: 2377 (1966).

The bounce average of (6) gives an equation for $f_0^{(o)}$:

$$0 = \{C(f_0^{(o)}) + Q(f_0^{(o)})\}. \quad (9)$$

This is the equation for the modified electron distribution due to RF effects. The bootstrap current is contained in the $f_1^{(o)}$ term, so we only solve for $f_0^{(o)}$ and $f_1^{(o)}$. From (7) and (3), we find the θ -dependent part of $f_1^{(o)}$:

$$f_1^{(o)} = \frac{-m}{eB_0} v_{||} \frac{\partial f_0^{(o)}}{\partial r} + \bar{f}_1^{(o)}. \quad (10)$$

Finally, to find the θ -independent quantity $\bar{f}_1^{(o)}$, we must bounce average (8).

Alternatively, we can use the adjoint technique,²⁴ which may allow us to solve for the plasma current without finding all the details of the electron distribution. This technique makes use of the self-adjoint property of the linearized collision operator C in the DKE (1). For any two distribution functions f and g which are slightly perturbed from a Maxwellian f_M , the adjoint property can be written as

$$\int d^3v g f_M^{-1} C(f) = \int d^3v f f_M^{-1} C(g). \quad (11)$$

If f is the solution of (1), and we let g be the toroidal generalization of the Spitzer-Härm distribution function,²⁵ then we can express the parallel current in terms of g :

$$J_{||} = \frac{-eB}{2\pi q} \int_0^{2\pi} \frac{rd\theta}{B_\theta} \int d^3v \left(\vec{S}_{RF} \cdot \frac{\partial}{\partial v} + \frac{m}{eB_0} \frac{v_{||}}{r} v_{||} h \frac{\partial f}{\partial r} \frac{\partial}{\partial \theta} \right) g e^{-E/T_e}. \quad (12)$$

Although originally applied only to RF and beam driven currents, the adjoint technique has been used to predict the bootstrap current in the absence of RF waves.²⁶ We will use the adjoint technique to determine the effect of RF waves on the bootstrap current.

The equations discussed above can be solved analytically and numerically to study the net current produced by bootstrap in conjunction with several different types of RF waves, including lower hybrid waves, fast Alfvén waves, and electron cyclotron waves. This will allow us to predict an RF scheme which can modify the electron distribution to provide an enhanced bootstrap current. We are also in the process of solving the four-dimensional DKE in its complete form on a parallel processing machine.

1.2.3 Fast Ion Orbits in a Tokamak

Sponsor

U.S. Department of Energy
Grant DE-FG02-91-ER-54109

Ion cyclotron heating in a two ion-species plasma increases the perpendicular energy of resonant minority ions as experimental evidence shows.²⁷ As these particles gain energy, they also become increasingly trapped in the magnetic field of a tokamak. The particles are being scattered into the trapped region as pitch-angle scattering is not fast enough to scatter the particles back in the passing region. Resonant ions can become so energetic that their orbits touch the plasma edge and their banana widths reach dimensions comparable to the minor radius. The banana tips move toward the resonant layer as they gain perpendicular energy when they cross the resonant layer. To understand the transport of these energetic particles due to RF

²⁴ S.P. Hirshman, *Phys. Fluids* 23: 1238 (1980); T.M. Antonsen, Jr. and K.R. Chu, *Phys. Fluids* 25: 1295 (1982).

²⁵ L. Spitzer and R. Härm, *Phys. Rev.* 89: 977 (1953).

²⁶ Y.R. Lin-Liu, F.L. Hinton, C.F.F. Karney, and S.P. Hirshman, "A Numerical Study of the Neoclassical Bootstrap Current Using Adjoint Functions," *Proceedings of the International Sherwood Fusion Theory Conference*, Dallas, Texas, March 14-16, 1994, paper 3C37; O. Sauter, Y.R. Lin-Liu, F.L. Hinton, and J. Vaclavik, CRPP Report LRP 503/94, p. 41 (1994).

²⁷ J. Hosea, *Phys. Rev. Lett.* 43: 1802 (1979).

and collisions, their orbits need to be known in detail.²⁸ We restrict this study to barely-confined trapped particles that touch the plasma edge. These particles are mainly responsible for fast density and energy loss to the plasma wall. We label these particles by the position of their banana tips.

We work in a tokamak cross section where the radial coordinate is $x = r/a$ and the poloidal coordinate is θ . a is the tokamak minor radius, while the major radius is given by R_0 . The geometric factor is $h = 1 + x \frac{a}{R_0} \cos\theta$. The parallel and perpendicular velocities of a particle are respectively $v_{||}$ and v_{\perp} . An algebraic equation for particle orbits can be derived by making use of the integrals of motion. These are the energy, the magnetic moment and the toroidal momentum, given respectively by equations (1), (2) and (3):

$$\bar{v}^2 = \frac{v^2}{v_{th}^2} \quad (1)$$

$$\bar{\mu} = h \bar{v}_{\perp}^2 \quad (2)$$

$$\bar{p} = -h \bar{v}_{||} + A_c x^2 \quad (3)$$

where the parameter A_c is defined as follows

$$A_c = \frac{\mu_0 q I}{4\pi m v_{th}} \quad (4)$$

where I is the total plasma current. We solve for $\bar{v}_{||}$ using (1) and (2), and substitute it into the expression for the toroidal momentum to get an equation in θ and x . The orbit equation is quartic in x :

$$ax^4 + c(\theta)x^2 + d(\theta)x + e = 0 \quad (5)$$

where

$$a = A_c^2; \quad c = -2\bar{p}A_c - \left(\frac{a}{R_0}\right)^2 \bar{v}^2 \cos^2\theta \quad (6)$$

and

$$d = \cos\theta \left(-2 \frac{a}{R_0} \bar{v}^2 + \frac{a}{R_0} \bar{\mu} \right); \quad e = \bar{p}^2 - \bar{v}^2 + \bar{\mu}. \quad (7)$$

The orbit equation describes all particle trajectories in a tokamak as functions of the constants of motion. We assume $\cos\theta = 1$; the orbit equation then becomes

$$ax^4 + c_1 x^2 + d_1 x + e = 0 \quad (8)$$

where our coefficients are

$$c_1 = -2\bar{p}A_c - \left(\frac{a}{R_0}\right)^2 \bar{v}^2 \quad (9)$$

and

$$d_1 = -2 \frac{a}{R_0} \bar{v}^2 + \frac{a}{R_0} \bar{\mu}. \quad (10)$$

To study the orbits of barely-confined particles, we let $x = 1$. This yields an equation for our constants of motion:

$$A_c^2 - 2\bar{p}A_c - \left(\frac{a}{R_0}\right)^2 \bar{v}^2 - 2\bar{v}^2 \frac{a}{R_0} + \bar{\mu} \frac{a}{R_0} + \bar{p}^2 - \bar{v}^2 + \bar{\mu} = 0. \quad (11)$$

Our choice of the constants of motion is now restricted to a two-dimensional space rather than a three-dimensional one. We can also let the inverse-aspect ratio equal one-third without too much loss of generality.

Energetic trapped particles that interact resonantly with the fast Alfvén wave eventually end up having their banana tips close to the resonant layer. These particles have a strong resonant interaction with the ion-cyclotron wave and therefore deserve careful study. They can be easily identified in phase space by looking at their constants of motion. By setting the parallel velocity of the particle at its banana tip to zero, one can easily derive the following relations for the momentum and the energy:

$$p = A_c x_0^2; \quad \bar{v}^2 = \bar{\mu} \quad (12)$$

where x_0 is the radial coordinate of the banana tip of the trapped particle. By substituting these relations in the orbit equation we get:

$$A_c^2 - 2A_c^2 x_0^2 - \frac{4\bar{v}^2}{9} + A_c^2 x_0^4 = 0. \quad (13)$$

²⁸ T.E. Stringer, *Plas. Phys.* 16: 651 (1973); J. Rome and Y.K.M. Peng, *Nuclear Fusion* 19: 1193 (1979).

Solving for x_0^2 :

$$x_{01}^2 = 1.0 + \frac{1}{3A_c/2} \sqrt{\bar{v}^2} \quad (14)$$

and

$$x_{02}^2 = 1.0 - \frac{1}{3A_c/2} \sqrt{\bar{v}^2}. \quad (15)$$

The first root x_{01} can be discarded because it gives a trajectory that goes outside the torus on the resonance layer. Solving (15) for the energy, we obtain:

$$\bar{v}^2 = \frac{9}{4} A_c^2 (1 - x_0^2)^2. \quad (16)$$

The energy has been normalized to 1 KeV. We are interested in particles whose energies are well above the thermal energy. One can observe that the most energetic trapped particles have their tips close to the center of the plasma. As the energy decreases, the tips move radially outward along the resonance layer. The maximum energy that such particles can have while still being confined is 1.2 MeV. In general, the maximum energy is determined by the toroidal current flowing in the tokamak. The maximum confined energy scales approximately as the total current squared.

We now generalize the approach which we took to study the trapped particles whose tips touch the resonant layer. We let the parallel velocity be equal to zero at some point and compute the constants of the motion as functions of the coordinate of this point. Doing so, we obtain

$$\bar{\mu} = \left(1 + \frac{1}{3} \cos\theta_0 x_0\right) \bar{v}^2; \bar{p} = A_c x_0^2 \quad (17)$$

where x_0 and θ_0 are the radial and poloidal angle coordinates of the tip of the banana. By substituting these expressions into (16) we obtain:

$$\bar{v}^2 = \frac{9}{4} A_c^2 \frac{(x_0^2 - 1)^2}{1 - x_0 \cos\theta_0}. \quad (18)$$

These expressions allow us to find the constants of motion given the location of the banana tips.

We are studying barely-confined trapped particles in phase space. We have shown that the location of their tips is the most convenient phase space label to study the orbits of these particles. Passing particles are not included in this analysis because only a small fraction of these particles are barely-confined. In the future, we will discuss the effect

that the fast Alfvén wave and collisions have on the unperturbed orbits.

1.2.4 Publications

Bers, A. "Simple Physics of LH $k_{||}$ Upshift Due to Density Gradient Along \vec{B}_0 ." *Proceedings of the U.S.-Japan Workshop on RF Heating and Current Drive*, MIT Plasma Fusion Center, Cambridge, Massachusetts, November 15-17, 1994.

Bers, A., A.K. Ram, and C.C. Chow. "Saturation of SRS by Spatiotemporal Chaos in Coupled Langmuir Decay." *Bull. Amer. Phys. Soc.* 39: 1754 (1994).

Chan, K.P. *Stochasticity Induced by Electrostatic Waves in Magnetized Plasma*. S.M. thesis. Dept. of Electr. Eng. and Comput. Sci. and Dept. of Physics, MIT, 1994.

Chow, C.C., A.K. Ram, and A. Bers. "Saturation of SRS by Spatiotemporal Chaos in Coupled Langmuir Decay." Revised Report PFC/JA-94-8-REV. Cambridge, Massachusetts: MIT Plasma Fusion Center, 1994.

Delcroix, J.L., and A. Bers. *Physique des Plasmas*. Vols. 1 and 2. Paris, France: InterÉditions/CNRS Éditions, 1994.

Fuchs, V., A.K. Ram, S.D. Schultz, A. Bers, and C.N. Lashmore-Davies. "Mode Conversion and Electron Damping of the Fast Alfvén Wave in a Tokamak at the Ion-Ion Hybrid Frequency." CCFM Report RI 447e. Quebec, Canada: Centre Canadien de Fusion Magnétique, October 1994.

Fuchs, V., S.D. Schultz, A.K. Ram, A. Bers, and C.N. Lashmore-Davies. "Mode Conversion of the Fast Alfvén Wave in a Tokamak at the Ion-Ion Hybrid Frequency." *Bull. Amer. Phys. Soc.* 39: 1627 (1994).

Ram, A.K., and A. Bers. "Hamiltonian Chaos in Wave-Particle Interactions." Invited paper presented at the 1993 Cambridge Workshop on Theoretical Geoplasma Physics. In *Physics of Space Plasmas, SPI Conference Proceedings and Reprint Series Number 13*. Eds. T. Chang and J.R. Jasperse. Cambridge, Massachusetts: Scientific Publishers, 1993.

Ram, A.K., and A. Bers. "Hamiltonian Chaos in Wave-Particle Interactions." Report

PFC/JA-94-22. Cambridge, Massachusetts: MIT Plasma Fusion Center, 1994.

Ram, A.K., A. Bers, V. Fuchs, and S.D. Schultz. "Current Drive by the Combination of Lower Hybrid and ICRF Waves." *Proceedings of the 21st European Physical Society Conference on Controlled Fusion and Plasma Physics*, Montpellier, France, June 27 - July 1, 1994. 3: 1134-1137 (1994).

Ram, R.K., A. Bers, V. Fuchs, and S.D. Schultz. "Current Drive by the Combination of Lower Hybrid and ICRF Waves." Report PFC/JA-94-18. Cambridge, Massachusetts: MIT Plasma Fusion Center, 1994.

Ram, A.K., A. Bers, V. Fuchs, and S.D. Schultz. "Enhanced Current Drive with Lower-Hybrid and Ion-Bernstein Waves." *Proceedings of the 15th International Atomic Energy Agency Conference on Plasma Physics and Controlled Nuclear Fusion*, Seville, Spain, September 26 - October 1, 1994. Vienna, Austria: IAEA. Paper IAEA-CN-60/D-P-I-15. Forthcoming.

Ram, A.K., A. Bers, V. Fuchs, and S.D. Schultz. "Enhanced Current Drive with Lower-Hybrid and Ion-Bernstein Waves." Report PFC/JA-94-34. Cambridge, Massachusetts: MIT Plasma Fusion Center, 1994.

Ram, A.K., A. Bers, V. Fuchs, and S.D. Schultz. "Enhancing Lower Hybrid Current Drive Efficiency with Fast Alfvén Waves and Ion-Bernstein Waves." 7th Boulder International RF Advanced Tokamak Workshop, Boulder, Colorado, April 6-8, 1994.

Ram, A.K., A. Bers, V. Fuchs, and S.D. Schultz. "Enhancing Lower Hybrid Current Drive with ICRF Waves." *Proceedings of the International Sherwood Fusion Conference*, Dallas, Texas, March 14-16, 1994. Paper 1C49.

Ram, A.K., A. Bers, V. Fuchs, and S.D. Schultz. "Heating and Current Drive by Mode-Converted Ion-Bernstein Waves." *Proceedings of the U.S.-Japan Workshop on RF Heating and Current Drive*, MIT Plasma Fusion Center, Cambridge, Massachusetts, November 15-17, 1994.

Ram, A.K., A. Bers, S.D. Schultz, and V. Fuchs. "Interaction of Ion-Bernstein Waves with Electrons." *Bull. Amer. Phys. Soc.* 39: 1626 (1994).

Ram, A.K., C.C. Chow, and A. Bers. "Saturation of SRS by Spatiotemporal Chaos in Coupled

Langmuir Decay." *Proceedings of the 21st European Physical Society Conference on Controlled Fusion and Plasma Physics*, Montpellier, France, June 27 - July 1, 1994, 3: 1460-1463 (1994).

Schultz, S.D., A. Bers, and A.K. Ram. "Effect of RF Waves on Bootstrap Current in Tokamaks." *Bull. Amer. Phys. Soc.* 39: 1625 (1994).

1.3 Physics of Thermonuclear Plasmas

Sponsor

U.S. Department of Energy
Contract DE-FGO2-91ER-54109

Project Staff

Professor Bruno Coppi, Dr. Giuseppe Bertin, Dr. Francesca Bombarda, Franco Carpignano, William S. Daughton, Dr. Paolo Detragiache, Darin R. Ernst, Andrew J. Kerman, Catherine Lorusso, Dr. Stefano Migliuolo, Gregory E. Penn, Darren M. Pierre, Caterina Riconda, Todd H. Rider, Suraj D. Salihu, Dr. Linda E. Sugiyama, George M. Svolos, Miriam Weiner

As our primary activity in this research program, we study the physics of magnetically confined plasmas in regimes relevant to present-day advanced experiments on high-temperature plasmas and to near-future thermonuclear reactors. The main objective of these experiments is to bring the plasma ("thermonuclear fuel") produced in toroidal magnetic confinement configurations to ignition conditions. The first generation fuel consists of deuterium-tritium mixtures (considered for the Ignitor and ITER experimental programs), and this should be followed by experiments with more advanced fuels such as deuterium-deuterium or deuterium-helium mixtures that have a lower rate of neutron production (CANDOR program).

The Ignitor-Ult machine is now in the early stages of construction in Europe. At MIT, the Alcator C-MOD experiment combines the favorable features of an elongated plasma cross section with a high magnetic field to produce high-plasma currents and sustain high-plasma densities with the high degree of purity that is required for fusion reactors. This is, in fact, consistent with a research program that we had formulated in the early 1970s with the proposal of a high-field, elongated plasma machine called Megator. Megator was capable of producing megampere plasma currents in a compact configuration. The Megator concept, with similar parameters to those of Alcator C-MOD, had been studied

as a logical evolution of the Alcator program that had been established at MIT since 1989.

First, the basic physical processes that characterize the properties and the dynamics of thermonuclear plasmas are being studied as they apply to existing or near-term future systems. In this effort, we closely collaborate with our experimental colleagues, as well as theorists from other research groups (e.g., Columbia, JET, Phillips Laboratory, Princeton, University of Texas, Lawrence Livermore National Laboratories). This work also involves time-dependent simulations of plasma discharges in the Ignitor-Ult experiment. We focus particular attention on the evolution of spatial profiles of plasma current and temperature. Collaboration with our colleagues at the E.N.E.A. laboratories of Italy (Ente per le Nuove Tecnologie, l'Energia e l'Ambiente), as well as in-house code development, plays a major role in this endeavor.

Second, we explore advanced regimes of thermonuclear burning, including those employing low neutron yield fuels ($D-^3He$, and "catalyzed" $D-D$). We consider both the design of machines that will contain these very high temperature plasmas as well as the physics that govern their behavior. Below, we discuss some salient results of work completed or presently being carried out by members of our research group.

1.3.1 Isotopic Effect in Transport and the Ubiquitous Mode

We have investigated the linear stability of the collisionless trapped electron mode (first called "the ubiquitous mode")²⁹ in plasmas with two or more ion species. In addition to this mode, whose perturbed electrostatic potential has even-parity about the midplane of the torus $\phi(-\theta) = \phi(\theta)$, the toroidal ion temperature gradient (ITG) mode with odd-parity is also investigated.²⁹ The calculations are performed in a low- β toroidal geometry. Two L-mode discharges in the JET and TFTR experiment are used to provide reference parameters for this study.³⁰ This work is carried out in the intermediate frequency regime, $k_{\parallel}v_{Ti} \ll \omega \ll k_{\parallel}v_{Te}$, appropriate to describe the perturbations that are

observed to dominate the spectrum in poloidal wavenumber (i.e., those with $k_{\theta}v_{Ti}/\omega_{ci} \sim 1$).³¹

The linear stability analysis shows that the $\gamma(k_{\theta})$ spectrum has no maximum in the regime of interest, $\partial\gamma/\partial|k_{\theta}| > 0$, and that the presence of an impurity ion species leads to a moderate decrease in the growth rate (at constant poloidal wavenumber), simply due to an effect of dilution of the primary (hydrogenic) ion: $n_i = n_e - Z_in_i$. This holds true for both even-parity (ubiquitous) and odd-parity (ITG) modes. An important detail to remember is that this stabilization exhibits no particular scaling with isotopic mass; indeed the stabilizing trend saturates quite quickly (around $A_i \sim 12$, i.e., carbon) and is a stronger function of impurity charge concentration (Z_in_i).

The realization that the single-ion dispersion relation is a function of a set of parameters where mass and charge occur only in the Larmor radius, $\rho_i \propto A_i/Z_i$, leads to the realization that a change in the ion species constituting the thermonuclear fuel (for instance, from Deuterium to Tritium) automatically entails a shift of the linear wave spectrum, in poloidal wavenumber, so that $k_{\theta}\rho_i$ remains constant. We speak of "poloidal wavenumber" only for convenience. In reality, many poloidal harmonics are coupled toroidally to create the unstable eigenmode in our analysis (carried out via the "ballooning representation"). The one true "quantum number" here is the toroidal wavenumber, n , so that $k_{\theta} = nq(r_s)/r_s$ where r_s is the radius of the reference rational surface and $q = rB/RB_{\theta}$. This conclusion in turn makes any model that relies on a mixing length formula, $D \propto \gamma/k_{\theta}$, exhibit an anti-isotopic effect whereby transport (measured by the particle diffusion coefficient D) increases with isotopic mass, in contradiction with experimentally observed trends.

The resolution lies apparently in adopting a description in which turbulence in experiments (e.g., JET)³² where an isotopic effect is observed ($D \propto A_i^{-1/2}$) is mostly determined by the quasilinear spectrum of linearly unstable modes. A simple calculation then shows that the quasilinear particle flux is due to the quasi-circulating electrons (the ones that have undergone drift-reversal), for cases with

²⁹ B. Coppi and F. Pegoraro, *Nucl. Fusion* 17: 969 (1977).

³⁰ S. Migliuolo, "Isotopic Effect in Transport and the Ubiquitous Mode," *Phys. Lett. A* 198: 341 (1995).

³¹ R.J. Fonck, G. Cosby, R.D. Durst, S.F. Paul, N. Bretz, S. Scott, E. Synakowski, and G. Taylor, *Phys. Rev. Lett.* 70: 3736 (1993).

³² F. Tibone, B. Balet, M. Bures, J.G. Cordey, T.T.C. Jones, P.J. Lomas, K. Lawson, H.W. Morsi, P. Nielsen, D.F.H. Start, A. Tanga, A. Taroni, K. Thomsen, and D.J. Ward, *Nucl. Fusion* 22: 413 (1993).

standard profiles ($\nabla T \cdot \nabla n > 0$), and that this flux is of the type:

$$\Gamma = 2\sqrt{\pi} \frac{cT_e}{eB} \sum_{k_\theta} k_\theta \Gamma_k$$

where Γ_k is a function of dimensionless variables that are invariant under isotopic substitution (for constant density and temperature profiles). This then leads, in a natural fashion, both to the isotopic effect (D decreasing with isotopic mass) as well as to the inverse dependence on charge, specifically $D \propto Z$ in this model. We note that the first theoretical model³³ to explain the observation of the isotopic effect was based on the excitation of third species ("impurity") driven modes at the edge of the plasma column.

1.3.2 Ideal-MHD Stability of Ignition Experiments

We have undertaken a study of the linear stability of toroidal plasmas in fully shaped toroidal configurations (i.e., including effects due to finite aspect ratio, ellipticity and triangularity) in parameter regimes relevant to ignition experiments, such as Ignitor and ITER. The analysis is carried out within the ideal magnetohydrodynamic (MHD) approximation, using the numerical equilibrium and stability code PEST-1 developed at Princeton University.³⁴ The input pressure and q profiles are taken in accordance with ITER design specifications and transport modeling:

$$P(\psi) = P_0(1 - \psi)^{3/2} \quad q(\psi) = q_0 + (q_a - q_0)\psi^3$$

Computations indicate that a pressure driven internal mode is unstable, with low threshold value (~ 1) in the parameter $\beta_N = \beta(\%)a(m)B(T)/I_p(MA)$, where $\beta = 8\pi \langle p \rangle / B^2$ and $\langle p \rangle$ is the volume averaged plasma pressure. This is in agreement

with practically all other stability analyses that have been carried out with $q_0 < 1$.

As is well known,³⁵ the physical parameter of relevance is β_p , the poloidal beta averaged within the $q \leq 1$ volume, and Ignitor is designed to operate at values of this parameter that are below critical ($\beta_p^{crit} \sim 0.3$). ITER, on the other hand, does not have this "safety feature" in its design and we expect it to be subject to an ideal MHD instability, which may lead to either large sawteeth, reconnection, and/or disruptions. A sample curve of the normalized growth rate as a function of $\beta(\%)$ is shown in figure 10. These instabilities are not amenable to wall stabilization, owing to their internal nature. The eigenfunction is dominated by the $m=1,2$ poloidal harmonics which mostly affect the $q \leq 2$ volume. See figure 11, we fix the toroidal mode number $n=1$; this is the most unstable case. Since this volume encompasses nearly 75 percent of the plasma, these modes which tend to mix the plasma via a macroscopic convective cell are likely to be extremely detrimental to the fusion reactivity in the experiments.

In addition, it should be noted that fast particle stabilization, by fusion α -particles, will not be effective in ITER. On the contrary, a preliminary calculation performed in collaboration with F. Porcelli from the Politechnic of Turin, indicates that the energy content in the α population is large enough to cause the appearance of the trapped particle branch of the fishbone. This is the high frequency³⁶ counterpart of the resonant $m=1$ oscillation³⁷ that is responsible for the scattering and ejection from the plasma of energetic ions in neutral beam-heated experiments.

Finally, we note that ignition experiments operate in regimes that are more collisional than present-day high temperature devices such as JET and TFTR and, in the case of Ignitor, with thermal plasmas. Thus, the physics of reconnecting modes³⁸ will be important and the subject of future study.

³³ B. Coppi, in *Plasma Physics and Controlled Nuclear Fusion Research*, (Vienna: I.A.E.A., 1991).

³⁴ R.C. Grimm, R.L. Dewar, and J. Manickam, *J. Comp. Phys.* 4: 94 (1983).

³⁵ M.N. Bussac, R. Pellat, D. Edery, and J.L. Soulé, *Phys. Rev. Lett.* 35: 1638 (1975); L.E. Zakharov, *Sov. J. Plasma Phys.* 4: 503 (1978); A.C. Coppi and B. Coppi, *Nucl. Fusion* 32: 205 (1992).

³⁶ L. Chen, R.B. White, and M.N. Rosenbluth, *Phys. Rev. Lett.* 52: 1122 (1984).

³⁷ B. Coppi and F. Porcelli, *Phys. Rev. Lett.* 57: 2272 (1986).

³⁸ G. Ara, B. Basu, B. Coppi, G. Laval, M.N. Rosenbluth, and B.V. Waddell, *Ann. Phys.* 112: 443 (1978).

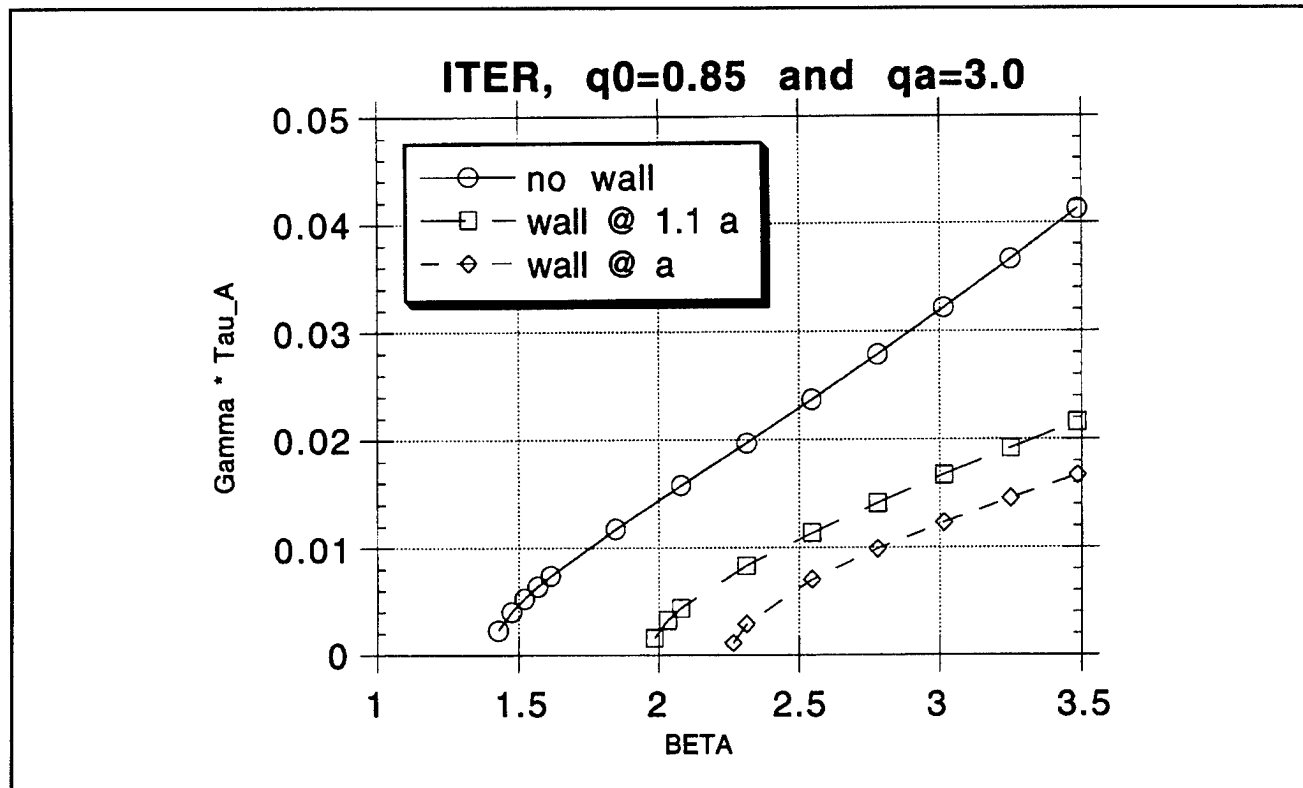


Figure 10.

1.3.3 Analysis of Disruptions in the TFTR Experiment

Disruptions (i.e., the sudden loss of control of the plasma, followed by a quench of the current and termination of the discharge) are a serious problem in toroidal magnetic confinement experiments. Disruptions limit the regime of operation (either in density, current, or pressure) and can have deleterious effects on the structural integrity of the Tokamak vacuum vessel due to the electromotive forces induced by the disruption.

In collaboration with Professor Jeffrey P. Freidberg, Dr. Jay Kesner, and Dr. Jesus Ramos we have begun an analysis of the plasma properties leading to disruption in the TFTR experiment at Princeton University. We have concentrated on events where pressure played a role such as the so-called "beta limit", where the plasma is unable to exceed a maximum value in the parameter $\beta = 8\pi \langle p \rangle / B^2$, the ratio of the volume averaged plasma pressure to the magnetic field energy density. The parameter of merit, $\beta_N = \beta(\%)B(T)a(m)/I(MA)$, rarely reaches the expected maximum value (~ 3) in TFTR.

Instead, a macroscopic phenomenon appears around $\beta_N \sim 2$ to limit the discharge.

Our original goal was to understand the physical cause of these disruptions and to deduce a cure for the relatively low values of β_N in TFTR. While this remains a major objective of our project, our work has pointed to an apparent major problem in the use of ideal-MHD linear stability codes as predictive tools for the TFTR tokamak, as well as, probably, other auxiliary heated experiments with substantial nonthermal populations of ions. The numerical codes predict the appearance of pressure-driven modes (with toroidal number $n=1$) well before any external manifestation occurs in the experiment. This occurs in the analysis of TFTR discharges where $q(0) < 1$, and it has been reported also to be the case for DIII-D plasmas.³⁹ The numerical analysis predicts the appearance of a linearly unstable mode whose dominant poloidal component is $m=1$ and with measurable $m=2,3$ components present due to toroidal coupling. Among the discharges analyzed was a high power shot 76778 (at the time, record) which achieved 10 MW fusion power. A careful modeling, employing $p(\psi)$ and $q(\psi)$ profiles, where $0 \leq \psi \leq 1$ is the normalized poloidal flux,

³⁹ T. Taylor, private communication.

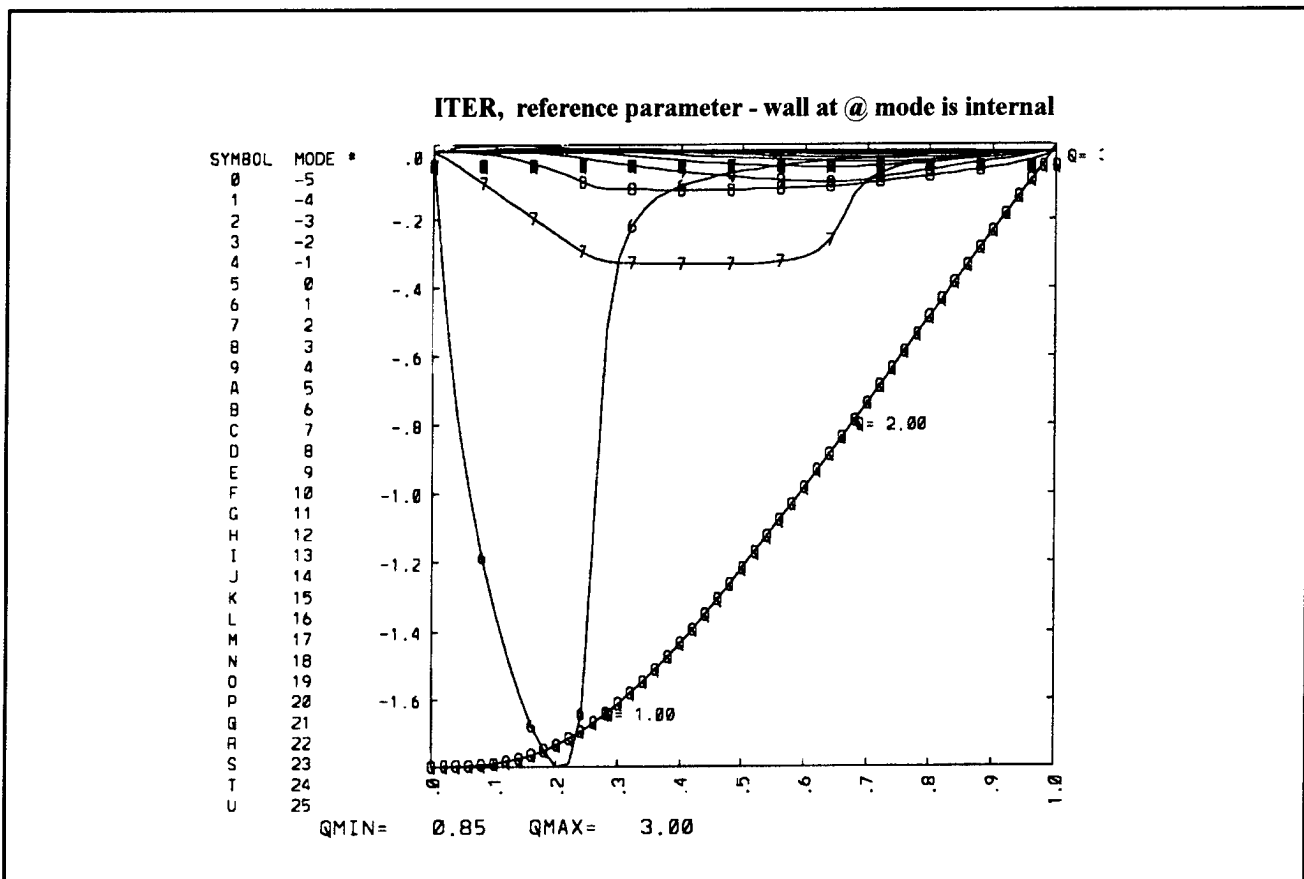


Figure 11.

obtained from TRANSP was performed using both PEST-1 and PEST-2 stability codes with the aforementioned results.

Resolutions of this apparent discrepancy are being sought at this time. They include the role of so-called "FLR stabilization" due to finite ion diamagnetic frequency either in the linear or nonlinear⁴⁰ regimes as well as other effects that involve breaking the single-fluid approximation.

Ongoing analysis includes discharges involving plasmas without a $q=1$ surface. These configurations involve reversed magnetic shear profiles, e.g., $q(0) > 2$, $q_{\min} < 2$, and $q(a) \sim 5 - 6$. In those cases, an $n=1$ and (dominant) $m=2$ appears at sufficiently high pressures. At present, results are mixed, with the linear code underestimating threshold in some

cases, relative to the value of β_N at the time of the disruption, and overestimating in others. Apparently, the problem resides in the fact that the q -profiles are known with less accuracy in these instances (and the value of q_{\min} is crucial for the analysis) rather than in the presence of additional physics.

1.3.4 Emissions at the Harmonics of the Cyclotron Frequency

An important source of information on the distribution of α -particles in DT fusion plasmas is the spectrum of radiation emission in the range of the α -particle cyclotron frequency and above.

Localized magnetosonic-whistler modes are thought to lie⁴¹ behind this emission, observed in JET⁴² and

⁴⁰ L. Zakharov, J. Manickam, W. Park, and B. Rogers, "Sawtooth Stabilization and Triggering of High-Beta Disruptions in TFTR," International Sherwood Theory Conference, Incline Village, Nevada, 1995.

⁴¹ B. Coppi, *Phys. Lett. A* 172: 439 (1993).

⁴² G.A. Cottrell et al., *Nuc. Fusion* 33: 1365 (1993).

TFTR.⁴³ These modes would interact resonantly with the harmonic of the α -particle cyclotron frequency, giving rise to a growth rate.

We have extended our previous work on the subject by studying the spatial structure of the magnetosonic-whistler wave.⁴⁴ We found that two classes of toroidal modes exist within the part of the spectrum where the whistler contribution is significant. One class is radially localized within a narrow shell near the outer edge of the plasma column. The distance of the shell from the axis of symmetry is found to be close to that estimated from the experiments.⁴² The other class propagates almost perpendicularly to the magnetic field and

can extend radially to well inside the plasma column.

Moreover, we have investigated the effects related to the inhomogeneity of the magnetic field on the instability, particularly how the growth rate is affected by toroidicity⁴⁵ for frequencies at or above the ion cyclotron frequency in the resonant case (i.e., $\omega \sim p\Omega_\alpha$).

We are now in the process of studying how the nature of the interaction is sensitive to the type of orbits along which the resonant particle travels, since we found that only trapped particles can reach the resonance region.

⁴³ S. Cauffman and R. Majeski, *Rev. Sc. Instrum.* 66: 819 (1995).

⁴⁴ B. Coppi, *Phys. Lett. A* 172: 439 (1993); C. Riconda, B. Coppi, and N. Asherie, "Spatial Structure of Magnetosonic Whistler Eigenmodes in Cylindrical Geometry," *Bull. Am. Phys. Soc.* 39: 1553 (1994).

⁴⁵ C. Riconda, B. Coppi, and G. Penn, "Emission above the Ion Cyclotron Frequency in a Nonhomogeneous Magnetic Field," International Sherwood Conference, Incline Village, Nevada, 1995.

Section 3 Electromagnetics

Chapter 1 Electromagnetic Wave Theory and Applications

Chapter 1. Electromagnetic Wave Theory and Applications

Academic and Research Staff

Professor Jin Au Kong, Dr. Kung Hau Ding, Dr. Robert T. Shin, Dr. Y. Eric Yang

Visiting Scientists and Research Affiliates

Dr. Yasunori Kanamaru,¹ Dr. Francesca Scire-Scappuzzo,² Dr. Leung Tsang,³ Dr. Lars H. Bomholt,⁴ Dr. Arthur K. Jordan,⁵ Dr. Kevin O'Neill,⁶ Dr. Jean-Claude Souyris,⁷ Dr. Michael Tsuk,⁸ Dr. Jiqing Xia⁹

Graduate Students

Jerome J. Akerson, Robert G. Atkins, William W. Au, Hong Tat Ewe, Tza Jing Gung, Chih-Chien Hsu, Gregory T. Huang, Joel T. Johnson, Jenn-Huei Kuan, Kevin Li, Christina Manolatou, John H. Oates, Ante Salcedo, Shih-En Shih, Prathet Tankuranun, M. Ali Tassoudji, Murat E. Veysoglu, Li-Fang Wang, Jun Yan, Chen-Pang Yeang, Yan Zhang, William W. Zhou

Undergraduate Students

William Lee, Grant Smith

Technical and Support Staff

Kit-Wah F. Lai

1.1 Remote Sensing of Earth Terrain

Sponsors

California Institute of Technology/
Jet Propulsion Laboratory
Contract 959548

National Aeronautics and Space Administration
Grant NAGW-1617
Contract 958461

U.S. Navy - Office of Naval Research
Grant N00014-92-J-1616
Grant N00014-92-J-4098

Project Staff

Professor Jin Au Kong, Dr. Francesca Scire-Scappuzzo, Dr. Leung Tsang, Dr. Kung Hau Ding, Dr. Robert T. Shin, Dr. Jean-Claude Souyris, Robert G. Atkins, William W. Au, Hong Tat Ewe, Chih-Chien Hsu, Joel T. Johnson, Ante Salcedo, Shih-En Shih, Murat E. Veysoglu, Li-Fang Wang, Jun Yan, Yan Zhang

In this project area, we investigate the active and passive remote sensing of forest, vegetation canopy, snow, sea ice, and ocean wind directions. Vegetation canopy can be modeled as either a mixture of multiple-species discrete scatterers described by a certain size, shape, and orientation

¹ Professor, Kanazawa Institute of Technology, Ishikawa, Japan.

² Professor, Istituto di Informatica e Telecomunicazioni, Catania, Italy.

³ Professor, University of Washington, Seattle, Washington.

⁴ Swiss Federal Institute of Technology, Lausanne, Switzerland.

⁵ U.S. Navy, Office of Naval Research, Arlington, Virginia.

⁶ U.S. Army, Cold Regions Research and Engineering Laboratory, Hanover, New Hampshire.

⁷ Centre D'Etude Spatiale des Rayonnements, Toulouse Cedex, France.

⁸ Digital Equipment Corporation, Tewksbury, Massachusetts.

⁹ Schlumberger-Doll Research, Ridgefield, Connecticut.

distributions, or as a continuous random medium characterized by correlation functions. A layer model is developed and applied to interpret radar backscattering coefficients and radiometric brightness temperatures collected from forest and vegetation fields.

For sea ice data interpretation and inversion, we have developed a random medium model using radiative transfer theory. An optimization approach is used for inversion. The discrepancy between the data and the results of the forward model is minimized by changing the inversion parameters according to a nonlinear programming scheme. Reconstruction of correlation lengths in the horizontal and vertical dimensions has been accomplished using the polarimetric backscattering coefficients at different angles of incidence as input data. Effects of data diversity and noise on the reconstruction of the physical parameters of sea ice from the backscattering coefficients are being investigated.

Polarimetric passive remote sensing of wind-generated ocean surfaces is investigated with emphasis on the third Stokes parameter. A numerical study of the polarimetric thermal emission from ocean surfaces randomly rough in one dimension using a Monte Carlo technique is carried out. A set of finite length surface profiles with desired statistics is generated using a spectral method. Each surface is extended periodically to create an infinite rough surface, and the thermal emission is computed using the extended boundary condition method (EBC) and the method of moments (MOM). The results of the study show that the third Stokes parameter is sensitive to the azimuthal angle between the surface periodicity and the looking angle, the rms height of the surface, and the surface power law spectrum slope. The results also show that this parameter is insensitive to variations in polar angle, permittivity, and surface spectrum high frequency content.

1.2 Electromagnetic Waves in Multilayer Media

Sponsors

Digital Equipment Corporation
AGMT DTD 11/16/93
Joint Services Electronics Program
Contract DAAL03-92-C-0001
Grant DAAH04-95-1-0038

MIT Lincoln Laboratory
P.O. No. BX-5424
U.S. Navy - Office of Naval Research
Grant N00014-90-J-1002
Grant N00014-89-J-1019

Project Staff

Professor Jin Au Kong, Dr. Lars H. Bomholt, Dr. Robert T. Shin, Dr. Michael Tsuk, Dr. Jiqing Xia, Dr. Y. Eric Yang, Robert G. Atkins, Hong Tat Ewe, Chih-Chien Hsu, Gregory T. Huang, Joel T. Johnson, Kevin Li, Christina Manolatou, John H. Oates, Prathet Tankuranun, M. Ali Tassoudji, Murat E. Veysoglu

In this project area, we apply both analytical and numerical methods to the solution of electromagnetic wave problems in layered media and microstrip structures. The analytical technique included the double deformation method performed on complex planes and the numerical technique include the integral equation methods and the finite difference time domain (FDTD) methods together with the absorbing boundary conditions (ABC).

The electromagnetic radiation from a VLSI chip package and heatsink structure is analyzed by means of the finite-difference time-domain (FDTD) technique. The dimensions of a typical configuration calls for a multizone gridding scheme in the FDTD algorithm to accommodate fine grid cells in the vicinity of the heatsink and package cavity and sparse gridding in the remainder of the computational domain. The issues pertaining to the effects of the heatsink in influencing the overall radiating capacity of the configuration are addressed. Analyses are facilitated by using simplified heatsink models and by using dipole elements as sources of electromagnetic energy to model the VLSI chip. The potential for enhancement of spurious emissions by the heatsink structure is illustrated. For heatsinks of typical dimensions, resonance is possible within the low gigahertz frequency range. The exploitation of the heatsink as an emissions shield by appropriate implementation schemes is discussed and evaluated.

The media that we studied included electrically and magnetically anisotropic material, superconductors, and chiral media made of helical elements. For helical chiral media, we derived the constitutive relations and studied their potential use as absorbing material. Anisotropic media are also investigated for applications as modulators in microstrip configurations.

1.3 Simulation of Electromagnetic Wave Scattering

Sponsors

DEMACO

Agreement 11/15/93

Federal Aviation Administration

Grant 94-G-007

U.S. Army Cold Regions Research and Engineering Laboratory

Contract DACA89-93-K-0009

Project Staff

Professor Jin Au Kong, Dr. Kevin O'Neill, Dr. Y. Eric Yang, Hong Tat Ewe, Tza Jing Gung, Chih-Chien Hsu, Jenn-Huei Kuan, William Lee, Grant Smith, M. Ali Tassoudji, Li-Fang Wang, Chen-Pang Yeang, Yan Zhang, William W. Zhou

In this project area, we concentrate on the development of the computer simulation software for electromagnetic modeling of scattering applied to remote sensing and applied to landing systems for airplanes. This is a long-term project for the development of comprehensive theoretical model for the computer simulation of three-dimensional microwave and millimeter wave scattering and emission phenomena. Major tasks include (1) Simulation Program—development of baseline simulation that include the effects of environments, hard targets, atmospheric absorption and scattering, and ground reflection; (2) Validation and Documentation—generation of synthetic scene for comparison with real data and production of user manuals and validation reports; and (3) Upgrade Assessment—studies into models that can be added to the baseline simulation and the ways to integrate them.

The goals are (1) to assemble available physical models that satisfy the minimum requirement defined above and (2) to build a preliminary simulation package using these models to demonstrate the process of generating scenes from standard input data sets and possibly of direct or indirect comparison with recorded images. We have developed a baseline simulation package with X-window/Motif graphical user interface. This program (1) first accesses GIS feature map and elevation map and create displays of both, (2) allows a user to identify and highlight particular terrain features in the map region from a menu, and then (3) interfaces with background terrain scattering coefficient database, which has been created by EMSARS program and a clutter statistics model to generate simulated radar images. A simple terrain shadowing effect is included. The current database is created using the random medium

volume scattering model and composite rough surface scattering model.

A study is also underway to model the effects of interference on the safety of ILS Category III operations. The intention is to gain a full understanding of radio interference on aircraft performance and to determine an acceptable level of interference for use in autoland certification. Previously a computer package had been developed to assess the electromagnetic compatibility in ILS/MLS channel planning. It is proposed that this model be enhanced to include the industrial, scientific, and medical (ISM) sources in the interference study. The aircraft automatic flight control system (AFCS) model will be integrated with the receiver model to simulate the effect of interference on autoland performance. Ultimately a standard on acceptable exposure time of FM broadcast interference will be developed from the study.

1.4 Publications

Au, W.C., J.A. Kong, and L. Tsang. "Absorption Enhancement of Scattering of Electromagnetic Waves by Dielectric Cylinder Clusters." *Micro-wave and Opt. Tech. Lett.* 7(10): 454-457 (1994).

Gu, Q., A.M. Tassoudji, S.Y. Poh, R.T. Shin, and J.A. Kong. "Coupled Noise Analysis for Adjacent Vias in Multilayered Digital Circuits." *IEEE Trans. Circuits and Sys.* 41(12): 796-804 (1994).

Hara, Y., R.G. Atkins, S.H. Yueh, R.T. Shin, and J.A. Kong. "Application of Neural Networks to Radar Image Classification." *IEEE Trans. Geosci. Remote Sensing* 32(1): 100-109 (1994).

Hsu, C.C., H.C. Han, R.T. Shin, J.A. Kong, A. Beaudoin, and T. Le Toan. "Radiative Transfer Theory for Polarimetric Remote Sensing of Pine Forest at P band." *Int. J. Remote Sensing* 15(14): 2943-2954 (1994).

Johnson, J., J.A. Kong, R.T. Shin, S.H. Yueh, S.V. Nghiem, and R. Kwok. "Polarimetric Thermal Emission from Rough Ocean Surfaces." *J. Electromag. Waves Appl.* 8(1): 43-59 (1994).

Lee, C.F., B.J. McCartin, R.T. Shin, and J.A. Kong. "A Triangular-Grid Finite-Difference Time-Domain Method for Electromagnetic Scattering Problems." *J. Electromag. Waves Appl.* 8(4): 449-470 (1994).

Lim, H.H., M.E. Veysoglu, S.H. Yueh, R.T. Shin, and J.A. Kong. "Random Medium Model

- Approach to Scattering from a Random Collection of Discrete Scatterers." *J. Electromag. Waves Appl.* 8(7): 801-817 (1994).
- Xia, J.J., T.M. Habashy, and J.A. Kong. "Profile Inversion in a Cylindrically Stratified Lossy Medium." *Radio Sci.* 29(4): 1131-114 (1994).
- Xia, J., A.K. Jordan, and J.A. Kong. "Electromagnetic Inverse Scattering Theory for Inhomogeneous Dielectric: the Local Reflection Model." *Opt. Soc. Am. A* 11(3): 1081-1086 (1994).
- Xia, J.J., J.A. Kong, and R.T. Shin. "A Macroscopic Model of Nonlinear Constitutive Relations in Superconductors." *IEEE Trans. Microwave Theory Tech.* 42(10): 1951-1957 (1994).
- Yueh, S.H., R. Kwok, F.K. Li, S.V. Nghiem, W.J. Wilson, and J.A. Kong. "Polarimetric Passive Remote Sensing of Ocean Wind Vectors." *Radio Sci.* 29(4): 799-814 (1994).
- Yueh, S.H., S.V. Nghiem, R. Kwok, W.J. Wilson, F.K. Li, J.T. Johnson, and J.A. Kong. "Polarimetric Thermal Emission from Periodic Water Surfaces." *Radio Sci.* 29(1): 87-96 (1994).
- #### 1.4.1 Meeting Papers
- Hsu, C.C., J.A. Kong, T. Le Toan, S. Paloscia, and P. Pampaloni. "Microwave Emission and Backscattering from Crops." Paper presented at the 1994 Progress in Electromagnetics Research Symposium, Noordwijk, The Netherlands, July 11-15, 1994.
- Johnson, J.T., J.A. Kong, Shin, and L. Tsang. "Theory and Experiments in Polarimetric Passive Remote Sensing." Paper presented at the National Radio Science Meeting, Boulder, Colorado, January 5-8, 1994.
- Nghiem, S.V., R. Kwok, S.H. Yueh, J.A. Kong, M.A. Tassoudji, C.C. Hsu, A.J. Gow, and D.K. Perovich. "Polarimetric Backscattering from Thin Saline Ice Related to Ice Physical and Morphological Characteristics." Paper presented at the International Geoscience and Remote Sensing Symposium, Pasadena, California, August 8-12, 1994.
- Nghiem, S.V., R. Kwok, S.H. Yueh, J.A. Kong, M.A. Tassoudji, C.C. Hsu, A.J. Gow, and D.K. Perovich. "Polarimetric Backscattering Signatures from Thin Saline Ice under Controlled Laboratory Conditions." Paper presented at the International Geoscience and Remote Sensing Symposium, Pasadena, California, August 8-12, 1994.
- Scire-Scapuzzpo, F., C.C. Hsu, L. Wang, J.A. Kong, and T. Le Toan. "Inversion of Biomass of Pine Forest using Theoretical Models." Paper presented at the 1994 Progress in Electromagnetics Research Symposium, Noordwijk, The Netherlands, July 11-15, 1994.
- Tsang, L., Z. Chen, G. Zhang, K.H. Ding, C. Hsu, and J.A. Kong. "Microwave Scattering by Vegetation Based on Wave Approach." Paper presented at the 1994 Progress in Electromagnetics Research Symposium, Noordwijk, The Netherlands, July 11-15, 1994.
- Yang, Y.E., H.T. Ewe, C.C. Hsu, L. Wang, S.E. Shih, K.H. Ding, J.A. Kong, R.T. Shin, H. Nguyen, T. Nguyen, J.Y. Ho, K. O'Neill. "A GIS Driven Interactive Radar Simulation using EMSARS Model." Paper presented at the International Geoscience and Remote Sensing Symposium, Pasadena, California, August 8-12, 1994.
- Yang, Y.E., M.A. Tassoudji, H.T. Ewe, J.A. Kong, and G.J. Markey. "Examination of Electromagnetic Interference to Civil Aviation GPS Receivers." Paper presented at the International Union of Radio Science (URSI) meeting, Seattle, Washington, June 19-24, 1994.

Section 4 Radio Astronomy

Chapter 1 Radio Astronomy

Chapter 1. Radio Astronomy

Academic and Research Staff

Professor Bernard F. Burke, Professor Jacqueline N. Hewitt, Professor David H. Staelin, Dr. Philip W. Rosenkranz, John W. Barrett

Visiting Scientists and Research Affiliates

Dr. Ann B. Saust-Rossi

Graduate Students

Ian M. Avruch, William J. Blackwell, Carlos R. Cabrera, Grace H. Chen, John D. Ellithorpe, Charles A. Katz, Deborah J. Becker-Haarsma, John K. Cartwright, Samuel R. Conner, Fronefield Crawford, André Fletcher, Lori K. Herold-Jacobson, Rizwan R. Koita, Christopher B. Moore, Mark A. Rawizza, Michael J. Schwartz, Michelle S. Spina

Undergraduate Students

Lauren B. Klatsky, Mark D. Messier

Technical and Support Staff

Anne E. Conklin

1.1 Extragalactic Radio Source Studies

Sponsor

National Science Foundation
Grant AST 92-24191

Project Staff

Professor Bernard F. Burke, Ian M. Avruch, Deborah J. Becker-Haarsma, John K. Cartwright, Samuel R. Conner, Fronefield Crawford, André Fletcher, Lori K. Herold-Jacobson

The research during the second year of the grant, "Extragalactic Radio Astronomy," has continued to focus on five general areas: (1) analysis of gravitational lensing by galaxies, (2) searching for new examples of gravitational lensing by galaxies, (3) studies of individual radio sources in our extensive VLA mapping study of MG radio sources, (4) completion of the Parkes-MIT-NRAO (PMN) survey of radio surveys in the southern sky, and (5) a search for distant neutral hydrogen concentrations beyond redshift 5.

This year, our study of gravitational lensed systems has concentrated on reducing our extended synoptic data on the twin quasar, B0957+561. We have published a value for the radio time delay between the two quasar images—a quantity of some cosmological significance because it gives a value for the Hubble constant that is based on

entirely different assumptions from the traditional optical methods. Since we have continued to observe the system with the VLA during the four years that have elapsed since the previous value was published, we can now refine the propagation delay significantly. A major change has occurred in the fluxes of both components, and a new value for the time delay will be determined soon. The reduction is being carried out by Ms. Deborah Becker-Haarsma.

The gravitational lens search is proceeding along the same lines as in the previous year. The search starts with VLA snapshots of radio sources from the MIT-Green Bank (MG) survey, taken with the VLA and reduced to well-calibrated maps. The work this year is concentrated on optical observations that are needed to provide the verification that radio sources, having promising structures that suggest lensing, have multiple structure at optical wavelengths. The radio reductions have been carried out by Mr. Samuel Conner, and the optical observations are being made by Ms. Lori Herold-Jacobson and Mr. André Fletcher. The MDM 1.3 m telescope on Kitt Peak was used to observe 160 sources at r-band, and the identifications support both the lens search and the studies of individual sources.

Compact radio double sources form one particularly interesting subsample of the MG collection of VLA snapshots. We observed a collection of 24 of these objects, using the Jodrell Bank MERLIN array to gain higher angular resolution. This study shows

polarization asymmetry between the radio lobes as a frequently-occurring phenomenon (the Laing effect), and a publication is in preparation. The optical studies of the compact double sources, noted earlier, are being reduced at the present time and will form the Ph.D. dissertation of Ms. Herold-Jacobson. A second set of individual source studies is being worked on by Mr. Fletcher, as a part of his Ph.D. dissertation. The sources are taken from either the equatorial or tropical section of the PMN survey and will form a link between identification work in the northern and southern hemispheres.

The Parkes-MIT-NRAO (PMN) survey of the southern sky has been completed. Three sections, the southern, tropical, and equatorial surveys, have been published; and the final section, the Zenith survey, is being prepared for publication.

The survey for pre-galactic condensations of neutral hydrogen, beyond redshift 5, is underway. Preliminary observations were made in the fall of 1994, using the 4000-channel spectrometer developed in collaboration with Professor Paul Horowitz of Harvard University. The particular feed structures that were used turned out to be vulnerable to interference received in their far sidelobes, and a new feed is under construction. The system must contend with terrestrial interference in the 200-250 MHz band that we are using. However, we are optimistic that enough clear spots in the spectrum can be found to yield results that should give information on the state of the medium after the recombination era ($z=1000$) and before the galaxy formation era (after $z=5$).

1.1.1 Publications

Fletcher, A., S.R. Conner, and B.F. Burke. "First Results from 8.4 GHz VLA Imaging of 1800 Southern Sky Parkes-MIT-NRAO (PMN) Radio Sources." *Bull. A.A.S.* 26: 1503 (1994). (abstract)

Griffith, M.R., A.E. Wright, R.D. Ekers, and B.F. Burke. "The Parkes-MIT-NRAO (PMN) Surveys: VI. Source Catalogue for the Equatorial Survey (covering -9.5 degrees <gamma<+10 degrees)." *Astrophys. J. Suppl.* 97: 347 (1995).

Tasker, N.J., J.J. Condon, A.E. Wright, and M.R. Griffith. "The Parkes-MIT-NRAO (PMN) Surveys V: Maps for the Tropical Survey (covering -29 degrees <gamma<-9 degrees)" *Astron. J.* 107: 2115 (1994).

Wright, A.E., M.R. Griffith, B.F. Burke, and R.D. Ekers. "The Parkes-MIT-NRAO (PMN) Surveys: II. Source Catalogue for the Southern Survey (covering -87.5 degrees <S<-37 degrees)." *Astrophys. J. Suppl.* 90: 179-295 (1994).

Wright, A.E., M.R. Griffith, B.F. Burke, and R.D. Ekers. "The Parkes-MIT-NRAO (PMN) Surveys: III. Source Catalogue for the Tropical Survey (covering -29 degrees <S<-9.5 degrees)." *Astroph. J. Suppl.* 91: 111-308 (1994).

1.2 Studies of Gravitational Lenses

Sponsors

MIT Class of 1948/Career Development Chair

National Science Foundation
Presidential Young Investigator Award

David and Lucile Packard Fellowship

Project Staff

Professor Jacqueline N. Hewitt, Grace H. Chen, John D. Ellithorpe, Charles A. Katz, Mark D. Messier, Christopher B. Moore, Dr. Ann B. Saust-Rossi

Gravitational lenses provide radio astronomers with the opportunity to re-examine many long-standing problems in astrophysics. Two of these problems, addressed by the work described here, are the nature and distribution of luminous and dark matter in galaxies, and the calibration of the age and scale of the universe (i.e., the determination of the present value of the cosmological Hubble parameter).

Both applications require the inference of the distribution of gravitating matter from the observed imaging properties of the lens. This, in turn, requires detailed measurements of the brightness distribution of the image. Detailed radio maps of two gravitationally lensed extragalactic sources, MG1131+0456 and MG0414+0534, are being compiled from data taken with the National Radio Astronomy Observatory (NRAO) Very Large Array (VLA) radio telescope and the recently completed telescopes of the NRAO Very Long Baseline Array (VLBA). The high resolution data of figure 1 have been analyzed by an application of the LensClean algorithm developed by Professors Christopher S. Kochanek and Ramesh Narayan of Harvard University. The figure shows the 8 GHz VLA image, model background source, model gravitationally lensed source, and residuals of the model fit. The model, which is a good fit to the data, is highly con-

strained. However, a significant number of residuals remain, and our effort to reconstruct the mass distribution in this lens is continuing.

The analysis depicted in Figure 1 was carried out using the images generated by the VLA. The image reconstruction techniques introduce errors into the process. To eliminate this source of error, we have developed a modified version of the LensClean algorithm, Visibility LensClean, that operates directly on the interferometer data. This algorithm is being tested and applied to VLBA data. We anticipate that it will be a critical resource in the interpretation of data from sparse antenna arrays such as the VLBA.

In a gravitational lens system, there are differences in the propagation time on the order of days to months for the different ray paths associated with

the images of the background source. Monitoring programs aimed at measuring these time delays are being carried out with the VLA. Analysis of the light curves has shown that the variations of the images of MG0414+0534 are correlated, providing further evidence that the MG0414 system is indeed gravitationally lensed. Furthermore, the monitoring data suggest that the third brightest of the four gravitationally lensed images leads the rest, a result that excludes certain models for the lensing mass distribution. Monitoring of the gravitational lens MG1131+0456 (at radio wavelengths) and PG1115+080 (at optical wavelengths, in collaboration with R. Schild of the Harvard-Smithsonian Center for Astrophysics) has detected significant variability in these objects, indicating that time delay measurements should be pursued. Measurements of the time delays would provide a measurement of

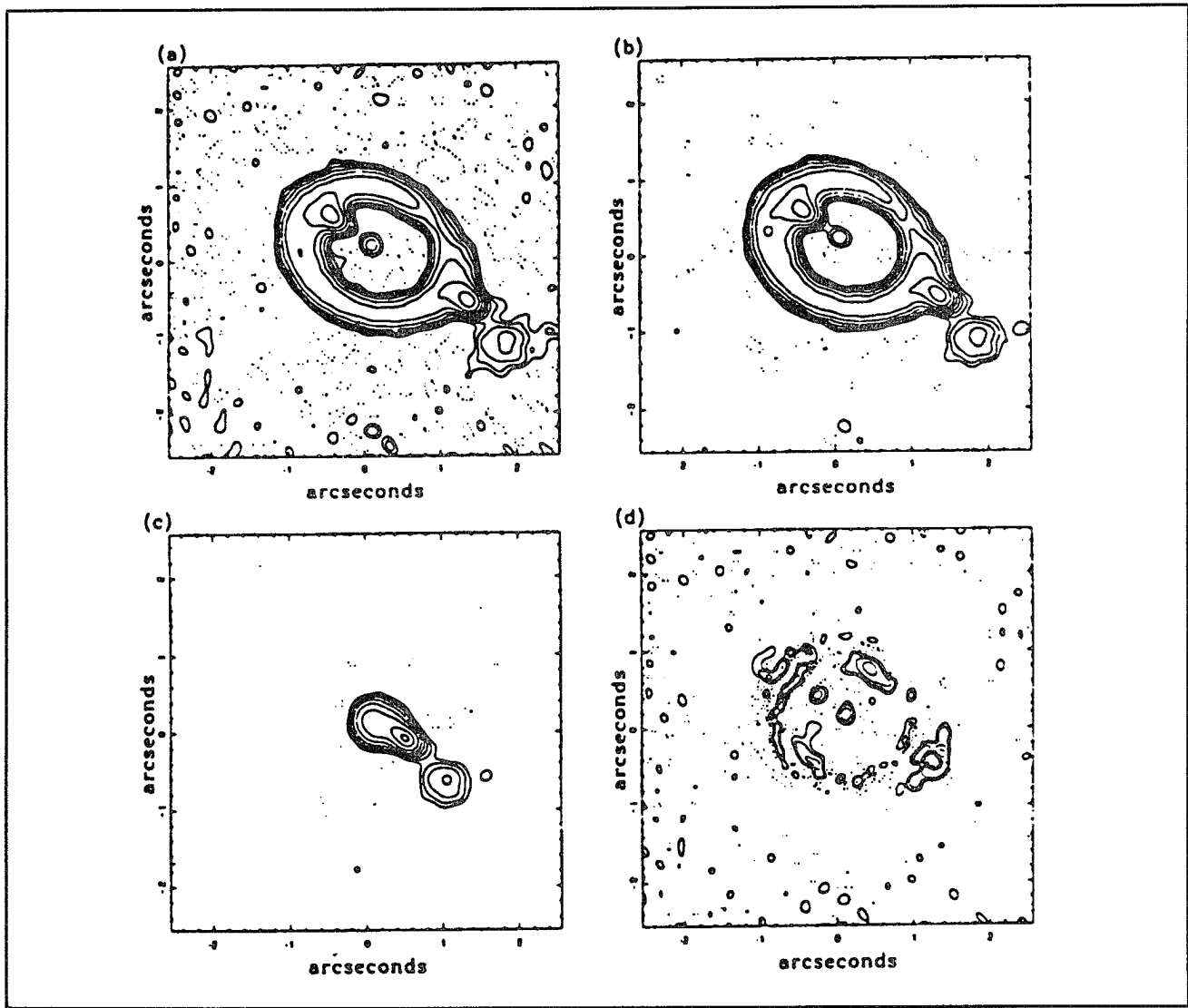


Figure 1. The 8 GHz VLA image, model background source, model gravitationally lensed sources, and residuals of the model fit.

the distances involved in the geometry of the gravitational lens system. Such an independent measure of distance provides a calibration of the present value of the cosmological Hubble parameter.

The time delay measurement techniques used in these investigations are general, so they have also been applied to the multifrequency monitoring data for the BL Lac object PKS2155-304.

1.2.1 Publications

Chen, G.H., C.S. Kochanek, and J.N. Hewitt. "The Mass Distribution of the Lens Galaxy in MG1131+0456." *Astrophys. J.* Forthcoming.

Edelson, R., J. Krolik, G. Madejski, L. Maraschi, G. Pike, C.M. Urry, W. Brinkmann, W., T.J.-L. Courvoisier, J. Ellithorpe, K. Horne, A. Treves, S. Wagner, W. Wamsteker, R. Warwick, H.D. Aller, M.F., Aller, M. Ashley, A. Blecha, P. Bouchet, P. Bratschi, J.N. Bregman, M. Carini, A. Celotti, M. Donahue, E. Feigelson, A.V. Filippenko, H. Fink, I. George, I. Glass, J. Heidt, J.N. Hewitt, P. Hughes, R. Kollgaard, Y. Kondo, A. Koratkar, K. Leighly, A. Marscher, T. Matheson, P.G. Martin, H.R. Miller, J.C. Noble, P. O'Brien, E. Pian, G. Reichert, J.M. Saken, J.M. Shull, M. Sitko, P.S. Smith, W.-H. Sun, and G. Tagliaferri. "Multi-Wavelength Monitoring of the BL Lac Object PKS 2155-304. IV. Multi-Wavelength Analysis." *Astrophys. J.* Forthcoming.

Hewitt, J.N., G.H. Chen, and M.D. Messier. "Variability in the Einstein Ring Gravitational Lens MG1131+0456." *Astronom. J.* Forthcoming.

Moore, C.B., and J.N. Hewitt. "Time Delay Observations and Variability of the Gravitational Lens MG0414+0534." Submitted to *Astrophys. J.*

Invited Talks

Hewitt, J.N. "Gravitational Lenses: A New Tool for Astrophysicists." U.S. Coast Guard Academy, Lecture, February 15, 1994.

Hewitt, J.N. "Gravitational Lenses and Cosmology." Argonne National Laboratory Physics Division Colloquium, April 1, 1994.

Hewitt, J.N. "Gravitational Lenses, Time Delays, and Hubble's Constant." University of California, Berkeley, Department of Astronomy Colloquium, April 7, 1994.

Hewitt, J.N. "Gravitational Lenses, Time Delays, and Hubble's Constant." Lawrence Livermore National Laboratory Colloquium, April 8, 1994.

Hewitt, J.N. "Gravitational Lenses - Observations." Fourth New England Regional Quasar/AGN Meeting, Brandeis University, review talk, May 6, 1994.

Hewitt, J.N. "Gravitational Lenses, Time Delays, and Hubble's Constant." California Institute of Technology Colloquium, May 25, 1994.

1.3 The Detection of Astronomical Radio Transients

Sponsors

MIT Class of 1948/Career Development Chair

National Science Foundation
Presidential Young Investigator Award
David and Lucile Packard Fellowship

Project Staff

Professor Jacqueline N. Hewitt, John W. Barrett, Charles A. Katz, Lauren B. Klatsky, Christopher B. Moore, John D. Ellithorpe

The detection of radio transients of astrophysical origin is of interest for a number of reasons. First, some already well studied sources are known to exhibit radio transients, and further characterizing their nature would increase our understanding of the emission processes involved. Examples include the sun, flare stars, and interacting stellar systems. Second, there have been serendipitous discoveries of radio transients, apparently of astrophysical origin, but with no known counterpart at other wavelengths. Since these may represent a new class of object, we would like to establish whether they are natural phenomena and to determine how frequently they occur.

Third, transients at other wavelengths are known to exist. The Compton Observatory is detecting gamma ray bursts at a rate of approximately one per day. X-ray transients have also been detected, many associated with radio outbursts. In the near future, all-sky monitors will be launched on the X-ray Transient Explorer and the High Energy Transient Experiment. An all-sky radio monitor is needed to detect any radio counterparts to the x-ray and gamma ray transients and to place upper limits on their fluence. Finally, because of the confusion with man-made interference, the investigation of radio phenomena on short time scales is an area

that has not been fully explored. As such, there is potential for the discovery of new phenomena.

To address the scientific questions outlined above, we are proposing the construction of a network of geographically separated correlating arrays. Prototype receivers, antennas, and data acquisition systems have been designed and constructed and are currently undergoing testing. The design of correlating arrays has begun.

This project is being carried out in collaboration with Alan E.E. Rogers and Brian E. Corey of MIT's Haystack Observatory.

1.3.1 Publications

Katz, C.A., J.N. Hewitt, C.B. Moore, and J.D. Ellithorpe. "The STARE Project: A Search for Transient Astronomical Radio Emission." *Bull. Am. Astronom. Soc.* Forthcoming.

Invited Talks

Hewitt, J.N. "Detecting Astronomical Radio Transients." Talk presented to the Radio Astronomy and Geodesy Group, Harvard-Smithsonian Center for Astrophysics, March 5, 1994.

1.4 Algorithms for Advanced Microwave Sounding Unit Operational Use

Sponsor

MIT Lincoln Laboratory
Agreement BX-4975

Project Staff

Dr. Philip W. Rosenkranz, Michael J. Schwartz

This project provides scientific support to the National Oceanic and Atmospheric Administration (NOAA), for the Advanced Microwave Sounding Units A and B (AMSU-A, AMSU-B) which are scheduled for launch on NOAA polar-orbiting weather satellites starting in 1996, and also for instrument improvements. The effort emphasizes development of atmospheric transmittance algorithms, estimation of surface emissivity and precipitation, issues related to instrument design and specification, and general retrieval methods.

Measurements from the MIT aircraft-based Microwave Temperature Sounder and from present satellite radiometers, such as the Microwave Sounding

Unit, are used to develop and test prototype algorithms.

1.4.1 Publications

Rosenkranz, P.W. "A Rapid Transmittance Algorithm for Microwave Sounding Frequencies," *Digest of the International Geoscience and Remote Sensing Symposium*, Pasadena, California, August 8-12, 1994.

Rosenkranz, P.W. "A Rapid Atmospheric Transmittance Algorithm for Microwave Sounding Frequencies." submitted to *IEEE Trans. Geosci. Rem. Sensing*.

Schwartz, M.J., J.W. Barrett, P.W. Rosenkranz, and D.H. Staelin. "Atmospheric Transmittance Measurements Near 118 GHz." *Digest of the International Geoscience and Remote Sensing Symposium*, Pasadena, California, August 8-12, 1994.

1.5 Earth Observing System: Advanced Microwave Sounding Unit

Sponsor

National Aeronautics and Space Administration/
Goddard Space Flight Center
Grant NAS 5-31276

Project Staff

Professor David H. Staelin, Dr. Philip W. Rosenkranz, John W. Barrett, William J. Blackwell, Carlos R. Cabrera, Michael J. Schwartz, Michelle S. Spina

The AMSU will provide microwave-band measurements to the Atmospheric Infrared Sounder (AIRS), which will be a facility instrument on NASA's planned Earth Observing System (EOS). This effort is directed toward developing algorithms for the retrieval of temperature and humidity profiles, precipitation, sea ice, land snow cover, and other parameters. The temperature and humidity profiles obtained from AMSU are intended to provide initial conditions for the AIRS infrared cloud-correction and profile retrieval algorithms. Work to date has focused on simulation efforts.

Artificial neural network techniques have been applied to retrievals of humidity profiles from simulated microwave spectral observations; to estimation of the altitudes of precipitation cell tops using data from the Microwave Temperature

Sounder; and to compact representation of radiometric data.

1.5.1 Publications

Cabrera-Mercader, C.R., and D.H. Staelin. "Passive Microwave Humidity Profile Retrievals Using Neural Networks." *Digest of the International Geoscience and Remote Sensing Symposium*, Pasadena, California, August 8-12, 1994.

Cabrera-Mercader, C.R., and D.H. Staelin. "Passive Microwave Relative Humidity Retrievals using Feedforward Neural Networks." submitted to *IEEE Trans. Geosci. Rem. Sens.*

Kuo, C.C., D.H. Staelin, and P.W. Rosenkranz. "Statistical Iterative Scheme for Estimating Atmospheric Relative Humidity Profiles." *IEEE Trans. Geosci. Rem. Sens.* 32(2): 254-260 (1994).

Rosenkranz, P.W. "A Rapid Transmittance Algorithm for Microwave Sounding Frequencies." *Digest of the International Geoscience and Remote Sensing Symposium*, Pasadena, California, August 8-12, 1994.

Rosenkranz, P.W. "A Rapid Atmospheric Transmittance Algorithm for Microwave Sounding Frequencies." submitted to *IEEE Trans. Geosci. Rem. Sens.*

Spina, M.S., M.J. Schwartz, D.H. Staelin, and A.J. Gasiewski. "Application of Multilayer Feedforward Neural Networks to Precipitation Cell-top Altitude Estimation." *Digest of the International Geoscience and Remote Sensing Symposium*, Pasadena, California, August 8-12, 1994.

Spina, M.S., M.J. Schwartz, D.H. Staelin, and A.J. Gasiewski. "Application of Multilayer Feedforward Neural Networks to Precipitation Cell-top Altitude Estimation." submitted to *IEEE Trans. Geosci. Rem. Sens.*

Thesis

Spina, Michelle S. *Application of Multilayer Feedforward Neural Networks to Precipitation Cell-Top Altitude Estimation*. M.S. thesis. Dept. of Electr. Eng. and Comput. Sci., MIT, 1994.

1.6 High-Resolution Passive Microwave Imaging of Atmospheric Structure

Sponsor

National Aeronautics and Space Administration/
Goddard Space Flight Center
Grant NAG5-10

Project Staff

Professor David H. Staelin, John W. Barrett, Dr. Philip W. Rosenkranz, Michael J. Schwartz

The MIT Microwave Temperature Sounder (MTS) is a dual-band radiometer, incorporating an imaging spectrometer at 118 GHz and a tunable fixed-beam radiometer at 52-54 GHz. This instrument is flown on the NASA ER-2 high-altitude aircraft.

High-resolution 118-GHz measurements of tropical cyclone Oliver (obtained in 1993) were processed. They show warming of approximately 10K in the eye relative to the environment, and the convective cloud structure of the eyewall and cloud bands. Cloud-top altitudes were inferred from the data using a neural-network algorithm.

Upward-observing profiles of atmospheric brightness temperature at 52-54 and 118 GHz are being used to test atmospheric transmittance algorithms.

1.6.1 Publications

Schwartz, M.J., J.W. Barrett, P.W. Rosenkranz, and D.H. Staelin. "Atmospheric Transmittance Measurements Near 118 GHz." *Digest of the International Geoscience and Remote Sensing Symposium*, Pasadena, California, August 8-12, 1994.

Schwartz, M.J., J.W. Barrett, P.W. Fieguth, P.W. Rosenkranz, M.S. Spina, and D.H. Staelin. "Passive Microwave Imagery of a Tropical Storm Near 118 GHz: Thermal and Precipitation Structure." *Digest of the International Geoscience and Remote Sensing Symposium*, Pasadena, California, August 8-12, 1994.

1.7 Reduction of Variation

Sponsor

MIT Leaders for Manufacturing Program

Project Staff

Professor David H. Staelin, Rizwan R. Koita, Mark A. Rawizza, Michelle S. Spina

Reduction of process and product variation is a primary economic goal in most manufacturing operations. Progress this year has centered in two areas: 1) continued development of "conformal experiment design" techniques which seek to optimize and characterize processes with as few as $2N$ experiments, where N is the approximate number of important parameters, and 2) development of "data-rich" data analysis techniques which most efficiently identify the nature and origin of the principal sources of variation in products and processes.

A previously developed software tool proposed sets of experiments which preferentially evaluate potential two-parameter interactions of greatest concern, based on the user's *a priori* knowledge about the process. If analysis of that block of experimental results suggests not all process variables or interactions have been identified, a second set of experiments is often desirable. Two methods for generating such a second block of experiments were developed. One method generates a set of experiments half the size of the original block, and the other method generates a second set of size equal to the original set. These new methods thus supplement the design software developed previously. This new method produces new factorial experiment designs with confounding patterns maximally different from those of the first block of experiments. These subsequent designs can be directed to focus on certain interactions of potential interest. The power of these new methods for sequential block design is limited, however, to identifying only one or a few new interactions per block of experiments.

A new method for sequentially designing experiments one-at-a-time was also developed. After an initial block of experiments has been performed, certain columns in the experiment matrix may be significant and also contain more than one potentially significant contributing interaction. The one-at-

a-time method can be used to identify which interactions are dominant in each column, and permits optimization of the process with a minimum number of experiments, typically on the order of the number of significant variables. The method involves iteratively hypothesizing on the basis of all prior data the most probable process model consistent with prior experiments, and then designing and performing that one experiment which should yield maximum quality. If the recommended experiment has been previously performed, then the next most likely process model is selected and its corresponding optimum process parameters are tested experimentally. This process is iterated until the process model predicts with adequate accuracy the outcomes of all experiments performed to date. These methods are particularly important when experiments can be conducted one at a time efficiently, and each experiment is costly in time or money.

Methods for identifying and controlling principal sources of variation in manufacturing processes are being developed by testing them on actual manufacturing data from LFM partner companies, including Alcoa, General Motors, Intel, Kodak, and potentially others. The commercially significant processes examined to date are typically characterized by multi-variant linear relationships between process observations and the resulting product characteristics. These relationships exhibit systematic drifting and discontinuities in process characteristics which are often hidden in superficial process noise and which, when identified, should permit improved process control and reduction in variation.

1.7.1 Thesis

Koita, Rizwan R. *Strategies for Sequential Design of Experiments*. M.S. thesis. Dept. of Electr. Eng. and Comput. Sci., MIT, 1994.

Part III Systems and Signals

Section 1 Computer-Aided Design

Section 2 Digital Signal Processing

Section 1 Computer-Aided Design

Chapter 1 Custom Integrated Circuits

Chapter 2 Computer-Integrated Design and Manufacture
of Integrated Circuits

Chapter 1. Custom Integrated Circuits

Academic and Research Staff

Professor Jonathan Allen, Professor John L. Wyatt, Jr., Professor Jacob K. White, Professor Srinivas Devadas, Professor Dimitri A. Antoniadis, Professor Berthold K.P. Horn, Professor Hae-Seung Lee, Professor Steven B. Leeb, Professor Terry P. Orlando, Professor Martin A. Schmidt, Professor Stephen D. Senturia, Professor Charles G. Sodini, Dr. Robert C. Armstrong

Visiting Scientists and Research Affiliates

Dr. Andrew Lumsdaine,¹ Dr. Ichiro Masaki,² Dr. Mark W. Reichelt,³ Dr. Herre S.J. van der Zant, Dr. He Yie⁴

Graduate Students

Donald G. Baltus, Xuejun Cai, Michael T. Chou, Steven J. Decker, Ibrahim M. Elfadel, Michael S. Ehrlich, George I. Hadjiiannis, Frederick P. Herrmann, Mattan Kamon, Stan Y. Liao, David R. Martin, Yehia M. Massoud, Robert G. McDonald, Ignacio S. McQuirk, José C. Monteiro, Keith S. Nabors, Ognen J. Nastov, Erkki Oja, Edward J. Ouellette, Joel R. Phillips, Mark N. Seidel, Luis M. Silveira, Chin Hwee Tan, Christopher B. Umminger, Paul C. Yu

Technical and Support Staff

Susan E. Chafe, Dorothy A. Fleischer

1.1 Custom Integrated Circuits

Sponsors

IBM Corporation

National Science Foundation

Project Staff

Professor Jonathan Allen, Dr. Robert C. Armstrong, Donald G. Baltus, Michael S. Ehrlich, Robert G. McDonald, Chin Hwee Tan

The overall goal of VLSI computer-aided design (CAD) research is to provide the means to produce custom integrated circuits quickly, correctly, and economically. Traditionally, correctness has been verified at several representational levels of abstraction, such as required topologies for given circuit families (e.g., precharge/evaluate CMOS circuits) and stipulated logic formalisms (such as binary decision diagrams). These techniques for checking correctness are usually local to the partic-

ular representational level involved and, while they are important components of the overall design testing procedure, they do not attempt to provide for the alignment and consistency checks between the different abstract representational levels and the provided input behavioral specification. In addition, they do not characterize the set of possible designs at each representational level corresponding to the initial functional specification in a way that ranges over the wide variety of possible performance levels. For this reason, there is a large need to provide CAD tools that serve as a framework for design exploration with performance as a parameter, thus providing the designer with the ability to achieve a desired performance together with consistently aligned representations at all levels.

This research group studies a variety of topics with an emphasis on performance-directed synthesis of custom VLSI designs. An overview of the viewpoint that motivates these projects is provided in a major survey paper⁵ in which the need for coordinating the design optimization process over the several

¹ Notre Dame University, Notre Dame, Indiana.

² Computer Science Department, General Motors Research Laboratory, Warren, Michigan.

³ Mathworks, Natick, Massachusetts.

⁴ Microelectronics Center, Southeast University, Nanjing, China.

⁵ J. Allen, "Performance-Directed Synthesis of VLSI Systems," *Proc. IEEE* 78(2): 336-355 (1990).

levels of representation is emphasized. Since design exploration is so central to the production of high-performance designs, emphasis is placed on how performance can be characterized at the several levels of representation and how overall design performance can be achieved in an integrated way.

During this past year, Donald G. Baltus finished his doctoral dissertation on the conversion of high-level functional specifications to a detailed mask layout.⁶ This research was motivated by the need for high-performance designs oriented toward signal processing tasks that can be implemented in optimal systolic arrays, where the predominant architectural feature is nearest neighbor communication. Because of this restricted architecture, it is possible to reflect performance considerations normally associated with physical design at the architectural level, since communication delays can be accurately modeled within the architectural domain of systolic arrays. The system designed by Baltus, called DESCARTES, uses a high-level linguistic specification of the design as input in a language called FLASH. These algorithmic specifications are then converted to data-dependence graphs which are augmented to provide indexed representations (where the index may range over space or time), thus allowing compact representation of calculations that do not grow with the size of the array.

Through the introduction of several constraints represented formally, it has been possible to substantially reduce the design space without rejecting any architectural candidates that might lead to an optimal design. The introduction of these constraints in the search process provides both comprehensive design exploration while providing an exact, optimal solution in terms of delay without the necessity to introduce any heuristic techniques. This overall design process sets the state of the art for systolic array synthesis, with particular emphasis on signal processing tasks. Attractive visual displays have also been generated that provide the designer with an insightful means to understand how the calculation is embedded in space and time. Experience with this system has shown that novel, unexpected solutions are frequently generated.

Yet, there were no cases in which known optimal designs have not been generated.⁷

In recent years, there has been a growing interest in the design of integrated circuits, subject to constraint and power dissipation. During this year, Chin Hwee Tan completed her master's thesis, in which she developed a set of heuristic techniques to manipulate transistor sizes and input ordering in order to minimize power under a delay constraint while utilizing statistical power estimation techniques.⁸ This research builds on new capabilities to estimate the switching frequencies of nodes within a circuit, and hence, provides a statistically accurate estimation of the average power dissipation at such nodes. Since both the capacitance and the voltage swing of the node are known, it is only necessary to obtain an accurate estimate of the number of voltage transitions per cycle at that node, together with the cycle time, in order to accurately estimate power.

The basic idea that motivated this research involves the situation when a node is in the longest delay path of a circuit and switches slowly, then it may be possible to increase the size of the transistors that drive the node, and hence speed up the switching of the node. There is little impact on power dissipation if the switching frequency of that node is relatively low when compared to the other nodes in the circuit. A small but complete standard cell library was laid out and circuit models were accurately extracted to provide accurate delay estimates. In her thesis, Tan investigated several techniques that have led to the accurate and effective minimization of power under delay constraints. She also combined the statistical techniques to estimate power, with careful attention to the reordering of inputs to nodes. The design process is iterative, so that optimal node ordering is in fact utilized. In this way, early arriving inputs at a gate are positioned close to the rails; while late arriving inputs are attached close to the output, thus minimizing or eliminating body effect on late switching transistors, with corresponding speed up. Experience with a wide class of combinational circuits has shown that it is possible to reduce delay up to 43 percent with only an 8 percent increase in power. These results were

⁶ D.G. Baltus, *Efficient Exploration of Affine Space-Time Transformations for Optimal Systolic Array Synthesis*, Ph.D. diss., Dept. of Electr. Eng. and Comput. Sci., MIT, 1994.

⁷ D.G. Baltus and J. Allen, "Efficient Exploration of Space-Time Transformations for Systolic Array Synthesis," paper presented at the International Conference on Application-Specific Array Processors, Venice, Italy, October 25-27, 1993.

⁸ C.H. Tan, *Optimization of Power and Delay in VLSI Circuits Using Transistor Sizing and Input Ordering*, Ph.D. diss., Dept. of Electr. Eng. and Comput. Sci., MIT, 1994.

presented at the 1994 International Workshop on Low Power Design.⁹

Dr. Robert C. Armstrong continues to improve the capability of the FICOM incremental consistency-based database.¹⁰ Emphasis is now placed on the use of schema compilation techniques to generate complete design systems centered around the design database. Substantial schemas have been designed that allow: the compiled generation of the design system user interface, the application interface from a variety of external applications to the database manager, and the database manager together with a data repository itself. Since the schema can be described in high-level language, it is possible to rapidly configure custom design systems that are appropriate to the needs of specific applications and individual users.

During this year, the schema compilation capability was further refined and the levels of representation utilized within the database were extended. A representation for physical layout was completed, and it is now being implemented in the overall system. In addition, application interfaces to several standard CAD applications were provided. The most useful one to date has been to the SPICE circuit simulator. By using this application, it is possible to automatically trigger a circuit simulation whenever a change is made in the design database. A timing estimation client is also being designed. This will be coupled with a transistor sizing scheme so that transistor sizes can be systematically manipulated in order to achieve timing performance specifications while maintaining consistent design representation at all levels through the use of the integrated database. The capability of the database to efficiently manage constraints has been particularly useful with the addition of the mask layout representation, since the same mechanism is used both to enforce design rules and to maintain display presentations for the user.

The database manager has been generalized in such a way that it not only accepts input from clients explicitly anticipated, but a general "CFI"-compliant interface is also provided so that any application that conforms to the CAD framework initiative specifications can readily be connected to this database manager and repository. This gives the system great flexibility, and it also

means that CFI-compliant applications do not have to be rewritten in order to use this incremental consistency database system. This avoids a large rewriting task and ensures that the database system can be broadly used over many applications.

During this year, Robert McDonald has continued to study the design of self-resetting CMOS circuits as an alternative circuit style that can provide very fast operation. A general organizational hierarchy was established for these circuits, which allows any logical function to be implemented. The general timing constraints for self-resetting operation are formulated, thus ensuring accurate operation. Several design variations were provided and methods for interfacing self-resetting CMOS circuits with standard static and precharge/evaluate circuits were generated. In addition, the overall logic partitioning of the system utilizing these circuits, as well as strategies for power reduction, are being developed. Several self-resetting logic blocks were designed, and techniques for composing these into networks of self-resetting circuits were developed. During 1995, these contributions will be integrated into an overall design system, thus providing a means for translating high-level logic specifications directly to very high-performance circuits.

During 1994, a 12-node IBM Scalable Parallel 2 computer system was installed in our laboratory. This is a state-of-the-art system that provides very high-performance computation nodes connected by a very high-speed crossbar switch. While this system provides general parallel computational capability for many research projects within the laboratory, it will be especially utilized in CAD applications where there is a high degree of parallelism. Many circuit simulation algorithms permit parallel partitioning, and the efficient parallel searching of design databases will also be explored using this facility. Our plans include the provision of additional nodes so that the effects of parallelism can be quantitatively described, as well as permitting the exploration of exceedingly large design spaces.

Professor Jonathan Allen is designing an interactive learning environment for VLSI design education. This environment includes the provision of new texts that cover basic VLSI design together with built-in hypertext links that allow navigation through

⁹ C.H. Tan and J. Allen, "Minimization of Power in VLSI Circuits Using Transistor Sizing Input Ordering, and Statistical Power Estimation," paper presented at the International Workshop on Low Power Design, Napa, California, April 24-27, 1994.

¹⁰ R.C. Armstrong and J. Allen, "FICOM: A Framework for Incremental Consistency Maintenance in Multi-Representation, Structural VLSI Design Databases," *Digest of Technical Papers*, IEEE/ACM International Conference on Computer-Aided Design, Santa Clara, California, November 8-12, 1992, 336-343.

the textual material in many different orders. In this way, students will not be constrained to follow the normal linear order of a text. Instead, they will be able to jump from topic to topic and explore issues at a depth that is appropriate for each individual student. This hypertext system will also be coupled to a circuit simulator, so it will be possible for the student to interactively explore the behavior of circuits as both device sizes and circuit topology are manipulated. Experience with the FICOM system¹¹ has provided interesting techniques that allow the student to compare a variety of designs. For example, six different inverter styles were implemented in the FICOM database and compared. This allowed the student to see what device sizes were necessary in order to provide equivalent performance between different circuit styles. In another comparison, a variety of circuit drivers (ranging from super buffers to push-pull drivers to bootstrap drivers) were implemented and their performance compared. Once again, this provided the student with ready insight into how these circuits can drive large loads. The goal is to implement this entire system on a laptop computer, so that the interactive learning environment can be used at any time or place by students as an individualized learning laboratory where each student can build experience with and understanding of the material.

1.1.1 Meeting Paper

Tan, C.H., and J. Allen, "Minimization of Power in VLSI Circuits Using Transistor Sizing Input Ordering, and Statistical Power Estimation." Paper presented at the International Workshop on Low Power Design, Napa, California, April 24-27, 1994.

1.2 Analog VLSI Systems for Integrated Image Acquisition and Early Vision Processing

Sponsor

National Science Foundation/
Advanced Research Projects Agency
Grant MIP 91-17724

Project Staff

Professor John L. Wyatt, Jr., Professor Berthold K.P. Horn, Professor Hae-Seung Lee, Professor Charles G. Sodini, Professor Jacob K. White, Dr. Ichiro Masaki, Steven J. Decker, Ibrahim M. Elfadel, Frederick P. Herrmann, David R. Martin, Ignacio S. McQuirk, Erkki Oja, Mark W. Reichelt, Mark N. Seidel, Luis M. Silveira, Christopher B. Umminger, Paul C. Yu

1.2.1 Project Summary

In real-time machine vision, the sheer volume of image data to be acquired, managed and processed leads to communications bottlenecks between imagers, memory and processors, as well as to very high computational demands. We are designing and testing experimental *analog* VLSI systems to overcome these problems. The goal is to determine how the advantages of analog VLSI—high speed, low power and small area—can be exploited, and its disadvantages—limited accuracy, inflexibility and lack of storage capacity—can be minimized. The work is concentrated on *early* vision tasks, i.e., tasks that occur early in the signal flow path of animal or machine.

The next section details substantial progress on eight different designs, including systems for automatic alignment to calibration marks, brightness adaptive imaging, video rate A/D conversion, a content-addressable digital image processor, and a focus-of-expansion motion chip. These are all now in the test phase, and we report primarily on the construction of test systems and on test results.

1.2.2 Vision Chip Designs

Single-Chip Alignment Sensor

Chris Umminger, working with Professors Charles Sodini and Berthold Horn, has been researching implementations of single-chip sensors to measure alignment error for tasks in automated manufacturing. These sensors will optically acquire an image of the alignment marking and output a measure of the misalignment. Currently they have settled on two methods for the task of aligning a mark to the sensor. The first is based on the surveyor's mark. The sensor consists of a four quad-

¹¹ R.C. Armstrong and J. Allen, "FICOM: A Framework for Incremental Consistency Maintenance in Multi-Representation, Structural VLSI Design Databases," *Digest of Technical Papers, IEEE/ACM International Conference on Computer-Aided Design*, Santa Clara, California, November 8-12, 1992, 336-343.

rant photodiode combined with an edge detection circuit to provide extra fine alignment accuracy. The second sensor design uses a square grating mark. A position sensitive moiré fringe pattern formed between the sensor and the marking is used to achieve accurate alignment.

The first version of the surveyor's mark sensor was fabricated in 1992 and was used to characterize the imaging photodiodes and associated amplification circuits. A second sensor was completed in October 1993. This sensor incorporated a larger imaging area and an improved amplifier capable of higher speed operation. Since January, the revised sensors have been tested in a mock alignment system consisting of an alignment target on a motor-controlled positioning table with a lens focusing the image onto the chip. Error signals from the sensor successfully detect misalignment of the target and are used to move the target back into its aligned position. Preliminary results indicate the sensor can detect displacements down to 30 PPM of the size of the sensor. Alignment repeatability is at least 300 PPM.

The moiré sensor design was completed in July 1993. Electrical testing revealed that the edge detecting circuits used to generate the coarse alignment signal were suffering from larger device mismatch than had been anticipated. When placed into the mock alignment system, the sensor was able to successfully generate the fine alignment signal from the resulting moiré fringe pattern. However, the coarse alignment signal was substantially degraded due to the device mismatch problems noted above. The fine alignment accuracy and repeatability are comparable to the surveyor's mark sensor.

Revisions to the chips were made and new designs were submitted for fabrication in April 1994. Modifications were made to improve the coarse alignment performance of both sensors. The revised sensors will be tested in July 1995. Testing with the current chips continues in order to more fully characterize their alignment accuracy, speed, and performance with degraded alignment markings. Papers reporting the results of this research are currently being written and should be completed in the fall of 1995.

Brightness Adaptive CCD Imager with Analog and Digital Output

Steve Decker, working with Professor Charles Sodini, has been designing an imager to act as the front end of a modular vision system. It will feature a 64 x 64 array of pixels, large fill factor, operating speed on the order of 1000 frames/sec, column parallel output, brightness adaptation capability, and user selectable analog or 10-bit digital output.

A test chip was laid out with a small array of each of the basic structures. It has a 4 x 4 array of wide dynamic range pixels, four adjacent A/D converters, and four adjacent analog output circuits. The chip was designed in the MIT CCD/CMOS 1.75 micron process.

The test chip was first fabricated over the summer and early fall of 1993. Due to excess leakage current in the NMOS devices, a second lot was processed over the first three months of 1994. The leakage current on the second lot is low enough to allow further testing. Initial testing has focused on the wide dynamic range pixel. The operation of the output buffer has been verified through direct electrical measurement of the transfer function from the floating gate input to the on-chip output source follower. The pixel and associated shift register has been operated as one big pixel by setting all gates at a high potential, so that photogenerated charge immediately flows to the output diffusion. The diffusion potential is periodically reset. The pixel behaves as expected; the buffer output is high when the reset device is on, and decreases linearly in time when the reset device turns off. When the output voltage reaches a certain minimum value, it remains constant until the reset device turns on again. The lateral overflow drain also works essentially as expected; the minimum output voltage increases or decreases as the overflow gate voltage increases or decreases. Further testing will focus on clocking the integrated charge packet to the output circuit and applying a time-varying voltage to the lateral overflow drain during the integration period.

A printed circuit board is used to test the chip. The board layout was completed in March 1994 and submitted to the MOSIS PC board fabrication service. The completed board has been returned and completely populated. Board testing has been done in conjunction with the chip testing, so that those circuits on the board needed to test the wide dynamic range pixel have been verified. This includes the clock drivers, the off-chip buffer for the floating diffusion output, and the voltage sources.

Video Rate Analog-to-Digital Conversion

Paul Yu, working with Professor H.-S. Lee, has been working on various techniques of achieving low-power video-rate analog-to-digital conversion using CMOS technology.

One of the most interesting techniques involves removing the capacitor-mismatch constraint on the differential linearity of the converter. This technique is simple, effective, and does not require any self-calibration. Therefore, it is not necessary to interrupt the converter during its operation to perform a calibration. Other advantages include area and power savings due to the absence of the calibration logic. Having removed the differential-linearity constraint, the limit to the minimum size of the sampling capacitor is governed by the $\frac{KT}{C}$ noise which is a fundamental physical constraint.

The performance bottleneck of a pipelined ADC is the op-amp. At 3-V supply, it is extremely critical to have an op-amp that not only has high gain, and high-speed, but also high swing. After careful examination of many different amplifier topologies, a two-stage op-amp is chosen. The output stage of the amplifier utilizes no cascode to achieve high swing. The amplifier settles within 20 ns to 12-bit accuracy.

The power dissipation of a pipelined converter is dominated by that of the operational amplifiers. Another proposed technique, using a system optimization, allows approximately between 25 percent to 40 percent saving in power dissipation by the op-amps. This technique has shown to be feasible in a SPICE simulation. As a result, we are currently pursuing a patent on this technique.

A combination of techniques such as the ones described previously are used to minimize the power consumption while maximizing the performance of the ADC. A preliminary design analysis, together with SPICE simulation, has shown that our targeted performance of 12-bit, 20-MHz conversion with 100 mW power dissipation should be achievable in a standard digital 1.2 μm double-poly process.

Content-Addressable Parallel Digital Image Processor

Massively parallel associative processors may be well suited as co-processors for accelerating machine vision applications. They achieve very fine granularity, as every word of memory functions as a simple processing element. A dense, dynamic, content-addressable memory cell supports fully-parallel operation, and pitch-matched word logic

improves arithmetic performance with minimal area cost. An asynchronous reconfigurable mesh network handles interprocessor communication and image input/output, and an area-efficient pass-transistor circuit counts and prioritizes responders.

Frederick P. Herrmann has completed the design of a 16K-trit associative processing chip, under the supervision of Professor Charles Sodini. The chip integrates 256 processing elements, each with 64 trits of memory. A 16 x 16 mesh network connects the processing elements, and larger meshes may be constructed using several chips. The chip was fabricated through the MOSIS service, using Orbit's 1.2 μm double-poly process. Conservative design rules were used to ensure functionality in this experimental process. Packaged parts were received in September 1993.

Chip testing has now been completed, and the full functionality of all subsystems has been demonstrated. A 6-V supply is used to compensate for the high (2 V) second-poly thresholds in this process. The chip performs match and write instructions in 175 ns. Power dissipation is highly dependent on the activity of the processing elements and the instructions being executed, but typical applications require about 220 mW.

BiCMOS/CCD Focus-of-Expansion Chip for Camera Motion

Ignacio McQuirk, working with Professors Berthold Horn and Hae-Seung Lee, has continued working on a real-time analog VLSI chip that determines the direction of camera translation directly from time-varying image sequences acquired with an on-chip CCD imager. His approach assumes a camera moving through a fixed world with translational velocity. The focus of expansion (FOE) is the projection of the camera translation vector onto the image plane and hence gives the direction of camera motion. Intuitively, the FOE is the image of the point towards which the camera is moving; other image points appear to be expanding outward from this point. An algorithm for estimating the FOE based on least squares minimization of the differences at stationary points between the observed time variation of brightness and the predicted variation has been implemented in a BiCMOS/CCD chip with an embedded CCD imager and a row-parallel processing scheme. A complete 64 x 64 version of this chip has been fabricated through MOSIS.

A complete test setup for the chip has been constructed and is currently used in the process of testing the chip. This setup involved the fabrication of a printed circuit board with all of the support

components required for operation of the FOE system. This board consists of a pattern generator, CCD clock drivers, chip bias and testing circuitry, a Feedback Control Processor, and an interface to the Vision Chip Test System. The latter will permit testing of the FOE chip with electrical data, allowing for algorithmic, system, and circuit level characterization. Additionally, for operation using input from the on-chip imager, a completed setup will optically present the FOE chip with a real-time image sequence due to 3-D motion. This is accomplished using a flexible fiber optic image guide with a proximal relay lens to transmit the image from a distal lens system mounted on a precision linear track to the FOE test board. The orientation of the viewpoint of the cable can be precisely positioned relative to the motion of the linear track, allowing the FOE to be placed anywhere in the image plane in order to quantify system performance.

Switched-Capacitor System for Merging Depth and Slope Estimates

Mark Seidel, working with Professors John Wyatt and Tom Knight, has completed the design, fabrication, and testing of a switched-capacitor chip to robustly compute the depth of a scene by merging depth estimates (possibly from a stereo algorithm) with surface slope estimates (possibly from a shape-from-shading algorithm). This multisensor image fusion design uses the least-squares properties of certain switched-capacitor systems to compute a dense depth map given noisy or sparse depth and slope input. Bench testing of the final 1-D version of the network showed excellent agreement with theoretical predictions of the steady-state network response. The testing demonstrated that compensation of floating capacitor parasitic capacitance can be achieved and, with proper design, the network behaves nearly ideally even without compensating for clock feedthrough and channel charge. The results were described in the thesis document. The doctoral thesis was completed and signed.

1.2.3 Analog versus Digital Approaches to Machine Vision Hardware

David Martin, under the supervision of Professor Hae-Seung Lee, Steve Decker under the supervision of Professor Charles Sodini, and Ichiro Masaki are developing a stereo vision system in collaboration with Professors John L. Wyatt, Berthold Horn, and Jacob K. White. The goals of this project are twofold: comparison of analog versus digital approaches and development of a practical stereo distance measurement system.

A case study to compare analog versus digital approaches is important in identifying what kinds of processing are suitable for analog implementation. An array processing function was chosen as the case for the comparison. The level of this function-definition is high enough for the generality of the result and, at the same time, it is low enough to make the result independent from the algorithm. A hybrid analog/digital array processor chip is being developed as an example of the analog implementation. The chip will consist of 32x32 hybrid analog/digital processing elements which will work in an MIMD (Multi-Instruction Multiple-Data) scheme. Each processing element will include a digital memory unit which will control an analog arithmetic unit and a data flow network. Examples of the digital array processors, for this comparison, include various schemes such as a pixel-parallel array processor architecture. With this scheme, a digital processing element is assigned for each pixel and multiple processing elements work in a SIMD (Single-Instruction Multiple-Data) fashion. The accuracy of the analog arithmetic unit will be limited by two factors: nonlinearity and transistor mismatch.

In the first step, the vision algorithms that will run on the array processor were simulated to determine their accuracy and speed requirements. These simulations revealed that the algorithms could tolerate random errors of up to 10 percent as long as no information was lost from arithmetic overflow. In the second step, key circuits were designed, simulated, fabricated, and tested. As a result of these tests, it was demonstrated that an analog processing unit would be about seven times smaller than a digital processing unit, but that the analog unit would be significantly slower than the digital circuit. This made it possible to perform a detailed comparison of the digital and analog approaches in terms of area, speed, and overall system requirements. A second version of the processor will be designed and fabricated after the tests of the first version are complete. The circuit design for this new processing element is underway and should be completed by June 30, 1995.

1.2.4 Mixed Circuit/Device Simulation Vision Systems

Dr. Abe Elfadel and Mark Reichelt, under the supervision of Professor Jacob K. White and in collaboration with Professor Andrew Lumsdaine of Notre Dame, are working on algorithms for efficiently including distributed devices in circuit simulation programs like SPICE. Such algorithms are needed to accurately simulate integrated vision systems because such systems make use of sensing

devices with distributed characteristics, such as CCDs and photodiodes.

Our primary work is on accelerating mixed circuit-device simulation, as this kind of analysis is required to properly simulate the performance of CCD-based analog vision circuits. Since such analyses are computationally very expensive, we have been investigating waveform-relaxation based techniques to show that in convolution-SOR or generalized conjugate-residual acceleration such methods can effectively exploit loosely coupled scalable parallel processors. (This work is also partly funded by the ARPA VLSI contract N00014-91-J-1698). The algorithms developed, although effective, force a fixed time discretization. For a robust practical program, adaptive timestep control is essential. They will investigate how to extend the acceleration techniques to this more general case. The most recent efforts have led to a better theoretical understanding of the conjugate-direction acceleration and may lead to even better accelerators.

In general, any linear distributed element, such as a transmission line or a linearized photodiode model, can be represented using scattering parameter descriptions. That is, the element can be represented in the form of a frequency-domain model or a table of measured frequency-domain data. There has been recent completion of an implementation of a new, robust, frequency-dependent voltage-controlled current-source (VCCS) element in SPICE3. The implementation has been used to analyze circuits combined with 3-D packaging. The frequency-dependent VCCS element uses a section-by-section approach to find a rational function approximation of the model, and then reduces the order, while still maintaining accuracy, using guaranteed stable balanced realization techniques. Finally, the reduced-order model is efficiently implemented in the time-domain using fast recursive convolution.

1.2.5 Solutions of Theoretical Problems in Analog Hardware and Machine Vision

Switched-Capacitor Network Theory

Mark Seidel, working with Professor John Wyatt, has been studying general networks of switches, capacitors, and sources. These networks are important in the implementation of computational and image processing problems formulated as minimization algorithms. The general theory of these networks in steady-state formed a major portion of the doctoral thesis, which has been completed and signed. This theory, which comprises Chapters 2 through 6 of the thesis document, includes a study

of the continuous-time network of real nonlinear capacitors, real nonlinear resistive MOSFET switches, and ideal voltage sources, and the conditions for its transformation to an ideal switched-capacitor network. Stability of the resulting discrete-time system is investigated, and its transient response is bounded for a large class of such systems. Resistive equivalent networks are found for general steady-state switched-capacitor networks, and the problem of synthesizing a switched-capacitor network given an arbitrary linear resistive network is addressed. Finally, several of the analysis and synthesis results are extended to the nonlinear resistive case, allowing for the implementation of arbitrary networks of two-terminal voltage-controlled conductances, two-terminal positive linear resistors, and lossy two-port transformers. One such example network is the one- and two-dimensional resistive fuse grid.

During this period, energy arguments were used to prove the uniqueness of steady-state transferred charge as seen from the sources. This result shows that a network of positive linear capacitors and ideal switches controlled by a multiphase clock has exactly one multiport resistive equivalent element as seen from the sources, regardless of charge trapped on plates of capacitors internal to the network. Also during this period, the analysis theory was applied to the study of multiple-frequency switched-capacitor lines, which are used to implement resistive lines with a controllable space constant. Experimental results on a fabricated VLSI circuit indicate excellent agreement with the predicted response.

Dynamics of Hebbian Unsupervised Learning

Within the domain of subspace methods for unsupervised learning, Erkki Oja has developed a nonlinear version of Hebb's rule that converges to a set of orthonormal weight vectors that are linear combinations of the dominant eigenvectors of the correlation matrix of the inputs, and hence are useful in principal components analysis. The mean or drift term of this system satisfies a nonlinear matrix differential equation. A number of *local* stability results already exist in the literature for this equation. However, the problem of its *global* behavior under arbitrary initial conditions is still largely open. Professor John Wyatt and Dr. Abe Elfadel have been investigating this difficult problem. Their results so far include an explicit solution of Oja's equations in the single neuron case as well as a proof that under an appropriate change of coordinates, these equations are a gradient descent system in both the single-neuron and multineuron case.

Reduced-Order Models for Interconnect Simulation

In order to analyze the effects of packaging parasitics on circuit performance, these parasitics are frequently modeled with equivalent circuits which are then included in a circuit simulation. Complicated packages or interconnect can generate extremely large equivalent circuits which must then be simplified, or reduced, for efficient use in a circuit simulator. The most commonly used Padé, or moment-matching, approaches to performing this model order reduction can generate unstable equivalent circuits. To overcome the instability problems, Dr. Luis Miguel Silveira and Dr. Abe Elfadel, under the guidance of Professor Jacob K. White, have been investigating a state-space algorithm for model-order reduction based on truncating a balanced system realization. This algorithm has the important characteristic that the reduced order model resulting from the truncation is *guaranteed to be stable*. The simulation of simple RLC circuits modeling transmission lines has demonstrated that the balanced-realization approach generates accurate, stable reduced-order models, whereas the Padé method does not.

1.2.6 Publications

Journal Articles

Elfadel, I.M., and R.W. Picard. "Gibbs Random Fields, Co-Occurrences, and Texture Modeling." *IEEE Trans. Pattern Anal. and Mach. Intell.* 16(1): 24-37 (1994).

Lumsdaine, A., and J. White. "Accelerating Waveform Relaxation Methods with Application to Parallel Semiconductor Device Simulation." *Numerical Functional Anal. and Optimization*. Forthcoming.

Reichelt, M., J. White, and J. Allen. "Optimal Convolution SOR Acceleration of Waveform Relaxation with Application to Parallel Simulation of Semiconductor Devices." *SIAM J. Sci. Stat. Comp.* Forthcoming.

Silveira, M., I. Elfadel, J. White, M. Chilukuri, and K. Kundert. "Efficient Frequency-Domain Modeling and Circuit Simulation of Transmission Lines." *IEEE Trans. Components, Hybrids, Manufact. Tech.* 17(4): 505-513 (1994). Special issue on Electrical Performance of Electronic Packaging.

Wyatt, J.L., Jr., and I.M. Elfadel. "Time-Domain Solutions of Oja's Equations." *Neural Comput.* 7(5): (1995).

Yu, P.C., and H.-S. Lee. "Settling-Time Analysis of a Replica-Amp Gain Enhanced Operational Amplifier." *IEEE Trans. Circ. Sys. II: Analog Digit. Signal Proc.* Forthcoming.

Conference Papers

Elfadel, I.M. "Approximate Covariance Functions for Gray-Level Gibbs Random Fields." Paper presented at IEEE International Symposium on Acoustics, Speech and Signal Processing, Adelaide, Australia, April 1994.

Elfadel, I.M. "Lyapunov Functions for Rotor Neural Networks." Paper presented at the American Control Conference (ACC '94). Submitted to *Neural Info. Proc. Syst.*

Herrmann, F.P., and C.G. Sodini. "A 256-Element Associative Parallel Processor." Symposium on VLSI Circuits, Honolulu, Hawaii, June 1994, pp. 99-100.

Masaki, I. "Vehicle-Based Vision Sensors for Intelligent Highway Systems." *SPIE Vol. TTS2 Technologies for Intelligent Vehicle Highways*, Boston, Massachusetts, November 1994, pp. 156-174.

Masaki, I. "Vision-Based Collision Avoidance Systems." American Fourth Annual Meeting, Atlanta, Georgia, April 1994. Forthcoming in proceedings.

Masaki, I., S. Decker, A. Gupta, B.K.P. Horn, H-S. Lee, D.A. Martin, C.G. Sodini, J.K. White, and J.L. Wyatt, Jr. "Cost-Effective Vision Systems for Intelligent Vehicles." *Proceedings of the IEEE International Intelligent Vehicles Symposium*, Paris, France, October 1994, pp. 39-43.

Silveira, L.M., I.M. Elfadel, J. White, M. Chilukuri, and K. Kundert. "An Efficient Approach to Transmission Line Simulation using Measured or Tabulated S-parameter Data." *Proceedings of the 31st Design Automation Conference*, San Diego, California, June 1994, pp. 634-639.

Silveira, L.M., M. Kamon, and J. White. "Direct Computation of Reduced-Order Models for Circuit Simulation of 3-D Interconnect Structures." *Proceedings of the 3rd Topical Meeting on Electrical Performance of Electronic Pack-*

aging, Monterey, California, November 1994, pp. 245-248.

Silveira, L.M., M. Kamon, and J. White. "Efficient Reduced-Order Modeling of Frequency-Dependent Coupling Inductances Associated with 3-D Interconnect Structures." Forthcoming in the *Proceedings of the European Design and Test Conference*, Paris, France, March 1995.

Umminger, C.B., and C.G. Sodini. "Integrated Analog Sensor for Automatic Alignment." Forthcoming *IEEE International Solid-State Circuits Conference*, San Francisco, California, February 1995.

Wyatt, J.L., and I.M. Elfadel. "On the Solution of Oja's Equations." Poster session, *Neural Networks for Computing Conference*, Snowbird, Utah, April 1994.

Wyatt, J.L., Jr., and I.M. Elfadel. "Time-Domain Solutions of Oja's Equations." Paper presented at the *Neural Information Processing Systems Conference*, Vail, Colorado, December 1994.

Book Chapters

Elfadel, I.M., and J.L. Wyatt, Jr. "The 'Softmax' Nonlinearity: Derivation Using Statistical Mechanics and Useful Properties as a Multiterminal Analog Circuit Element." In *Advances in Neural Information Processing Systems 6*. Eds. J.D. Cowan, G. Tesauro, and J. Alspector. San Mateo, California: M. Kaufmann Publishers, 1994.

Umminger, C.B. and C.G. Sodini. "Switched Capacitor Networks for Focal Plane Image Processing Systems." In *Vision Chips: Implementing Vision Algorithms with Analog VLSI Circuits*. Eds. C. Koch and H. Li. Los Alamitos, California: IEEE Computer Society Press, 1994.

Wyatt, J.L., Jr. "Little-Known Properties of Resistive Grids that are Useful in Analog Vision Chip Design." In *Vision Chips: Implementing Vision Algorithms with Analog VLSI Circuits*. Eds. C. Koch and H. Li. Los Alamitos, California: IEEE Computer Science Press, 1994.

Theses

Dron, L.G. *Computing 3-D Motion in Custom Analog and Digital VLSI*. Ph.D. diss. Dept. of Electr. Eng. and Comput. Sci., MIT, 1994.

Herrmann, Frederick P. *An Integrated Associative Processing System*. Ph.D. diss. Dept. of Electr. Eng. and Comput. Sci., MIT, 1994.

Seidel, M.N. *Switched-Capacitor Networks for Image Processing: Analysis, Synthesis, Response Bounding, and Implementation*. Sc.D. diss. Dept. of Electr. Eng. and Comput. Sci., MIT, 1994.

Silveira, L.M. *Model Order Reduction Techniques for Circuit Simulation*. Ph.D. diss. Dept. of Electr. Eng. and Comput. Sci., MIT, 1994.

Invited Talks

Mann, J., D. Edell, J.F. Rizzo, J. Raffel, and J.L. Wyatt. "Development of a Silicon Retinal Implant: Microelectronic System for Wireless Transmission of Signal and Power." Association for Research in Vision and Ophthalmology (ARVO) Meeting, Sarasota, Florida, May 1994.

Narayanan, M.V., J.F. Rizzo, D. Edell, and J.L. Wyatt. "Development of a Silicon Retinal Implant: Cortical Evoked Potentials Following Focal Stimulation of the Rabbit Retina with Light and Electricity." Association for Research in Vision and Ophthalmology (ARVO) Meeting, Sarasota, Florida, May 1994.

Wyatt, J.L., Jr., and J. Rizzo. "Steps Toward the Development of a Silicon Retinal Implant to Aid Patients Suffering from Certain Forms of Blindness." Talk given at the following: Smith-Kettlewell Eye Research Institute, San Francisco, California, January 1994; University of California, San Diego, California, January 1994; Steen-Hall Eye Institute, Shreveport, Louisiana, January 1994; Neural Networks for Computing Conference, Snowbird, Utah, April 1994; Caltech lecture, Pasadena, California, April 1994; Retinitis Pigmentosa Foundation, Boston, Massachusetts, May 1994.

Wyatt, J.L., J.F. Rizzo, A. Grumet, D. Edell, and R.J. Jensen. "Development of a Silicon Retinal Implant: Epiretinal Stimulation of Retinal Ganglion Cells in the Rabbit." Association for Research in Vision and Ophthalmology (ARVO) Meeting, Sarasota, Florida, May 1994.

Internal Publications

Lumsdaine, A., M. Silveira, and J. White. *CMVSIM User's Guide*. RLE TR-590. Cambridge: MIT Research Laboratory of Electronics, 1994.

Lumsdaine, A., M. Silveira and J. White. *SIMLAB Programmer's Guide*. RLE TR-589. Cambridge: MIT Research Laboratory of Electronics, 1994.

Silveira, M., A. Lumsdaine and J. White. *SIMLAB User's Guide*. RLE TR-588. Cambridge: MIT Research Laboratory of Electronics, 1994.

1.3 Parallel Algorithms for Device Simulation

Sponsors

Advanced Research Projects Agency/
U.S. Navy - Office of Naval Research
Contract N00014-94-1-0985

IBM Corporation

National Science Foundation/
Advanced Research Projects Agency
Grant MIP 91-17724

Project Staff

Dr. Andrew Lumsdaine,¹² Mark W. Reichelt,¹³ Professor Jacob K. White, Professor Jonathan Allen

The growing importance of mixed circuit/device simulation, its enormous computational expense, as well as the increasing availability of parallel computers, have made the development of specialized, easily parallelized, algorithms for transient simulation of MOS devices necessary. In earlier work

on the Waveform Overrelaxation Device Simulator (WORDS) program, the easily parallelized waveform relaxation (WR) algorithm was shown to be a computationally efficient approach to device transient simulation even on a serial machine. The WR algorithm, though, typically requires hundreds of iterations to achieve an accurate solution.

To use WORDS in a mixed circuit/device simulator, we have been investigating ways of making the program more robust and efficient. We determined how to compute the terminal currents accurately using different timepoints at different mesh nodes. We also improved the timestep selection procedure by determining how to refine the timesteps as WR iterations proceed and reducing the total computation by as much as a factor of 2 by using only a few coarse timesteps in early iterations. The more accurate, electric field dependent mobility model was also implemented. Recent work on theoretical aspects of these methods have answered several long-standing questions about multirate stability.¹⁴

We found experimental evidence that WR using standard overrelaxation acceleration can produce oscillatory results, and are investigating methods for eliminating this phenomenon. A frequency-dependent overrelaxation algorithm using lowpass filtering was developed, as well as a waveform conjugate-direction approach.¹⁵ Experimental results indicate that both approaches reduces the number of waveform iterations required by more than a factor of seven. Finally, experimental results using a parallel computer show that although the accelerated WR methods are only competitive with the best of the standard algorithms for device transient simulation on a serial machine, the WR algorithms are substantially faster on a parallel machine.¹⁶

¹² Notre Dame University, Notre Dame, Indiana.

¹³ Mathworks, Natick, Massachusetts.

¹⁴ M. Reichelt, F. Odeh, and J. White, "A-Stability of Multirate Integration Methods, with Application to Parallel Semiconductor Device Simulation," invited Paper, *Proceedings of the SIAM Meeting on Parallel Processing for Scientific Computing*, Norfolk, Virginia, March 1993.

¹⁵ A. Lumsdaine and M. Reichelt, "Waveform Iterative Techniques for Device Transient Simulation on Parallel Machines," invited Paper, *Proceedings of the SIAM Meeting on Parallel Processing for Scientific Computing*, Norfolk, Virginia, March 1993; A. Lumsdaine and J. White, "Accelerating Waveform Relaxation Methods with Application to Parallel Semiconductor Device Simulation," *Numerical Functional Analysis and Optimization*, forthcoming; M. Reichelt, "Optimal Convolution SOR Acceleration of Waveform Relaxation with Application to Semiconductor Device Simulation," Third place, best student paper competition, *Proceedings of the Copper Mountain Conference on Multigrid Methods*, Copper Mountain, April 1993; M. Reichelt, J. White, and J. Allen, "Optimal Convolution SOR Acceleration of Waveform Relaxation with Application to Parallel Simulation of Semiconductor Devices," *SIAM J. Sci. Stat. Comput.*, forthcoming.

¹⁶ A. Lumsdaine and M. Reichelt, "Waveform Iterative Techniques for Device Transient Simulation on Parallel Machines," invited Paper, *Proceedings of the SIAM Meeting on Parallel Processing for Scientific Computing*, Norfolk, Virginia, March 1993; M. Reichelt, J. White, and J. Allen, "Optimal Convolution SOR Acceleration of Waveform Relaxation with Application to Parallel Simulation of Semiconductor Devices," *SIAM J. Sci. Stat. Comput.*, forthcoming.

1.4 Numerical Simulation of Short Channel MOS Devices

Sponsors

IBM Corporation
U.S. Navy
Contract N00174-93-C-0035

Project Staff

Khalid Rahmat, Professor Dimitri A. Antoniadis,
Professor Jacob K. White

The model used in conventional device simulation programs is based on the drift-diffusion model of electron transport, and this model does not accurately predict the field distribution near the drain in small geometry devices. This is of particular importance for predicting oxide breakdown due to penetration by "hot" electrons. There are two approaches for more accurately computing the electric fields in MOS devices, one is based on adding an energy equation to the drift-diffusion model and the second is based on direct solution of Boltzman's equation.

In the first approach, an energy balance equation is solved along with the drift-diffusion equations so that the electron temperatures are computed accurately. This combined system is numerically less tame than the standard approach and must be solved carefully. We have developed a two-dimensional device simulator in which an energy balance equation is solved for electron temperature along with the usual drift-diffusion equations. The program avoids temperature instabilities produced by previous discretization approaches through the use of a careful application of exponential-fitting to the energy equation. Drain currents for silicon MOSFETs predicted by the simulator, using one set of model parameters, match well with experimental data for devices over a range of channel lengths from $0.90\text{ }\mu\text{m}$ to $0.16\text{ }\mu\text{m}$. Also, a method to compute substrate current has been derived which uses the electron temperature provided by the simulator. The computed substrate currents match well with measured data, for the regime above sub-

threshold, for MOSFETs with channel lengths as short as $0.16\text{ }\mu\text{m}$.¹⁷

The limited ability to accurately predict hot-electron effects from an energy-balance based simulator has led to our current investigation. We are now trying to solve the full Boltzman equation, using a spherical harmonics based approach, but only in portions of the MOS device which are likely to create hot carriers. We have implemented a Galerkin method for the solution of the Boltzmann equation which allows arbitrary order spherical harmonic expansions in momentum space. A self-consistent solution is obtained by directly solving the Boltzmann and Poisson equations simultaneously. The boundary conditions and discretization methods necessary for the arbitrary order method are also presented. Results up to third order in one real space dimension show the importance of including harmonics beyond first order to accurately calculate the distribution function in high field regions.¹⁸

1.5 Coupled Simulation Algorithms for Microelectromechanical CAD (MEMCAD)

Sponsors

Analog Devices, Inc.
Federal Bureau of Investigation
Contract J-FBI-92-196

Project Staff

Xuejun Cai, Mattan Kamon, He Yie,¹⁹ Professor Martin A. Schmidt, Professor Stephen D. Senturia, Professor Jacob K. White

High fabrication costs and increasing microsensor complexity is making computer simulation of the realistic geometries necessary, both to investigate design alternatives and to perform verification before fabrication. At MIT, we are developing a MicroElectroMechanical Computer-Aided Design (MEMCAD) system to make it possible for microsensor designers to easily perform realistic simulations. Carefully selected commercial software packages have been linked with specialized data-

¹⁷ K. Rahmat, J. White, and D. Antoniadis, "Simulation of Very Short Channel MOSFET's Including Energy Balance," *IEEE Trans. Comput.-Aided Design*, 12(6): 817-825 (1993).

¹⁸ K. Rahmat, J. White, and D. Antoniadis, "A Galerkin Method for the Arbitrary Order Expansion in Momentum Space of the Boltzmann Equation using Spherical Harmonics," *Proceedings of NUPAD V*, Honolulu, Hawaii, June 1994, forthcoming; K. Rahmat, J. White, and D.A. Antoniadis, "Solution of the Boltzmann Transport Equation in Two Real-Space Dimensions using a Spherical Harmonic Expansion in Momentum Space," *Proceedings of the International Electron Devices Meeting*, San Francisco, California, forthcoming December 1994.

¹⁹ Visiting Scientist, Microelectronics Center, Southeast University, Nanjing, China.

base and numerical programs to allow a designer to easily enter a three-dimensional microsensor geometry and quickly perform both mechanical and electrical analysis. The system currently performs electromechanical analyses, such as calculating the capacitance versus pressure (or force) curve for both a square diaphragm deformed by a differential pressure, and can be used to calculate levitation forces in structures as complicated as a comb drive.²⁰

To support design of electromechanical structures, we are currently investigating two approaches to combining finite-element mechanical analysis with multipole-accelerated electrostatic analysis. The first method is the obvious relaxation algorithm, and the second method is a more sophisticated surface/Newton generalized conjugate-residual scheme. By comparing the two methods, we have demonstrated both theoretically and by example that our surface/Newton-GCR algorithm is faster and more robust than the simpler relaxation scheme.²¹ We have also been working on the multipole accelerated Galerkin implementation of our electrostatic analysis program FASTCAP. Galerkin is less sensitive to the mesh of the structure than the original collocation approach and always yields more accurate results particularly with dielectric interfaces.²²

We have also been investigating how to apply CAD to MEMS with the level of complexity of a practical, high-volume manufacturable sensor while avoiding computationally impractical models. Two methods were developed. One was a simple analysis method in which the ideal structure was assumed. This allowed prediction of the stability and the effects of structure misalignment on a surface-micromachined accelerometer. However, the simple method is limited because the actual structure has fabrication induced nonidealities, such as

warpage, which can cause the simple method to be significantly in error. The second method discarded the ideal structure assumption and analyzed the nonideal structure via a self-consistent analysis. This method is based on the calculation of an intermediate look-up table from which the electrostatic forces are obtained directly from the position of the moving mass, greatly reducing computation time and memory requirements in comparison to a standard self-consistent electromechanical analysis scheme. Using this lumped-model self-consistent scheme, we analyzed an Analog Devices, Inc., non-ideal ADXL50 accelerometer including fabrication non-idealities (warpage, over-etching, residual stress, etc.).²³

Finally, our latest work is in investigating the coupling of fluid forces and mechanical deformation to add additional capabilities to our existing MEMCAD system. To first gain more control over the underlying algorithms of the current MEMCAD system, we are currently implementing an elastostatic solver to replace the commercial mechanical solver used in the MEMCAD system.

1.6 Numerical Techniques for Simulating Josephson Junction Arrays

Sponsors

Advanced Research Projects Agency/
Consortium for Superconducting Electronics
Contract MDA972-90-C-0021
National Defense Science and Engineering
Graduate Fellowship

Project Staff

Joel R. Phillips, Dr. Herre S.J. van der Zant, Professor Terry P. Orlando, Professor Jacob K. White

²⁰ J.R. Gilbert, P.M. Osterberg, R.M. Harris, D.O. Ouma, X. Cai, A. Pfajfer, J. White, and S.D. Senturia, "Implementation of a MEMCAD System for Electrostatic And Mechanical Analysis of Complex Structures From Mask Descriptions," *Proceedings of the IEEE Micro-Electro Mechanical Systems* Fort Lauderdale, February 1993; X. Cai, H. Yie, P. Osterberg, J. Gilbert, S. Senturia, and J. White, "A Relaxation/Multipole-Accelerated Scheme for Self-Consistent Electromechanical Analysis of Complex 3-D Microelectromechanical Structures," *Proceedings of the International Conference on Computer-Aided Design*, Santa Clara, California, November 1993, pp. 270-274.

²¹ X. Cai, P. Osterberg, H. Yie, J. Gilbert, S. Senturia, and J. White, "Self-Consistent Electromechanical Analysis of Complex 3-D Microelectromechanical Structures using a Relaxation/Multipole Method," *Int. J. Sensors and Mat.*, forthcoming; H. Yie, X. Cai, P. Osterberg, S. Senturia, and J. White, "Convergence Properties of Relaxation Versus the Surface-Newton Generalized-Conjugate Residual Algorithm for Self-consistent Electromechanical Analysis of 3-D Micro-Electro-Mechanical Structures," *Proceedings of NUPAD V*, Honolulu, Hawaii, June 1994, forthcoming.

²² X. Cai, K. Nabors, and J. White, "Efficient Galerkin Techniques for Multipole-Accelerated Capacitance Extraction of 3-D Structures with Multiple Dielectrics," *Proceeding of the 16th Conference on Advanced Research in VLSI*, Chapel Hill, North Carolina, March 1995, forthcoming.

²³ H. Yie, S.F. Bart, J. White, and S.D. Senturia, "Computationally Practical Simulation of a Surface-Micromachined Accelerometer with True Fabrication Non-idealities." *Proceedings of MEMS 95*, forthcoming.

Vortices play a central role in determining the static and dynamic properties of two-dimensional (2D) superconductors. Artificially fabricated networks of superconducting islands weakly coupled by Josephson junctions are model systems to study the behavior of vortices. Through simulation, we have discovered that the static properties of vortices in an array of Josephson junctions can be significantly influenced by magnetic fields induced by the vortex currents. The energy barrier for vortex motion is enhanced, nearly doubling for penetration depths on the order of a cell size. Moreover, we have found that correct calculation of the vortex current distribution, the magnetic moment, and the lower critical field require modeling mutual inductance interactions between all cell pairs in the array. To make numerical simulation of the system with all inductive effects computationally feasible, a novel FFT-accelerated integral equation solver was derived. This algorithm is sufficiently efficient to allow study of large (500x500 cells) arrays.²⁴

The development of the FFT-accelerated algorithm for inductance effects in Josephson Junction arrays led to a more general result useful for packaging analysis. For the important special case of conductors over non-ideal ground planes, extremely fast FFT-accelerated inductance extraction methods have been developed. The FFT technique is so fast compared to its direct method rival, that it reduces analysis time from hours to seconds even for relatively simple problems.²⁵

1.7 Efficient 3-D Interconnect Analysis

Sponsors

Advanced Research Projects Agency/
Consortium for Superconducting Electronics
Contract MDA972-90-C-0021
Digital Equipment Corporation

IBM Corpotation
National Defense Science and Engineering
Graduate Fellowship
Semiconductor Research Corporation
Contract SRC 93-SJ-360
U.S. Navy - Office of Naval Research
Contract N00014-91-J-1698

Project Staff

Michael T. Chou, Mattan Kamon, Yehia M. Massoud, Keith S. Nabors, Joel R. Phillips, Professor Jacob K. White

We have developed multipole-accelerated algorithms for computing capacitances and inductances of complicated 3-D geometries and implemented these algorithms in the programs FASTCAP and FASTHENRY. The methods are accelerations of the boundary-element or method-of-moments techniques for solving the integral equations associated with the multiconductor capacitance or inductance extraction problem. Boundary-element methods become slow when a large number of elements are used because they lead to dense matrix problems which are typically solved with some form of Gaussian elimination. This implies that the computation grows as n^3 , where n is the number of panels or tiles needed to accurately discretize the conductor surface charges.

Our new algorithms, which use generalized conjugate residual iterative algorithms with a multipole approximation to compute the iterates, reduce the complexity so that accurate multiconductor capacitance and inductance calculations grow nearly as nm where m is the number of conductors. For practical problems which require as many as 10,000 panels or filaments, FASTCAP and FASTHENRY are more than two orders of magnitude faster than standard boundary-element based programs.²⁶ Manuals and source code for

²⁴ J.R. Phillips, H. Van der Zant, J. White, and T. Orlando, "Influence of Induced Magnetic Fields on the Static Properties of Josephson-Junction Arrays," *Phys. Rev. B* 47: 5219-5229 (1993); J.R. Phillips, H.S.J. van der Zant, J. White, and T.P. Orlando, "Influence of Induced Magnetic Fields on Shapiro Steps in Josephson-junction Arrays," *Phys. Rev. B* 50(13): 9387-9398 (1994); J.R. Phillips, H.S.J. van der Zant, and T.P. Orlando, "Dynamics of Row-switched States in Josephson-junction Arrays," *Phys. Rev. B* 50: 9380-9386 (1994).

²⁵ J.R. Phillips, M. Kamon, and J. White, "An FFT-Based Approach to Including Non-ideal Ground Planes in a Fast 3-D Inductance Extraction Program," *Proceedings of the Custom Integrated Circuits Conference*, San Diego, California, May 1993.

²⁶ M. Chou, M. Kamon, K. Nabors, J. Phillips, and J. White, "Extraction Techniques for Signal Integrity Analysis of 3-D Interconnect," Invited paper, to appear in *Proceedings of the Custom Integrated Circuits Conference*, May, 1995; K. Nabors, F.T. Korsmeyer, F.T. Leighton, and J. White, "Multipole Accelerated Preconditioned Iterative Methods for Three-Dimensional Potential Integral Equations of the First Kind," *SIAM J. on Sci. and Stat. Comp.* 15(3): 713-735 (1994); M. Kamon and J.R. Phillips, "Preconditioning Techniques for Constrained Vector Potential Integral Equations, with Application to {3-D} Magnetoquasistatic Analysis of Electronic Packages," *Proceedings of the Colorado Conference on Iterative Methods*, Breckenridge, Colorado, April 1994; M. Kamon, M.J. Tsuk, and J. White, "FASTHENRY: A Multipole-Accelerated 3-D Inductance Extraction Program," *IEEE Trans. Microwave Theory Tech.*, special issue on Electrical Performance of Electronic Packaging, forthcoming; T. Korsmeyer, D.K.P. Yue, K. Nabors, and J. White, "Multipole-

FASTCAP and FASTHENRY are available directly from MIT.

In our latest work, we have developed an alternative to the fast-multipole approach to potential calculation. The new approach uses an approximate representation of charge density by point charges lying on a uniform grid instead of by multipole expansions. For engineering accuracies, the grid-charge representation has been shown to be a more efficient charge representation than the multipole expansions. Numerical experiments on a variety of engineering examples arising indicate that algorithms based on the resulting "precorrected-FFT" method are comparable in computational efficiency to multipole-accelerated iterative schemes, and superior in terms of memory utilization.²⁷

The precorrected-FFT method has another significant advantage over the multipole-based schemes, in that it can be easily generalized to some other common kernels. Preliminary results indicate that the precorrected-FFT method can easily incorporate kernels arising from the problem of capacitance extraction in layered media.²⁸ More importantly, problems with a Helmholtz equation kernel have been solved at moderate frequencies with only a modest increase in computational resources over the zero-frequency case. An algorithm based on the precorrected-FFT method which efficiently solves the Helmholtz equation could form the basis for a rapid yet accurate full-wave electromagnetic analysis tool.²⁹

In order to accurately compute the RC delay and cross-talk noise in complicated three-dimensional interconnects, it is necessary to numerically solve Maxwell's equation in the electro-quasistatic regime.

It has been suggested that the analysis be performed by computing the time evolution of the electric field both inside and outside the conductors via a finite-difference discretization of Laplace's equation. While this method leads to a sparse matrix problem, it requires discretization of the entire physical domain, and generates a large number of unknowns. More recently, a boundary-element approach based on Green's theorem was proposed, which performs the calculation using the same surface discretization used for ordinary capacitance extraction. However, this leads to dense matrix problems which are too expensive to solve directly. When the fast-multipole algorithm is applied to the iterative solution in the boundary-element method, we find that the small multipole errors are magnified to unacceptable levels due to the ill-conditioning in the steady-state problem.

We have formulated a new, mixed surface-volume approach, which requires both the conductor surfaces and interior volume be discretized. Given the conductor surface potentials, Laplace's equation is solved independently inside each conductor via the finite-difference method to determine the internal current flow. The vector of internal and external currents cause charging of conductor surfaces, which is used to compute the time-rate of change of surface potentials via the boundary-element method. The interior problem is sparse and thus inexpensive to solve. The boundary-element problem is dense, but its solution can be accelerated by the fast-multipole algorithm to improve efficiency of the overall scheme. In this approach, accuracy is not affected by the ill-conditioning because the perturbed system has a physical analog close to the exact problem. Numerical experiments on realistic interconnect problems show that the new method can run twenty times

Accelerated Preconditioned Iterative Methods For Three-Dimensional Potential Problems," *Boundary Element Methods 15 (BEM15)*, Worcester, Massachusetts, August 1993.

²⁷ J. White, J.R. Phillips, and T. Korsmeyer, "Comparing Precorrected-FFT and Fast Multipole Algorithms for Solving Three-Dimensional Potential Integral Equations," *Proceedings of the Colorado Conference on Iterative Methods*, Breckenridge, Colorado, April 1994; K. Nabors, J. Phillips, F.T. Korsmeyer, and J. White, "Multipole and Precorrected-FFT Accelerated Iterative Methods For Solving Surface Integral Formulations of Three-dimensional Laplace Problems," *Proceedings of the Domain-Based Parallelism and Problem Decomposition Methods in Computational Science and Engineering Workshop*, Minnesota, July 1993, forthcoming; J.R. Phillips and J. White, "A Precorrected-FFT Method for Capacitance Extraction of Complicated 3-D Structures," *International Conference on Computer-Aided Design*, Santa Clara, California, November 1994.

²⁸ J.R. Phillips and J. White, "A Precorrected-FFT method for Capacitance Extraction of Complicated 3-D Structures," *International Conference on Computer-Aided Design*, Santa Clara, California, November 1994.

²⁹ J.R. Phillips and J. White, "Efficient Capacitance Extraction of 3D Structures Using Generalized Pre-corrected FFT methods," *Proceedings of the IEEE 3rd Topical Meeting on Electrical Performance of Electronic Packaging*, Monterey, California, November 1994, forthcoming; J.R. Phillips and J.K. White, "Preccorrected-FFT Methods for Electromagnetic Analysis of Complex 3-D Interconnect and Packages," invited paper, *Progress in Electromagnetic Research Symposium*, Seattle, Washington, July 1995, forthcoming; J. Phillips, "Error and Complexity Analysis for a Collocation-Grid-Projection plus Preccorrected-FFT Algorithm for solving Potential Integral Equations with Laplace or Helmholtz Kernels," 2nd Place, Student Paper Competition, Colorado Conference on Multigrid Methods, April 1995.

faster and use two orders of magnitude less memory than using dense iterative methods.³⁰

1.8 Adaptive Gridding Techniques for Multipole-Accelerated Solution of Integral Equations

Sponsors

National Science Foundation/
Advanced Research Projects Agency
Grant MIP 91-17724
Semiconductor Research Corporation
Contract SRC 93-SJ-558

Project Staff

Michael T. Chou, F. Thomas Korsmeyer,³¹ Professor Jacob K. White

Finding computationally efficient numerical techniques for simulation of three dimensional structures has been an important research topic in almost every engineering domain. Surprisingly, the most numerically intractable problem across these various disciplines can be reduced to the problem of solving a three-dimensional Laplace problem. Such problems are often referred to as potential problems, and application examples include electrostatic analysis of sensors and actuators; electro- and magneto-quasistatic analysis of integrated circuit interconnect and packaging; and potential flow based analysis of wave-ocean structure interaction.

The recent development of extremely fast multipole-accelerated iterative algorithms for solving potential problems has renewed interest in integral equation formulations. In such methods, the fast multipole algorithm is used to implicitly construct a sparse representation of the dense matrix associated with a standard integral equation formulation, and this implicit representation is used to quickly compute the matrix-vector products required in a Krylov subspace based iterative method like GMRES. That the multipole-accelerated approach leads to prac-

tical engineering analysis tools has been demonstrated for electrostatic analysis of integrated circuit interconnect and packaging problems,³² as well as general Laplace problems.³³

We are extending our own work on multipole-accelerated iterative methods for potential problems to address what we see is the key difficulty preventing such techniques from finding broader use in engineering applications, that of automatic error control. In particular, we are interested in first investigating the straight-forward problem of how best to include higher-order boundary or volume elements. We are then planning to use such a result, along with other error estimation procedures, to perform automatic element refinement. The spatial hierarchy already introduced by the multipole algorithm, and our use of a locally preconditioned iterative scheme, makes it possible to perform very efficient local element refinement, and may even allow for an efficient variable element order scheme. And, as we have been using realistic examples from a wide variety of engineering disciplines, we will be able to determine the robustness of our procedures.

1.9 Circuit Simulation Algorithms

Sponsors

IBM Corporation
National Science Foundation
Advanced Research Projects Agency
Grant MIP 91-17724
Semiconductor Research Corporation
Contract SRC 93-SJ-558

Project Staff

Ognen J. Nastov, Luis M. Silveira, Professor Steven B. Leeb, Professor Jacob K. White

The determination of the steady-state distortion of clocked analog circuits such as switching filters and phase-locked loops, using conventional circuit simu-

³⁰ M. Chou and J. White, "A Multipole-Accelerated Boundary-Element Approach To Transient Simulations of Three-Dimensional Integrated Circuit Interconnect," *Proceedings of the IEEE 3rd Topical Meeting on Electrical Performance of Electronic Packaging*, Monterey, California, November 1994; M. Chou and J. White, "Transient Simulations of Three-dimensional Integrated Circuit Interconnect using a Mixed Surface-Volume Approach," invited paper, *Progress in Electromagnetic Research Symposium*, Seattle, Washington, July 1995, forthcoming.

³¹ Research Staff, Department of Ocean Engineering, MIT.

³² K. Nabors, F.T. Korsmeyer, F.T. Leighton, and J. White, "Multipole Accelerated Preconditioned Iterative Methods for Three-Dimensional Potential Integral Equations of the First Kind," *SIAM J. Sci. Stat. Comput.* 15(3): 713-735 (1994).

³³ T. Korsmeyer, D.K.P. Yue, K. Nabors, and J. White, "Multipole-Accelerated Preconditioned Iterative Methods For Three-Dimensional Potential Problems," *Boundary Element Methods 15 (BEM15)*, Worcester, Massachusetts, August 1993.

lation techniques, is an extraordinarily computationally intensive task. This is because the period of the clock is orders of magnitude smaller than the required time interval to reach the steady-state. One approach to computing steady-state distortion is the mixed frequency-time method (MFT). This method is based on the observation that the node waveforms in a particular high-frequency clock cycle are similar to the node waveforms in the neighboring cycles. Therefore, this suggests that by calculating the solution accurately over a few selected clock cycles, a solution accurate over many cycles can be constructed.

We are developing a generalization of the MFT algorithm which can be used to calculate the steady-state and intermodulation distortion for analog circuits whose inputs are a sum of periodic signals at unrelated frequencies. For example, computing the intermodulation distortion of narrow-band amplifiers by traditional circuit simulation is very difficult since the maximum usable time step is much smaller than the period of the difference frequency of the two frequencies in the input signal. The period of the difference frequency is large since the two input frequencies are required to be close in order for the distortion products to be within the bandwidth of the amplifier. If the amplifier is high-Q, the required simulation time interval will be many times larger than the period of the difference frequency. We are also exploring other possible extensions of the MFT ideas and their application to other hard-to-simulate nonlinear analog circuits.

To help support our work in interconnect analysis, we are developing algorithms for efficient SPICE-level simulation of elements with arbitrary frequency-domain descriptions, such as scattering parameters. That is, an element can be represented in the form of a frequency-domain model or a table of measured frequency-domain data. Our approach

initially uses a forced stable decade-by-decade ℓ_2 minimization approach to construct a sum of rational functions approximation, but the approximation has dozens of poles and zeros. This unnecessarily high-order model is then reduced using a guaranteed stable model order reduction scheme based on balanced realizations. Once the reduced-order model is derived, it can be combined with any inherent delay (for transmission line models) to generate an impulse response. Finally, following what is now a standard approach, the impulse response is efficiently incorporated in the circuit simulator SPICE3 using recursive convolution.³⁴

Reduced-order modeling techniques are now commonly used to efficiently simulate circuits combined with interconnect. Generating reduced-order models from realistic 3-D structures, however has received less attention. Recently we have been studying an accurate approach to using the iterative method in the 3-D magnetoquasistatic analysis program FASTHENRY to compute reduced-order models of frequency-dependent inductance matrices associated with complicated 3-D structures. This method, based on a Krylov-subspace technique, namely the Arnoldi iteration, reformulates the system of linear ODEs resulting from the FASTHENRY equation into a state-space form and directly produces a reduced-order model in state-space form. The key advantage of this method is that it is no more expensive than computing the inductance matrix at a single frequency. The method compares well with the standard Padé approaches and may present some advantages because in the Arnoldi-based algorithm, each set of iterations produces an entire column of the inductance matrix rather than a single entry, and if matrix-vector product costs dominate then the Arnoldi-based algorithm produces a better approximation for a given amount of work.³⁵

³⁴ L.M. Silveira, I.M. Elfadel, J. White, M. Chilukuri, and K. Kundert, "An Efficient Approach to Transmission Line Simulation using Measured or Tabulated S-parameter Data," *Proceedings of the 31st Design Automation Conference*, San Diego, California, June 1994, pp. 634-639; L.M. Silveira, I. Elfadel, J. White, M. Chilukuri, and K. Kundert, "Efficient Frequency-Domain Modeling and Circuit Simulation of Transmission Lines," *IEEE Trans. Compon., Hybrids, Manuf. Technol.*, special issue on Electrical Performance of Electronic Packaging, forthcoming.

³⁵ L.M. Silveira, M. Kamon, and J.K. White, "Algorithms for Coupled Transient Simulation of Circuits and Complicated 3-D Packaging," *IEEE Trans. Compon., Hybrids, Manuf. Technol.*, special issue on the Electrical Performance of Electronic Packaging; L.M. Silveira, M. Kamon, and J.K. White, "Direct Computation of Reduced-Order Models for Circuit Simulation of 3-D Interconnect Structures," *Proceedings of the 3rd Topical Meeting on Electrical Performance of Electronic Packaging*, Monterey, California, November 1994; L.M. Silveira, M. Kamon, and J. White, "Efficient Reduced-Order Modeling of Frequency-Dependent Coupling Inductances Associated with 3-D Interconnect Structures," *Proceedings of the European Design and Test Conference*, Paris, France, March 1995, forthcoming; L. Silveira, M. Kamon, and J. White, "Direct Computation of Reduced-Order Models for Circuit Simulation of 3-D Interconnect Structures," invited paper, *Progress in Electromagnetic Research Symposium*, Seattle, Washington, July 1995, forthcoming.

1.10 Techniques for High-Performance Low-Power Embedded System Design

Sponsors

Advanced Research Projects Agency/
U.S. Army Intelligence Center
Contract DABT63-94-C-0053
National Science Foundation
Young Investigator Award with matching funds
from Mitsubishi Corporation
Fellowship MIP 92-58376

Project Staff

Professor Srinivas Devadas, Edward J. Ouellette,
José C. Monteiro, George I. Hadjiiannis, Stan Y.
Liao

Our focus is on solving several critical problems in the design of large-scale digital systems containing both application-specific and reprogrammable hardware. In the near future, most, if not all, of the circuitry for such systems will be integrated on a single chip. We are developing a design methodology that optimizes the power dissipation of the embedded system while meeting area and performance constraints, as described in the following sections.

1.10.1 Embedded Systems

An increasingly common micro-architecture for embedded systems is to integrate a microprocessor or microcontroller, a ROM and an ASIC all on a single integrated circuit (IC). Such a micro-architecture can currently be found in many diverse embedded systems: for example, FAX modems, laser printers, cellular telephones, and portable computers.

The programmable component in embedded systems can be an application-specific instruction processor (ASIP), a general-purpose microprocessor such as the SPARC, a microcontroller such as the INTEL 8051, or a digital signal processing (DSP) microprocessor such as the TMS320C25. We are currently focusing on the DSP application domain, where embedded systems are increasingly used. Many of these systems use processors from the TMS320C2x, 56K or ADSP families, all fixed-point DSP microprocessors with irregular datapaths.

As the complexity of embedded system grows, the need to decrease development costs and time to market mandates the use of high-level languages

(HLLs) in programming DSP processors; only short, time-critical portions of the program can be assembly-coded. Recent statistics from Dataquest support this trend: high-level languages (HLLs) such as C (and C++) are gradually replacing assembly language, because using HLLs greatly lowers the cost of development and maintenance of embedded systems. However, current compilers for fixed-point DSP microprocessors generate poor code—thus programming in a HLL can incur significant code performance and code size penalties.

Need for Optimizing DSP Compilers

While optimizing compilers has proved effective for RISC processors, the irregular datapaths and small number of registers found in DSP processors remain a challenge to compilers. The direct application of conventional code optimization methods has, so far, been unable to generate code that efficiently uses the features of fixed-point DSP microprocessors.

Code size matters a great deal in embedded systems since program code resides in on-chip ROM, the size of which directly translates into silicon area and cost. Designers often devote a significant amount of time to reducing code size so that the code will fit into available ROM; as exceeding on-chip ROM size could require expensive redesign of the entire IC. As a result, a compiler that automatically generates small, dense code will result in a significant productivity gain as well.

Code Optimization for Irregular Datapaths

We are developing code optimization techniques for DSP microprocessors with irregular datapaths that improve code performance and reduce code size. While we focus on the TMS320C25 processor, our techniques are applicable to a broad class of DSP microprocessors, including those in the 56K and ADSP series. The optimization problems we target include instruction scheduling and register allocation. We have also formulated the *accumulator spilling* and *mode selection* problems that arise in DSP microprocessors. The individual problems of scheduling and register allocation have traditionally been solved independently in compilers. We have developed optimal and heuristic algorithms that determine an instruction schedule while simultaneously optimizing accumulator spilling and mode selection. The preliminary results we have obtained show significant improvements over existing code generation methods.

1.10.2 Design for Low Power Dissipation

Average power dissipation has emerged as an important parameter in the design of general-purpose and application-specific integrated circuits, as well as in embedded system design. For embedded systems used in portable applications such as cellular telephones, laptops and notebooks, low power dissipation has emerged as the most important design parameter.

Optimization for low power can be applied at many different levels of the design hierarchy. For instance, algorithmic and architectural transformations can trade off throughput, circuit area, and power dissipation, and logic optimization methods have been shown to have a significant impact on the power dissipation of combinational logic circuits.

It is important to develop optimization methods that are applicable to a broad class of circuits. To this end, we are developing a logic synthesis system capable of synthesizing low-power digital combinational and sequential circuits. Some of our research in this area is described below. We have also begun a hardware design project involving the design of a portable graphics terminal to better understand system-level issues, before we develop CAD methodologies for the design of entire systems for low power (see *Demonstration Vehicle: A Portable Graphics Terminal*).

Logic Synthesis Methods

We are addressing the problem of optimizing logic-level sequential circuits for low power. In collaboration with Dr. Abhijit Ghosh of Mitsubishi Electric Research Laboratories, Sunnyvale, California, we have developed a powerful sequential logic optimization method that is based on selectively *pre-computing* the output logic values of the circuit one clock cycle before they are required, and using the precomputed values to reduce internal switching activity in the succeeding clock cycle. We have developed several different precomputation architectures which exploit this observation.

The primary optimization step is the synthesis of the precomputation logic, which computes the output values for a *subset* of input conditions. If the output values can be precomputed, the original logic circuit can be "turned off" in the next clock cycle and will have substantially reduced switching activity. The size of the precomputation logic determines power dissipation reduction, area increase and delay increase relative to the original circuit.

Given a logic-level sequential circuit, we are developing automatic method of synthesizing precomputation logic so as to achieve maximal reductions in

power dissipation. Preliminary experiments indicate that up to 75 percent reductions in average switching activity and power dissipation are possible with marginal increases in circuit area and delay.

Demonstration Vehicle: A Portable Graphics Terminal

The work described in this section is being done in collaboration with Professor A. Chandrakasan.

We propose to design and implement an ultralow-power portable graphics transceiver using a comprehensive system-level approach to power minimization. Our approach incorporates algorithmic, architectural, logical and circuit optimization techniques for low power and exploits novel fabrication and antenna technology. We hope to demonstrate a power reduction of over an order of magnitude with respect to currently available transceivers.

Our proposed wireless system supports color graphics processing using a simple user interface, providing access to a various graphics databases (e.g., maps). On the down-link, the raw data from the *RF* module is decoded using a *communication decoder* which performs synchronization and error decoding. The decoded data goes to a low-power *graphics processor* which takes high-level graphics commands (e.g., draw square) and produces the bit-mapped data required by the *LCD display*. The bit-mapped data will be stored in a low-power DRAM frame-buffer memory and will be read off to refresh the LCD. On the up-link from the portable terminal to the base-station, data from the keyboard or pen will be sent, which is low-bandwidth in nature.

A major focus of the proposed system is to minimize the power consumption so that the battery life of the portable unit can be extended. A system-level approach to power minimization will be taken, exploiting novel fabrication technologies, circuit design techniques, architectures and algorithms. At the highest level, system partitioning will be optimized to trade power consumption in the transceiver and the bandwidth used in the wireless link. The goal is to display high resolution color graphics (640 x 480). We will investigate various partitioning schemes including a pure bit-map approach, a full X-server implementation, compressed X, and several solutions which lie in between a pure bit-map approach and a full X-server. Various power reduction techniques will be developed for the graphics processor including an optimized instruction set architecture, techniques for efficient power down of blocks, logic-level shutdown, circuit and device modifications for low-

voltage operation (e.g., 1.5 V), etc. We plan to fabricate the graphics processor in a standard 1.0 μm CMOS technology. We are also investigating the problem of generating code for the graphics processor so that the overall power consuming transitions is minimized. Using a whole slew of techniques, we hope to demonstrate two orders of magnitude reduction in power over existing "optimized" commercial processors.

The graphics processor will require a *frame-buffer* ($640 \times 480 \times 8$) to interface to a display which uses 256 colors. Though current TFT color displays consume as much as 20 W, recent advances in LCD displays indicate that the power consumption of active matrix color displays using reflective technology can be as low as 100 mW.

The *communications encoder* module performs error correction on pen and keyboard data and formats the data to be sent over the wireless link. We are investigating error correction algorithms that efficiently utilize the spectrum. Similarly, the communications decoder will perform error decoding on graphics packets and send the data to the processor. If so many errors occurred that data could not be reliably decoded, a retransmission request will be sent to the base-station.

1.10.3 Publications

Alidina, M., J. Monteiro, S. Devadas, A. Ghosh, and M. Papaefthymiou. "Precomputation-Based Sequential Logic Optimization for Low Power." *IEEE Trans. VLSI Syst.* 2(4): 426-436 (1994).

Devadas, S., K. Keutzer, S. Malik, and A. Wang. "Verification of Asynchronous Interface Circuits with Bounded Wire Delays." *J. VLSI Sig. Process.* 7(1): 161-182 (1994).

Devadas, S., K. Keutzer, S. Malik, and A. Wang. "Event Suppression: Improving the Efficiency of Timing Simulation for Synchronous Digital Circuits." *IEEE Trans. Comput.-Aided Des.* 13 (6): 814-822 (1994).

Devadas, S., K. Keutzer, S. Malik, and A. Wang. "Certified Timing Verification and the Transition Delay of a Circuit." *IEEE Trans. VLSI Syst.* 2(3): 333-342 (1994).

Shen, A., S. Devadas, and A. Ghosh. "Probabilistic Manipulation of Boolean Functions Using Free Boolean Diagrams." *IEEE Trans. on Comput.-Aided Des.* 14(1): 87-95 (1995).

Tsui, C.-Y., J. Monteiro, M. Pedram, S. Devadas, A. M. Despain, and B. Lin. "Exact and Approximate Methods of Switching Activity Estimation in Sequential Logic Circuits." *IEEE Trans. VLSI Syst.* March 1995.

Van Aelten, F., J. Allen, and S. Devadas. "Event-Based Verification of Synchronous Globally Controlled Logic Designs against Signal Flow Graphs." *IEEE Trans. Comput.-Aided Des.* 13(1): 122-134 1994.

1.10.4 Conference Proceedings

Alidina, M., J. Monteiro, S. Devadas, A. Ghosh, and M. Papaefthymiou. "Precomputation-Based Sequential Logic Optimization for Low Power." *Proceedings of the International Conference on Computer-Aided Design*, Santa Clara, California, November 1994, pp. 74-81.

Bhagwati, V., and S. Devadas. "Automatic Verification of Pipelined Microprocessors." *Proceedings of the 31st Design Automation Conference*, San Diego, California, June 1994, pp. 603-608.

Liao, S., S. Devadas, and K. Keutzer. "Code Density Optimization for Embedded DSP Processors Using Data Compression Techniques." *Proceedings of the 1995 Chapel Hill Conference on Advanced Research in VLSI*, Chapel Hill, North Carolina, March 1995.

Liao, S., S. Devadas, K. Keutzer, S. Tjiang, and A. Wang. "Code Optimization Techniques in Embedded DSP Microprocessors." *Proceedings of the 32nd Design Automation Conference*, San Francisco, California, June 1995.

Liao, S., S. Devadas, K. Keutzer, S. Tjiang, and A. Wang. "Storage Assignment to Decrease Code Size." *Proceedings of the SIGPLAN Programming Language Design and Implementation Symposium*, Princeton, New Jersey, June 1995.

Lin, B., and S. Devadas. "Synthesis of Hazard-Free Multilevel Logic Under Multiple-Input Changes from Binary Decision Diagrams." *Proceedings of the International Conference on Computer-Aided Design*, Santa Clara, California, November 1994, pp. 542-549.

Monteiro, J., S. Devadas, and B. Lin. "A Methodology for Efficient Estimation of Switching Activity in Sequential Logic Circuits." *Proceedings of the 31st Design Automation Conference*, San Diego, California, June 1994, pp. 12-17.

Monteiro, J., J. Rinderknecht, S. Devadas, and A. Ghosh. "Optimization of Combinational and Sequential Logic Circuits for Low Power Using Precomputation." *Proceedings of the 1995 Chapel Hill Conference on Advanced Research in VLSI*, Chapel Hill, North Carolina, March 1995.

Yun, K., B. Lin, D. Dill, and S. Devadas. "Performance-Driven Synthesis of Asynchronous Controllers." *Proceedings of the International Conference on Computer-Aided Design*, Santa Clara, California, November 1994, pp. 550-557.



*Research Scientist Michael B. McIlrath (left) and Professor Donald E. Troxel
(Photo by John F. Cook)*

Chapter 2. Computer-Integrated Design and Manufacture of Integrated Circuits

Academic and Research Staff

Professor Dimitri A. Antoniadis, Professor Duane S. Boning, Professor Donald E. Troxel, Linus F. Cordes, Gregory T. Fischer, Stanley B. Gershwin, Thomas J. Lohman, Michael B. McIlrath, James E. Murgua

Graduate Students

Asbjørn M. Bonvik, John C. Carney, Lynn D. Gabbay, Jarvis B. Jacobs, James T. Kao, Jimmy Y. Kwon, Nicole S. Love, William P. Moyne, Miltiadis A. Stamatopoulos, Evren R. Unver

Undergraduate Students

Victor E. Chin, Nadir E. Rahman, Kit Yan Tso

Technical and Support Staff

Francis M. Doughty

2.1 Introduction

Sponsors

Advanced Research Projects Agency
U.S. Navy
Contract N00174-93-K-0035

Computer aided fabrication environment (CAFE) is a software system being developed at MIT for use in the fabrication of integrated circuits and microstructures. The distinguishing feature of CAFE is that it can be used in all phases of process design, development, planning, and manufacturing of integrated circuit wafers. CAFE presently provides day-to-day support to research and production facilities at MIT with both flexible and standard product capabilities. This manufacturing software system is unique in the development of a process flow representation and its integration into actual fabrication operations. CAFE provides a platform for work in several active research areas, including technology (process and device) computer aided design (TCAD), process modeling, manufacturing quality control, and scheduling.

2.1.1 Architecture

The CAFE architecture is a computer integrated manufacturing (CIM) framework for the deployment and integration of integrated circuit (IC) and process design and manufacturing software. CAFE uses an object oriented database model which is implemented in a layered manner on top of a relational database. Our database schema is based on GESTALT, an object oriented, extensible data

model. GESTALT is a layer of abstraction which maps user defined objects onto existing database systems (e.g., a relational DBMS) and shields application programs from the details of the underlying database. The integration architecture includes the conceptual schema and models used to represent the IC manufacturing domain in CAFE, and the user and programmatic interfaces to the various applications. Two important CAFE applications relate process simulation and actual wafer fabrication to the very same process flow representation.

2.2 CAFE Applications

The fabrication of wafers with a process represented as a process flow representation (PFR) involves several steps. A suitable PFR for the specific process must be created and installed. Wafer lots must be created and associated with this specific PFR. These lots must then be "started" to create a task data structure which is isomorphic to the hierarchical structure of the PFR.

At this point, actual machine operations can be scheduled and reservations made for both machines and operators. Finally, the machine operations can be performed, instructions given to the operator and machines, and data collected from the operator or machine and entered into the database.

Current work involves the implementation of hierarchical scheduling, development of factory design tools, real time process control using the PFR, and integration of a TCAD system using the PFR.

2.3 Organization of Data and Algorithms for Factory Design and Control

Project Staff

Miltiadis A. Stamatopolous, Stanley B. Gershwin,
Professor Donald E. Troxel

A methodology for the design, redesign, dynamic reconfiguration, and operation of production systems is proposed. A set of tools and data abstractions provide aid in decision making for the whole life cycle of factories.

An important aspect of our approach is the use of common data and, when appropriate, common code, both in the analysis and simulation as well as in the operation of production systems. This way, the analysis and simulation are more realistic; and the tools provided for the operation are extensively tested before they are put in use.

In order to effectively tackle such problems as factory design, redesign, dynamic reconfiguration, and operation of production systems, it is necessary to have an efficient way of organizing all the relevant data. This data can be abstracted in information about *where* to produce, *how* to produce, as well as *what* and *how much* to produce. Furthermore, a performance matrix according to which systems can be evaluated (*how well*) in a consistent manner is required. This information must be specified conveniently and in a way that allows several application programs to access and use the same data. In this way, consistency in different experiments and analytical calculations will be guaranteed.

It is very important to ensure the commonality of the data in all applications that require it. In particular, the same data, as well as scheduling algorithms and code, must be used both in the simulation and in the real time control of production systems. In this way, the simulation will be more realistic; and the scheduling code can be extensively tested before it is put in use.

Several commercial simulation packages exist, but none can guarantee the consistency of data and algorithms used in the design process and in real time control of production systems. In this paper, we develop a methodology that incorporates all stages of factory life, from design to operation. To realize this task, we break it into meaningful abstractions both in data organization and in the procedures used.

2.4 Statistical Process Control Charts for the Computer Aided Fabrication Environment

Project Staff

Nicole S. Love

Statistical process control (SPC) charts are means of improving process performance through the analysis of post-process measurements. SPC charts for the computer aided fabrication environment were developed to assist in the manufacturing of integrated circuits. This thesis describes the application program to produce the SPC charts focusing on four main objectives: generating the control charts, accessing the data from the database, caching the data, and combining control charts. The generation of the control chart is independent of the data and requires a data file of the correct format. The control chart user interface is implemented using the Tcl/Tk scripting language along with [incr Tcl], an extension to Tcl. Accessing the data is accomplished by using the PFR to link a process step with the corresponding inspection step. Caching the data is accomplished using a Gestalt object to store the time frame of the data, the data, and other information used in generating the control chart. The advantages and disadvantages of combining control charts, including multiple machines running the same recipe, and multiple recipes on the same machine, are examined.

2.5 Run-by-Run Control: Interfaces, Implementations, and Integration

Project Staff

William P. Moyne

One of the largest barriers to implementing run-by-run (RbR) control of manufacturing processes is compatibility with existing systems. Manufacturers are reluctant to modify "working" equipment to implement an unproven modification. The RbR controller will attempt to remedy this. The controller will use layered messaging as its interface model. Multiple layers will be designed to interact with external data sources at different levels of abstraction, from objects to primitive scalars. Internally, the controller will use an object based interface to its data as well as a well-defined algorithmic interface. These interfaces are needed for implementation of existing algorithms as well as future algorithmic development. Finally, as a test of the above goals, the RbR controller will be integrated into a variety of systems including both a

local CIM system and a control framework being developed as a joint university and corporate effort.

RbR control is a form of process control. It uses post-process measurements and possibly *in situ* data to modify models of the process, and based on these adaptive models recommends new equipment settings for the next run. Although RbR may use *in situ* data, it differs from real time control in that it only adjusts process variables between runs. RbR control can be effective in keeping a process on target and in statistical control in the presence of process noise and drift.

There are many approaches to RbR control. One basic approach is gradual mode control. This method assumes that the actual changes in the process are minor (less than three standard deviations) and only small changes in the control parameters are required in order to compensate. Usually, an exponentially weighted moving average filter is used to distinguish between random noise and real disturbances, thus smoothing the control decisions. This form of control complements existing systems well by suggesting new recipes to the operators of the equipment.

A modified version of gradual mode which was developed at Texas Instruments is predictor corrector control (PCC). This method more explicitly models the time dependence of disturbances. Trends in the drift are monitored over many runs and are factored into the suggested recipes. This method requires the addition of state to the process model, but has shown improved performance over gradual mode when persistent drift is present. An example cause of such drift is equipment aging.

Another approach to RbR control is the rapid mode. This addition integrates control with more traditional statistical process control (SPC) charting and alarm methods. Using statistical rules, the performance of a process is classified as either in-control or out-of-control. Gradual mode control is used for an in-control process, while a more aggressive control strategy (rapid mode) is used to bring out-of-control processes back on target. This provides both rapid correction for statistically large variations such as step changes, while reducing the risk of over control through filtered gradual mode control decisions.

In addition to the methods already discussed, neural networks have also been applied with some success. In this method, a neural network is trained on the inputs and outputs present after a shift has

occurred. The controller then uses this information to immediately compensate for disturbances after a shift rather than waiting for convergence in the case of gradual mode. Gradual mode control may then be applied once the shift has been compensated for. Experiments have shown that this method does reduce process variation when compared to pure gradual mode.

The concept of a clean and open interface to the above algorithms has not been studied as well as the algorithms themselves. However, there have been several attempts at defining the form of the data needed for RbR control as well as presenting the controller in a user friendly and easy to use manner. The control algorithms have also been converted to "C".

Incompatibilities between existing equipment and current control implementations are a barrier to adoption of RbR control routines in the VLSI fabrication environment. The RbR controller will attempt to address some of the leading issues blocking existing implementations. In order to communicate with existing systems, the RbR controller will use layered messaging as its interface model. Multiple levels of communication will be possible to provide a wide range of interaction, from complete object interaction to primitive scalar data passing. There will be well defined boundaries between each layer, and translation modules will be written to promote multiple primitive data items into complete objects. The controller itself will use an object based communication model and rely on these translations for interaction with non-object based external sources.

Once the communication model has been defined, the controller will provide a well-defined interface to existing algorithms to ensure that maintenance of code and integration of new algorithms will be as efficient as possible. This interface will embrace ideas such as a programmatic interface, data abstraction, and ANSI "C" coding techniques.

Finally, as a test of the above techniques, the controller will be integrated into an existing CIM system (CAFE), a control framework (GCC), and a locally produced RbR graphical user interface (GUI). These widely varying implementations will test the robustness of the RbR controller's communication model as well as its performance in a wide variety of implementations. It is hoped that by providing a generic and robust model of communication, the RbR controller can become both a test bed for further algorithmic development as well as a model for RbR messaging techniques.

2.6 Hardware Setup for a Remote Microscope

Project Staff

James T. Kao

We have defined the equipment needed to set up a remote microscope (inspection) unit. Although our test unit will not be mounted on a microscope initially, this could be easily accomplished in the future by using a special mount. The hardware for the remote inspection unit basically consists of a PC (connected to the network) installed with a framegrabber board, which will grab images from a video camera.

After capturing images with a framegrabber board, we will save these files to the network using PC-NFS and an ethernet adapter such as the Interlan PCI Ethernet card. The remote microscope user interface software will then be responsible for processing this image and transferring it to remote inspection sites.

Typically in a remote microscope setup, the RGB video signal from the camera's DSUB connector will be sent to the Targa+ DSUB input using a CCXC9DD cable. However, to view the live video image, a separate video monitor must be used. By getting the monitor's video signal from the Targa+ instead of the video camera, one can view the video exactly as seen by the framegrabber board. On the other hand, if one would rather use the camera-monitor setup without going through the computer first, the camera can be attached directly to the monitor. The CCXC9DD monitor has a horizontal resolution (420 lines) that matches the capabilities of the DXC151 camera (440 lines RGB or 460 lines Y/C or VBS); but depending on one's desired applications, a lower resolution (cheaper) monitor might be preferable (for example, if the monitor is used only as a view finder and not as a detailed display). Regardless of the resolution of the video monitor, the frame captured by the Targa+ board will still be very high quality, since the capture resolution of the Targa+ is 640x480.

We are now developing software to control the system. One possible approach is to have the remote inspection site's terminal serve as a client that will connect to a local server that can request grabbed frames from the PC. Another approach would be to have the PC become the actual local server to which a remote client would connect. In either case, the hardware described here (Targa+, camera, lens, power supply, cables, Pentium computer, ethernet card, and video monitor) will still be required in order to provide capability for capturing

video frames and passing them through the network.

2.7 First-Order Model for Remote Fabrication

Project Staff

Jimmy Y. Kwon

The first-order processing model makes explicit the information transfer stage during remote processing. The processing of information might proceed as follows. The user writes the process flow text, installs it into the CAFE database, and then creates a new lot and task tree. The local machine operations are then done in the typical operate machine/next operation cycle. When a remote machine operation comes up, the operate machine/next operation cycle breaks in preparation for the remote operation. The first step is the locking of data.

The locking step is needed to provide some measure of data security in the local database. Assume for simplicity that both the local and remote facilities are running CAFE. When a lot leaves the local facility, the database should reflect that state and prevent any changes to the information associated with the lot until the lot returns. This could be thought of as a delayed evaluation. Suppose one wants to compute the product $7*17$ on a remote processor. The value 7 is stored in a variable x and the value 17 is stored in y. After storing the values in the variables and sending the computation request, one cannot change the values in x and y until the computation is complete; or else the result one gets will be wrong for the original problem. Similarly in CAFE, appropriate objects in the database should be protected from changes while the lot is away.

We need to consider what sort of objects should be locked in CAFE while operations are done remotely, since in CAFE objects typically contain references to other objects. To begin with, the lot object itself needs to be locked. Lots contain wafer sets, which contain wafers, so these also should be locked. The lot has an associated task tree, so the parts of the process flow and task tree that are sent to the remote facility should also be locked and protected from tampering. In this case, we can lock only the portion of the task and flow tree that involves the remote operations, leaving the other parts free for modification (i.e., the present group of remote operations are locked, but future operations may be modified). Leaf tasks have opinst objects that may also need to be locked.

2.8 Estimating the Lead Time Distribution of Priority Lots in a Semiconductor Factory

Project Staff

Asbojorn M. Bonvik

We consider the lead time of priority lots in a semiconductor factory. The main cause of delays is waiting for repairs of failed machines, and the failures are mainly caused by power disturbances. This can be modeled as an exogenous time-dependent failure process, and we develop a probabilistic model of the system based on this. Using this model, a convolution algorithm for finding the lead time distribution is described.

We describe a method of creating synthetic samples of the lead time from historical failure and repair data collected in the factory. Based on such a sample from the MIT Integrated Circuits Laboratory, we approximate the distribution of lead times by a gamma probability density function shifted by the smallest possible lead time for the product type. The parameters of the gamma distribution are found by using a maximum likelihood estimator. The resulting distribution gives good agreement with the synthetic data for values less than two standard deviations above the mean lead time.

Since our procedure depends only on a description of the process and the failure and repair history of the factory, it can also be used to obtain lower bounds on the lead time for new product types.

2.9 Factory Display Software

Project Staff

John C. Carney

A semiconductor manufacturing facility contains several machines, each of which operates on lots. At any given time the state of a machine may change. The machine might go down for repairs or might receive a new lot on which to operate. Status information of this sort is of great importance to managers and workers of the facility. Factory display software has been developed which makes this information available graphically. By providing the user a map of the facility, with iconic representations of machines, the user can quickly and easily view the status of the facility. In addition, the user can probe the map to obtain other desired information about the machines and lots within the facility.

It is intended that the factory display software will be used in real time, showing the current status of

machines and lots with an active display that dynamically changes as the status information changes. However, there are other important uses. The factory display can also be used to "play back" the events of a facility much faster than real time. This would allow a user to perhaps view the entire previous week's events in just a few minutes. The graphical manner in which a user can see all machines at every instant in time can convey an enormous amount of information in a very suitable way. While a view of the facility's historical information is useful, also very useful is a view of simulated information. The factory display software has been designed with this in mind. It can be integrated with facility scheduling and simulation software to provide an "output device" for the data produced by such programs.

The factory display software is written in Tcl/Tk, a scripting language and toolkit for creating graphical user interfaces under X Windows. The display program uses a message passing system to dynamically receive messages containing status information about the facility. The message passing nature of the display program allows it to be easily integrated with other existing or developing systems. The factory display program has successfully been integrated with CAFE.

2.10 Message Passing Tools for Software Integration

Project Staff

John C. Carney

Unix-based environments typically provide a rich abundance of tools. Generally these tools are integrated by operating on a common set of files. There are no interactions among tools and each provides its own interface. One approach for integrating tools is through the use of a message passing system. The goal of a message passing system is to provide a method by which structured information can be exchanged between two or more running processes. These processes may all run on a single workstation or on separate workstations connected by a network.

A flexible peer-to-peer approach to message passing has been developed. This approach allows an enormous variety of connection architectures, where each program establishes one or many connections with various other programs. The communications handling application tools (CHAT) suite has been developed, providing the programmer with a suite of libraries which can be used to integrate software based on the peer-to-peer message passing approach. The suite contains three libraries

of routines which provide support for packaging of data into messages, handling of incoming messages, and establishment of connections between programs. All three libraries are written in C and in Tcl/Tk. The CHAT suite will allow for arbitrary combinations and architectures of "C" programs and Tcl/Tk programs to exchange messages.

Libraries within the CHAT suite have been used to integrate a new factory display program into CAFE. Libraries have also been used to integrate a graphical user interface and simulation environment with an RbR control server. Plans have been made to use the CHAT suite in research work being done on the remote fabrication and remote inspection projects within MIT's computer integrated design and manufacturing (CIDM) project.

2.11 CAFE at MIT Lincoln Laboratory

Project Staff

Gregory T. Fischer

MIT Lincoln Laboratory is using CAFE as the CIM system for use in their IC processing facility. Multiple lots are being processed daily via PFR based fabrication. Lincoln Laboratory is committed to having 100 percent of their wafers in this facility processed with PFR based fabrication.

Release 5.3 of CAFE was installed at both MIT and Lincoln Laboratory. A number of enhancements and improvements have been made to CAFE in response to user requests and feedback both at Lincoln and at our campus fabrication facilities. They are described below. Perhaps most noteworthy is the substantial speed-up of Generate Traveller and Operate Machine.

Generate Traveller has been modified extensively due to previous speed problems and corrupted traveller cache files at Lincoln Laboratory. The traveller report for a PFR lot is precalculated and stored in files for faster generation of a traveller report upon request by a user. In previous releases of CAFE, the initial traveller cache for a PFR lot was calculated the first time a user selected the "Generate Traveller" menu option. For CAFE release 5.3, the initial traveller cache is now calculated at "Start Lot" time, cutting the initial cache creation time by a factor of at least five.

The caching scheme for a traveller report was also altered. The old caching scheme involved up to three files for a PFR lot: a past report file, a present report file, and a future report file. "Generate Traveller" would check the lot to see which operations had been performed since the last traveller

report generation and would update the three files accordingly. With CAFE release 5.3, a traveller cache file is created for each top-level upset task in a lot's task tree. These files are stored in a /usr/cafe/cache/traveller/<lotname> directory. Each filename is a number, such as 003; and listing the directory will display the files in the same order as they appear in the task tree. A schema change was made to add an "advice" slot to TASK database objects, providing a place to store the traveller cache filename which belongs to a given top-level upset task.

The updating process for an existing traveller report has also been enhanced. Any function which alters a task's status, such as "Operate Machine", now updates the correct traveller cache file for that task upon exiting. Any function which alters a lot's task tree must delete the appropriate traveller cache file for recalculation at a later date. Upon invoking "Generate Traveller", if only task status has been modified, generation of the traveller report now takes three to five seconds. If a lot's task tree has been altered, only the top-level upset tasks which have no traveller cache file are updated before the full traveller report is generated. This takes about half the time it took to update the traveller cache in previous versions of CAFE.

Enhancements to the speed of "Operate Machine" have also been performed. The functions which calculate the WAFERSET and/or WAFER display have been optimized. Also, at "Start Lot" time, the Fabform user interface screen for each fringe task is calculated and stored in the PLANNEDOPINST object for that task. In tests on cafe.mit.edu and garcon.mit.edu, these enhancements have dropped the time to get into "Operate Machine" from twenty seconds to around five seconds. The time to get out of "Operate Machine" has been slightly retarded due to traveller cache file updating, seven seconds in the previous version of CAFE to twelve seconds in CAFE release 5.3.

"Operate Machine" and "Next Operation" have been modified to allow users to continue from one "Operate Machine" to the next without getting back to the "Fabrication Tools" menu. Once an operation is completed in "Operate Machine", a message is displayed informing the user of the next machine operation to be performed; and the user is asked if he wishes to indeed operate the next machine. If the response is "yes", "Next Operation" is called. If there is only one machine choice for the next operation, "Operate Machine" is immediately entered again for that machine. If more than one machine is valid for the next operation, a cleaner "Next Operation" screen is presented which allows the user to choose which machine to operate.

"Start Lot" has been modified to check a lot's wafer sets against the wafer sets specified by the PFR process. If a lot is found to be lacking wafer sets needed by the process, an error message is displayed informing the user as to which wafer sets are missing. "Start Lot" also generates the initial traveller cache for the lot.

New trend chart applications are now under the "Reports" "Trend" menu. Tcl/Tk graphical user interfaces allow users to design, edit, display and plot SPC charts for PFR-based diffusion processes which have been performed.

Traveller caches for all PFR lots are now updated overnight via backgrounded cache update functions. Invoking these functions during nightly cafe maintenance will insure up-to-date traveller reports each morning.

A new Tcl/Tk graphical user interface has been developed to replace the current Fabform user interface. The new interface combines graphical menus with Fabform-based application interfaces. Users can toggle between the new interface and Fabform via the "General Purpose" "Change Interface" application.

A new PFR-based process rule checking capability is now available via the "Task Editor". This allows a user to test a process and check for possible problems and safety hazards, such as placing wafers which are still coated with photoresist into a diffusion furnace. Eighteen rules are currently checked.

A new user interface has been developed for the "Modify Machine Status" application which allows users to modify the status of multiple machines within a facility without having to return to the "Labstaff Tools" menu.

A new subclass of the OPINST database object was created: REALOPINST. Subtypes of a REALOPINST are ACTIVEOPINST and COMPLETEDOPINST. The TASK schema was modified to use the REALOPINST in the "opinst" slot. This change will prevent PLANNEDOPINSTs from incorrectly pointing to a TASK's "opinst" slot.

It is now possible to view CAFE Help and Lab Manual text via the World Wide Web and xmosaic. Options have been added under the "Help" and "Help" "Equipment Help" menus which will initiate

an xmosaic window displaying the specified help text section.

2.12 Error Handling Within CAFE

Project Staff

Gregory T. Fischer, Thomas J. Lohman

CAFE users were frequently encountering errors within the CAFE software package, both at the MIT Microsystems Technology Laboratories (MTL) and at Lincoln Laboratory. These errors would often result in the user being dumped in to the Lisp debugger and/or having the CAFE session abort completely. After investigation, new methods of catching these errors were developed and incorporated into the CAFE software.

The interception of the Lisp error handlers and the ability to disable CTRL-C signals have been instrumental in tracking and preventing CAFE errors. The frequency of error email messages has dropped dramatically from an average of five a day to only one or two per week, suggesting that the previous user CTRL-C interrupts were causing more wide-ranging problems than was first thought.

2.13 Semiconductor Manufacturing Process Flow Representation

Project Staff

Michael B. McIlrath, Professor Donald E. Troxel, Professor Duane S. Boning, Evren R. Unver

2.13.1 Introduction

The PFR and its integration into both design and fabrication operations is central to the CIDM program and the CAFE software system.¹ CAFE is currently being used at the semiconductor fabrication processing facilities of the MTL, Lincoln Laboratory, and Case Western University. Activities in this area include both formal methods for process modeling and the practical application of process representation to process design and execution.

For high performance computing systems and other advanced technology, concurrence in the design of the product, manufacturing process, and factory is crucial. The goal is to achieve fully integrated

¹ M.B. McIlrath, D.E. Troxel, D.S. Boning, M.L. Heytens, and P. Penfield, Jr., "CAFE - The MIT Computer-Aided Fabrication Environment," *IEEE Trans. Comp., Hybrids, and Manuf. Tech.* 15(2): 353-360 (1992).

design and manufacture, in which the boundary between design and manufacturing domains is eliminated: in particular, information from the manufacturing floor is continuously available from the earliest stages of process and device design onward. Conversely, the manufacturing process, developed concurrently with the product, continues to undergo design via improvement and modification while in production. Computer integrated design and manufacture, therefore, requires a coherent manufacturing process representation capable of storing information from a variety of different knowledge domains and disciplines, and supporting access to this information in a consistent manner. We believe that our general semiconductor process modeling framework organizes the complexity of this interrelated information and puts our PFR on a sound footing by giving it clear semantics.

A high level conceptual model for describing and understanding semiconductor manufacturing processing is a crucial element of both the CIDM research program and software frameworks for TCAD and CIM, including MIT CAFE. Initially a two-stage generic process step model was used, which described processing steps in terms of two independent components: (1) an equipment-dependent, wafer-independent stage, which maps equipment settings to physical processing environments; and (2) an equipment-independent, wafer-dependent stage, which relates physical environments to changes in the input wafers. Driven by the needs of process control and optimization research, including sophisticated modeling, design, and experimental model verification, our fundamental conceptual process model has evolved from the two-stage generic process model into one which is part of a more general process modeling framework, in which the earlier two-stage model is a special case. Our approach to process representation for both TCAD and CIM is based on this general modeling framework for semiconductor processing. In this framework, state information (e.g., wafer, environment, and equipment state), and models, or transformations, that describe relationships between state descriptions, are formally identified and described. The purpose of this comprehensive framework is to enable an effective representation that can be used throughout the IC semiconductor process life cycle, from early conception and design phases through fabrication and maintenance.

In the MIT CAFE system, the PFR is expressed in a textual (ASCII) format and then converted into Gestalt objects and loaded into the CAFE database. The textual language of the PFR is extensible, so that it can flexibly accommodate

changes and extensions to both the underlying modeling methodology and the needs of specific applications. The object-oriented nature of the Gestalt database interface enables the convenient evolutionary development of CAFE software applications built around the PFR. The PFR allows process step descriptions to be underdetermined; for example, by expressing only the wafer-state change, making it possible to develop a process incrementally with increasing degrees of detail. In addition to expressing the fundamental concepts of wafer transformation within individual process steps, the PFR supports both hierarchical and parameter abstraction and embedded computation, thereby providing support for modular process design and development. Processes expressed in the PFR can be simulated using a variety of technology CAD tools; PFR extensibility allows the incorporation of both simulator-dependent and simulator-independent information. A simulation manager application uses the appropriate information in the PFR along with knowledge of specific simulators to invoke simulation tools and maintain simulation state.

2.13.2 Process Development and Execution

The PFR has been used to develop and execute all of the fabrication processing at Lincoln Laboratory during the last two years. Over five hundred fabrication runs have been completed with around forty lots in process at any given time. These lots represent a variety of technologies, including CCD, low power CMOS, and SOI. All of the Lincoln facility processing uses CAFE and the CAFE PFR.

Additionally, at MIT the PFR is used for both baseline and research processing: in particular, in support of other CIDM and MTL research activities including hot carrier reliability and extreme submicron technology design.

2.13.3 Design Rule Checking for Wafer Fabrication Using CAFE

We have developed an extensible and general framework for process design rule checking. A table-driven approach used is to check for rule constraints at each processing step, based on the current state of the wafers. By wafer state here we refer not only to the simulated or measured process effects but also to the process history. The rule checker can be used in two ways: on-line, to prevent unsafe operations from occurring during fabrication; and during process development, to warn a user that an illegal or incorrect process flow has been specified.

Each design rule is a separate entity and can be developed and applied independently. Customized groups of rules can be created. Each rule is a constraint associating wafer state information and process step information. Rules may be based on any process attribute or set of attributes, e.g., wafer state, physical treatment, equipment, etc. The constraint is active just when the process step information matches the attributes of the process step specified in the PFR. If a constraint is not satisfied, an error is signaled. Unsatisfied constraints thus "block" further execution of the process. If the step can proceed (that is, all rules are satisfied) the running wafer state is updated with the necessary information, determined from the process attributes. Rules are applied in parallel in a single walk through the process; it is not necessary to sequentially run multiple design rule checking programs. Splits and joins are supported.

In on-line (fabrication) rule checking, running wafer state information is maintained in the task tree. The on-line wafer state can also be used to verify the correctness of changes made to a flow during processing by inserting, deleting or modifying the nodes of the task tree associated with the flow.

2.13.4 Conceptual Graphs Applied to Semiconductor Processing

Conceptual graphs are known to be relevant to a broad spectrum of problems in knowledge representation, including modeling of physical processes. We have applied the conceptual graph formalism to the general process modeling framework underlying the PFR² and are working on the application of conceptual graphs to semiconductor problems including process control and design.

2.13.5 Investigation of PFR Requirements for Factory Design and Real Time Scheduling

We have begun investigation of PFR requirements for factory modeling and design, simulation, and real time scheduling. The goal is to be able to support the development of methods for the design of an efficient factory and the efficient operation of a factory to meet production requirements. Among

the needs that have been identified are a more sophisticated and precise definition of operation time, including setup time, initial operator time, unattended operation time, and final operator time; and the proper handling of PFR conditionals for scheduling, including predictive branching.

2.13.6 Extension Language Interface

An extension language provides a programmable way for users to extend an application software tool or framework. An extension language interface to the CAFE system has been implemented and is designed to be compatible with the CAD framework initiative (CFI) extension language (EL), which is based on Scheme. Because the PFR has a programmatic, textual form, designed for extensibility, extension language forms may be embedded in the PFR to access the CAFE database and services and express computations. An extension language interpreter has been integrated into the PFR interpreter, and we are experimenting with the use of this capability in process design and fabrication.

2.13.7 Ongoing Standards Activities

Work is continuing in conjunction with the CFI working group on semiconductor process representation (SPR). A pilot implementation of SPR is being built at Technology Modeling Associates (TMA) and an early version is in use in the Sematech Lithography Modeling Workbench. We are working closely with TMA and Sematech to insure compatibility with larger integrated design and manufacturing framework principles and goals. A formal base information model for SPR, developed largely from MIT work, is currently being considered by the SPR working group and Sematech reviewers.

2.14 Computer-Aided Technology Design

Project Staff

Professor Dimitri A. Antoniadis, Professor Duane S. Boning, Lynn D. Gabbay, Jarvis B. Jacobs, Michael B. McIlrath, Nadir E. Rahman, Kit Yan Tso

² D.S. Boning, M.B. McIlrath, P. Penfield, Jr., and E. Sachs, "A General Semiconductor Process Modeling Framework," *IEEE Trans. Semicond. Manufact.* 5(4): 266-280 (1992).

2.14.1 Introduction

The design of advanced integrated circuit microsystems is increasingly linked to the design of both the component devices of the microsystem and the microfabrication process used in its manufacture. Traditionally, the devices and manufacturing process used in building integrated circuits are collectively called the technology. The objective of microsystems technology design is to devise a fabrication process sequence which yields structures with some desired characteristics. Actually, two activities proceed in parallel: design of (1) the device structures and (2) the process to fabricate them. In general, the design space for both is explored by the technology designer using a combination of physical experiments and numerical simulation.

The microsystem (circuit) designer typically views the technology through a very limited interface; usually a set of process parameters, which describe electrical behavior of underlying structures (for example, resistance of polysilicon), and the design rules, which express the allowable manufacturing limits in geometrical terms (i.e., minimum line width). The high-level goal of this project area is the development of tools and methodologies for more fully integrating the technology design with both the product design and the manufacture of integrated circuit microsystems.

2.14.2 Technology CAD Framework

Contemporary large-scale software system engineering emphasizes frameworks, wherein common structure and interface specifications enable both current and future software components to be integrated in a flexible and modular way. Frameworks have been particularly successful in the development of electronic circuit CAD systems. Software may be generally divided into (1) tools, such as a simulator, which perform some part of an application task, and (2) services, such as a database, which provide some necessary support capability used by various tools.

With framework standards, reusable, interchangeable software components from various suppliers may be deployed in systems which comply with the standard. In the broad sense, a framework standard specifies:

- data representations for the objects of discourse in the application domain and their

semantics, and programmatic interfaces to those representations; and

- architecture; that is, interactions among software components (tools and services), and how tools fit together to perform application tasks for the user.

Standards for CAD frameworks are currently being established by the CAD framework initiative (CFI), a broad organization of vendor and user companies which has expanded its scope to include technology CAD. Technology CAD (TCAD) framework components include programming representations for the fundamental objects of process and device CAD: the physical structures on the wafer, the manufacturing process, and the structure and behavior of the resulting devices. A TCAD framework standard should also specify how application software is structured to use these representations and the underlying software services in process and device design and simulation activities.

The problem of wafer representation can be divided into geometry (shapes of regions and their relations) and fields (variations of properties over a region). A wafer representation for two dimensional simulation has been designed and prototyped and proposed through the CFI semiconductor wafer representation (SWR) working group. Current research is focused on three-dimensional representations.

An information model for semiconductor manufacturing processes has been proposed through the CFI working group on semiconductor process representation (SPR). A pilot implementation of SPR is being built at TMA and an early version is in use in the Sematech Technology CAD Workbench.

2.14.3 Process Capabilities Database

As semiconductor manufacturing becomes increasingly expensive, few institutions can maintain complete processing capability at the leading edge of research. We have built an information entry and retrieval system for data about university fabrication facilities collected by the Semiconductor Research Corporation (SRC). The system is accessible through the World Wide Web (WWW). Through a web-based query interface, remote users can find university facilities with particular fabrication capabilities and resources. Owners of remote fabrications in the database can update information about their own facility.

2.14.4 Advanced Process Simulation and Design Environments

We are looking at higher-level architectural issues, such as the interrelationships between the framework data representations and the connection of compliant tools to achieve end-user design objectives. We are also investigating the larger questions of the relationship between frameworks for different related domains (e.g., circuit CAD and TCAD), and the integration of design frameworks into frameworks for computer integrated manufacturing (CIM).

Commercial one- and two-dimensional process simulators have been integrated into the CAFE system through a simulation manager interface to the process flow representation (PFR). Full two-dimensional physical simulation of the MIT CMOS baseline process and research processes have been performed from CAFE.

Through a description formalism for device structural and behavioral goals, we hope to be able to extend traditional process and device simulation further towards actual design. Such goals may be direct structural goals (e.g., junction depth, sidewall slope), or they may be electrical, mechanical, or thermal goals (e.g., threshold voltage or impact ionization current at a specified bias).

2.14.5 Conceptual Graphs and Manufacturing Processes

Conceptual graphs are known to be relevant to a broad spectrum of problems in knowledge representation, including modeling of physical processes. We have been working on the development and application of conceptual models of semiconductor manufacturing processes, applying the conceptual graph formalism to the representation of state (wafer, physical variables, and equipment, including actuators and sensors) and relationship information. Specifically, we are investigating: (1) descriptions of the causal chain of effects in manufacturing; and (2) a predictor concept for expressing in detail how effects propagate.

Applications of the conceptual graph formalism to semiconductor manufacturing include causal reasoning about manufacturing processes, process synthesis, diagnosis, and control. In particular, the determination of potential opportunities for closed loop process control is becoming more important given the increasing quality and repeatability demands of semiconductor manufacturing. Analysis of the possibilities for control (e.g., of equipment state, physical variables, or intermediate or

final wafer state, via open or closed loop) may be made from the paths in the conceptual graph of process effects. Specific controller synthesis requires predictors detailing the relationship between states in the graph.

2.14.6 Determination of Doping Profiles from Electrical Device Data

We are exploring a novel method for the determination of a two-dimensional (2D) doping profile of a MOSFET using inverse modeling. With the advent of shallow junction technologies using preamorphization acceptor implants, e.g., indium, determination via simulation of the 2D doping profile near the drain/source junctions has been made more difficult. In the case of indium, the basic implant statistics and diffusion coefficients used in simulators are not as well-characterized as are the data for boron and arsenic. Inverse modeling provides an alternative methodology to understand the 2D doping profile. These methods utilize one-dimensional (1D) experimental doping profile data and measured device data. The 1D experimentally extracted long-channel doping profiles and measured device data consist of: 1D channel profile and 1D extension drain profile versus depth into the silicon; and the threshold voltage versus channel length, drain-induced barrier lowering versus channel length, and threshold voltage versus substrate bias as a function of channel length, respectively. We have found that it is possible to generate a 2D doping profile which matches the above data. To show that our result is unique, the experimentally extracted doping profile data at the center of the channel as a function of channel length is being incorporated into this analysis to reduce the chances of error. Different approaches are being explored for automation of the inverse doping profile modeling process, including both heuristic and purely numerical methods. Understanding the exact nature of the implant profiles enhances our ability to design next generation technologies.

2.15 Publications

2.15.1 Journal Article

Giles, M.D., D.S. Boning, G.R. Chin, W.C. Dietrich, M.S. Karasick, M.E. Law, P.K. Mozumder, L.R. Nackman, V.T. Rajan, D.M.H. Walker, R.H. Wang, and A.S. Wong. "Semiconductor Wafer Representation for TCAD." *IEEE Trans. Comput. Aided Design.* 13(1): 82 (1994).

2.15.2 Internal Publications

Antoniadis, D., D.E. Troxel, D. Boning, S. Gershwin, M. McIlrath, and J. White. "ARPA HPC/Microsystems PI Meeting - Poster Session and Demonstrations." CIDM Memo 94-14. MIT, 1994.

Bonvik, A.M. "A Program for Historical Sample Path Analysis of Cycle Times in Semiconductor Manufacturing." CIDM Memo 94-3. MIT, 1994.

Bonvik, A.M. "Design Proposal for the CAFE Scheduling Application." CIDM Memo 94-6. MIT, 1994.

Bonvik, A.M. "Estimating the Lead Time Distribution of Priority Lots in a Semiconductor Factory." CIDM Memo 94-13. MIT, 1994.

Bonvik, A.M. "Introduction to the CAFE Scheduling and Simulation Testbed." CIDM Memo 94-11. MIT, 1994.

Carney, J. "An Implementation of a Layered Message Passing System." CIDM Memo 94-15. MIT, 1994.

Fischer G. "New Traveller Generator and Operate Machine Speed Enhancements." CIDM Memo 94-8. MIT, 1994.

Fischer, G. "Release 5.3 of CAFE (Version 3.0)." CIDM Memo 94-10. MIT, 1994.

Gabbay, L. "Assessment of Caesar v1.1.0." CIDM Memo 94-9. MIT, 1994.

Gabbay, L. "Backgrounded Lot Traveller Report Caching." CIDM Memo 94-2. MIT, 1994.

Kwon, J. "First-Order Model for Remote Fabrication." CIDM Memo 94-18. MIT, 1994.

Kao, J. "Hardware Setup for Remote Microscope." CIDM Memo 94-19. MIT, 1994.

Kwon, J. "Zeroth-Order Model for Remote Fabrication." CIDM Memo 94-17. MIT, 1994.

Kwon, J., and J. Kao. "Remote Fabrication/Remote Inspection - Work in Progress." CIDM Memo 94-16. MIT, 1994.

Love, N. "SPC Charts for CAFE." CIDM Memo 94-4. MIT, 1994.

Stamatopoulos, M., S.B. Gershwin, and D.E. Troxel. "Organization of Data and Algorithms for Factory Design and Control." CIDM Memo 94-12. MIT, 1994.

Stamatopoulos, M., D.E. Troxel, and S.B. Gershwin. "Microsystems Factory Representation." CIDM Memo 94-7. MIT, 1994.

Troxel, D.E. "Caching of Data Base Objects in CAFE." CIDM Memo 94-5. MIT, 1994.

Troxel, D.E. "Tasks and PFR based Fabrication." CIDM Memo 94-1. MIT, 1994.

2.15.3 Meetings and Presentations

McIlrath, M.B. SWIM Meeting at SEMATECH, Austin, Texas, February 17, 1994.

Troxel, D.E., and M.B. McIlrath. CIM Application Framework Review at SEMATECH, Austin, Texas, May 4, 1994.

2.15.4 Theses

Love, N.S. *Statistical Process Control Charts for the Computer-Aided Fabrication Environment*. S.M. thesis. Dept. of Electr. Eng. and Comput. Sci., MIT, 1994.

Stamatopoulos, M. *A Factory Representation as a Design Tool in a Computer Integrated Manufacturing Environment*. S.M. thesis. Dept. of Electr. Eng. and Comput. Sci., MIT, 1994.

Unver, E.R. *Implementation of a Design Rule Checker for Silicon Wafer Fabrication*. M.E. thesis. Dept. of Electr. Eng. and Comput. Sci., MIT, 1994.

2.15.5 Conference Proceedings

Boning, D.S., and M.B. McIlrath. "Conceptual Graphs and Manufacturing Processes." Second International Conference on Conceptual Structures, College Park, Maryland, August 15, 1994.

Section 2 Digital Signal Processing

Chapter 1 Digital Signal Processing Research Program

Chapter 2 Advanced Telecommunications and Signal Processing Program

Chapter 3 Combined Source and Channel Coding for High-Definition Television

Chapter 1. Digital Signal Processing Research Program

Academic and Research Staff

Professor Alan V. Oppenheim, Professor Arthur B. Baggeroer, Professor Gregory W. Wornell, Giovanni Aliberti

Visiting Scientists and Research Affiliates

Dr. Bernard Gold, Dr. Bruce R. Musicus,¹ Dr. S. Hamid Nawab,² Dr. James C. Preisig, Dr. Ehud Weinstein³

Graduate Students

John R. Buck, Kevin M. Cuomo, Christoforos N. Hadjicostis, Steven H. Isabelle, Jacek Jachner, Warren M. Lam, Jeffrey T. Ludwig, John P. Mann, James M. Ooi, Haralabos C. Papadopoulos, Denis J. Peregrym, Brian M. Perreault, Michael D. Richard, Stephen F. Scherock, Li Shu, Andrew C. Singer, Shawn M. Verbout, Kathleen E. Wage, Kambiz C. Zangi

Technical and Support Staff

Margaret S. Beucler, Sally C. Santiago

1.1 Introduction

The field of digital signal processing grew out of the flexibility afforded by the use of digital computers in implementing signal processing algorithms and systems. It has since broadened into the use of a variety of both digital and analog technologies, spanning a broad range of applications, bandwidths, and realizations. The Digital Signal Processing Group carries out research on algorithms for signal processing and their applications. Current application areas of interest include signal enhancement, active noise cancellation, processing of speech, music and underwater acoustic signals, advanced beamforming for radar and sonar systems, and signal coding and transmission.

In some of our recent work, we have developed new methods for signal enhancement and noise cancellation with single or multisensor measurements. We have also been developing new methods for representing and analyzing fractal signals. This class of signals arises in a wide variety of physical environments and also has potential in problems involving signal design. We are also exploring potential uses of nonlinear dynamics and chaos theory for signal design and analysis.

In other research, we are investigating applications of signal and array processing to ocean and structural acoustics and geophysics. These problems require the combination of digital signal processing tools with a knowledge of wave propagation to develop systems for short time spectral analysis, wavenumber spectrum estimation, source localization, and matched field processing. We emphasize the use of real-world data from laboratory and field experiments such as the Heard Island Experiment for Acoustic Monitoring of Global Warming and several Arctic acoustic experiments conducted on the polar ice cap.

The group is also involved in research on new signal processing techniques for multiuser wireless communication systems. The intended applications range from mobile radio networks to indoor personal wireless systems to digital audio and television broadcast systems. Of special interest are broadband spread spectrum systems and code-division multiple access networks both for conventional and secure transmission.

Much of our work involves close collaboration with the Woods Hole Oceanographic Institution, MIT Lincoln Laboratory, and a number of high technology companies in the Boston Area.

¹ Bolt, Beranek, and Newman, Inc., Cambridge, Massachusetts.

² Associate Professor, Boston University, College of Engineering, Boston, Massachusetts.

³ Department of Electrical Engineering, Systems Division, Faculty of Engineering, Tel-Aviv University, Israel; adjunct scientist, Department of Applied Ocean Physics and Engineering, Woods Hole Oceanographic Institution, Woods Hole, Massachusetts.

1.2 Single Mode Excitation in the Shallow Water Acoustic Channel

Sponsor

MIT-Woods Hole Oceanographic Institute
Joint Graduate Program in Oceanographic Engineering

Project Staff

John R. Buck, Professor Alan V. Oppenheim, Dr. Josko Catipovic

Under appropriate conditions, the ocean acts as an acoustic waveguide with sound propagation occurring almost entirely through a discrete set of normal modes. Shallow water is one such condition. The goal of this research is to use a vertical array to excite the underwater channel so that, as nearly as possible, only one of these discrete modes is propagating into the far field. Knowing that the propagating field consisted originally of only a single mode, tomographic techniques can characterize and locate ocean features by observing the distribution of modes received downrange.

The problem of exciting only a single mode is easily solved analytically for the time-invariant case with a uniform sound speed profile and bottom topography. However, it is much more challenging in a realistic ocean environment due to propagation losses and coupling between modes caused by time-varying inhomogeneities in the medium and range-dependent irregularities in the seafloor and water column. Our strategy is to use a reference array of receivers at the start of the far field to obtain information about the coupling in the channel, and then adaptively update the source array weights to obtain a single mode at this reference array.

Currently, we are focusing our attention on developing and investigating strategies for estimating the coupling between the sources and the reference array, and tracking the variations in this coupling over time due to a variety of ocean processes. We are using detailed ocean acoustic modeling programs such as SAFARI to simulate a realistic ocean environment for the work.

1.3 Self-Synchronization of Chaotic Systems: Analysis, Synthesis, and Applications

Sponsors

Advanced Research Projects Agency/
U.S. Navy - Office of Naval Research
Grant N00014-93-1-0686
Lockheed Sanders Inc./
U.S. Navy - Office of Naval Research
Contract N00014-91-C-0125
U.S. Air Force - Office of Scientific Research
Grant AFOSR-91-0034

Project Staff

Kevin M. Cuomo, Professor Alan V. Oppenheim

Chaotic systems provide a rich mechanism for signal design and generation, with potential applications to communications and signal processing. Because chaotic signals are typically broadband, noise-like, and difficult to predict, they can be used in various contexts for masking information-bearing waveforms and as modulating waveforms in spread spectrum systems. A particularly useful class of chaotic systems are those which possess a self-synchronization property. Specifically, two identical chaotic systems may synchronize when the second system is driven by the first.⁴ This property enables chaotic systems to be exploited for private communications.⁵ A potential difficulty, however, is that the analysis and synthesis of chaotic systems is not well understood because of the highly nonlinear nature of these systems.

In this research, we are developing new methods for analyzing and synthesizing a class of high-dimensional dissipative chaotic systems which possess the self-synchronization property. For the class of chaotic systems that we consider, the synchronization is global and highly robust to perturbations in the drive signal. Synchronization error models are derived which provide a deeper understanding of the inherent robustness of these systems. We also develop several methods for embedding an information-bearing waveform in a chaotic carrier signal and for recovering the information at the synchronizing receiver. In addition, the practical aspects of synchronized chaotic

⁴ L.M. Pecora and T.L. Carroll, "Synchronization in Chaotic Systems," *Phys. Rev. Lett.* 64(8): 821-824 (1990); T.L. Carroll and L.M. Pecora, "Synchronizing Chaotic Circuits," *IEEE Trans. Circuits Syst.* 38(4): 453-456 (1991).

⁵ K.M. Cuomo, A.V. Oppenheim, and S.H. Isabelle, *Spread Spectrum Modulation and Signal Masking Using Synchronized Chaotic Systems*, RLE TR-570 (Cambridge: MIT Research Laboratory of Electronics, 1992); A.V. Oppenheim, G.W. Wornell, S.H. Isabelle, and K.M. Cuomo, "Signal Processing in the Context of Chaotic Signals," *Proc. IEEE ICASSP* 4: 117-120 (1992).

systems are demonstrated using a transmitter and receiver circuit with dynamics governed by the chaotic Lorenz system.⁶

1.4 Algebraic and Probabilistic Structure in Fault-Tolerant Computation

Sponsor

Advanced Research Projects Agency/
U.S. Navy - Office of Naval Research
Grant N00014-93-1-0686

Project Staff

Christoforos N. Hadjicostis, Professor George C. Verghese, Professor Alan V. Oppenheim

The traditional approach towards fault-tolerant computation has been modular redundancy. Although universal and simple, modular redundancy is inherently expensive and inefficient in its use of resources. Recently developed Algorithm Based Fault Tolerance (ABFT) techniques offer more efficient fault coverage, but their design is specific to each application. A particular class of ABFT techniques involves the design of arithmetic codes that protect elementary computations. For the case of computations that can be represented as operations in a group, the recent doctoral thesis by Beckmann⁷ has shown how to obtain a variety of useful results and systematic constructive procedures.

We are exploring the extension of this work to other algebraic structures. Our current studies indicate that much of Beckmann's framework can be generalized to the case of semigroups. In the other direction, we are examining refinements for the case of computations occurring in rings, modules, fields, or vector spaces. Beckmann's thesis shows how to take advantage of the underlying group structure in all these instances, but we expect that the additional structure that they possess can lead to stronger results and more efficient implementations of fault-tolerant schemes. Another objective of our research is to fold probabilistic models for failures and errors into the design and analysis of arithmetic codes. This will allow us to better characterize and design fault-tolerant systems.

1.5 Signal Processing Applications of Chaotic Dynamical Systems

Sponsors

AT&T Bell Laboratories Doctoral Support Program
Advanced Research Projects Agency/
U.S. Navy - Office of Naval Research
Grant N00014-89-J-1489
Grant N00014-93-1-0686
Lockheed Sanders, Inc./
U.S. Navy - Office of Naval Research
Contract N00014-91-C-0125
U.S. Air Force - Office of Scientific Research
Grant AFOSR-91-0034

Project Staff

Steven H. Isabelle, Professor Alan V. Oppenheim,
Professor Gregory W. Wornell

Researchers in areas ranging from animal behavior and medicine to economics and geophysics have found evidence of chaotic behavior in an enormous number of empirically gathered time series. Indeed, the sheer volume of apparently random phenomena which appear to have a deterministic explanation underscores the need for signal processing techniques specifically tailored to the unique characteristics of chaotic signals. In particular, because chaotic signals can generally be observed only indirectly, e.g., through some propagation channel or nonideal laboratory instrumentation, a signal's chaotic structure may be partially obscured by additive noise and convolutional distortion. Consequently, algorithms for reducing these distortions are an important component of signal processing systems for chaotic signals. This research explores effects of convolutional distortion on chaotic signals along with techniques for reducing such distortions.

In general, the limiting trajectory of a chaotic system will be a highly structured set in the state space, while the scalar output will appear erratic and unstructured. It is this "hidden" structure that makes the signal interesting and allows for a simple description. One measure of structure which has been used to characterize a chaotic signal is the fractal dimension of its strange attractor. We are

⁶ K.M. Cuomo and A.V. Oppenheim, *Synchronized Chaotic Circuits and Systems for Communications*, RLE TR-575 (Cambridge: MIT Research Laboratory of Electronics, 1992); K.M. Cuomo and A.V. Oppenheim, "Chaotic Signals and Systems for Communications," *Proc. IEEE ICASSP* 3: 137-140 (1993); K.M. Cuomo and A.V. Oppenheim, "Circuit Implementation of Synchronized Chaos with Applications to Communications," *Phys. Rev. Lett.* 71: 65-68 (1993).

⁷ P.E. Beckmann, *Fault-Tolerant Computation using Algebraic Homomorphisms*, RLE TR-580 (Cambridge: MIT Research Laboratory of Electronics, 1993).

examining the effect of convolution on fractal dimension and using these results to develop deconvolution algorithms. The major challenge here is developing optimal computationally efficient techniques which are uniformly applicable to a broad class of chaotic signals.

1.6 Wavelet-Based Representation and Algorithms for Generalized Fractal Signals

Sponsors

AT&T Bell Laboratories Doctoral Support Program
Advanced Research Projects Agency/
U.S. Navy - Office of Naval Research
Grant N00014-89-J-1489
Grant N00014-93-1-0686

Lockheed Sanders, Inc./
U.S. Navy - Office of Naval Research
Contract N00014-91-C-0125

U.S. Air Force - Office of Scientific Research
Grant AFOSR-91-0034

Project Staff

Warren M. Lam, Professor Gregory W. Wornell

While the $1/f$ family of fractal processes have become increasingly appealing for modeling statistically scale-invariant phenomena, we study a generalization of this signal model to account for more general scaling behavior found in a wide variety of natural phenomena. While many phenomena exhibit scaling behavior, a great number of them do so only over a finite range of scales. For example, while seafloor morphology is observed to be self-similar at fine scales, such scaling behavior is absent in long length scales due to the lack of correlation among points far apart.⁸ On the other hand, many phenomena exhibit scaling behavior which varies over scales. For instance, such varying scaling behavior is encountered in the study of diluted gels and colloidal aggregates in the field of materials science.⁹

In this work, we focus on the development of a class of generalized fractal processes for capturing such nonuniform scaling behavior. Exploiting the role of the wavelet transformation as a whitening filter for such processes, we formulate algorithms

for addressing a number of practical estimation problems involving such signals. Adopting a maximum-likelihood criterion and invoking an estimate-maximize algorithm, we derive consistent, computationally-efficient spectral parameter estimators which are useful for the classification of generalized fractals. We also formulate a Bayesian minimum mean-squares error signal estimation scheme which is directly applicable in a variety of signal separation and signal recovery scenarios.

1.7 Approximate Signal Processing

Sponsor

U.S. Navy - Office of Naval Research
Grant N00014-93-1-0686

Project Staff

Jeffrey T. Ludwig, Professor S. Hamid Nawab

In any given problem-solving domain, an algorithm, A , may be considered an approximation to another algorithm, B , provided A is more computationally efficient than B by virtue of A being designed to yield a lower quality answer than B . Such approximate algorithms are said to carry out *approximate processing* with respect to the problem-solving domain under consideration. The need for such algorithms arises in applications with real-time constraints.

Within the context of real-time systems, a signal processing task may have to be performed within a time interval whose duration may or may not be determined prior to run time. In the case of a predetermined time allocation, an approximate processing algorithm may be used to obtain the highest quality answer possible within the allotted time. In cases where the time allocation is not predetermined, it is desirable to use an approximate processing algorithm which produces an answer of improving quality as a function of time. This allows the algorithm to be terminated whenever desired and the quality of the resulting answer is directly proportional to the actual execution time. These types of approximate processing algorithms are said to carry out *incremental refinement* of their answers.

In previous research it has been demonstrated that approximate processing algorithms can be effective

⁸ J.A. Goff and T.H. Jordan, "Stochastic Modeling of Seafloor Morphology: Inversion of Sea Beam Data for Second-Order Statistics," *J. of Geophys. Res.* 93(B11): 13589-13608 (1988).

⁹ *Fractals in the Natural Sciences*, eds. M. Fleischmann, D.J. Tildesley, and R.C. Ball (Princeton, New Jersey: Princeton University Press, 1989), pp. 35-53.

in the real-time analysis of music, speech, and synthetic signals. For example, approximations to the short-time Fourier transform (STFT) have been shown to retain prominent time-frequency characteristics of such signals while improving computational efficiency by an order of magnitude over FFT-based calculations of the exact STFT.

Our aim is to develop a formal structure for using approximate processing concepts in designing novel signal processing algorithms in areas such as time-frequency analysis, cepstral analysis, multi-pass analysis, adaptive filtering, and adaptive beamforming.

1.8 CDMA for Digital Storage

Sponsor

U.S. Air Force - Office of Scientific Research
Grant AFOSR-91-0034

Project Staff

James M. Ooi, Professor Gregory W. Wornell

Code division multiple access (CDMA) is an active area of communications research. It is a method by which multiple users superpose their transmissions on top of one another throughout an entire symbol period and throughout a larger frequency bandwidth than required. Although the technique was once primarily associated with military spread spectrum systems, designers today are finding that it has properties which are desirable outside of military use. These properties include automatic interference reduction when other users are not transmitting, ease of adding new users, graceful degradation as channel capacity is exceeded, and robustness against intentional jamming and multipath interference.

The goal of this research is to extend the CDMA concept to computer storage devices in order to reap some of the above advantages. The analogous behavior on which the work will focus is graceful degradation as capacity is exceeded, tolerance to faulty memory, ease of adding new users, and an automatic improvement in fidelity as the storage requirements decrease. It is also hoped that this may also lead to a more general theory of distributed coding for the storage channel.

1.9 Estimation and Detection of a Class of Chaotic Signals

Sponsors

Advanced Research Projects Agency/
U.S. Navy - Office of Naval Research
Grant N00014-89-J-1489
Grant N00014-93-1-0686
U.S. Air Force - Office of Scientific Research
Grant AFOSR-91-0034

Project Staff

Haralabos C. Papadopoulos, Professor Gregory W. Wornell

Chaos arises in a broad range of physical and man-made systems. Naturally, there is a need for efficient and robust algorithms for estimation and detection of chaotic signals in the presence of noise. We have obtained Maximum Likelihood algorithms for signal filtering, smoothing, and prediction for a class of chaotic signals, which although nonlinear, possess very convenient recursive implementations that are efficient both in terms of computation and storage. Generalized estimation algorithms are suggested for a much broader class of chaotic signals.

The pseudorandom, broadband characteristics, and ease of generation of chaotic signals make them appealing candidates for signaling waveforms in secure and low probability of intercept communication systems. We explore the viability of spread spectrum communication schemes using chaotic signals, and consider generalized antipodal coding schemes which possess attractive properties for secure communications. Optimal discrimination strategies for a class of these chaotic signaling schemes and robust, computationally efficient demodulators have been obtained. Monte Carlo simulations reveal that chaotic signaling is potentially useful for the particular communication applications mentioned above.

1.10 Real Time Active Noise Cancellation

Sponsor

National Science Foundation Fellowship

Project Staff

Brian M. Perreault, Professor Alan V. Oppenheim

In many industrial and consumer settings, there often exists undesired acoustic noise. In many cases, the noise is obtrusive enough to warrant an

effort to reduce its effect. In situations where the noise cannot be reduced using physical, passive methods, active noise cancellation (ANC) techniques are a suitable alternative. Many types of noise have certain predictable characteristics; active noise cancellation exploits these characteristics, and uses destructive interference from a secondary acoustic source to eradicate the noise.

One algorithm for active noise cancellation results from approaching the problem from a control perspective. If the noise is measured at a single sensor, the essence of the technique is to use a control algorithm to give feedback through an actuator, constraining the measurement at the sensor to zero.

In many applications, such as airplane cockpits, high levels of narrowband noise are present. This type of algorithm may be useful for the cancellation of these narrow bands of noise. This algorithm is being investigated to determine its effectiveness in such an environment. A set of headphones, utilizing a microphone and speaker in each ear cup, is being developed to cancel the cockpit noise. Such a set of headphones is very desirable for a pilot, especially considering that passive attenuation of the headphones is not enough to fully compensate for the noise.

Digital predictive techniques are being used in conjunction with analog to digital (A/D) and digital to analog (D/A) converters in order to implement the active noise cancellation techniques. A digital signal processor is employed to execute the algorithms, due to its high computational ability. A flexible set of hardware has been developed in order to evaluate different ANC algorithms in real time.

1.11 State and Parameter Estimation with Chaotic Systems

Sponsors

Augmentation Awards/ Science and Engineering
Research Training Program
Lockheed Sanders, Inc./
U.S. Navy - Office of Naval Research
Contract N00014-91-C-0125

U.S. Air Force - Office of Scientific Research
Grant F49620-92-J-0255
Grant AFOSR-91-0034
U.S. Navy - Office of Naval Research
Grant N00014-93-1-0686

Project Staff

Michael D. Richard, Professor Alan V. Oppenheim

Chaotic systems are nonlinear dynamical systems characterized by extreme sensitivity to initial conditions. A signal generated by a chaotic system may appear random, despite its having been generated by a low-order, deterministic dynamical system. Both random and chaotic signals lack long-term predictability; but, in contrast to truly random signals, chaotic signals exhibit short-term predictability. Evidence of chaotic behavior has been reported in many diverse disciplines including physics, biology, engineering, and economics.

We are exploring techniques for state and parameter estimation with chaotic systems. We have implemented the extended Kalman filter,¹⁰ a recursive state estimator for nonlinear systems, and several related algorithms¹¹ and have evaluated their effectiveness as state estimators for chaotic systems. Preliminary results have shown these algorithms to perform reasonably well. But, these results have also shown these algorithms to suffer potentially unacceptable deficiencies when applied to chaotic systems.

More recently, we have developed and begun testing several related novel, state-estimation techniques loosely motivated by maximum likelihood state estimation. The techniques exploit a distinguishing property of all chaotic systems—the simultaneous existence of stable and unstable manifolds.¹² The combination of these techniques with an estimate-maximize (EM) algorithm is also being considered. Finally, we plan to ascertain the value of various state-estimation techniques in improving the short-term predictability of chaotic signals.

¹⁰ A. Jazwinski, *Stochastic Processes and Filtering Theory* (New York: Academic Press, 1970); M.D. Richard, *State Estimation with Discrete-Time Chaotic Systems*, RLE TR-571 (Cambridge: MIT Research Laboratory of Electronics, 1992).

¹¹ A. Willsky, Course Notes for 6.433 "Recursive Estimation," Unpublished, 1989.

¹² J. Eckmann and D. Ruelle, "Ergodic Theory of Chaos and Strange Attractors," *Rev. of Mod. Phys.* 57(3) Part 1: 617-656 (1985).

1.12 Model Based Analysis of Music

Sponsors

Defense Advanced Research Projects Agency/
U.S. Navy - Office of Naval Research
Grant N00014-89-J-1489

National Science Foundation Graduate Fellowship

Project Staff

Stephen F. Scherock, Dr. Bernard Gold

Many digital audio signals can be broadly classified as speech or music. Speech signals have been studied extensively since the 1950s, for the purposes of automatic speech recognition, production, and data compression. Work has advanced toward each of these goals in part because of the development of models for speech production and recognition. While physically based models exist for music production, applying these models to synthetic music production or data compression has not been fully exploited. This research involves model-based compression of music from a single instrument, the trumpet.

1.13 Nonlinear Models for Signal Processing

Sponsors

Advanced Research Projects Agency/
U.S. Navy - Office of Naval Research
Grant N00014-89-J-1489
Grant N00014-93-1-0686

Lockheed Sanders Inc./
U.S. Navy - Office of Naval Research
Contract N00014-91-C-0125

Project Staff

Andrew C. Singer, Professor Alan V. Oppenheim

This research involves the use of nonlinear system models in signal processing. Predominantly, linear models and algorithms have been employed in this field due to the tractability of their analysis and the richness of the class of signals for which these models are well-suited. However, by trading complexity for tractability, we can further broaden the boundaries of signal processing. For example, we have recently shown that nonlinear signal modeling techniques are both useful and practical for modeling a variety of signals for which linear techniques have proven inadequate. Further, we have begun to find practical applications for nonlinear dynamic systems in chaos, which until recently were thought of as more paradoxical than practical. Another interesting phenomenon whose curious behavior

has crossed many disciplines of science, is the theory of solitons. It is our goal to exploit the behavior these solitary waves and other nonlinear phenomena in search of new paradigms and new directions in signal processing.

1.14 Environmental Robustness in Automatic Speech Recognition

Sponsor

Maryland Procurement Office
Contract MDA904-93-C-4180

Project Staff

Shawn M. Verbout, Professor Alan V. Oppenheim

As the technology in automatic speech recognition (ASR) becomes increasingly advanced, greater consideration is given to speech as a viable means of interaction between humans and machines. However, as more ASR systems become incorporated into real-world applications, greater attention must be devoted to making these systems robust with respect to changes in their operating environments. The need for environmental robustness is clear when we consider the difficulties presently encountered in attempting to make ASR systems yield consistently high performance in practical settings. In particular, even the most sophisticated ASR systems today are extremely sensitive to variations in recording conditions, and must be carefully retrained for each new environment in which they are deployed.

In the context of ASR, environmental variability is a broad notion encompassing the various changes that can occur in any factor affecting acoustic measurements. For example, environmental changes can be due to physiological differences between different speakers, variations in loudness for a single speaker, differences in the physical relationship between the speaker and the microphone, changes in the ambient noise level, differences in recording equipment, and differences in room acoustics. In addition to these factors, which may be termed "physical," there are yet other environmental factors that may be viewed as "situational." For example, consider the operation of an ASR system in the relatively benign setting of a typical business office. In this environment, a speech signal can be corrupted during a recording session by unanticipated acoustic events such as sudden activation of a manifold system, intermittent keyboard clicking, background conversations, slamming doors and file cabinet drawers, and reverberation due to acoustic reflections from walls, floors, and various objects in the room.

The long-term objective of our research in this area is to determine the signal processing technology required to make the performance of an ASR system relatively insensitive to these kinds of changes in the recording environment, while keeping the performance at a consistently high level. One viable method for making an ASR system more robust is to replace the single sensor in a typical recording environment with multiple sensors located in various parts of the room. This multisensor approach affords some redundancy in the measurement of the primary speech signal, and simultaneously provides a diverse set of reference measurements for noise events throughout the room. The resulting multiple signal measurements may then be processed to extract the primary speech signal from the interfering noise sources.¹³ Important intermediate goals in our investigation of the multisensor robustness approach will include quantifying the performance of an existing ASR system with and without preprocessing of the sensor measurements using algorithms such as those mentioned above.

1.15 Active Noise Cancellation

Sponsors

Advanced Research Projects Agency/
U.S. Navy - Office of Naval Research
Grant N00014-89-J-1489
Grant N00014-93-1-0686

U.S. Air Force - Office of Scientific Research
Grant AFOSR-91-0034

Project Staff

Kambiz C. Zangi, Professor Alan V. Oppenheim

Unwanted acoustic noise is a by-product of many industrial processes and systems. With active noise cancellation (ANC), one introduces secondary noise sources to generate an acoustic field that interferes destructively with the unwanted noise, thereby eliminating it. Examples of such unwanted noise include machinery noise, aircraft cabin noise, and fan noise.

Traditional active noise cancellation systems assume that the statistical characteristic of the primary noise is known *a priori*. Furthermore, almost all of the existing systems use two microphones, and as result suffer from an *acoustic feedback* between the canceling speaker and the input microphone.¹⁴

We have developed an adaptive active noise cancellation system which only uses one microphone, and therefore has no feedback problem. This system uses the estimate maximize (EM) algorithm to simultaneously estimate the noise statistics and the transfer function between the canceling speaker and the microphone. An optimal canceling signal is then generated based on these estimates.¹⁵

We have also developed a two microphone version of the above system which does not suffer from the feedback problem and is more intelligent in using the outputs of the microphones.

We are currently studying the problem of noise cancellation in a volume. A topic of fundamental interest is to find analytically simple ways to describe the sound field over a volume from measurements made at a finite set of points in that volume. Similarly, we would like to find ways to alter the sound field in a desired manner using only a finite number of sources.

1.16 Oceanographic Signal Processing

Sponsors

U.S. Navy - Office of Naval Research
Grant N00014-91-J-1628
University of California SCRIPPS
Contract 1003-73-59

Project Staff

Professor Arthur B. Bagherer

Our research programs involve the application of signal and array processing to problems in ocean acoustics and geophysics. They require an understanding of both signal processing and wave propaga-

¹³ K.M. Cuomo, A.V. Oppenheim, and S.H. Isabelle, *Spread Spectrum Modulation and Signal Masking Using Synchronized Chaotic Systems*, RLE TR-570 (Cambridge: MIT Research Laboratory of Electronics, 1992); E. Weinstein, M. Feder, and A.V. Oppenheim, *Multi-Channel Signal Separation Based on Decorrelation*, RLE TR-573 (Cambridge: MIT Research Laboratory of Electronics, 1992).

¹⁴ L.J. Eriksson, M.C. Allie, and C.D. Bremigan, "Active Noise Control Using Adaptive Digital Signal Processing," *Proc. ICASSP 4*: 2594-2597 (1988).

¹⁵ E. Weinstein, A. Oppenheim, and M. Feder, *Signal Enhancement Using Single and Multi-Sensor Measurements*, RLE TR-560 (Cambridge: MIT Research Laboratory of Electronics, 1990); K. Zangi, "A New Two Sensor Active Noise Cancellation Algorithm," *Proc. ICASSP 1*: (1992).

gation; moreover, most use data from laboratory or field experiments, so an appreciation of real world issues such as noise, sensor calibrations and modeling errors is needed. Several of the topics provide opportunities to participate in oceanographic cruises.

1.16.1 Acoustic Thermometry of Ocean Climate

The Heard Island Feasibility Test demonstrated that coded acoustic signal can be transmitted over 10,000 km ranges. This has led to the Acoustic Thermometry of Ocean Climate (ATOC) program by ARPA. A network of acoustic sources and receivers is being deployed in the Pacific ocean this spring to monitor the ocean by measuring changes in acoustic travel times. These changes will be used to infer temperature changes.

1.16.2 Directional Spectrum Estimation: a Maximum Likelihood Method

Project Staff

John P. Mann, Professor Arthur B. Baggeroer

Antenna arrays can be used to estimate the direction of arrival of signals incident upon the array. Capon's minimum variance method is commonly used to estimate the frequency spectrum arriving from a desired direction. However, this method has some limitations. A finite set of samples from the array is used to form a sample covariance, which must then be inverted to calculate the minimum variance estimate of the spectrum. In order for the sample covariance to provide reasonable results, it has been shown that the number of samples necessary is approximately twice the number of sensors in the array.¹⁶ In cases where the signal environment changes fast enough, this requirement becomes a problem. Estimates need to be updated faster than is possible given this constraint.

In this research, we will investigate methods of directional spectrum estimation when the number of samples available is limited. In addition to some commonly used algorithms, a maximum likelihood method for estimating frequency wavenumber spectra has been derived and will be evaluated and

refined.¹⁷ The performance of the different methods will be compared through simulations on a series of different array geometries and signal environments. The effect of errors in the gain and position of sensor elements will also be investigated.

1.16.3 Single Mode Excitation in the Shallow Water Acoustic Channel

Project Staff

Denis J. Peregrym, Professor Arthur B. Baggeroer

Acoustic signals can be described as a sum of normal modes or eigenfunctions of a waveguide. Under certain conditions in shallow water, a small set of discrete modes carries almost all of the acoustic energy. Our goal is to design a source which excites only a single mode in the waveguide at a reference receiver some distance down the guide from the source. The signal at this receiver is used to adaptively update the source weights and converge to a single mode. Our current research involves investigating the field shape in the waveguide and deciding on an optimum position for the reference array in the near field/far field boundary. In addition, we are investigating how the mode shapes or weights at the source array required to generate a single mode can be used to characterize the channel.

1.16.4 Estimation of Normal Mode Amplitudes for Underwater Acoustics

Project Staff

Kathleen E. Wage, Professor Arthur B. Baggeroer

In underwater acoustics, signals are often efficiently represented as weighted sums of the normal modes or eigenfunctions associated with the waveguide. The weights are usually estimated from data obtained with a vertical array of hydrophones. The purpose of this research is to investigate methods for estimating the modal amplitudes (i.e., weights). In addition to studying modal amplitude estimation techniques previously developed, this work also applies several bearing estimation algorithms to the modal amplitude problem. A least squares formulation is the most common in the literature, and

¹⁶ I.S. Reed, J.D. Mallett, and L.E. Brennan, "Rapid Convergence Rate in Adaptive Arrays," *IEEE Trans. Aerosp. Electron. Syst.* AES-10: 853-863 (1974).

¹⁷ A.B. Baggeroer, "A True Maximum Likelihood Method for Estimating Frequency Wavenumber Spectra," *Proc. Inst. Acoust.* 13(2): 217-224 (1991).

several variations of this generalized approach are under consideration. The three-bearing estimation algorithms which will be implemented were developed in the context of direction-of-arrival location for diversely-polarized antennas.¹⁸ This thesis considers the effects of noise, modeling assumptions, mode coherence, and multiple modal sources on the behavior of each estimator.

The motivation for this work is twofold. First, modal decomposition is a natural way to approach solutions to the acoustic wave equation, and a knowledge of the modal structure is often helpful in exploring the effects of a particular channel on a transmitted signal. Specifically, mode attenuation is

important in many acoustic and oceanographic processes, e.g., Kuperman and Ingenito have explored the attenuation of modes due to scattering at rough boundaries.¹⁹ A second motivating factor is that the modal amplitudes are useful in matched mode processing and in matched field tomography. Recent papers indicate that source range and depth information may be obtained by performing matched field beamforming using the modal coefficients.²⁰ Shang has also used adiabatic normal mode theory to develop a method for acoustic tomography.²¹ Obviously, the ability to estimate the mode coefficients accurately and efficiently is essential to the success of these types of algorithms.

¹⁸ E.R. Ferrara and T.M. Parks, "Direction Finding with an Array of Antennas Having Diverse Polarizations," *IEEE Trans. Antennas Propagat.* AP-31(2): 231-236 (1983).

¹⁹ W.A. Kuperman and F. Ingenito, "Attenuation of the Coherent Component of Sound Propagating in Shallow Water with Rough Boundaries," *J. Acoust. Soc. Am.* 61(5): 1178-1187 (1977).

²⁰ S.M. Jesus, "Normal-mode Matching Localization in Shallow Water: Environmental and System Effects," *J. Acoust. Soc. Am.* 90(4): 2034-2041 (1991); E.C. Shang, "An Efficient High-resolution Method of Source Localization Processing in Mode Space," *J. Acoust. Soc. Am.* 86(5): 1960-1967 (1989); T.C. Yang, "A Method of Range and Depth Estimation by Modal Decomposition," *J. Acoust. Soc. Am.* 82(2): 1736-1745 (1987).

²¹ E.C. Shang, "Ocean Acoustic Tomography Based on Adiabatic Mode Theory," *J. Acoust. Soc. Am.* 85(4): 1531-1537 (1989).

Chapter 2. Advanced Telecommunications and Signal Processing Program

Academic and Research Staff

Professor Jae S. Lim

Visiting Scientists and Research Affiliates

Dr. Hae-Mook Jung

Graduate Students

John G. Apostolopoulos, David M. Baylon, Shiufun Cheung, Raynard O. Hinds, Kyle K. Iwai, Peter A. Monta, Julien J. Nicolas, Alexander Pfajfer, Eric C. Reed, Lon E. Sunshine, Carl Taniguchi, Chang Dong Yoo

Technical and Support Staff

Cindy LeBlanc, Denise M. Rossetti

2.1 Introduction

The present television system was designed nearly 40 years ago. Since then, there have been significant developments in technology which are highly relevant to the television industries. For example, advances in very large scale integration (VLSI) technology and signal processing make it feasible to incorporate frame-store memory and sophisticated signal processing capabilities into a television receiver at a reasonable cost. To exploit this new technology in developing future television systems, Japan and Europe have established large laboratories, funded by government or industry-wide consortia. The need for this type of organization in the United States was considered necessary for the broadcasting and equipment manufacturing industries. In 1983 the advanced television research program (ATRP) was established at MIT by a consortium of U.S. companies.

The major objectives of the ATRP are:

- To develop the theoretical and empirical basis for improving existing television systems, as well as the design of future television systems;
- To educate students through television-related research and development and motivate them to pursue careers in television-related industries;
- To facilitate the continuing education of scientists and engineers already working in the industry;
- To establish a resource center where problems and proposals can be brought for discussion and detailed study; and

- To transfer the technology developed from the ATRP program to the television-related industries.

Research areas of the program include the design of a receiver-compatible advanced television (ATV) system and digital ATV system, as well as the development of transcoding methods. Significant advances have already been made in some of these research areas. A digital ATV system was designed and tested in the fall of 1992 by the FCC for its possible adoption as the U.S. HDTV standard for terrestrial broadcasting. Some elements of this system are likely to be included in the U.S. HDTV standard.

In addition to research on advanced television systems, our research program also includes research on speech processing. Current research topics include the development of a new speech model and algorithms to enhance speech degraded by background noise.

2.2 ATRP Facilities

The ATRP facilities are currently based on a network of eight SUN workstations and three DecStation 5000 workstations. There is approximately 14.0 GB of disk space, distributed among the various machines. Attached to one of the SUN workstations is a VTE display system with 256 MB of RAM. This display system is capable of driving the Sun-4 monitors, or a 29-inch Conrac monitor, at rates up to 60 frames/sec. In addition to displaying high-resolution real-time sequences, the ATRP facilities include a Metheus frame buffer which drives a

Sony 2Kx2K monitor. For hard copy output, the lab uses a Kodak XL7700 thermal imaging printer which can produce 2Kx2K color or black and white images on 11x11 inch photographic paper.

Other peripherals include tape drives (Exabyte 8 mm and AMPEX DST600), a 16-bit digital audio interface with two channels and sampling rates up to 48 kHz per channel, and an audio workstation with power amplifier, speakers, CD player, tape deck, etc. In addition, the lab has a 650 MB optical disk drive, a CD-ROM drive, two laser printers, and one color printer. The ATRP facilities also include a PowerMacintosh, two Mac II computers, and an Apple LaserWriter for preparing presentations.

A fast network (FDDI) is under consideration to augment the current 10 Mbps Ethernet. The new network would enable much faster data transfer to display devices and would support large NFS transfers more easily.

2.3 Signal Representations for Very-low-bit-rate Video Compression

Sponsors

AT&T Fellowship
Advanced Telecommunications Research Program

Project Staff

John G. Apostolopoulos

Video, which plays an important role in many applications today, is expected to become even more important in the near future with the advent of multimedia and personal communication devices. The large amount of data contained in a video signal, together with the limited transmission capacity in many applications, requires the compression of a video signal. A number of video compression algorithms have been developed for different applications from video-phone to high-definition television. These algorithms perform reasonably well at respective bit rates of 64 kb/s to tens of Mb/s. However, many applications, particularly those associated with portable or wireless devices, will probably be required in the near future to operate at considerably lower bit rates, possibly as low as 10 kb/s. The video compression methodologies developed to date cannot be applied at such low bit rates. The goal of this research is to create efficient signal representations which can lead to acceptable video quality at extremely low bit rates.

Conventional video compression algorithms may be described as block-based coding schemes; they

partition each frame into square blocks and then independently process each block. Examples of these compression techniques include block-based temporal motion-compensated prediction and spatial block discrete-cosine transformation. Block-based processing is the basis for virtually all video compression systems today because it is a simple and practical approach for achieving acceptable video quality at required bit rates. However, block-based coding schemes can not effectively represent a video signal at very low bit rates because the source model is extremely limited: Block-based schemes inherently assume a source model of (translational) moving square blocks, but a typical video scene is not composed of translated square blocks. In effect, block-based schemes impose an artificial structure on the video signal before encoding, instead of exploiting the structure inherent to a particular video scene.

The goal of this research is to develop signal representations that better match the structure that exists within a video scene. By identifying and efficiently representing this structure, it may be possible to produce acceptable video quality at very low bit rates. For example, since real scenes contain objects, a promising source model is one with two- or three-dimensional moving objects. This approach may provide a much closer match to the structure in a video scene than the block-based schemes mentioned above. Three fundamental issues must be addressed for the success of this approach: (1) appropriate segmentation of the video scene into objects, (2) encoding the segmentation information, and (3) encoding the object interiors. In regard to the third issue, significant statistical dependencies exist in regions belonging to each object and must be exploited. Conventional approaches to encoding arbitrarily shaped regions are typically simple extensions of the block-based approaches, and hence suffer from inefficiencies. A number of novel methods for efficiently representing the interior regions have been developed.

2.3.1 Publication

Apostolopoulos, J., A. Pfajfer, H.M. Jung, and J.S. Lim. "Position-Dependent Encoding." *Proceedings of ICASSP V*: 573-576 (1994).

2.4 Constant Quality Video Coding

Sponsors

INTEL Fellowship
Advanced Telecommunications Research Program

Project Staff

David M. Baylon

Traditional video compression algorithms for fixed bandwidth systems typically operate at fixed targeted compression ratios. A problem with fixed bit rate systems is that video quality can vary greatly within an image and across an image sequence. In regions of low image complexity, quality is high, whereas in regions of high image complexity, quality can be low due to coarse quantization.

Recently, with the development of asynchronous transfer mode (ATM) switching for broadband networks, there has been increasing interest in variable rate video coding. Asynchronous channels can use bandwidth efficiently and provide a time varying bit rate well suited for the nonstationary characteristics of video. By allowing the compression ratio to vary with scene contents and complexity, constant quality video can be delivered.

This research focuses on methods for encoding high-definition video to yield constant high quality video while minimizing the average bit rate. Simple mean square error approaches are insufficient for measuring video quality, therefore distortion functions which incorporate visual models are being investigated. Adaptive quantization schemes to maintain constant quality are being studied also. This study includes development of a spatially and temporally adaptive weighting matrix for frequency coefficients based upon a visual criterion. For example, high-frequency coefficients corresponding to edges can be more visually important than those corresponding to texture. By studying how to vary bit allocation with scene contents to maintain a specified level of quality, a statistical characterization of the variable bit rate video coding can be obtained.

2.5 Signal Representations in Audio Compression

Sponsor

Advanced Telecommunications Research Program

Project Staff

Shiufun Cheung

The demand for high-fidelity audio in transmission systems such as digital audio broadcast (DAB) and high-definition television (HDTV) and in commercial products such as MiniDisc and Digital Compact Cassette has generated considerable interest in audio compression schemes. The common objec-

tive is to achieve high quality at a rate significantly smaller than the 16 bits/sample used in current CD and DAT systems. We have been considering applications to HDTV; an earlier implementation, the MIT Audio Coder (MIT-AC), is one of the systems that was considered for inclusion in the U.S. HDTV standard. In this research, we seek to build upon our previous efforts by studying an important aspect of audio coder design: the selection of an appropriate and efficient acoustic signal representation.

In conventional audio coders, short-time spectral decomposition serves to recast the audio signal in a representation that is not only amenable to perceptual modeling but also conducive to deriving transform coding gains. This is commonly achieved by a multirate filter bank, or, equivalently, a lapped transform.

In the first stage of this research, we replace our original uniform multirate filter bank with a nonuniform one. Filter banks with uniform subbands, while conceptually simpler and easier to implement, force an undesirable tradeoff between time and frequency resolution. For example, if the analysis bandwidth is narrow enough to resolve the critical bands at low frequencies, poor temporal resolution can result in temporal artifacts such as the "pre-echo" effect. A nonuniform filter bank, on the other hand, allows enough flexibility to simultaneously satisfy the requirements of good pre-echo control and frequency resolution consistent with critical-band analysis. In our prototype implementation, we use a hierarchical structure based on a cascade of M-band perfect-reconstruction cosine-modulated filter banks. Testing the new representation has shown improvement over a uniform filter bank scheme. While pre-distortion still exists in transient signals, listening sessions show that pre-echo is inaudible with the new filter bank.

In the second stage of this research, we are studying the incorporation of biorthogonality into Malvar's lapped transforms. Lapped transforms are popular implementations of cosine-modulated filter banks. They form the major building blocks in both our uniform and nonuniform signal decomposition schemes. Conventional lapped transforms are designed to be orthogonal filter banks in which the analysis and synthesis filters are identical. By allowing the analysis and synthesis filters to differ, we create a biorthogonal transform with additional degrees of freedom over the orthogonal case. This increased flexibility is very important for achieving a spectral analysis that approximates the critical bands of the human ear well enough for subsequent perceptual modeling.

2.5.1 Publications

Cheung, S., and J.S. Lim. "Incorporation of Biorthogonality into Lapped Transforms for Audio Compression." *Proceedings of ICASSP*. Forthcoming.

Monta, P.A., and S. Cheung. "Low Rate Audio Coder with Hierarchical Filter Banks and Lattice Vector Quantization." *Proceedings of ICASSP II*: 209-212 (1994).

2.6 Pre-Echo Detection and Reduction

Sponsor

Advanced Telecommunications Research Program

Project Staff

Kyle K. Iwai

In recent years, there has been an increasing interest in data compression for storage and data transmission. In the field of audio processing, various varieties of transform coders have successfully demonstrated reduced bit rates while maintaining high audio quality. However, there are certain coding artifacts which are associated with transform coding. The pre-echo is one such artifact. Pre-echos typically occur when a sharp attack is preceded by silence. Quantization noise added by the coding process is normally hidden within the signal. When the coder is stationary over the window length, an assumption breaks down in a transient situation. The noise is unmasked in the silence preceding the attack, creating an audible artifact called a pre-echo.

If the length of the noise can be shortened to about 5 ms, psycho-acoustic experiments tell us that the noise will not be audible. Using a shorter window length shortens the length of the pre-echo. However, shorter windows also have poorer frequency selectivity and poorer coder efficiency. One solution is to use shorter windows only when there is a quiet region followed by a sharp attack.

In order to use adaptive window length selection, a detector had to be designed. A simple detector was implemented which compares the variance within two adjacent sections of audio. In a transient situation, the variance suddenly increases from one section to the next. The coder then uses short windows to reduce the length of the pre-echo, rendering the artifact inaudible.

2.7 Video Source Coding for High-Definition Television

Sponsor

Advanced Telecommunications Research Program

Project Staff

Peter A. Monta

Efficient source coding is the technology for high-definition television (HDTV) which will enable broadcasting over the relatively narrow channels (e.g., terrestrial broadcast and cable) envisioned for the new service. Coding rates are on the order of 0.3 bits/sample, and high quality is a requirement. This work focuses on new source coding techniques for video relating to representation of motion-compensated prediction errors, quantization and entropy coding, and other system issues.

Conventional coders represent video with the use of block transforms with small support (typically 8x8 pixels). Such independent blocks result in a simple scheme for switching a predictor from a motion-compensated block to a purely spatial block; this is necessary to prevent the coder from wasting capacity in some situations.

Subband coders of the multiresolution or wavelet type—with their more desirable localization properties, lack of "blocking" artifacts, and better match to motion-compensated prediction errors—complicate this process of switching predictors, since the blocks now overlap. A novel predictive coding scheme is proposed in which subband coders can combine the benefits of good representation and flexible adaptive prediction.

Source-adaptive coding is a way for HDTV systems to support a more general imaging model than conventional television. With a source coder that can adapt to different spatial resolutions, frame rates, and coding rates, the system may then make tradeoffs among the various imagery types (for example, 60 frames/s video, 24 frames/s film, highly detailed still images, etc.). In general, this is an effort to make HDTV more of an image transport system rather than a least-common-denominator format to which all sources must either adhere or be adjusted to fit. These techniques are also applicable to NTSC to some extent; one result is an algorithm for improved chrominance separation for the case of "3-2" NTSC, that is, NTSC upsampled from film.

2.8 Transmission of HDTV Signals in a Terrestrial Broadcast Environment

Sponsor

Advanced Telecommunications Research Program

Project Staff

Julien J. Nicolas

High-definition television (HDTV) systems currently being developed for broadcast applications require 15-20 Mbps to yield good quality images for roughly twice the horizontal and vertical resolutions of the current NTSC standard. Efficient transmission techniques must be found in order to deliver this signal to a maximum number of receivers while respecting the limitations stipulated by the FCC for over-the-air transmission. This research focuses on the principles that should guide the design of such transmission systems.

The major constraints related to the transmission of broadcast HDTV include (1) a bandwidth limitation (6 MHz, identical to NTSC), (2) a requirement for simultaneous transmission of both NTSC and HDTV signals on two different channels (Simulcast approach), and (3) a tight control of the interference effects between NTSC and HDTV, particularly when the signals are sharing the same frequency bands. Other considerations include complexity and cost issues of the receivers and degradation of the signal as a function of range.

A number of ideas are currently being studied; most systems proposed to date use some form of forward error-correction to combat channel noise and interference from other signals. The overhead data reserved for the error-correction schemes represents up to 30 percent of the total data, it is therefore well worth trying to optimize these schemes. Current work is focusing on the use of combined modulation/coding schemes capable of exploiting the specific features of the broadcast channel and the interference signals. Other areas of interest include the use of combined source/channel coding schemes for HDTV applications and multi-resolution coded modulation schemes.

2.8.1 Publication

Nicolas, J., and J.S. Lim. "On the Performance of Multicarrier Modulation in a Broadcast Multipath Environment." *Proceedings of ICASSP III*: 245-248 (1994).

2.9 Position-Dependent Encoding

Sponsor

Advanced Telecommunications Research Program

Project Staff

Alexander Pfajfer

In typical video compression algorithms, the DCT is applied to the video, and the resulting DCT coefficients are quantized and encoded for transmission and storage. Some of the DCT coefficients are set to zero. Efficient encoding of the DCT coefficients is usually achieved by encoding the location and amplitude of the nonzero coefficients. Since in typical MC-DCT compression algorithms, up to 90 percent of the available bit rate is used to encode the location and amplitude of the nonzero quantized DCT coefficients, efficient encoding of the location and amplitude information is extremely important for high quality compression.

A novel approach to encoding of the location and amplitude information, position-dependent encoding, is being examined. Position-dependent runlength encoding and position-dependent encoding of the amplitudes attempts to exploit the inherent differences in statistical properties of the runlengths and amplitudes as a function of their position. This novel method is being compared to the classical, separate, single-codebook encoding of the runlength and amplitude, as well as to the joint runlength and amplitude encoding.

2.9.1 Publication

Apostolopoulos, J., A. Pfajfer, H.M. Jung, and J.S. Lim. "Position-Dependent Encoding." *Proceedings of ICASSP V*: 573-576 (1994).

2.10 MPEG Compression

Sponsors

U.S. Navy - Office of Naval Research
NDSEG Graduate Fellowship
Advanced Telecommunications Research Program

Project Staff

Eric C. Reed

In a typical MC-DCT compression algorithm, almost 90 percent of the available bit rate is used to encode the location and amplitude of the non zero quantized DCT coefficients. Therefore efficient encoding of the location and amplitude information

is extremely important. One novel approach to encoding the location and amplitude information of the nonzero coefficients is position-dependent encoding. Position-dependent encoding, in contrast to single-codebook encoding, exploits the inherent differences in statistical properties of the runlengths and amplitudes as a function of position.

Position-dependent encoding has been investigated as an extension to separate encoding of the runlengths and amplitudes and has proven to provide a substantial reduction in the overall bit rate compared to single-codebook methods. However, MPEG compression does not allow separate encoding of the runlengths and amplitudes. Therefore, this research involves developing a position-dependent extension to encode the runlengths and amplitudes jointly as a single event. Rather than having two separate codebooks for the runlengths and amplitudes, one two-dimensional codebook will be utilized. This method will be compared to conventional approaches as well as the position-dependent encoding approach using separate codebooks.

2.11 HDTV Transmission Format Conversion and the HDTV Migration Path

Sponsor

Advanced Telecommunications Research Program

Project Staff

Lon E. Sunshine

The current proposal for terrestrial HDTV broadcasting allows for several possible transmission formats. Because production and display formats may differ, it will be necessary to convert between formats effectively. Since HDTV will presumably move toward progressive display systems, de-interlacing non-progressive source material will be a key process. This research will consider topics relating to conversion among the six formats being proposed for the U.S. HDTV standard.

As HDTV evolves, it is probable that more transmission formats will be accepted. Furthermore, additional bandwidth may be allocated for some channels (terrestrial and/or cable). This research will consider the issues related to the migration of HDTV to higher resolutions. Backward compatibility and image compression and coding issues will be addressed.

2.12 Removing Degradations in Image Sequences

Sponsor

Advanced Telecommunications Research Program

Project Staff

Carl Taniguchi

The development of two-dimensional noise smoothing algorithms have been an active area of research since the 1960s. Many of the traditional algorithms fail to use the temporal correlation that exists between frames when processing image sequences. However, with the increasing speed of microprocessors and the rising importance of video, three-dimensional algorithms have not only become feasible, but also practical.

Three-dimensional median filters that are sensitive to motion is the first step in using the temporal correlation in images. Existing algorithms of this type effectively reduce to two-dimensional median filters under areas of the image undergoing motion. An improvement in the use of temporal correlation can be obtained by using a motion estimation algorithm before filtering the image with a three-dimensional median filter. Various median filters and motion compensation algorithms will be tested in the presence of noise.

Uniform processing of an image tends to unnecessarily blur areas of the image that are not affected by noise. In this case, a degradation detector may be of practical use.

2.13 Speech Enhancement

Sponsor

Maryland Procurement Office
Contract MDA904-93-C-4180

Project Staff

Chang Dong Yoo

The development of the dual excitation (DE) speech model has led to some interesting insights into the problem of speech enhancement. Based on the ideas of the DE model, a new speech model is being developed. The DE model provides more flexible representation of speech and possesses features which are particularly useful to the problem of speech enhancement. These features, along with a variable length window, are the backbone of the new speech model being developed.

Because the DE model does not place any restrictions on its characterization of speech, the enhancement system based on the DE model performs better than the one based on any of the previous speech models. While a model should be inclusive in its characterization, it should have some restrictions. Specifically, a speech model should pertain to speech. The DE model is somewhat unrestrictive and simple in its characterization of speech. It is solely based on the separation of the voiced and unvoiced components. Whether it makes sense to represent a stop as a voiced and an unvoiced component is only one of many interesting issues which are being investigated. An extension of the DE model which deals with these issues better is currently being studied.

All model-based enhancement methods to date have been formulated on the premise that each segment of speech is stationary for a fixed window length. The performance of these enhancement algorithms depends on the validity of this assumption. We use a variable-length window to capture varying durations of stationarity in the speech. There are several algorithms which adaptively detect changes in auto-regressive model parameters in quasi-stationary signals which have been successfully used in speech recognition. We propose to investigate some of these algorithms. Using a variable length window will allow (1) better and "cleaner" separation of the voiced and unvoiced components, and (2) a greater reduction in the number of characteristic parameters, such as the amplitudes of the voiced components and the LP coefficients of the unvoiced component.



Professor Emeritus William F. Schreiber (Photo by John F. Cook)

Chapter 3. Combined Source and Channel Coding for High-Definition Television

Academic and Research Staff

Professor Emeritus William F. Schreiber

Graduate Students

Michael O. Polley, Susie J. Wee

Technical and Support Staff

Deborah S. Manning

3.1 Project Description

Sponsor

Scitex America Corporation

The purpose of this project is to develop a high-definition television (HDTV) system for terrestrial broadcasting. Under decisions previously made by the Federal Communications Commission, each current broadcaster will be given a second channel. This channel is to be used for HDTV, transmitting the same program as the standard NTSC channel in a procedure called simulcasting. Fifteen years after the commencement of high-definition broadcasting, NTSC is to go off the air, the original channels being returned to the FCC for reassignment. In many cases, the new assignments will be taboo channels not usable for NTSC because of interference. This obviously requires that the HDTV transmissions have excellent interference performance. Coverage must be comparable to what is now achieved with NTSC.

The system being developed in this project is intended to be more useful than the all-digital scheme that has evolved from the FCC process [the Grand Alliance (GA) system]. Its features have been chosen specifically to be acceptable to the various stakeholders including broadcasters, equipment manufacturers, program producers, regulatory authorities, and viewers. The most important performance factors are efficient use of spectrum, coverage versus quality, cost, and interoperability. In addition, it must have a feasible transition scenario. We have concluded that all receivers need not have

the same picture quality and that low-cost receivers must be available for less-critical applications. We have therefore designed a multiresolution (MR) system, in which a hierarchy of encoders of different price/performance can communicate with a hierarchy of decoders, also of varying cost and quality. As compared with the Grand Alliance system, the new scheme features:

1. Extended coverage, albeit at lower quality in the extra area,
2. Higher quality, albeit only in the central portion of the service area,
3. Comparable quality in a large portion of the service area,
4. Support for single-frequency networks (SFNs), which make the most efficient use of spectrum,¹
5. Support for less expensive receivers for less demanding applications, and
6. Automatic optimization of image quality as a function of signal quality and receiver complexity.

(The price for features 1-3 is somewhat lower quality in a part of the service area.)

The multiresolution (MR) feature makes possible the design of cheaper receivers for small sizes and other noncritical applications. It also permits higher performance receivers to optimize their image quality as a function of received signal quality, thus improving spectrum utilization.

¹ SFNs make the signal level more uniform across the population of receivers by utilizing a cellular network of low-power transmitters, all operating in the same channel. The several signals sensed at each receiver appear to be ghosts, so very good ghost suppression is required.

The MR feature is achieved using combined source and channel coding employing a pyramid technique. The coded video and audio data is divided into a number (typically 3 or 4) of data streams. The quality of the reconstructed video depends on the number of streams recovered and their signal-to-noise ratio. Thus the lowest stream provides a picture somewhat better than studio-quality NTSC to the least-expensive receivers and/or under poor reception conditions. The higher streams are used to enhance image quality. The streams are packaged by the channel coder so that the number recovered depends on the signal strength and receiver performance. The lowest quality level features standard MPEG-2 coding so that the cheapest receivers can use single-chip MPEG decoders.²

3.2 Technology

In the GA system, digital source coding is used to get very high compression, which is needed, in part, because all-digital channel coding does not make best use of the analog channel capacity. Our system uses multiresolution hybrid analog/digital coding, which permits both high compression and efficient use of spectrum.

The source coder uses some MPEG features, but produces data in a form suitable for hybrid channel coding. This data is not all of one kind; some require essentially perfect transmission, and some can tolerate a certain amount of noise and distortion.

The channel coder uses spread spectrum and orthogonal frequency-division multiplex (OFDM),³ which, in combination, give good resistance to analog channel impairments and facilitate multiresolution operation. The coder transmits the more sensitive data digitally and the less sensitive data in analog form. The received signal "looks" simple to a low-performance receiver, while a high-performance receiver, with its more powerful decoder, "knows" where to look in the signal for the higher streams of data. These are recoverable at

locations where the signal strength is higher and/or where the receiver is of better quality. Digital performance is enhanced by extensive forward error correction. The simpler receivers are expected to be substantially cheaper than those used in the GA system, while the higher-performance receivers will be of comparable complexity and cost.

3.3 Current Status

All the novel elements of the system have been simulated and picture quality at the first three levels has been demonstrated. These have resolutions of 384 x 640 (better than NTSC), 576 x 960, and 768 x 1280, all 60 frames/sec progressively scanned compared to 720 x 1280 for the GA system. It is believed that further system optimization will permit substantially higher resolution for all levels above the first.

3.4 Future Plans

One small coding job remains, which is the coding of the coefficient identification data. Based on previous work, we expect no problem with this. We shall continue to improve the system. There is little doubt that the quality at the middle and highest levels will become better. (It is already very good.) These levels, at present, must cope with distortions introduced by MPEG at the lowest level. Although the MPEG pictures are good when displayed at 60 fps, there are significant frame-to-frame errors that place a burden on the motion compensation at levels two and three. This is so much the case that we can get nearly as good results using intraframe coding only at these levels.

If we retain motion compensation at levels two and three, we plan to go to a scheme in which the motion vectors will be calculated for all three levels from the original high-resolution sequence. This may well solve some of the problems we are now having at the lowest level, and it also will facilitate the coding of the vectors for levels two and three.

² The Motion Picture Experts Group has promulgated an international all-digital standard for TV source coding, which has been adopted by many groups. Inexpensive coder and decoder chips are becoming available, which makes the use of MPEG coding very attractive.

³ OFDM was invented in the US, but in recent years has been developed in Europe for digital audio broadcasting. It is also intended for use in digital TV terrestrial broadcasting in Europe. The coded form is referred to as COFDM.

Table 1. Composition, Rates, and Thresholds of the MR Data Streams. This table shows details of the three levels of performance. Note that it is possible to transmit only the lowest level, or only the lowest two levels, in which case the threshold is reduced and coverage increased.

Class	Composition		Incremental Rate	Total Rate	Threshold
low-res 384 x 640	MPEG stream audio ancillary data	digital	4 Mb/s	4 Mb/s	6 dB CNR
medium-res 576 x 960	enhanced motion vectors, selection information, additional audio	digital	4 Mb/s	8 Mb/s	17 dB CNR
	selected residual coeffs.	analog	2.5 Ms/s	2.5 Ms/s	
high-res 768 x 1280	enhanced motion vectors, selection information, additional audio	digital	4 Mb/s	12 Mb/s	29 dB CNR
	selected residual coeffs.	analog	2.5 Ms/s	5 Ms/s	

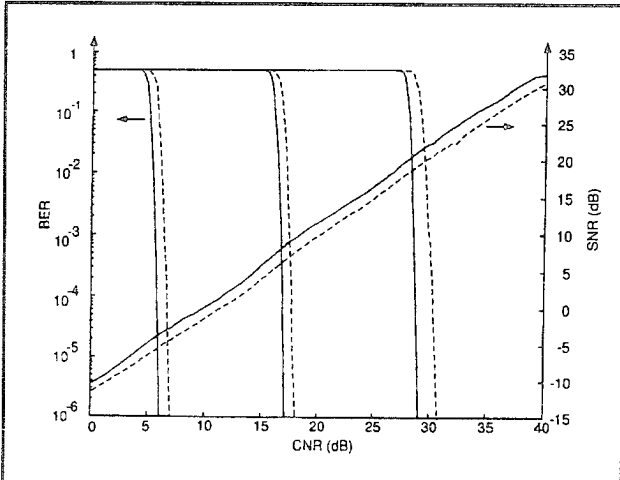


Figure 1. Noise Performance With and Without Echoes. This figure shows the performance of both the digital and the analog data streams as a function of the receiver CNR. (We use CNR to mean the signal/noise ratio of the radio-frequency carrier and SNR to apply to the recovered baseband signal representing the analog data.) The solid lines represent the no-echo situation, while the dotted lines represent the performance in the presence of five echoes ranging from -10 to -20 dB.

3.5 Publications

Polley, M.O., S.J. Wee, and W.F. Schreiber. "Hybrid Channel Coding for Multiresolution HDTV Terrestrial Broadcasting." *Proceedings of the IEEE International Conference on Image Processing*. November 1994.

Schreiber, W.F. "A Unified Approach to Moving Image Coding for Most Media and Most Applications." *Sig. Proc.* Forthcoming.

Schreiber, W.F. "Advanced Television Systems for Terrestrial Broadcasting: Some problems and some proposed solutions." *Proc. IEEE*. Forthcoming.

Wee, S.J., M.O. Polley, and W.F. Schreiber. "A Scalable Source Coder for a Hybrid Transmission HDTV System." *Proceedings of the IEEE International Conference on Image Processing*. November 1994.

Part IV Bioelectronics

Section 1 Genetic Analysis

Section 1 Genetic Analysis

Chapter 1 Genosensor Technology Development

The development of genosensor technology has been a significant area of research in recent years, driven by the need for more accurate and efficient methods of detecting genetic variations. This chapter will provide an overview of the current state of genosensor technology, focusing on its applications and challenges.

Genosensors are devices that can detect specific genetic markers or mutations in a sample. They typically consist of a sensor array, which is a collection of small sensors that can detect different types of genetic material. The sensor array is usually made of a polymer or metal film, and it is designed to bind to specific DNA sequences. When a sample is applied to the array, the sensors can detect the presence of specific genetic markers, such as single nucleotide polymorphisms (SNPs), insertions, or deletions.

There are several types of genosensors, each with its own advantages and disadvantages. One type of genosensor is a microarray, which consists of a grid of thousands of small sensors. Microarrays are highly sensitive and can detect many different types of genetic markers at once. However, they are also expensive and require a large amount of sample material.

Another type of genosensor is a nanowire-based sensor, which consists of a single nanowire that is coated with a specific antibody or probe. These sensors are very sensitive and can detect very small amounts of genetic material. However, they are less versatile than microarrays and may not be able to detect all types of genetic markers.

Genosensors have a wide range of potential applications, including medical diagnostics, environmental monitoring, and food safety. In medicine, genosensors could be used to quickly and accurately diagnose genetic disorders or predict the effectiveness of certain treatments. In environmental monitoring, genosensors could be used to detect genetic changes in populations of organisms, such as bacteria or viruses, that are exposed to pollutants or other stressors. In food safety, genosensors could be used to detect genetic changes in food products, such as fruits or vegetables, that are contaminated with harmful bacteria or viruses.

However, there are also several challenges associated with the development and use of genosensors. One challenge is the cost of the equipment and reagents required for their use. Another challenge is the need for specialized expertise and training to operate and interpret the results of genosensors. Additionally, there are concerns about the privacy and security of genetic data, as well as the potential for discrimination based on genetic information.

Chapter 1. Genosensor Technology Development

Academic and Research Staff

Dr. Daniel J. Ehrlich, Dr. Mark A. Hollis, Dr. Dennis D. Rathman

1.1 Introduction

The primary objective of this cooperative work with the Houston Advanced Research Center (HARC) is to develop a novel method for automated, low-cost, high-throughput DNA sequence analysis. The overall goal is to demonstrate laboratory prototypes that provide a substantial increase in speed over the conventional DNA sequencing methods now used in the biomedical, pharmaceutical, and agricultural industries.

The basic approach is shown in figure 1. In a hypothetical DNA sequencing test, a solution of single-stranded "target" DNA strands of identical but unknown sequence is washed onto a specialized microelectronic chip called a genosensor. The genosensor surface contains a large array of test sites, each site containing short pieces of single-stranded DNA known as "probes." These probes are chemically attached to the site. All probes in a given site have the same sequence, and the sequence for each site is unique on the chip. The target DNA strands will bond, or hybridize, very strongly to probes containing their exact Watson-Crick complement, but much less strongly to probes on other sites. The sites containing hybridized DNA are identified via electronic sensing on the chip, and this information is used by off-chip instrumentation to reconstruct the sequence of the target strands. MIT's role in this effort is primarily in the design and fabrication of the genosensor chips.

1.2 Development of Genosensor Arrays for DNA Decoding

Sponsor

Houston Advanced Research Center
Contract HRC-HG00665-01

Project Staff

Dr. Daniel J. Ehrlich, Dr. Mark A. Hollis, Dr. Dennis D. Rathman

1.2.1 Genosensor Electronic-Detection Principle

The simplest electrical measurement that can be made at a test site to detect hybridization is probably a measurement of the change in local permittivity due to the addition of long target strands to the site. The complex permittivity $\epsilon' - j\epsilon''$ of an aqueous solution containing DNA exhibits a dispersion around a relaxation frequency which is a function of the size and conformation of the DNA molecule. A measurement of the capacitance and/or conductance between two electrodes in the solution over a range of frequency can therefore differentiate between a site that contains only short probe strands and one that contains long target strands hybridized to the probe strands. From these measurements the relative permittivity ϵ' , the dielectric loss ϵ'' , and the dissipation factor ϵ''/ϵ' can be obtained for the cell.

The ideal electrode structure in a test well consists of two parallel plates spaced so that the entire volume between them is filled by the hybridized DNA globules in aqueous solution. For the sizes of target DNA envisioned, this spacing ranges from approximately 200 to a few thousand angstroms. A practical, easily fabricated structure that approximates this ideal is an interdigitated design shown in figure 2. Fabricated by a combination of wet and dry etching with metal liftoff, this design can achieve the required spacings between the upper and lower electrodes at their edges. Figure 3 shows various aspects of completed genosensor devices.

1.2.2 Genosensor Fabrication Development

The primary emphasis of this project is on the process development and feasibility exploration for the genosensor design of figure 2. For this chip, conventional 2- μm photolithography, wet and dry etching techniques, and electron-beam evaporation and liftoff processes are used to fabricate an interdigitated electrode structure in which the opposing electrodes are separated vertically.

During this past year, significant progress has been made in process development. Yield and reproducibility of 6x6 passive arrays of various

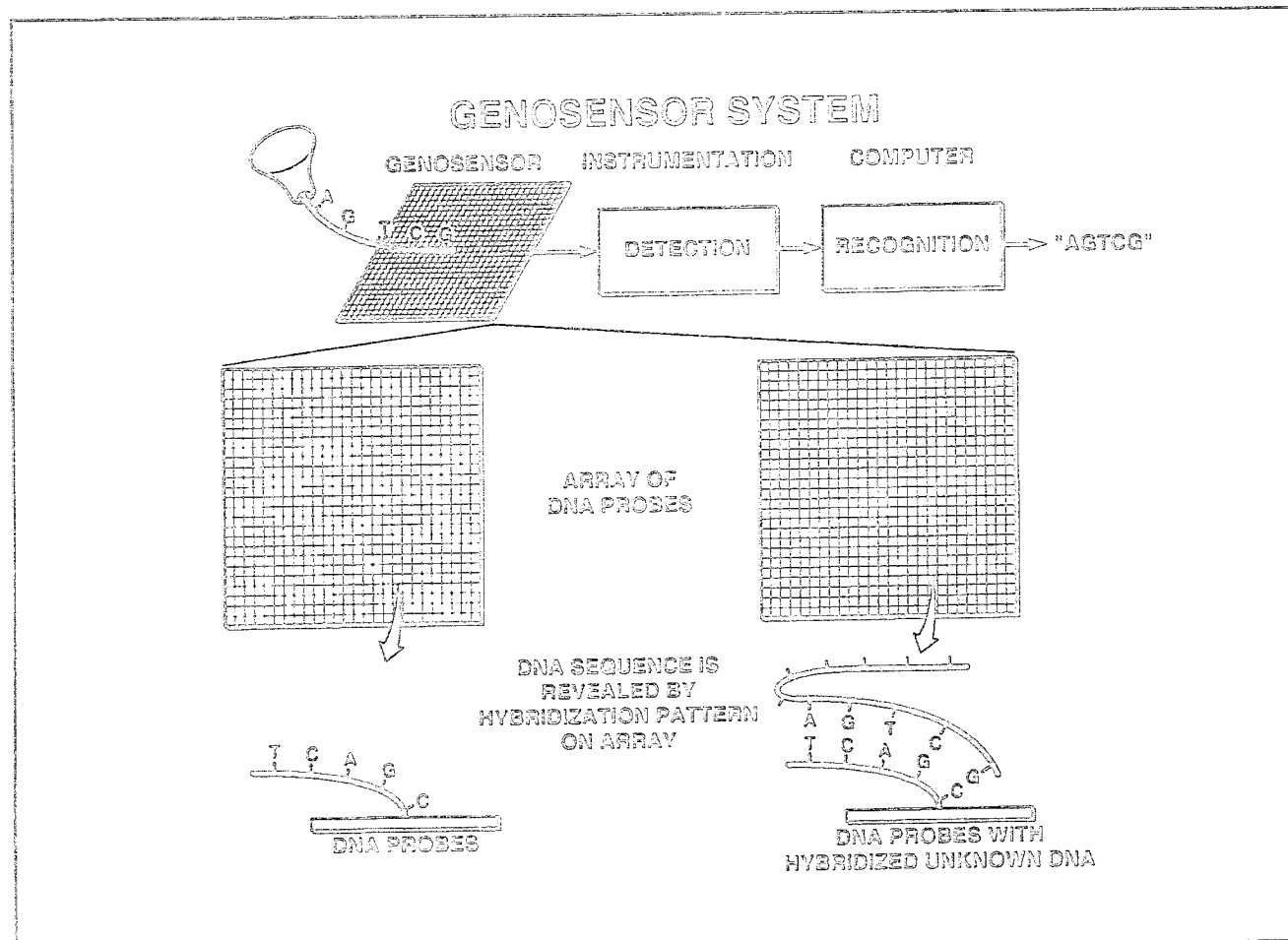


Figure 1. Conceptual genosensor system.

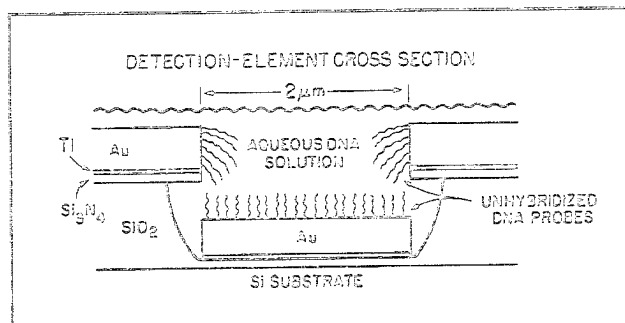


Figure 2. Electrode design for a permittivity genosensor. The unit cell shown is repeated many times across a test well to form an interdigitated test structure with the top Au electrodes connected to one access line and the bottom Au electrodes to the other.

active-area sizes have been dramatically improved to greater than 90 percent for all array sizes. Problems described in last year's report related to the patterning of the narrow Pt interconnect lines have been solved. In addition, the use of thicker Ti layers underneath the Pt lines has resulted in better adhesion of both the interconnects and the active-area electrodes to the substrates. We have also

developed techniques to connect Al wires directly to Pt electrodes, eliminating the need for evaporation and liftoff of Au bonding pads.

One of the more challenging fabrication efforts successfully completed this year was the development of a buried-interconnect, or insulated-lead, process. (The motivation for developing this process is discussed in Section 1.2.3 below). This involves the use of photosensitive polyimide as a second-layer dielectric which is deposited on the completed device. The active electrode area is opened through the polyimide by conventional photolithography, where the polyimide behaves like positive photoresist which can be developed out after exposure. The polyimide is then hard baked at 200°C or greater and remains on the genosensor chip to insulate the interconnect leads from the chemical solutions used in the attachment and measurement of DNA. In initial tests, the polyimide does seem to be somewhat degraded by the chemical treatments required for DNA strand attachment, but not so severely that the electrical measurements are compromised. Investigation of these matters is continuing.

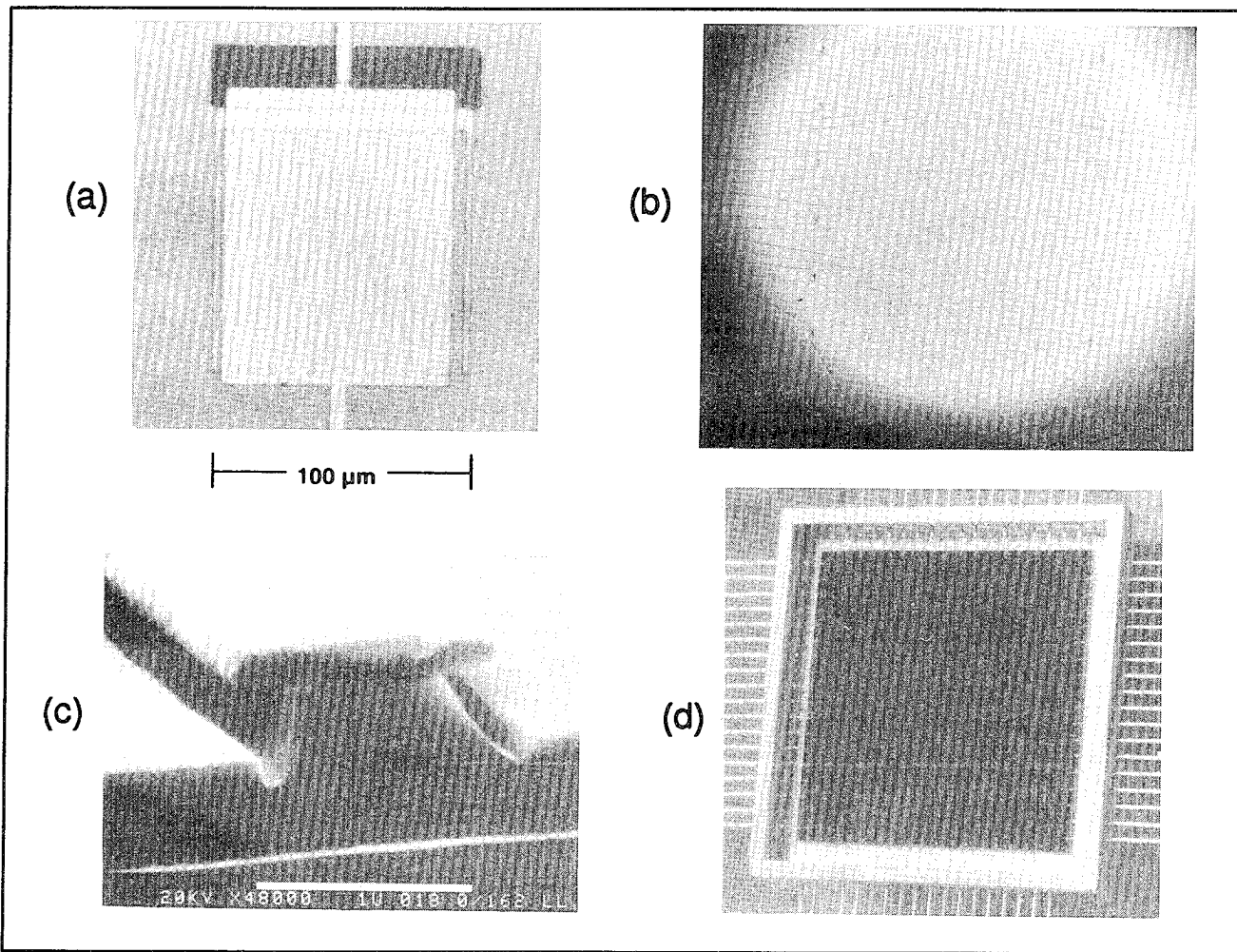


Figure 3. Collection of photographs showing various views of a complete genosensor device. (a) Top view of the standard 100 μm X 100 μm single test cell. (b) Top view of the 6 X 6 passive array of test cells. (c) Scanning electron micrograph (SEM) closeup of the interdigitated electrode fingers. (d) Genosensor chip in electronic package.

During this past year, we have delivered 30 packaged devices (and several unpackaged chips for DNA attachment experiments) to HARC for tests for this project. At present, several additional wafers are in various stages of processing.

1.2.3 Genosensor Test Results

Extensive experimental and theoretical studies of genosensor electrical properties have been carried out this past year. It has been found that the preliminary data showing peaks in dissipation factor for DNA probes and hybridized DNA that were shown in figure 4 in last year's report are actually artifacts of parasitic effects. The first-generation genosensor used for those measurements did not have insulated interconnect leads on the chip surface, thus the leads were exposed to the aqueous saline solution used during the electrical tests. Extensive electromagnetic modeling has shown that the par-

ticular parasitic resistance and capacitance associated with the leads combined with the high dielectric constant and conductivity of the saline can reduce the phase velocity of electromagnetic propagation along the leads by as much as a factor of 100. This slow-wave effect produces an anomalous inductive behavior in the measurement circuit, causing spurious resonances which show up as the peaks in last year's data. These findings are the motivation behind the development of the insulated-lead process described above. It should be stressed that this effect is only important in interconnect leads that run across the chip surface from the bonding pads to the sensor sites and is not important in the interdigitated electrodes in the sensor sites themselves.

Measurements on the new devices having insulated leads are being performed presently. It appears that the permittivity of DNA in aqueous solution can be sensed, especially below 300 kHz. Detailed test

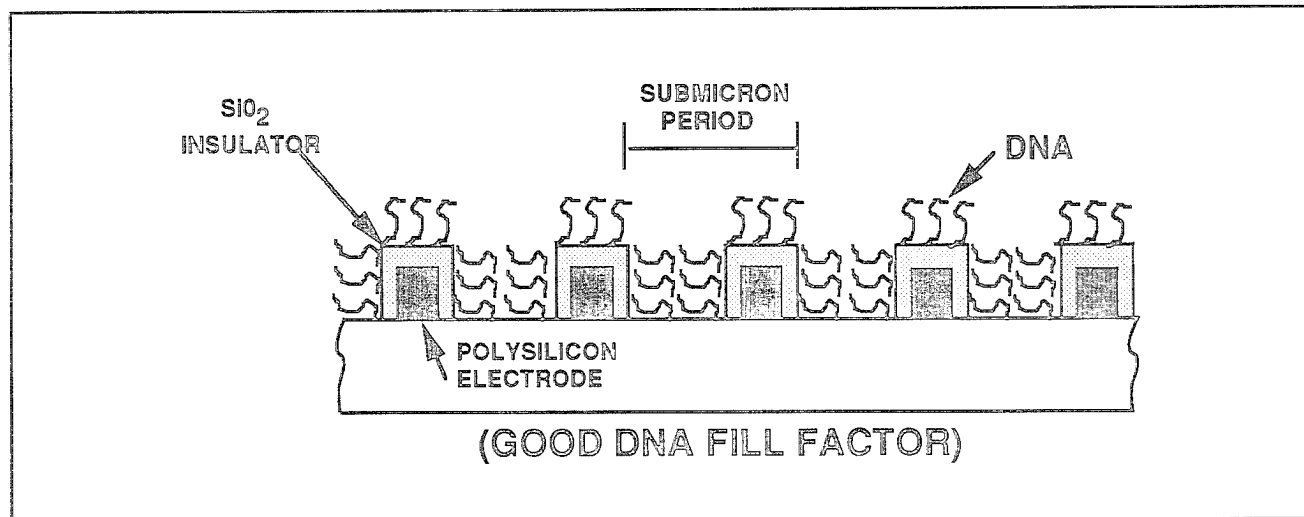


Figure 4. Advanced genosensor design with high-aspect-ratio insulated electrodes.

results will be reported next year after the data have been extensively analyzed.

1.3 Microdetection Technology for Automated DNA Sequencing

Sponsor

Houston Advanced Research Center
Contract HRC-HG00776-01

Project Staff

Dr. Daniel J. Ehrlich, Dr. Mark A. Hollis, Dr. Dennis D. Rathman

The primary emphasis of this effort is to complement the program described above by optimizing the electrode geometry for maximum sensitivity. Initial work for this contract began with the electrode configuration illustrated in figures 2 and 3. Subsequently, both experimental studies and theoretical modeling have shown a need to design and fabricate more aggressive electrode geometries, which are now being developed as described below.

Measurements by our colleagues at HARC and Baylor College of Medicine have shown that DNA attachment to SiO_2 is more easily achieved than attachment to Pt or Au. In fact, surface-attachment densities of DNA probes are typically one order of

magnitude higher on oxide-coated polysilicon compared to the Pt electrodes of our conventional permittivity chip designs. The exact reasons for this are not yet known but may be related to the different linker chemistries used for attachment or to the strong ionic and polarization effects observed at liquid-metal interfaces. In either case, the fabrication of a permittivity chip incorporating oxide-coated polysilicon electrodes is currently underway. Because sophisticated dry-etching technology is available for patterning polysilicon, electrode structures having large height-to-spacing ratios should be possible. Several wafers are currently in process which have coplanar, nonself-aligned oxide-insulated polysilicon electrodes. This design is conceptually illustrated in figure 4.

In addition to this coplanar design, we are also fabricating one using the self-aligned electrode architecture illustrated in figure 2 but having submicrometer-periodicity oxide-insulated polysilicon electrodes. The patterning of the electrodes is being done by a combination of laser interferometric lithography and reactive ion etching. For the attachment chemistry that will be used with these devices, the DNA probes will probably attach not only to the electrodes but also to the oxide/nitride sidewalls of the wells. This will substantially increase the probe density in each sensor site and possibly the detection sensitivity. Several wafers in which we use this approach are currently in process as well.

Part V Language, Speech and Hearing

Section 1 Speech Communication

Section 2 Sensory Communication

Section 3 Auditory Physiology

Section 4 Linguistics

Section 1 Speech Communication

Chapter 1 Speech Communication

Chapter 1. Speech Communication

Academic and Research Staff

Professor Kenneth N. Stevens, Professor Jonathan Allen, Professor Morris Halle, Professor Samuel J. Keyser, Dr. Melanie L. Matthies, Dr. Joseph S. Perkell, Dr. Stefanie Shattuck-Hufnagel, Dr. Mario A. Svirsky, Dr. Alice Turk, Dr. Yi Xu, Peter C. Guiod, Seth M. Hall, Joyce Manzella,

Visiting Scientists and Research Affiliates

Dr. Vladimir M. Barsukov, Dr. Corine A. Bickley, Dr. Suzanne E. Boyce,¹ Dr. Carol Espy-Wilson,² Dr. Richard S. Goldhor,¹ Dr. Robert E. Hillman,³ Dr. Caroline Huang, Dr. Harlan Lane,⁴ Dr. John Locke,⁵ Dr. John I. Makhoul,⁶ Dr. Sharon Manuel, Dr. Jorgen Pind,⁷ Dr. Reiner Wilhelms-Tricarico, Dr. David R. Williams, Sergio Basalo,⁸ Anna Esposito,⁹ Helen Hanson,¹⁰ Eva B. Holmberg,¹¹ Clay T. Mitchell, Jane W. Wozniak³

Graduate Students

Hwa-Ping Chang, Marilyn Y. Chen, Karen Chenausky, David M. Horowitz, Mark A. Johnson, Hong-Kwang J. Kuo, Sharlene A. Liu, Noel Massey, Katerina Nguyen, Kelly L. Poort, Lorin F. Wilde

Undergraduate Students

Howard Cheng, Laura C. Dilley, Helena Geng, Brett A. Geoffroy, John Hardy, Marnie L. Harker, Henry Lu, Rebecca Mallin, Rachel Molinaar, Laura M. Sever

Technical and Support Staff

D. Keith North, Arlene E. Wint

Sponsors

C.J. Lebel Fellowship

Dennis Klatt Memorial Fund

National Institutes of Health

Grant R01-DC00075

Grant R03-DC01721

National Institutes of Health

Grant R01-DC01291

Grant R01-DC00261¹²

Grant P01-DC00361-06A1¹²

Grant R01-DC00776¹³

¹ Audiofile, Inc., Lexington, Massachusetts.

² Boston University, Boston, Massachusetts.

³ Massachusetts Eye and Ear Infirmary, Boston, Massachusetts.

⁴ Department of Psychology, Northeastern University, Boston, Massachusetts.

⁵ Massachusetts General Hospital, Boston, Massachusetts.

⁶ Bolt, Beranek and Newman, Inc., Cambridge, Massachusetts.

⁷ University of Iceland, Reykjavík, Iceland.

⁸ Hospital de Clinicas, Universidad de la Republica, Montevideo, Uruguay.

⁹ Department of Physics, Salerno University, Italy.

¹⁰ Harvard University, Cambridge, Massachusetts.

¹¹ MIT Staff Member and Massachusetts Eye and Ear Infirmary, Boston, Massachusetts.

¹² Under subcontract to Massachusetts Eye and Ear Infirmary.

¹³ Under subcontract to Massachusetts General Hospital.

National Science Foundation
Grant IRI 89-05439¹⁴
Grant IRI 89-10561
Grant INT 90-24713¹⁵

1.1 Studies of Normal Speech Production

1.1.1 Articulatory Evidence for Acoustic Goals for Consonants: a Pilot Study

In previous work, we found evidence for trading relations between tongue-body raising and upper lip protrusion (measured with an EMMA system) for the vowel /u/, reflecting a "motor equivalence" strategy that should help to constrain acoustic variation. Theoretically, analogous relations in the transformation between the area function and the acoustic transfer function are possible for the consonants /r/ and /ʃ/, which are also produced with two independently-controllable constrictions, formed by the tongue and by the lips. Such relations might occur more among tokens that are least prototypical, i.e., closest to perceptual boundaries. In a preliminary test of these hypotheses, a single speaker has produced the sounds /r/, /ʃ/ and /u/, embedded in contexts designed to induce differences in prototypicality. Motor equivalence was observed for the /u/ in /ut/ (least prototypical, with the highest F2 values) but not in /pub/ or /hud/. For /r/ and /ʃ/, anterior displacement of the tongue constriction was positively correlated with upper lip protrusion, providing initial support for the hypothesis that movement goals for the consonants also include acoustic components. These components are manifested in a tendency to maintain sufficient front-cavity length to help assure acoustic-phonetic distinctiveness. These findings were also confined to less prototypical tokens. A second subject has been recorded with the same paradigm.

1.1.2 Clarity versus Effort in Speech Production: Initial Results of a Pilot Study

The goal of this research is to test the hypothesis that there is a trading relation between clarity (measured acoustically and in intelligibility tests) and articulatory effort in speech production. We have recorded midsagittal-plane articulatory move-

ments of points on the tongue body, tongue blade, lips and mandible (with an EMMA system), as well as the acoustic signal from a male talker in five speaking conditions: normal, clear, clear plus fast, fast, and slow. Different CVC words were embedded in two positions in a carrier phrase (called "one" and "two"). Kinematic analyses were performed as a function of speaking condition and position in the phrase. As an example result, CV movements of a point on the tongue body for the word "cab" have the following characteristics. Movement duration was shorter for position two; in both positions, it followed the order: slow > clear > normal > clear plus fast > fast. The range of distance traveled was greater for both slow and clear than for the other conditions. Peak velocity was higher for fast and clear plus fast than the other conditions. Midsagittal plane location at movement end was less variable for the tokens in position one (longer duration movements). A measure of effort was higher for clear, clear plus fast and fast, than for normal or slow, in both word positions. Acoustic analyses and the construction of intelligibility tests are in progress. Most recently, the same kind of recordings have been made for a second subject.

1.1.3 Articulatory Processes

A chapter called "Articulatory Processes" was prepared for a forthcoming book, *A Handbook of Phonetic Science*, edited by W.J. Hardcastle and J. Laver (Blackwell Publishers, Oxford, England). The chapter presents the following view of speech production.

Articulatory processes are actions of the respiratory, laryngeal, and vocal-tract systems that convert linguistic messages to an intelligible signal. The linguistic message is encoded in acoustic characteristics of individual sound segments and in superimposed prosodic patterns of sound level, fundamental frequency and duration. Important additional influences are listener needs, which are determined by factors such as the level of environmental noise and the listener's familiarity with the language, speaker, and subject matter. Kinematic adjustments are used to help convey some linguistically-contrastive information; however, the large amount of variability inherent in speech and the lack of truly comprehensive kinematic data currently make it difficult to provide a systematic account of articulatory kinematics. Some prelimi-

¹⁴ Under subcontract to Boston University.

¹⁵ U.S.-Sweden Cooperative Science Program.

nary ideas about articulatory dynamics indicate that the biomechanical response properties of articulators and effort minimization strategies have roles in shaping the control of articulatory processes; on the other hand, it is very likely that perceptually-related factors are at least as important in this regard.

1.1.4 Modeling Vocal-fold Vibration

The goal of the modeling work is to use a relatively simple model of glottal function to infer approximate relative values of three important physiological parameters that cannot be measured directly: vocal fold stiffness, degree of adduction of the membranous folds, and size of an inter-arytenoid chink. It is hoped that the models will help us to understand more about the mechanisms that underlie our aerodynamic and acoustic measurements. We have extended our implementation of the two-mass model of Ishizaka and Flanagan (1972) to account for two frequently-made observations: (1) gradual closure that propagates along the folds in the antero-posterior direction and (2) the presence of a chink. We assume that stiffness parameters in the model are roughly analogous to vocal-fold stiffness, and rest positions of the masses are analogous to the degree of intra-membranous vocal-fold adduction. We intend to employ the model in an analysis-by-synthesis approach. Using inputs consisting of the measured value of subglottal air pressure and F_0 and estimates of gender-specific values of parameters such as vocal-fold mass and length, values will be estimated for the model's stiffness parameters, rest positions of the masses, and chink size. The estimates will be adjusted so that the model's flow output matches the measured glottal airflow waveform.

The original model of Ishizaka and Flanagan contains a linear relation between the displacements of the two masses and the areas. For sufficiently large amplitudes of the oscillations of the masses, the minimum area between them is zero, and the closure becomes unrealistically abrupt. In our first modification, to simulate gradual closure, the positive ramp relation between mass displacement and glottal area was replaced by a function that maintains minimal opening areas greater than zero, and a smooth quadratic function which, for small openings, computes the areas from the oscillator amplitudes. Our second modification has been to introduce a chink which represents the opening between the arytenoid cartilages. In the equivalent circuit, the acoustic effects of this chink are represented by a parallel impedance running from below to above (across) the glottis. In preliminary simu-

lation experiments, waveforms were computed as the sum of air flow through the glottis and the chink. These waveforms were quantitatively within reasonable ranges, and they looked qualitatively very similar to observed waveforms.

1.1.5 Physiological Modeling of Speech Production

In the past year, Dr. Reiner Wilhelms-Tricarico joined the Speech Group to continue work on physiological modeling of speech production that he had begun at Ohio State University and continued at ATR Laboratories, Kyoto, Japan.

During this year, previously-developed finite element code for modeling the behavior of the tongue was installed on a DEC Alpha PC; an altered, more realistic muscle model was incorporated; and a number of computational improvements were implemented. Improvements were also made in programs for displaying the computational results. The possibility of building finite element code based on Matlab was evaluated and compared with the current C++ programming approach. The result is that Matlab is just as good for this purpose and may be easier to maintain. A number of computational experiments were performed to clarify stability limitations of the current method. Theoretical studies were performed to determine what type of element needs to be used to avoid instabilities; results indicate the need to develop a mixed tri-quadratic type of element with four degrees of freedom of the pressure field. Implementation of this type of element in Matlab code has been initiated. The code makes use of vector and matrix commands wherever possible. The resulting code should be portable to any machine that runs Matlab, including the Cray supercomputer, which is the target platform once the described refinements are completed.

1.1.6 Stop Consonant Production: An Articulation and Acoustic Study

Articulation and acoustic data for stop consonant production have been examined with the aims of (1) describing the movements and coordination of the articulatory structures and (2) developing procedures for interpreting acoustic data in terms of articulatory movements. Movements in the midsagittal plane of points on the lower jaw, lips, tongue blade, and tongue body were measured using the EMMA system. Acoustic data were recorded simultaneously. Three normal hearing, normal speaking male subjects spoke single-syllable words /CVt/, composed of a voiceless stop

consonant C followed by the vowel /a/ or /i/ and the consonant /t/, placed in a carrier phrase. Half the tokens were preceded by the fricative consonant /s/. An estimate of the constriction cross-sectional area change with time following the release of each of the stops was calculated with the aid of the articulation data. For example, the cross-sectional area of the lips in the labial /p/ in **spot** increases by approximately 35 cm²/sec within the first 5-10 ms following the stop release. During the first few ms following the release, the constriction cross-sectional area change with time can be related to the corresponding acoustics in two important ways: (1) by modeling the vocal tract as a series of tubes of varying cross-sectional area (in the case of a labial stop, a Helmholtz resonator) and calculating the transition of the first formant frequency *F*₁; and (2) by calculating the time course of the burst when the constriction cross-sectional area is used as a parameter in a circuit model of the vocal tract. The articulation data were also studied to determine the effects of phonetic context. Findings include a constraint on lower jaw position during /s/ production, maximum downward velocity for the lower jaw occurring approximately at the time of the consonant release, and a correlation between the distance articulators must travel and rates of movement. The inferences made from the detailed examination of the articulation and acoustic data will aid in developing a more comprehensive model of stop consonant production.

1.2 Speech Research Relating to Special Populations

1.2.1 Speech Production of Cochlear Implant Patients

This project is funded under a subcontract to the Massachusetts Eye and Ear Infirmary in collaboration with Drs. Harlan Lane, Donald K. Eddington, and Joseph Nadol.

This research aims to characterize the speech production of postlingually deafened adults before and after they receive cochlear implants, in order to contribute to the development of models of the role of hearing in speech. The findings can also contribute to evaluating and improving prostheses and to focusing speech therapy for implant users. Toward these goals, we have been measuring: vowel acoustics (vowel formants, *F*₀, SPL, duration, and a measure of inferred glottal aperture); consonant acoustics (voice-onset time, fricative and plosive spectra); and speech aerodynamics (speech initiation and termination lung volumes, volume of air per syllable, inferred subglottal pressure, oral

and nasal airflow, peak glottal airflow, minimum flow, AC flow, open quotient, and maximum flow declination rate). Generally, our findings continue to indicate significant deterioration of acoustic and articulatory speech parameters in postlingually deafened adults, and substantial long-term changes, generally in the direction of normalcy, following activation of the cochlear implant. During this last year, we have made the following specific findings.

Voice Onset Time (VOT)

The effects on VOT of turning subjects' speech processors off and on within an experimental session were generally consistent with, but smaller than, the long-term effects of deafening and restoration of some hearing. Data were analyzed for two implant users who participated in a longitudinal study of VOT described in last year's report. Only their voiced plosives and not the voiceless showed significant increases in VOT when comparing mean values in the first processor-off condition with the following processor-on condition. Changes in processor state produced widespread postural changes (in average SPL, *F*₀ and speaking rate). Those changes may be responsible for the observed changes in voiced VOT.

We have begun perceptual tests using synthetic speech stimuli in order to assess whether Ineraid implant users can discriminate VOT differences of the order of magnitude of the discrepancy between their VOT values and normative data. We tested a voicing contrast in syllable-initial plosives, created with the Klatt synthesizer. Onset frequencies of *F*₀ and *F*₁ varied across the series. Two psychometric functions were determined, one for voiced and one for voiceless syllables. In this initial experiment, one implant user yielded jnd values of 50 and 35 ms for voiceless and voiced plosives VOTs respectively. These jnd's are more than twice as large as the discrepancies between her pre-implant VOTs and normative values, suggesting that, in her case, changes in VOT with the speech processor on are not due to auditory validation of the VOT contrast. A subject with normal hearing gave jnd's of 15 and 5 ms, respectively.

Syllable-to-syllable Regulation of *F*₀ and SPL

Syllable-to-syllable fluctuation of *F*₀ and SPL were measured in readings of a passage by four postlingually deafened adults, recorded before and after they received cochlear implants, and one adult with neurofibromatosis-2 (NF2—see section 1.2.3 below), who was initially profoundly deaf in one ear

and had a mild to moderate hearing loss in the other (aided). Three of the four cochlear implant users reliably reduced syllable-to-syllable fluctuation in *F0* and SPL following the activation of their speech processors. The fourth speaker began with and maintained the regularity achieved by the others post-activation. In recordings made following the onset of bilateral profound deafness, the NF2 subject showed increased syllable-to-syllable fluctuation in *F0* and SPL. Results from another experiment,¹⁶ in which multiple repetitions of vowels in an /hVd/ context were produced by cochlear implant users with their processors turned off and on, suggest that some subjects showed less token-to-token variability in *F0* and SPL with their processors turned on. The present results indicate that auditory feedback may also constrain the syllable-to-syllable variability of *F0* and SPL contours.

1.2.2 Speech Perception by Cochlear Implant Users

The two long-term goals of this research are (1) to understand the acoustic cues that underlie speech reception by cochlear implant users and (2) to find the optimal stimulation strategies for different subjects and different types of cochlear implants.

Development of Software and Hardware Tools

The Nucleus device has an external part (including microphone, speech processor and transmitter) and an internal implanted receiver that receives power and stimulation information via a radio frequency link. In order to meet the goal of optimizing speech processing strategies, we have implemented an interface to encode computer-stored stimuli for presentation to users of the Nucleus cochlear implant. This interface bypasses the external part of the Nucleus device and can be used to stimulate subjects in an unrestricted fashion, constrained only by the limitations of the Nucleus device. Our system includes software running on two different CPUs: a PC and a Texas Instruments 320C25 fixed-point digital signal processor installed in the PC. The PC performs high-level functions (such as processing input speech signals according to different strategies); it downloads stimulation information to the 320C25 DSP chip and sends a signal to the DSP to start stimulation. The DSP sends appropriate electrical signals to a custom made

hardware driver that generates the radio frequency pulses that are sent to the implanted receiver.

We have written code to run a number of psycho-physical and speech perception tests. Psychophysical tests include determination of threshold (T) and maximum comfortable stimulation level (C); loudness balancing of two channels; and pitch ranking of different channels. Speech processing is done off-line (not in real time), and it involves a number of steps. Files are either synthesized with KLSYN88 or digitized from a speech signal, and then converted to a standard binary format. Files are then processed according to a subject's T and C levels and to different stimulation strategies. We find the power density in a set of frequency bands that may or may not overlap, covering the speech range up to 6 kHz. Any arbitrary function may be used to map a specified acoustic range into the subject's electrical dynamic range. Finally, the program chooses what channels will be stimulated and in what sequence and outputs a subject-specific stimulus file to disk. We have already digitized and converted a large number of vowel and consonant tokens, and these files have been processed for presentation to specific subjects. Stimulus presentation and recording of subject responses will be done with a program developed at the Sensory Communications Group (see section 2).

Pitch Ranking

Three subjects were tested with a pitch ranking task to assess their channel discrimination. Two adjacent channels were stimulated in sequence and the subject was asked whether the first or the second stimulus was higher pitched. We then calculated *d'* values for all pairs of adjacent channels. Subjects 1 and 2 were tested with the standard clinical interface. Subject 1 had 19 active channels. Nine of the 18 channel pairs were perfectly discriminated and correctly pitch-ranked (i.e., more basal channels sounded higher pitched). Of the remaining nine channel pairs, seven were adequately discriminated (*d'* values between 1 and 2) and correctly pitch ranked; channels 13 and 14 were totally indiscriminable, and channels 10 and 11 were well discriminated (*d'*=1.9), but their pitch was reversed (that is, the more basal channel had a lower pitch). Subject 2 also had 18 pairs of adjacent channels, but only three of those pairs were perfectly discriminated and pitch ranked. Ten additional channel pairs were correctly pitch ranked. Five of those

¹⁶ M.A. Svirsky, H.L. Lane, J.S. Perkell, and J.F. Wozniak, *J. Acoust. Soc. Am.* 92(3): 1284-1300 (1992).

were adequately discriminated ($1 < d' < 2$), and the other five were poorly discriminated ($0.4 < d' < 1$). The four remaining pairs had reverse pitch ranking, three of them with low discriminability ($0.4 < d' < 1$) and one pair with perfect discrimination. The third subject was tested with our interface and software. Nineteen pairs of channels were tested. Six of them were perfectly discriminated and correctly pitch ranked. Four additional pairs were correctly pitch ranked, but only three of those showed adequate discrimination ($1 < d' < 2$). The remaining nine channel pairs had reverse pitch ranking, with three showing perfect discriminability and two more showing adequate discriminability ($1 < d' < 2$). In summary, all subjects showed marked differences in channel discriminability across the electrode array, and the nominally more basal channels did not always sound higher pitched than their nominally more apical neighbors. This may have important consequences in our thinking about speech processing strategies. For example, we may choose to implement strategies that only include stimulation channels that are well discriminated from their neighboring channels, and correctly pitch-ranked.

Mathematical Model of Vowel Perception with the Ineraid Cochlear Implant

The Ineraid cochlear implant has been used successfully to help deaf subjects understand speech. The incoming speech signal is filtered into four overlapping frequency bands, with crossover frequencies at approximately 700 Hz, 1.4 kHz and 2.3 kHz. The filters are broad, with slopes of 12 dB per octave. An analog representation of each filter output is delivered to an intracochlear electrode. Electrodes are placed at 4 mm intervals, spanning a range of 8 mm to 20 mm from the cochlear base. Electrodes closer to the base of the cochlea are associated with filters that have higher cutoff frequencies. Using this strategy, a typical patient can have a fluent one-on-one conversation (with the help of lipreading) and he also has significant speech reception scores without lipreading. However, there is still controversy about the cues employed by users of the Ineraid device to understand speech.

The aim of the current study was to determine the cues employed by users of the Ineraid cochlear implant to identify vowels. Our approach was to implement various mathematical decision models and determine which one gives the best fit to data on vowel perception reported by Dorman et al. (1992). In particular, we implemented models that used only temporal cues, only amplitude cues, or both kinds of cues at the same time. Our preliminary conclusion was that perceptual models with

only one type of cue (either temporal or amplitude cues) may be insufficient to explain important characteristics of the data. A simple model incorporating both kinds of cues appears to succeed where other models fail. The most successful model gave a good fit to actual speech reception data, for all vowels used in the study. This model used one temporal dimension (an estimate of $F1$ obtained from the temporal stimulation waveform delivered to channel 1) and three amplitude dimensions, namely the ratios of stimulation amplitude delivered to channels 2, 3 and 4 with respect to the stimulation amplitude delivered to channel 1.

Our main conclusion is that it is very difficult to explain vowel perception by Ineraid patients based only on the time waveforms delivered to each channel, or only on the distribution of energy among channels. Users of the Ineraid device seem to integrate temporal and channel amplitude information in order to understand speech.

1.2.3 Degradation of Speech and Hearing with Bilateral Acoustic Neuromas

In this project, we are studying the relation between speech and hearing in people who become deaf from bilateral acoustic neuromas (auditory nerve tumors) associated with the genetic disorder neurofibromatosis type II (NF2). The primary goal of the study is to increase our understanding of the role of hearing in the control of adult speech production. The rationale and approach for this work are similar to those of our ongoing work on the speech production of cochlear implant patients. Speech acoustic and physiological parameters have been recorded and speech perception has been tested in a group of 40 (still hearing) NF2 patients. Then the same parameters are recorded at intervals for any patients who suffer further hearing loss.

Two of the enrolled patients have suffered further hearing loss, and we have obtained post-loss recordings on both of them. We have analyzed the pre- and post-loss recordings from one of the two, who lost her hearing due to tumor surgery and received a multichannel auditory brainstem implant (ABI), which restored some limited hearing. Recordings have been made longitudinally prior to and following hearing loss, covering a period of about two years. Perceptual testing following surgery showed that the subject (when using the ABI) had an awareness of sounds but poor (i.e., ineffective) speech discrimination ability. Informal observations indicate a slowly progressing, slight decrease in intelligibility. Longitudinal production changes appear to fall into three categories: changes in baseline values of the postural parame-

ters of SPL, speaking rate and F_0 , some changes in phonemic contrasts, and changes in the syllable-to-syllable regulation of F_0 and SPL (reported above in section 1.2.1). These changes are roughly consistent with an initial inability to make much use of the auditory feedback provided by the ABI, followed by a period of accommodation in which postural parameters appear to be returning to pre-loss values, but phonemic and syllable-to-syllable parameters continue to move away from pre-loss values. (The surgery also resulted in facial paralysis on one side, which is taken into account when interpreting speech production results.)

Several post-implant sessions have also included a recording made after 24 hours with the speech processor of the ABI turned off. Multiple repetitions of the speech material were recorded first with the processor off, then with it turned on for a number of minutes, then with it off again. Analysis of these recordings is almost complete.

1.2.4 Objective Assessment of Vocal Hyperfunction

This project is funded under a subcontract to the Massachusetts Eye and Ear Infirmary in collaboration with Dr. Robert E. Hillman.

The major goal of this project is to further develop and use quantitative measures of voice production to provide objective descriptions of conditions referred to as vocal hyperfunction. This work involves the use of noninvasive acoustic, aerodynamic and physiologic measures to study both organic (nodules, polyps, contact ulcers) and nonorganic (functional dysphonia/aphonia) manifestations of vocal hyperfunction. These measures are examined in relation to encoded descriptions of the pathophysiologic status of the larynx (from videolaryngoscopy/stroboscopy), pertinent medical and psychosocial factors, and judgments about perceptual characteristics of the voice. Interpretation of results will be aided through use of a simple model of vocal-fold vibration, as described in section 1.1.4.

Comparisons Among the Glottal Airflow Waveform, the Electroglottographic Signal, and the Acoustic Spectrum

The inverse filtering technique used in this work is not without problems: the potential for an air leak between the subject's face and the mask; cases of unsuccessful inverse filtering resulting in formant residuals (although some F_1 ripple may be due to subglottal coupling); and smoothing effects of low-pass filtering at around 1 kHz, resulting in a

rounding of an otherwise-abrupt change in the flow waveform that occurs at the moment of vocal-fold closure. Therefore, we added measures of the acoustic spectrum slope (at low and high frequencies) to our paradigm that have been found salient for vocal intensity as well as voice quality. We also calculated an indirect measure of vocal fold closure (adduction quotient), obtained from an electroglottographic (EGG) signal. The goal was to improve methods of evaluating voice disorders and their treatment by finding complements and/or substitutes for those airflow measures that are especially sensitive to recording and analysis difficulties. In addition, relationships among the aerodynamic, acoustic, and EGG measures were studied for two speech tasks; strings of repeated /pæ/ syllables and sustained phonation of /æ/. Each task is needed for different kinds of voice analyses.

The main results for group and individual data led to the following conclusions: (1) Adduction quotient, measured from the waveform, is sensitive enough to differentiate between waveforms with gradual versus abrupt vocal-fold closing movements. (2) Measurements of the spectrum slope (especially A1-A3, the difference in amplitudes of the spectrum prominences of F_1 and F_3) may add important information to glottal waveform measures about voices with high vocal-fold closing velocities, often found for patients with hyperfunctionally-related voice disorders. (3) Some measures differ significantly depending upon whether energy in the F_3 region is comprised predominantly of harmonics or noise. (4) The EGG-based adduction quotient can serve as a complement to flow measures when there are problems with formant residuals that make the flow-based adduction quotient less reliable. (5) Large inter-speaker and session-to-session intra-speaker variation in DC flow may be at least partly due to air leakage not noticed during the recording. Thus, DC flow data must be interpreted with caution, and the value of DC flow as a clinical tool seems questionable. (6) Cross-task comparisons of measures obtained from /æ/ and /pæ/ can be made after adjustments for SPL differences.

Phonatory Function in Women with Vocal Nodules

In initial work we conducted a study that compared phonatory function of a group of 12 adult female bilateral vocal-fold nodules patients with a group of age matched normal female controls. After modifying our signal processing system, we reanalyzed the recordings from the initial study and combined the data with data for new subjects to yield a study comparing a group of 22 adult female nodules patients with 22 matched normal controls.

Statistical analyses of these data lead to the suggestion that bilateral vocal-fold nodules are associated with a pathophysiological phonation mechanism in which normal relationships between SPL and underlying vocal parameters are disrupted, i.e., there is reduction in the efficiency with which aerodynamic energy is converted into SPL, potentially contributing to ever-increasing vocal hyperfunction. Nodules patients appeared to expend higher than normal levels of aerodynamic energy (reflected in higher levels of subglottal pressure, peak flow, and AC flow) to attain a given SPL. These results also support our previous hypothesis about the potential existence of a "vicious cycle" in which the presence of lesions makes voice production more difficult (disrupts the normal vibratory mechanism), requiring higher levels of aerodynamic driving and myoelastic restoring forces. Such increases in the forces underlying phonation may lead to excessively stiff folds and a further increase in the collision forces and the further development of nodules. The tendency for subjects with nodules to speak louder than normal may exacerbate the problem and could conceivably accelerate the pathological process. The existence of this hypothesized pathophysiological mechanism should also be apparent in acoustic spectral measures (e.g., steeper spectral slope). We are currently examining acoustic spectra for such evidence of this mechanism.

1.2.5 Acoustic and Perceptual Effects of Endoscopic Nasal Surgery

This project is carried out in collaboration with Dr. Ralph Metson of the Massachusetts Eye and Ear Infirmary. The aim of this research is to determine the effects of surgical alterations of nasal anatomy on the spectral characteristics and perceptual attributes of speech. Five patients who underwent endoscopic nasal surgery were recorded prior to surgery, then one week and one month after surgery. The utterances were six vowel types adjacent to nasal consonants and stop consonants. In addition to endonasal surgery enlarging the sinus openings, some patients had a correction of deviated septum, resection of a turbinate, or removal of polyps. Acoustic analysis was carried out for nasalized vowels, nonnasalized vowels, and the nasal consonants /m/ and /n/. Significant differences in spectral properties were observed in the consonants and nasalized vowels recorded before and after surgery. For example, changes were found in the prominence of extra peaks due to nasalization and the first formant bandwidth was narrower for the nasal consonants and nasalized vowels. All except one patient perceived a change in their speech post-operatively. Attempts have

been made to account for the speech changes by incorporating the anatomical alterations caused by surgery into a speech production model. In particular, the removal of surfaces within the nasal cavity reduces the acoustic loss and leads to narrower bandwidths for some resonances.

1.2.6 Aiding Dysarthric Speakers

One practical aim of this research is to determine how best to use speech recognition techniques for augmenting the communication abilities of dysarthric speakers. As a first step toward this goal, we have performed the following kinds of analyses and tests on words produced by eight dysarthric speakers: a closed-set intelligibility test, critical listening and transcription, acoustic analysis of selected utterances, and an evaluation of the recognition of words by a commercial speech recognizer. An outcome of this evaluation is a description of attributes of vowels and consonants which are produced adequately and consistently and those which are produced in a distorted or inconsistent manner. The analysis and testing have led to several conclusions concerning the control of the articulators for these speakers: production of obstruent consonants was a particular problem, whereas sonorant consonants were less of a problem. Of the obstruent errors, most were place errors for alveolar consonants (particularly fricatives), but voicing errors were also high. These obstruent consonants were often produced inconsistently, as inferred from acoustic analysis and from low scores from the recognizer for words with these consonants. In comparison, vowel errors were less prevalent. The practical use of a speech recognizer for augmenting the communication abilities of the speakers requires the selection of an inventory of utterances that are produced consistently and consequently are recognized with reasonable accuracy. Based on the experimental data, word lists that lead to the enhancement of recognition accuracy for each speaker have been designed.

1.3 Speech Production Planning and Prosody

1.3.1 Interaction Between Prosody and Planning

Our work in speech production planning is focused on the interaction between prosody and other aspects of planning, such as segmental serial ordering, glottalization and error detection/correction. To facilitate these studies, we have spent

several years developing a range of speech databases for prosodic analysis. The largest database, consisting of seven hours of speech read "on air" by seven different professional FM radio news broadcasters, has been digitized, orthographically transcribed, automatically phonetically aligned and labeled for the occurrence of audible breath intakes. It will be made available to the research community via the Linguistics Data Consortium (LDC) at the University of Pennsylvania. In addition, we have helped to develop a new prosodic labeling system (ToBI), which was recently evaluated for reliability across more than a dozen transcribing sites.¹⁷ Using this transcription system, we have marked the pitch accents, boundary tones and prosodic constituent boundaries of four stories that were read by six of the seven speakers, and more than 50 stories recorded in the broadcast studio by several of the speakers. These prosodic labels, which will also be made available via the LDC, are the basis for the analyses described below. Finally, we are prosodically labeling digitized versions of 200 spoken errors from the ATIS and Switchboard corpora of spontaneous speech, as well as 400 utterances read by nonprofessional speakers as part of a corpus developed for the study of lexical access. Training of new prosodic labelers and evaluation of the labeling conventions are ongoing in our lab.

In recent studies, the FM radio news database has provided evidence for the view that speakers signal the onset of a new intonational phrase using an early pitch accent where possible (as in e.g., "In MASSachusetts HOSpitals"), and prefer to avoid the pitch accent clash that results when two adjacent syllables in the same intonational phrase are pitch accented. These two factors together, phrase onset marking and pitch accent clash avoidance, provide an alternative account of what has been called "stress shift", and provide substantial support for the claim that constituents of the prosodic hierarchy play an active role in speech production planning.

Further evidence for this hypothesis has been derived from the study of glottalization of vowel-onset syllables. In earlier work, we demonstrated that speakers glottalize vowel onsets at prosodically significant locations, i.e., at the beginning of a new intonational phrase, or when the syllable is pitch-accented, in a subset of the BU FM news database containing more than 2000 candidate syllables in a

range of prosodic and segmental contexts. More recently, we have shown that this pattern of glottalization of prosodically significant syllables holds for nonprofessional read speech as well. We are currently examining the glottalization of vowel-onset syllables in spontaneous (nonread) speech.

Examining the role of glottal gestures in speech production more extensively, we are also testing the hypothesis that when speakers detect an error and interrupt an utterance to correct it, the interruption is accomplished via a relatively sudden glottal closure. While some of the errors in our recorded corpus show this pattern, particularly if the interruption occurs within a syllable, others appear to be characterized by completion of the word with a diminution in amplitude that is more characteristic of an utterance-final word. We are currently examining the correlation of this contrast with the type of error being corrected.

1.3.2 Some Phrase-level Influences on the Glottal Waveform

The prosody of an utterance is often described in terms of the locations of attributes such as pitch accents, boundary tones, and vowel reduction. These prosodic descriptions are usually represented in the sound by changes in fundamental frequency, duration, and other temporal and spectral attributes of the segments. We have collected data showing that the amplitude and spectrum of the glottal pulses, as well as their frequency, undergo modification depending on locations of pitch accents and boundary tones and depending on vowel reduction. The following results were obtained: (1) Reduced vowels tend to have significantly lower amplitude (7 to 13 dB) than nonreduced vowels, together with an increased first-formant bandwidth and an increased tilt in the source spectrum. (2) A nonreduced vowel has a somewhat reduced amplitude (by about 6 dB) when it follows a nuclear pitch accent. (3) A nonreduced vowel in utterance-final position in a declarative sentence shows a decreased amplitude of the first-formant peak, an increased open quotient, and an increased spectrum tilt. Production mechanisms that could account for these changes include modifications in subglottal pressure, adjustments of the glottal configuration, and influences of constrictions in the supraglottal airway.

¹⁷ J.F. Pitrelli, M.E. Beckman, and J. Kirschberg, *Proceedings of the International Conference on Spoken Language Processing 3*, Yokohama, Japan, 1994, pp. 123-126.

1.4 Studies of the Acoustics, Perception, and Modeling of Speech Sounds

1.4.1 Use of Transient Response to Determine the Natural Frequencies of the Nasal Cavity

Direct estimates of the natural frequencies of the nasal cavity are difficult to make, and these frequencies must often be inferred from calculations based on anatomical data or from measurements of the spectra of nasal consonants and vowels. In our present research, we have attempted to determine these natural frequencies based on measurements of the transient response of the nasal cavity. An abrupt excitation of the nasal cavity is obtained by first creating a continuous flow of air through the nasal passages with the velum lowered and the lips closed. The velum is then raised abruptly so that there is rapid closure of the velopharyngeal port, aided by the buildup of intraoral pressure near the instant of closure. This closure creates an acoustic transient that excites the nasal cavity. A spectral analysis of this transient response reveals peaks that represent the natural frequencies of the nasal cavity when it is closed at the posterior end. Some of these peaks are well-defined and consistent for a given subject, and others are less prominent. The latter are probably resonances of the sinuses, which appear as pole-zero pairs in the transfer function, whereas the former represent natural frequencies of the nasal cavity proper.

Measurements of the two lowest natural frequencies of the nasal cavity proper for six adult speakers give an average value of 540 Hz (range of 400-640 Hz) and 2160 Hz (range of 1880-2420 Hz). Additional resonances, presumably due to sinuses, appear for some subjects at frequencies of 210-250 Hz and 1150-1420 Hz. The values of the natural frequencies of the nasal cavity proper are consistent with sweep-tone measurements reported by others, and with estimates of these resonances based on anatomical data. There appears to be some variability in estimates of the natural frequencies of the sinuses.

1.4.2 Modification of /ð/ by a Preceding Nasal Consonant

Presumably as a result of coarticulation, /ð/ often assimilates to a preceding /n/ in phrases like "win those," but this assimilation is not complete for all features. With respect to the feature [nasal], the assimilation is often radical. The entire consonant

region in the middle of the two-word sequence is nasalized. However, acoustic evidence suggests that contextually-nasalized /ð/ retains its dental place of articulation. Specifically, $F2$ is considerably lower at the release of a contextually-nasalized /ð/ than at the release of a true /n/, as would be expected for a dental consonant. Perception tests show that listeners can generally tell the difference between natural tokens of pairs like "win nos" and "win those," even when the /ð/ is completely nasalized. In addition, a synthetic stimulus continuum was constructed in which items differed only with respect to $F2$ frequency in the vicinity of the nasal consonant regions of phrases like "win nos". Listeners systematically reported hearing "those" more often when $F2$ was low at the release of the nasal consonant. These results are consistent with the claim of Krakow, Fowler, and others, that listeners can at least sometimes factor out coarticulatory effects.

1.4.3 Glottal Characteristics of Female Speakers—Acoustic, Physiological, and Perceptual Correlates

In a previous study of vowels produced by female speakers, we showed substantial individual differences in acoustic parameters related to glottal characteristics. Based on measurements taken on the speech signal or spectrum, inferences were made about glottal configuration during phonation and the nature of the glottal pulse. Subjects fell into two groups based on the acoustic measurements: Group 1, assumed to have abrupt glottal closure, and Group 2, assumed to have nonsimultaneous closure. Results of a listening test have shown that members of Group 2 are perceived to be breathier than members of Group 1. Our present research extends the earlier work in several ways. Physiological measurements have been made for four subjects, including inverse filtered airflow recordings and glottal images obtained by fibrescopy. Also, listening tests using synthesized speech have been carried out to study the role of glottal characteristics in speaker discrimination, and the usefulness of the acoustic measures for guiding the synthesis of natural sounding speech. The physiological and perceptual data are found to be consistent with the earlier interpretations of the acoustic measures of glottal characteristics.

1.4.4 The Effect of Emphatic Accent on Contextual Tonal Variation

Recent data show that the F_0 contour of a tone in Mandarin is perturbed differently by the tone preceding it than by the tone following it: the influence of the preceding tone (carryover effect) is assimilatory—the beginning of the F_0 contour of a tone becomes similar to the ending pitch value of the preceding tone; the influence of the following tone (anticipatory effect) is mostly dissimilatory—the F_0 maximum of a tone dissimilates from the F_0 minimum of the following tone. The present study examines the effect of emphatic accent on different syllables in disyllabic words in order to learn more about the nature of contextual tonal variation.

Native speakers of Mandarin produced /mama/ with different tone combinations. They were requested to produce those utterances with emphasis on the first or last syllable, or with no emphasis on either syllable. Various F_0 measurements were taken, including maximum and minimum F_0 values and F_0 values at different locations in the vowel and the nasal segments. Comparisons among the three accent conditions confirm that carryover assimilation is strongest when the first syllable is emphasized. As for the anticipatory effect, dissimilation is found in all three accent conditions, but the magnitude of the effect is strongest when the second syllable receives accent. In summary, for both carryover and anticipatory effects, the accented syllables are found to exert greater influence on the unaccented syllables than the other way around, regardless of the nature of the influence.

1.4.5 Time-variation in Mandarin Voiceless Sibilant Spectra

The three Mandarin sibilant fricatives, [s], [ʂ], and [ʂ̥], were studied using a combination of time-averaging and ensemble-averaging of the spectra. Ten native speakers of Beijing Mandarin (five male and five female) produced these fricatives followed by both unrounded and rounded high vowels. Time-averaged spectra were obtained by averaging thirteen consecutive 8-ms FFT windows over 20-ms intervals. Token-ensemble-averaged spectra were then obtained by averaging over the time-averaged spectra of ten repetitions of each sentence produced by each speaker at time-normalized locations in the utterances. Further ensemble-

averaging was also performed over the male and female speakers separately to obtain group-ensemble-averaged spectra. Preliminary examination of both token-ensemble-averaged and group-ensemble-averaged spectra reveals that (a) Mandarin sibilants have substantial time-variation in their noise spectra, indicating continuous articulatory movement throughout the production of the frication; and (b) all three sibilants manifest substantial spectral variation due to anticipatory coarticulation with the following vowel. This kind of variation is evident from the very beginning of the frication noise, indicating that the extent of the anticipatory coarticulation may go beyond the beginning of the frication.

1.4.6 Acoustic and Perceptual Attributes of Fricative Consonants

Our studies of fricative consonants have been extended to include examination of the spectra of the fricative consonants in relation to adjacent vowels and the time variation of these spectra at the boundaries between fricatives and adjacent vowels. The following results emerged from the acoustic analyses:

1. For the strident fricatives /s ʂ ʂ̥/, the maximum spectrum amplitude in the frequency range of the third formant and higher is 15-22 dB higher than the corresponding spectrum amplitude for the weak fricatives /f θ/. Most of this difference can be accounted for by the influence of the resonance of the front cavity (or tongue blade channel) on the transfer function from the turbulence noise source to the output.
2. The changes in the spectrum that occur in a time of 20-odd ms preceding voicing onset for the vowel generally consist of a reduction in high-frequency amplitude for strident consonants and the appearance of aspiration noise in the region of the second and third formants.

Perceptual experiments with synthesis of fricative-vowel syllables showed the importance of maintaining a strong high-frequency spectrum amplitude for the consonant /s/, but with limits on the range of amplitudes that was acceptable. Listeners accepted a wider range of amplitudes for the weak fricative /f/.

1.5 Models for Lexical Representation and Lexical Access

1.5.1 Theoretical Background

Our work on the development of models for lexical access stems from a view that the lexical items that underlie an utterance are stored in memory in terms of sequences of segments, each of which is classified by a set of distinctive features. The retrieval of these segments and features from the speech signal as produced by a speaker is a two-stage process. (1) The locations of a sequence of landmarks are determined, and these landmarks identify critical regions in the signal where acoustic information about individual segments is concentrated. The landmarks are the result of implementing articulator-free features, and each landmark is labeled with these features. (2) A directed search for acoustic properties is carried out in the vicinity of these landmarks, leading to estimates of the articulator-bound features of the segments.

1.5.2 Identification of Landmarks

This work is a component of a proposed knowledge-based speech recognition system which uses *landmarks* to guide the search for *distinctive features*. An algorithm has been developed for automatically detecting acoustically-abrupt landmarks. The algorithm is hierarchically-structured, and is rooted in linguistic and speech production theory. It uses several factors to detect landmarks: energy abruptness in six frequency bands and at two levels of temporal resolution, segmental duration, broad phonetic class constraints, and constraints imposed by articulation on landmark sequences. Tested on a database of continuous, clean speech of women and men, the landmark detector has detection rates 90 percent and above, substitution rates between 1 percent and 3 percent, and insertion rates 16 percent and below. The effects of landmark type, phonetic class, and prosody have been evaluated. These promising results indicate that landmarks are robustly-identifiable points in a speech waveform and that a landmark detector as a front-end in a speech recognition system could be feasible.

1.5.3 Automatic Context-sensitive Estimation of Distinctive Features at Landmarks

We have continued to develop procedures for estimation of distinctive feature values at articulatory landmarks. Toward this end, we are modeling each distinctive feature as a table containing phonetic contexts, a list of signal measurements (acoustic correlates) which provide information about the feature in each context, and, for each context, a statistical model for evaluating the feature given the measurements. The model of a distinctive feature may include several sets of acoustic correlates, each indexed by a different set of context features. Context features are typically lower-level features of the same segment; for example, manner features ([continuant, sonorant]) provide context for the identification of articulator-bound features ([lips, blade]). The acoustic correlates of a feature can be any static or kinematic spectral measurements defined relative to the time of the landmark. The statistical model is a simple N-dimensional Gaussian hypothesis test. A measurement program has been developed to test the usefulness of user-defined phonetic contexts. Measures of voice-onset time and formant locus classification are being developed as examples.

1.6 Development of Computer and Data Processing Facilities

A program has been written to display high-quality spectrograms on our engineering workstations. The spectrogram display includes a cursor which can be time-aligned with cursors in MITSYN-based programs for interactive data extraction or in the Klatt software used for acoustic analyses. This display will facilitate the identification of abrupt spectral transitions in acoustic signals.

The KLSYN88 speech synthesis facility has been augmented to include a transient source, consisting of a single sample, which can be filtered in the same way as the frication source. This new source is used to simulate the transients that occur at the release of stop or affricate consonants.

1.7 Publications

1.7.1 Papers Published

- Holmberg, E., J. Perkell, R. Hillman, and C. Gress. "Individual Variation in Measures of Voice." *Phonetica* 51(1-3): 30-37 (1994).
- Holmberg, E., R. Hillman, J. Perkell, and C. Gress. "Relationships between Intra-speaker Variation in Aerodynamic Measures of Voice Production and Variation in SPL Across Repeated Recordings." *J. Speech Hear. Res.* 37: 484-495 (1994).
- Johnson, M.A. "Automatic Context-Sensitive Measurement of the Acoustic Correlates of Distinctive Features at Landmarks." *Proceedings of the International Conference on Spoken Language Processing* 3, Yokohama, Japan, 1994, pp. 1639-1642.
- Lane, H., J. Wozniak, and J.S. Perkell. "Changes in Voice-Onset Time in Speakers with Cochlear Implants." *J. Acoust. Soc. Am.* 96(1): 56-64 (1994).
- Matthies, M.L., M.A. Svirsky, H. Lane, and J.S. Perkell. "A Preliminary Study of the Effects of Cochlear Implants on the Production of Sibilants." *J. Acoust. Soc. Am.* 96 (3): 1367-1373 (1994).
- Perkell, J., R. Hillman, and E. Holmberg. "Group Differences in Measures of Voice Production and Revised Values of Maximum Airflow Declination Rate." *J. Acoust. Soc. Am.* 96 (2): 695-698 (1994).
- Shattuck-Hufnagel, S. "Stress Shift as Early Pitch Accent Placement: A Comment on Beckman and Edwards." In *Phonological Structure and Phonetic Form, Papers in Laboratory Phonology III*. Ed. P.A. Keating. Cambridge, Massachusetts: Cambridge University Press, 1994, pp. 34-42.
- Shattuck-Hufnagel, S., M. Ostendorf, and K. Ross. "Stress Shift and Early Pitch Accent Placement in Lexical Items in American English." *J. Phonetics* 22: 357-388 (1994).
- Sperry, E., R. Hillman, and J.S. Perkell. "Use of Inductance Plethysmography to Assess Respiratory Function in a Patient with Vocal Nodules." *J. Med. Speech-Language Path.* 2: 137-145 (1994).

Stevens, K.N. "Phonetic Evidence for Hierarchies of Features." In *Phonological Structure and Phonetic Form, Papers in Laboratory Phonology III*. Ed. P.A. Keating. Cambridge, Massachusetts: Cambridge University Press, 1994, pp. 242-258.

Stevens, K.N. "Scientific Substrates of Speech Production." In *Introduction to Communication Sciences and Disorders*. Ed. F. Minifie. San Diego: Singular, 1994, pp. 399-437.

Stevens, K.N., C.A. Bickley, and D.R. Williams. "Control of a Klatt Synthesizer by Articulatory Parameters." *Proc. Int. Conf. on Spoken Language Process.* 1: 183-186 (1994).

Stevens, K.N., and H.M. Hanson. "Classification of Glottal Vibration from Acoustic Measurements." In *Vocal Fold Physiology: Voice Quality Control*. Eds. O. Fujimura and M. Hirano. San Diego: Singular, 1994, pp. 147-170.

Wilhelms-Tricarico, R., and J.S. Perkell. "Biomechanical and Physiologically based Speech Modeling." *Proceedings of the 2nd ESCA/IEEE Workshop on Speech Synthesis*, New Paltz, New York, 1994, pp. 17-20.

1.7.2 Papers Accepted for Publication

- Hillman, R.E., E.B. Holmberg, J.S. Perkell, J. Kobler, P. Guiod, C. Gress, and E.E. Sperry. "Speech Respiration in Adult Females with Vocal Nodules." *J. Speech Hear. Res.* Forthcoming.
- Keyser, J.S., and K.N. Stevens. "Feature Geometry and the Vocal Tract." *Phonology*. Forthcoming.
- Perkell, J.S. "Articulatory Processes." In *Handbook of Phonetic Science*. Eds. W. Hardcastle and J. Laver. Oxford: Blackwell. Forthcoming.
- Perkell, J.S., M.L. Matthies, M.A. Svirsky, and M.I. Jordan. "Goal-based Speech Motor Control: A Theoretical Framework and Some Preliminary Data." *J. of Phonetics*. Forthcoming.
- Shattuck-Hufnagel, S. "The Importance of Phonological Transcription in Empirical Approaches to 'Stress Shift' vs. Early Accent: a Commentary on Grabe and Warren Stress Shift: Do Speakers do it or do Listeners hear it? and Vogel, Bunnell and Hoskins The Phonology and Phonetics of the Rhythm Rule." In *Papers in Laboratory Phonology IV*. Eds. B.A. Connell and A. Arvaniti. Cambridge, Massachusetts: Cambridge University Press. Forthcoming.

Shattuck-Hufnagel, S. "Slips of the Tongue." In *Encyclopedia of Language and Linguistics*. Eds. R.E. Asher and J.M.Y. Simpson. Oxford: Pergamon Press. Forthcoming.

Stevens, K.N. "Articulatory-acoustic-auditory Relationships." In *Handbook of Phonetic Sciences*. Eds. W. Hardcastle and J. Laver. Blackwell: Oxford. Forthcoming.

Wilhelms-Tricarico, R. "Physiological Modeling of Speech Production: Methods for Modeling Soft-tissue Articulators." *J. Acoust. Soc. Am.* Forthcoming.

1.7.3 Papers Submitted for Publication

Chen, M. "Acoustic Parameters of Nasalized Vowels in Hearing-impaired and Normal-hearing Speakers." Submitted to *J. Acoust. Soc. Am.*

Dilley, L., S. Shattuck-Hufnagel, and M. Ostendorf. "Glottalization of Vowel-Initial Syllables as a Function of Prosodic Structure." Submitted to *J. Phonetics*.

Holmberg, E.B., R.E. Hillman, J.S. Perkell, and S. Goldman. "Comparisons Among Aerodynamic, Electroglottographic, and Acoustic Spectrum Measures of Female Voices." Submitted to *J. Speech Hear. Res.*

Lane, H., J. Wozniak, M.L. Matthies, M.A. Svirsky, and J.S. Perkell. "Phonemic Resetting vs. Postural Adjustments in the Speech of Cochlear Implant Users: an Exploration of Voice Onset Time." Submitted to *J. Acoust. Soc. Am.*

Manuel, S.Y. "Speakers Nasalize /g/ After /n/, But Listeners Still Hear /g/." Submitted to *J. Phonetics*.

Ostendorf, M., P. Price, and S. Shattuck-Hufnagel. "A Database of Prosodically Labelled Speech." In preparation.

Perkell, J.S., Matthies, M.L., and Svirsky, M.A. "Goal-based Speech Motor Control: A Theoretical Framework and some Preliminary Data." Submitted to *J. Phonetics*.

Perkell, J.S. "Properties of the Tongue Help to Define Vowel Categories: Hypotheses Based on Physiologically-oriented Modeling." Submitted to *J. Phonetics*.

Shattuck-Hufnagel, S., L. Dilley, and M. Ostendorf. "Prosodic Constraints on Glottalization of Vowel-initial Syllables in American English." Abstract submitted for Accoustical Society of America Meeting, June 1994.

Stevens, K.N. "Models of Speech Production." In *Handbook of Acoustics*. Ed. M. Crocker. New York: Wiley.

Wilhelms-Tricarico, R. "Biomechanical and Physiologically Based Speech Modeling." Submitted to *J. Phonetics*.

1.7.4 Thesis

Massey, N.S. *Transients at Stop Consonant Releases*. S.M. thesis. Dept. of Electr. Eng. and Comput. Sci., MIT, 1994.

Section 2 Sensory Communication

Chapter 1 Sensory Communication

Chapter 1. Sensory Communication

Academic and Research Staff

Professor Louis D. Braida, Nathaniel I. Durlach, Professor Richard M. Held, Professor Anuradha M. Annaswamy, Dr. David L. Brock, Dr. Donald K. Eddington, Dr. Susan L. Goldman, Dr. Julie E. Greenberg, Dr. Lynette A. Jones, Dr. Jeng-Feng Lee, Dr. William M. Rabinowitz, Dr. Christine M. Rankovic, Dr. Charlotte M. Reed, Dr. Wendelin L. Sachtler, Dr. J. Kenneth Salisbury, Dr. Barbara G. Shinn-Cunningham, Dr. Mandayam A. Srinivasan, Dr. Anne H. Takeuchi, Dr. Thomas E.v. Wiegand, Dr. David Zeltzer, Dr. Patrick M. Zurek, Lorraine A. Delhorne, Seth M. Hall, Dorrie Hall

Visiting Scientists and Research Affiliates

Dr. Paul Duchnowski, Geoffrey L. Plant, Dr. Matthew Power

Graduate Students

Walter A. Aviles, Gerald L. Beauregard, Maroula Bratakos, Jyh-Shing Chen, Kiran Dandekar, Joseph Desloge, Eric M. Foxlin, Joseph A. Frisbie, Rogeve J. Gulati, Rakesh Gupta, Louise Jandura, Jean C. Krause, David S. Lum, Hugh B. Morgenbesser, Philip M. Nadeau, Michael P. O'Connell, Nicholas Pioch, Hong Z. Tan, Daniel P. Welker, Craig B. Zilles

Undergraduate Students

Walter E. Babiec, Stephen V. Baird, James H. Bandy, Susan E. Born, Erika N. Carmel, Gail Denesvich, Ashanthi Gajaweera, Dorrie Hall, Gabrielle Jones, Steingrimur P. Karason, Danielle G. Lemay, David C. Lossos, Jonathan Pfautz, Frederick L. Roby, Tomas Rodriguez-Perez, Jonathan R. Santos, Matthew Sexton, Ranjini Srikantiah, Joseph D. Towles, Lukasz A. Weber, Evan F. Wies

Technical and Support Staff

Ann K. Dix, Eleanora M. Luongo, Mabayoje Tuyo

1.1 Research on Hearing, Hearing Aids, and Tactile Communication of Speech

1.1.1 Hearing Aid Research

Sponsor

National Institutes of Health
Contract 2 R01 DC00117

Project Staff

Professor Louis D. Braida, Dr. Paul Duchnowski, Dr. Matthew Power, Dr. Christine M. Rankovic, Dr. Anne H. Takeuchi, Seth M. Hall, Dr. Patrick M. Zurek, Joseph A. Frisbie, Ann K. Dix, Danielle G. Lemay, Matthew Sexton, Ranjini Srikantiah, Jean C. Krause, David S. Lum

Characteristics of Sensorineural Hearing Impairment

Although there is no satisfactory model of sensorineural hearing impairment, several *functional models* that allow listeners with normal hearing to experience the perceptual distortions and speech-reception problems of hearing-impaired listeners are emerging. Our past work has documented the effectiveness of masking noise that elevates the tone-detection thresholds of normal-hearing listeners to those of listeners with hearing impairments in simulating limitations on speech-reception associated with the impairment.¹ More recently, Duchnowski and Zurek² have shown that a type of multiband amplitude expansion proposed by

¹ P.M. Zurek and L.A. Delhorne, "Consonant Reception in Noise by Listeners With Mild and Moderate Hearing Impairment," *J. Acoust. Soc. Am.* 82: 1548-1559 (1987).

² P. Duchnowski and P.M. Zurek, "Villchur Revisited: Another Look at AGC Simulation of Recruiting Hearing Loss," *J. Acoust. Soc. Am.*, forthcoming.

Villchur³ is also capable of simulating these limitations.

Both the noise and expansion simulations of hearing loss are addressed nominally at the minimal factors of audibility and abnormal loudness growth. These simulations differ both with respect to phenomenological realism and in the relation of the acoustic properties of processed stimuli to the normal listener's hearing. Current research is directed towards understanding the ability of the two simulation approaches to account for the impaired perception of nonspeech sounds. To evaluate the ability of the expansion simulation to reproduce the effects of hearing impairment for such sounds, we have developed a version of the simulator that operates in real time. This simulator uses a digital signal processor to filter signals into fourteen bands (with widths comparable to critical bands), estimates the short-term energy in each band, applies a level-dependent attenuation based on this estimate, and sums the resulting attenuated band signals. Measurements⁴ of simultaneous narrowband masking patterns and forward-masked psychophysical tuning curves indicate that both simulation techniques produce reductions in frequency selectivity that are similar to those observed in listeners with sensorineural hearing impairments (e.g., Dubno and Schaefer⁵). By contrast, the expansion simulation preserves the microstructure of the normal-hearing listener's audiogram, while the masking simulation does not.

Characteristics of the Speech Signal

Token Variability

The goal of this research is to understand the limitations on speech intelligibility associated with natural variations in the utterances of the same speech sound. Although differences in the acoustic realization of speech elements associated with the

identity of the speaker are typically large enough to have stable perceptual effects, subtler differences associated with context and variability of production in a fixed context can also be discerned⁶ and effect the ability to identify speech sounds, particularly when the speech signal is degraded by noise or other distortions. Although the difficulties posed by such variation for automatic speech recognition systems are increasingly appreciated, their effects on human speech reception have not been studied systematically.

To obtain insight into the combined effects of multiple sources of acoustic variability, Takeuchi and Braida⁷ measured the ability of listeners to identify /b/-V-/t/ syllables in which the vowel was selected from 9 monophthongs of American English. To make the identification task nontrivial, the syllables were distorted by a multiplicative noise process. In one stimulus set, the three tokens of each syllable were produced by a single speaker, but each token was distorted by three different noises. In a second set, the tokens were produced by three talkers, but each token was distorted by a single noise. The effects of speaker variability were generally greater than the effects of token variability or noise variability. Token variability tended to have a greater effect when the stimulus set varied in distorting noise than when the stimulus set varied in speaker, suggesting that the degree of variability effect depends upon the context provided by the other stimuli in a set. The effects of speaker and token variability, as well as of token and noise variability, were generally additive. Blocking the stimuli by holding one or both sources of variability constant reduced, but did not eliminate, these effects.

Clear Speech

We have initiated a new study of the changes that occur in the acoustic speech signal associated with the attempt to speak clearly. Previous studies (e.g.,

³ E. Villchur, "Electronic Models to Simulate the Effect of Sensory Distortions on Speech Perception by the Deaf," *J. Acoust. Soc. Am.* 62: 665-674 (1977).

⁴ D.S. Lum, *Evaluation of a Hearing Loss Simulator*, Advanced Undergraduate Project Report, Dept. of Electr. Eng. and Comput. Sci., MIT, 1994.

⁵ J.R. Dubno, and A.B. Schaefer, "Frequency Selectivity for Hearing-Impaired and Broadband-Noise-Masked Normal Listeners," *Quart. J. Exp. Psych.* 43A: 543-564 (1991).

⁶ R.M. Uchanski, L.D. Braida, C.M. Reed, and N.I. Durlach, "Speaking Clearly for the Hard of Hearing. IV: Further Studies of the Role of Speaking Rate," *J. Speech Hear. Res.*, forthcoming.

⁷ A.H. Takeuchi and L.D. Braida, "Effects of Multiple Sources of Variability on the Accuracy of Vowel Identification," submitted to *J. Acoust. Soc. Am.*

Uchanski et al.⁸ have demonstrated that clear speech is generally enunciated more slowly than conversational speech, but the degree to which the reduction in rate is essential to clarity has not been established. To improve our understanding of the importance of reduced speaking rate to improved intelligibility, we plan to measure the intelligibility of speech produced by "professional" talkers under nine different speaking modes. The talkers will be individuals, such as debaters, public speakers, and actors who have been trained to adopt speaking styles that differ from everyday conversational speech. The speaking modes will differ with respect to both speaking rate and other speech characteristics. Four of the modes will be at a conversational speaking rate: soft, loud, conversational, and clear speech at conversational rate. Two modes will be at a quick speaking rate: quick speech and clear speech at quick rates. Three modes will be at a slow rate: slow speech, clear speech, and conversational speech with pauses between words (as if speaking to a discrete-word automatic speech recognition system).

Preliminary measurements of the intelligibility of speech produced in the traditional conversational and clear styles suggests that there may be a simple relation between the word score W and average speaking rate R (with sentence durations corrected for pauses between words): $W = a - bR$, where a but not b depends on the identity of the talker. Based on this observation we plan to select talkers with relatively high values of a and attempt to train them using techniques similar to those developed by Chen⁹ to increase their speaking rate while maintaining the intelligibility of clear speech and intelligibility while maintaining the speaking rate of conversational speech.

Models of Speech Intelligibility

Speech Transmission Index

Unlike the Articulation Index (AI), (e.g., Dugal et al.¹⁰) which bases predictions of speech intelligibility on the long-term power spectrum of speech, the Speech Transmission Index (STI), (e.g., Houtgast et al.¹¹) bases predictions on the intensity modulation spectra for individual frequency bands. This distinction is fundamental to the understanding of the dependence of intelligibility on speaking mode. Whereas clear and conversational speech have roughly the same long-term spectrum,¹² they are likely to have different modulation spectra because of differences in speaking rate and consonant-vowel energy (CV) ratios. Also the effects of reverberation and multiband amplitude compression on the speech signal are likely to be more evident in the intensity modulation spectra than in the power spectrum.

Although the STI is typically computed from estimates of modulated spectra derived from theoretical considerations or from measurements of modulation transfer functions made with intensity modulated noise, we are attempting to base this calculation on measurements of real speech waveforms. However, these attempts have been obstructed by artifacts that distort the envelope spectra of speech that has been degraded by noise and reverberation. Specifically, we observe a "noise floor" in the envelope spectra if any background noise is present. For power spectra of white noise, the expected power spectral level is proportional to the variance of the noise. In our case, we compute power spectra of filtered noise envelopes. The variance of the envelopes is inversely proportional to the bandwidth of the octave filters we use. We have confirmed that the noise floors we observe vary in level according to the bandwidth of the filters. We are currently examining various ways to remove or compensate for these noise floor effects.

⁸ R.M. Uchanski, S. Choi, L.D. Braida, C.M. Reed, and N.I. Durlach, "Speaking Clearly for the Hard of Hearing IV: Further Studies of the Role of Speaking Rate," *J. Speech Hear. Res.*, forthcoming.

⁹ F.R. Chen, *Acoustic Characteristics and Intelligibility of Clear and Conversational Speech at the Segmental Level*, S.M. thesis, Dept. of Electr. Eng. and Comput. Sci., MIT, 1980.

¹⁰ R.L. Dugal, L.D. Braida, and N.I. Durlach, "Implications of Previous Research for the Selection of Frequency-Gain Characteristics," in *Acoustical Factors Affecting Hearing Aid Performance and Measurement*, eds. G.A. Studebaker and I. Hochberg (New York: Academic Press).

¹¹ T. Houtgast and H.J.M. Steeneken, "A Review of the MTF Concept in Room Acoustics and Its Use for Estimating Speech Intelligibility in Auditoria," *J. Acoust. Soc. Am.* 77: 1069-1077 (1985).

¹² M.A. Picheny, N.I. Durlach, and L.D. Braida, "Speaking Clearly for the Hard of Hearing II: Acoustic Characteristics of Clear and Conversational Speech," *J. Speech Hear. Res.* 29(4): 4344-446 (1986).

Even if they work on noise alone, none of the strategies tested have resulted in speech in noise spectra as we would expect.

We have also examined some alternative techniques to calculate the STI. Ludvigsen et al.¹³ have developed a technique in which the squared envelopes of octave bands of undistorted speech are correlated with those of degraded speech using a linear regression analysis. The slope of the regression is used, along with the squared envelope means, to compute a transmission index for each octave band. When we implemented their algorithm, we found that it is extremely sensitive to the existence of delays between the original and corrupted speech envelopes and would thus be difficult to apply to reverberant speech. Since, in many other ways this technique holds promise, we will continue studying this idea.

Publications

Duchnowski, P., and P.M. Zurek. "Villchur Revisited: Another Look at AGC Simulation of Recruiting Hearing Loss." *J. Acoust. Soc. Am.* Forthcoming.

Lum, D.S. *Evaluation of a Hearing Loss Simulator*. Advanced Undergraduate Project Report, Dept. of Electr. Eng. and Comput. Sci., MIT, 1994.

Maxwell, J.A., and P.M. Zurek. "Feedback Reduction in Hearing Aids." *IEEE Trans. Speech Audio Proc.* Forthcoming.

1.1.2 Enhanced Speechreading

Sponsor

National Institutes of Health
Contract 1 R01 DC02032

Project Staff

Professor Louis D. Braida, Dr. Susan L. Goldman, Charlotte M. Reed, Lorraine A. Delhorne, Dr. Paul Duchnowski, Maroula Bratakos, Gabrielle Jones, Mabayoje Tuyo, Philip M. Nadeau, Danielle G. Lemay, Matthew Sexton

Basic Studies of Audiovisual Integration

The McGurk effect¹⁴ demonstrates that visual lip movements can influence perception of auditory speech even when auditory and visual cues are in conflict. For example, when auditory /ma/ is dubbed onto visual lip movements of /ta/, the auditory-visual stimulus is often perceived as "na." Whereas this effect has been found to be robust for American perceivers, it is generally much weaker for Japanese perceivers when the stimuli are produced by Japanese speakers.¹⁵ Although this finding suggests that linguistic and/or cultural factors affect the integration process, it may also reflect the properties of the utterances of the single Japanese speaker who produced the utterances used in these studies.

We conducted an experiment with new stimuli to explore this issue. These stimuli consisted of utterances of the syllables /ba,da,ga,pa,ta,ka,ma,na/ produced by two Japanese and two American speakers. Recorded sound and videotaped lip movements from each speaker were combined to create 16 pairs, half of which consisted of concordant AV components (e.g., A=/ba/, V=/ba/) the remainder consisted of discrepant components (e.g., A=/ba/, V=/ga/). Since Japanese vowels are typically shorter than English vowels, the Japanese speakers were instructed to produce sounds with the same duration as those produced by the English speakers. This is in contrast to our previous study in which the American speaker was instructed to produce shorter vowels. The slower Japanese articulations were more easily lipread than those used in earlier studies.

The stimuli were presented in auditory-visual (AV), visual only (V), and auditory only (A) conditions. Subjects wrote what they heard (AV and A conditions), or what they thought the speaker was saying (V condition), with no restrictions on the response set. The size of the McGurk effect was estimated as the increase in percentage of auditory place of articulation errors (labial versus nonlabial) caused by discrepant visual cues. Results indicated that although the group difference was replicated, the Japanese subjects showed a stronger McGurk effect than before for auditory labials, although

¹³ C. Ludvigen, *Acta Otol. Suppl* 469: 190-195 (1990).

¹⁴ H. McGurk and J. MacDonald, "Hearing Lips and Seeing Voices," *Nature* 264: 746-748 (1976).

¹⁵ K. Sekiyama and Y. Tohkura, "McGurk Effect in Non-English Listeners," *J. Acoust. Soc. Am.*, 90: 1797-1805 (1991); K. Sekiyama, "Differences in Auditory-Visual Speech Perception Between Japanese and Americans," *J. Acoust. Soc. Japan (E)* 15: 143-158 (1994).

there were large individual differences. Unlike our previous study,¹⁶ there was no difference between the Japanese and English stimuli. The strong effect of the visual stimulus on Japanese subjects appears to be related to the auditory ambiguity and visual robustness of the stimuli for these listeners. For the American perceivers, on the other hand, the size of the McGurk effect was comparable to that found previously and relatively unaffected by the ambiguity of the auditory stimuli.

Supplements Based on Automatic Speech Recognition

The goal of this work is to develop systems for producing and displaying discrete speechreading supplements that can be derived from the acoustic signal by speech recognition technology. Current efforts are focused on supplements related to the Manual Cued Speech System used in some educational and communication settings by deaf individuals.

Although previous studies of the reception of Manual Cued Speech and of the performance of ASR systems suggests that current technology may provide an adequate basis for the design of an automatic cueing system,¹⁷ the effects of speech recognition errors and delays associated with the recognition process on cue reception and integration are not well understood. To estimate the effects of such imperfections, we have initiated a study of the reception of synthetically generated cues characterized by errors and delays. The visual cues are static handshapes that correspond to the nominal shapes and positions of manual cued speech but lack fluid articulation. These cues are dubbed onto video images of a face that were recorded simultaneously with the acoustic speech signal. In preliminary tests on one skilled receiver of Manual Cued Speech, scores for words in IEEE sentences were 48 percent for speechreading alone, 92 percent for Manual Cued Speech, 84

percent for error-free static handshapes, and 72-74 percent for cues derived from phones recognized with 10-20 percent errors. Although scores for error-free cues are lower than for manual cued speech, this may result from the reduced speaking rate that accompanies cue production (100 versus 150 wpm). The scores obtained with cues derived from a simulation of recognition errors are sufficiently encouraging to warrant further study of this approach.

Supplements Based on Signal Processing

Listeners who have severe to profound hearing impairments typically rely heavily on speechreading to communicate and often receive little benefit from conventional hearing aids in the absence of speechreading. We are attempting to develop aids that present simplified representations of the speech waveform acoustically to the impaired ear. These simplified signals consist of tones that are amplitude modulated by the amplitude envelopes of filtered bands of speech. Research in this area is focused on the effect of background noise on the benefit provided by the signals, and with perceptual interference between pairs of modulated tones.

Envelopes Derived from Noisy Speech

The amplitude envelopes of filtered bands of speech, when derived from clean speech and presented as amplitude modulations of tones located at the centers of the bands, substantially improve the speechreading ability of listeners with normal hearing.¹⁸ To assess the effectiveness of these supplements when the band-envelopes are extracted from noisy speech, Lemay and Braida¹⁹ tested four young adults with normal hearing and superior speechreading abilities on word reception in both highly contextual (CUNY) and low-context sentences (IEEE). The interference was additive Gaussian noise filtered to have a speech-like power spectrum. The noisy speech was filtered into

¹⁶ K. Sekiyama, "Differences in Auditory-Visual Speech Perception Between Japanese and Americans," *J. Acoust. Soc. Japan E* 15: 143-158 (1994).

¹⁷ R.M. Uchanski, L.A. Delhorne, A.K. Dix, L.D. Braida, C.M. Reed, and N.I. Durlach, "Automatic Speech Recognition to Aid the Hearing Impaired. Prospects for the Automatic Generation of Cued Speech," *J. Rehabil. Res. and Dev.* 31: 20-41 (1994).

¹⁸ M. Breeuwer and R. Plomp, "Speechreading Supplemented With Frequency Selective Sound-Pressure Information," *J. Acoust. Soc. Am.* 76: 686-691 (1984); M. Breeuwer and R. Plomp, "Speechreading Supplemented With Auditorily Presented Speech Parameters," *J. Acoust. Soc. Am.* 79: 481-499 (1986); K.W. Grant, L.D. Braida, and R.J. Renn, "Single Band Amplitude Envelope Cues as an Aid to Speechreading," *Quart. J. Exp. Psych.* 43: 621-645 (1991); K.W. Grant, L.D. Braida, and R.J. Renn, "Auditory Supplements to Speechreading: Combining Amplitude Envelope Cues From Different Spectral Regions of Speech," *J. Acoust. Soc. Am.* 95: 1065-1073 (1994).

¹⁹ D.G. Lemay and L.D. Braida, "Band Envelope Speechreading Supplements Derived From Noisy Speech," *J. Acoust. Soc. Am.* 95: 3014 (1994).

octave bands centered at 500, 1600, and 3300 Hz, fullwave rectified, and low pass filtered (50 Hz bandwidth) to create band-envelope signals. The resulting low-bandwidth signals were then used to amplitude-modulate one or more tones centered in the passbands.

For the CUNY sentences, word intelligibility scores increased from 31.4 percent for speechreading alone to 67.4 percent, 68.3 percent, and 47.8 percent when single band supplements derived from noiseless speech were presented at 500, 1600, and 3300 Hz respectively, and to 93.9 percent when all three envelope signals were presented. For the IEEE sentences, these scores were 14.5 percent for speechreading alone; 36.0 percent, 26.5 percent, and 18.3 percent for the single envelope signals, and 82.0 percent for the multiple envelope signal. These results are similar to the findings of Grant, Braida, and Renn (1991).²⁰ When the envelopes are derived from noisy speech, scores in the audiovisual condition are reduced, but higher than for speechreading alone for $S/N > -4$ dB (CUNY) and $S/N > 0$ dB (IEEE) for the multiple envelope supplement. Roughly half of the increase in score (relative to speechreading alone) is retained at $S/N = 0$ dB (60 percent words correct) for the CUNY sentences. These results suggest that the band envelope signals can be successfully adapted for presentation to listeners with severely restricted dynamic ranges, since at a S/N of 0 dB, excursions of the component envelope signals are limited to roughly 12-15 dB by the relatively constant background noise. Moreover, all subjects were able to utilize the envelopes regardless of lipreading ability while the best lipreaders derived the greatest benefits.

Supplements Derived from Multiple Band Envelopes

Although speechreading can be considerably enhanced when a normal hearing listener receives a single tone modulated by the amplitude envelope of a single octave speech band, even larger gains are possible when additional envelopes are used to modulate tones at the center frequencies of the bands from which they were derived. To benefit a

listener with high-frequency hearing loss, these modulated signals must be presented at low frequencies in close spectral proximity. However, when two or more modulated tones are simultaneously presented, regardless of the frequency separation between the tones, there may be perceptual interactions that can enhance or interfere with the perception of the modulation patterns.

In previous work, Takeuchi and Braida²¹ reported that the ability of normal-hearing listeners to compare amplitude modulation patterns was adversely affected by the presence of simultaneous ipsilateral amplitude-modulated distractors. Perceptual interference effects, although generally small in magnitude, were greatest when the distractor envelope was uncorrelated with the target pattern and was greater when the separation between carrier and distractor carrier frequencies was small (200 and 250 Hz) than when it was large (200 and 500 Hz). To determine whether this finding results from the effects of peripheral masking (which typically decreases with spectral separation), Takeuchi and Braida²² extended these experiments to include conditions in which the distractor consisted of an unmodulated tone or was presented dichotically. In general, the amount of interference found in the present experiment was smaller than that found in the earlier one, but the dependence on correlation and separation was similar for replicated conditions. Dichotic presentation produced roughly the same amount of interference as diotic presentation, for both correlated and uncorrelated distractors. This indicates that interference is unlikely to be of peripheral origin and also suggests that listeners can perceive correlations between envelopes equally well under diotic and dichotic presentation. Unmodulated distractors did not degrade envelope comparisons when the frequency separation was large and reduced performance when the frequency separation was small only for two of the four listeners tested.

Field Studies

To obtain insight into the benefits provided to hearing impaired listeners by band-envelope supplements in everyday situations, we plan to provide

²⁰ K.W. Grant, L.D. Braida, and R.J. Renn, "Single Band Amplitude Envelope Cues as an Aid to Speechreading," *Quart. J. Exp. Psych.* 43: 621-645 (1991); K.W. Grant, L.D. Braida, and R.J. Renn, "Auditory Supplements to Speechreading: Combining Amplitude Envelope Cues from Different Spectral Regions of Speech," *J. Acoust. Soc. Am.* 95: 1065-1073 (1994).

²¹ A.H. Takeuchi and L.D. Braida, "Recognition of Amplitude Modulation Patterns in the Presence of a Distractor: I. Effects of Correlation and Frequency Relation," *J. Acoust. Soc. Am.*, forthcoming.

²² A.H. Takeuchi and L.D. Braida, "Recognition of Amplitude Modulation Patterns in the Presence of a Distractor: II. Effects of Dichotic Presentation and Unmodulated Distractors," *J. Acoust. Soc. Am.*, forthcoming.

wearable DSP-based SiVo Aids²³ that have been programmed to produce these supplements to listeners with severe to profound impairments. In preliminary work, digital oscillators and filters have been implemented on the TMS320C50 processor used in the SiVo Aid and found capable of producing signals similar to those studied previously. Preliminary evaluations of these amplitude envelope signals as aids to speechreading have been performed by one hearing-impaired listener using tests of word intelligibility in (IEEE) sentences. For that listener, who is an effective hearing aid user, the increase in intelligibility provided by the single-band envelope cues was found to be roughly equal to that provided by her own aid. Detailed planning of the field study and recruitment of participants is now underway.

Publications

Grant, K.W., L.D. Braida, and R.J. Renn. "Auditory Supplements to Speechreading: Combining Amplitude Envelope Cues From Different Spectral Regions of Speech." *J. Acoust. Soc. Am.* 95: 1065-1073 (1994).

Takeuchi, A.H., and L.D. Braida. "Recognition of Amplitude Modulation Patterns in the Presence of a Distractor: I. Effects of Correlation and Frequency Relation." *J. Acoust. Soc. Am.* Forthcoming.

Takeuchi, A.H., and L.D. Braida. "Recognition of Amplitude Modulation Patterns in the Presence of a Distractor: II. Effects of Dichotic Presentation and Unmodulated Distractors." *J. Acoust. Soc. Am.* Forthcoming.

Uchanski, R.M., L.A. Delhorne, A.K. Dix, L.D. Braida, C.M. Reed, and N.I. Durlach. "Automatic Speech Recognition to Aid the Hearing Impaired. Prospects for the Automatic Generation of Cued Speech." *J. Rehab. Res. Dev.* 31: 20-41 (1994).

1.1.3 Cochlear Implants

Sponsor

National Institutes of Health
Contract 2 P01 DC00361²⁴
Contract N01 DC22402

Project Staff

Professor Louis D. Braida, Lorraine A. Delhorne, Dr. Donald K. Eddington, Dr. William M. Rabinowitz

The use of cochlear implants is directed at aiding individuals with profound sensorineural deafness who are unable to derive useful benefits from acoustic input to the ear. The prosthesis bypasses the impaired acoustic transduction mechanism and directly stimulates surviving auditory nerve fibers with currents delivered via an electrode array implanted within the cochlea. The overall goal of our research is to understand the mechanisms responsible for the improved hearing provided by these prostheses and to exploit this understanding for the development of improved systems. Our program uses a dedicated group of postlingually deafened adults implanted with a multichannel cochlear prosthesis (Ineraid, Richards Medical Corporation), who participate in intensive multifactorial studies. The research capitalizes on having direct accessibility to the implanted electrode array via a percutaneous connector.

During the past year, work has involved (1) analysis of cue integration in audiovisual speech reception, (2) studies of interactions among different implant channels, and (3) alternative speech processing for improved implant performance. The work in (3) is performed with Joseph Tierney and Dr. Marc Zissman (see also part 5 section 3 chapter 1.7).

The work on audiovisual integration assesses the ability of an implantee to combine cues that are available from separately using vision and audition. Since most implantees require audiovisual input for reliable communication, analysis of integration is of particular significance.

A series of experiments on audiovisual integration with speech segments has been essentially completed. Closed-set identification for a set of ten vowels, a set of the 12 most frequently occurring consonants, and the full set of 24 (initial-position) consonants was tested. Results have been

²³ A. Faulkner, V. Ball, S. Rosen, B.C.J. Moore, and A. Fourcin, "Speech Pattern Hearing Aids for the Profoundly Hearing Impaired: Speech Perception and Auditory Abilities," *J. Acoust. Soc. Am.* 91: 2136-215 (1992).

²⁴ Subcontract from Massachusetts Eye and Ear Infirmary. Dr. Joseph P. Nadol, M.D., Principal Investigator.

obtained using vision alone, audio (the implant) alone, and audiovisually. Analyses to determine the efficiency with which the information available separately from vision and audition is utilized in the combined audiovisual condition are underway.²⁵ Initial analysis of the 12-consonant results suggests that (1) confusion patterns for the vision-alone condition are more consistent and more highly structured than are those for the audition-alone condition, and (2) most subjects make efficient use of the unimodal results in the combined condition.

The work in channel interactions is designed to assess the perceptual independence among different channels of an implant. Current spread from intracochlear electrodes is extensive²⁶ and psycho-physical studies with simple stimuli reveal substantial interelectrode interactions.²⁷ However, the consequences of these interactions for speech reception are not clear.

In one set of experiments, consonant identification was measured using each of four individual intracochlear electrodes (driven from their corresponding individual processor channels), using different pairs of electrodes, and using all four electrodes (the normal system). Analysis of multielectrode integration uses the same models being applied to study audiovisual intergration. These models quantify the extent to which the results from multielectrode conditions reflect optimum use of the information available from the separate electrode conditions versus interference from electrode interactions. The models indicate that predicted optimum performance with multiple electrodes sometimes exceeds observed performance by substantial amounts (e.g., 85 percent-correct predicted versus 65 percent-correct observed). In these cases, however, large response biases are evident in the results from the separate electrode conditions. When the integration models are constrained to maintain these same biases, the predicted and observed multichannel results are generally more similar.

Another set of experiments assessed multichannel saliency with the Ineraid prosthesis by altering the normal tonotopic mapping between the sound-processor's four filter channels and the intracochlear electrode array.²⁸ A single high-performing subject was tested with (1) the normal four channel processing system, (2) a "single-channel" processor, formed by summing the outputs of the four processor filters and delivering the resulting current to a single electrode, and (3) a tonotopically "reversed" system, formed by connecting the four processor filter outputs to four intracochlear electrodes in reversed order. When using the implant in conjunction with speechreading, all three mappings showed a large improvement on the recognition of words in sentences over speechreading alone. When using the implant alone (without speechreading), tests of consonant and vowel recognition, and the recognition of words in isolation and in sentences all showed a substantial decrease in performance across the three mappings: normal > single-channel > reversed. The patterns of segmental confusions and the relations among scores on different tests were highly consistent.²⁹ Overall, the results indicate that, despite the extensive spread of current associated with monopolar intracochlear stimulation, the Ineraid electrode array affords a degree of perceptual selectivity that substantially aids speech reception.

The work on altered speech processing involves evaluation of the recently developed continuous-interleaved-stimulation (CIS) strategy. Each channel of a CIS processor uses the compressed envelope of its bandpass filtered output to modulate biphasic current pulses that are delivered to an intracochlear electrode. Pulses are interleaved across channels to avoid simultaneous field interactions, and pulse rates are high (~2000 pps/channel) to preserve temporal waveform cues. Using up to six monopolar electrodes directly accessible with the Ineraid implant, this strategy has shown considerable promise in acute evaluations conducted in the labo-

²⁵ L.D. Braida, "Crossmodal Integration in the Identification of Consonant Segments," *Quart. J. Exp. Psychol.* 43A: 647-677 (1991).

²⁶ C. van den Honert and P.H. Stypulkowski, "Single Fiber Mapping of Spatial Excitation Patterns in the Electrically Stimulated Auditory Nerve," *Hear. Res.* 29: 195-206 (1987).

²⁷ R.V. Shannon, "Multichannel Electrical Stimulation of the Auditory Nerve in Man: II. Channel Interaction," *Hear. Res.* 18: 135-143 (1983).

²⁸ W.M. Rabinowitz and D.K. Eddington, "Effects of Channel-to-Electrode Mappings on Speech Reception With the Ineraid Cochlear Implant," *Ear Hear.*, forthcoming.

²⁹ W.M. Rabinowitz, D.K. Eddington, L.A. Delhorne, and P.A. Cuneo, "Relations Among Different Measures of Speech Reception in Subjects Using a Cochlear Implant," *J. Acoust. Soc. Am.* 92: 1869-1881 (1992).

ratory.³⁰ In collaboration with a group in Innsbruck, a prototype portable real-time system has been developed (based on a DSP56001) that can realize some CIS implementations. Two subjects with nine years of experience using the standard Ineraid analog sound processor are now wearing the CIS system on a full-time basis. After several weeks, one subject prefers the CIS strategy; however, objective measures of speech reception show no gain (re the standard processor). The second subject shows a large gain with CIS and some evidence of continuing improvement. On relatively difficult sentences presented in quiet and without lipreading cues, the subject scores near perfectly with CIS versus 65 percent with the standard processor. For speech reception in noise, he shows a deficit of 7 dB re normal-hearing listeners, which compares favorably to deficits of 10 to 15 dB obtained with the standard analog processor.

Publication

Rabinowitz, W.M., and D.K. Eddington. "Effects of Channel-to-Electrode Mappings on Speech Reception With the Ineraid Cochlear Implant." *Ear Hear.* Forthcoming.

1.1.4 Binaural Hearing

Sponsor

National Institutes of Health
Grant R01-DC00100³¹

Project Staff

Nathaniel I. Durlach, Dr. Patrick M. Zurek

The long-term goal of this program is (1) to develop an integrated, quantitative theory of binaural interaction that is consistent with psychophysical and physiological data on normal and impaired auditory systems and (2) to apply our results to the diagnosis and treatment of hearing impairments.

Recent work has examined the precedence effect that is observed when leading and lagging sounds occupy different frequency regions.³² Subjects were asked to match the intracranial lateral position of an acoustic pointer to that of a test stimulus composed

of two binaural noise bursts with asynchronous onsets, parametrically-varied frequency content, and different interaural delays. The precedence effect was measured by the degree to which the interaural delay of the matching pointer was independent of the interaural delay of the lagging noise burst in the test stimulus. Results show an asymmetric frequency effect in which the lateralization influence of a lagging high-frequency burst is almost completely suppressed by a leading low-frequency burst, whereas a lagging low-frequency burst is weighted equally with a leading high-frequency burst. This asymmetry is shown to be the result of an inherent low-frequency dominance that is seen even with simultaneous bursts. When this dominance is removed (by attenuating the low-frequency burst), the precedence effect operates equally effectively both upward and downward in frequency.

1.1.5 Multimicrophone Hearing Aids

Sponsor

National Institutes of Health
Grant R01-DC00270

Project Staff

Joseph Desloge, Nathaniel I. Durlach, Dr. Julie E. Greenberg, Michael P. O'Connell, Dr. William M. Rabinowitz, Daniel P. Welker, Dr. Patrick M. Zurek

The goal of this research is to determine the improvements that can be provided to hearing aids through the use of multiple microphones. The work is directed toward developing algorithms for processing the signals from a head-worn microphone array for the primary goal of improving the intelligibility of speech (assumed to arise from a known direction) in the presence of noise and reverberation. Ideally, this intelligibility enhancement would be achieved without compromising the listener's ability to monitor and localize sound sources from all directions. Array processing algorithms are first implemented and evaluated in terms of signal-to-noise improvement in computer simulations. The most promising approaches are then implemented in real-time with wearable devices (tethered to a computer) for laboratory evaluations

³⁰ B.S. Wilson, C.C. Finley, D.T. Lawson, R.D. Wolford, D.K. Eddington, and W.M. Rabinowitz, "Better Speech Reception With Cochlear Implants," *Nature* 352: 236-238 (1991).

³¹ Subcontract from Boston University, Professor H. Steven Colburn, Principal Investigator.

³² B.G. Shinn-Cunningham, P.M. Zurek, N.I. Durlach, and R.K. Clifton, "Cross-frequency Interactions in the Precedence Effect," *J. Acoust. Soc. Am.*, forthcoming.

in terms of speech reception in noise and sound localization by normal and hearing-impaired listeners. Some devices will be made portable for field studies.

Work in the past year has focused on algorithmic design and analysis. One particular area concerns controlling the adaptation of time-varying processing schemes to minimize signal cancellation and misadjustment. These problems arise when the array is not perfectly aligned to the desired source and in the presence of strong source signals. They are especially bothersome in the hearing aid application because: (1) hearing aid users cannot be expected to hold their heads rigidly pointing at the signal source; and (2) often the signal is larger than the interference and so it degrades the precision of interference cancellation that can be achieved. These issues were outlined previously, along with ad hoc solutions, by Greenberg and Zurek.³³ Recent work has thoroughly analyzed and refined those ad hoc solutions, producing a modified adaptive algorithm that includes two additional features. One modification is to adjust the steps taken by the adaptive algorithm in order to reduce misadjustment when the output power is strong, and the other is to inhibit adaptation based on the correlation between microphone signals. Guidelines have been established for selecting the relevant processing parameters in a variety of acoustic environments.

Another problem with adaptive systems is that reverberation results in a signal that does not arrive from the source direction, but that is correlated with the source signal. A simple solution to the problem of reverberation-induced signal cancellation has been studied.³⁴ By reducing the amount by which the adaptive filter can "look ahead in time" (by a bulk processing delay), signal cancellation can be avoided with little loss in noise-reduction performance.

The result of this design and analysis work is a specification for a relatively simple and robust broadside adaptive array.³⁵ Computer simulations have evaluated this system in a variety of acoustic

environments. Steady-state results show that it provides very large improvements in relatively anechoic environments. Substantial benefits are obtained in moderate reverberation, particularly if relatively long filters are used. In extreme reverberation, performance is comparable to that of the underlying nonadaptive microphone array. Transient results indicate that convergence of the adaptive algorithm is sufficiently rapid for processing speech signals. In addition, this work has considered the use of directional microphones and the number of microphones required in a practical system.

Work to date on multimicrophone arrays for hearing aids has been aimed at processing the microphone signals to form a single output signal. Such monaural-output systems contain none of the information about the location of sound sources that is normally conveyed primarily by differences between the signals at the two ears. In addition to sound localization ability, binaural hearing provides a sensation of auditory space and improved speech reception in noise. In an attempt to provide these natural benefits of binaural hearing along with improvements from multimicrophone array processing, we have been exploring ways of combining them. In one project, we have been exploring designs of a fixed four-microphone array in which, by choice of a frequency-dependent parameter, directivity can be traded with fidelity of interaural time delay (the most important binaural cue).³⁶ At one extreme in this trade maximal directivity is achieved, while at the other extreme the outermost microphone signals are simply passed to the two ears. In another project, we are exploring the design of a two-microphone adaptive binaural array, with the microphones worn at the ears.³⁷

In both projects a very promising approach is a particularly simple one that exploits the psychoacoustic finding that sound localization is dominated by low-frequency interaural delay cues. Using this fact, we allocate the lowpass part of the signal spectrum for transmitting natural binaural cues by simply passing

³³ J.E. Greenberg and P.M. Zurek, "Evaluation of an Adaptive Beamforming Method for Hearing Aids," *J. Acoust. Soc. Am.* 91: 1662-1676 (1992).

³⁴ J.E. Greenberg and P.M. Zurek, "Preventing Reverberation-Induced Target Cancellation in Adaptive-array Hearing Aids," *J. Acoust. Soc. Am.* 95: 2990-2991 (1994).

³⁵ J.E. Greenberg, *Improved Design of Microphone-Array Hearing Aids*, Ph.D. diss., Division of Health Sciences and Technology, MIT, 1994.

³⁶ J.G. Desloge, *A Fixed Microphone Array Hearing Aid with a Binaural Output*, M.S. Thesis, Dept. of Electr. Eng. and Comput. Sci., MIT, 1994.

³⁷ D.P. Welker, *A Binaural-Output Adaptive-Beamforming Hearing Aid*, M.S. Thesis, Dept. of Electr. Eng. and Comp. Sci., MIT, 1994.

the lowpass-filtered microphone signals to the ears. The highpass part is the output of the array, presented diotically. This approach allows source localization via the low frequencies and an enhanced signal via the high frequencies.

1.1.6 Tactile Communication of Speech

Sponsor

National Institutes of Health
Grant 5 R01 DC00126

Project Staff

Lorraine A. Delhorne, Gail Denesovich, Nathaniel I. Durlach, Ashanthi Gajaweera, Geoffrey L. Plant, William M. Rabinowitz, Dr. Charlotte M. Reed, Dr. Mandayam A. Srinivasan, Hong Z. Tan, Jonathan R. Santos

The ultimate goal of this research is to develop tactial aids for the deaf and deaf-blind that can serve as substitutes for hearing in speech communication. Research is conducted in three major areas summarized below.

Basic Study of Encoding and Display Schemes

This research is designed to develop methods of displaying acoustic signals to the tactial sense for optimal information transfer. Research in this area includes measurements of basic resolution and information transfer for tasks involving active finger motions and for those involving motional or vibratory stimulation of the finger, in addition to work on

the design and construction of a multifinger tactal stimulator. Studies employing active finger motions include measurements of the ability to discriminate and identify joint-angle rotation, measurements of the ability to discriminate the thickness of materials with different bending moduli,³⁸ and measurements of manual perception of compliance with work cues eliminated and force cues minimized.³⁹ Studies employing motional or vibratory stimulation include measurement of amplitude and frequency discrimination for motional (i.e., low-frequency, high-amplitude) signals⁴⁰ and a study of the reception of Morse Code sequences employing motional and vibratory stimulation.⁴¹ In addition, work has been conducted on the design and construction of a multifinger tactal device capable of providing stimulation along the frequency continuum from motion to vibration.

Tactical Supplements to Speechreading

This research is designed to lead towards the development of tactal aids to supplement information available through speechreading. Recent research in this area has been concerned with describing and understanding differences in performance achieved through auditory and tactal presentation of a simple acoustic-based supplement to speechreading. Data comparing the two modes of presentation were obtained for various tasks, including sentence, prosodic, and segmental reception.⁴² In addition, related nonspeech psychophysical measurements for tactal and auditory presentation were obtained to increase our understanding of the differential results observed in aided speechreading tasks.⁴³

³⁸ A. Gajaweera, *Tactal Discrimination of Thickness*, B.S. thesis, Dept. of Mech. Eng., MIT, 1994.

³⁹ H.Z. Tan and N.I. Durlach, "Manual Discrimination Using Active Finger Motion: Compliance, Force, and Work," *Percept. Psychophys.*, forthcoming.

⁴⁰ G.L. Beauregard, W.M. Rabinowitz, H.Z. Tan, and N.I. Durlach, "Amplitude and Frequency Resolution for Motional Stimulation," Third International Conference on Hearing Aids, Tactile Aids, and Cochlear Implants, Miami, Florida, May 2-5, 1994.

⁴¹ H.Z. Tan and N.I. Durlach, "A Study of the Tactal Perception of Motor Input Sequences," Third International Conference on Hearing Aids, Tactile Aids, and Cochlear Implants, Miami, Florida, May 2-5, 1994; H.Z. Tan, N.I. Durlach, W.M. Rabinowitz, and C.M. Reed, "Tactal Performance with Motional Stimulation of the Index Finger," (Abstract) *J. Acoust. Soc. Am.* 95: 2986 (1994).

⁴² J.M. Bising, C.M. Reed, and N.I. Durlach, "A Comparison of Auditory and Tactal Presentation of a Single-band Envelope Cue as a Supplement to Speechreading," submitted to *Seminars in Hearing*, 1994; M.S. Bratakos, *Supplements to Speechreading: A Comparison of Auditory and Tactile Presentation of a Single-band Envelope Cue*, B.S. thesis, Dept. of Electr. Eng. and Comput. Sci., MIT, 1993; C.M. Reed, M.S. Bratakos, L.A. Delhorne, and G. Denesovich, "A Comparison of Auditory and Tactile Presentation of a Single-band Envelope Cue as a Supplement to Speechreading," Third International Conference on Hearing Aids, Tactile Aids, and Cochlear Implants, Miami, Florida, May 2-5, 1994.

⁴³ W.M. Rabinowitz, C.M. Reed, L.A. Delhorne, and J.M. Bising, "Tactile and Auditory Measures of Modulation Resolution," (Abstract) *J. Acoust. Soc. Am.* 95: 2987 (1994); W.M. Rabinowitz, C.M. Reed, and L.A. Delhorne, "Tactile and Auditory Measures of Modulation Resolution," Third International Conference on Hearing Aids, Tactile Aids, and Cochlear Implants, Miami, Florida, May 2-5, 1994.

Evaluation of Practical Aids

This research is designed to evaluate the speech-reception performance of experienced users of portable, wearable tactile aids and to compare this performance to that of users of other types of auditory prostheses. Research in this project area includes (1) laboratory evaluations of tactile devices with artificially deafened subjects, (2) a field study of the performance of deaf adult users of tactile aids,⁴⁴ (3) a study of the effects of training on adult performance with a tactile device, and (4) a study of the effects of training on the use of a tactile device by deaf children.⁴⁵ The tactile devices used in this research include two commercially available, wearable tactile aids: Tactaid 2 and Tactaid 7 (both products of Audiological Engineering Corporation), with research focused primarily on the Tactaid 7 as a multichannel display of the first and second speech formants. The Tactaid 2, by comparison, is a two-channel tactile display of one lowpass frequency region of speech and one highpass band. In addition, some data have been obtained on several nonwearable laboratory-based systems, including a nine-channel laboratory implementation of the Queen's University vocoder (Brooks and Frost, 1983) and a high-performance single-channel vibrator (the Alpha-M AV6 Minishaker) used to present speech-envelope supplements to speechreading.

Publications

Besing, J.M., C.M. Reed, and N.I. Durlach. "A Comparison of Auditory and Tactile Presentation of a Single-band Envelope Cue as a Supplement to Speechreading." Submitted to *Seminars in Hearing* (1994).

Rabinowitz, W.M., D. Henderson, C.M. Reed, L.A. Delhorne, and N.I. Durlach. "Development and Evaluation of an Improved Synthetic Tadoma System." *J. Acoust. Soc. Am.* Forthcoming.

Reed, C.M., and L.A. Delhorne. "Current Results of a Field Study of Adult Users of Tactile Aids." Submitted to *Seminars in Hearing* (1994).

Reed, C.M., L.A. Delhorne, N.I. Durlach, and S.D. Fischer. "A Study of the Tactual Reception of Sign Language." *J. Speech Hear. Res.* Forthcoming.

Tan, H.Z., and N.I. Durlach. "Manual Discrimination Using Active Finger Motion: Compliance, Force, and Work." *Percept. Psychophys.* Forthcoming.

Thesis

Gajaweera, A. *Tactual Discrimination of Thickness.* B.S. thesis, Dept. of Mech. Eng., MIT, 1994.

1.2 Haptics Research

1.2.1 Introduction

In the following subsections, we describe work performed during the past year on a wide variety of projects concerned with manual sensing and manipulation (i.e., haptics). Further work on haptics, oriented specifically toward the use of virtual environments for training, is discussed in section 1.3 below.

1.2.2 Mechanistic Modeling of the Primate Fingerpad

Sponsor

National Institutes of Health
Grant R29-DC00625

Project Staff

Dr. Mandayam A. Srinivasan, Kiran Dandekar, Walter E. Babiec, Rogeve J. Gulati

When we touch an object, the source of all tactile information is the spatio-temporal distribution of mechanical loads on the skin at the contact interface. The relationship between these loads and the resulting stresses and strains at the nerve terminals within the skin plays a fundamental role in the neural coding of tactile information. Although empirical determination of the stress or strain state

⁴⁴ C.M. Reed, L.A. Delhorne, and N.I. Durlach, "Results obtained with Tactaid 2 and Tactaid 7," *Proceedings of the 2nd International Conference on Tactile Aids, Hearing Aids, and Cochlear Implants*, eds. A. Risberg, S. Felicetti, G. Plant, and K.-E. Spens, (Stockholm, Sweden: Dept. of Speech Comm. Music Acoust., KTH, 1992), pp. 149-155; C.M. Reed and L.A. Delhorne, "Current Results of a Field Study of Adult Users of Tactile Aids," submitted to *Seminars in Hearing*, 1994.

⁴⁵ G. Plant, "The Development of a Training Program for Profoundly Deaf Children Fitted with Tactaid 7," Third International Conference on Hearing Aids, Tactile Aids, and Cochlear Implants, Miami, Florida, May 2-5, 1994.

of a mechanoreceptor is not possible at present, mechanistic models of the skin and subcutaneous tissues enable generation of testable hypotheses on skin deformations and associated peripheral neural responses. The hypotheses can then be verified by comparing the calculated results from the models with biomechanical data on the deformation of skin and subcutaneous tissues and neurophysiological data from recordings of the responses of single neural fibers. The research under this grant is directed towards applying analytical and computational mechanics to analyze the biomechanical aspects of touch—the mechanics of contact, the transmission of the mechanical signals through the skin, and their transduction into neural impulses by the mechanoreceptors.

Determination of the Shape and Compressibility of the Primate Fingertip (distal phalanx)

The first step in performing mechanistic analyses of the primate fingertip is to determine its geometric and material properties. The three-dimensional (3D) external geometry of primate fingertips was determined from accurate epoxy replicas of human and monkey fingertips. Using a videomicroscopy setup, we obtained images of orthographic projections of the epoxy replicas at various known orientations. The images were then digitized and processed to determine the boundary of the finger at each orientation. By combining the boundary data for all the different orientations, we were able to reconstruct the 3D external geometry of the fingertip.⁴⁶ We have reconstructed several human and monkey fingertips using this method. For mechanistic modeling of the human fingerpad, the Poisson's ratio, which is a measure of its compressibility, is required as an input to the mathematical models. The Poisson's ratio for the human fingerpad *in vivo* is unknown at present. In previous noninvasive experiments on human subjects, we have measured the change in volume of

the fingerpad under static indentations with different indentors.⁴⁷ Our results show that increases in either the depth of indentation or the contact area with the indentor increased the compressibility of the fingertip. The highest change in fingertip volume was about 5 percent.

We have now developed an experimental setup involving a computer controlled linear actuator for fingertip volume change measurements under dynamic conditions.⁴⁸ We measured volume changes of the fingerpad under three types of indentors (point, circular flat and flat plate) imposing constant velocity ramps (1 to 8 mm/s), several depths of indentation (1 to 4 mm) and sawtooth stimulation (1 and 2 mm amplitude; 0.25 to 2Hz frequency). The fingerpad, encased in a thin latex fingercot, was placed in a fluid-filled chamber and indented by using a computer controlled stepper motor. The resulting fingertip volume changes were calculated (resolution ~1/100 ml) by video recording the fluid level in a small diameter pipette, transcribing the data frame-by-frame, and subtracting out the fluid level changes due to indentor displacement. The results show that reductions in fingertip volume are small and in phase with stimulus variations, with an increase in their mean value over time. The volume changes during the ramp phase increase linearly with indentor displacement and are independent of velocity; during sawtooth stimulations, however, the nature of the hysteresis loops depend on velocity of indentation. We have analyzed such data for four subjects.

Fingertip Models and Finite Element Analysis

We have performed linear and nonlinear finite element analysis of a series of mechanistic models of the fingerpad under a variety of mechanical stimuli.⁴⁹ The models range from a semi-infinite medium to a three-dimensional (3D) model based on the actual finger geometry, and composed of a

⁴⁶ T.R.R. Perez, K. Dandekar, and M.A. Srinivasan, *Videomicroscopic Reconstruction of the Human Finger*, Project report to the MIT Minority Summer Science Research Program, 1992.

⁴⁷ M.A. Srinivasan, R.J. Gulati, and K. Dandekar, "In vivo Compressibility of the Human Fingertip," *Advances in Bioengineering*, ed. M.W. Bidez (Chicago: ASME, 1992), vol. 22, pp. 573-576.

⁴⁸ W.E. Babiec, *In vivo Volume Changes of the Human Fingerpad under Indentors*, B.S. thesis, Dept. of Mech. Eng., MIT, 1994.

⁴⁹ M.A. Srinivasan and K. Dandekar, "Role of Fingertip Geometry in the Transmission of Tactile Mechanical Signals," *Advances in Bioengineering*, ed. M.W. Bidez (Chicago: ASME, 1992), vol. 22, pp. 569-572 (1992); M.A. Srinivasan and K. Dandekar, "An Investigation of the Mechanics of Tactile Sense Using Two Dimensional Models of the Primate fingertip," *J. Biomech. Eng.*, forthcoming; K. Dandekar and M.A. Srinivasan, "Tactile Coding of Object Curvature by Slowly Adapting Mechanoreceptors," in *Advances in Bioengineering*, ed. M.J. Askew. Chicago: ASME, 1994, vol. 28, pp. 41-42; K. Dandekar and M.A. Srinivasan, "A Three-dimensional Finite Element Model of the Monkey Fingertip for Predicting Responses of Slowly Adapting Mechanoreceptors," ASME summer annual meeting, Beaver Creek, Colorado, 1995.

homogeneous elastic material, a thick elastic shell containing a fluid or a multilayered medium. Simulations of the mechanistic aspects of neurophysiological experiments involving mapping of receptive fields with single point loads, determination of spatial resolution of two-point stimuli, and indentations by single bars as well as periodic and aperiodic gratings have been carried out for the two-dimensional (2D) and 3D models. We have also solved the nonlinear contact problem of indentations by cylindrical objects and sinusoidal step shapes. The large number of numerical calculations needed even for the linear two-dimensional models necessitated the use of the Cray-C90 at the NSF Pittsburgh Supercomputer Center.

The results show that the model geometry has a significant influence on the spatial distribution of the mechanical signals, and that the elastic medium acts like a low-pass filter in causing blurring of the mechanical signals imposed at the surface. Multi-layered 3D models of monkey and human fingertips accurately predicted the surface deformations under a line load, experimentally observed by Srinivasan.⁵⁰ The same models predicted the experimentally observed surface deformations under cylindrical indentors as well. These 3D finite element models were used to simulate neurophysiological experiments involving indentation by rectangular bars, aperiodic gratings, cylindrical indentors and step shapes. Several strain measures at typical mechanoreceptor locations were matched with previously obtained neurophysiological data to determine the relevant mechanical signal that causes the receptors to respond. In the simulations, the strain energy density at the receptor location was found to be directly related to the static discharge rate of the slowly adapting (SA) afferents. In addition, strain energy density is a scalar that is invariant with respect to receptor orientations and is a direct measure of the distortion of the receptor caused by loads imposed on the skin. We have therefore hypothesized that the strain energy density at the receptor site is the relevant stimulus to the slowly adapting receptors. In summary, this research project has resulted in mechanistic models of the primate fingertip whose predictions match a variety of biomechanical and neurophysiological data. The models can also be used to generate hypotheses to be tested in future biomechanical and neurophysiological experiments.

1.2.3 Peripheral Neural Mechanisms of Haptic Touch

Sponsor

U.S. Navy - Office of Naval Research
Grant N00014-88-K-0604

Project Staff

Dr. Mandayam A. Srinivasan, Professor Anuradha M. Annaswamy, Dr. Robert H. LaMotte,⁵¹ Steingrimur P. Karason

We have been collaborating with Dr. Robert LaMotte, Yale University School of Medicine, in conducting psychophysical and neurophysiological studies on the tactile perception of the microtexture, shape and softness of objects. We have shown that humans can detect extremely fine textures composed of 50 nm-high parallel bars on plane glass plates.⁵² Our neurophysiological recordings indicate that when such fine textures are stroked on the fingerpad skin, the fingerprint ridges vibrate and cause Pacinian Corpuscles to respond, thus enabling detection of the microtexture.⁵³

In studies of the tactile perception of shape, a series of two- and three-dimensional objects (e.g., cylinders, spheres, ellipsoids and wavy surfaces) were pressed or stroked across the fingerpads of anesthetized monkeys and evoked responses in cutaneous mechanoreceptive primary afferent nerve fibers were recorded.⁵⁴ Major geometrical properties of the shapes were well represented in the spatio-

⁵⁰ M.A. Srinivasan, "Surface Deflection of Primate Fingertip Under Line Load," *J. Biomech.* 22(4): 343-349 (1989).

⁵¹ Yale University School of Medicine, New Haven, Connecticut.

⁵² R.H. LaMotte and M.A. Srinivasan, "Surface Microgeometry: Neural Encoding and Perception," in *Information Processing in the Somatosensory System*, eds. O. Franzen and J. Westman, Wenner-Gren International Symposium Series (New York: Macmillan Press, 1991).

⁵³ M.A. Srinivasan, J.M. Whitehouse, and R.H. LaMotte, "Tactile Detection of Slip: Surface Microgeometry and Peripheral Neural Codes," *J. Neurophys.* 63(6): 1323-1332 (1990).

⁵⁴ M.A. Srinivasan and R.H. LaMotte, "Tactile Discrimination of Softness," *J. Neurophys.* 73(1): 88-101 (1995); R.H. LaMotte and M.A. Srinivasan, "Responses of Cutaneous Mechanoreceptors to the Shape of Objects Applied to the Primate Fingerpad," *Acta Psychologica* 84: 41-51 (1993); R.H. LaMotte, M.A. Srinivasan, C. Lu, and A. Klusch-Petersen, A., "Cutaneous Neural Codes for Shape," *Can. J. Physiol. Pharm.* 72: 498-505 (1994).

temporal responses of SA and RA afferent fiber populations, particularly those of the SAs. The results show that the following hypothesis explains qualitatively the data we have obtained: the depth of indentation and the change in curvature of the skin surface are encoded by the discharge rates of SAs; in addition, the velocity and the rate of change in skin surface curvature are encoded by the discharge rates of both SAs and RAs.

Thus, the intensive parameters of shapes, such as the magnitude of change in skin curvature produced by contact with the object surface were encoded in the discharge rates of SAs and RAs, but this neural code was also influenced by changes in stroke velocity. Spatial parameters of shapes such as the curvature width and the changes in contour that characterize a shape as belonging to a particular category (such as a sphere as opposed to a cylinder) are encoded in the spatially distributed discharge rates of the SA population. This spatial response profile provides a neural code that is probably invariant with moderate changes in the parameters that govern contact conditions between the object and the skin, such as the contact force or orientation and velocity of its trajectory. Therefore, among the different possible geometric representations of the shape of objects, the intrinsic description, i.e., the surface curvature as a function of the distance along the surface, seems to be relevant for tactile sensing of shape.

Based on a theoretical analysis of the mechanics of contact, we have proposed a mechanism by which shapes of objects within contact regions are perceived through the tactile sense. The curvature of the skin surface under an object, which we know from differential geometry is approximated by the second spatial derivative of surface deflection, is coded without differentiating (which is a noise enhancing process), but by exploiting its relation to surface pressure. Pressure peaks occur where the depths of indentation and/or changes in the skin surface curvature are large. The skin effectively acts as a low-pass filter in transmitting the mechanical signals, and the mechanoreceptors respond to the blurred versions of the surface pressure dis-

tribution, thus encoding the shape of the object in terms of its surface curvatures.⁵⁵

We have also shown that the human discriminability of softness or compliance of objects depends on whether the object has a deformable or rigid surface.⁵⁶ When the surface is deformable, the spatial pressure distribution within the contact region is dependent on object compliance, and hence information from cutaneous mechanoreceptors is sufficient for discrimination of subtle differences in compliance. When the surface is rigid, kinesthetic information is necessary for discrimination, and the discriminability is much poorer than that for objects with deformable surfaces.

Development of a Computational Theory of Haptics

Our research on the computational theory of haptics is focused on developing a theoretical framework for studying the information processing and control strategies common to both humans and robots performing haptic tasks. For example, although the "hardware" of the tactile apparatus in humans and robots are different, they have the common feature of mechanosensors embedded in a deformable medium. Therefore the mechanistic analyses needed to solve the computational problem of coding (predicting sensor response for a given mechanical stimulus at the surface) and decoding (inferring the mechanical stimulus at the surface by suitably processing the sensor response) are similar for human and robot tactile sensing systems.

We first developed such a computational theory using a simplified 2D half-space model of the human or robot finger subjected to arbitrary pressure or displacement loading conditions normal to the surface and then gave explicit formulae for coding and decoding problems.⁵⁷ We have now expanded these results to a more general 3D half-space model where the load direction can be completely arbitrary.⁵⁸ Explicit solutions for the coding problem are given and enable the selection of a useful set of relevant stimuli as well as the choice of sensors appropriate for maximizing the informa-

⁵⁵ M.A. Srinivasan and R.H. LaMotte, "Encoding of Shape in the Responses of Cutaneous Mechanoreceptors," in *Information Processing in the Somatosensory System*, eds: O. Franzen and J. Westman, Wenner-Gren International Symposium Series (New York: Macmillan Press, 1991).

⁵⁶ M.A. Srinivasan and R.H. LaMotte, "Tactile Discrimination of Softness," *J. Neurophys.* 73(1): 88-101 (1995).

⁵⁷ M.A. Srinivasan, "Tactile Sensing in Humans and Robots: Computational Theory and Algorithms," Newman Laboratory Technical Report, Department of Mechanical Engineering, MIT, 1988.

⁵⁸ S.P. Karason, M.A. Srinivasan, and A.M. Annaswamy, "Tactile Sensing of Shape," Center for Information Driven Mechanical Systems (CIDMS) Workshop Proceedings, Dept. of Mech. Eng., MIT, 1994.

tion about the stimulus on the skin surface. The solution of the decoding problem is also given, both for the idealized noise-free case and for the realistic case with measurement noise. For the latter, the solutions are shown to be numerically stable and optimal.

In our work during the previous years, we were successful in answering basic identification and control issues that arise during manipulation of compliant objects using compliant fingerpads.⁵⁹ In order to understand the fundamental aspects of these tasks, we have analyzed the problem of identification of compliant objects with a single finger contact, as well as under a two-finger grasp. Using lumped parameter models, we have carried out the identification of human and object parameters, using either force or displacement inputs to the rigid backing of the end-effector. Based on identified parameters, control strategies are developed to achieve a desired manipulation of the object in the workspace. We have also modeled the dynamic interactions that occur between compliant end-effectors and deformable objects by a class of nonlinear systems. It was shown that standard geometric techniques for exact feedback linearization techniques were inadequate. New algorithms were developed by using adaptive feedback techniques which judiciously employed the stability characteristics of the underlying nonlinear dynamics. In both theoretical and simulation studies, it was shown that these adaptive control algorithms led to successful manipulation. The theoretical results can be used to generate testable hypotheses for experiments on human or robot haptics.

1.2.4 Biomechanics of Human Fingerpad-Object Contact

Sponsor

U.S. Navy - Office of Naval Research
Grant N00014-91-J-1454

Project Staff

Dr. Mandayam A. Srinivasan, Jyh-Shing Chen,
Kiran Dandekar, Rogeve J. Gulati, Tomas

Rodriguez-Perez, Frederick L. Roby, Joseph D. Towles

Although physical contact is ubiquitous in our interactions with objects in the environment, we do not yet understand the mechanistic phenomena occurring at the skin-object interface. As mentioned before, the spatio-temporal distribution of mechanical loads on the skin at the contact interface is the source of all tactile information. These loads, specified as pressure, displacements, etc., depend on the geometrical and material properties of both the contacting entities, as well as the overall forces of interaction.

The goals of this project are (1) determination of the growth and motion of contact regions and the associated force variations over time between the human fingerpad and carefully chosen transparent test objects whose microtexture, shape or softness is varied in a controlled manner, (2) experimental measurement of the surface deformations of human fingertips under shaped indentors, and (3) characterization of the mechanical properties of the human fingerpad. The results obtained are being used to gain a deeper understanding of the neurophysiological and psychophysical data we have already obtained for the same test objects.

To measure the *in vivo* surface deformations of the fingerpad under various tactile stimuli, we have designed a videomicroscopy system together with high precision force sensors. The videomicroscopy system consists of a set of video zoom lenses attached to a high-resolution CCD camera, whose output can either be digitized directly at about 5 frames/s, or stored on a laserdisk at real-time frame rates (30 frames/s) for off-line digitization. The zoom lenses allow continuous variation of magnification, with the field of view covering the entire fingerpad, or just a few fingerprint ridges. High contrast images are achieved with coaxial and other fiberoptic lighting. In collaboration with our colleagues at the Artificial Intelligence Laboratory at MIT, we designed and built two 6-axis force sensors that are customized to our application. These sensors have much higher resolutions (10 bit) than commercial sensors operating in comparable range of forces (5 Newtons). Transparent test objects can be attached to these sensors for both biomechanical and psychophysical experiments.

⁵⁹ A.M. Annaswamy and D. Seto, "Object Manipulation Using Compliant Fingerpads: Modeling and Control," *ASME J. Dynam. Syst. Measure, Control* (1993); A.M. Annaswamy and M.A. Srinivasan, "A Study of Dynamic Interactions between Haptic Interfaces and Compliant Fingerpads," *Proceedings of the Motion Control Workshop*, Berkeley, California, March 1994; A.M. Annaswamy and M.A. Srinivasan, "The Role of Compliant Fingerpads in Grasping and Manipulation: Identification and Control," Institute of Mathematics (New York: Springer Verlag, 1995).

During the past year, we enhanced the videomicroscopy system to be able to acquire images when the human subject's finger remained passive. A linear stepper motor with a microstepping drive was added to the system. Transparent compliant specimens can be mounted on the motor to indent a stationary finger at a given velocity. The motor is controlled by a 80386 PC, with a specified indentation velocity commanded by a 80486 PC via a digital link. A strain gage based single degree of freedom force sensor is mounted between the specimen and the motor to record contact force. With this setup, we will be able to investigate how the skin-object contact region changes with indentation velocity and force. During the indentation, the contact force and the video signal generated by the CCD camera focused on the contact region are recorded. A new video grabber was incorporated into the system to allow video data to be digitized into the computer system memory in real time. This method allows the force and video data to be synchronized. The video data can be digitized at rates up to 20 frames/sec. For the processing of contact images, a computer program which uses mouse cursor input to manually extract the border of an contact image was developed. Although this method is slow, it serves to calibrate more automated image processing methods under development.

Videomicroscopy of the Fingerpad-object Contact Regions

Using the test facility described above, we have performed a set of experiments with human subjects to investigate the relationship between the contact force, contact area and compliance of the object. The experiments involved active indentation of transparent compliant rubber specimens and a glass plate with the subjects' fingerpads. Static video images of the contact regions were captured at various force levels and magnifications. In order to minimize the effects of nonuniform illumination, we implemented homomorphic image processing algorithms with or without image decimation. The processed images showed that contact regions consisted of discontinuous "islands" along each finger ridge, with clear distinction between contact and noncontact regions over the entire field of view.

Results show that for objects whose compliances are discriminable, even when the overall contact areas under a given contact force are the same, the actual contact areas can differ by a factor of two or more. The actual pressure distribution, which acts only within the discontinuous contact islands on the skin, will therefore be radically different for the objects. Consequently, a spatio-temporal neural code for object compliance emerges with far higher resolution than an intensive code such as the average pressure over the overall contact area. These results are in agreement with our hypothesis that the neural coding of objects with deformable surfaces (such as rubber) is based on the spatio-temporal pressure distribution on the skin. This was one of the conclusions from our psychophysical, biomechanical and neurophysiological experiments in a companion project conducted in collaboration with Professor LaMotte of the Yale University School of Medicine.

Measurement of Surface Deformation of Human Fingerpads

The finite element models described previously need to be verified by comparing the experimentally observed skin surface deformations with those predicted by the finite element models under the same mechanical stimuli. The experimental data was obtained by indenting human fingerpads with several cylindrical and rectangular indentors and acquiring images of the undeformed and deformed fingerpad using the videomicroscopy setup.⁶⁰ Fine markers were placed on the fingerpad and the skin surface deformation was measured by tracking the displacements of the markers in the high resolution video images. The same experiment was simulated using the finite element models of the human fingertip and the displacements of corresponding points were compared with the experimental data. The displacements predicted by the multilayered 3D model matched the experimental data quite well.

Force Response of the Human Fingerpad to Indentation

A 2-DOF robot designed by Dr. Howe of the Harvard group was modified to serve as a "Tactile Stimulator" capable of delivering static and dynamic

⁶⁰ F.L. Roby, K. Dandekar, and M.A. Srinivasan, *Study of Fingertip Deformation Under Indentations by Circular and Rectangular Indentors*, Report to the MIT Summer Research Program, 1994.

stimuli to the human fingerpad.⁶¹ Three types of indentors (point, flat circular, and a flat plate) attached to the stimulator imposed a variety of constant velocity ramps (1 to 32 mm/s), depths of indentation (0.5 to 3 mm), and sinusoids (0.25 mm to 0.5 mm amplitude; 0.125 to 16 Hz frequency) under displacement control (resolution ~ 20 microns). The resulting normal and shear forces were measured by a 2-axis force sensor (resolution ~ 10 mN). The results showed a pronounced nonlinear force-indentation depth relationship under both static and dynamic conditions, viscoelastic effects of force relaxation under constant depth of indentation, and hysteresis under sinusoidal displacements. There was wide variability in the magnitude of response for the five subjects who were tested, and their fingertip diameter or volume did not account for the observed variability. A piecewise linear, lumped parameter model with spring and dashpot elements was developed to identify the mechanical parameters causing the nonlinear response. The model predictions with only one set of parameters for each subject matched the empirical data very well under a wide variety of stimuli. The model represents a compact description of the data and will be used to verify and tune our finite element models of the fingertip.

Force Response of the Human Fingerpad to Shear Displacement

The 2-DOF tactile stimulator was also used to deliver shear displacement ramp (0.5 to 16 mm/sec for a total shear displacement of 7 mm) at various depths of indentation of the fingerpad (0.5 to 3 mm) by a flat, smooth aluminum plate.⁶² Only one subject has been tested so far under these stimuli, and the resulting data has been analyzed with a view towards fine tuning the experimental protocol and parameters. The results show that at each depth of indentation, the shear displacement initially caused increasing skin stretch and shear force, followed by slipping of the plate across the skin surface. The shear force-shear displacement was almost linear and slip occurred at around 3 mm shear displacement at all velocities. Low velocities tended to cause stick-slip (as indicated by oscillatory shear force during slip), whereas the shear force decreased smoothly at higher velocities.

At increasing depths of indentation, slip occurred at larger shear displacements, as is to be expected. The coefficient of static friction was obtained by measuring the slope of the normal and shear forces at the incipience of slip for a given shear velocity. To a first approximation, it was found to be independent of shear velocity. More experiments on different subjects are being initiated.

1.2.5 Human and Robot Hands: Mechanics, Sensorimotor Functions and Cognition

Sponsor

U.S. Navy - Office of Naval Research
Grant N00014-92-J-1814

Project Staff

Dr. Mandayam A. Srinivasan, Dr. J. Kenneth Salisbury, Nathaniel I. Durlach, Dr. Robert H. LaMotte, Dr. Robert D. Howe,⁶³ Jyh-Shing Chen, Kiran Dandekar, Louise Jandura, Steingrimur P. Karason

The premise of this University Research Initiative project is that the integrated study of human and robot haptics can provide complementary knowledge of the processes of prehension and manipulation. From the human side, we wish to understand the basic mechanical, perceptual and strategic capabilities that lead to the dexterity and deftness we observe in human task performance. By studying the underlying competences that humans bring to bear on task performance, we seek guidelines on how to build better robots. From the robotic side, we wish to understand how mechanism and sensor design choices can best be made to maximize grasping and manipulative competences. By better understanding the mechanical demands of task performance, we seek to understand the performance demands which underlie skillful human manipulation.

The main components of the research conducted under this project during the past year are (1) development of new hardware for robotic and human studies, (2) processing of robot sensor signals and task-level control of the devices, (3)

⁶¹ R.J. Gulati and M.A. Srinivasan, "Human Fingerpad under Indentation. I: Static and Dynamic Force Response," ASME summer annual meeting, forthcoming.

⁶² J.D. Towles and M.A. Srinivasan, *Frictional Properties of the Human Fingerpad*, Report to the MIT Summer Research Program, 1994.

⁶³ Harvard University, Cambridge, Massachusetts.

experiments on human perception and control of forces using some of the devices. The subsections to follow provide descriptions of the results obtained in each of the three topics.

Development of New Hardware for Robotic and Human Studies

During the past year, we have completed a high-precision glass smooth actuator (GSA) test bed that was used for experiments in human perception and dual actuator control. A force sensing fingertip has been integrated with a 3-degree-of-freedom force exerting device (the PHANTOM) to provide an apparatus for conducting force-based touch perception experiments. A passive three-finger hand, known as the Talon, has been instrumented with a coarse array of tactile sensors and multiple grasp force sensors for use in grasp quality assessment experiments. A high-performance 8x8 tactile array has been developed and interfaced. Several one- and two-axis force sensors were fabricated for experiments to determine mechanical properties of the human fingerpad as well as ability of humans to control forces. For psychophysical and neurophysiological experiments on tactile information obtained through tool contact, an instrumented stylus was constructed to measure three-axis force signals. An apparatus capable of measuring human fingerpad volume changes to a resolution of 1/100 ml was built to investigate the compressibility of the fingerpads. An "Instrumented Active Object" which could be made to expand or collapse rapidly under computer control was developed and used in experiments on human grasp control.

Robot Sensing, Actuation, Control and Planning

Sensing and Interpretation of Tactile and Contact Force Information

Significant effort in the development of sensors and interpretation methods has been undertaken at both Harvard University and at MIT's Artificial Intelligence (AI) Laboratory. Dr. Howe's group at Harvard has developed greatly improved tactile array sensors. Work on the manufacturing process has created sensors that are easily made with a photolithography-etching process. The resulting sensors are thin and flexible and easily attached to a wide range of robot finger tip shapes and sizes. In combination with new readout and signal processing electronics, this has resulted in very fast and sensitive sensors: less than 0.1 gram noise per element with complete readout of an 8x8 array in 5 msec.

At the Artificial Intelligence Laboratory, we have focused on perception of contact states observable from contact temporal force data. This work has progressed in four areas. Low frequency measured force data reflects information about contact constraints. Estimating the form of these constraints from force and motion measurements is essential to unstructured robot force control. A procedure was developed for estimating the directions of constraint, and the geometric parameters defining the constraint equations, for points in a Cartesian space and for the interaction of planar polygons. These results may be applied to three-dimensional problems by taking planar slices of three-dimensional space.

A procedure using the force and motion measurement residual from the sensor was also developed for selecting the type of the contact constraint. After each new force and motion measurement, the best estimate of the geometric parameters can be computed. These can then be used in conjunction with an assumed form of the contact constraints to compute a measurement error or residual. By testing the size of the error for all possible measurement models, the model which best fits the data can be determined.

A theoretical foundation and set of definitions for representing the forces and motions in contact tasks was defined. The forces and motions are represented as a network of measurement models (task network). Each node in the network represents a particular measurement model. A set of points in configuration space can be associated with each and every node. The points in configuration space then define the connections in the network. These definitions provide a starting point for learning and computing networks for given tasks from models of the geometry and desired actions.

A task state observer was developed that determines the probable current state of a task given a task network for the task. An observer was coded for a network and set of measurement models for the energy in the derivative of the strain energy. This signal is a good representation for high frequency short duration events. The observer was implemented in real-time and achieved 72 percent labeling accuracy on a test data set. A simple demonstration event driven robot program was also written. The robot program uses the most probable robot state, determined by the observer, to select an action.

High-Precision Actuation

The high precision actuator project has designed and built a prototype glass smooth actuator (GSA).

The basic design relies on a dual actuator concept, in which a small actuator runs a high-frequency torque control loop, and a large actuator creates a low frequency force bias using a large spring in the transmission. The GSA has been used both as a stimulation device for psychophysical experiments and as a platform for advancing robot actuator concepts. It has been used in an initial set of experiments in human force control in which the subject attempts to track a moving endpoint, while exerting constant force. Another set of experiments is underway in which the actuator follows a moving environment, while acting to maintain constant force. The current performance of the GSA is very good. The actuator has a force control dynamic range of 500:1. It is also capable of controlling force at 40 Hz bandwidth.

Grasp Quality Assessment

In conjunction with Dr. Salisbury's group, Dr. Pratticizzo from the University of Pisa (while on a five-month fellowship at the MIT Artificial Intelligence Laboratory) has developed an approach for measuring the quality of whole hand grasps. The work combines a solid theoretical approach to measuring the "distance" from losing the grasp with a practical computational approach to real-time measurement of grasp quality. The approach utilizes contact geometric and friction information to define the maximum possible grasp quality; with the measurement of contact forces, it also permits assessment of the instantaneous quality as a percentage of the maximum attainable quality. The approach provides a means for estimating the maximum quality possible even in the absence of full sensory information, provides a method for optimizing internal grasp forces and can be used to specify limits on dynamic motions to avoid grasp failure. Real-time processing of touch and force sensor data from the talon hand has been implemented to demonstrate online grasp quality assessment.

Grasp Gaits

We have developed an approach for planning multi-finger grasp gaits. Truly dexterous manipulation of objects with the fingers requires repeated sequences of moving the object and repositioning of the fingers. Our approach permits planning sequences of repositioning and regrasping an object with two and three finger grasps. It considers loss of mobility due to figure range limits and loss of constraint due to friction and force closure limitations. The enormous search tree has been suffi-

ciently reduced by a series of planning heuristics that real-time planning for rotation of an unknown planar object is possible. A real-time graphic simulation permits viewing progress of the planned actions.

Robot Control

Professor Howe's group at Harvard has implemented a Cartesian stiffness controller on the two-fingered Planar Manipulator in the Harvard Robotics Laboratory. This controller permits accurate control of the apparent stiffness and the center of compliance of a grasped object. The controller will be used in planned experiments on the role of tactile information in real-time control of precision manipulation tasks.

Human Perception and Control

The Human Haptics Group at MIT has investigated (1) the mechanics of the human fingerpad and its role in tactile sensing, and (2) human perception and control of forces exerted by the fingerpads. The former, described earlier and partially supported by this grant, includes experiments to determine the mechanical behavior of the fingerpad under normal and shear forces, as well as the compressibility of the fingerpad. Nonlinear lumped parameter models were developed and finite element analysis of multilayered 3D fingertip models were carried out to match biomechanical and neurophysiological data.

To quantify human perception and control of forces, experiments were conducted under a wide variety of conditions: (1) tracking of visual displays of static and dynamic force traces with a stationary fingerpad (isometric case), (2) maintaining constant contact force on a moving robot end-effector (isotonic case), (3) sensing and control of torque applied on the shaft of an "Instrumented Screw Driver", and (4) control of grasp forces on an "Instrumented Active Object". The data from each of these experiments have been analyzed with the viewpoint of developing engineering specifications of human haptic performance. The Yale group has performed psychophysical and neurophysiological experiments on perception and control of tactile information obtained by touching an object with a tool. An instrumented stylus was used in both active and passive touch experiments on the discrimination of softness by human subjects and in recording cutaneous neural responses to the same stimuli applied to monkey fingerpads. Brief descriptions of each of the experiments and models described above are given in the sections below.

Isometric Force Tracking Ability of Humans

In the experimental setup, a human subject tracks visual images of force traces displayed on the monitor by applying appropriate normal forces through a fingerpad that is in contact with a force sensor. In these experiments, the finger moves by only fractions of a millimeter, thus approximating isometric muscular contraction conditions. We had completed one set of experiments on such force tracking last year, and now we have expanded the range of target forces and their frequency. During tracking constant and sinusoidal force targets (three subjects with three trials per stimulus), the mean absolute error increased with constant force magnitude, target sinusoid frequency and amplitude. The errors for a sinusoid of a given amplitude are 5 to 40 times higher than those for constant force targets with the same magnitude. Even at relatively low frequency of 2 Hz, the errors can be higher than 50 percent of the sinusoid amplitude at all amplitudes.

Isotonic Force Control Ability of Humans

We employed the high-precision glass smooth actuator (GSA) to measure the ability of human subjects to maintain a constant force (0.1 to 0.8 N) by pressing their fingerpads on the actuator's end effector while it was moving sinusoidally (2 to 16 degrees in amplitude; 0.5 to 16 Hz frequency). During each trial, the robot maintained a constant position for the first 10 seconds, and during the first 8 seconds, the subjects tracked a constant target force displayed as a line on a monitor. The monitor screen was then blanked out, and after two seconds, the actuator started moving sinusoidally at a preprogrammed frequency and amplitude, but the subjects were asked to maintain the same force as before. All the subjects were able to perform the task with very little drift in mean force. However, the deviations from the mean were in phase with the actuator motion, and various error measures changed differently with stimulus parameters. The mean absolute error increased with frequency and amplitude almost linearly, but remained constant with respect to target force magnitude.

Torque Sensing and Control

The human ability to sense and control torque was investigated in experiments with the Instrumented ScrewDriver (ISD).⁶⁴ The ISD is comprised of a

single shaft, which is supported by low friction bearings, and is connected to a reaction torque sensor and a magnetic particle brake. Angular position of the shaft is measured by an incremental optical encoder. In all cases the subjects grasped the handle of the ISD between the thumb and index finger of their dominant hand and turned the shaft clockwise for 180 degrees against a constant resistive torque applied by the magnetic particle brake. The magnitude of this resistive torque was varied across different trials. Two types of experiments were conducted: discrimination experiments to determine the human resolution in sensing torque and control experiments to determine the human motor capability in controlling torque.

All torque discrimination experiments used a one-interval, two-alternative, forced-choice paradigm with no feedback to the subject. The reference torque value was 60 mN-m and the comparison values were equal to 5 percent, 10 percent, 20 percent and 30 percent of the reference torque. In addition, training runs were conducted with a comparison value of 50 percent of the reference torque until the subject response was 90 percent correct. The just noticeable difference for torque was found to be 12.7 percent for the reference torque of 60 mN-m. During some of the trials, in addition to recording the stimulus and the subject's response, the resistive torque, the output of the torque sensor and the angular position of the shaft over time were also recorded. These data are used to make comparisons between the motor performance in the discrimination task and the control task.

For the control experiments, subjects were asked to maintain a constant angular velocity while turning against the constant resistive torque. The value of the angular velocity was up to the subject to choose, but they were asked to try and use the same value for each trial. Because of the physics of the ISD, attempting to maintain a constant angular velocity is directly related to attempting to apply and maintain a constant torque during shaft motion. The constant resistive torque values used were the same as for the discrimination experiments. As before, the resistive torque, the output of the torque sensor, and the angular position of the shaft were recorded over time. Comparison of the time profiles of angular velocity indicate that even when subjects were trying to maintain a constant angular velocity in the control experiments, their performance was not significantly better than when they were trying to discriminate the torques.

⁶⁴ L. Jandura and M.A. Srinivasan, "Experiments on Human Performance in Torque Discrimination and Control," in *Dynamic Systems and Control*, Ed. C.J. Radcliffe (Chicago: ASME, 1994), DSC-Vol. 55-1.

A curious phenomena observed rather consistently in all of the data is the occurrence of peaks in the velocity and acceleration profiles at about 0.1 second intervals. To further investigate this phenomena, the power spectral density of the middle third of the angular velocity profile was calculated. Although there is some tendency for the discrimination PSDs to be single-peaked while the control PSDs are double-peaked, this was not observed consistently across all subjects. However, in all subjects, most of the frequency content was less than about 15 Hz for both the discrimination and control experiments.

Grasp Control of an Instrumented Active Object

Most of the investigations of human grasp control reported in the literature pertain to passive objects. In order to test the limitations of the human motor system in compensating for sudden disturbances, we fabricated an "Instrumented Active Object."⁶⁵ It mainly consisted of a pneumatic cylinder whose piston could expand or contract through the operation of computer controlled valves. A position sensor monitored the motion of the piston while two 2-axis force sensors measured the normal and shear forces applied by a subject's fingerpads on two circular plates when the object was held in a pinch grasp. The plate surfaces were either polished aluminum or sandpaper depending on the experiment. A visual display on a computer monitor indicated the force of pinch grasp the subjects were required to apply, and when subjects achieved it, after a random time-delay the object contracted suddenly (170 to 240 mm/s velocity; 19 mm displacement). When initial grasp forces were less than 1.8 N, the subjects dropped the object all the time (three subjects; ten trials per grasp force value per subject), whereas they held it in increasing number trials as the grasp forces increased. No significant difference between aluminum and sand paper surfaces were observed. In one trial where there was a small slip, a perturbation in force applied by the thumb is seen at around 100 ms, but the object did not drop. In another trial in which the subject dropped the object, oscillations in force applied by the middle finger began at 60 ms, and those oscillations in force applied by the thumb began at about 80 ms. Both these kinds of oscillations continued until the object was dropped at about 100 ms. These data are being analyzed further for a deeper understanding of the dynamics of grasping.

Processing of Tactile Information Obtained by Touching an Object with a Tool

The capacity of humans to discriminate the softness of rubber specimens differing in compliance by means of a tool (stylus) was measured under a variety of experimental conditions. Under active touch (AT), the observer held the stylus in a pinch grip and either tapped, pressed or bounced it against the rubber specimens during tests requiring either ranking or pairwise discrimination. Under passive touch (PT), one end of the stylus indented the stationary fingerpad with a base force maintained by a torque motor while the other end was tapped, pressed or bounced (dropped onto) by the rubber specimen. Discrimination of softness was superior during AT than during PT for both tapping and pressing, suggesting that proprioceptive cues contribute to optimal tactual performance. The fact that discrimination was more accurate for tapping than for pressing under PT suggests the importance of tactile cues generated by the initial impact of the stylus against the surface of the rubber. Bouncing the specimen (attached to a pivoted arm) against the stylus under PT produced characteristic oscillatory contact forces on the skin that subjects could readily discriminate indicating the usefulness of vibratory signals generated by the impact of a lightly held tool against an object.

The same stimuli used in the PT tests in humans were applied via the stylus to the fingerpad of the anesthetized monkey. Evoked nerve impulse activity was recorded electrophysiologically from slowly-adapting type I and rapidly-adapting type I (RA) and type II (PC) mechanoreceptive peripheral nerve fibers. Increases in the hardness of the specimen tapped or bounced against the stylus elicited nerve-impulse trains with shorter interspike intervals and shorter durations for all three fiber types. Fiber responses of SAs during pressing were related only to the force rate (velocity of pressing) and did not discriminate between specimens. Thus, the psychophysical measures can be accounted for by the responses of cutaneous mechanoreceptors. An implication of this research for the development of robotic hands is the need to develop sensors and decoding algorithms for transducing and recognizing dynamic changes in contact force produced by the impact of a tool against an object.

⁶⁵ S.P. Karason and M.A. Srinivasan, "Human Grasp Control of an Instrumented Active Object," submitted to the 1995 ASME winter annual meeting, San Francisco, California.

1.2.6 Publications

- Annaswamy, A.M., and M.A. Srinivasan. "A Study of Dynamic Interactions between Haptic Interfaces and Compliant Fingerpads." *Proceedings of the Motion Control Workshop*, Berkley, California, March 1994.
- Annaswamy, A.M., and M.A. Srinivasan. "The Role of Compliant Fingerpads in Grasping and Manipulation: Identification and Control." Institute of Mathematics, Springer Verlag. Forthcoming.
- Bicchi, A., and D. Prattichizzo. "A Standard Form for the Dynamics of General Manipulation Systems." Submitted to the IEEE International Conference on Robotics and Automation, 1995.
- Bicchi, A., P. Petreschi, and D. Prattichizzo. "Control of Force Decomposition in Enveloping Grasping." In *Proceedings of the Symposium on Robot Control*, 1994.
- Bicchi, A., and D. Prattichizzo. "Controllability of Whole-Arm Manipulation." 33rd CDC, forthcoming.
- Dandekar, K., and M.A. Srinivasan. "Tactile Coding of Object Curvature by Slowly Adapting Mechanoreceptors." In *Advances in Bioengineering*. Ed. M.J. Askew. Chicago: ASME, 1994, BED-Vol. 28, pp. 41-42.
- Dandekar, K., and M.A. Srinivasan. "A three-dimensional Finite Element Model of the Monkey Fingertip for Predicting Responses of Slowly Adapting Mechanoreceptors." ASME summer annual meeting. Beaver Creek, Colorado. Forthcoming.
- Eberman, B., and J.K. Salisbury. "Application of Change Detection to Dynamic Contact Sensing." *Int. J. Robotics Res.* 12(5): (1994).
- Gulati R.J. and Srinivasan M.A. "Human Fingerpad under Indentation. I: Static and Dynamic Force Response." ASME summer annual meeting. Forthcoming.
- Jandura, L., and M.A. Srinivasan. "Experiments on Human Performance in Torque Discrimination and Control." In *Dynamic Systems and Control*, Ed: C.J. Radcliffe. Chicago: ASME, 1994, DSC-Vol. 55-1, pp. 369-375.
- Karason, S.P., M.A. Srinivasan, and A.M. Annaswamy. "Tactile Sensing of Shape." Center for Information Driven Mechanical Systems (*CIDMS*) Workshop Proceedings, Dept. of Mech. Eng., MIT, September 1994.
- Karason, S.P., and M.A. Srinivasan. "Human Grasp Control of an Instrumented Active Object." Submitted to the 1995 ASME winter annual meeting.
- LaMotte, R.H., M.A. Srinivasan, C. Lu, and A. Klusch-Petersen. "Cutaneous Neural Codes for Shape." *Can. J. Physiol. Pharm.* 72: 498-505 (1994).
- LaMotte, R.H., J. Zhang, and J. Yan. "Tactile Signals Generated by a Tool Used to Discriminate the Softness of Objects." *Soc. Neurosci. Abstr.* 20: 1381 (1994).
- Peine, W.J., J.S. Son, and R.D. Howe. *A Palpation Device for Artery Localization in Laparoscopic Surgery*. Harvard University, Robot Sensor Laboratory Technical Report, September 1994.
- Petreschi, P., D. Prattichizzo, and A. Bicchi. "Articulated Structures with Tendon Actuation for Whole-Limb Manipulation," *Proceedings of the 1994 International Conference on Robotics and Automation*, San Diego, California, May 1994.
- Roby, F.L., K. Dandekar and M.A. Srinivasan. *Study of Fingertip Deformation Under Indentations by Circular and Rectangular Indentors*. Report to the MIT Summer Research Program, 1994.
- Son, J.S., E.A. Monteverde, and R.D. Howe. *A Tactile Sensor for Localizing Transient Events in Manipulation*. Harvard University, Robot Sensor Laboratory Technical Report, May 1994.
- Srinivasan, M.A., and K. Dandekar. "An Investigation of the Mechanics of Tactile Sense Using Two-dimensional Models of the Primate Fingertip." *J. Biomech. Eng.* Forthcoming.
- Srinivasan, M.A., and R.H. LaMotte. "Tactual Discrimination of Softness." *J. Neurophys.* 73(1): 88-101 (1995).
- Towles, J.D., and M.A. Srinivasan. *Frictional Properties of the Human Fingerpad*. Report to the MIT Summer Research Program, 1994.
- Thesis**
- Babiec, W.E. *In vivo Volume Changes of the Human Fingerpad under Indentors*. S.B. thesis. Dept. of Mech. Eng., MIT, 1994.

1.3 Virtual Environment Technology for Training

1.3.1 Research Testbed

Sponsor

U.S. Navy - Naval Air Warfare Center Training Systems Division
Contract N61339-94-C-0087

Project Staff

Nathaniel I. Durlach, Dr. David Zeltzer, Dr. Jeng-Feng Lee, Walter A. Aviles, James H. Bandy, Rakesh Gupta, Dorrie Hall, Jonathan Pfautz, Nicholas Pioch

During the second year of the Virtual Environment Technology for Training (VETT) program, the major goal of the Testbed project was to continue development of the basic facilities and architecture of the Testbed so that meaningful training experiments could be initiated. The following efforts were completed or are underway during the second year.

Implementation of Research Support Methods and Tools

Testbed personnel have worked closely with personnel of the Satellite projects in an effort to refine the software and hardware interfaces that each Satellite will require to conduct experimental research using the Testbed. We have recently completed the Phase-1 implementation of the Experimenters' Interface (EI), a distributed software package that will allow experimenters—either VETT investigators, or personnel from other military or government laboratories—to make use of the VETT Testbed as a research tool.

Performance Characterization

Test hardware and software for measuring the performance of the Testbed have been completed. Using these tools the performance of the Testbed (e.g., graphics, auditory, and haptic update rates and delays) has been precisely measured. This is important to characterize the system itself for development purposes, but it is also necessary to provide baseline data for Satellite experiments which will be run on the Testbed.

Development of Requirements and Specifications for Software Architecture and Multimodel VE Database Required to Support Physically-based Modeling of Objects and Actions within Virtual Environments

In collaboration with the Haptics and Sensorimotor groups, the design of a common representational framework is underway, beginning with physically based, articulated, rigid bodies. This representational framework will be utilized to model and render the visual, auditory, and haptic interactions which characterize virtual environments.

Upgrade Testbed Graphics Capabilities and Performance

A RealityEngine2 graphics subsystem was purchased and integrated into our SGI Onyx system. This system not only allows improved graphics performance but also increases compatibility with Naval Air Warfare Center Training Systems Division (NAWCTSD) systems. The Core Testbed VE-prototyping software, known as 3D, now makes use of the anti-aliasing capabilities of the RealityEngine2. In addition, work is currently underway to utilize more than one processor within our Onyx system to support graphics and general computation. As one aspect of this, Core Testbed personnel are exploring the substitution of the SGI Performer software library for the SGI GL graphics library used in the 3D system. The Performer library directly supports the use all RealityEngine2 features and the use of multiple processors for graphics processes. A Virtual Research VR4 head-mounted display was recently purchased and has been integrated into the Testbed. This LCD-based HMD has a larger horizontal field-of-view (~ 40° horizontal) than our previous HMD.

Integration and Evaluation of Improved Haptic Interfaces, Speech Interaction Systems, and Auditory Displays

The PHANToM haptic display device was incorporated into the Testbed, and several demonstration applications have been implemented. A BBN Hark speaker-independent, connected speech recognition system was purchased and integrated. The auditory event representation, modeling, and rendering process received particular attention during the second year. As part of the aforementioned multimodal object database efforts, initial methods of representing and modeling acoustic events have been developed. In addition, an audio-event server and sound spatialization system were developed.

The audio-event server allows the playback of pre-recorded audio sounds (i.e., based either upon recordings or generated by physical models). Hundreds of sounds may be simultaneously generated, mixed, and output on eight physical output channels. These output channels in turn are spatialized using commercial sound spatializers.

A Crystal River Engineering BEACHTRON 2-channel sound spatializer has been integrated into the Core Testbed. Three new spatialization systems (the Ctronll and the Gargantutron from Crystal River Engineering and the system from Tucker-Davis Technologies) were acquired under Grant N61339-93-C-0104. The goal of this grant was to create a "next-generation" system with expanded capabilities to further the field of sound spatialization for auditory virtual environments. Since no single system appeared capable of delivering all of the envisioned needs of the field (e.g., enhanced computational throughput, increased internal storage, use of off-the-shelf rather than special-purpose hardware, greater programmability, etc.), three solutions were simultaneously developed. The Gargantutron, based on mature hardware and software, was developed to ensure continuity between existing technology and new approaches while increasing throughput and effective storage by a factor of four. The Gargantutron will be used primarily for generation of "natural-sounding" spatial sound, including environments with reflective surfaces. The Ctronll was developed using off-the-shelf DSP cards and frequency-domain filtering techniques. As such, the Ctronll should prove to be a fairly inexpensive system for the simulation of relatively simple echoic environments and a proof of concept for frequency-domain representations of HRTFs in real-time environments. Finally, the system developed by Tucker-Davis technologies is highly modular and extremely flexible.

All three of the new sound spatialization systems will be tested to ensure that they meet their design specifications. Following this initial evaluation, the systems will be employed in various projects under the VETT program. Both the Gargantutron and the Ctronll will be used primarily in generating natural-sounding spatial sound for projects running on the Core Testbed. While developed primarily for the simulation of natural-sounding acoustic environments, the Tucker-Davis system's flexibility makes it an ideal tool for use in further auditory-motor experiments in the Sensorimotor Loop project.

Implementation of the Officer of the Deck Training Application and Pilot Experiments

The first training system under development on the Core Testbed involves training a submarine officer of the deck (OOD) to perform in-harbor navigation on a surfaced submarine. This is a task that involves a dozen or more personnel, most of whom make up the below-deck piloting team that operates periscopes, radar and sonar systems, and performs basic navigational calculations. The OOD, stationed on the conning tower of the surfaced boat during this task, is essentially responsible for monitoring the progress of the boat as it negotiates a marked channel. This officer verifies that the navigational suggestions of the piloting team are correct and that the course of the submarine is indeed conforming to the navigational plan.

The U.S. Navy, in fact, currently has simulator systems for the below-deck piloting team, but there is no corresponding simulator or formal training program for junior officers who must learn to perform this task—essentially in an informal on-the-job apprenticeship. As part of the VETT program, a VE system has been developed that allows an OOD trainee to view a particular harbor and associated waterway through a head-mounted display, receive spoken reports from a simulated piloting team, give spoken commands to the helmsman, and receive verbal confirmation of command execution from the helm. The training effectiveness of the system—including instructional aids unique to VE systems—will be evaluated experimentally with a small number of subjects.

The design of the OOD application has been accomplished with the close cooperation of the Training Satellite at BBN, and the members of this group have designed the experimental program for evaluating the OOD training application.

1.3.2 Sensorimotor Satellite

Sponsor

U.S. Navy - Naval Air Warfare Center
Training System Division
Contract N61339-93-C-0055
Contract N61339-94-C-0087

Project Staff

Nathaniel I. Durlach, Professor Richard M. Held, Dr. Thomas E.v. Wiegand, Dr. Wendelin L. Sachtler, Dr. Barbara G. Shinn-Cunningham, Evan F. Wies, David C. Lossos, Susan E. Born, Stephen V. Baird, Lukasz A. Weber, Erika N. Carmel

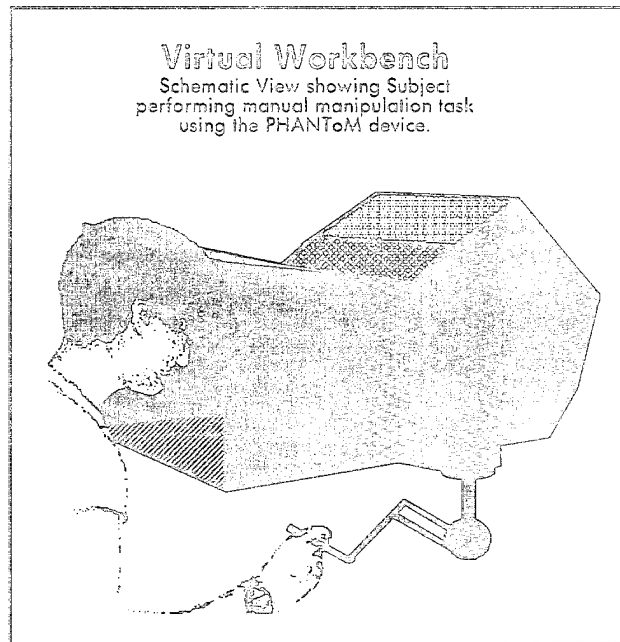


Figure 1. The virtual workbench concept in schematic form.

Work on the sensorimotor satellite in the VETT program is directed towards evaluating human response to alterations in sensorimotor loops associated with the use of virtual environment (VE) technology. Even in cases in which the design goal is complete realism, alterations in the form of distortions, time delays, and statistical variability ("noise") are inevitable (1) in the presentation of information to the human operator (because of limitations in displays), and (2) in the sensing of the operator's responses via the controls in the human-machine interface. Such alterations will occur in all sensorimotor loops involved in the system, including, for example: (1) those associated with visual and proprioceptive sensing, and motor control of hand position and posture; and (2) those associated with visual and auditory images of computer generated scenes and motor control and proprioceptive sensing of head position and orientation. Furthermore, in some cases, it appears that specific training goals can be achieved more efficiently by purposefully introducing distortions to highlight or magnify certain features or relationships in the training situation. In these cases, as well as those in which the alterations are the result of technological limitations, it is essential to determine the human response to the altered characteristics of the sensorimotor loops involved.

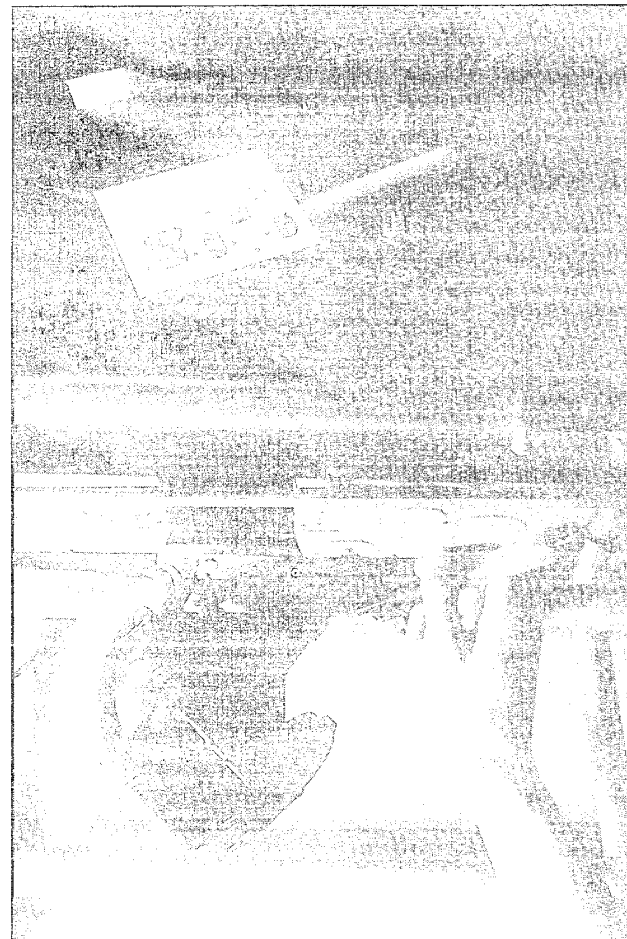


Figure 2. The virtual circuit board display and PHANTOM™ unit mounted below the mirror.

In the past year, we have addressed these issues in three areas. First, we have continued our basic psychophysical experiments in the area of adaptation to alterations in the visual-proprioceptive sensorimotor loop (using the apparatus and paradigm described in *RLE Progress Report No. 136*). Second, we have completed a set of experiments elucidating a model of adaptation to alterations in the loop involving auditory localization.

Third, we have begun a new area of research utilizing a VE system that includes an alternative man-machine interface: the virtual workbench. The multimodal virtual workbench was developed to both study human sensorimotor capabilities in near-field space and to explore cognitive performance and training in complex tasks involving spatialization of information in VEs. The system combines state-of-the-art haptic feedback and visual display technologies with audio capabilities to create an alternative "front-end" interface for the core VETT testbed.

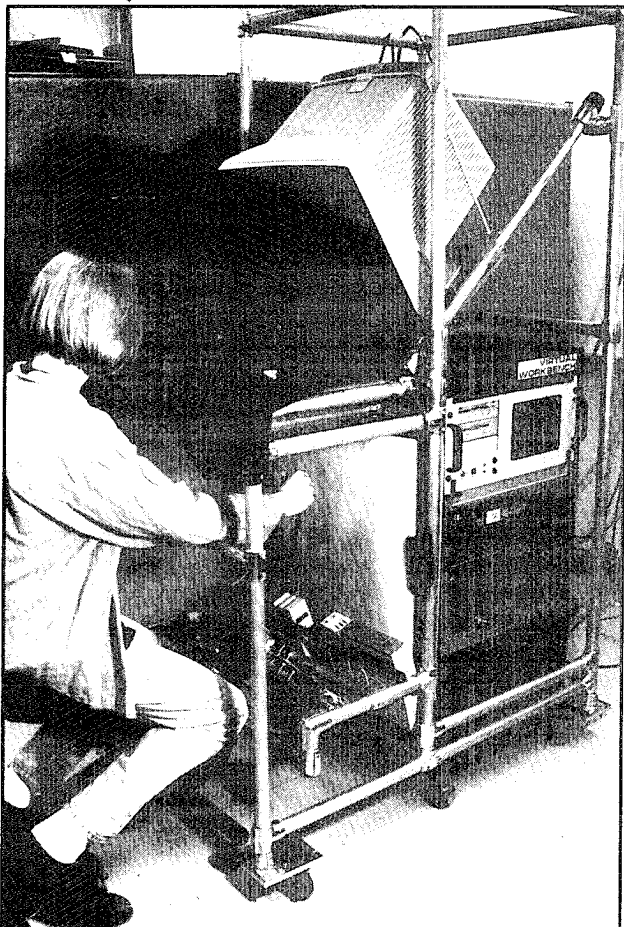


Figure 3. Photograph of subject seated at the virtual workbench.

Currently available HMDs and their associated tracking and graphics rendering systems operate at the limits of current technology. Despite their great cost, these systems are still insufficient to present a virtual world free of performance-reducing and nauseogenic effects. In the virtual workbench, we combine visual display and haptic feedback technologies into a form in which the user looks and reaches into a virtual space (as opposed to trying to immerse the entire body). In this way, we are able to sidestep many of the technical shortcomings of HMDs, enabling the virtual workbench to serve as a precision instrument for measuring human sensory and cognitive performance. The virtual workbench was specifically designed for precise overlay of visual and haptic spaces, providing a cohesive world percept. The effects (on human performance) of deviations from precise registration of the spaces, as well as distortions, delays, and other manipulations (e.g., modification of forces in haptic space), will be studied using this system. In addition to these sensorimotor effects, we are preparing experiments designed to examine the influence of the manipulations mentioned above on cognitive

performance (using memory and reasoning tasks). Development efforts are also being directed toward producing a highly veridical training task involving manual interaction with virtual electronic circuit boards and components.

1.3.3 Haptics Satellite

Project Staff

Dr. J. Kenneth Salisbury, Dr. Mandayam A. Srinivasan, Nathaniel I. Durlach, Dr. Lynette A. Jones, Dr. David L. Brock, Gerald L. Beauregard, Hugh B. Morgenbesser, Hong Z. Tan, Craig B. Zilles

In the past year, we have developed device hardware, interaction software and psychophysical experiments pertaining to haptic interactions with virtual environments. Two major devices for performing psychophysical experiments, the Linear and Planar Graspers, have been fitted with additional sensors for improved performance. Another haptic display device developed previously, the PHANTOM, has been used to prototype a wide range of force-based haptic display primitives. The three devices were used to perform psychophysical experiments. Copies of the PHANTOM, along with demonstration software, have been delivered to the sponsor and the core testbed. In addition, two full-scale tool-handle haptic interface devices have been designed and constructed.

We had previously developed software for the demonstration of haptic displays with the PHANTOM, such as interactions with virtual pushbuttons, sliding friction and surface texture displays, virtual screw turning, and virtual grasping as well as two-person haptic "pong" with two PHANTOMs. Additional software was developed for visual and haptic rendering of deformable toroids and needle biopsy procedures. Different algorithms for rendering Coulomb and static friction in haptic displays were developed. Stroking of surfaces with varying compliance in the normal direction was demonstrated and experiments revealed a need for preserving passivity of interaction. Stable two-finger grasping and stacking of two virtual blocks was demonstrated with two tool-handle haptic interfaces. Network communication between a haptic renderer (Pentium PC) and graphics renderer (Silicon Graphics) was implemented. The development and specification of a software format to facilitate standard multimodal representation of convex and concave polyhedral objects was started. This format is necessary to allow consistent visual and haptic rendering of objects in virtual environments. Multimodal rendering of a triangular meshed polyhedron

of moderate complexity (200 facets) was demonstrated.

Software was also developed for the conduction of psychophysical experiments with the linear grasper, planar grasper and the PHANTOM. The linear grasper is now capable of simulating fundamental mechanical properties of objects such as compliance, viscosity and mass during haptic interactions. Virtual wall and corner software algorithms were developed for the planar grasper, in addition to the simulation of two springs within its workspace. A variety of haptic rendering algorithms for displaying the shape, texture and friction of solid surfaces have been implemented on the PHANTOM. We completed a series of psychophysical experiments with the Linear Grasper to characterize the ability of the human haptic system to discriminate fundamental mechanical properties of objects.⁶⁶ These included several experiments to measure the manual resolution of viscosity and mass. In addition, experiments were also performed to study the influence of mechanical work and terminal force on the perception of compliance.

Utilizing the planar grasper, we have completed a set of multimodal psychophysical experiments investigating the influence of visual information on the haptic perception of stiffness in virtual workspaces. Results indicate that the perception of stiffness for objects like virtual pushbuttons can be significantly altered by presenting visually skewed positional information to the subject. We have initiated psychophysical experiments using the PHANTOM to determine the feasibility of various haptic display algorithms for shape, texture and friction of solid surfaces. The results show that even when the user is exploring nominally flat surfaces, he can be made to feel as if he is interacting with a shaped and textured surface by appropriately varying the direction of the force reflected back to the user. These new algorithms permit the mapping of a shape or texture onto a polygon, so that they may be used in haptic rendering in the same way that texture mapping and color shading are used in graphics rendering. Our psychophysical experiments are aimed at characterizing the effectiveness of such computationally efficient simulations and rendering algorithms in conveying the desired object properties to the human user.

Publications

Beauregard, G.L., M.A. Srinivasan, and N.I. Durlach. "Manual Resolution of Viscosity and Mass," Submitted for presentation at the ASME winter annual meeting, San Francisco, California, 1995.

Srinivasan, M.A. "Haptic Interfaces." In *Virtual Reality: Scientific and Technical Challenges*. Eds. N.I. Durlach and A.S. Mavor. Report of the Committee on Virtual Reality Research and Development. Washington, D.C.: National Research Council, National Academy Press, 1994.

Srinivasan M.A. "Virtual Haptic Environments: Facts Behind the Fiction," *Proceedings of the Eighth Yale Workshop on Adaptive and Learning Systems, Center for Systems Science*, New Haven, Connecticut: Yale University, 1994.

Tan, H.Z., and N.I. Durlach, G.L. Beauregard, and M.A. Srinivasan. "Manual Discrimination of Compliance Using Active Pinch Grasp: the Roles of Force and Work Cues." *Percept. Psychophys.* Forthcoming.

Tan H.Z., M.A. Srinivasan, B. Eberman, and B. Cheng. "Human Factors for the Design of Force-reflecting Haptic Interfaces." In *Dynamic Systems and Control*, Ed. C.J. Radcliffe. Chicago: ASME, 1994, DSC-Vol.55-1, PP. 353-359.

1.4 Research on Improved Sonar Displays: A Human/Machine Processing System

Sponsor:

U.S. Navy - Office of Naval Research
Grant N00014-93-1-1198

Project Staff:

Dr. David Zeltzer, Dr. Jeng-Feng Lee, Nathaniel I. Durlach

The human/machine processing system (HMPS) program began August 1, 1993. The overall objec-

⁶⁶ H.Z. Tan, N.I. Durlach, G.L. Beauregard, and M.A. Srinivasan, "Manual Discrimination of Compliance Using Active Pinch Grasp: the Roles of Force and Work Cues," *Percept. Psychophys.*, forthcoming; G.L. Beauregard, M.A. Srinivasan, and N.I. Durlach, "Manual Resolution of Viscosity and Mass," submitted to the 1995 ASME winter annual meeting, San Francisco, California.

tives of this research, as discussed in the proposal, are to:

- explore general techniques for multisensory interaction with sonar data in light of an acoustic propagation model,
- develop a working human-machine processing system (HMPS) testbed embodying the most promising of these techniques, and
- evaluate the effectiveness of the experimental HMPS.

Nearly all the first year objectives have been met. A significant effort was required to become familiar with naval sonar operations; interviews with domain experts (i.e., sonar technicians) and a task analysis based on these interviews were required before system design could begin. At present, the user-centered system design of the HMPS is largely accomplished, and HMPS implementation is underway.

An extensive literature review and a survey of available undersea acoustic propagation models were conducted; this included discussions with undersea acoustics experts at MIT and elsewhere. No extant models were deemed appropriate for the HMPS project. The ray tracing paradigm has been identified as the most appropriate and effective technique for computing undersea sound propagation. A modeling and simulation package based on modifications to ray tracing algorithms reported in Ziomek⁶⁷ is currently being implemented.

In order to design a human/machine interface for improved sonar display, it is necessary to understand and analyze the tasks actually performed by sonar crews. To this end, a number of interviews have been conducted with two domain experts, both active-duty sailors, one of whom has served as sonar supervisor, and the other as a sonar technician, on a U.S. Navy fast attack submarine. Based on these interviews, we have developed a task analysis of the functions performed by the sonar supervisor, and we have subsequently designed the functional architecture of the HMPS. In addition, we have been in contact with a number of other submarine officers in the course of the VETT project, and their input has been valuable for the HMPS work as well.

We have chosen to focus the HMPS on the requirements of the fast attack submarine, rather than a

ballistic missile submarine or a surface ship, for the following reasons. First, a ballistic missile submarine is a strategic asset and does not pursue offensive tactical operations. Sonarmen on a fast attack submarine, therefore, have a range of offensive tactical operations to be supported by an HMPS that are simply not encountered on a ballistic missile submarine. Surface ships, unlike either class of submarines, can often call on support from aircraft, other naval vessels and satellites in support of tactical operations. The fast attack submarine, however, must operate as a self-contained sensor and weapons platform in a complex and noisy undersea environment.

Once an acoustic contact is detected on a fast attack sub, it is the responsibility of a single individual—the sonar supervisor—to form a coherent picture of the immediate tactical situation, and to make recommendations to the conn regarding control of the vessel. In addition to viewing "waterfall" and similar displays and interacting with the sonar technicians in the sonar shack, the sonar supervisor must construct a "mental model" of the tactical situation with essentially no supporting documentation, hardware, or software. It all must be done "in his head", based on his knowledge and experience. The purpose of the HMPS, then, is to provide tools for enhancing situational awareness and to support "what if" simulations of sensor, vessel, and weapons operations.

We have obtained undersea terrain data from several sources, and we have selected a data set appropriate for initial HMPS implementation. In addition, we have acquired several geometric models of submarines which have also been integrated into the HMPS. Furthermore, we found that ocean eddy data is available from researchers at Woods Hole.

The initial implementation of the HMPS is in progress. The ray tracing model is being coded; a large effort has gone into programming an efficient ray tracing package and programming efficient graphics modules to display ray tracing results and acoustic shadow volumes.

Once the initial HMPS implementation is complete, work will begin on a multimodal operator interface. We expect this work to be underway late in the third quarter of the second year, with subject evaluations to begin in the fourth quarter, as called for in the original proposal.

⁶⁷ L.J. Ziomek, "The RRA Algorithm: Recursive Ray Acoustics for Three-Dimensional Speeds of Sound, *IEEE J. Oceanic Eng.* 18(1): 25-30 (1993).

We have identified sources for platform and biological signatures, and we are prepared to incorporate such acoustic databases into the HMPS. As time permits, we may investigate cooperative antisubmarine warfare (ASW) techniques. In particular, we will be able to simulate remote active sources which serve as acoustic illuminators for the passive sensors of an attack submarine.

1.5 Development of Inertial Head-Tracking Technology

Sponsor

National Aeronautics and Space Administration/
Ames Research Center
Grant NCC 2-771

Project Staff

Eric M. Foxlin, Nathaniel I. Durlach

The inertial head-tracker program began in September 1992. Our objective is to develop a new head-tracking technology for HMD applications which offers large working volume, high fidelity, and unencumbered operation.

Commercially available tracking systems suffer from a variety of limitations which restrict their use in human-machine interfaces. Mechanical trackers offer fast response times and good accuracy, but require physical attachment to the head which limits range of motion and user comfort. Optical methods are expensive, require a clear line-of-sight, and usually necessitate a trade-off between precision and working volume. Magnetic trackers (such as those available through Polhemus or Ascension Technologies) are reasonably priced, but have a small working volume and suffer from noise and magnetic field distortions caused by metallic objects. Finally, acoustic systems based upon a transmitted signal's time-of-flight are available at reasonable cost and offer a large working volume. However, the speed of these systems is limited by the speed of sound, and they are sensitive to acoustic interference.

Our system departs from the prior state-of-the-art in head-tracking by relying on inertial sensors for its primary measurements. This offers the potential advantage of a self-contained head-mounted measurement device that does not rely on signals from other equipment in the lab, making possible large range and freedom from interference. The main difficulty with inertial systems is drift, which we correct with an inclinometer and compass. The orientation

tracker therefore retains its large range and relative invulnerability to interference. Position can be tracked more accurately than orientation by optical and acoustic systems, but provides greater difficulties for inertial systems. We propose to build a system which combines an inertial orientation tracker with a hybrid acoustic-inertial position tracker because this would overcome most of the problems of either technology used alone.

1.5.1 Orientation Tracker First Prototype

In the first year of the grant, an initial prototype orientation tracker was built. The tracker consisted of three Systron-Donner GyroChips mounted on an aluminum bracket, together with a fluid inclinometer for drift compensation. It was large and heavy, but provided a convincing demonstration of the potential usefulness of inertial orientation tracking. Methods were developed for bench-testing the performance of the prototype and a simple apparatus built for this purpose. Detailed testing of drift, accuracy, resolution, noise, and dynamic response began late in the first year.

Testing of the initial prototype inertial head-orientation tracker was completed early in the second grant year. Three new projects were started to further develop the inertial head-tracking concept: (1) development of a second prototype orientation tracker, (2) construction of a general tracker testing facility, and (3) six-degrees-of-freedom (6 DOF) inertial tracker concept development and research on its underlying device technologies.

1.5.2 Orientation Tracker Second Prototype

The second prototype effort is now nearing completion. Its primary purpose is to take the inertial tracker from the proof-of-concept phase through to the demonstration of a practical tracking device that can be used in real applications including auditory experiments. Several improvements were needed to accomplish this goal. The sensor assembly, entirely redesigned to incorporate a two-axis fluxgate compass for yaw drift compensation, weighs just four ounces. The electronics were improved and transferred to a circuit board which installs in an expansion slot of a PC. Finally, a variety of improvements to the software were made including the addition of rs-232 host interface capability, more systematic sensor error compensation, and a new demonstration and testing program that runs on a separate PC connected to the tracker through the rs-232 interface.

1.5.3 Calibration and Test Facility

A second new project, which is now well underway, is the design and construction of a facility for calibrating our inertial trackers and evaluating all types of head-trackers. We would like to be able to evaluate the performance of our tracker as it would behave in a real VE system, including the effect of the serial interface. In the testing procedure used to evaluate our first prototype, the testing was performed by the same program running on the same PC that integrates the sensor signals. Therefore, any delays that would result from the interface were not included in our measurements. It was also impossible to measure the performance of other common trackers such as those manufactured by Polhemus, Ascension Technologies, and Shooting Star Technologies, and thereby perform a fair comparative evaluation of our inertial tracker versus other tracking systems.

We set out to design an autonomous system which could meet several needs: (1) testing any type of head tracker by stimulating it with a very well-known mechanical input motion and comparing the tracker output with the known mechanical input; (2) obtaining calibration data for inertial trackers by applying well-known mechanical input motions and recording all the sensor outputs simultaneously; and (3) testing the dynamic performance of a complete virtual environment system by applying mechanical motions to the head-tracker and measuring resulting changes directly from the surface of the visual display using photodiodes. For the first task, it is desirable to provide arbitrary 6 DOF mechanical input motions to identify any nonlinear interactions between the input axes. However, a full 6 DOF rate table was too expensive, so we devised other simpler means for determining the degree of nonlinearity. We designed a mechanical motion stimulus generator that is capable of applying controlled motion to any one of the 6 degrees of freedom at a time. The 6 DOFs comprise three linear translation axes for position and three angular rotation axes for orientation; therefore, one linear motor and one rotary motor, of which one may be operated at any given time, and means for mounting any head tracker in any of three orthogonal orientations on either motor, were deemed sufficient. This equipment is also adequate for the second and third tasks. The motion stimulator package needs to generate significant output up to 15 Hz for both linear and rotational motion, up to 1000 degrees rotation rate; and the

linear and rotary axes must be provided with encoders accurate to 0.01 mm and 0.005 degrees respectively.

1.5.4 Six-Degrees-of-Freedom Inertial Tracker

Investigation has begun into the possibility of augmenting the inertial orientation tracker with triaxial accelerometers to track position as well as orientation. Background reading has been done in the field of strapdown inertial navigation to identify any existing theory that can be applied to the head-tracking problem. A thorough review of the state-of-the-art in accelerometer technologies has also been conducted, including both library research and extensive telephone inquiries. A renewed effort to identify small, more accurate gyros has also been made, because the orientation subsystem in the 6 DOF inertial tracker must be accurate to 1 mrad. Drawings and clay models of the five most promising combinations of sensors have been prepared in order to balance size, cost and performance. A combination has been selected to provide three axes of acceleration and three axes of angular rate with navigation-grade performance in a package of only 1.6 cubic inches and three ounces weight. A hybrid 6-DOF tracking system is currently being designed which uses a Kalman filter to achieve efficient sensor data fusion of the signals from the three rate gyroscopes, three linear accelerometers, and an ultrasonic time-of-flight position triangulation system. When completed, this system will offer the highest resolution-range product ever achieved for a human motion-tracking system.

1.5.5 Publications

Foxlin, E. *Inertial Orientation Tracker Apparatus Having Automatic Drift Compensation for Tracking Human Head and Other Similarly Sized Body.* U.S. Patent Application No. U.S.S.N. 261,364, 1994.

Foxlin, E., and N. Durlach. "An Inertial Head-Orientation Tracker with Automatic Drift Compensation for Use with HMDs." Virtual Reality Software and Technology Conference, Singapore, August 23-26, 1994. In *Proceedings VRST '94*. Eds. G. Singh, S.K. Feiner, and D. Thalmann. Singapore: World Scientific, 1994.

Section 3 Auditory Physiology

Chapter 1 Signal Transmission in the Auditory System

Chapter 1. Signal Transmission in the Auditory System

Academic and Research Staff

Professor Lawrence S. Frishkopf, Professor Nelson Y.S. Kiang, Professor William T. Peake, Professor William M. Siebert, Professor Thomas F. Weiss, Dr. Peter Cariani, Dr. Bertrand Delgutte, Dr. Donald K. Eddington, Dr. Dennis M. Freeman, Dr. John J. Guinan, Jr., Dr. William M. Rabinowitz, Dr. John J. Rosowski, Dr. Christopher A. Shera, Marc A. Zissman

Visiting Scientists and Research Affiliates

Dr. Sunil Puria, Dr. Jay T. Rubinstein,¹ Dr. Devang M. Shah, Joseph Tierney

Graduate Students

C. Cameron Abnet, Alexander J. Aranyosi, C. Quentin Davis, Scott B.C. Dynes, Sridhar Kalluri, Zoher Z. Karu, Christopher J. Long, Martin F. McKinney, Pankaj Oberoi, Lisa F. Shatz, Konstantina Stankovic, Thomas M. Talavage, Su W. Teoh, Susan E. Voss

Technical and Support Staff

Janice L. Balzer, Gregory T. Huang, Michael E. Ravicz, David A. Steffens

1.1 Introduction

Research on the auditory system is carried out in cooperation with two laboratories at the Massachusetts Eye and Ear Infirmary (MEEI). Investigations of signal transmission in the auditory system involve the Eaton-Peabody Laboratory for Auditory Physiology, whose long-term objective is to determine the anatomical structures and physiological mechanisms that underlie vertebrate hearing and to apply this knowledge to clinical problems. Studies of cochlear implants in humans are carried out at the MEEI Cochlear Implant Research Laboratory. Cochlear implants electrically stimulate intracochlear electrodes to elicit patterns of auditory nerve fiber activity that the brain can learn to interpret. The ultimate goal for these devices is to provide speech communication for the profoundly deaf.

1.2 Signal Transmission through the External and Middle Ear

The goal of our work is generate and test physical rules that relate specific external and middle-ear structures to the overall function of the external and middle ear.

1.2.1 Structure-Function Relations in Middle Ears

Sponsor

National Institutes of Health
Grant RO1-DC-00194-11

Project Staff

Dr. John J. Rosowski, Professor William T. Peake, Janice L. Balzer, Greg T. Huang, Michael E. Ravicz, David A. Steffens, Su W. Teoh, Susan E. Voss

The external and middle ear transform environmental sound from airborne atmospheric vibrations to sound pressures and vibrations in the fluid-filled inner ear. This transformation results from the action of specific structures including (1) the funnel-like shape of the external ear tube, (2) the pressure-transformer mechanism of the tympanic membrane and the stapes footplate, and (3) the lever mechanism of the ossicles. The transformation is greatly influenced by the acoustical and mechanical properties of the ear's structures. Our aim last year was to elucidate the function of three important structural features.

¹ Research Affiliate, Massachusetts Eye and Ear Infirmary, Boston, Massachusetts.

The Cochlear Windows

We continued our efforts to test and refine the classic assumption that the cochlea responds to the pressure difference between the cochlear windows within the middle ear. Cats were prepared so that we could independently control the sound pressure magnitudes and angles of stimuli presented to the two windows. Measurements of cochlear responses to these stimuli were analyzed using linear systems theory to determine the common-mode and difference-mode gain of the inner ear. These measurements suggest that the common-mode gain is 20-40 dB smaller than the difference mode gain. This work is included in a master's thesis submitted to the Department of Electrical Engineering and Computer Science on January 20, 1995.²

Middle-Ear Size

We have also investigated the effect of ear size on middle-ear function by examining middle-ear structure and its acoustic function in members of the cat family. Three different kinds of measurements were made: (1) Anatomical measurements of skull and bony ear size were made from more than 100 museum specimens that included 32 of the 36 living species of cat. Middle-ear volume was demonstrated to be proportional to the square of skull length, while the cross-sectional area of bony ear canal and tympanic ring grows as the square-root of skull length. This dichotomy suggests changes in function with animal size. (2) The middle-ear air spaces of a deceased domestic cat and a lion were serially reconstructed from anatomical and CT scanned sections. These data were consistent with the museum data in that while the volume of the lion middle-ear air spaces was nearly 20 times that of the domestic cat, the area of the lion's tympanic membrane is only three times larger. (3) Acoustic measurements of middle-ear function were made in the deceased lion which suggest rules that relate impedance to size in this family. This work is the

subject of a poster at the Association for Research in Otolaryngology meeting.³

Pars Flaccida of the Tympanic Membrane

We are also investigating the contribution of the *pars flaccida* of the tympanic membrane to middle-ear mechanics. The tympanic membrane of many mammals is composed to two parts. The *pars tensa* is stiff and is attached to the ossicles, while the compliant *pars flaccida* is generally small and distant from the ossicular attachment. Most treatments of middle-ear mechanics ignore the *flaccida*. We have investigated the role of *pars flaccida* in the gerbil ear where the *flaccida* takes up about 20 percent of the total membrane area. Measurements of middle-ear input impedance, middle-ear pressure and middle-ear transmission made with normal, stiffened and absent *flaccida* have demonstrated that the *flaccida* has a significant effect on middle-ear mechanics especially at low frequencies. Improved middle-ear models that include *pars flaccida* effects are being investigated. Part of this work is the subject of S.W. Teoh's master's thesis.⁴

1.2.2 Basic and Clinical Studies of Middle-Ear Function

Sponsor

National Institutes of Health
Grant PO1-DC00119 Sub-Project 1
Grant F32-DC00073-3

Project Staff

Dr. John J. Rosowski, Professor William T. Peake, Janice L. Balzer, Dr. Sunil Puria, Michael E. Ravicz, David A. Steffens

We have spent the last year testing and revising our models of human middle-ear function. New model analyses of the effects of middle-ear reconstructive procedures were prepared and published.⁵

² S.E. Voss, *Is the Pressure Difference Between the Oval and Round Window the Effective Acoustic Stimulus to the Inner Ear*, S.M. thesis, Dept. of Electr. Eng. and Comput. Sci., MIT, 1995.

³ J.J. Rosowski, W. T. Peake, G. T. Huang, and D. T. Flandermeier, "Middle-ear Structure and Function in Felidae," *Abstracts of the 18th Midwinter Meeting of the Association for Research in Otolaryngology*, forthcoming.

⁴ S.W. Teoh, "Effects of Pars Flaccida in Middle-Ear Acoustic Transmission", S.M. thesis, Dept. of Electr. Eng. and Comput. Sci., MIT, forthcoming.

These analyses made predictions about the effect of variations in ossicular prosthetic shapes and implantation procedures. The predictions of outcome for one class of surgical procedures (Type IV Tympanoplasty for severely diseased middle ears) were demonstrated to compare well with real surgical cases⁶ and point out the importance of considering the acoustic effects of the surgical procedure on hearing outcome. Empirical tests of the Type IV model were also performed using a cadaveric human temporal-bone preparation. Measurements were made of the stapes motion in a mock Type-IV preparation that allows manipulation of middle-ear volume and tympanic-graft stiffness. The results of these tests were consistent with model predictions.

1.2.3 Publications

Journal Articles

Merchant, S.N., J.J. Rosowski and M.E. Ravicz. "Mechanics of Type IV and V Tympanoplasty. II. Clinical Analysis and Surgical Implications." *Am. J. Otol.* Forthcoming.

Rosowski, J.J., S.N. Merchant and M.E. Ravicz. "Mechanics of Type IV and V Tympanoplasty. I. Model Analysis and Predictions." *Am. J. Otol.* Forthcoming.

Rosowski, J.J. and S.N. Merchant. "Mechanical and Acoustical Analyses of Middle-ear Reconstruction." *Am. J. Otol.* Forthcoming.

Meeting Paper

Rosowski, J.J., W. T. Peake, G. T. Huang and D. T. Flandermeyer. "Middle-ear Structure and Function in Felidae." *Abstracts of the Eighteenth Midwinter Meeting of the Association for Research in Otolaryngology*, St. Petersburg, Florida, February 5-9, 1995. Forthcoming.

Theses

Teoh, S.W. *Effects of Pars Flaccida in Middle-Ear Acoustic Transmission*. M.S. thesis. Dept. of Electr. Eng. and Comput. Sci., MIT. Forthcoming.

Voss, S.E. *Is the Pressure Difference between the Oval and Round Window the Effective Acoustic Stimulus to the Inner Ear*. M.S. thesis. Dept. of Electr. Eng. and Comput. Sci., MIT, 1995.

1.3 Cochlear Mechanisms

Sponsor

National Institutes of Health
Contract P01-DC00119
Grant R01 DC00238

Project Staff

Professor Thomas F. Weiss, Dr. Dennis M. Freeman, Dr. Devang M. Shah, C. Cameron Abnet, Alexander J. Aranyosi, C. Quentin Davis, Zoher Z. Karu, Lisa F. Shatz

Our goal is to study the cochlear mechanisms by which motions of macroscopic structures in the inner ear produce discharges in nerve fibers that innervate the hair cells.

1.3.1 Osmotic Responses of the Tectorial Membrane in the Mouse, Chick, and Alligator Lizard

We completed studies of osmotic responses of the isolated tectorial membrane (TM) in response to changes in bath ion composition in the chick⁷ and the mouse cochlea.⁸ We have also presented a comparative study of the osmotic responses in

⁵ J.J. Rosowski and S.N. Merchant, "Mechanical and Acoustical Analyses of Middle-ear Reconstruction," *Am. J. Otol.*, forthcoming; J.J. Rosowski, S.N. Merchant and M.E. Ravicz, "Mechanics of Type IV and V Tympanoplasty. I. Model Analysis and Predictions," *Am. J. Otol.*, forthcoming.

⁶ S.N. Merchant, J.J. Rosowski and M.E. Ravicz "Mechanics of Type IV and V Tympanoplasty. II. Clinical Analysis and Surgical Implications," *Am. J. Otol.*, forthcoming.

⁷ D.M. Freeman, D.A. Cotanche, F. Ehsani, and T.F. Weiss, "The Osmotic Response of the Isolated Tectorial Membrane of the Chick to Isosmotic Solutions: Effect of Na⁺, K⁺, and Ca²⁺ Concentration," *Hear. Res.* 79: 197-215 (1994).

⁸ D.M. Shah, D.M. Freeman, and T.F. Weiss, "The Osmotic Response of the Unfixed Mouse Tectorial Membrane to Isosmotic Solutions: Effect of Na⁺, K⁺, and Ca²⁺ Concentration," submitted to *Hear. Res.* 1995; D.M. Shah, D.M. Freeman, and T.F. Weiss, "The

three species—mouse, chick, and alligator lizard.⁹ TMs from all three species show qualitatively similar osmotic responses. In all three species, increasing the calcium concentration from the low values typical for endolymph to the higher concentrations found in perilymph causes the TM to shrink reversibly. In all three species, for solutions with low calcium concentrations, the TM swells when isosmotic, high-sodium solutions are substituted for high-potassium solutions. These qualitative similarities suggest that common mechanisms are at work in all three species. However, the magnitudes of osmotic responses of the chick TM are much greater than are those of either the mouse or lizard TM. Furthermore, the spatial pattern of swelling differs across these three species. Osmotic responses for the mouse are primarily changes in thickness with little change in the orthogonal directions. For the chick, radial displacements are often larger than thickness changes. Osmotic responses of the lizard are largely isotropic. These differences in response patterns suggest that there are intrinsic differences in the TMs of these three species. The differences may well be related to differences in ultrastructure and biochemical composition that have been described.

Our measurements of osmotic responses of the tectorial membranes are consistent with simple gel models that are similar to those used to describe other connective tissues. Biochemical studies have shown that the TM contains fixed (nondiffusible), ionizable charge groups that can bind ions differentially. The binding of ions (1) modulates the fixed charge density, (2) changes the concentration of mobile counterions in the tissue, and (3) causes water to flow into or out of the tissue. Thus, the tissue can shrink and swell in response to changes in bath composition, even those that are isosmotic.

In principle, the state of ionization of any of the fixed, ionizable groups in the TM that can bind hydrogen ions will depend upon pH. Thus, we might expect a change in pH to result in shrinking or swelling of the TM. In other connective tissues, it has been possible to infer important properties,

such as the charge density of the fixed charges, from measurements of hydration (shrinking/swelling) as a function of pH. Therefore, we have initiated a study of the effect of pH on the isolated mouse TM. Preliminary results have shown that changes in pH in the range 3-11 cause large, rapid osmotic responses. In general, the TM swells for both low and high pH, but is independent of pH for pH in the range 6-8.

1.3.2 Measurement of Sound-Induced Motion of Cochlear Structures

We have developed a system to measure the sound-induced motion of key structures in the cochlea of the alligator lizard, including the basilar and tectorial membranes, the hair bundles of hair cells, and even individual stereocilia. The capabilities of the system have been examined in preliminary experiments. The basic idea is to obtain images of the receptor organ under stroboscopic illumination synchronized with the hydrodynamic stimulus to the organ. Motion information is calculated from pairs of images obtained at different phases of the motion. The methods for extracting motion estimates from the images are described in a manuscript¹⁰ and preliminary results have been presented.¹¹

1.3.3 Publications

Journal Articles

Davis, C.Q., and D.M. Freeman. "Statistics of Sub-Pixel Motion Estimates Based on Optical Flow." Submitted to *IEEE Trans. Pattern Anal. Mach. Intellig.*

Freeman, D.M., D.A. Cotanche, F. Ehsani, and T.F. Weiss. "The Osmotic Response of the Isolated Tectorial Membrane of the Chick to Isosmotic Solutions: Effect of Na^+ , K^+ , and Ca^{2+} Concentration." *Hear. Res.* 79: 197-215 (1994).

Osmotic Response of the Isolated, Unfixed Mouse Tectorial Membrane: Effect of Na^+ , K^+ , and Ca^{2+} Concentration," presented at the 18th Midwinter Research Meeting of the Association for Research in Otolaryngology, St. Petersburg, Florida, February 5-9, 1995.

⁹ D.M. Freeman and T.F. Weiss, "Species Dependence of Osmotic Responses of the Tectorial Membrane: Implications of Structure and Biochemical Composition," presented at the 18th Midwinter Research Meeting of the Association for Research in Otolaryngology, St. Petersburg, Florida, February 5-9, 1995.

¹⁰ C.Q. Davis and D.M. Freeman, "Statistics of Sub-Pixel Motion Estimates Based on Optical Flow," submitted to *IEEE Trans. Pattern Anal. Mach. Intellig.*

¹¹ C.Q. Davis and D.M. Freeman, "Direct Observations of Sound-Induced Motions of the Reticular Lamina, Tectorial Membrane, Hair Bundles, and Individual Stereocilia," presented at the 18th Midwinter Research Meeting of the Association for Research in Otolaryngology, St. Petersburg, Florida, February 5-9, 1995.

Shah, D.M., D.M. Freeman, and T.F. Weiss. "The Osmotic Response of the Isolated, Unfixed Mouse Tectorial Membrane to Isosmotic Solutions: Effect of Na^+ , K^+ , and Ca^{2+} Concentration." Submitted to *Hear. Res.*

Meeting Papers

Davis, C.Q., and D.M. Freeman. "Direct Observations of Sound-Induced Motions of the Reticular Lamina, Tectorial Membrane, Hair Bundles, and Individual Stereocilia." Presented at the 18th Midwinter Research Meeting of the Association for Research in Otolaryngology, St. Petersburg, Florida, February 5-9, 1995.

Freeman, D.M., and T.F. Weiss. "Species Dependence of Osmotic Responses of the Tectorial Membrane: Implications of Structure and Biochemical Composition." Presented at the 18th Midwinter Research Meeting of the Association for Research in Otolaryngology, St. Petersburg, Florida, February 5-9, 1995.

Shah, D.M., D.M. Freeman, and T.F. Weiss. "The Osmotic Response of the Isolated, Unfixed Mouse Tectorial Membrane: Effect of Na^+ , K^+ , and Ca^{2+} Concentration." Presented at the 18th Midwinter Research Meeting of the Association for Research in Otolaryngology, St. Petersburg, Florida, February 5-9, 1995.

1.4 Stimulus Coding in the Auditory Nerve and Cochlear Nucleus

Sponsor

National Institutes of Health
Grant P01-DC00119
Grant T32-DC00038

Project Staff

Dr. Bertrand Delgutte, Dr. Peter Cariani, Martin F. McKinney

This research investigates neural mechanisms underlying auditory perception at the level of the auditory nerve and cochlear nucleus. In the past year, we have focused on two projects: (1) correlates of the "stretched octave" in interspike intervals of auditory-nerve fibers, and (2) representation of

vowels in the auditory nerve. We have also written a review of models¹² that predict performance in basic psychophysical tasks based on the activity of auditory-nerve fibers.

When listeners are asked to adjust the frequencies of two pure tones so that they sound one octave apart, they choose frequency ratios slightly greater than 2:1. In order to investigate possible correlates of this "octave stretch" phenomenon in the temporal patterns of neural discharges, we recorded the activity of auditory-nerve fibers in anesthetized cats for low-frequency pure-tone stimuli, taking particular care to obtain very precise measurements of spike times. As is well known, interspike intervals for low-frequency (< 4-5 kHz) tones occur approximately at the stimulus period and its multiples. Our results show that the earlier modes of interspike interval histograms (ISIH) actually occur slightly, but systematically later than the times expected from the stimulus period. These mode offsets are consistent with the refractory properties of neurons: they are significant for interspike intervals smaller than 5 msec, and decrease monotonically with increasing length of the interspike interval.

Two models were investigated for their ability to predict an octave stretch based on the offsets of modes of ISIHs. The first model matches modes of the ISIH for the lower-frequency tone with even-ordered modes of the ISIH for the higher-frequency tone. Subjective octave corresponds to the frequency ratio giving the best match. This model predicts no octave stretch because mode offsets depend primarily on the length of the interspike interval regardless of stimulus frequency. The second model scales the time scale of the higher-frequency ISIH by a factor of two before matching its modes with corresponding modes for the lower-frequency ISIH. This model was found to predict an octave stretch consistent with psychophysical data. In particular, the trend of increasing stretch with increasing frequency was correctly predicted. These results provide support for temporal models of pitch perception.

Our research on the auditory representation of vowels is carried out in collaboration with Dr. Tatsuya Hirahara from the NTT Basic Research Laboratory in Tokyo. Dr. Hirahara's psychophysical experiments suggest that the identity of front vowels depends primarily on the amplitude ratio of two harmonics of the fundamental frequency in the vicinity of the first formant. Our experiments aimed at

¹² B. Delgutte, "Physiological Models for Basic Auditory Percepts," in *Auditory Computation*, eds. H. Hawkins and T. McMullen (New York: Springer-Verlag, forthcoming).

determining how these "crucial" harmonics are encoded in both the average discharges rates and the temporal discharge patterns of auditory-nerve fibers. Preliminary results using vowel stimuli with a wide range of fundamental frequencies suggest that profiles of average rates against CF show broad local maxima near the frequencies of the crucial harmonics and that the relative amplitude of these peaks varies in an orderly fashion with formant frequency. These results generally support the concept of crucial harmonics as a possible basis for vowel distinctions and suggest that the auditory nerve may convey more rate-place information than previously thought about voice pitch and vowel identity.

Publications

Cariani, P.A., and B. Delgutte. "Transient Changes in Neural Discharge Patterns may Enhance the Separation of Concurrent Vowels with Different Fundamental Frequencies." *J. Acoust. Soc. Am.* 95: 2842 (1994).

Delgutte, B. "Physiological Models for Basic Auditory Percepts." In *Auditory Computation*. Eds. H. Hawkins and T. McMullen. New York: Springer-Verlag. Forthcoming.

Delgutte, B. "Neural Correlates of Basic Psycho-physical Functions." *Abstracts of the 18th Midwinter Meeting of the Association for Research in Otolaryngology*, St. Petersburg, Florida, February 5-9, 1995.

McKinney, M.F., and B. Delgutte. "Physiological Correlates of the Stretched Octave in Interspike Intervals of Auditory-Nerve Fibers." *Abstracts of the 18th Midwinter Meeting of the Association for Research in Otolaryngology*, St. Petersburg, Florida, February 5-9, 1995.

1.4.1 Binaural Interactions in Auditory Brainstem Neurons

Sponsor

National Institutes of Health
Grant P01-DC00119

Project Staff

Dr. Bertrand Delgutte, Dr. Ruth Y. Litovsky

We are studying neural mechanisms for sound localization in the auditory midbrain in collaboration with Dr. T.C.T. Yin and his colleagues at the University of Wisconsin in Madison. Our specific aim is to determine which of many acoustic cues for sound localization, including interaural time (ITD), interaural level (ILD) differences, and spectral shape, are most important for the directional sensitivity of cells in the central nucleus of the inferior colliculus (IC). We use "virtual-space" (VS) stimuli that use closed acoustic systems to mimic the sound pressure waveforms that are produced in the ear canals for free-field stimuli. VS stimuli are ideally suited for our aims because they are realistic and rich in localization cues, and they provide precise control over each individual cue. We have previously reported that for IC neurons with high characteristic frequencies (> 5 kHz), ILD is generally the most potent cue, followed by spectral shape, and by ITD. In the past year, we wrote a brief report of these findings,¹³ and extended our work in two directions: (1) comparing the response of IC neurons to VS stimuli with responses to simpler stimuli, and (2) investigating the response to stimuli that produce a precedence effect.

Central auditory neurons can be classified into binaural types by comparing their responses to monaural stimuli with responses to binaural stimuli. For example, binaural interactions for IC neurons are classified as being either inhibitory or facilitatory depending on whether the response to binaural stimuli is smaller or larger than the response to the most effective monaural stimulus (usually the contralateral one). We found that binaural interactions measured with VS stimuli were consistent with those determined from responses to broadband noise. The most common type of interaction was mixed, with the ipsilateral ear being inhibitory for ILDs favoring the ipsilateral side, and facilitatory for ILDs favoring the contralateral ear. The effect of such mixed interactions is to enhance the directional sensitivity of IC neurons because the response to stimuli located on the contralateral side is enhanced while the response to ipsilateral stimuli is suppressed. A more quantitative attempt to predict responses to VS stimuli from responses to broadband noise was made by (1) measuring discharge rate versus ILD for broadband noise, and (2) transforming these rate-ILD functions into rate-

¹³ B. Delgutte, P.X. Joris, R.Y. Litovsky, and T.C.T. Yin, "Relative Importance of Different Acoustic Cues to the Directional Sensitivity of Inferior-Colliculus Neurons," in *Advances in Hearing Research*, G.A. Manley, G.M. Klump, C. Kppi, H. Fastl and H. Oeckinghaus, eds., (Singapore: World Scientific, forthcoming).

azimuth functions using head-related transfer functions for frequencies near the CF. Predicted rate-azimuth functions were in good agreement with responses to VS stimuli for about half of the cells tested. We are currently investigating whether predictions can be improved by an appropriate choice of the linear filter representing the frequency selectivity of each neuron.

The precedence effect is an auditory illusion important for accurate sound localization in echoic environment. Drs. Yin and Litovsky have previously reported correlates of the precedence effect in the responses of IC neurons: When two brief binaural stimuli are presented in succession, the response to the lagging stimulus (which simulates an echo) is suppressed for a majority of neurons. Such echo suppression is found for both free-field and dichotic stimuli, and has a time course ranging from 1 msec to 100 msec. Recent pilot experiments show that echo suppression also occurs with VS stimuli, and that the time course of suppression is similar to that observed for free-field and traditional dichotic stimuli. Our data further suggest that echo suppression is largest for leading VS stimuli that produce the largest response, consistent with free-field results. These pilot experiments show the feasibility of using VS stimuli for studying which localization cues are the most important for the precedence effect.

Publications

Delgutte, B., P.X. Joris, R.Y. Litovsky, and T.C.T. Yin. "Relative Importance of Different Acoustic Cues to the Directional Sensitivity of Inferior-Colliculus Neurons." In *Advances in Hearing Research*. Eds. G.A. Manley, G.M. Klump, C. Kpli, H. Fastl and H. Oeckinghaus. Singapore: World Scientific. Forthcoming.

Delgutte, B., P.X. Joris, R.Y. Litovsky, and T.C.T. Yin. "Different Acoustic Cues Contribute to the Directional Sensitivity of Inferior-Colliculus Neurons as Studied with Virtual-Space Stimuli." *Abstr. Assoc. Res. Otolaryngol.* 17: 86 (1994).

1.4.2 Electrical Stimulation of the Auditory Nerve

Sponsor

National Institutes of Health
Contract P01-DC00361

Project Staff

Dr. Bertrand Delgutte, Scott B.C. Dynes

We are studying physiological mechanisms of electrical stimulation of the cochlea in the hope that such information will help design improved speech processing schemes for cochlear implants. During the past year, we have investigated auditory-nerve fiber correlates of interactions observed psychophysically when pulsatile electric stimuli are applied in rapid succession. Specifically, experiments consisted in modifying the state of an auditory-nerve fiber using one or more monophasic current pulses, and then probing the threshold characteristics of this modified state using a single monophasic pulse. The probe pulse is used to measure the threshold and the dynamic range of the neural response for several intervals following the conditioning stimulus.

For single subthreshold cathodic conditioning pulses, the probe threshold was decreased for short (< 600 *sec) probe delays. Following this, the probe threshold increased above its resting threshold about 1 dB for delays between 1 and 4 msec, after which it relaxed to its resting value. For anodic conditioners followed by a cathodic probe, the probe threshold was increased for short probe delays, followed by a short period when the threshold decreased below its resting value. For both anodic and cathodic conditioners, the initial phases are qualitatively consistent with a passive model in which the threshold change is due to a residual charge left by the conditioner on the neural membrane. However, the "overshoot" phases cannot be explained by a first-order passive model. Modeling studies suggest that this behavior can be reproduced using active models of nerve membranes that show large potassium currents (Hodgkin-Huxley, Rothman-Young-Manis) but not by models in which potassium currents are smaller (Frankenhaeuser-Huxley, Chiu et al., Schwarz-Eikhof).

Our results with subthreshold conditioners contrast with those of similar studies in other (nonauditory) systems. These studies show a monotonic relaxation of probe threshold to the resting value, contrary to the multiple-phase effects that we observe. Thus, the auditory nerve may well be specialized in its ability to respond to pulses presented in rapid succession. In support of this interpretation, the most successful model in predicting our data was originally developed for bushy cells in the cochlear nucleus. Bushy cells are thought to be specialized for fine timing. The finding that classic mammalian node models do not predict auditory nerve behavior as well as the bushy-cell model will impact the development of future models of the response of auditory neurons to electrical stimulation.

The relative spread of threshold (RS) is a measure of the variability in the neural threshold. It can also

been considered as a measure of the dynamic range of nerve fibers. Analysis of the RS of auditory-nerve fibers as a function of probe delay shows an increase in the RS for short probe delays for subthreshold conditioners, but not for suprathreshold conditioners. This result means that a subthreshold conditioning pulse effectively increases the dynamic range of the fiber for a brief period of time. This finding may partly explain why cochlear-implant patients show improved speech reception when the pulse rate of continuous-interleaved sampling processors is increased. The increase in the dynamic range may allow a more precise encoding of stimulus intensity and may create a more natural pattern of neural activity than that created by a slower pulse rate.

Publication

Dynes, S.B.C., and B. Delgutte. "Temporal Mechanisms of Auditory-Nerve Fiber Response to Multiple Electric Pulses." *Abstr. Assoc. Res. Otolaryngol.* 17: 163 (1994).

1.5 Interactions of Middle-Ear Muscles and Olivocochlear Efferents

Sponsor

National Institutes of Health
Grant PO1-DC00119

Project Staff

Dr. John J. Guinan, Jr.

Our aim is to determine the actions and interactions of the acoustically elicited middle-ear muscle reflexes and the olivocochlear efferent reflexes.

During the past year, we have continued work to measure and understand the effects of medial efferent-inhibition in the cochlea on sound activation of the middle-ear muscle reflexes. We activate medial efferents by electrical stimulation with an electrode at the midline of the floor of the fourth ventricle and monitor middle-ear-muscle (MEM) acoustic reflexes by measurements of the reflex-induced changes in ear-canal sound pressure level. Our results to date show relatively small changes in

MEM reflex thresholds and level-function growth due to activation of medial efferents. This contrasts with reductions of 20 dB or more in the responses of auditory-nerve fibers with low spontaneous rates (SRs) at sound levels near the MEM reflex threshold and with the same activation of medial efferents. Our results contradict the hypothesis that low-SR fibers activate the MEM reflexes.

1.6 Cochlear Efferent System

Sponsor

National Institutes of Health
Grant RO1-DC00235

Project Staff

Dr. John J. Guinan, Jr., Dr. Christopher A. Shera, Konstantina Stankovic

Our aim is to understand the physiological effects produced by efferents in the mammalian inner ear including medial olivocochlear efferents, which terminate on outer hair cells, and lateral efferents, which terminate on auditory-nerve fibers.

During the past year, two papers were published describing a new class of vestibular primary afferent neurons which respond to sound at moderately high sound levels.¹⁴ These papers show responses of these fibers to clicks and tones, how these responses change with efferent stimulation, and demonstrate that the fibers originate in the saccule.

Tuning curves and other properties of acoustically-responsive vestibular afferents are described in a third paper.¹⁵ Acoustically-responsive vestibular afferents in the cat have broad tuning curves centered at 800 Hz. At their best frequencies (BFs), the minimum thresholds for rate increases are 90 dB SPL or higher. At levels 10-15 dB lower than the rate thresholds, responses of these fibers synchronize to low-frequency tones. There was a slight tendency for fibers with higher BFs to have higher thresholds and wider tuning curves. With two sound sources, one tightly coupled to the skull and one loosely coupled, almost identical tuning curves were obtained. This is consistent with the adequate stimulus for acoustically responsive vestibular afferents being the sound conducted

¹⁴ McCue, M.P., and J.J. Guinan, Jr., "Acoustically-Responsive Fibers in the Vestibular Nerve of the Cat," *J. Neurosci.* 14: 6058-6070 (1994); McCue, M.P., and J.J. Guinan, Jr., "Influence Of Efferent Stimulation On Acoustically-Responsive Vestibular Afferents in the Cat," *J. Neurosci.* 14: 6071-6083 (1994).

¹⁵ McCue, M.P., and J.J. Guinan, Jr., "Spontaneous Activity and Frequency Selectivity of Acoustically Responsive Vestibular Afferents in the Cat," submitted to *J. Neurophysiol.*

through the tympanic membrane and ossicles, rather than vibration from bone conduction. Sensitivity of the saccule to sound has a long phylogenetic history in vertebrates and our data show that this sensitivity is present in the cat.

We also studied the statistical properties of the spontaneous activity of these acoustically responsive vestibular afferents. Acoustically responsive vestibular afferents have spike interval distributions which are similar to those of the irregular vestibular neurons reported by Walsh et al.¹⁶ Also, acoustically responsive vestibular afferents are virtually indistinguishable from the irregular vestibular afferents of Walsh et al. in plots of coefficient of variation versus skew from interval histograms. A detailed examination of the statistical properties of these fibers shows that their firing patterns can be closely modeled by probability density functions from the Erlang family. Although there are many possible explanations for the generation of such functions, one simple one is worth stating: The inter-spike intervals from acoustically responsive vestibular afferents are equivalent to those of a unit which, after it fires becomes unresponsive for about 9 ms, and then at the arrival of the second of two events from a Poisson event generator, it fires again. How this relates to the actual spike generation mechanism is not known. Since there is a strong correlation between threshold and spontaneous rate in cochlear auditory-nerve fibers, we looked for such a correlation in acoustically responsive vestibular afferents. We found no obvious relationship. There was, however, a slight tendency for more irregular fibers to have lower thresholds. These data are described by McCue and Guinan.¹⁵

During the past year, we have completed a project and submitted a paper comparing efferent effects measured by compound action potentials versus by ear-canal distortion products.¹⁷ This work was done so that we could understand the reasons why measurements of efferent responses in humans show lower values than measurements of efferent responses in cats. Efferents were activated by sound in the contralateral ear in cats in which the middle-ear muscles had been cut, or in which middle-ear muscle reflexes were abolished by barbiturate anesthesia. Cochlear mechanical effects were monitored by measuring the distortion product otoacoustic emission (DPOAE) evoked by

two-tone stimuli (frequency: $f_1 < f_2$) in the external ear. Cochlear neural effects were monitored by measuring the compound action potential of the auditory nerve in response to tone pips at the f_2 frequency of the DPOAE measurement. Contralateral sound suppressions of CAPs and DPOAEs were qualitatively similar in all animals, but suppression of CAPs was always as large, or larger, than suppression of DPOAEs. Thus, the reported differences in efferent reflex strength between human work (which used DPOAEs) and animal work (which used CAPs) may arise from inherent differences between the CAP and the DPOAE tests, rather than from a species difference in efferent effects.

During the past year, we have worked on a project to compare efferent-evoked effects on auditory-nerve fibers with different spontaneous rates and to compare the time course of efferent effects. An abstract by Guinan and Stankovic has been submitted describing this work.

1.6.1 Publications

Guinan J.J., Jr., K.M. Stankovic. "Medial Olivocochlear Efferent Inhibition of Auditory-Nerve Firing Mediated by Changes in Endocochlear Potential." *Abstr. Assoc. Res. Otolaryngol.* 18: 172 (1995).

McCue, M.P., and J.J. Guinan, Jr. "Acoustically Responsive Fibers in the Vestibular Nerve of the Cat." *J. Neurosci.* 14: 6058-6070 (1994).

McCue, M.P., and J.J. Guinan, Jr. "Influence Of Efferent Stimulation On Acoustically-Responsive Vestibular Afferents in the Cat." *J. Neurosci.* 14: 6071-6083 (1994).

McCue, M.P., and J.J. Guinan, Jr. "Spontaneous Activity and Frequency Selectivity of Acoustically Responsive Vestibular Afferents in the Cat." Submitted to *J. Neurophysiol.*

Puria, S., J.J. Guinan, Jr., and M.C. Liberman. "Olivocochlear Reflex Assays: Effects of Contralateral Sound on Compound Action Potentials vs. Ear-Canal Distortion Products." Submitted to *J. Acoust. Soc. Am.*

¹⁶ B.T. Walsh, J.G. Miller, R.R. Gacek, and N.Y.S. Kiang, "Spontaneous Activity in the Eighth Cranial Nerve of the Cat," *Intern. J. Neurosci.* 3: 221-236 (1972).

¹⁷ Puria, S., J.J. Guinan, Jr., and M.C. Liberman, "Olivocochlear Reflex Assays: Effects of Contralateral Sound on Compound Action Potentials vs. Ear-Canal Distortion Products," submitted to *J. Acoust. Soc. Am.*

1.7 Cochlear Implants

Sponsor

National Institutes of Health
 Contract PO1-DC00361
 Contract NO1-DC22402

Project Staff

Dr. Donald K. Eddington, Dr. William M. Rabinowitz,
 Dr. Jay T. Rubinstein, Christopher J. Long, Joseph
 Tierney, Marc A. Zissman

Most people who suffer profound hearing impairment have lost the ability to translate the acoustic energy of sound into electrical signals carried to the brain by the auditory nerve. Cochlear implants are electronic devices designed to bypass the external and middle ears and reintroduce these signals by exciting the auditory nerve directly. These devices include a microphone connected to a belt-worn package of electronics (called a sound processor) that translates acoustic signals to electric stimuli. When these stimuli are directed to auditory nerve fibers using an array of electrodes implanted in the deaf patient's cochlea (inner ear), they elicit patterns of nerve activity that the brain interprets as sound.

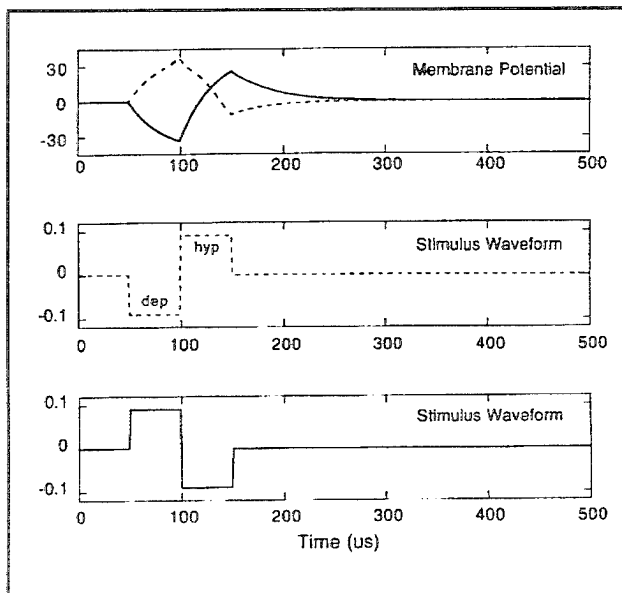


Figure 1. The top panel shows the responses of the membrane potential predicted by a model "nerve fiber" to the two, subthreshold biphasic stimuli ($50 \mu\text{s}/\text{phase}$) plotted in the lower two panels. Each of the 15 nodes of the myelinated axon model consist of a variable, nonlinear conductance (based on the characteristics of voltage dependent sodium channels) and a linear membrane resistance and capacitance. The nodal parameters were derived from measurements in mammal at 37°C and the internodal parameters are from frog (with C_m adjusted to give an appropriate conduction velocity).

Our work is directed at understanding the fundamental mechanisms underlying the sound sensations produced by electrical stimulation of the auditory system and using that information to develop cochlear implant systems that improve speech reception. One of our ongoing efforts is directed at reducing the interference between electrical stimuli that can occur when they are presented close together in time.

In figure 1, the top panel shows the predicted response of a model axon's membrane potential for the two biphasic stimuli ($50 \mu\text{s}/\text{phase}$) plotted in the lower two panels. Note that at $t = 150 \mu\text{s}$, when the biphasic pulses are completed, the membrane potential is nonzero and takes 150 to 200 μs to return to its resting state. Thus, when the cathodic (depolarizing) phase is last, the membrane remains partially depolarized (solid line of top panel) and will tend to reduce the threshold of subsequent stimuli delivered within this "sensitized" period.

This effect is seen in figure 2 where probe threshold (in dB relative to the nonmasked probe threshold) is plotted as a function of the delay between the onset of the subthreshold masker stimulus and the onset of the probe stimulus. In this case, the stimuli are directed to the most apical electrode of a subject's Ineraid electrode array (return electrode in the temporalis muscle) and an adaptive, forced-choice procedure is used to measure psychophysical threshold.

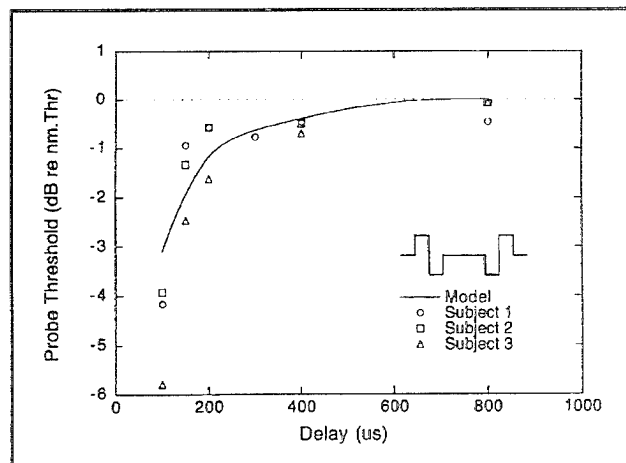


Figure 2. Forward masking results for a subthreshold, anodic-phase-first biphasic masker followed by a cathodic-phase-first, biphasic probe. Probe threshold is plotted in dB relative to the nonmasked threshold and as a function of the delay between the onset of the masker and the onset of the probe. The masker is presented 2 dB below its nonmasked threshold. Subject results are represented by symbols and the model axon predictions by the solid line.

The model and subject data of figure 2 show that the overall influence of the masker is to reduce the probe's threshold. When compared to the dynamic range of electrical stimulation (4 to 20 dB), the maximum threshold shifts of 4 to 6 dB are relatively large, and it is clear that unintended deviations in fiber sensitivity of even 1 dB could have significant perceptual consequences.

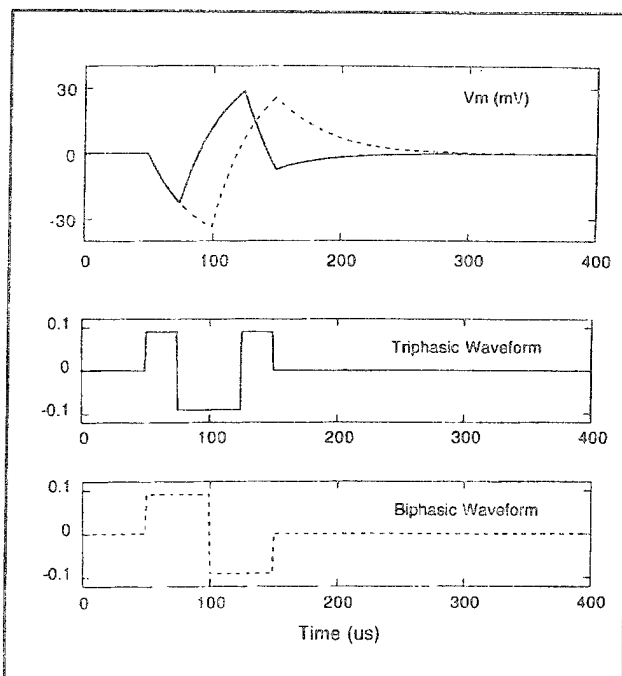


Figure 3. The top panel shows the membrane potential responses predicted by the same model axon of figure 1 to the subthreshold, triphasic and biphasic stimuli plotted in the lower two panels.

One approach to reduce these nonsimultaneous interactions uses triphasic stimulus waveforms. In the top panel of figure 3, the membrane potential of the model axon is plotted for two different waveforms, each presented at levels 2 dB below their respective unmasked thresholds. The broken line shows the model's response to the anodic-first biphasic waveform plotted in the bottom panel and the solid line represents the response to the triphasic waveform shown in the middle panel. Note that at $t = 150 \mu\text{s}$, the predicted deviation from the resting potential is considerably less for the triphasic than for the biphasic waveform. This suggests that a triphasic waveform may reduce the forward masking demonstrated in the results of figure 2.

The results of an initial test of this idea are shown in figure 4 where the effect of the triphasic masker on the probe's threshold is plotted as a function of masker's first phase duration. Although these data are preliminary, they show a significant null in

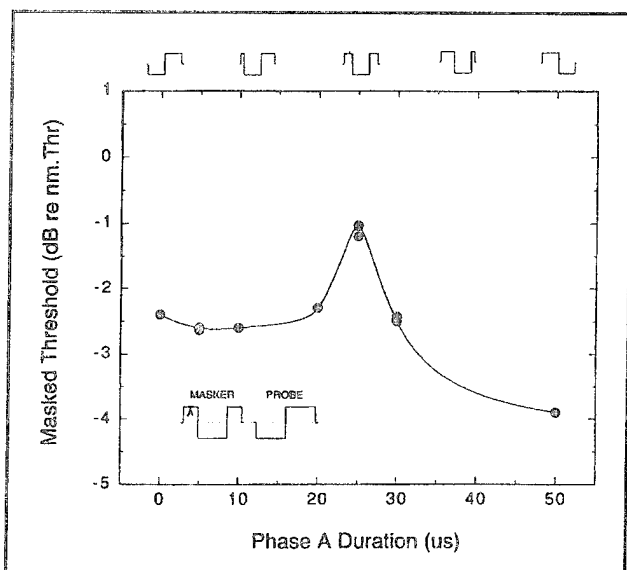


Figure 4. Forward masking results from a single Ineraid subject for the subthreshold, triphasic masker followed by a cathodic-phase-first, biphasic probe ($50 \mu\text{s}/\text{phase}$) shown as an inset in the lower left corner of the figure. The masker was composed of three phases (A,B,C) and constrained as follows: (1) charge-balanced, (2) total duration of $100 \mu\text{s}$, (3) 2nd phase (B) cathodic and $50 \mu\text{s}$ in duration, and (4) level = 2 dB below the unmasked waveform's threshold. Because of these masker constraints, as the duration of the first phase (A) was varied from zero to $50 \mu\text{s}$, the masker waveform changed from a cathodic-first, biphasic stimulus ($A = 0 \mu\text{s}$, $B = C = 50 \mu\text{s}$) to a symmetric triphasic stimulus ($A = C = 25 \mu\text{s}$, $B = 50 \mu\text{s}$) to an anodic-first biphasic stimulus ($A = B = 50 \mu\text{s}$, $C = 0$) as shown by the masker waveforms plotted along the top abscissa of the figure. Probe threshold is plotted in dB relative to the nonmasked threshold and as a function of the duration of the "A" phase of the triphasic masker.

forward masking for the balanced triphasic waveform and suggest that manipulation of the stimulating waveform can substantially reduce distortions caused by these nonsimultaneous interactions.

1.7.1 Publications

Eddington, D.K. "Recent Developments in Sound Processing." British Society of Audiology Annual Conference, Bath, England, September 15-17, 1993.

Eddington, D.K. "Forward Masking During Intracochlear Electrical Stimulation: Models, Physiology and Psychophysics." *J. Acoust. Soc. Am.* 95: 2904 (1994).

Rabinowitz, W.M., and D.K. Eddington. "Effects of Channel-to-Electrode Mappings on Speech

Chapter 1. Signal Transmission in the Auditory System

Reception with the Ineraid Cochlear Implant."
Submitted to *Ear Hear.*

Section 4 Linguistics

Chapter 1 Linguistics

Linguistics is the study of language. It is concerned with the structure of language, how it is used, and how it changes over time. Linguistics is a scientific discipline, and its methods are based on observation and analysis. Linguists use a variety of approaches to study language, including descriptive linguistics, which aims to describe the structure of a language; prescriptive linguistics, which aims to provide rules for the use of a language; and historical linguistics, which studies the development of languages over time.

Language is a complex system of communication that involves the production, transmission, and reception of linguistic signals. These signals can be vocal, written, or signed. Language is used for a wide range of purposes, such as expressing thoughts, emotions, and ideas; conveying information; and maintaining social relationships. Language is also used for practical purposes, such as giving directions, ordering food, and conducting business.

The study of language has many applications in various fields, such as education, psychology, and computer science. In education, linguistics can help teachers understand how children learn language and develop effective teaching strategies. In psychology, linguistics can help researchers understand the relationship between language and thought. In computer science, linguistics can be used to develop natural language processing systems that can understand and generate human language.

There are many sub-fields of linguistics, each focusing on a specific aspect of language. Some of the most well-known sub-fields include phonetics, which studies the physical production of speech sounds; phonology, which studies the abstract patterns of speech sounds; morphology, which studies the structure of words; syntax, which studies the structure of sentences; semantics, which studies the meaning of words and sentences; and pragmatics, which studies the context in which language is used.

In conclusion, linguistics is a fascinating field that explores the intricate details of language. By understanding the structure and function of language, we can gain a deeper appreciation for the complexity of human communication and the importance of language in our daily lives.

Chapter 1. Linguistics

Academic and Research Staff

Professor Morris Halle, Professor Noam A. Chomsky

1.1 Introduction

The work of the Linguistics group is directed towards a better understanding of the mental capacities of human beings through the study of the nature, acquisition and use of language. Language is a uniquely human faculty: only humans appear to be capable of learning and using a language, and every normal human acquires knowledge of one or more languages.

We are trying to understand how this linguistic knowledge is represented in the speaker's mind. The central issues of linguistics research are:

1. What is the nature of linguistic knowledge? What do speakers of a particular language such as Latvian, Spanish or Walpiri know, and how does knowledge of one language resemble or differ from that of another language?
2. How do speakers acquire this knowledge?
3. How do speakers put this knowledge to use in producing and understanding utterances?
4. What are the physiological mechanisms that provide the material basis for storage, acquisition and utilization of linguistic knowledge?

Our ability to answer these questions differs considerably, and our research reflects these differences. At present, we have progressed further with regard to answering the questions posed by item one and have made less progress with item four. Currently, our research is heavily concentrated on issues concerned with the nature of the knowledge that characterizes fluent speakers of various languages. However, we are making a significant effort to solve the other questions also.

We are studying these topics along a number of parallel lines. Linguists have investigated the principles by which words are concatenated to form meaningful sentences. These principles have been the primary domain of inquiry into the disciplines of syntax and semantics. Phonology studies the sound structure of words while morphology examines the manner in which different languages combine different meaning-bearing units (specifically, stems, prefixes, suffixes and infixes) to form

words. The latter topic has attracted increasing interest in recent years and will probably become more prominent in our research efforts in the future.

1.2 Abstracts of Doctoral Dissertations

The following are abstracts of dissertations submitted in 1994 to the Department of Linguistics and Philosophy in partial fulfillment of the requirements for the degree of Doctor of Philosophy in Linguistics.

1.2.1 How Some So-called "Thematic Roles" that Select Animate Arguments are Generated, and How these Roles Inform Control

Seth Aaron Minkoff

Abstract

This thesis presents a theory of how the shape of lexical syntax constrains the generation of those thematic relations that require animacy in the argument to which they are attributed. The thesis also shows how these relations, termed "logophoric roles," licence logophoric dependencies.

First, I show that all logophoric roles are licensed by a single syntactic relation: Given any two coarguments X and Y, a logophoric role can be assigned to X only if X occupies the highest theta-position within some maximal projection, and there is no logophoric role assigned to Y. This finding lends support to a modified version of Hale and Keyser's hypotheses that all thematic relations ultimately reduce to configurations in lexical syntax.

Next, I show that the relations of reflexive-binding and control divide themselves into two classes of dependencies: local and logophoric.

Local reflexive binding holds whenever a binder and reflexive are coarguments of each other. Local control holds whenever a controller and the relevant infinitival clause are attached within the same

maximal projection. I argue that control, properly understood, holds between the controller and the entire infinitival clause. Therefore, I conclude that a single dependency of either kind is local only when it holds between two constituents attached within the same maximal projection.

A logophoric control or (reflexive) binding dependency is one whose acceptability requires the assignment of a logophoric role to its antecedent argument. Since all the dependencies at issue are either local or logophoric, the creation of non-local dependencies effectively "forces" the assignment of a logophoric role. Hence the formulation of locality, with its implicit revision of standard notions of Condition A, accounts for the distribution of dependencies whose antecedents appear to require the assignment of a logophoric role.

Finally, I argue that so-called "backwards binding" dependencies are logophoric, not licensed by the satisfaction of locality (Condition A) at d-structure as other researchers have claimed. There are cases of backwards binding that cannot realistically be held to satisfy locality at d-structure or anywhere else. And moreover, in these cases and all others, the "backwards antecedent" (i.e., binder) displays the hallmark trait of a logophoric dependency, namely the appearance of requiring a logophoric role.

1.2.2 On Economizing the Theory of A-Bar Dependencies

Wei-Tien Tsai

Abstract

This dissertation aims to derive linguistic variations of *wh*-question and syntactic asymmetries among *wh*-expressions from a fairly restricted set of factors under the minimalist approach: (1) binary vs. singulary substitution (i.e., Generalized Transformation vs. Chain formation), (2) noun vs. adverb, and (3) weak vs. strong operator features. Correlations have been established between *wh*-question formation and quantification in terms of the structural height of binders, as well as the magnitude of unselective binding. Chinese, English, Hindi, and Japanese are examined to give a selective but representative spectrum of this correlation.

On empirical grounds, we demonstrate that unselective binding and (A'-)Chain formation are different breeds of construal. It is shown that the asymmetries between unselective binding and long *wh*-movement in general reflect the distinction between binary and singulary substitution.

Our second goal is to relate the (in)definiteness/specifity of nominals to their structural properties. By extending Diesing's (1992) mapping hypothesis, we present a fairly explicit mechanism of mapping syntactic representations to their corresponding logical forms, centering on the notion of syntactic predicate. This move provides us a simple and optimal way to characterize the interaction between predication and quantification. Existential closure is also shown to observe the Greed principle if understood properly, i.e., as an interpretation procedure rather than a syntactic operation. We also explore the possibility of eliminating the lowering mechanism in favor of the copy theory, and initiate an attempt to reduce the stage-individual asymmetries to the distinction between degree and individual variables in the sense of Heim (1987) and Frampton (1990).

Appendices

Appendix A RLE Publications and Papers Presented

Appendix B Current RLE Personnel

Appendix C Milestones

Appendix D RLE Research Support Index

Appendix A. RLE Publications and Papers Presented

The first section of this bibliography includes papers and talks presented by RLE faculty, staff and students during 1994 and is in alphabetical order by conference name. Reprints of these papers may be obtained by contacting the authors directly.

Section 2 includes an alphabetical listing by author of journal articles that were published and accepted or submitted for publication. Book chapters by RLE authors are listed in section 3. Section 4 of this bibliography lists RLE general publications and technical reports, and section 5 is a list of RLE theses submitted during 1994. Theses and technical reports may be ordered from Document Services, MIT Libraries, Room 14-0551, 77 Massachusetts Avenue, Cambridge, Massachusetts 02139-4307; telephone (617) 253-5668; email: docs@mit.edu; fax: (617) 253-1690.

A.1 Meeting Papers

A.1.1 Papers Presented

- Acoustical Society of America Meeting*, Austin, Texas, November 28-December 2, 1994.
- Chen, M.Y. "Baseline Acoustic Parameters for Nasalized Vowels on English and French."
- Liu, S.A. "Landmark Detection for Distinctive Feature-based Speech Recognition."
- Advanced Research Projects Agency Optoelectronics Program Review*, Monterey, California, June 13-17, 1994.
- Villeneuve, P.R., and J.D. Joannopoulos. "The Development of New Periodic Dielectric Material Waveguides for Compact Integrated Optics."
- Advanced Solid-State Lasers Topical Meeting*, Salt Lake City, Utah, February 7-10, 1994.
- Wong, N.C., and D. Lee. "Frequency Tuning and Phase Locking of an Ultrastable Doubly Resonant Optical Parametric Oscillator."
- Advanced Research Projects Agency DS Research Council Summer Conference Workshop on Fundamental Limits to Optoelectronic Devices*, La Jolla, California, July 5, 1994.
- Haus, H.A. "Quantum Limits in Optical Devices."
- Advances in Optical Imaging and Photon Migration Conference*, Orlando, Florida, March 21-23, 1994.
- Hee, M.R., J.A. Izatt, D. Huang, E. Swanson, C.P. Lin, J.S. Schuman, C. Puliafito, and J.G. Fujimoto. "Micron-resolution Optical Coherence Tomography of the Human Eye."
- Izatt, J.A., M.R. Hee, G. Tearney, G.M. Owen, E. Swanson, and J.G. Fujimoto. "Optical Coherence Microscopy."
- American Astronomical Society Meeting*, Washington, DC, January 11-14, 1994.
- Avruch, I.M., S.R. Conner, D.J. Becker, and B.F. Burke. "Low Surface Brightness Structure in the Field of the Gravitational Lens 0957+561." (poster session)
- Ellithorpe, J.D., and J.N. Hewitt. "VLBI Observations of the Gravitational Lens, MG0414+0534."
- American Astronomical Society Meeting*, 184th, Minneapolis, Minnesota, May 29-June 2, 1994.
- Herold, L.K., B.F. Burke, S.R. Conner, and E.J. Gaidos. "Compact Double Radio Sources in the MIT-Green Bank-VLA (MGV) Gravitational Lens Search Sample."
- American Physical Society Meeting*, Pittsburgh, Pennsylvania, March 21-25, 1994
- Cho, K. "STM Tip-Surface Interactions."
- Hui, K., and A.N. Berker. "Analytic Expression for the Exact Boundary of the Superantiferromagnetic Phase of the Ising Model with Nearest- and Next-Nearest-Neighbor Interactions."
- Falicov, A., and A.N. Berker. "Finite-Temperature Phase Diagram of the tJ Model: Renormalization-Group Theory."
- Schapers, T., R.A. Wyss, Q. Hu, M. Krueger, A. Foster, A. van der Hecht, and H. Lueth. "Far-

Appendix A. RLE Publications

- infrared Studies of Planar Resonant Tunneling Field Effect Transistors."
- Verghese, S., R.A. Wyss, T. Schapers, Q. Hu, E.R. Brown, K.A. McIntosh, and M.R. Melloch. "Broad-band Far-infrared Spectroscopy of Mesoscopic Devices."
- Wyss, R.A., C.C. Eugster, J. del Alamo, Q. Hu, M.J. Rooks, and M.R. Melloch. "Far-Infrared Radiation-Induced Thermopower in an Antenna-Coupled Quantum Point Contact."
- Wyss, R.A., Q. Hu, M. Krueger, A. Foerster, A. van der Hart, and H. Lueth. "Far-Infrared Studies of Planar Resonant Tunneling Field Effect Transistors."
- American Physical Society, Division of Atomic, Molecular, and Optical Physics Meeting, Crystal City, Virginia, April 18-22, 1994.*
- Andrews, M.R., D. Pelly, K. Davis, M-O. Mewes, and W. Ketterle. "Improved Design of Neutral Atom Magnetic Traps."
- Hammond, T.D., M.S. Chapman, C.R. Ekstrom, J. Schmiedmayer, and D.E. Pritchard. "Interferometry with Atoms and Molecules."
- American Physical Society, Division of Plasma Physics Meeting, 36th Annual, Minneapolis, Minnesota, November 7-11, 1994.*
- Bers, A., A.K. Ram, C.C. Chow. "Saturation of SRS by Spatiotemporal Chaos in Coupled Langmuir Decay." (poster session)
- Carpignano, F., B. Coppi, and M. Nassi. "Prototypes Construction in the Ignitor Program."
- Migliuolo, S., S. Luckhardt, J. Kesner, F. Paoletti, P. Zolfaghari, S. Bernabei, and M. Ohabayashi. "Prompt Sawtooth Stabilization in Lower Hybrid RF Experiments on PBX-M."
- Nassi, M., F. Carpignano, and B. Coppi. "The Ignitor Project."
- Penn, G., Y.K. Pu, S. Migliuolo, and B. Coppi. "The Isotopic Effect: Particles and Energy."
- Ram, A.K., A. Bers, S.D. Schultz, and V. Fuchs. "Interaction of Ion-Bernstein Waves with Electrons." (poster session)
- Schultz, S.D., A. Bers, and A.K. Ram. "Effect of RF Waves on Bootstrap Current in Tokamaks." (poster session)
- American Society for Mass Spectrometry Conference on Mass Spectrometry, Chicago, Illinois, May 29-June 3, 1994.*
- Bradley, M., F. DiFilippo, V. Natarajan, F. Palmer, and D.E. Pritchard. "Mass Spectrometry At and Below 0.1 Parts Per Billion."
- Applied Superconductivity Conference, Boston, Massachusetts, October 16-21, 1994.*
- de Lange, G., B.R. Jacobson, and Q. Hu. "Micromachined Millimeter-wave SIS Mixers."
- Argonne National Laboratory Physics Division Colloquium, Chicago, Illinois, April 1, 1994.*
- Hewitt, J.N. "Gravitational Lenses and Cosmology."
- Association for Research in Otolaryngology Meeting, 17th Mid-Winter, St. Petersburg, Florida, February 6-10, 1994.*
- Delgutte, B., P.X. Joris, R.Y. Litovsky, and T.C.T. Yin. "Different Acoustic Cues Contribute to the Directional Sensitivity of Inferior-Colliculus Neurons as Studied with Virtual-Space Stimuli."
- Ravicz, M.E., and J.J. Rosowski. "The Effect of Middle-ear Cavity Size on Acoustic Power Flow in the Ear of the Mongolian Gerbil." (poster session)
- Voss, S.E., J.J. Rosowski, and W.T. Peake. "Is the Pressure Difference Between the Oval and Round Windows the Stimulus for Cochlear Responses?" (poster session)
- Association for Research in Vision and Ophthalmology, Annual Meeting, Sarasota, Florida, May 1-6, 1994.*
- Hee, M.R., J.A. Izatt, E.A. Swanson, D. Huang, C.P. Lin, J.S. Schuman, C.A. Puliafito, J. Inderfurth, R. Birngruber, and J.G. Fujimoto. "In Vivo Optical Coherence Tomography of the Anterior Segment."
- Izatt, J.A., M.R. Hee, D. Huang, E.A. Swanson, C.P. Lin, J.S. Schuman, C.A. Puliafito, and J.G. Fujimoto. "High-Speed In Vivo Retinal Imaging with Optical Coherence Tomography."
- Mann, J., D. Edell, J.F. Rizzo, J. Raffel, and J.L. Wyatt, Jr. "Development of a Silicon Retinal Implant: Microelectronic System for Wireless Transmission of Signal and Power."
- Narayanan, M.V., J.F. Rizzo, D. Edell, and J.L. Wyatt, Jr. "Development of a Silicon Retinal Implant: Cortical Evoked Potentials Following Focal Stimulation of the Rabbit Retina with Light and Electricity."

- Wyatt, J.L., Jr., J.F. Rizzo, A. Grumet, D. Edell, and R.J. Jensen. "Development of a Silicon Retinal Implant: Epiretinal Stimulation of Retinal Ganglion Cells in the Rabbit."
- Atmospheric Infrared Spectrometer/Advanced Microwave Sounding Unit Team Meeting*, Washington, DC, May 17-18, 1994.
- Staelin, D.H. "Status Report: MTS, TOGA, COARE, and CAMEX Data."
- Board on Mathematical Sciences National Research Council Symposium on Large-Scale Structures in Acoustics and Electromagnetics*, Washington, DC, September 26-27, 1994.
- Haus, H.A. "Distributed Feedback Resonators."
- California Institute of Technology Colloquium*, Pasadena, California, May 25, 1994.
- Hewitt, J.N. "Gravitational Lenses, Time Delays, and Hubble's Constant."
- Colorado Conference on Iterative Methods*, Breckenridge, Colorado, April 5-9, 1994.
- Kamon, M., and J.R. Phillips. "Preconditioning Techniques for Constrained Vector Potential Integral Equations, with Application to 3-D Magnetoquasistatic Analysis of Electronic Packages."
- White, J., J.R. Phillips, and T. Korsmeyer. "Comparing Precorrected-FFT and Fast Multipole Algorithms for Solving Three-Dimensional Potential Integral Equations."
- Conference on Fundamental Problems in Quantum Mechanics Theory*, Baltimore, Maryland, June 17-21, 1994.
- Pritchard, D.E. "Interferometry with Atoms and Molecules."
- Conference on Motor Speech*, Sedona, Arizona, March 24-27, 1994.
- Perkell, J.S., M. Matthies, and M. Svirskey. "Factors Underlying Findings of Motor Equivalence in the Relation between the Vocal Tract Area Function and the Acoustic Transfer Function."
- Conference on Neural Networks for Computing*, Snowbird, Utah, April 5-8, 1994.
- Wyatt, J.L., Jr., and I.M. Elfadel. "On the Solutions of Oja's Equations." (poster session)
- Wyatt, J.L., Jr., and J. Rizzo. "Steps Toward the Development of a Silicon Retinal Implant to Aid Patients Suffering from Certain Forms of Blindness."
- Conference on Nonlinear Optics: Materials, Fundamentals, and Applications*, Waikoloa, Hawaii, July 25-29, 1994.
- Ippen, E.P., K.R. Tamura, L.E. Nelson, and H.A. Haus. "Ultrashort-pulse Fiber Ring Lasers."
- Shapiro, J.H., and K-X. Sun. "Semiclassical versus Quantum Behavior in Fourth-Order Interference."
- Shapiro, J.H., and L.G. Joneckis. "Enhanced Fiber Squeezing Via Local-Oscillator Pulse Compression."
- Conference on Precision Electromagnetic Measurements*, Boulder, Colorado, June 27-July 1, 1994.
- DiFilippo, F., V. Natarajan, M. Bradley, F. Palmer, S. Rusinkiewicz, and D.E. Pritchard. "Mass Spectrometry at 0.1 Part Per Billion for Fundamental Metrology."
- Conference on Quantum Nonintegrability*, Philadelphia, Pennsylvania, September 8-11, 1994.
- Kleppner, D. "Advances in Periodic Orbit Spectroscopy."
- Conference on Quantum Theory of Real Materials*, Berkeley, California, August 11-15, 1994.
- Joannopoulos, J.D. "Photonic Crystals." (talk)
- CLEO/QELS-Conference on Lasers and Electro-Optics/Quantum Electronics and Laser Science*, Anaheim, California, May 5-13, 1994.
- Adams, L.E., E.S. Kintzer, C.-K. Sun, M. Ramaswamy, J.G. Fujimoto, U. Keller, and M.T. Asom. "Mode Locking of a Broad Area Semiconductor Laser Using a Multiple-Quantum-Well Saturable Absorber."
- Boivin, L., F.X. Kartner, and H.A. Haus. "Quantum Theory of Self-Phase Modulation with Finite Response Time."
- Chapman, M.S. "Atomic and Molecular Interferometry."
- Cheng, T.K., M.S. Dresselhaus, and E.P. Ippen. "Direct Observation of Ultrafast Ionic Screening."
- Doerr, C.R., W.S. Wong, H.A. Haus, and E.P. Ippen. "Additive-Pulse Mode Locking/Limiting Storage Ring."

Appendix A. RLE Publications

- Dougherty, D.J., F.X. Kartner, H.A. Haus, and E.P. Ippen. "Direct Measurement of the Raman Gain Spectrum of Glass Fibers with Femtosecond Pulses."
- Hultgren, C.T., and E.P. Ippen. "Femtosecond Band-edge Index Nonlinearities in Active AlGaAs Waveguides."
- Izatt, J.A., M.R. Hee, G.M. Owen, G. Tearney, E.A. Swanson, and J.G. Fujimoto. "Optical Coherence Microscopy."
- Ketterle, W., K.B. Davis, M.A. Joffe, M-O. Newes, and D.E. Pritchard. "Dark Cold Atoms at High Densities."
- Lee, D., and N.C. Wong. "Tuning Characteristics of a CW Dual-cavity KTP Optical Parametric Oscillator."
- Paye, J., M. Ramaswamy, J.G. Fujimoto, and E.P. Ippen. "How to Measure the Amplitude and Phase of Ultrashort Light Pulses with an Autocorrelator and a Spectrometer."
- Ramaswamy-Paye, M., and J.G. Fujimoto. "Compact Dispersion-Compensating Geometry for Kerr-Lens Modelocked Femtosecond Lasers."
- Shirasaki, M., C.R. Doerr, I. Lyubomirsky, and H.A. Haus. "Harmonically Modelocked Fiber Laser with Hybrid Gain."
- Wong, N.C., D. Lee, and L.R. Brothers. "Optical Frequency Measurement and Synthesis Using Nonlinear Optical Techniques."
- Dagstuhl Workshop on Code Generation*, First, Schloss Dagstuhl, Wadern, Germany, August 29-September 6, 1994.
- Liao, S.Y., S. Devadas, and K. Keutzer. "On Code Size Minimization Using Data Compression Techniques."
- Department of Electrical Engineering Seminar*, Madison, Wisconsin, January 14-18, 1994.
- Beketi, G. "Free Electron Research at MIT."
- Design Automation Conference*, 31st, San Diego, California, June 6-10, 1994.
- Bhagwati, V., and S. Devadas. "Automatic Verification of Pipelined Microprocessors."
- Monteiro, J., S. Devadas, and B. Lin. "A Methodology for Efficient Estimation of Switching Activity in Sequential Logic Circuits."
- Silveira, L.M., I.M. Elfadel, M. Chilukuri, K.S. Kundert, and J.K. White. "An Efficient Approach to Transmission Line Simulation Using Measured or Tabulated S-parameter Data."
- Silveira, L.M., I.M. Elfadel, M. Chilukuri, K.S. Kundert, and J.K. White. "Efficient Frequency-Domain Modeling and Circuit Simulation of Transmission Lines."
- Device Research Conference*, 52nd Annual, Boulder, Colorado, June 20-22, 1994.
- Berthold, G., E. Zanoni, M. Manfredi, M. Pavesi, C. Canali, J.A. del Alamo, and S.R. Bahl. "Electroluminescence and Gate Current Components of InAlAs/InGaAs HFETs."
- Electrical Performance of Electronic Packaging Meeting*, Third, Monterey, California, November 2-4, 1994.
- Chou, M., and J.K. White. "A Multipole-accelerated Boundary-element Approach to Transient Simulations of Three-dimensional Integrated Circuit Interconnect."
- Silveira, L.M., M. Kamon, and J. White. "Direct Computation of Reduced-order Models for Circuit Simulation of 3-D Interconnect Structures."
- Electronic Components and Technology Conference*, Washington, DC, May 1-4, 1994.
- Silveira, L.M., M. Kamon, and J.K. White. "Algorithms for Coupled Transient Simulation of Circuits and Complicated 3-D Packaging."
- European Conference on Computer Vision*, Third, Stockholm, Sweden, May 1994.
- Elfadel, I.M. "On the Convergence of Relaxation Labeling Processes."
- European Physical Society's Conference on Controlled Fusion and Plasma Physics*, 21st, Montpellier, France, June 27-July 1, 1994.
- Ram, A.K., A. Bers, V. Fuchs, and S.D. Schultz. "Current Drive by the Combination of Lower Hybrid and ICRF Waves."
- Ram, A.K., C.C. Chow, and A. Bers. "Saturation of SRS by Spatiotemporal Chaos in Coupled Langmuir Decay."
- European Quantum Electronics Conference*, Fifth, Amsterdam, The Netherlands, August 28-September 2, 1994.
- Fujimoto, J.G., J.A. Izatt, M.R. Hee, B. Bouma, E.A. Swanson, C.P. Lin, and C.A. Puliafito. "Biological Imaging Using Optical Coherence Tomography and Microscopy."

European Science Foundation Study Centre Workshop on Nonlinear Optics and Guided Waves, Edinburgh, Scotland, August 1-20, 1994.

Moores, J.D., W.S. Wong, and H.A. Haus. "Overcoming Limitations to High Bit-Rate Soliton Transmission and Storage."

European Speech Communication Association/IEEE Workshop on Speech Synthesis, Second, New Paltz, New York, September 12-15, 1994.

Wilhelms-Tricarico, R., and J.S. Perkell. "Biomechanical and Physiologically Based Speech Modeling."

Integrated Photonics Research Topical Meeting, San Francisco, California, February 17-19, 1994.

Chen, J.C., and S. Jungling. "Efficient Eigenmode Calculations Using Imaginary-distance Beam Propagation Method."

Ferrera, J., J.N. Damask, V.V. Wong, H.I. Smith, and H.A. Haus. "High-Coherence QWS Gratings for Optoelectronic Devices: Why Spatial-Phase-Locked E-Beam Lithography is Necessary."

International Clinical Phonetics and Linguistics Association Conference and American Speech and Hearing Association Conference, New Orleans, Louisiana, November 13-21, 1994.

Chang, H.-P. "Speech Input for Dysarthric Computer Users."

International Conference on Computer-Aided Design, San Jose, California, November 7-10, 1994.

Alidina, M., J. Monteiro, S. Devadas, A. Ghosh, and M. Papaefthymiou. "Precomputation-Based Sequential Logic Optimization for Low Power."

Lin, B., and S. Devadas. "Synthesis of Hazard-Free Multilevel Logic Under Multiple-Input Changes from Binary Decision Diagrams."

Yun, K., B. Lin, D. Dill, and S. Devadas. "Performance-Driven Synthesis of Asynchronous Controllers."

International Conference on InP and Related Compounds, Santa Barbara, California, March 1994.

Choi, W.Y., V.V. Wong, J.C. Chen, H.I. Smith, and C.G. Fonstad. "Design and Fabrication Using X-ray Lithography of Ridge-Waveguide Distribution Feedback Structures on InP."

International Conference on Laser Applications in Life Sciences, Fifth, Minsk, Belarus, June 28-July 2, 1994.

Fujimoto, J.G., J.A. Izatt, M.R. Hee, B. Bouma, E.A. Swanson, C.P. Lin, and C.A. Puliafito. "Biological Imaging Using Optical Coherence Tomography and Microscopy." (plenary session)

International Conference on Molecular Beam Epitaxy, Eighth, Osaka, Japan, August 29-September 2, 1994.

Fisher, P.A., E. Ho, J.L. House, G.S. Petrich, L.A. Kolodziejewski, J. Walker, and N.M. Johnson. "P- and N-type Doping of ZnSe: Effects of Hydrogen Incorporation."

International Conference on Spoken Language Processing, Yokohama, Japan, September 18-22, 1994.

Johnson, M. "Automatic Context-Sensitive Measurement of the Acoustic Correlates of Distinctive Features at Landmarks."

International Conference on Tactile Aids, Hearing Aids and Cochlear Implants, Third, Miami, Florida, May 2-5, 1994.

Beauregard, G.L., W.M. Rabinowitz, H.Z. Tan, and N.I. Durlach. "Amplitude and Frequency Resolution for Motional Stimulation."

Delhorne, L.A., C.M. Reed, and N.I. Durlach. "Current Results of a Field Study of Tactile Aid Users."

Rabinowitz, W.M., J.M. Bising, C.M. Reed, and L.A. Delhorne. "Tactile and Auditory Measures of Amplitude Modulation Discrimination."

Reed, C.R., S. Bratakos, L.A. Delhorne, and G. Denesvich. "A Comparison of Auditory and Tactile Presentation of a Single-Band Envelope Cue as a Supplement to Speechreading."

Tan, H.Z. "A Study of the Tactual Perception of Motor Input Sequences."

International Conference on VLSI Design, Seventh, Calcutta, India, January 5-8, 1994.

Bamji, C.S., and J. Allen. "GLOVE: A Graph-Based Layout Verifier."

International Geoscience and Remote Sensing Symposium, Pasadena, California, August 8-12, 1994.

Appendix A. RLE Publications

- Cabrera-Mercader, C.R., and D.H. Staelin. "Passive Microwave Humidity Profile Retrievals Using Neural Networks."
- Nghiem, S.V., R. Kwok, S.H. Yueh, J.A. Kong, M.A. Tassoudji, C.C. Hsu, A.J. Gow, and D.K. Perovich. "Polarimetric Backscattering Signatures from Thin Saline Ice Under Controlled Laboratory Conditions."
- Rosenkranz, P.W. "A Rapid Transmittance Algorithm for Microwave Sounding Frequencies."
- Schwartz, M.J., J.W. Barrett, P.W. Fieguth, P.W. Rosenkranz, M.S. Spina, and D.H. Staelin. "Passive Microwave Imagery of a Tropical Storm Near 118 GHz."
- Schwartz, M.J., J.W. Barrett, P.W. Rosenkranz, and D.H. Staelin. "Atmospheric Transmittance Measurements Near 118 GHz."
- Spina, M.S., M.J. Schwartz, D.H. Staelin, and A.J. Gasiewski. "Application of Multilayer Feedforward Neural Networks to Precipitation Cell-Top Altitude Estimation."
- Yang, Y.E., H.T. Ewe, C.C. Hsu, L. Wang, S.E. Shih, K.H. Ding, J.A. Kong, R.T. Shin, H. Nguyen, T. Nguyen, J.Y. Ho, and K. O'Neill. "A GIS-Driven Interactive RAdar Image Simulation Using EMSARS Model."
- International RF Advanced Tokamak Workshop*, Seventh, Boulder, Colorado, April 6-8, 1994.
- Ram, A.K., A. Bers, V. Fuchs, and S. Schultz. "Enhancing Lower Hybrid Current Drive Efficiency with Fast Alfvén Waves and Ion-Bernstein Waves."
- International Scanning Microscopy Conference*, Toronto, Canada, May 7-12, 1994.
- Cho, K., and J.D. Joannopoulos. "Tip-induced Modifications in STM and AFM."
- International Sherwood Fusion Theory Conference*, Dallas, Texas, March 14-16, 1994.
- Coppi, B., L.E. Sugiyama, and M. Greenwald. "Global Thermal Transport and Indications from the Alcator-CM Experiment."
- Detragiache, P., B. Coppi, S. Migliuolo, M. Nassi, and B. Rogers. "Advanced Fusion in ICRF Heated Plasmas."
- Migliuolo, S., B. Coppi, B. Rogers, and L. Zakharov. "Analysis of $m=1$ Mode Stability in D-T Plasmas with Fusion Alpha Particles."
- Ram, A.K., A. Bers, V. Fuchs, and S.D. Schultz. "Enhancing Lower Hybrid Current Drive with ICRF Waves."
- Sugiyama, L.E., and W. Park. "Separation of Plasma Pressure and Magnetic Field Evolution in a Two Fluid $m=1$ Reconnection Process."
- International Symposium on Electron, Ion and Photon Beams*, 38th, New Orleans, Louisiana, May 31-June 3, 1994.
- Burkhardt, M., H.I. Smith, D.A. Antoniadis, T.P. Orlando, M.R. Melloch, K.W. Rhee, and M.C. Peckerar. "Fabrication Using X-ray Nanolithography and Measurement of Coulomb Blockade in a Variable-sized Quantum Dot."
- Hector, S.D., V.V. Wong, H.I. Smith, M.A. McCord, A. Wagner, and K.W. Rhee. "Printability of sub-150 nm Features in X-ray Lithography: Theory and Experiments."
- Mondol, M., H. Li, G. Owen, and H.I. Smith. "Uniform-Stress Tungsten on X-ray Mask Membranes via He-Backside Temperature Homogenization."
- Wong, V.V., J. Ferrera, J. Damask, J. Carter, E. Moon, H.A. Haus, H.I. Smith, and S. Rishton. "Spatial-Phase Locked E-Beam Lithography and X-ray Lithography for Fabricating First-Order Gratings on Rib Waveguides."
- Yang, I.Y., H. Hu, L.T. Su, V.V. Wong, M. Burkhardt, E. Moon, J. Carter, D.A. Antoniadis, H.I. Smith, K.W. Rhee, and W. Chu. "High Performance Self-Aligned Sub-100 nm MOSFETs Using X-ray Lithography."
- International Symposium on Guided-Wave Optoelectronics: Device Characterization, Analysis and Design*, Brooklyn, New York, October 26-28, 1994.
- Chen, J.C., H.A. Haus, J.N. Winn, and J.D. Joannopoulos. "Narrow-band Optical Filters from Photonic Band Gap Gratings."
- Haus, H.A., J.N. Damask, and M.J. Khan. "Distributed Feedback Channel Dropping Filters."
- International Symposium on Integrated Optics Conference on Nanofabrication Technologies and Device Integration*, Lindau, Germany, April 11-15, 1994.
- Damask, J.N., J. Ferrera, V.V. Wong, H.I. Smith, L.A. Kolodziejski, and H.A. Haus. "Limitations and Solutions for the Use of Integrated QWS-DBR Resonators in WDM Applications."

- International Ultrafast Phenomena Conference*, Ninth, Dana Point, California, May 2-6, 1994.
- Bouma, B., A. Gouveia-Neto, J. Russell, R. Sierra, J.A. Izatt, U. Keller, and J.G. Fujimoto. "Passive Modelocking of a Flashlamp Pumped Ti:Al₂O₃ Laser."
- Sun, C.-K., B. Golubovic, H.K. Choi, C.A. Wang, G.D. Sanders, C.J. Stanton, and J.G. Fujimoto. "Femtosecond Spectral Hole Burning in InGaAs/AlGaAs Strained-Layer Single-Quantum-Well Diode Lasers."
- International Union of Radio Science Meeting*, Seattle, Washington, June 20-24, 1994.
- Yang, Y.E., M.A. Tassoudji, H.T. Ewe, J.A. Kong, and G.J. Markey. "Examination of Electromagnetic Interference to Civil Aviation GPS Receivers."
- International Workshop on Low Power Design*, Napa, California, April 24-27, 1994.
- Alidina, M., J.S. Monteiro, S. Devadas, A. Ghosh, and M. Papaefthymiou. "Precomputation-Based Sequential Logic Optimization for Low Power."
- Monteiro, J., S. Devadas, B. Lin, C-Y. Tsui, M. Pedram, and A.M. Despain. "Exact and Approximate Methods of Switching Activity Estimation in Sequential Logic Circuits."
- Tan, C.H., and J. Allen. "Minimization of Power in VLSI Circuits Using Transistor Sizing, Input Ordering, and Statistical Estimation."
- International Workshop on Numerical Modeling of Process and Devices for Integrated Circuits V*, Honolulu, Hawaii, June 5-6, 1994.
- Rahmat, K., J. White, and D.A. Antoniadis. "A Galerkin Method for the Arbitrary Order Expansion in Momentum Space of the Boltzmann Equation Using Spherical Harmonics."
- Yie, H., X. Cai, and J. White. "Analysis of 3-D Micro-Electro-Mechanical Structures. Convergence Properties of Relaxation Versus the Surface-Newton Generalized-Conjugate Residual Algorithm for Self-consistent Electro-mechanical."
- Istanbul Technical University Statistical Physics Days*, Istanbul, Turkey, July 14-15, 1994.
- Falicov, A., and A.N. Berker. "Finite-Temperature Phase Diagram of the tJ Model: Renormalization-Group Theory."
- IEEE Digital Signal Processing Workshop*, Yosemite, California, October 3-5, 1994.
- Lam, W.M., and G.W. Wornell. "Multiscale Synthesis and Analysis of Fractal Renewal Processes."
- IEEE International Conference on Acoustics, Speech, and Signal Processing*, Adelaide, Australia, April 18-23, 1994
- Apostolopoulos, J.G., A. Pfajfer, H.M. Jung, and J.S. Lim. "Position-Dependent Encoding."
- Cheung, S., and P. Monta. "Low-Rate Audio Coder with Hierarchical Filterbanks and Lattice Vector Quantization."
- Elfadel, I.M. "Approximate Covariance Function for Gray-Level Gibbs Random Fields."
- IEEE International Conference on Plasma Science*, 21st, Santa Fe, New Mexico, June 6-8, 1994.
- Bekefi, G., B. Chen, I. Mastovsky, and P. Volpbeyn. "Experimental Studies of a High Gradient RF Accelerating Structure Driven by a 33 GHz Free Electron Laser Amplifier."
- Joint Automatic Target Recognizer Systems and Technology Conference IV and Imaging Understanding Workshop*, Monterey, California, November 14-17, 1994.
- Fung, I., and J.H. Shapiro. "Multiresolution Laser Radar Range Profiling with the Expectation-Maximization Algorithm."
- Lawrence Livermore National Laboratory Colloquium*, Livermore, California, April 8, 1994.
- Hewitt, J.N. "Gravitational Lenses, Time Delays, and Hubble's Constant."
- Materials Research Society*, Spring Meeting, San Francisco, California, April 4-8, 1994.
- Ho, E., P.A. Fisher, J.L. House, C.A. Coronado, G.S. Petrich, L.A. Kolodziejski, M.S. Brandt, and N.M. Johnson. "P- and N-Type Doping of ZnSe Using GSMBE."
- Lu, K., P.A. Fisher, E. Ho, J.L. House, C.A. Coronado, G.S. Petrich, and L.A. Kolodziejski. "GSMBE of ZnSe on (In,Ga)P."
- Micro- and Nano-Engineering Meeting*, Davos, Switzerland, September 26-29, 1994.
- Burkhardt, M., S. Silverman, H.I. Smith, D.A. Antoniadis, K.W. Rhee, and M.C. Peckerar. "Gap Control in the Fabrication of Quantum-Effect Devices Using X-ray Nanolithography."

Appendix A. RLE Publications

- National Center for Integrated Photonics Workshop*, Princeton, New Jersey, July 17-19, 1994.
Ippen, E.P. "Femtosecond Dynamics in Semiconductor Optical Amplifiers."
- National Radio Science Meeting*, Boulder, Colorado, January 5-8, 1994.
Johnson, J.T., J.A. Kong, R.T. Shin, and L. Tsang. "Theory and Experiments in Polarimetric Passive Remote Sensing."
- National Research Council Meeting*, Washington, DC, June 18, 1994.
Joannopoulos, J.J. "Photonic Crystals."
- Neural Information Processing Systems Conference*, Vail, Colorado, December 1994.
Wyatt, J.L., Jr., and I.M. Elfadel. "Time-Domain Solutions of Oja's Equations."
- Neural Prosthesis Workshop*, 25th, Washington, DC, October 20-21, 1994.
Wyatt, J.L., and J.F. Rizzo. "Retinal Implant." (poster session)
- New England Regional Quasar/AGN Meeting*, Fourth, Brandeis University, Waltham, Massachusetts, May 6, 1994.
Hewitt, J.N. "Gravitational Lenses - Observations."
- Optical Fiber Communication Conference*, San Jose, California, February 20-25, 1994.
Damask, J.N., V.V. Wong, J. Ferrera, H.I. Smith, and H.A. Haus. "High-coherence QWS Gratings for Optoelectronic Devices: Why Spatial-phase-locked E-beam Lithography is Necessary."
- Optical Society of America Meeting*, Annual, Dallas, Texas, October 2-7, 1994.
Chapman, M.S., C.R. Ekstrom, J. Schmiedmayer, T.D. Hammond, S. Wehinger, and D.E. Pritchard. "Interferometry with Atoms and Molecules." (talk)
- Chen, J.C., and C. Seo. "Novel Reduction of Losses in Bent Waveguides."
- Davis, K.B., M.-O. Mewes, M.A. Andrews, and W. Ketterle. "Transfer of Laser-Cooled Atoms into a Magnetic Trap."
- Davis, K.B., M.-O. Mewes, P. Yesley, M.A. Joffe, D.E. Pritchard, and W. Ketterle. "A Spin-Flip Zeeman Slower for the Production of Intense Slow Sodium Beams."
- Haus, H.A. "From Classical to Quantum Noise."
- Shapiro, J.H. "An Eclectic Tour of Quantum Optical Communications."
- Tamura, K.R., H.A. Haus, and E.P. Ippen. "Femtosecond Fiber Lasers."
- Plasma Fusion Seminar*, Fusion Research Center, Austin, Texas, March 22, 1994.
Sugiyama, L.E. "Nonlinear Magnetic Reconnection and Two Fluid Models."
- Progress in Electromagnetics Research Symposium*, Noordwijk, the Netherlands, July 11-15, 1994.
Hsu, C.C., J.A. Kong, T. Le Toan, S. Paloscia, and P. Pampaloni. "Microwave Emission and Back-scattering from Crops."
- Scire-Scapuzzpo, F., C.C. Hsu, L. Wang, J.A. Kong, T. Le Toan. "Inversion of Biomass of Pine Forest Using Theoretical Models."
- Tsang, L., Z. Chen, G. Zhang, K.H. Ding, C. Hsu, and J.A. Kong. "Microwave Scattering by Vegetation Based on Wave Approach."
- Radio Astronomy and Geodesy Group Meeting*, Harvard-Smithsonian Center for Astrophysics, Cambridge, Massachusetts, March 5, 1994.
Hewitt, J.N. "Detecting Astronomical Radio Transients."
- Speech Research Symposium*, 14th, Baltimore, Maryland, June 22-23, 1994.
Verbout, S.M. "Signal Enhancement for Automatic Recognition of Noisy Speech."
- Statistical Mechanics Meeting*, 71th, New Brunswick, New Jersey, May 11-13, 1994.
Aalberts, D.P., and A.N. Berker. "Spin-Wave Bound-State Energies from an Ising Model."
- Falicov, A., and A.N. Berker. "A Correlated Random-Chemical-Potential Model for the Phase Transitions of Helium Mixtures in Porous Media."
- Hui, K., and A.N. Berker. "Expression for the Superantiferromagnetic Boundary of the Ising Model with Nearest- and Next-Nearest-Neighbor Interactions on the Square Lattice."
- Steen-Hall Eye Institute Meeting*, Shreveport, Louisiana, January 31-February 1, 1994.

- Wyatt, J.L., Jr. "Retinal Implant Project with Dr. Joseph Rizzo of Massachusetts Eye and Ear Infirmary."
- Symposium on VLSI Technology*, Honolulu, Hawaii, June 7-9, 1994.
- Herrmann, F.P., and C.G. Sodini. "A 256-Element Associative Parallel Processor."
- Hu, H., L.T. Su, I.Y. Yang, D.A. Antoniadis, and H.I. Smith. "Channel and Source/Drain Engineering in High-Performance Sub-0.1 μm NMOSFETs Using X-ray Lithography."
- Synopsis Workshop on Embedded Systems*, Berkeley, California, January 19-25, 1994.
- Devadas, S. "Retargetable Code Generation."
- Joannopoulos, J.D. "Ab-initio Statistical Mechanics."
- SEMATECH Company*, Austin, Texas, February 17, 1994.
- McIlrath, M.B. "SEMATECH Workbench for Integrated Modelling Meeting."
- SEMATECH Company*, Austin, Texas, May 4, 1994.
- Troxel, D.E. "Computer Integrated Manufacturing Application Framework Review."
- SPIE Conference on Laser Beams*, San Diego, California, June 16-24, 1994.
- Bekefi, G., B. Chen, M.E. Conde, I. Mastovsky, K. Ricci, C.J. Taylor, and P. Volfbeyn. "Observations of Frequency Chirping and Phase of a Free Electron Laser Amplifier."
- Catravas, P., W. Hu, C. Chen, I. Mastovsky, and G. Bekefi. "Experimental Studies of the MIT 3.3 GHz Relativistic Klystron Amplifier."
- Larrabee, J. V. Baisley, R. Huffman, R. Meade, and J.D. Joannopoulos. "Detectivity of a UB-B Photodiode."
- Stoner, R., J. Blastos, and G. Bekefi. "Radiation Studies Using the MIT Microwiggler for Free Electron Lasers."
- SPIE International Society for Optical Engineering Conference*, Los Angeles, California, January 22-29, 1994.
- Catravas, P., W. Hu, C. Chen, I. Mastovsky and G. Bekefi. "Studies of the MIT 3.3 GHz Relativistic Klystron Amplifier."
- Chen, C., G. Bekefi, W. Hu, and P. Catravas. "Advanced Two-Stream Relativistic Klystron Amplifier Research."
- Hu, Q., J.H. Smet, and C.G. Fonstad. "Terahertz Lasers Using Quantum-well Structures." (invited talk)
- Hu, Q., R. Gupta, D. Terpstra, G.J. Gerritsma, and H. Rogalia. "Response of High-Tc Ramp-type Josephson Junctions to Near-millimeter-wave Radiation."
- Izatt, J.A., M.R. Hee, D. Huang, E.A. Swanson, C.P. Lin, J.S. Schuman, C.A. Puliafito, and J.G. Fujimoto. "In Vivo Ophthalmic Imaging with Optical Coherence Tomography."
- Jerby, E., and G. Bekefi. "Traveling-Wave Cyclotron Maser Amplifier and Oscillator Experiments."
- Ricci, K., P. Volfbeyn, B. Chen, and G. Bekefi. "Observations of Frequency Chirping and Spatial Phase Variations of a Raman, Free-Electron Laser Amplifier."
- Wong, N.C., D. Lee, and L.R. Brothers. "CW Phase-locked Optical Parametric Oscillator as a Tunable Source for Terahertz Radiation."
- Technologies for Intelligent Vehicle Highways Conference*, Boston, Massachusetts, November 1994.
- Masaki, I. "Vehicle-Based Vision Sensors for Intelligent Highway Systems."
- The Future of Spectroscopy: From Astronomy to Biology Meeting*, Quebec, Canada, September 1994.
- Ketterle, W. "Cooling and Trapping of Neutral Atoms."
- Tokamak Physics Experiment Physics Meeting*, Princeton, New Jersey, September 11-12, 1994.
- Ram, A.K., A. Bers, S. Schultz, and V. Fuchs. "Current Drive Synergism in TPX."
- Towards Teraflop Computing Conference*, Baton Rouge, Louisiana, February 9-12, 1994.
- Cho, K., and J.J. Joannopoulos. "The Enchanting World of Surfaces."
- U.S. Coast Guard Academy Lecture*, New London, Connecticut, February 15, 1994.
- Hewitt, J.N. "Gravitational Lenses: A New Tool for Astrophysicists."

Appendix A. RLE Publications

Ultrafast Phenomena Conference, Dana Point, California, May 2-6, 1994.

Bouma, B., A. Gouveia-Neto, J. Russell, R. Sierra, J.A. Izatt, U. Keller, and J.G. Fujimoto. "Passive Modelocking of a Flashlamp Pumped Ti:Al₂O₃ Laser."

Fujimoto, J.G. "Biological Spectroscopy and Medical Applications." (session)

Sun, C.-K., B. Golubovic, H.K. Choi, C.A. Wang, G.D. Sanders, C.J. Stanton, and J.G. Fujimoto. "Femtosecond Spectral Hole Burning in InGaAs/AlGaAs Strained-Layer Single-Quantum-Well Diode Lasers."

University of California Department of Astronomy Colloquium, Berkeley, California, April 7, 1994.

Hewitt, J.N. "Gravitational Lenses, Time Delays, and Hubble's Constant."

Virtual Reality Software and Technology Meeting, Singapore, August 23-26, 1994.

Foxlin, E., and N. Durlach. "An Inertial Head-Orientation Tracker with Automatic Drift Compensation for Use with HMD's."

Vocal Fold Physiology Conference, Eighth, Kurume, Japan, April 7-9, 1994.

Stevens, K.N., and H.M. Hanson. "Classification of Glottal Vibration from Acoustic Measurements."

Workshop for the Detection of Dark Matter, Berkeley, California, February 20-22, 1994.

Kleppner, D. "Application of Rydberg Atoms to the Detection of Microwave Photons."

Workshop on Quantum Communications and Measurements, Nottingham, United Kingdom, July 11-16, 1994.

Boivin, L., C.R. Doerr, K. Bergman, and H.A. Haus. "Quantum Noise Reduction Using a Nonlinear Sagnac Loop with Positive Dispersion."

Workshop on Quantum Field Theory of Cold Atoms, Boulder, Colorado, July 25-29, 1994.

Davis, K.B., M-O. Mewes, M.A. Joffe, and W. Ketterle. "Evaporative Cooling of Sodium Atoms."

Workshop on Singularities In Patterns and Collapse, Cork, Ireland, August 21-26, 1994.

Bouma, B., and J.G. Fujimoto. "Nonlinear Propagation Effects in Ultrashort Pulse Generation."

A.1.2 Published Meeting Papers

Bers, A. "Simple Physics of LH K_{||} Upshift Due to Density Gradient Along B₀" *Proceedings of the U.S.-Japan Workshop on RF Heating and Current Drive*, MIT Plasma Fusion Center, Cambridge, Massachusetts, November 15-17, 1994.

Berthold, G., M. Mastrapasqua, C. Canali, M. Manfredi, E. Zanoni, S.R. Bahl, and J.A. del Alamo. "Electron and Hole Real Space Transfer in InAlAs/InGaAs Heterostructure Device." *Proceedings of the 24th European Solid State Device Research Conference*, Edinburgh, Scotland, September 11-15, 1994.

Bhagwati, V., and S. Devadas. "Automatic Verification of Pipelined Microprocessors." *Proceedings of the 31st Design Automation Conference*, San Diego, California, June 1994.

Boning, D.S., and M.B. McIlrath. "Conceptual Graphs and Manufacturing Processes." *Proceedings of the Second International Conference on Conceptual Structures*, College Park, Maryland, August 15, 1994.

DiFilippo, F., V. Natarajan, M. Bradley, F. Palmer, and D.E. Pritchard. "Accurate Atomic Mass Measurements from Penning Trap Mass Comparisons of Individual Ions." *Proceedings of the Fourteenth International Conference on Atomic Physics*, Boulder, Colorado, July 31-August 5, 1994.

Elfadel, I.M. "Lyaponov Functions for Rotor Neural Networks." *Proceedings of the American Control Conference (ACC '94)*, Baltimore, Maryland, June 1994.

Fisher, P.A., E. Ho, G.S. Petrich, L.A. Kolodziejski, M.S. Brandt, and N.M. Johnson. "N- and P-Type Doping of ZnSe Using Gas Source Molecular Beam Epitaxy." *Proceedings of the Material Research Society Symposium*, San Francisco, California, March 1994.

Kleppner, D. "Quantum Chaos and Laser Spectroscopy." *Proceedings of the Enrico Fermi International School of Physics*, Varenna, Italy, June 2-12, 1993.

- Masaki, I., S. Decker, A. Gupta, B.K.P. Horn, H.-S. Lee, D.A. Martin, C.G. Sodini, J.K. White, and J.L. Wyatt, Jr. "Cost-Effective Vision Systems for Intelligent Vehicles." *Proceedings of the IEEE International Intelligent Vehicles Symposium*, Paris, France, October 1994.
- Monteiro, J., J. Kukula, S. Devadas, and H. Neto. "Bitwise Encoding of Finite State Machines." *Proceedings of the 7th International Conference on VLSI Design*, Calcutta, India, January 1994.
- Monteiro, J., S. Devadas, and B. Lin. "A Methodology for Efficient Estimation of Switching Activity in Sequential Circuits." *Proceedings of the 31st Design Automation Conference*, San Diego, California, June 1994.
- Oppenheim, A.V., S.H. Nawab, G.C. Verghese, and G.W. Wornell. "Algorithms for Signal Processing." *Proceedings of the First Annual Rapid Prototyping of Application Specific Signal Processors Conference*, Arlington, Virginia, August 15-18, 1994.
- Polley, M.O., S.J. Wee, and W.F. Schreiber. "Hybrid Channel Coding for Multiresolution HDTV Terrestrial Broadcasting." *Proceedings of the IEEE International Conference on Image Processing*, Austin, Texas, November 1994.
- Pritchard, D.E., M.S. Chapman, C.R. Ekstrom, T.D. Hammond, J. Schmiedmayer, A. Lenef, R. Rubenstein, and S. Wehinger. "Interferometry with Atoms and Molecules." *Proceedings of the New York Academy of Sciences*, Baltimore, Maryland, June 18-22, 1994.
- Ram, A.K., A. Bers, V. Fuchs, and S.D. Schultz. "Heating and Current Drive by Mode-Converted Ion-Bernstein Waves." *Proceedings of the U.S.-Japan Workshop on RF Heating and Current Drive*, MIT Plasma Fusion Center, Cambridge, Massachusetts, November 15-17, 1994.
- Ram, A.K., A. Bers, V. Fuchs, and S.D. Schultz. "Enhanced Current Drive with Lower-Hybrid and Ion-Bernstein Waves." *Proceedings of the 15th International Atomic Energy Agency Conference on Plasma Physics and Controlled Nuclear Fusion*, Seville, Spain, September 26-October 1, 1994.
- Schattenburg, M.L., R.J. Aucoin, R.C. Fleming, I. Plotnick, J. Porter, and H.I. Smith. "Fabrication of High Energy X-ray Transmission Gratings for AXAF." *SPIE Proceedings 2280, EUV, X-ray and Gamma-Ray Instrumentation for Astronomy V*, San Diego, California, July 24-29, 1994.
- Silveira, L.M., M. Kamon, and J. White. "Direct Computation of Reduced-Order Models for Circuit Simulation of 3-D Interconnect Structures." *Proceedings of the 3rd Topical Meeting on Electrical Performance of Electronic Packaging*, Monterey, California, November 1994.
- Stevens, K.N., C.A. Bickley, and D.R. Williams. "Control of a Klatt Synthesizer by Articulatory Parameters." *Proceedings of the International Conference on Spoken Language Processing*, Yokohama, Japan, September 18-22, 1994.
- Tan, H.Z., M.A. Srinivasan, B. Eberman, and B. Cheng. "Human Factors for the Design of Force-Reflecting Haptic Interfaces." *Proc. ASME: Dynamic Systems and Control*. Ed. C.J. Radcliffe. Vol. 55-1, pp. 353-359.
- van der Zant, H.S.J., T.P. Orlando, S. Watanabe, and S.H. Strogatz. "Vortex Propagation in Discrete Josephson Rings." *Proceedings of the ICTP Workshop on Quantum Dynamics of Submicron Structures*, Trieste, Italy, June 13-July 1, 1994.
- Wee, S.J., M.O. Polley, and W.F. Schreiber. "A Scalable Source Coder for a Hybrid Transmission HDTV System." *Proceedings of the IEEE International Conference on Image Processing*, Austin, Texas, November 1994.
- Wilhelms-Tricarico, R., and J.S. Perkell. "Biomechanical and Physiologically Based Speech Modeling." *Proceedings of the Second European Speech Communication Association/IEEE Workshop on Speech Synthesis*, New Paltz, New York, September 12-15, 1994.
- Yang, Y.E., H.T. Ewe, C.C. Hsu, L. Wang, S.E. Shih, K.H. Ding, J.A. Kong, R.T. Shin, H. Nguyen, T. Nguyen, J.Y. Ho, and K. O'Neill. "A GIS-Driven Interactive Radar Image Simulation Using EMSARS Model." *IEEE Proc. IGARSS '94*.

A.2 Journal Articles

A.2.1 Published Journal Articles

- Abernathy, D.L., S. Song, K.I. Blum, R.J. Birgeneau, and S.G.J. Mochrie. "Chiral Melting of the Si(113) Reconstruction." *Phys. Rev. B* 49: 2691 (1994).
- Alidina, M., J. Monteiro, S. Devadas, A. Ghosh, and M. Papaefthymiou. "Precomputation-Based Sequential Logic Optimization for Low Power." *IEEE Trans. VLSI Syst.* 2(4): 426-436 (1994).
- Altshuler, B.L., L.S. Levitov, and A.Y. Yakovets. "Non-equilibrium Noise in a Mesoscopic Conductor: Microscopic Analysis." *JETP Lett.* 59: 857 (1994).
- Arias, T.A., and J.D. Joannopoulos. "Electron Trapping and Impurity Segregation Without Defects: Ab initio Study of Perfectly Rebonded Grain Boundaries." *Phys. Rev. B* 49(7): 4525-4531 (1994).
- Arias, T.A., and J.D. Joannopoulos. "Ab Initio Theory of Dislocation Interactions: From Close-Range Spontaneous Annihilation to the Long-Range Continuum Limit." *Phys. Rev. Lett.* 73(5): 680-683 (1994).
- Au, W.C., J.A. Kong, and L. Tsang. "Absorption Enhancement of Scattering of Electromagnetic Waves by Dielectric Cylinder Clusters." *Microwave Opt. Tech. Lett.* 7(10): 454-457 (1994).
- Bahl, S.R., and J.A. del Alamo. "Physics of Breakdown in InAlAs/n-InGaAs Heterostructure Field-Effect Transistors." *IEEE Trans. Electron Dev.* 41(12): 2268-2275 (1994).
- Bekefi, G., B. Chen, M.E. Conde, I. Mastovsky, K. Ricci, C.J. Taylor, and P. Volfbeyn. "Observations of Frequency Chirping and Phase of a Free Electron Laser Amplifier." *Nucl. Instrum. Methods Phys. Res. A* 341: 119-123 (1994).
- Bergman, K., H.A. Haus, E.P. Ippen, and M. Shirasaki. "Squeezing in a Fiber Interferometer with a Gigahertz Pump." *Opt. Lett.* 19(4): 290-292 (1994).
- Berman, D., H.S.J. van der Zant, T.P. Orlando, and K.A. Delin. "Discrete Superconducting Vortex Flow Transistors." *IEEE Trans. Appl. Superconduct.* 4: 161-168 (1994).
- Bers, A., A.K. Ram, and C.C. Chow. "Saturation of SRS by Spatiotemporal Chaos in Coupled Langmuir Decay." *Bull. Am. Phys. Soc.* 39: 1754 (1994).
- Bock, R.D., J.R. Phillips, H.S.J. van der Zant, and T.P. Orlando. "Influence of Induced Magnetic Fields on the Static Properties of One-Dimensional Parallel Josephson-junction Arrays." *Phys. Rev. B* 49: 10009-10012 (1994).
- Boivin, L., F.X. Kartner, and H.A. Haus. "Analytical Solution to the Quantum Field Theory of Self-Phase Modulation with a Finite Response Time." *Phys. Rev. Lett.* 73(2): 240-243 (1994).
- Bouma, B., A. Gouveia-Neto, J.A. Izatt, J. Russell, R. Sierra, U. Keller, and J.G. Fujimoto. "Hybrid Mode-locking of a Flash-lamp-pumped Ti:Al₂O₃ Laser." *Opt. Lett.* 19(22): 1858-1860 (1994).
- Bouma, B., A. Gouveia-Neto, J.A. Izatt, J. Russell, R. Sierra, U. Keller, and J.G. Fujimoto. "Hybrid Mode Locking of a Flash-lamp-pumped Ti:Al₂O₃ Laser." *Opt. Lett.* 19(22): 1858-1860 (1994).
- Bounds, J.K., and H.A. Haus. "Quantum Noise of Raman Amplification." *Quantum Opt.* 6: 79-85 (1994).
- Bozler, C.O., C.T. Harris, S. Rabe, D.D. Rathman, W.D. Goodhue, M.A. Hollis, and H.I. Smith. "Arrays of Gated Field-Smitter Cones Having 0.32 μm Tip-to-Tip Spacings." *J. Vac. Sci. Technol. B* 12: 629-632 (1994).
- Brommer, K., M. Clavan, A. Dal Pino, and J.D. Joannopoulos. "Theory of Adsorption of Atoms and Molecules on Si(111)-(7x7)." *Surf. Sci.* 314: 57 (1994).
- Brothers, L.R., D. Lee, and N.C. Wong. "Terahertz Optical Frequency Comb Generation and Phase Locking of an Optical Parametric Oscillator at 665 GHz." *Opt. Lett.* 19(4): 245-247 (1994).
- Burkhardt, M., H.I. Smith, D.A. Antoniadis, T.P. Orlando, M.R. Melloch, K.W. Rhee, and M.C. Peckerar. "Fabrication Using X-ray Nanolithography and Measurement of Coulomb Blockade in a Variable-Sized Quantum Dot." *J. Vac. Sci. Technol. B* 12(6): 3611-3613 (1994).
- Capaz, R.B., A. Dal Pino, Jr., and J.D. Joannopoulos. "Identification of the Migration Path of Interstitial Carbon in Silicon." *Phys. Rev. B* 50(11): 7439-7442 (1994).

- Cariani, P.A., and B. Delgutte. "Transient Changes in Neural Discharge Patterns May Enhance the Separation of Concurrent Vowels with Different Fundamental Frequencies." *J. Acoust. Soc. Am.* 95: 2842 (1994).
- Coppi, B., and the Ignitor Project Group. "Highlights of the Ignitor Project Group." *J. Fusion Energy* 13(2/3): 111-119 (1994).
- Coronado, C.A., E. Ho, P.A. Fisher, J.L. House, K. Lu, G.S. Petrich, and L.A. Kolodziejski. "Gas Source Molecular Beam Epitaxy of ZnSe and ZnSe:N." *J. Electron. Mater.* 23: 269-274 (1994).
- Courtney, M., H. Jiao, N. Spellmeyer, and D. Kleppner. "Long-Period Orbits in the Stark Spectrum of Lithium." *Phys. Rev. Lett.* 73(10): 1340-1343 (1994).
- Delgutte, B., P.X. Joris, R.Y. Litovsky, and T.C.T. Yin. "Different Acoustic Cues Contribute to the Directional Sensitivity of Inferior-Colliculus Neurons as Studied with Virtual-Space Stimuli." *Abstr. Assoc. Res. Otolaryngol.* 17: 86 (1994).
- Devadas, S., K. Keutzer, S. Malik, and A. Wang. "Event Suppression: Improving the Efficiency of Timing Simulation for Synchronous Digital Circuits." *IEEE Trans. Comput.-Aided Des.* 13(6): 814-822 (1994).
- Devadas, S., K. Keutzer, S. Malik, and A. Wang. "Certified Timing Verification and the Transition Delay of a Circuit." *IEEE Trans. VLSI Syst.* 2(3): 333-342 (1994).
- Devadas, S., K. Keutzer, S. Malik, and A. Wang. "Verification of Asynchronous Interface Circuits with Bounded Wire Delays." *J. VLSI Sig. Process.* 7(1): 161-182 (1994).
- Devenyi, A., K. Cho, T.A. Arias, and J.D. Joannopoulos. "Adaptive Riemannian Metric for All-Electron Calculations." *Phys. Rev. B* 49(19):13 373-13 376 (1994).
- DiFilippo, F., V. Natarajan, K.R. Boyce, and D.E. Pritchard. "Accurate Atomic Masses for Fundamental Metrology." *Phys. Rev. Lett.* 73(11): 1481-1484 (1994).
- Doerr, C.R., F.I. Khatri, and M. Shirasaki. "Simulation of Pulsed Squeezing in Optical Fiber with Chromatic Dispersion." *J. Opt. Soc. Am. B* 11(1): 143-149 (1994).
- Doerr, C.R., H.A. Haus, and E.P. Ippen. "Asynchronous Soliton Mode Locking." *Opt. Lett.* 19(23): 1958-1960 (1994).
- Doerr, C.R., H.A. Haus, E.P. Ippen, M. Shirasaki, and K. Tamura. "Additive-pulse Limiting." *Opt. Lett.* 19(1): 33-36 (1994).
- Doerr, C.R., K. Tamura, M. Shirasaki, H.A. Haus, and E.P. Ippen. "Orthogonal Polarization Fiber Gyroscope with Increased Stability and Resolution." *Appl. Opt.* 33(34): 8062-8068 (1994).
- Doerr, C.R., M. Shirasaki, and F.I. Khatri. "Simulation of Pulsed Squeezing in Optical Fiber with Chromatic Dispersion." *J. Opt. Soc. Am. B* 11(1): 143-149 (1994).
- Doerr, C.R., W.S. Wong, H.A. Haus, and E.P. Ippen. "Additive-Pulse Mode Locking/Limiting Storage Ring." *Opt. Lett.* 19(21): 1747-1749 (1994).
- Dynes, S.B.C., and B. Delgutte. "Temporal Mechanisms of Auditory-Nerve Fiber Response to Multiple Electric Pulses." *Abstr. Assoc. Res. Otolaryngol.* 17: 163 (1994).
- Eddington, D.K. "Forward Masking During Intracochlear Electrical Stimulation: Models, Physiology and Psychophysics." *J. Acoust. Soc. Am.* 95: 2904 (1994).
- Elfadel, I.M., and R.W. Picard. "Gibbs Random Fields, Co-Occurrences, and Texture Modeling." *IEEE Trans. Pattern Anal. Mach. Intell.* 16(1): 24-37 (1994).
- Ellithorpe, J.D., and J.N. Hewitt. "VLBI Observations of the Gravitational Lens MG0414+0543." *Bull. Am. Astron. Soc.* 25: 1409 (1994).
- Fan, S., P.R. Villeneuve, R.D. Meade, and J.D. Joannopoulos. "Design of Three-Dimensional Photonic Crystals at Submicron Lengthscales." *Appl. Phys. Lett.* 65(11): 1466-1468 (1994).
- Fieguth, P.W., and D.H. Staelin. "High-accuracy Profiler That Uses Depth From Focus." *Appl. Opt.* 33(4): 686-689 (1994).
- Fletcher, A., S.R. Conner, and B.F. Burke. "First Results from 8.4 GHz VLA Imaging of 1800 Southern Sky Parkes-MIT-NRAO (PMN) Radio Sources." *Bull. Am. Astron. Soc.* 26: 1503 (1994).
- Foxman, E.P., U. Meirav, P.L. McEuen, M.A. Kastner, O. Klein, P.A. Belk, D.M. Abusch, and

- S.J. Wind. "Crossover from Single-Level to Multilevel Transport in Artificial Atoms." *Phys. Rev. B* 50: 14193 (1994).
- Freeman, D.M., D.A. Cotanche, F. Ehsani, and T.F. Weiss. "The Osmotic Response of the Isolated Tectorial Membrane of the Chick to Isosmotic Solutions: Effect of Na^+ , K^+ , and Ca^{2+} Concentration." *Hear. Res.* 79: 197-215 (1994).
- Fuchs, V., S.D. Schultz, A.K. Ram, A. Bers, and C.N. Lashmore-Davies. "Mode Conversion of the Fast Alfvén Wave in a Tokamak at the Ion-Ion Hybrid Frequency." *Bull. Am. Phys. Soc.* 39: 1627 (1994).
- Giles, M.D., D.S. Boning, G.R. Chin, W.C. Dietrich, M.S. Karasick, M.E. Law, P.K. Mozumder, L.R. Nackman, V.T. Rajan, D.M.H. Walker, R.H. Wang, and A.S. Wong. "Semiconductor Wafer Representation for TCAD." *IEEE Trans. Comput.-Aided Des.* 13(1): 82 (1994).
- Grant, K.W., L.D. Braida, and R.J. Renn. "Auditory Supplements to Speechreading: Combining Amplitude Envelope Cues from Different Spectral Regions of Speech." *J. Acoust. Soc. Am.* 95: 1065-1073 (1994).
- Green, T.J., Jr., and J.H. Shapiro. "Detecting Objects in Three-Dimensional Laser Radar Range Images." *Opt. Eng.* 33(3): 865-874 (1994).
- Gu, Q., M.A. Tassoudji, S.Y. Poh, R.T. Shin, and J.A. Kong. "Coupled Noise Analysis for Adjacent Vias in Multilayered Digital Circuits." *IEEE Trans. Circuits Syst.* 41(12): 796-804 (1994).
- Guo, J.Z.Y., G.K. Celler, J.R. Maldonado, and S.D. Hector. "Wavelength Dependence of Exposure Window and Resist Profile in X-ray Lithography." *J. Vac. Sci. Technol. B* 12: 4044-4050 (1994).
- Gupta, R., Q. Hu, D. Terpstra, G.J. Gerritsma, and H. Rogalla. "A Noise Study of a High-T_c Josephson Junction under Near-millimeter-wave Irradiation." *Appl. Phys. Lett.* 64(7): 927-929 (1994).
- Hall, K.L., G. Lenz, A.M. Darwish, and E.P. Ippen. "Subpicosecond Gain and Index Nonlinearities in InGaAsP Diode Lasers." *Opt. Commun.* 111: 589-612 (1994).
- Hara, Y., R.G. Atkins, S.H. Yueh, R.T. Shin, and J.A. Kong. "Application of Neural Networks to Radar Image Classification." *IEEE Trans. Geosci. Remote Sensing* 32(1): 100-109 (1994).
- Haus, H.A., E.P. Ippen, and K. Tamura. "Additive-Pulse Modelocking in Fiber Lasers." *IEEE J. Quantum Electron.* 30(1): 200-208 (1994).
- Hector, S.D., H.I. Smith, N. Gupta, M.L. Schattenburg. "Optimizing Synchrotron-based X-ray Lithography for 0.1 μm Lithography." *Microelectron. Eng.* 23: 203-206 (1994).
- Hector, S.D., V.V. Wong, H.I. Smith, M.A. McCord, and K.W. Rhee. "Printability of Sub-150 nm Features in X-ray Lithography: Theory and Experiments." *J. Vac. Sci. Technol. B* 12(6): 3965-3969 (1994).
- Hemmer, P.R., M.S. Shahriar, M.K. Kim, K.Z. Cheng, and J. Kierstead. "Time Domain Optical Data Storage Using Raman Coherent Population Trapping." *Opt. Lett.* 19: 296 (1994).
- Ho, E., P.A. Fisher, J.L. House, G.S. Petrich, and L.A. Kolodziejksi. "The Doping of ZnSe Using Gas Source Molecular Beam Epitaxy." *SPIE Proc.* 2346: 61-69 (1994).
- Holmberg, E., J.S. Perkell, R. Hillman, and C. Gress. "Individual Variation in Measures of Voice." *Phonetica* 51(1-3): 30-37 (1994).
- Holmberg, E., R. Hillman, J.S. Perkell, and C. Gress. "Relationships Between Intra-speaker Variation in Aerodynamic Measures of Voice Production and Variation in SPL Across Repeated Recordings." *J. Speech Hear. Res.* 37: 484-495 (1994).
- Hsu, C.C., H.C. Han, R.T. Shin, J.A. Kong, A. Beaudoin, and T. Le Toan. "Radiative Transfer Theory for Polarimetric Remote Sensing of Pine Forest." *J. Remote Sensing* 15(14): 2943-2954 (1994).
- Hu, H., J.B. Jacobs, J.E. Chung, and D.A. Antoniadis. "The Correlation Between Gate Current and Substrate Current in 0.1 μm NMOSFETs." *IEEE Electron Dev. Lett.* 11: 418 (1994).
- Izatt, J.A., M.R. Hee, D. Huang, J.G. Fujimoto, E.A. Swanson, C.P. Lin, J.S. Schuman, C.A. Puliafito. "Optical Coherence Tomography for Medical Diagnostics." *SPIE Proceed.* IS11: 450-472 (1994).
- Izatt, J.A., M.R. Hee, E.A. Swanson, C.P. Lin, D. Huang, J.S. Schuman, C.A. Puliafito, and J.G. Fujimoto. "Micrometer-Scale Resolution Imaging of the Anterior Eye In Vivo with Optical

- Coherence Tomography." *Arch. Oph.* 112:1584-1589 (1994).
- Izatt, J.A., M.R. Hee, G.M. Owen, E.A. Swanson, and J.G. Fujimoto. "Optical Coherence Microscopy in Scattering Media." *Opt. Lett.* 19(8): 590-592 (1994).
- Jerby, E., G. Bekefi, and A. Shahadi. "Observation of Chirping in a Traveling-Wave Cyclotron Maser Experiment." *Nucl. Inst. Meth.* A341: 115-118 (1994).
- Johnson, J., J.A. Kong, R.T. Shin, S.H. Yueh, S.V. Nghiem, and R. Kwok. "Polarimetric Thermal Emission from Rough Ocean Surfaces." *J. Electromag. Waves Appl.* 8(1): 43-59 (1994).
- Jose, J.V., G. Ramirez-Santiago, and H.S.J. van der Zant. "Critical Exponents of Frustrated Josephson-junction Arrays." *Physica B* 194-196: 1671-1672 (1994).
- Jungling, S., and J.C. Chen. "A Study and Optimization of Eigenmode Calculations Using the Imaginary-Distance Beam-Propagation Method." *IEEE J. Quantum Electron.* 30(9): 2098-2105 (1994).
- Kamon, M., M.J. Tsuk, and J.K. White. "FASTHENRY: A Multipole-Accelerated 3-D Inductance Extraction Program." *IEEE Trans. Microwave Theory Tech.* 42(9): 1750-1758 (1994).
- Kartner, F.X., D. Dougherty, H.A. Haus, and E.P. Ippen. "Raman Noise and Soliton Squeezing" *J. Opt. Soc. Am. B* 11(7): 1267-1276 (1994).
- Kartner, F.X., D. Dougherty, H.A. Haus, and E.P. Ippen. "Raman Noise and Soliton Squeezing." *J. Opt. Soc. Am. B* 11(7): 1267-1276 (1994).
- Khatri, F.I., G. Lenz, J.D. Moores, H.A. Haus, and E.P. Ippen. "Extension of Coupled-cavity Additive Pulse Mode-locked Laser Theory." *Opt. Commun.* 110: 131-136 (1994).
- Knecht, W.G. "Nonlinear Noise Filtering and Beamforming Using the Perceptron and Its Volterra Approximation." *IEEE Trans. Speech Audio Process.* 2(1): 55-62 (1994).
- Kuo, C.C., D.H. Staelin, and P.W. Rosenkranz. "Statistical Iterative Scheme for Estimating Atmospheric Relative Humidity Profiles." *IEEE Trans. Geosci. Remote Sens.* 32(2): 254-260 (1994).
- Lane, H., J. Wozniak, and J.S. Perkell. "Changes in Voice-Onset Time in Speakers with Cochlear Implants." *J. Acoust. Soc. Am.* 96(1): 56-64 (1994).
- Lee, C.F., B.J. McCartin, R.T. Shin, and J.A. Kong. "A Triangular-Grid Finite-Difference Time-Domain Method for Electromagnetic Scattering Problems." *J. Electromag. Waves Appl.* 8(4): 449-470 (1994).
- Lee, L.H., T.P. Orlando, and W.G. Lyons. "Current Distribution in Superconducting Thin-Film Strips." *IEEE Trans. Appl. Superconductivity* 4(1): 41-44 (1994).
- Lemay, D.G., and L.D. Braida. "Band Envelope Speechreading Supplements Derived From Noisy Speech." *J. Acoust. Soc. Am.* 95: 3014 (1994).
- Lim, J.S. "A Migration Path to a Better Digital Television System." *SMPTE J.* January (1994).
- Linden, D.S., T.P. Orlando, and W.G. Lyons. "Modified Two-Fluid Model for Superconductor Surface Impedance Calculation." *IEEE Trans. Appl. Superconduct.* 4: 136 (1994).
- Lu, K., J.L. House, P.A. Fisher, C.A. Coronado, E. Ho, G.S. Petrich, and L.A. Kolodziejski. "(In,Ga)P Buffer Layers for ZnSe-Based Visible Emitters." *J. Cryst. Growth* 138: 1-7 (1994).
- Lu, K., P.A. Fisher, E. Ho, J.L. House, G.S. Petrich, L.A. Kolodziejski, G.C. Hua, and N. Otsuka. "Gas Source Molecular Beam Epitaxy Growth of ZnSe on (In,Ga)P." *Mat. Res. Soc. Symp. Proc.* 340: 497-502 (1994).
- Lu, K., P.A. Fisher, J.L. House, E. Ho, C.A. Coronado, G.S. Petrich, L.A. Kolodziejski, G.-C. Hua, and N. Otsuka. "Gas Source Molecular Beam Epitaxy Growth of ZnSe on Novel Buffer Layers." *J. Vac. Sci. Tech. B* 12(2): 1153-1155 (1994).
- Lynch, T.J. III, W.T. Peake, and J.J. Rosowski. "Measurements of the Acoustic Input Impedance of Cat Ears: 10 Hz to 20 kHz." *J. Acoust. Soc. Am.* 96(4): 2184-2209 (1994).
- Matthies, M.L., M.A. Svirsky, H.L. Lane, and J.S. Perkell. "A Preliminary Study of the Effects of Cochlear Implants on the Production of Sibilants." *J. Acoust. Soc. Am.* 96(3): 1367-1373 (1994).

Appendix A. RLE Publications

- Matveev, K.A. "Change Fluctuations Under the Coulomb Blockade Conditions." *Physica B* 203: 404 (1994).
- McCue, M.P., and J.J. Guinan, Jr. "Influence of Efferent Stimulation on Acoustically-Responsive Vestibular Afferents in the Cat." *J. Neurosci.* 14: 6071-6083 (1994).
- McCue, M.P., and J.J. Guinan, Jr. "Acoustically-Responsive Fibers in the Vestibular Nerve of the Cat." *J. Neurosci.* 14: 6058-6070 (1994).
- Meade, R.D., A. Devenyi, J.D. Joannopoulos, O.L. Alerhand, D.A. Smith, and K. Kash. "Novel Applications of Photonic Band Gap Materials: Low-loss Bends and High Q Cavities." *J. Appl. Phys.* 75(9): 4753-4755 (1994).
- Mondol, M.K., H. Li, G. Owen, and H.I. Smith. "Uniform-Stress Tungsten on X-ray Mask Membranes via He-Backside Temperature Homogenization." *J. Vac. Sci. Technol. B* 12(6): 4024-4027 (1994).
- Moolji, A.A., S.R. Bahl, and J.A. del Alamo. "Impact Ionization in InAlAs/InGaAs HFET's." *IEEE Electron Dev. Lett.* 15(8): 313-315 (1994).
- Moores, J.D., W.S. Wong, and H.A. Haus. "Stability and Timing Maintenance in Soliton Transmission and Storage Rings." *Opt. Comm.* 113: 153-175 (1994).
- Mucciolo, E., R. Capas, B. Altshuler, and J.D. Joannopoulos. "Manifestation of Quantum Chaos in Electronic Band Structures." *Phys. Rev. B* 50: 8254 (1994).
- Nuttall, W.J., D.Y. Noh, B.O. Wells, and R.J. Birgeneau. "Synchrotron X-ray Scattering Study of the Pressure Melting of Near-monolayer Xenon on Single Crystal Graphite at 140K." *Surf. Sci.* 307-309: 768 (1994).
- Oppenheim, A.V., E. Weinstein, K.C. Zangi, M. Feder, and D. Gauger. "Single-Sensor Active Noise Cancellation." *IEEE Trans. Speech Audio Process.* 2(2): 285-290 (1994).
- Payton, K.L., R.M. Uchanski, and L.D. Braida. "Intelligibility of Conversational and Clear Speech in Noise and Reverberation for Listeners with Normal and Impaired Hearing." *J. Acoust. Soc. Am.* 95(3): 1581-1592 (1994).
- Perkell, J.S., R.E. Hillman, and E.B. Holmberg. "Group Differences in Measures of Voice Production and Revised Values of Maximum Airflow Declination Rate." *J. Acoust. Soc. Am.* 96(2): 695-698 (1994).
- Phillips, J.R., H.S.J. van der Zant, and T.P. Orlando. "Dynamics of Row-switched States in Josephson-junction Arrays." *Phys. Rev. B* 50: 9380-9386 (1994).
- Phillips, J.R., H.S.J. van der Zant, and T.P. Orlando. "Numerical Study of Self-field Effects on Dynamics of Josephson-junction Arrays." *Physica B* 194-196: 1777-1779 (1994).
- Phillips, J.R., H.S.J. van der Zant, J. White, and T.P. Orlando. "Influence of Induced Magnetic Fields on Shapiro Steps in Josephson-junction Arrays." *Phys. Rev. B* 50: 9387-9396 (1994).
- Preisig, J.C. "A Minmax Approach to Adaptive Matched Field Processing in an Uncertain Propagation Environment." *IEEE Trans. Signal Process.* 42(6): 1305-1316 (1994).
- Prigodin, V.N., B.L. Altshuler, K.B. Efetev, and S. Lida. "Mesoscopic Dynamical Echo in Quantum Dots." *Phys. Rev. Lett.* 72: 546 (1994).
- Ram, A.K., A. Bers, S.D. Schultz, and V. Fuchs. "Interaction of Ion-Bernstein Waves with Electrons." *Bull. Am. Phys. Soc.* 39: 1626 (1994).
- Ramaswamy-Paye, M., and J.G. Fujimoto. "Compact Dispersion-Compensating Geometry for Kerr-Lens Modellocked Femtosecond Lasers." *Opt. Lett.* 19(21): 1756-1758 (1994).
- Schmiedmayer, J., C.R. Ekstrom, M.S. Chapman, T.D. Hammond, S. Wehinger, and D.E. Pritchard. "Magnetic Coherences in Atom Interferometry." *J. Phys. II (France)* 4: 2029 (1994).
- Schultz, S.D., A. Bers, and A.K. Ram. "Effect of RF Waves on Bootstrap Current in Tokamaks." *Bull. Am. Phys. Soc.* 39: 1625 (1994).
- Sekiyyama, K. "Differences in Auditory-Visual Speech Perception Between Japanese and Americans." *J. Acoust. Soc. Japan E* 15: 143-158 (1994).
- Shapiro, J.H., and K-X. Sun. "Semiclassical Versus Quantum Behavior in Fourth-Order Interference." *J. Opt. Soc. Am. B* 11(6): 1130-1141 (1994).
- Shattuck-Hufnagel, S., M. Ostendorf, and K. Ross. "Stress Shift and Early Pitch Accent Placement in Lexical Items in American English." *J. Phon.* 22: 357-388 (1994).

- Shirasaki, M., I. Lyubomirski, and H.A. Haus. "Noise Analysis of Mach-Zehnder Squeezer for Nonclassical Input State." *J. Opt. Soc. Am. B* 11(5): 857-863 (1994).
- Singer, A.C., G.W. Wornell, and A.V. Oppenheim. "Nonlinear Autoregressive Modeling and Estimation in the Presence of Noise." *Digit. Signal Process.* 4: 207-221 (1994).
- Smet, J.H., L.H. Peng, Y. Hirayama, and C.G. Fonstad. "Electron Intersubband Transitions to 0.8 eV (1.55 μ m) in InGaAlAs/AlAs Single Quantum Wells." *Appl. Phys. Lett.* 64: 986-987 (1994).
- Smith, H.I. "Microlithography." *Encycl. Appl. Phys.* 10: 281-295 (1994).
- Song, S., and S.G.J. Mochrie. "Tricriticality in the Orientational Phase Diagram of Stepped Si(113) Surfaces." *Phys. Rev. Lett.* 73(7): 995-998 (1994).
- Sperry, E., R. Hillman, and J.S. Perkell. "Use of Inductance Plethysmography to Assess Respiratory Function in a Patient with Vocal Nodules." *J. Med. Speech-Language Path.* 2: 137-145 (1994).
- Sun, C.-K., F. Vallee, L.H. Acioli, E.P. Ippen, and J.G. Fujimoto. "Femtosecond-tunable Measurement of Electron Thermalization in Gold." *Phys. Rev. B* 50(20): 337-348 (1994).
- Tamura, K., C.R. Doerr, H.A. Haus, and E.P. Ippen. "Soliton Fiber Ring Laser Stabilization and Tuning with a Broad Intracavity Filter." *IEEE Photonic Technol. Lett.* 6(6): 697-699 (1994).
- Tamura, K., C.R. Doerr, L.E. Nelson, H.A. Haus, and E.P. Ippen. "Technique for Obtaining High-energy Ultrashort Pulses from an Additive-pulse Mode-locked Erbium-doped Fiber Ring Laser." *Opt. Lett.* 19(1): 46-48 (1994).
- Tamura, K., L.E. Nelson, H.A. Haus, and E.P. Ippen. "Soliton Versus Non-soliton Operation of Fiber Ring Lasers." *Appl. Phys. Lett.* 64(2): 149-151 (1994).
- Tasker, N.J., J.J. Condon, A.E. Wright, and M.R. Griffith. "The Parkes-MIT-NRAO (PMN) Surveys: V. Maps for the Tropical Survey (covering -29 degrees < gamma < 9 degrees)." *Astron. J.* 107: 2115 (1994).
- Uchanski, R.M., L.A. Delhorne, A.K. Dix, L.D. Braida, C.M. Reed, and N.I. Durlach. "Automatic Speech Recognition to Aid the Hearing Impaired. Prospects for the Automatic Generation of Cued Speech." *J. Rehabil. Res. Dev.* 31: 20-41 (1994).
- Van Aelten, F., J. Allen, and S. Devadas. "Event-Based Verification of Synchronous Globally Controlled Logic Designs Against Signal Flow Graphs." *IEEE Trans. Comput.-Aided Des.* 1(1): 122-134 (1994).
- van der Zant, H.S.J., and T.P. Orlando. "Eck Peak in Underdamped Discrete Superconducting Vortex Flow Devices." *J. Appl. Phys.* 76: 7606-7612 (1994).
- van der Zant, H.S.J., D. Berman, T.P. Orlando, and K.A. Delin. "Fiske Modes in One-Dimensional Parallel Josephson-junction Arrays." *Phys. Rev. B* 49: 12945-12952 (1994).
- van der Zant, H.S.J., K.A. Delin, R.D. Bock, D. Berman, and T.P. Orlando. "Resonance Modes in One-dimensional Parallel Arrays of Josephson-junctions." *Physica B* 194-196: 1779-1780 (1994).
- van der Zant, H.S.J., M.N. Webster, J. Romijn, and J.E. Mooij. "Vortices in Two-dimensional Superconducting Weakly Coupled Wire Networks." *Phys. Rev. B* 50: 340-350 (1994).
- van der Zant, H.S.J., R.A.M. Receveur, T.P. Orlando, and A.W. Kleinsasser. "One-dimensional Parallel Josephson-junctions Arrays as a Tool for Diagnostics." *Appl. Phys. Lett.* 65: 2102-2104 (1994).
- van der Zant, H.S.J., T.P. Orlando, S. Watanabe, and S.H. Strogatz. "Vortices Trapped in Discrete Josephson Rings." *Physica B* 203: 490-496 (1994).
- Volfbeyn, P., K. Ricci, B. Chen, and G. Beketi. "Measurement of the Temporal and Spatial Phase Variations of a Pulsed Free Electron Laser Amplifier." *IEEE Trans. Plasma Sci.* 22(5): 659-665 (1994).
- Weinstein, E., A.V. Oppenheim, M. Feder, and J.R. Buck. "Iterative and Sequential Algorithms for Multisensor Signal Enhancement." *IEEE Trans. Signal Process.* 42(4): 846-859 (1994).
- Weinstein, E., M. Feder, and A.V. Oppenheim. "Multi-Channel Signal Separation by Decorre-

- lation." *IEEE Trans. Speech Audio Process.* 1(4): 405-413 (1994).
- Winn, J., R. Meade, and J.D. Joannopoulos. "Two Dimensional Photonic Band Gap Materials." *J. Opt.* 41: 257-273 (1994).
- Wong, V.V., J. Ferrera, J.N. Damask, J.M. Carter, E.E. Moon, H.A. Haus, H.I. Smith, and S. Rishton. "Spatial-Phase-Locked E-Beam Lithography and X-ray Lithography for Fabricating First-Order Gratings on Rib Waveguides." *J. Vac. Sci. Technol. B* 12(6): 3741-3745 (1994).
- Wright, A.E., M.R. Griffith, B.F. Burke, and R.D. Ekers. "The Parkes-MIT-NRAO (PMN) Surveys: II. Source Catalog for the Southern Survey (covering -87.5 degrees < S < -37 degrees)." *Astron. J. Suppl.* 90: 179-295 (1994).
- Wright, A.E., M.R. Griffith, B.F. Burke, and R.D. Ekers. "The Parkes-MIT-NRAO (PMN) Surveys: III. Source Catalog for the Tropical Survey (covering -29 degrees < S < -9.5 degrees)." *Astron. J. Suppl.* 91: 111-308 (1994).
- Xia, J.J., A.K. Jordan, and J.A. Kong. "Electromagnetic Inverse Scattering Theory for Inhomogeneous Dielectric: the Local Reflection Model." *Opt. Soc. Am. A* 11(3): 1081-1086 (1994).
- Xia, J.J., T.M. Habashy, and J.A. Kong. "Profile Inversion in a Cylindrically Stratified Lossy Medium." *Radio Sci.* 29(4): 113-114 (1994).
- Yang, I.Y., H. Hu, L.T. Su, V.V. Wong, M. Burkhardt, E.E. Moon, J.M. Carter, D.A. Antoniadis, H.I. Smith, K.W. Rhee, and W. Chu. "High Performance Self-Aligned Sub-100 nm MOSFETs Using X-ray Lithography." *J. Vac. Sci. Technol. B* 12(6): 4051-4054 (1994).
- Yang, Y.E., H.T. Ewe, C.C. Hsu, L. Wang, S.E. Shih, K.H. Ding, J.A. Kong, R.T. Shin, H. Nguyen, T. Nguyen, J.Y. Ho, and K. O'Neill. "A GIS-Driven Interactive Radar Image Simulation Using EMSARS Model." *IEEE Proc. IGARSS '94* 857-859 (1994).
- Yueh, S.H., R. Kwok, F.K. Li, S.V. Nghiem, W.J. Wilson, and J.A. Kong. "Polarimetric Passive Remote Sensing of Ocean Wind Vectors." *Radio Sci.* 29(4): 799-814 (1994).
- Yueh, S.H., S.V. Nghiem, R. Kwok, W.J. Wilson, F.K. Li, J.T. Johnson, and J.A. Kong. "Polarimetric Thermal Emission from Periodic Water Surfaces." *Radio Sci.* 29(1): 87-96 (1994).
- ### A.2.2 Journal Articles Accepted for Publication
- Bergman, K., H.A. Haus, E.P. Ippen, and M. Shirasaki. "Squeezing in a Fiber Interferometer with a GHz Pump." *Opt. Lett.*
- Besing, J.M., C.M. Reed, and N.I. Durlach. "A Comparison of Auditory and Tactual Presentation of a Single-band Envelope Cue as a Supplement to Speechreading." *Seminars Hear.*
- Brothers, L.R., D. Lee, and N.C. Wong. "Terahertz Optical Frequency Comb Generation and Phase Locking of an Optical Parametric Oscillator at 665 GHz." *Opt. Lett.*
- Burkhardt, M., S. Silverman, H.I. Smith, D.A. Antoniadis, K.W. Rhee, and M.C. Peckerar. "Gap Control in the Fabrication of Quantum-Effect Devices Using X-ray Nanolithography." *J. Microelectron. Eng.*
- Cabrera-Mercader, C.R., and D.H. Staelin. "Application of Multilayer Feedforward Neural Networks to Precipitation Cell-top Altitude Estimation." *IEEE Trans. Geosci. Rem. Sens.*
- Cabrera-Mercader, C.R., and D.H. Staelin. "Passive Microwave Relative Humidity Retrievals Using Feedforward Neural Networks." *IEEE Trans. Geosci. Rem. Sens.*
- Chapman, M.S., C.R. Ekstrom, T.D. Hammond, R. Rubenstein, J. Schmiedmayer, S. Wehinger, and D.E. Pritchard. "Optics and Interferometry with Molecules." *Phys. Rev. Lett.*
- Chen, G.H., C.S. Kochanek, and J.N. Hewitt. "The Mass Distribution of the Lens Galaxy in MG1131+0456." *Astrophys. J.*
- Chen, M. "Acoustic Parameters of Nasalized Vowels in Hearing-impaired and Normal-hearing Speakers." *J. Acoust. Soc. Am.*
- Coppi, B. "Astrophysical and Laboratory Experiments and Theories on High Energy Plasmas." *Plasma Phys. Controlled Fusion.*
- Courtney, M., and D. Kleppner. "Core-Induced Chaos in Diamagnetic Lithium." *Phys. Rev. A.*
- Courtney, M., H. Jiao, N. Spellmeyer, and D. Kleppner. "Quantum Chaos and Rydberg Atoms in Strong Fields." *Drexel Conf. Proc.*

- Courtney, M., H. Jiao, N. Spellmeyer, D. Kleppner, J. Gao, and J.B. Delos. "Closed Orbit Bifurcations in Continuum Stark Spectra." *Phys. Rev. Lett.*
- Courtney, M., N. Spellmeyer, H. Jiao, and D. Kleppner. "Classical, Semiclassical, and Quantum Dynamics in the Lithium Stark System." *Phys. Rev. A*.
- Davis, C.Q., and D.M. Freeman. "Statistics of Sub-Pixel Motion Estimates Based on Optical Flow." *IEEE Trans. Pattern Anal. Mach. Intellig.*
- Davis, K.B., M.-O. Mewes, M.A. Joffe, M.R. Andrews, and W. Ketterle. "Evaporative Cooling of Sodium Atoms." *Phys. Rev. Lett.*
- de Lange, G., B.R. Jacobson, and Q. Hu. "Micro-machined Millimeter-wave SIS Mixers." *IEEE Trans. Appl. Superconduct.*
- DiFilippo, F., V. Natarajan, M. Bradley, F. Palmer, and D.E. Pritchard. "Accurate Atomic Mass Measurements from Penning Trap Mass Comparisons of Individual Ions." *Phys. Scr.*
- Dilley, L., S. Shattuck-Hufnagel, and M. Ostendorf. "Glottalization of Vowel-Initial Syllables as a Function of Prosodic Structure." *J. Phon.*
- Duchnowski, P., and P.M. Zurek. "Villchur Revisited: Another Look at AGC Simulation of Recruiting Hearing Loss." *J. Acoust. Soc. Am.*
- Edelson, R., J. Krolik, G. Madejski, L. Maraschi, G. Pike, C.M. Urry, W. Brinkmann, T.J.-L. Courvoisier, J. Ellithorpe, K. Home, et al. "Multi-Wavelength Monitoring of the BL Lac Object PKS 2155-304. IV. Multi-Wavelength Analysis." *Astrophys. J.*
- Ekstrom, C.R., J. Schmiedmayer, M.S. Chapman, T.D. Hammond, and D.E. Pritchard. "Measurement of the Electric Polarizability of Sodium with an Atom Interferometer." *Phys. Rev. A*.
- Fan, S., A. Devenyi, R. Meade, and J.D. Joannopoulos. "Guided Modes in Periodic Dielectric Materials." *J. Opt. Soc. Am.*
- Grayson, M., D.C. Tsui, M. Shayegan, K. Hirakawa, R.A. Ghanbari, and H.I. Smith. "Far Infrared Emission from Hot Quasi-One Dimensional Quantum Wires in GaAs." *App. Phys. Lett.*
- Hammond, T.D., D.E. Pritchard, M.S. Chapman, A. Lenef, and J. Schmiedmayer. "Multiplex Velocity Selection for Precision Matter Wave Interferometry." *Appl. Phys. B*.
- Haus, H.A. "From Classical to Quantum Noise." *J. Opt. Soc. Am. B*.
- Haus, H.A., K. Tamura, L.E. Nelson, and E.P. Ippen. "Stretched Pulse Additive Pulse Modelocking of Fiber Lasers." *IEEE J. Quantum Electron.*
- Hee, M.R., J.A. Izatt, E.A. Swanson, D. Huang, J.S. Schuman, C.P. Lin, C.A. Puliafito, and J. G. Fujimoto. "Optical Coherence Tomography of the Human Retina." *Arch. Oph.*
- Hewitt, J.N., G.H. Chen, and M.D. Messier. "Variability in the Einstein Ring Gravitational Lens MG1131+0456." *Astronom. J.*
- Hillman, R.E., E.B. Holmberg, J.S. Perkell, J. Kobler, P. Guiod, C. Gress, and E.E. Sperry. "Speech Respiration in Adult Females with Vocal Nodules." *J. Speech Hear. Res.*
- Ho, E., P.A. Fisher, J.L. House, G.S. Petrich, L.A. Kolodziejski, J. Walker, and N.M. Johnson. "Hydrogen Passivation in Nitrogen- and Chlorine-Doped ZnSe Films Grown by Gas Source Molecular Beam Epitaxy." *Appl. Phys. Lett.*
- Holmberg, E.B., R.E. Hillman, J.S. Perkell, and S. Goldman. "Comparisons Among Aerodynamic, Electroglossographic, and Acoustic Spectrum Measures of Female Voices." *J. Speech Hear. Res.*
- Jerby, E., A. Shadhadi, V. Grinberg, V. Dikhtiar, M. Sheinin, E. Agmon, H. Golombek, V. Trebich, M. Bensal, and G. Bekefi. "Cyclotron Maser Oscillator Experiments in a Periodically Loaded Waveguide." *IEEE J. Quantum Electron.*
- Katz, C.A., J.N. Hewitt, C.B. Moore, and J.D. Ellithorpe. "The STARE Project: A Search for Transient Astronomical Radio Emission." *Bull. Am. Astron. Soc.*
- Keyser, J.S., and K.N. Stevens. "Feature Geometry and the Vocal Tract." *Phonology*.
- Klein, O., C. de C. Chamon, D. Tang, D.M. Abusch-Magder, S.-G. Wen, M.A. Kastner, and S.J. Wind. "Exchange Effects in an Artificial Atom at High Magnetic Fields." *Phys. Rev. Lett.*

Appendix A. RLE Publications

- Kuo, C.C., D.H. Staelin, and P.W. Rosenkranz. "Statistical Iterative Scheme for Estimating Atmospheric Relative Humidity Profiles." *IEEE Trans. Geosci. Remote Sensing*.
- Lane, H., J. Wozniak, M.L. Matthies, M.A. Svirsky, and J.S. Perkell. "Phonemic Resetting vs. Postural Adjustments in the Speech of Cochlear Implant Users: an Exploration of Voice Onset Time." *J. Acoust. Soc. Am.*
- Lumsdaine, A., and J. White. "Accelerating Waveform Relaxation Methods with Application to Parallel Semiconductor Device Simulation." *Numer. Funct. Anal. Optimiz.*
- Manuel, S.Y. "Speakers Nasalize /θ/ After /n/, But Listeners Still hear /θ/." *J. Phon.*
- Maxwell, J.A., and P.M. Zurek. "Feedback Reduction in Hearing Aids." *IEEE Trans. Speech Audio Proc.*
- McCue, M.P., and J.J. Guinan, Jr. "Spontaneous Activity and Frequency Selectivity of Acoustically-Responsive Vestibular Afferents in the Cat." *J. Neurophysiol.*
- Merchant, S.N., J.J. Rosowski, and M.E. Ravicz. "Mechanics of Type IV and V Tympanoplasty. II. Clinical Analysis and Surgical Implications." *Am. J. Otol.*
- Moore, C.B., and J.N. Hewitt. "Time Delay Observations and Variability of the Gravitational Lens MG0414+0534." *Astrophys. J.*
- Natarajan, V., F. DiFilippo, and D.E. Pritchard. "Squeezed States of Classical Motion in a Penning Trap." *Phys. Rev. Lett.*
- Perkell, J.S. "Properties of the Tongue Help to Define Vowel Categories: Hypotheses Based on Physiologically-oriented Modeling." *J. Phon.*
- Perkell, J.S., M.L. Matthies, M.A. Svirsky, and M.I. Jordan. "Goal-based Speech Motor Control: A Theoretical Framework and Some Preliminary Data." *J. Phon.*
- Phillips, J.R., H.S.J. van der Zant, T.P. Orlando, and E. Trias. "Self-field Effects in Two-Dimensional Nb Josephson-junction Arrays." *IEEE Trans. Appl. Superconduct.*
- Puria, S., J.J. Guinan, Jr., and M.C. Liberman. "Olivocochlear Reflex Assays: Effects of Contralateral Sound on Compound Action Potentials vs. Ear-Canal Distortion Products." *J. Acoust. Soc. Am.*
- Rabinowitz, W.M., and D.K. Eddington. "Effects of Channel-to-Electrode Mappings on Speech Reception with the Ineraid Cochlear Implant." *Ear Hear.*
- Rabinowitz, W.M., D. Henderson, C.M. Reed, L.A. Delhorne, and N.I. Durlach. "Development and Evaluation of an Improved Synthetic Tadoma System." *J. Acoust. Soc. Am.*
- Reed, C.M., and L.A. Delhorne. "Current Results of a Field Study of Adult Users of Tactile Aids." *Seminars Hear.*
- Reed, C.M., L.A. Delhorne, N.I. Durlach, and S.D. Fischer. "A Study of the Tactile Reception of Sign Language." *J. Speech Hear. Res.*
- Reichelt, M., J. White, and J. Allen. "Optimal Convolution SOR Acceleration of Waveform Relaxation with Application to Parallel Simulation of Semiconductor Devices." *J. Sci. Stat. Comp.*
- Rosenkranz, P.W. "A Rapid Atmospheric Transmittance Algorithm for Microwave Sounding Frequencies." *IEEE Trans. Geosci. Remote Sensing*.
- Rosowski, J.J., and S.N. Merchant. "Mechanical and Acoustical Analyses of Middle-ear Reconstruction." *Am. J. Otol.*
- Rosowski, J.J., S.N. Merchant, and M.E. Ravicz. "Mechanics of Type IV and V Tympanoplasty. I. Model Analysis and Predictions." *Am. J. Otol.*
- Schmiedmayer, J., M.S. Chapman, C.R. Ekstrom, T.D. Hammond, S. Wehinger, and D.E. Pritchard. "Index of Refraction of Various Gases for Sodium Matter Waves." *Phys. Rev. Lett.*
- Schreiber, W.F. "Advanced Television Systems for Terrestrial Broadcasting: Some Problems and Some Proposed Solutions." *IEEE Proc.*
- Schreiber, W.F. "A Unified Approach to Moving Image Coding for Most Media and Most Applications." *Sig. Proc.*
- Shapiro, J.H. "Phase Conjugate Quantum Communication with Optical Heterodyne Detection." *Opt. Lett.*

- Shapiro, J.H., and L. Boivin. "Raman-Noise Limit on Squeezing in Continuous Wave Four-Wave Mixing." *Opt. Lett.*
- Silveira, L.M., I.M. Elfadel, J.K. White, M. Chilukuri, and K.S. Kundert. "Efficient Frequency-Domain Modeling and Circuit Simulation of Transmission Lines." *IEEE Trans. Compon., Hybrids, Manuf. Technol.*
- Smet, J.H., C.G. Fonstad, and Q. Hu. "Intrawell and Interwell Intersubband Transitions in Multiple Quantum Wells." *J. Appl. Phys.*
- Smet, J.H., C.G. Fonstad, and Q. Hu. "Magnetotunneling Spectroscopy with both In-plane and Longitudinal Fields." *Phys. Rev. B*.
- Song, S., and S.G.J. Mochrie. "Attractive Interactions Between Steps, Tricriticality and Faceting in the Orientational Phase Diagram of Silicon Surfaces Between (113) and (114)." *Phys. Rev. B*.
- Sperry, E., R. Hillman, and J. Perkell. "Use of Inductance Plethysmography to Assess Respiratory Function in a Patient with Vocal Nodules." *J. Med. Speech-Language Path.*
- Spina, M.S., M.J. Schwartz, D.H. Staelin, and A.J. Gasiewski. "Application of Multilayer Feedforward Neural Networks to Precipitation Cell-top Altitude Estimation." *IEEE Trans. Geosci. Rem. Sens.*
- Stoner, R., and G. Bekefi. "A 70-Period High-Precision Microwiggler for Free Electron Lasers." *IEEE J. Quantum Electron.*
- Takeuchi, A.H., and L.D. Braida. "Recognition of Amplitude Modulation Patterns in the Presence of a Distractor: I. Effects of Correlation and Frequency Relation." *J. Acoust. Soc. Am.*
- Takeuchi, A.H., and L.D. Braida. "Recognition of Amplitude Modulation Patterns in the Presence of a Distractor: II. Effects of Dichotic Presentation and Unmodulated Distractors." *J. Acoust. Soc. Am.*
- Tamura, K., E.P. Ippen, and H.A. Haus. "Optimization of Filtering in Soliton Fiber Lasers." *Electron Lett.*
- Tan, H.Z. and N.I. Durlach. "Manual Discrimination Using Active Finger Motion: Compliance, Force, and Work." *Percept. Psychophys.*
- Uchanski, R.M., L.A. Delhorne, A.K. Dix, L.D. Braida, C.M. Reed, and N.I. Durlach. "Automatic Speech Recognition to Aid the Hearing Impaired. Prospects for the Automatic Generation of Cued Speech." *J. Rehab. Res. Dev.*
- van der Zant, H.S.J., T.P. Orlando, and A.W. Kleinsasser. "One-dimensional Parallel Josephson-junctions Arrays as a Tool for Circuit Diagnostics." *IEEE Trans. Appl. Superconduct.*
- Vergheese, S., R.A. Wyss, T. Schapers, A. Forster, M.J. Rooks, and Q. Hu. "Photon-assisted Transport Through Quantized Energy States in a Lateral Dual-Gate Device." *Phys. Rev. Lett.*
- Villeneuve, P.R., S. Fan, J.D. Joannopoulos, K.Y. Lim, G.S. Petrich, L.A. Kolodziejski, and R. Reif. "Air-Bridge Microcavities." *Phys. Rev. Lett.*
- Wilhelms-Tricarico, R. "Physiological Modeling of Speech Production: Methods for Modeling Soft-tissue Articulators." *J. Acoust. Soc. Am.*
- Wilhelms-Tricarico, R. "Biomechanical and Physiologically Based Speech Modeling." *J. Phon.*
- Xia, J.J., J.A. Kong, and R.T. Shin. "A Macroscopic Model of Nonlinear Constitutive Relations in Superconductors." *IEEE Trans. Microwave Theory Tech.*
- Yakubo, K., S. Feng, and Q. Hu. "Direct Simulation of Photon-assisted Quantum Transport." *Phys. Rev. B*.
- Yu, P.C., and H.-S. Lee. "Settling-Time Analysis of a Replica-Amp Gain Enhanced Operational Amplifier." *IEEE Trans. Circ. Sys. II: Analog Digit. Signal Process.*

A.3 Books/Chapters in Books

- Delgutte, B. "Physiological Models for Basic Auditory Percepts." In *Auditory Computation*. Eds. H. Hawkins and T. McMullen. New York: Springer-Verlag. Forthcoming.
- Delgutte, B., P.X. Joris, R.Y. Litovsky, and T.C.T. Yin. "Relative Importance of Different Acoustic Cues to the Directional Sensitivity of Inferior Colliculus Neurons." In *Advances in Hearing Research*. Eds. G.A. Manley, G.M. Klump, C. Kppl, H. Fastl, and H. Oeckinghaus. Singapore: World Scientific. Forthcoming.

Appendix A. RLE Publications

- Elfadel, I.M., and J.L. Wyatt, Jr. "The 'Softmax' Nonlinearity: Derivation Using Statistical Mechanics and Useful Properties as a Multiterminal Analog Circuit Element." In *Advances in Neural Information Processing Systems*. Ed. M. Kaufman. Amsterdam, the Netherlands: Elsevier Scientific Publishers, 1994.
- Ezekiel, S., S.P. Smith, and F. Zarinetchi. "Basic Principles of Fiber-Optic Gyroscopes." In *Optical Fiber Rotation Sensing*, pp. 3-25. Ed. W.K. Burns. San Diego, California: Academic Press, Inc., 1994.
- Hu, Q., R.A. Wyss, C.C. Eugster, J.A. del Alamo, and S. Feng. "Far-infrared Study of an Antenna-coupled Quantum Point Contact." In *Quantum Well Intersubband Transition Physics and Devices*, p. 553. Eds. H.C. Liu, B.F. Levine, and J.Y. Andersson. Boston: Kluwer Academic, 1994.
- Masaki, I. "Fuzzy Logic Technology and the Intelligent Highway System (IHS)." In *Fuzzy Logic Technology and Applications I*. New Jersey: IEEE Press, 1994.
- Perkell, J.S. "Articulatory Processes." In *Handbook of Phonetic Science*. Eds. W. Hardcastle and J. Laver. Oxford: Blackwell. Forthcoming.
- Pritchard, D.E. "Atom Interferometer." In *Proceedings of the 13th International Conference on Atomic Physics*. Eds. T.W. Hansch, H. Walther, and B. Neizert. New York: American Institute of Physics, 1994.
- Ram, A.K., and A. Bers. "Hamiltonian Chaos in Wave-Particle Interactions." In *Physics of Space Plasmas*. Eds. T. Chang and J.R. Jasperse. Cambridge, Massachusetts: Scientific Publishers, 1994.
- Shattuck-Hufnagel, S. "Slips of the Tongue." In *Encyclopedia of Language and Linguistics*. Eds. R.E. Asher and J.M.Y. Simpson. Oxford: Pergamon Press. Forthcoming.
- Shattuck-Hufnagel, S. "Stress Shift as Early Pitch Accent Placement: A Comment on Berkman and Edwards." In *Phonological Structure and Phonetic Form, Papers in Laboratory Phonology III*, pp. 34-42. Ed. P.A. Keating. Cambridge: Cambridge University Press, 1994.
- Smith, H.I. "Microlithography" In *Encyclopedia of Applied Physics*, 10: 281-295. Ed. G.L. Trigg. New York: VCH Publishers, 1994.
- Smith, H.I., and M.L. Schattenburg. "X-ray Nanolithography: Limits, and Application to Sub-100 NM Manufacturing." In *Nanolithography: A Borderland between STM, EB, IB, and X-Ray Lithographies*, pp. 103-119. Eds. M. Gentili et al. Dordrecht, the Netherlands: Kluwer Academic Publishers, 1994.
- Stevens, K.N. "Articulatory-acoustic-auditory Relationships." In *Handbook of Phonetic Sciences*. Eds. W. Hardcastle and J. Laver. Oxford: Blackwell. Forthcoming.
- Stevens, K.N. "Scientific Substrates of Speech Production." In *Introduction to Communication Sciences and Disorders*, pp. 399-437. Ed. F. Minifie. San Diego, California: Singular, 1994.
- Stevens, K.N. "Phonetic Evidence for Hierarchies of Features." In *Phonological Structure and Phonetic Form, Papers in Laboratory Phonology III*, pp. 242-258. Ed. P.A. Keating. Cambridge, Massachusetts: Cambridge University Press, 1994.
- Stevens, K.N., and H.M. Hanson. "Classification of Glottal Vibration from Acoustic Measurements." In *Vocal Fold Physiology: Voice Quality Control*, pp. 147-170. Eds. O. Fujimura and M. Hirano. San Diego, California: Singular, 1994.
- Umminger, C.B., and C.G. Sodini. "Switched Capacitor Networks for Focal Plane Image Processing Systems." In *Vision Chips: Implementing Vision Algorithms with Analog VLSI Circuits*. Eds. C. Koch and H. Li. Los Alamitos, California: IEEE Computer Society Press, 1994.
- Wyatt, J.L., Jr. "Little-Known Properties of Resistive Grids that are Useful in Analog Vision Chip Design." In *Vision Chips: Implementing Vision Algorithms with Analog VLSI Circuits*. Eds. C. Koch and H. Li. Los Alamitos, California: IEEE Computer Society Press, 1994.

A.4 RLE Publications

- RLE 45th Anniversary Brochure*. MIT, 1991. 72 pp. No charge.
- RLE currents* 7(2): (1994). Topic: Solid-State Secrets: Probing the Mysteries of Surface Physics at RLE. 28 pp. No charge.
- RLE Progress Report No. 136*: January-December 1993. MIT, 1994. 488 pp. No charge.

- Cuomo, K.M. *Analysis and Synthesis of Self-Synchronizing Chaotic Systems*. RLE TR-582. MIT, 1994.
- Lumsdaine, A., M. Silveira, and J. White. *SIMLAB Programmers's Guide*. RLE TR-589. MIT, 1994.
- Lumsdaine, A., M. Silveira, and J. White. *CMVSIM User's Guide*. RLE TR-590. MIT, 1994.
- Nicolas, J.J. *Investigation of Coding and Equalization for the Digital HDTV Terrestrial Broadcast Channel*. RLE TR-585. MIT, 1994.
- Richard, M.D. *Estimation and Detection with Chaotic Systems*. RLE TR-581. MIT, 1994.
- Silveira, M., A. Lumsdaine, and J. White. *SIMLAB User's Guide*. RLE TR-588. MIT, 1994.
- Verbout, S.M. *Signal Enhancement for Automatic Recognition of Noisy Speech*. RLE TR-584. MIT, 1994.
- Wage, K.E. *Adaptive Estimation of Acoustic Normal Modes*. RLE TR-586. MIT, 1994.
- Wornell, G.W. *Efficient Symbol-Spreading Strategies for Wireless Communication*. RLE TR-587. MIT, 1994.
- Zangi, K.C. *Optimal Feedback Control Formulation of the Active Noise Cancellation Problem: Pointwise and Distributed*. RLE TR-583. MIT, 1994.
- ## A.5 Theses
- Adams, T. *Gate Delay in InP Heterostructure Field-Effect Transistors*. S.B. thesis, Dept. of Electr. Eng. and Comput. Sci., MIT, 1994.
- Alidina, M.M. *Precomputation-Based Sequential Logic Optimization for Low Power*. S.M. thesis, Dept. of Electr. Eng. and Comput. Sci., MIT, 1994.
- Au, W.C. *Computational Electromagnetics in Microwave Remote Sensing*. Ph.D. diss., Dept. of Aero. and Astro., MIT, 1994.
- Bach, S. *Chirp Compensation in Active Mode-Locked Semiconductor Diode Laser Using a DFB*. M. Eng. thesis, Dept. of Electr. Eng. and Comput. Sci., MIT, 1994.
- Baltus, D.G. *Efficient Exploration of Affine Space-Time Transformations for Optimal Systolic Array Synthesis*. Ph.D. diss., Dept. of Electr. Eng. and Comput. Sci., MIT, 1994.
- Berman, D. *Discrete Superconducting Vortex Flow Transistors*. S.M. thesis, Dept. of Electr. Eng. and Comput. Sci., MIT, 1994.
- Bhagwati, V.L. *Automatic Verification of Pipelined Microprocessors*. S.M. thesis, Dept. of Electr. Eng. and Comput. Sci., MIT, 1994.
- Blastos, J.C. *The Spectral Analysis of the Spontaneous Emission of MITs 8.8 mm, Room Temperature, Pulsed Free Electron Laser Microwiggler*. S.M. thesis, Dept. of Physics, MIT, 1994.
- Brungart, D.S. *Distance Information Transmission Using First Order Reflections*. S.M. thesis, Dept. of Electr. Eng. and Comput. Sci., MIT, 1994.
- Catravas, P.E. *MIT 3.3 GHz Relativistic Klystron Amplifier: Experimental Study of Input Cavity and Beam Characteristics*. S.M. thesis, Dept. of Electr. Eng. and Comput. Sci., MIT, 1994.
- Chan, K.P. *Stochasticity Induced by Electrostatic Waves in Magnetized Plasma*. S.B. thesis, Dept. of Physics, MIT, 1994.
- Chen, B.-L.J. *Experimental Studies of a CERN-CLIC 32.98 GHz High Gradient RF Accelerating Structure Driven by a Free Electron Laser Amplifier*. S.B. thesis, Dept. of Physics, MIT, 1994.
- Cheng, T.K. *The Excitation and Dynamics of Coherent Lattice Vibrations in Semimetals and Narrow-gap Semiconductors*. Ph.D. diss., Dept. of Electr. Eng. and Comput. Sci., MIT, 1994.
- Coronado, C.A. *Growth and Characterization of ZnSe by Metalorganic and Gas Source Molecular Beam Epitaxy*. Ph.D. diss., Dept. of Mater. Sci. and Eng., MIT, 1994.
- Courtney, M. *Rydberg Atoms in Strong Fields: A Testing Ground for Quantum Chaos*. Ph.D. diss., Dept. of Physics, MIT, 1994.
- Cuomo, K.M. *Analysis and Synthesis of Self-Synchronizing Chaotic Systems*. Ph.D. diss., Dept. of Electr. Eng. and Comput. Sci., MIT, 1994.
- Daley, S.P. *The Role of Bulk Versus Surface Bound H in the Catalytic Hydrogenation of*

Appendix A. RLE Publications

- Methyl Radicals and Ethylene on Ni. Ph.D. diss., Dept. of Chem., MIT, 1994.
- DiFilippo, F. Precise Atomic Masses for Determining Fundamental Constants. Ph.D. diss., Dept. of Physics, MIT, 1994.
- Doerr, C.R. Toward a Noise-Free Interferometric Fiber Optic Gyroscope. Ph.D. diss., Dept. of Electr. Eng. and Comput. Sci., MIT, 1994.
- Dron, L.G. Computing 3-D Motion in Custom Analog and Digital VLSI. Ph.D. diss., Dept. of Electr. Eng. and Comput. Sci., MIT, 1994.
- Ewe, H.T. Radiative Transfer Theory for Active and Passive Remote Sensing of Sea Ice. S.M. thesis, Dept. of Electr. Eng. and Comput. Sci., MIT, 1994.
- Ferrera, J. Highly Coherent Gratings for Optoelectronics: An Application of Spatial-Phase-Locked Electron Beam Lithography. S.B. and S.M. thesis, Dept. of Electr. Eng. and Comput. Sci., MIT, 1994.
- Funatsu, J. Laser-Assisted Focused-Ion-Beam-Induced Deposition of Copper. S.M. thesis, Dept. of Mater. Sci. and Eng., MIT, 1994.
- Fung, I. Multiresolution Laser Radar Range Profiling with the Expectation-Maximization Algorithm. S.M. thesis, Dept. of Electr. Eng. and Comput. Sci., MIT, 1994.
- Gajaweera, A. Tactual Discrimination of Thickness. S.B. thesis, Dept. of Mech. Eng., MIT, 1994.
- Greenberg, J.E. Improved Design of Microphone-Array Hearing Aids. Ph.D. diss., Harvard-MIT Div. of Health Sci. and Technol., MIT, 1994.
- Grumet, A.E. Extracellular Electrical Stimulation of Retinal Ganglion Cells. S.M. thesis, Dept. of Electr. Eng. and Comput. Sci., MIT, 1994.
- Hector, S.D. Optimization of Image Formation in X-ray Lithography Using Rigorous Electromagnetic Theory and Experiments. Ph.D. diss., Dept. of Electr. Eng. and Comput. Sci., MIT, 1994.
- Herrmann, F.P. An Integrated Associative Processing System. Ph.D. diss., Dept. of Electr. Eng. and Comput. Sci., MIT, 1994.
- House, J.L. Optical Characterization of ZnSe by Photoluminescence. S.M. thesis, Dept. of Electr. Eng. and Comput. Sci., MIT, 1994.
- Hu, H. Experimental Study of Electron Velocity Overshoot in Silicon Inversion Layers. Ph.D. diss., Dept. of Physics, MIT, 1994.
- Hu, W. Generation of Coherent High-Power Microwave Radiation with Relativistic Electron Beams. S.M. thesis, Dept. of Physics, MIT, 1994.
- Hugunin, J.J. The Superconductor/Semiconductor Interface of V_3Si and Si. S.M. thesis, Dept. of Electr. Eng. and Comput. Sci., MIT, 1994.
- Hui, E.E-Y. Measurement of Photo-Induced Radiation in a Quantum Point Contact. S.B. thesis, Dept. of Physics, MIT, 1994.
- Hultgren, C.T. Femtosecond Nonlinearities in AlGaAs Diode Laser Amplifiers. Ph.D. diss., Dept. of Electr. Eng. and Comput. Sci., MIT, 1994.
- Iwai, K.K. Pre-Echo Detection and Reduction. S.M. thesis, Dept. of Electr. Eng. and Comput. Sci., MIT, 1994.
- Jacobson, B.R. A Micromachined SIS Mixer. S.M. thesis, Dept. of Electr. Eng. and Comput. Sci., MIT, 1994.
- Koita, R.R. Strategies for Sequential Design of Experiments. S.M. thesis, Dept. of Electr. Eng. and Comput. Sci., MIT, 1994.
- Kumar, A. Single Electron Charging Effects in Quantum Dot Nanostructures. Ph.D. diss., Dept. of Electr. Eng. and Comput. Sci., MIT, 1994.
- Li, H. Temperature Homogenization with Tungsten Absorber on X-ray Mask. S.B. and S.M. thesis, Dept. of Electr. Eng. and Comput. Sci., MIT, 1994.
- Love, N.S. Statistical Process Control Charts for the Computer-Aided Fabrication Environment. S.M. thesis, Dept. of Electr. Eng. and Comput. Sci., MIT, 1994.
- Lu, K. Lattice-Matched $(In,Ga)P$ Buffer Layers for ZnSe Based Visible Emitters. S.M. thesis, Dept. of Electr. Eng. and Comput. Sci., MIT, 1994.
- Lyubomirsky, I. Quantum Reality and Squeezed States of Light. S.M. thesis, Dept. of Electr. Eng. and Comput. Sci., MIT, 1994.
- Mann, J.P. A Maximum Likelihood Method for Directional Spectrum Estimation. S.M. thesis,

- Dept. of Electr. Eng. and Comput. Sci., MIT, 1994.
- Massey, N.S. *Transients at Stop Consonant Releases*. S.M. thesis, Dept. of Electr. Eng. and Comput. Sci., MIT, 1994.
- Moores, J.D. *All-Optical Soliton Communications: Devices and Limitations*. Ph.D. diss., Dept. of Electr. Eng. and Comput. Sci., MIT, 1994.
- Morshidi, W.Y. *Frequency Modulation Spectroscopy for Frequency Stabilization of Dye-laser*. S.B. thesis, Dept. of Physics, MIT, 1994.
- Mucciolo, E.R. *Universal Correlations in the Quantum Spectra of Chaotic Systems in Exactly Solvable Many-Body Problems*. Ph.D. diss., Dept. of Physics, MIT, 1994.
- Oates, J.H. *Propagation and Scattering of Electromagnetic Waves in Complex Environments*. Ph.D. diss., Dept. of Electr. Eng. and Comput. Sci., MIT, 1994.
- Owen, G.M. *Optical and Mechanical Characterization of Thin Membranes for X-ray Lithography*. S.M. thesis, Dept. of Electr. Eng. and Comput. Sci., MIT, 1994.
- Pfajfer, A. *Position-Dependent Encoding*. S.M. thesis, Dept. of Electr. Eng. and Comput. Sci., MIT, 1994.
- Reiner, J.W. *A Small-Signal Model for Surface Effects in InAlAs/InGaAs HFETs*. S.B. thesis, Dept. of Electr. Eng. and Comput. Sci., MIT, 1994.
- Richard, M.D. *Estimation and Detection with Chaotic Systems*. Sc.D. diss., Dept. of Electr. Eng. and Comput. Sci. 1994.
- Rinderknecht, W.R. *A Power Reduction Algorithm for Combinational CMOS Circuits Using Input Disabling*. S.M. thesis, Dept. of Electr. Eng. and Comput. Sci., MIT, 1994.
- Seidel, M.N. *Switched-Capacitor Networks for Image Processing: Analysis, Synthesis, Response Bounding, and Implementation*. Sc.D. diss., Dept. of Electr. Eng. and Comput. Sci. 1994.
- Shen, A.H. *Probabilistic Representation and Manipulation of Boolean Functions Using Free Boolean Diagrams*. Ph.D. diss., Dept. of Electr. Eng. and Comput. Sci., MIT, 1994.
- Shvets, G. *Interaction of Intense Lasers with Plasmas*. Ph.D. diss., Dept. of Physics, MIT, 1994.
- Silveira, L.M. *Model Order Reduction Techniques for Circuit Simulation*. Ph.D. diss., Dept. of Electr. Eng. and Comput. Sci., MIT, 1994.
- Sisson, D.L. *Magnetic Field in a Tunable Microwiggler*. S.B. thesis, Dept. of Physics, MIT, 1994.
- Smet, J.H. *Intrawell and Interwell Intersubband Transitions in Single and Multiple Quantum Well Heterostructures*. Ph.D. diss., Dept. of Electr. Eng. and Comput. Sci., MIT, 1994.
- Spina, M.S. *Application of Multilayer Feedforward Neural Networks to Precipitation Cell-Top Altitude Estimation*. S.M. thesis, Dept. of Electr. Eng. and Comput. Sci., MIT, 1994.
- Stamatopoulos, M. *A Factory Representation as a Design Tool in a Computer Integrated Manufacturing Environment*. S.M. thesis, Dept. of Electr. Eng. and Comput. Sci., MIT, 1994.
- Stoner, R.E. *Radiation from Relativistic Electron Beams in Periodic Structures*. Ph.D. diss., Dept. of Physics, MIT, 1994.
- Tan, C.H. *Optimization of Power and Delay in VLSI Circuits Using Transistor Sizing and Input Ordering*. S.M. thesis, Dept. of Electr. Eng. and Comput. Sci., MIT, 1994.
- Tannian, B. *Near Field Imaging of Atomic Diffraction Gratings: The Atomic Talbot Effect*. S.B. thesis, Dept. of Physics, MIT, 1994.
- Tassoudji, M.A. *Electromagnetic Interference in Electronic Circuits and Systems*. Ph.D. diss., Dept. of Electr. Eng. and Comput. Sci., MIT, 1994.
- Unver, E.R. *Implementation of a Design Rule Checker for Silicon Wafer Fabrication*. M.Eng. thesis, Dept. of Electr. Eng. and Comput. Sci., MIT, 1994.
- Vegsoglu, M.E. *Direct and Inverse Scattering Models for Random Media and Rough Surfaces*. Ph.D. diss., Dept. of Electr. Eng. and Comput. Sci., MIT, 1994.
- Volbeyn, P.S. *Measurements of the Temporal and Spatial Phase Variations of a 33 GHz Pulsed Free Electron Laser Amplifier and Applications*

Appendix A. RLE Publications

to RF Acceleration. S.M. thesis, Dept. of Physics, MIT, 1994.

Welker, D.P. *A Real-Time Binaural Adaptive Hearing Aid.* S.M. thesis, Dept. of Electr. Eng. and Comput. Sci., MIT, 1994.

Appendix B. Current RLE Personnel

Director: Jonathan Allen
Associate Director: Daniel Kleppner

Professors

Jonathan Allen	Hermann A. Haus	Miklos Porkolab
Boris Altshuler	Albert Hill ¹	David E. Pritchard
Dimitri A. Antoniadis	Erich P. Ippen	William F. Schreiber ¹
Arthur B. Baggeroer	John D. Joannopoulos	Campbell L. Searle
George Bekefi	Marc A. Kastner	Stephen D. Senturia
Abraham Bers	Nelson Y.-S. Kiang	Jeffrey H. Shapiro
Robert J. Birgeneau	John G. King	William M. Siebert ¹
Amar G. Bose	Daniel Kleppner	Henry I. Smith
Louis D. Braida	Leslie A. Kolodziejski	Charles G. Sodini
Bernard F. Burke	Jin A. Kong	David H. Staelin
Bruno Coppi	Patrick A. Lee	Kenneth N. Stevens
Srinivas Devadas	Jerome Y. Lettvin ¹	Donald E. Troxel
Shaoul Ezekiel	Jae S. Lim	Thomas F. Weiss
Clifton G. Fonstad, Jr.	Alan V. Oppenheim	John L. Wyatt, Jr.
Lawrence S. Frishkopf	William T. Peake	Henry J. Zimmermann ¹

Associate Professors

Jesús A. del Alamo	Qing Hu	Jacob K. White
James G. Fujimoto	Simon G.J. Mochrie	Jonathan S. Wurtele
Peter L. Hagelstein		

Assistant Professors

Raymond C. Ashoori	Jacqueline N. Hewitt	Gregory W. Wornell
Anantha P. Chandrakasan	Wolfgang Ketterle	

Senior Research Scientists

Nathaniel I. Durlach	Joseph S. Perkell	Robert H. Rediker
----------------------	-------------------	-------------------

Principal Research Scientists

Donald K. Eddington	Charlotte M. Reed	Mandayam A. Srinivasan
John J. Guinan, Jr.	Philip W. Rosenkranz	David Zeltzer
William M. Rabinowitz	J. Kenneth Salisbury	Patrick M. Zurek

¹ Professor Emeritus.

Research Scientists and Research Specialists

Giovanni Aliberti
John W. Barrett
James M. Carter
Bertrand Delgutte
Lorraine A. Delhorne
Gregory T. Fischer
David W. Foss
Dennis M. Freeman
David Gosalvez
Seth M. Hall

Thomas J. Lohman
Joyce Manzella
Ivan Mastovsky
Melanie L. Matthies
Michael B. McIlrath
Robert D. Meade
Stefano Migliuolo
Euclid E. Moon
Abhay K. Ram

Dennis D. Rathman
John J. Rosowski
Selim M. Shahriar
Stefanie Shattuck-Hufnagel
Scott E. Silverman
Linda E. Sugiyama
Mario A. Svirsky
Ngai Chuen Wong
Y. Eric Yang

Administrative Staff

Joseph F. Connolly
Virginia R. Lauricella
Barbara J. Passero

Gerrard F. Power
William H. Smith

Vicky-Lynn Taylor
Mary E. Young

Support and Technical Staff

Mary C. Aldridge
Janice L. Balzer
Felicia G. Brady
Margaret S. Beucler
Manuel Cabral, Jr.
Susan E. Chafe
Anne E. Conklin
John F. Cook
Carol A. Costa
Thomas L. DeFilippo
Ann K. Dix
Francis M. Doughty

Dorothy A. Fleischer
Donna L. Gale
Mary S. Greene
Peter C. Guiod
Maureen C. Howard
Cynthia Y. Kopf
Kit-Wah F. Lai
Cindy LeBlanc
Eleanora M. Luongo
Deborah S. Manning
Rita C. McKinnon

Mark K. Mondol
Edward R. Murphy
Denise M. Rossetti
Bruce A. Russell
Maxine P. Samuels
Robert D. Sisson
Mabayoje Tuyo
Laura M. von Bosau
Arlene E. Wint
Janice M. Zaganjori
Mary J. Ziegler

Postdoctoral Fellows and Associates

Robert C. Armstrong
Brett E. Bouma
Gerhard De Lange
Kung-Hau Ding
Chinnaswamy M. Harish
Jeng-Feng Lee
Alan L. Lenef

Fred L. Palmer
Anne Pepin
Matthew H. Power
Wendelin L. Sachtler
Ofir Shalvi
Barbara G. Shinn-Cunningham
Stephen P. Smith

Alice E. Turk
Simon Verghese
Pierre R. Villeneuve
Thomas E.v. Wiegand
Reiner Wilhelms-Tricarico
Yi Xu

Research Assistants

Charles C. Abnet
David M. Abusch
Joseph F. Ahadian
Michael R. Andrews
Mark A. Armstrong
Neer R. Asherie
Walter A. Aviles

Ian M. Avruch
James H. Bandy
Soosan Beheshti
Igor P. Bilinsky
William J. Blackwell
Roxann R. Blanchard
Luc Boivin

Jeffrey K. Bounds
Michael P. Bradley
Maroula S. Bratakos
Louis R. Brothers
Martin Burkhardt
Carlos R. Cabrera
Xuejun Cai

David J. Carter
 John K. Cartwright
 Palmyra E. Catravas
 Claudio L. Cesar
 Hwa-Ping Chang
 Michael S. Chapman
 Grace H. Chen
 Jerry C. Chen
 Jyh-Shing Chen
 Marilyn Y. Chen
 Shiufun Cheung
 Jeffrey T. Chiou
 Mike T. Chou
 Tzilgakis Constantine
 Geoffrey J. Coram
 Fronefield Crawford
 Jay H. Damask
 Kiran B. Dandekar
 Ali Darwish
 Charles Q. Davis
 Kendall Davis
 Timothy J. Derksen
 Joel C. DeVries
 Sean M. Donovan
 David J. Dougherty
 Dallin S. Durfee
 Scott B. Dynes
 Michael S. Ehrlich
 John D. Ellithorpe
 Shanhui Fan
 Juan Ferrera
 Siegfried B. Fleischer
 Andre B. Fletcher
 Eric M. Foxlin
 Joseph A. Frisbie
 Alan I. Gale
 Boris Golubovic
 James G. Goodberlet
 David Gosalvez
 Donald R. Greer
 Andrew E. Grumet
 Nitin Gupta
 Rakesh Gupta
 Deborah B. Haarsma
 Christoforos N. Hadjicostis
 George I. Hadjiyiannis
 Andrew K. Halberstadt
 Troy D. Hammond

Michael R. Hee
 Lori K. Herold
 Raynard O. Hinds
 Chih-Hao Ho
 Easen Ho
 Jeffrey R. Holley
 David M. Horowitz
 Jody House
 Chih-Chien Hsu
 Louise Jandura
 Xiaohu Jiang
 Hong Jiao
 Joel T. Johnson
 Mark A. Johnson
 David J. Jones
 Alkan Kabakcioglu
 Mattan Kamon
 Steingrimur Karason
 Zoher Z. Karu
 Charles A. Katz
 Mohammad J. Khan
 Farzana I. Khatri
 Jimmy Y. Kwon
 Warren M. Lam
 Dicky Lee
 Junehee Lee
 Laurence H. Lee
 Gadi Lenz
 Stan Y. Liao
 Kuo-Yi Lim
 Sharlene A. Liu
 Jeffrey T. Ludwig
 David S. Lum
 Robert I. Lutwak
 Ilya Lyubomirsky
 Christina Manolatou
 Elisabeth A. Marley
 Paul S. Martin
 Elliott J. Mason
 Marc O. Mewes
 José C. Monteiro
 Christopher B. Moore
 Hugh B. Morgenbesser
 William P. Moyne
 Thomas E. Murphy
 Philip M. Nadeau
 Ognen J. Nastov

Philip T. Nee
 Lynn E. Nelson
 Michael P. O'Connell
 Edward J. Ouellette
 Haralabos C. Papadopoulos
 Ickjin Park
 Steven G. Patterson
 Gregory E. Penn
 Joel R. Phillips
 Nicholas Pioch
 Arifur Rahman
 Khalid Rahmat
 Monte J. Ramstad
 Farhan Rana
 Mark A. Rawizza
 Richard A. Rubenstein
 Timothy A. Savas
 David W. Schloerb
 Steven D. Schultz
 Michael J. Schwartz
 Song Seungheon
 Lisa Shatz
 Shih-en Shih
 Andrew C. Singer
 Matthew T. Sinn
 Neal W. Spellmeyer
 Lon E. Sunshine
 Nitish Swarup
 Hong Z. Tan
 Xiaofeng Tang
 Carl Taniguchi
 Prathet Tankuranun
 Guillermo J. Tearney
 Kathleen E. Wage
 Li-Fang Wang
 Vincent V. Wong
 William S. Wong
 Rolf A. Wyss
 Bin Xu
 Jun Yan
 Anto Yasaka
 Kenneth W. Yee
 Chang D. Yoo
 Noah D. Zamdmmer
 Yan Zhang
 Craig B. Zilles

Teaching Assistants

John R. Buck
 Irfan U. Chaudhary
 Alan E. Freedman

James M. Ooi
 Magdalena A. Petryniak
 Caterina Riconda

Jennifer L. Stinn
 Catherine S. Trotter-Wilson

Appendix B. Current RLE Personnel

Graduate Students

Laura E. Adams	Shilpa M. Hattangadi	Diane E. Ronan
Jerome J. Akerson	Ljubomir Illic	Yakov Royter
Abdulaziz Al Jalal	Steven H. Isabelle	Jay Sarkar
John G. Apostolopoulos	Erik B. Iverson	Hugh E. Secker-Walker
Alexander Aranyosi	Megan C. Jasek	Laura Sever
Chalee Asavathiratham	James Kao	Satyen Shah
Richard J. Barron	Thomas C. Killian	Asif Shakeel
David M. Baylon	Jean C. Krause	Krishna V. Shenoy
Karl K. Berggren	Chwen-yuen Ku	Gennady Shvets
Stephen A. Boppart	Jenn-Huei J. Kuan	Edward T. Smith
Stanley W. Brown	Hong-Kwang J. Kuo	Araceli Soto
John C. Carney	Corinna Lathan	Michelle S. Spina
Shourov K. Chatterji	Daniel D. Lee	Konstantina Stankovic
Brian Chen	Kevin Li	Stanley H. Thompson
Karen Chenausky	Robert G. McDonald	Andrew Ugarov
William S. Daughton	Yehia M. Massoud	Christopher B. Umminger
Diana Dabby	Ignacio S. McQuirk	Luigi Vacca
Steven J. Decker	Marcelo M. Mizuki	Shawn M. Verbout
Joseph G. Desloge	Ann W. Morgenthaler	Mark M. Visosky
Shepard S. Doebleman	Katerina Nguyen	Susie J. Wee
James Ernstmeyer	Janet L. Pan	Chen-Hsiang Yeang
Ilya Entin	Darren M. Pierre	Peter S. Yesley
Anita M. Flynn	Adam D. Polcyn	Mirang Yoon
Eric J. Gaidos	Michael O. Polley	Michael J. Young
Felicisimo W. Galicia	Eric C. Reed	William W. Zhou
Tza-Jing Gung	Todd H. Rider	

Undergraduate Students

Catherine Bae	Everest W. Huang	Michelle M. Scheer
Stephen V. Baird	Owen D. Johnson	Sudeep Rangaswamy
Andrew W. Beharrie	Gabrielle A. Jones	Luz M. Rivas
Susan E. Born	Allen N. Jordan	Jonathan R. Santos
Erica N. Carmel	Lauren Klatsky	Matthew G. Sexton
Theodore C. Cha	Brian D. Lee	Han Shu
Brian P. Clarkson	Scott A. Lehman	Samad Soomro
Laura C. Dilley	Danielle G. Lemay	Ranjini Srikantiah
David Garrison	David C. Lossos	Christiana Toutet
Brett A. Geoffroy	Tina L. Lin	Lukasz A. Weber
William R. Godfrey	Russell A. Newman	Evan F. Wies
Arlene A. Hahn	Marsha F. Novak	Chiann J. Yeh
Philip M. Hinz	Jonathan D. Pfautz	Xiao Yu
Carmen Ho	Robert Powers	Lee Zamir

Visiting Scientists

Shari R. Baum	Yasunori Kanamaru	Kevin O'Neill
Gerald L. Beauregard	Hisashi Kanie	Karen L. Payton
Corine A. Bickley	Andrew J. Kerman	Geoffrey L. Plant
Marek K. Czachor	Jack Kotik	Helene Rieu
Paul Duchnowski	Stepan Kubasiak	Stanley J. Rosenthal
Julie E. Greenberg	Brent E. Little	Ann B. Rossi
Rogeve Gulati	Riccardo Maggiora	Hannes J. Schmiedmayer
Helen M. Hanson	Shu Namiki	Jean-Claude Souyris
Arthur K. Jordan	Suzanne Neil	Richard E. Stoner

Liguo Sun
George M. Svolos

Research Affiliates

John S. Barlow
Vladimir Barsukov
Herbert J. Bernstein
Giuseppe Bertin
Suzanne Boyce
Mark E. Brezinski
Elliott R. Brown
Frank S. Cardarelli
H. Steven Colburn
Theodore W. Ducas
Daniel J. Ehrlich
Ibrahim M. Elfadel
Carol Y. Espy-Wilson
Patrick N. Everett
Paul D. Fiore
Ignacio Garcia-Otero
Gad Geiger
Bernard Gold
Susan L. Goldman
Kenneth W. Grant
Katherine L. Hall
Robert D. Hall

Philip R. Hemmer
Robert E. Hillman
Mark A. Hollis
Eva B. Holmberg
Caroline B. Huang
Joseph A. Jarrell
Carlos Kennedy
John D. Kierstead
Harlan Lane
Charles P. Lin
John I. Makhoul
Sharon Y. Manuel
Sumiko Miller
Victor A. Noel
Gale S. Petrich
Leonard L. Picard
James C. Preisig
Mara G. Prentiss
Christine M. Rankovic
Michael E. Ravicz
Stephen A. Raymond

Joseph F. Rizzo
John J. Rosowski
Jay T. Rubinstein
Steven R. Rueman
Christopher A. Shera
Robert T. Shin
Richard J. Solomon
Frank J. Stefanov-Wagner
David A. Steffens
Annie H. Takeuchi
Joseph Tierney
Mark A. Tramo
Michael J. Tsuk
Kenneth P. Wacks
Ehud Weinstein
Lorin F. Wilde
David R. Williams
Jane W. Wozniak
Jiqing Xia
Marc Zissman

Appendix C. Milestones

C.1 New Faculty and Staff

Dr. Anantha P. Chandrakasan joined RLE's Circuits and Devices Group in September 1994. Concurrently, he was appointed as assistant professor and to the Analog Devices Career Development Professorship in MIT's Department of Electrical Engineering and Computer Science. Professor Chandrakasan came to MIT from the University of California/Berkeley (BS '89, MS '90, PhD '94), where he recently completed postgraduate research in low-power integrated circuit design.

C.2 Promotions

Dr. Qing Hu was promoted to associate professor in the Department of Electrical Engineering and Computer Science, effective February 1995. In RLE's Optical Communications Group, Professor Hu's research has focused on the response of solid-state devices to high-frequency radiation.

C.3 Appointments

Dr. Miklos Porkolab, Professor of Physics, was appointed director of MIT's Plasma Fusion Center (PFC), effective February 1, 1995. Professor Porkolab has served as PFC's associate director for plasma research since 1991, as well as acting head of the centers Toroidal Confinement Division since 1994.

C.4 Awards and Honors

Dr. Arthur B. Baggeroer (SM/EE '65, ScD '68), Ford Professor of Engineering, was elected to the National Academy of Engineering in 1995. Professor Baggeroer was cited for his contributions in signal processing that have been applied to sonar. As a principal investigator in RLE's Digital Signal Processing Group, Professor Baggeroer uses advanced signal processing techniques to explore underwater acoustics and geophysics.

An International Symposium on the Physics of Laboratory and Space Plasmas was held at MIT in honor of **Dr. Bruno Coppi**, Professor of Physics,

on January 19 and 20, 1995. Professor Coppi is a principal investigator in RLE's Plasma Physics Group.

Dr. Jacqueline N. Hewitt (PhD '86), Class of 1948 Associate Professor of Physics, received the American Physical Society's 1995 Maria Goeppert-Mayer Award sponsored by the General Electric Foundation. The award recognizes outstanding achievements by a women physicist in the early years of her career and provides opportunities to present these achievements through public lectures. Professor Hewitt received the award at ceremonies held during the American Physical Society meeting in San Jose, California, on March 20, 1995. She is a principal investigator in RLE's Radio Astronomy Group.

Dr. Wolfgang Ketterle, Assistant Professor of Physics, was named recipient of the Michael and Philip Platzman Award by MIT's Department of Physics. Professor Ketterle, a principal investigator in RLE's Atomic, Molecular, and Optical Physics Group, was cited for his emerging leadership in the field of laser cooling and trapping of atoms at high density.

Dr. William F. Schreiber, Professor Emeritus of Electrical Engineering and Computer Science, was elected to the National Academy of Engineering in 1995. Professor Schreiber was cited for his contributions to image processing, television technology, video compression, and color graphics. He has pioneered developments in the field of image processing, electronic imaging systems, and transmission coding for over four decades.

Dr. Henry I. Smith, Joseph F. and Nancy P. Keithley Professor of Electrical Engineering, was named the recipient of the 1995 IEEE Cleto Brunetti Award for his contributions to microfabrication science and technology, notably microlithography. Professor Smith is a principal investigator in RLE's Quantum-Effect Devices Group and director of MIT's NanoStructures Laboratory. The annual Brunetti Award, which recognizes outstanding contributions in the field of miniaturization in the electronic arts, will be presented to Professor Smith during the International Electron Devices Meeting in Washington, D.C., on December 12, 1995.

Appendix D. RLE Research Support Index

- Advanced Research Projects Agency
7-22, 27-28, 35-42, 70-74, 77-83, 150-151
273, 275-283, 285-296, 300-306
- Advanced Telecommunications Research
Program 309-315
- Analog Devices, Inc. 274-275
- AT&T Bell Laboratories 27, 301-302, 310
- California Institute of Technology/Jet
Propulsion Laboratory 245-246
- Consortium for Superconducting
Electronics 70-74
- DEMACO 247
- Digital Equipment Corporation
246, 276-278
- Draper (Charles S.) Laboratory
109-113
- Electric Power Research Institute 139-142
- ENECO 139-142
- Federal Aviation Administration 247
- Federal Bureau of Investigation 274-275
- Fujitsu Laboratories 112-113
- Hertz (Fannie and John) Foundation
7-10, 12-15, 17-18, 162
- Honeywell Technology Center 119
- Houston Advanced Research Center 325-328
- IBM Corporation 85-88, 263-266, 273, 276-280
- INTEL Corporation 310
- Joint Services Electronics Program 7-10, 29-33,
35-43, 49, 53-68, 75-88, 90-105, 109-111,
114-125, 167-181, 201-219, 246
- Klatt (Dennis) Memorial Fund 333-346
- LeBel (C.J.) Foundation 333-346
- Lockheed Sanders, Inc. 300-302
- Magnetic Fusion Science Fellowship Program
232-234
- Maryland Procurement Office 143-145, 305-306,
314-315
- MIT Leaders for Manufacturing Program 256-257
- MIT Lincoln Laboratory 43-46, 111-112, 130-137,
146-147, 155-157, 246, 255
- MIT Plasma Fusion Center 187-190
- MIT Research Laboratory of Electronics
155-156
- MIT-Woods Hole Oceanographic Institution
Joint Program 300
- Motorola Corporation 12-15
- National Aeronautics and Space Administration
83-85, 99-100, 150-151, 245-246, 255-256,
263-274, 378-379
- National Center for Integrated Photonic
Technology 7-22, 36-47, 113-117, 119-120
- National Institutes of Health 125-130, 333-346,
349-362, 383-394
- National Science Foundation 7-10, 12-15,
17-18, 22-28, 40-43, 47-49, 55-66,
69-74, 104-105, 111-114, 152-157,
201-211, 229, 232-234, 251-255, 263-274,
278-283, 303-305, 333-346
- National Security Agency 10-12
- Packard (David and Lucille) Foundation
104, 252-255
- Raytheon Corporation 29-33
- Scitex America Corporation 317-319
- Semiconductor Research Corporation
75-77, 276-279
- Sloan (Alfred P.) Fellowship 215-219
- Toshiba Corporation 25
- U.S. Air Force - Electronic Systems Division
71-72, 190-192, 194-196, 198-199
- U.S. Air Force - Office of Scientific Research
71-72, 90-92, 109-111, 114-130, 145-146,
211-215, 223-229, 300-304, 306
- U.S. Air Force - Rome Laboratory 158-160
- U.S. Army - Cold Regions Research and
Engineering Laboratory 247
- U.S. Army - Harry Diamond Laboratories
223-229
- U.S. Army Research Office 25-26, 35-40, 76-77,
89, 93-95, 146-147, 158-164, 211-215
- U.S. Department of Energy 223-242
- U.S. Navy 274, 285-296
- U.S. Navy - Naval Air Systems Command
77-83, 85-88, 372-376
- U.S. Navy - Office of Naval Research 22-24,
104-105, 120-130, 196-198, 201-205, 211-219,
223-228, 245-246, 276-278, 303-308, 362-371,
376-378
- University of California/Scripps Institution
306-308

Project Staff and Subject Index

Project Staff and Subject Index

A

Abnet, C. Cameron 383, 385
 Abusch-Magder, David M. 55
 Acoustic Thermometry of Ocean Climate Program 307
 Adams, Laura E. 109
 Adams, Tracy E. 29
 Advanced Telecommunications Research Program 309—315
 Aggarwal, Rajni J. 7, 8, 9
 Ahadian, Joseph F. 7, 10, 35, 46
 Akerson, Jerome J. 245
 Al-Jalal, Abdulaziz 223
 Aldridge, Mary C. 109
 Aliberti, Giovanni 299
 Allen, Jonathan 263—266, 273, 333
 Altshuler, Boris L. 53—54
 Andreev, Anton 53
 Andrews, Michael R. 201, 215
 Annaswamy, Anuradha M. 349, 362
 Antoniadis, Dimitri A. 71, 72, 86, 90, 92, 263, 274, 285, 293
 Apostolopoulos, John G. 309, 310
 Aranyosi, Alexander J. 383, 385
 Arias, Tomas A. 171
 Ariel, Imadiel 67, 171
 Armstrong, Robert C. 263
 Array processing 306
 Ashoori, Raymond C. 103—105
 AT&T Bell Laboratories 112, 117
 Atkins, Robert G. 245, 246
 Atomic physics 201—219
 Atoms
 Evaporative cooling 215
 Magnetic trapping 215
 Structure in magnetic fields 201—208
 Au, William W. 245
 Aucoin, Richard J. 75, 99
 Auditory system 383—394
 Aviles, Walter A. 349, 372
 Avruch, Ian M. 251

B

Babiec, Walter E. 349, 360
 Bach, Susan 109
 Baggeroer, Arthur B. 299, 306, 307, 433
 Baird, Stephen V. 349, 373

Baltus, Donald G. 263
 Balzer, Janice L. 383, 384
 Bandy, James H. 349, 372
 Barrett, John W. 251, 254, 255, 256
 Barsukov, Vladimir M. 333
 Basalo, Sergio 333
 Baylon, David M. 309, 311
 Baylor College of Medicine 328
 Beauregard, Gerald L. 349, 375
 Becker-Haarsma, Deborah J. 251
 Bekefi, George 223—228
 Bergman, Keren 109, 112
 Berman, David 69, 71, 103, 104, 105
 Bers, Abraham 223, 229—237
 Bertin, Giuseppe 237
 Beucler, Margaret S. 299
 Bickley, Corine A. 333
 Bilinsky, Igor P. 109, 122
 Birgeneau, Robert J. 167—169
 Birngruber, Reginald 125
 Blackwell, William J. 251, 255
 Blastos, James C. 223
 Bock, Robert D. 69
 Boivin, Luc 109, 112
 Bombarda, Francesca 223, 237
 Bomholt, Lars H. 245, 246
 Boning, Duane S. 285, 291, 293
 Bonvik, Asbjørn M. 289
 Boppert, Stephen A. 109, 125
 Born, Susan E. 349, 373
 Bose-Einstein condensation 215
 Bouma, Brett E. 109, 120, 122, 125
 Bounds, Jeffrey K. 143
 Boyce, Suzanne E. 333
 Bradley, Michael P. 201, 208
 Brady, Felicia G. 223
 Braida, Louis D. 349—379
 Bratakos, Maroula 349, 352
 Braun, Eric K. 7, 8
 Brezinski, Mark E. 109, 125
 Brock, David L. 349, 375
 Brodsky, Mikhail G. 103, 104
 Brommer, Karl 171
 Brookhaven National Laboratory 227
 National Synchrotron Light Source 167, 177
 Brothers, L. Reginald 143, 146
 Brown, Elliot 156
 Buck, John R. 299, 300
 Buffer layers 40
 Burke, Bernard F. 251—252
 Burkhardt, Martin 72, 75, 78, 90

C

Cabrera, Carlos R. 251, 255
Cai, Xuejun 263, 274
Cain, Clarence P. 125
California Institute of Technology 12
Canizares, Claude R. 99
Capaz, Rodrigo B. 171
Cariani, Peter 383, 387
Carmel, Erika N. 349, 373
Carney, John C. 285, 289
Carpignano, Franco 223, 237
Carter, David J. 69, 72, 75, 90
Carter, James M. 75, 76, 77, 78, 83, 86, 93, 100
Cartwright, John K. 251
Case Western Reserve University 291
Catipovic, Josko 300
Catravas, Palmyra E. 223
Chafe, Susan E. 263
Chan, Ho Bun 103, 104
Chan, Kai P. 223, 229
Chandrasekaran, Anantha P. 281, 433
Chang, Hwa-Ping 333
Channel-dropping filter 43
Chaotic systems 300, 301, 303, 304
Chapman, Michael S. 201, 211
Chen, Beth L. 223
Chen, Chiping 223
Chen, Grace H. 251, 252
Chen, Jerry C. 21, 109, 113
Chen, Jyh-Shing 349, 364, 366
Chen, Marilyn Y. 333
Chenausky, Karen 333
Cheng, Howard 333
Cheung, Shiufun 309, 311
Chin, Victor E. 285
Chklovskii, Dmitri 67
Cho, Kyeongjae 171
Choi, Woo-Young 7
Chomsky, Noam A. 397—398
Chou, Michael T. 263, 276, 278
Chow, Carson C. 223, 229
Chu, Arthur 187
Chun, Leo 109
Circuit design 263—283, 285—296
Cochlear efferents 390
Cochlear implants 355, 392
Cochlear mechanisms 383—394
Compound semiconductors 35
Conklin, Anne E. 251
Conner, Samuel R. 251
Cook, John F. 1, 34, 76, 82, 148, 170, 200, 284, 316

Coppi, Bruno 223, 237—242, 433
Cordes, Linus F. 285
Corey, Brian E. 254
Cornell University
 National Nanofabrication Facility 212
Corrugated surface 49
Costa, Carol A. 201
Coulomb blockade energy 67
Courtney, Michael W. 201
Crawford, Fronefield 251
Cudjoe-Flanders, Charmaine A. 7, 35, 69
Cuomo, Kevin M. 299, 300
Cutro, Janet A. 69

D

Damask, Jay N. 35, 43, 75, 95, 109, 113
Dandekar, Kiran 349, 360, 364, 366
Darwish, Ali M. 109, 119
Daughton, William S. 223, 237
Davis, C. Quentin 383, 385
Davis, Kendall B. 201, 215
de Lange, Gerhard 149, 150
Decker, Steven J. 263, 266
del Alamo, Jesús A. 152
Delgutte, Bertrand 383, 387, 388, 389
Delhorne, Lorraine A. 349, 352, 355, 359
Delin, K.A. 70, 71
Denesvich, Gail 349, 359
Desloge, Joseph 349, 357
Detragiache, Paolo 223, 237
Devadas, Srinivas 263, 280—283
DeVries, Joel C. 201, 205
DiCarlo, Cheryl D. 125
DiFilippo, Frank 201, 208
Digital signal processing 299—308, 309—314, 317—319
 Fractals 302
Dilley, Laura C. 333
Ding, Kung Hau 245
Dix, Ann K. 349
DNA decoding 325
DNA sequencing 325
Doan, Jonathan C. 223
Doerr, Christopher R. 109, 111, 112
Donnelly, J.P. 119
Donoghue, John J. 187
Donovan, Sean M. 35, 49, 75, 100
Dougherty, David J. 109, 116, 117, 119
Doughty, Francis M. 285
Dron, Lisa G. 263
Ducas, Theodore W. 201, 205

Duchnowski, Paul 349, 352
 Durlach, Nathaniel I. 349—379
 Duwel, Amy E. 69, 73
 Dynes, Scott B.C. 383, 389

E

Ear stapedius 390
 Eddington, Donald K. 336, 349, 355, 383, 392
 Ehrlich, Daniel J. 325, 328
 Ehrlich, Michael S. 263
 Elastic cross section 215
 Electromagnetic wave theory 245—248
 Electronic devices
 Quantum heterostructures 28
 Quantum-effect devices 75—102
 Superconducting transmission lines 69—74
 Superconductors 149—164
 X-ray lithography 75—102
 Electronic materials 7—28, 35—49
 (In,Ga)(As,P) 35, 43
 (In,Ga)P 35, 40, 46
 GaAs 42, 46, 49
 II-VI 35, 42
 III-V 35, 42
 Semiconductors 29—33, 177
 Si 49
 Silicon surfaces 177
 ZnSe 35, 36, 40, 42
 ZnSe:Cl 35, 36
 ZnSe:N 35, 36
 Elfadel, Ibrahim M. 263, 266
 Ellithorpe, John D. 251, 252, 254
 Entin, Ilya 201, 215
 Ernst, Darin R. 223, 237
 Ernstmeyer, James 149, 158
 Esposito, Anna 333
 Espy-Wilson, Carol 333
 Everett, Patrick N. 75, 81
 Ewe, Hong Tat 245, 246, 247
 Extragalactic radio sources 251
 Ezekiel, Shaoul 187—199

F

Feng, Shechao 153
 Ferrera, Juan 75, 76, 78, 83, 86, 93, 95, 113
 Fiberoptics 109, 144, 187
 Field-effect transistors 29—33
 InGaAs 29
 InP 29

Fischer, Gregory T. 285, 290, 291
 Fisher, Philip A. 35, 36, 40
 Fleischer, Dorothy A. 263
 Fleischer, Siegfried B. 109, 119
 Fleming, Robert C. 75, 83, 99
 Fletcher, Andre 251
 Fleury, Marc 109, 130, 134, 136
 Folch, Albert 103, 105
 Fonstad, Clifton G., Jr. 7—28, 46, 93, 160
 Foxlin, Eric M. 349, 378
 Free-electron lasers 223
 Freeman, Dennis M. 383, 385
 Freidberg, Jeffrey P. 240
 Frisbie, Joseph A. 349
 Frishkopf, Lawrence S. 383
 Fuchs, Vladimir 223, 229
 Fujimoto, James G. 109, 113, 120—130
 Fung, Irene 143, 145
 Fusion reactors 237

G

Gabbay, Lynn D. 285, 293
 Gajaweeda, Ashanthi 349, 359
 Gale, Donna L. 109
 Gavrilovich, Paul 7
 Gellerman, W. 115
 Genetic analysis 325—328
 Geng, Helena 333
 Genosensor technology 325—328
 Geoffroy, Brett A. 333
 Geophysics 306
 Geraci, James R. 35, 36
 Gershwin, Stanley B. 285, 286
 Gold, Bernard 299, 305
 Goldhaber-Gordon, David J. 55
 Goldhor, Richard S. 333
 Goldman, Susan L. 349, 352
 Golubovic, Boris 109, 122
 Goodberlet, James G. 109, 130, 134, 136
 Gravitational lenses 251, 252
 Greenberg, Julie E. 349, 357
 Greer, Donald R. 143
 Grimson, W. Eric L. 145
 Grot, A.C. 12
 Groves, S.H. 119
 GSMBE 36, 43
 Guinan, John J., Jr. 383, 390
 Guiod, Peter C. 333
 Gulati, Rogeve J. 349, 360, 364
 Gung, Tza Jing 245, 247
 Gupta, Nitin 75, 89

Gupta, Rakesh 349, 372
Gyroscopes
 Laser 187, 199

H

Hadjicostis, Christoforos N. 299, 301
Hadjiyannis, George I. 263, 280
Hagelstein, Peter L. 109, 130—142
Hall, Dorrie 349, 372
Hall, Seth M. 333, 349
Halle, Morris 333, 397—398
Hammond, Troy D. 201, 211
Hands 366, 371
 Fingertips 360
Hanson, Helen 333
Haptics 360—376
Hardy, John 333
Harker, Marnie L. 333
Harring, Debra L. 167
Harvard University 252
 Smithsonian Center for Astrophysics 253
Haus, Hermann A. 19, 21, 43, 95, 109—120
Hay, Todd A. 223
Head-tracking technology 378
Heard Island Feasibility Test 307
Hearing 349—360, 383—394
 Binaural 357
Hearing aids 349—360
Hearing-impaired individuals 349—360
Hector, Scott D. 75, 77, 78
Hee, Michael R. 109, 125
Heemeyer, Sven 103, 105
Held, Richard M. 349, 373
Hemmer, Philip R. 187
Herold-Jacobson, Lori K. 251
Herrmann, Frederick P. 263, 266
Heteroepitaxy 35, 40, 42, 49
Heterointerfaces 42
Heterostructures 29
Hewitt, Jacqueline N. 251, 252—255, 433
High-definition television 309—314, 317—319
Hijirida, David H. 223
Hillman, Robert E. 333, 339
Hinds, Raynard O. 309
Hinz, Philip M. 201, 215
Hirahara, Tatsuya 388
Ho, Easen 35, 36, 40
Holley, Jeffrey R. 201, 205
Hollis, Mark A. 325—328
Holmberg, Eva B. 333
Horn, Berthold K.P. 263, 266

Horowitz, David M. 333
Horowitz, Paul 252
Hoshino, Isako 7
House, Jody L. 35, 36, 40, 42
Houston Advanced Research Center 325
Howe, Robert D. 366
Hsu, Chih-Chien 245, 246, 247
Hu, Hang 75
Hu, Kan 35
Hu, Qing 25, 149—164, 433
Hu, Wen 223
Huang, Caroline 333
Huang, Everest W. 215
Huang, Gregory T. 245, 246, 383
Hugunin, James J. 69, 71, 75, 92
Hultgren, Charles T. 109, 116
Human/machine interfaces 373, 376, 378

I

Ignitor-Ult experiment 237
III-V lasers 46
Iisuka, Norio 7, 25
Image processing 266, 299—308, 309—314,
 317—319
Induced stochasticity and chaos 229
Integrated circuits
 Alignment and consistency 263
 Computer-aided design 263—283, 285—296
 Device simulation 273, 274
 Low-power embedded system 280
 Manufacturing processes 266, 285—296
 VLSI 7—49
 VLSI computer-aided design 263—283
Integration 49
Interferometry
 Atom wave 211
Ions
 Mass spectrometry 208
Ippen, Erich P. 42, 109—120, 122
Isabelle, Steven H. 299, 301
Ismail, Khalid 100
Iwai, Kyle K. 309, 312
Izatt, Joseph A. 109, 120, 125

J

Jachner, Jacek 299
Jackson, Keith 86
Jacobs, Jarvis B. 285, 293
Jacobson, Brian R. 149, 150

Jandura, Louise 349, 366
 Jesús A. del Alamo 29—33
 Jiao, Hong 201
 Joannopoulos, John D. 47, 113, 171—176
 Johnson, Joel T. 245, 246
 Johnson, Mark A. 333
 Joneckis, Lance G. 143
 Jones, David J. 109, 111
 Jones, Gabrielle 349, 352
 Jones, Lynette A. 349, 375
 Jordan, Arthur K. 245
 Jung, Hae-Mook 309

K

Kalluri, Sridhar 383
 Kamon, Mattan 263, 274, 276
 Kanamaru, Yasunori 245
 Kanie, Hisashi 35
 Kao, James T. 285, 288
 Karason, Steingrimur P. 349, 362, 366
 Karu, Zohar Z. 383, 385
 Kastner, Marc A. 55—66
 Katz, Charles A. 251, 252, 254
 Katz, Daniel 187
 Kaushik, Sumanth 109, 130, 134, 139
 Keller, Ursula 120
 Kesner, Jay 240
 Ketterle, Wolfgang 201, 215—219, 433
 Keyser, Samuel J. 333
 Khan, Mohammed J. 109, 113
 Khatri, Farzana I. 109, 112, 114
 Kiang, Nelson Y.S. 383
 Kierstead, John D. 187
 Klatsky, Lauren B. 251, 254
 Klein, Olivier 55
 Kleinsasser, A.W. 72
 Kleppner, Daniel 201—208
 Kochanek, Christopher S. 252
 Kohichi R., Tamura 109
 Koita, Rizwan R. 251, 256
 Kolodziejksi, Leslie A. 10, 35—49, 100, 113
 Kong, Jin Au 245—248
 Kopf, Cynthia Y. 109
 Korsmeyer, F. Thomas 278
 Krause, Jean C. 349
 Kuan, Jenn-Huei 245, 247
 Kumar, Arvind 69, 72, 75
 Kuo, Hong-Kwan J. 333
 Kwon, Jimmy Y. 285, 288

L

Lai, Bobby Y. 143, 146
 Lai, Kit-Wah F. 245
 Lam, Warren M. 299, 302
 LaMotte, Robert H. 362, 366
 Lane, Harlan 333, 336
 Laser cooling 215
 Lasers 7—28, 109—142
 Fiberoptic 109, 187—199
 Free-electron 223
 Medicine 125
 Semiconductor 19
 Le, H.Q. 119
 LeBlanc, Cindy 309
 Lee, Dicky 143, 146
 Lee, Hae-Seung 263, 266
 Lee, Jeng-Feng 349, 372, 376
 Lee, Laurence H. 69, 70
 Lee, Patrick A. 67—68
 Lee, William 245, 247
 Leeb, Steven B. 263, 278
 Lemay, Danielle G. 349, 352
 Lenef, Alan L. 201, 211
 Lenz, Gadi 109, 114, 115, 116, 119
 Li, Huiying 75, 78
 Li, Kevin 245, 246
 Liao, Stan Y. 263, 280
 Lim, Jae S. 309—315
 Lim, Kuo-Yi 35, 47
 Lin, Charles P. 109, 125
 Linden, Derek S. 69
 Linguistics 397—398
 Litovsky, Ruth Y. 388
 Little, Brent E. 109
 Liu, Sharlene A. 333
 Locke, John 333
 Lohman, Thomas J. 285, 291
 Long, Christopher J. 383, 392
 Lorusso, Catherine 223, 237
 Lossos, David C. 349, 373
 Love, Nicole S. 285, 286
 Lu, Henry 333
 Lu, Kan 40
 Ludwig, Jeffrey T. 299, 302
 Lum, David S. 349
 Lumsdaine, Andrew 263, 273
 Luongo, Eleanora M. 349
 Lutwak, Robert I. 201, 205
 Lyons, W.G. 70
 Lysczarz, Theodore M. 55
 Lyubomirsky, Ilya 149, 162

M

Makhoul, John I. 333
Mallin, Rebecca 333
Mankiewich, P. 55
Mann, John P. 299, 307
Manning, Deborah S. 317
Manolatou, Christina 245, 246
Manuel, Sharon 333
Manufacturing processes 256
Manzella, Joyce 333
Marley, Elisabeth A. 35, 43
Martin, David R. 263, 266
Martin, Paul S. 7, 17, 18, 19, 21, 22
Masaki, Ichiro 263, 266
Mason, Elliot J. 143
Massachusetts Eye and Ear Infirmary 340, 383
Massachusetts General Hospital 126
Massey, Noel 333
Massoud, Yehia M. 263, 276
Mastovsky, Ivan 223
Matthies, Melanie L. 333
Matveev, Konstantin 67
Max Planck Institute 100
McDonald, Robert G. 263
McIlrath, Michael B. 285, 291, 293
McKinney, Martin F. 383, 387
McQuirk, Ignacio S. 263, 266
Medical lasers 125
Meehan, Kathy 7
Melloch, Michael R. 90, 152, 156, 158, 162
Mervis, Juliet 187
Messier, Mark D. 251, 252
Metson, Ralph 340
Mewes, Marc-O. 201, 215
Microwaves
 Remote sensing 255
Middle ear 383—394
Migliuolo, Stefano 223, 237
Mikkelsen, J.M. 8
Minkoff, Seth Aaron 397
MIT Artificial Intelligence Laboratory 145, 367
MIT Haystack Observatory 254
MIT Laboratory for Information and Decision
 Systems 145
MIT Lincoln Laboratory 10, 111, 112, 119, 123,
 126, 145, 149, 291, 299
MIT Microsystems Technology Laboratories 291
MIT-Woods Hole Oceanographic Institution Joint
 Program 299
Mitchell, Clay T. 333
Mochrie, Simon G.J. 167, 177—181
Molinaar, Rachel 333

Mollenauer, Linn 112
Mondol, Mark K. 75, 78
Monta, Peter A. 309, 312
Monteiro, José C. 263, 280
Moolji, Akbar A. 75
Moon, Euclid E. 75, 77, 81
Moore, Christopher B. 251, 252, 254
Moores, John D. 109, 111, 112, 114
Morgan, Nicole Y. 55
Morgenbesser, Hugh B. 349, 375
Morshidi, Wan Y. 201, 215
Moyné, William P. 285, 286
Mucciolo, Eduardo R. 53
Muendel, Martin H. 109, 130, 134, 136
Murguia, James E. 285
Murphy, Edward 75, 78
Murphy, Thomas E. 75
Murray, Cade 7
Music
 Mathematical models 305
Musicus, Bruce R. 299

N

Nabors, Keith S. 263, 276
Nadeau, Philip M. 349, 352
Nadol, Joseph 336
Namiki, Shu 109
Narayan, Ramesh 252
Nastov, Ognen J. 263, 278
National Radio Astronomy Observatory
 Very Large Array 251, 252
 Very Long Baseline Array 251, 252
Nawab, S. Hamid 299, 302
Nee, Phillip T. 143
Nelson, Lynn E. 109
Nguyen, Katerina 333
Nicolas, Julien J. 309, 313
Noise
 Active noise cancellation 303, 306
Nonlinear optics 143
Nonlinear waves in plasmas 229
Noojin, Gary D. 125
North, D. Keith 333
Noshino, Isako 27
NTT Basic Research Laboratory 388

O

O'Connell, Michael P. 349, 357
O'Neill, Kevin 245, 247

Oates, John H. 245, 246
 Oberoi, Pankaj 383
 Oceanography
 Signal processing 306
 Odoardi, Angela R. 7, 35, 69
 Ohkawa, Hana 223
 Oja, Erkki 263, 266
 Ooi, James M. 299, 303
 Oppenheim, Alan V. 299—308
 Optical communication 143—147
 Devices 7—28
 Optics 109—142
 Femtosecond 120
 Nonlinear 143
 Opto-electronics 109—142, 146
 Integrated circuits 46
 Orlando, Terry P. 69—74, 90, 92, 263, 275
 Osgood, Gene T. 263
 Ouellette, Edward J. 263, 280
 Owen, Gabrielle M. 75, 77, 78

P

Palmer, Fred L. 201, 208
 Pan, Janet L. 7, 22, 25
 Pant, Amrit R. 201, 211
 Papadopoulos, Haralabos C. 299, 303
 Parkes-MIT-NRAO Survey 251
 Passive waveguides 43
 Patterson, Steven G. 143
 Peake, William T. 383, 384
 Peng, Lung-Han 7, 24, 25
 Penn, Gregory E. 223, 237
 Peregrym, Denis J. 299, 307
 Perkell, Joseph S. 333
 Perreault, Brian M. 299, 303
 Petrich, Gale S. 10, 35—49
 Pfajfer, Alexander 309, 313
 Pfautz, Jonathan 349, 372
 Phase transitions 167
 Phillips, Joel R. 69, 263, 275, 276
 Photonic bandgap 47
 Photonic devices 43
 Pierre, Darren M. 223, 237
 Pind, Jorgen 333
 Pioch, Nicholas 349, 372
 Plant, Geoffrey L. 349, 359
 Plasma physics 223—242
 Nonlinear waves in plasmas 229
 Relativistic electron beams 223
 RF Heating and Current Drive 229
 Thermonuclear plasmas 237

Polley, Michael O. 317
 Poort, Kelly L. 333
 Porkolab, Miklos 433
 Porter, Jeanne M. 75, 100
 Portnoy, Vladislav 223
 Power, Matthew 349
 Prasad, Sheila 7, 26
 Preisig, James C. 299
 Prentiss, Mara G. 187
 Pritchard, David E. 201, 208—215
 Process flow representation 285—296
 Psaltis, Demetri 12
 Puria, Sunil 383, 384

Q

Quantum heterostructures 7
 Quantum studies 55, 67, 72, 103—105
 Chaos 53
 Heterostructures 7—28
 Optics 109—142, 143
 Statistics 53

R

Rabinowitz, William M. 349, 355, 357, 359, 383, 392
 Radar
 Laser 145
 Radio astronomy 251—257
 Radio transients 254
 Rahman, Arifur 149, 150
 Rahman, Nadir E. 285, 293
 Rahmat, Khalid 274
 Ram, Abhay K. 223, 229
 Ramaswamy-Paye, Malini 109, 113, 120, 122
 Ramos, Jesus 240
 Ramstad, Monte J. 167
 Rana, Farhan 149
 Rankovic, Christine M. 349
 Rathman, Dennis D. 325, 328
 Ravicz, Michael E. 383, 384
 Rawizza, Mark A. 251, 256
 Receveur, Roger A.M. 69, 72
 Rediker, Robert H. 143
 Reed, Charlotte M. 349, 352, 359
 Reed, Eric C. 309, 313
 Reichelt, Mark W. 263, 266, 273
 Reif, L. Rafael 47
 Reiner, James W. 29
 Relativistic electron beams 223

Project Staff and Subject Index

- Remote sensing 245, 255
Ricci, Kenneth N. 223
Richard, Michael D. 299, 304
Riconda, Caterina 223, 237
Rider, Todd H. 223, 237
Roach, W.P. 125
Robots 366, 367, 368
Roby, Frederick L. 349, 364
Rodriguez-Perez, Tomas 349, 364
Rogers, Alan E.E. 254
Rooks, Michael J. 152
Rosenkranz, Philip W. 251, 255, 256
Rosenthal, Michael 7
Rosowski, John J. 383, 384
Rossetti, Denise M. 309
Royter, Yakov 7, 15
Rubenstein, Richard A. 201, 211
Rubinstein, Jay T. 383, 392
Rusinkiewicz, Szymon M. 201, 208
Russell, Jeffrey 120
- S**
- Sachtler, Wendelin L. 349, 373
Salcedo, Ante 245
Salihu, Suraj D. 223, 237
Salisbury, J. Kenneth 349, 366, 375
Santiago, Sally C. 299
Santos, Jonathan R. 349, 359
Saust-Rossi, Ann B. 251, 252
Savas, Timothy A. 75, 83, 100, 109, 130, 134
Schäpers, Thomas 149, 155
Schattenburg, Mark L. 75, 77, 78, 83, 99, 100
Scherock, Stephen F. 299, 305
Schild, R. 253
Schmidt, Martin A. 263, 274
Schmiedmayer, H. Jörg 201, 211
Schreiber, William F. 317—319, 433
Schultz, Steven D. 223, 229
Schwartz, Michael J. 251, 255, 256
Scire-Scappuzzo, Francesca 245
Seidel, Mark N. 263, 266
Sematech Corporation 293
Semiconductor Research Corporation 294
Semiconductors 103—105, 116
 Compound 29—33
 Fabrication 291
 II-VI 36, 40
 III-V 40
 Single-electron transistors 55
Sensorimotor satellite 373
Sensory aids 355, 392
Sensory communication 349—379
Senturia, Stephen D. 263, 274
Sever, Laura M. 333
Sexton, Matthew 349, 352
Shah, Devang M. 383, 385
Shah, Satyen 75, 83, 100
Shahriar, Selim M. 187
Shakeel, Asif 143
Shapiro, Jeffrey H. 143—147
Shattuck-Hufnagel, Stefanie 333
Shatz, Lisa F. 383, 385
Shaver, David C. 55
Shenoy, Krishna V. 7, 8, 10, 12, 13, 17, 46
Shera, Christopher A. 383, 390
Shih, Shih-En 245
Shin, Robert T. 245, 246
Shinn-Cunningham, Barbara G. 349, 373
Shirasaki, Matasaka 109, 112
Shu, Li 299
Shvets, Gennady 223
Siebert, William M. 383
Sierra, Raymond 120
Signal processing 7, 299—308, 353, 355, 392
 Chaotic systems 300, 301, 303, 304
 Mathematical models 305
 Noise 303, 306
 Speech 305
Silveira, Luis M. 263, 266, 278
Silverman, Scott E. 75, 76, 85, 86
Simons, Benjamin D. 53
Singer, Andrew C. 299, 305
Sisson, David 223
Sisson, Robert D. 75
Smet, Jurgen H. 7, 25, 149, 158, 160
Smith, Brian M. 75
Smith, Edward T. 201, 211
Smith, Grant 245, 247
Smith, Henry I. 43, 49, 71, 72, 75—102, 113, 433
Smith, Stephen P. 187
Sodini, Charles G. 263, 266
Sokolinski, Ilia 103
Somerville, Mark H. 29
Sonar 306, 376
Song, Seungheon 177
Souyris, Jean-Claude 245
Speech communication 333—346, 359
Speech processing 314
Speech recognition 305
Speechreading 352—355, 359
Spellmeyer, Neal 201
Spina, Michelle S. 251, 255, 256
Srikantiah, Ranjini 349
Srinivasan, Mandayam A. 349, 359, 360—371, 375

Staelin, David H. 251, 255—257
 Stamatopoulos, Miltiadis A. 285, 286
 Stankovic, Konstantina 383, 390
 Stanton, Christopher 122
 Steffens, David A. 383, 384
 Stevens, Kenneth N. 333—346
 Stoner, Richard E. 223
 Strogatz, Steven H. 72
 Stroock, Abraham D. 201
 Submarines 372
 Navigation systems 376
 Sugiyama, Linda E. 223, 237
 Sun, Chi-Kuang 109, 122
 Sunshine, Lon E. 309, 314
 Superconducting devices 69—74, 149—164
 Superconducting tokamak magnets 187, 188
 Surface studies 167—169
 Semiconductors 171—176, 177—181
 Svilan, Vjekoslav 69
 Svirsky, Mario A. 333
 Svolos, George M. 223, 237
 Swanson, Eric A. 119, 125

T

Tactile communication 359
 Takeuchi, Anne H. 349
 Talavage, Thomas M. 383
 Tamura, Kohichi R. 109, 115
 Tan, Chin Hwee 263
 Tan, Hong Z. 349, 359, 375
 Tang, Xiaofeng 35, 47
 Taniguchi, Carl 309, 314
 Taniguchi, Nobuhiko 53
 Tankuranun, Prathet 245, 246
 Tannian, Bridget E. 201, 211
 Tassoudji, M. Ali 245, 246, 247
 Tearney, Guillermo J. 109, 125
 Telecommunications 309—315
 Television research
 High-definition 309—314, 317—319
 Teoh, Su W. 383
 Thermonuclear plasmas 237
 Thompson, Carl V. 49, 100
 Thompson, Stanley H. 201, 215
 Tierney, Joseph 383, 392
 Toth, Cynthia A. 125
 Touch 360—371, 376
 Towles, Joseph D. 349, 364
 Trías, Enrique 69
 Troutman, Sarah 53
 Troxel, Donald E. 285—296

Tsai, Wei-Tien 398
 Tsang, Leung 245
 Tso, Kit Yan 285, 293
 Tsuk, Michael 245, 246
 Tufts University School of Medicine 126
 Turk, Alice 333
 Tuyo, Mabayoje 349, 352
 Tziligakis, Constantine 109

U

Ullschmied, Jiri 223
 Ulman, Morrison 109, 122
 Umminger, Christopher B. 263, 266
 Underwater acoustics 306
 University of Utah 115
 Unver, Evren R. 285, 291

V

Vacca, Luigi 223, 229
 van der Zant, Herre S.J. 69, 70, 71, 72, 73, 263, 275
 Verbout, Shawn M. 299, 305
 Vergheese, George C. 301
 Vergheese, Simon 149, 155, 156
 Very Large Array 251, 252
 Very Long Baseline Array 251, 252
 Vestibular system 390
 Veysoglu, Murat E. 245, 246
 Virtual environment technology 372—379
 Virtual workbench 373
 Visible emitters 36
 Vision chip designs 266
 VLSI computer-aided design 263—283
 VLSI systems
 Machine vision 266
 Volkbeyn, Pavel S. 223
 von Bosau, Laura 223
 Voss, Susan E. 383

W

Wage, Kathleen E. 299, 307
 Wang, Hao 7, 17, 22
 Wang, Li-Fang 245, 247
 Watanabe, Shinya 72
 Wave propagation 306
 Waveguides 47
 Weber, Lukasz A. 349, 373

Project Staff and Subject Index

Wee, Susie J. 317
Weinberg, Michael J. 29, 75
Weiner, Miriam 223, 237
Weinstein, Ehud 299
Weiss, Thomas F. 383, 385
Welker, Daniel P. 349, 357
Wellman Laboratories of Photomedicine 126
Wells, Barry 167
White, Jacob K. 69, 70, 263, 266, 273—279
Wiegand, Thomas E.v. 349, 373
Wies, Evan F. 349, 373
Wilde, Lorin F. 333
Wilhelms-Tricarico, Reiner 333
Williams, David R. 333
Willsky, Alan S. 145
Wind, Shalom 55
Wint, Arlene E. 333
Wong, Ngai C. 143, 146
Wong, Vincent V. 75, 76, 77, 78, 86, 93, 95, 113
Wong, William S. 109, 111, 112
Woods Hole Oceanographic Institution 299
Wornell, Gregory W. 299, 301, 302, 303
Wozniak, Jane W. 333
Wurtele, Jonathan S. 223
Wuu, John J. 201, 215
Wyatt, John L., Jr. 263, 266—273
Wyss, Rolf A. 149, 152, 155

Z

Zamdmmer, Noah D. 149, 156
Zangi, Kambiz C. 299, 306
Zeltzer, David 349, 372, 376
Zhang, Yan 245, 247
Zhou, William W. 245, 247
Zilles, Craig B. 349, 375
Zissman, Marc A. 383, 392
Zurek, Patrick M. 349, 357

X

Xia, Jiqing 245, 246
Xu, Bin 149, 158
Xu, Yi 333

Y

Yakubo, Kou 153
Yan, Jun 245
Yang, Isabel Y. 75, 77, 78, 86
Yang, Y. Eric 245, 246, 247
Yasaka, Anto 75, 85
Yeang, Chen-Pang 245, 247
Yesley, Peter S. 201, 215
Yie, He 263, 274
Yoo, Chang Dong 309, 314
Yoon, Mirang 177
Young, Michael J. 167
Yu, Charles 109
Yu, Paul C. 263, 266